# Radio Environment Maps, and Machine Learning Techniques for Spectral and Energy Efficiency Improvement of Wireless Communications, with Emphasis on Massive MIMO Systems.

Doctoral Dissertation


**Author**: mgr inż. Marcin Hoffmann
**Supervisor**: dr hab. inż. Paweł Kryszkiewicz, Prof. PUT

Poznań University of Technology
Faculty of Computing and Telecommunications
Institute of Radiocommunications

September 22, 2025

# Abstract

The evolution of mobile networks towards 5G and 6G introduces unprecedented challenges in simultaneously meeting diverse Quality of Service (QoS) requirements across enhanced Mobile Broadband (eMBB), Ultra-Reliable Low Latency Communications (URLLC), and massive Machine-Type Communications (mMTC). Central to this complexity are Massive Multiple-Input Multiple-Output (MMIMO) systems and their extensions, such as User-Centric Cell-Free (UCCF) MMIMO, which provide substantial spectral efficiency (SE) gains but demand significant hardware and computational resources, increasing the energy consumption. In this context, improving both SE and Energy Efficiency (EE) emerges as a critical research challenge.

This dissertation proposes the utilization of Radio Environment Maps (REMs) and Machine Learning (ML) techniques to enhance SE and EE in 5G and 6G networks. REMs, originally conceived for dynamic spectrum management within Cognitive Radio, are extended by the PhD candidate to store multidimensional location-dependent data, such as interference distributions, mobility patterns, or QoS metrics. The PhD candidate makes REM actionable through ML, including Reinforcement Learning (RL) and Federated Learning (FL), and demonstrates data-driven optimization strategies for wireless networks, overcoming the limitations of purely analytical approaches.

The research hypothesis of the dissertation is formulated as follows: **The usage of information stored in Radio Environment Maps can improve spectral and energy efficiency of wireless networks, especially those using massive MIMO, by utilizing machine learning.**

The PhD candidate confirmed the research hypothesis by demonstrating in the dissertation his contributions based on 16 peer-reviewed publications in the top journals and presented at renowned conferences. The contributions span three representative use cases. For V2X communications (URLLC), the PhD candidate proposed novel models of localization error, interference-aware frequency assignment, and beam management algorithms. In the MMIMO domain (eMBB), the PhD candidate designed REM-enhanced ML solutions for intelligent cell and antenna activation, dynamic optimization of power amplifier operation point, interference coordination, and management of UCCF MMIMO network, achieving substantial SE and EE gains validated using the realistic simulator of MMIMO network based on 3D ray-tracing radio channel models. For IoT (mMTC), the PhD candidate's work addresses vulnerabilities to Denial-of-Service attacks through a Signaling Storm Detection algorithm, validated in both simulations and a real-world 5G testbed.

# Streszczenie

Rozwój sieci 5G i 6G stawia nowe wyzwania związane z potrzebą jednoczesnego spełniania wymagań rożnych klas ruchu tzn. usług szerokopasmowych (ang. enhanced Mobile Broadband), dostępu ultra-niezawodnego o niskim opóźnieniu (ang. Ultra-Reliable Low Latency Communications), oraz masowej komunikacji między maszynami (ang. massive Machine-Type Communications). Dodatkowo, kluczowym elementem sieci 5G i 6G jest zastosowanie systemów wieloantenowych MMIMO (ang. Massive Multiple-Input Multiple-Output), które zapewniają poprawę efektywności widmowej, kosztem zużycia znacznych zasobów sprzętowych oraz energetycznych. W tym kontekście, zwiększenie zarówno efektywności widmowej, jak i energetycznej staje się kluczowym wyzwaniem badawczym dla nowoczesnych sieci mobilnych.

Niniejsza rozprawa doktorska proponuje wykorzystanie Map Środowiska Radiowego REM (ang. Radio Environment Maps) oraz uczenia maszynowego ML (ang. Machine Learning) do zwiększenia efektywności widmowej i energetycznej w sieciach 5G i 6G. REM'y, które pierwotnie wykorzystywano do dynamicznego zarządzania widmem, zostały rozszerzone przez doktoranta tak, aby przechowywały wielowymiarowe dane geolokalizacyjne, np. rozkłady interferencji. Dane zgromadzone w REM mogą być efektywnie wykorzystane dzięki technikom ML, w tym tzw. uczeniu ze wzmocnieniem oraz uczeniu federacyjnemu do optymalizacji sieci 5G/6G. Pozwala to przezwyciężyć ograniczenia metod analitycznych.

Hipoteza badawcza rozprawy brzmi: **Wykorzystanie informacji przechowywanych w REM'ach oraz metod ML, może poprawić efektywność widmową i energetyczną sieci bezprzewodowych, zwłaszcza tych wykorzystujących technikę MMIMO.**

Doktorant potwierdził hipotezę badawczą, prezentując w rozprawie swoje osiągnięcia oparte na cyklu 16 publikacji w najbardziej uznanych międzynarodowych czasopismach naukowych i materiałach konferencyjnych. W zakresie komunikacji między pojazdami doktorant zaproponował nowe modele błędu lokalizacji, algorytmy przypisywania częstotliwości dla konwoju pojazdów, oraz zarządzanie wiązkami. W domenie MMIMO doktorant opracował rozwiązania wykorzystujące REM i ML do inteligentnej aktywacji komórek i anten, optymalizacji punktu pracy wzmacniacza mocy, koordynacji interferencji oraz zarządzania siecią MMIMO zorientowaną na użytkownika, uzyskując poprawę efektywności widmowej i energetycznej, potwierdzoną za pomocą symulatora sieci MMIMO opartego na modelu kanału radiowego z śledzeniem promieni. W przypadku sieci IoT (ang. Internet of Things) doktorant zaproponował metodę wykrywania i przeciwdziałania atakom typu Denial-of-Service. Zaproponowane rozwiązanie zostało zweryfikowane poprzez symulacje, jak i w laboratoryjnej sieci 5G.

# Publication List

The dissertation is based on the following sixteen original publications (ordered based on Ministry points):

[P1] M. Hoffmann, S. Janji, A. Samorzewski, L. Kułacz, C. Adamczyk, M. Dryjański, P. Kryszkiewicz, A. Kliks, and H. Bogucka, "Open RAN xApps Design and Evaluation: Lessons Learnt and Identified Challenges," *IEEE Journal on Selected Areas in Communications*, vol. 42, no. 2, pp. 473–486, 2024.

MNiSW Points[1]: 200

Number of citations[2]:

- according to Web of Science: 13
- according to Google Scholar: 38

[P2] H. Bogucka, M. Hoffmann, P. Kryszkiewicz and L. Kulacz, "An Open-RAN Testbed for Detecting and Mitigating Radio-Access Anomalies," in *IEEE Communications Magazine*, early access, 2025.

MNiSW Points: 200

[P3] M. Hoffmann and P. Kryszkiewicz, "Signaling Storm Detection in IIoT Network based on the Open RAN Architecture," in *IEEE INFOCOM 2023 - IEEE Conference on Computer Communications Workshops (INFOCOM WKSHPS)*, pp. 1–2, 2023.

MNiSW Points: 200

Number of citations:

- according to Web of Science: 6
- according to Google Scholar: 28

[P4] M. Hoffmann and P. Kryszkiewicz, "O-RAN for Energy-Efficient Serving Cluster Formulation in User-Centric Cell-Free MMIMO," in *IEEE INFOCOM 2024 - IEEE Conference on Computer Communications Workshops (INFOCOM WKSHPS)*, pp. 1–2, 2024.

MNiSW Points: 200

Number of citations:

- according to Web of Science: 1

[1]Points assigned by the Polish Ministry of Science and Higher Education accoridng to information in `https://sin.put.poznan.pl/people/details/marcin.hoffmann`

[2]as on September 3, 2025

- according to Google Scholar: 1

[P5] M. Hoffmann, P. Kryszkiewicz, and A. Kliks, "Frequency selection for platoon communications in secondary spectrum using radio environment maps," *IEEE Transactions on Intelligent Transportation Systems*, vol. 23, no. 3, pp. 2637–2650, 2022.

MNiSW Points: 140

Number of citations:

- according to Web of Science: 9
- according to Google Scholar: 12

[P6] M. Hoffmann, P. Kryszkiewicz, and A. Kliks, "Increasing energy efficiency of massive-MIMO network via base stations switching using reinforcement learning and radio environment maps," *Computer Communications*, vol. 169, pp. 232–242, 2021.

MNiSW Points: 140

Number of citations:

- according to Web of Science: 20
- according to Google Scholar: 33

[P7] M. Hoffmann, A. Kliks, P. Kryszkiewicz, and G. P. Koudouridis, "A Reinforcement Learning Approach for Base Station On/Off Switching in Heterogeneous M-MIMO Networks," in *2020 IEEE 21st International Symposium on "A World of Wireless, Mobile and Multimedia Networks" (WoWMoM)*, pp. 170–172, 2020.

MNiSW Points: 140

Number of citations:

- according to Web of Science: 6
- according to Google Scholar: 7

[P8] M. Hoffmann and P. Kryszkiewicz, "Similarity Measures for Location- Dependent MMIMO, 5G Base Stations On/Off Switching Using Radio Environment Map," in *2021 IEEE 22nd International Symposium on a World of Wireless, Mobile and Multimedia Networks (WoWMoM)*, pp. 286–291, 2021.

MNiSW Points: 140

[P9] M. Hoffmann and P. Kryszkiewicz, "Reinforcement Learning for Energy-Efficient 5G Massive MIMO: Intelligent Antenna Switching," *IEEE Access*, vol. 9, pp. 130329–130339, 2021.

MNiSW Points: 100

Number of citations:

- according to Web of Science: 13
- according to Google Scholar: 26

[P10] M. Hoffmann and P. Kryszkiewicz, "Contextual Bandit-Based Amplifier IBO Optimization in Massive MIMO Network," *IEEE Access*, vol. 11, pp. 127035–127042, 2023.

MNiSW Points: 100

Number of citations:

- according to Web of Science: 1
- according to Google Scholar: 1

[P11] M. Hoffmann and M. Dryjański, "Energy Efficiency in Open RAN: RF Channel Reconfiguration Use Case," *IEEE Access*, vol. 12, pp. 118493–118501, 2024.

MNiSW Points: 100

Number of citations:

- according to Web of Science: 1
- according to Google Scholar: 5

[P12] M. Hoffmann and P. Kryszkiewicz, "Evaluation of User-Centric Cell-Free Massive Multiple-Input Multiple-Output Networks Considering Realistic Channels and Frontend Nonlinear Distortion," *Applied Sciences*, vol. 14, no. 5, p. 1684, 2024.

MNiSW Points: 100

Number of citations:

- according to Web of Science: 2
- according to Google Scholar: 7

[P13] M. Hoffmann and P. Kryszkiewicz, "Beam Management Driven by Radio Environment Maps in O-RAN Architecture," in *2023 IEEE International Conference on Communications Workshops (ICC Workshops)*, pp. 54–59, 2023.

MNiSW Points: 70

Number of citations:

- according to Web of Science: 4
- according to Google Scholar: 13

[P14] M. Hoffmann, P. Kryszkiewicz, and G. P. Koudouridis, "Modeling of real time kinematics localization error for use in 5G networks," *EURASIP Journal on Wireless Communications and Networking*, vol. 2020, no. 1, p. 31, 2020.

MNiSW Points: 70

Number of citations:

- according to Web of Science: 8
- according to Google Scholar: 15

[P15] M. Hoffmann, P. Kryszkiewicz, and A. Kliks, "Federated learning-based interference modeling for vehicular dynamic spectrum access," in *International Conference on Mobile and Ubiquitous Systems: Computing, Networking, and Services*, pp. 431–454, Springer, 2022.

MNiSW Points: 70

[P16] M. Hoffmann and P. Kryszkiewicz, "Radio Environment Map and Deep Q-Learning for 5G Dynamic Point Blanking," in *2022 International Conference on Software, Telecommunications and Computer Networks (SoftCOM)*, pp. 1–3, 2022.

MNiSW Points: 70

Number of citations:

- according to Web of Science: –
- according to Google Scholar: 4

# Contents

# List of acronyms

**3GPP** Third Generation Partnership Project

**ANOVA** ANalysis Of VAriance

**AP** Access Point

**API** Application Programming Interface

**BMM-xApp** Beam Mobility Management xApp

**BS** Base Station

**C-V2X** Cellular Vehicle to Everything

**CN** Core Network

**COBBIO** Contextual Bandit-Based IBO Optimization

**CoMP** Coordinated Multi-Point

**CP** Control Plane

**CPU** Central Processing Unit

**CR** Cognitive Radio

**DBSCAN** Density Based Spatial Clustering of Applications with Noise

**DGPS** Differential Global Positioning System

**DNN** Deep Neural Network

**DoS** Denial of Service

**DPB** Dynamic Point Blanking

**DPS** Dynamic Point Selection

**DRL** Deep Reinforcement Learning

**DSA** Dynamic Spectrum Access

**EE** Energy Efficiency

**EGT** Equal Gain Transmission

**FL** Federated Learning

**GMM** Gaussian Mixture Model

**GNSS** Global Navigation Satellite System

**GoB** Grid of Beams

**GPS** Global Positioning System

**HetNet** Heterogeneous Network

**eMBB** enhanced Mobile Broadband

**FCC** Federal Communications Commission

**IBO** Input Back-Off

**IEEE** Institute of Electrical and Electronics Engineers

**IoT** Internet of Things

**IQ** In-phase/Quadrature

**JT** Joint Transmission

**KPI** Key Performance Indicator

**KS** Kolmogorov–Smirnov

**LTE-A** Long-Term Evolution Advanced

**MCS** Modulation and Coding Scheme

**MDP** Markov Decision Process

**ML** Machine Learning

**MNO** Mobile Network Operator

**MMIMO** Massive Multiple-Input Multiple-Output

**MRT** Maximum Ratio Transmission

**mMTC** Massive Machine-Type Communications

**Near-RT** Near Real-Time

**Non-RT** Non Real-Time

**O-CU** Open RAN Centralized Unit

**O-DU** Open RAN Distributed Unit

**O-RU** Open RAN Radio Unit

**OFDMA** Orthogonal Frequency Division Multiple Access

**PA** Power Amplifier

**PDF** Probability Density Function

**RAN** Radio Access Network

**RB** Resource Block

**RCR-rApp** RF Channel Reconfiguration rApp

**REASA** REM-Empowered Action Selection Algorithm

**REM** Radio Environment Map

**REM-EA** REM-based Exploration Algorithm

**RIC** RAN Intelligent Controller

**RL** Reinforcement Learning

**RMSE** Root Mean Square Error

**RSM** Radio Service Map

**RSS** Received Signal Strength

**RTK** Real Time Kinematics

**RZF** Regularized Zero-Forcing

**SCF** Serving Cluster Formulation

**SDR** Software-Defined Radio

**SE** Spectral Efficiency

**SNR** Signal-to-Noise Ratio

**SGD** Stochastic Gradient Descent

**SSD** Signaling Storm Detection

**SSA** Signaling Storm Attack

**SWES** SWitching on/off-based Energy Saving

**TA** Timing Advance

**TVWS** TV White Space

**UCB** Upper Confidence Bound

**UCCF** User-Centric Cell-Free

**UCCF MMIMO** User-Centric Cell-Free MMIMO

**UE** User Equipment

**U.S.** United States

**URLLC** Ultra Reliable Low Latency

**V2V** Vehicle to Vehicle

**V2X** Vehicle to Everything

**QoS** Quality of Service

**ZF** Zero-Forcing

# 1 Introduction

The currently deployed 5G and future 6G mobile networks are expected to offer services for a variety of devices [1]. These devices can range from consumer electronics, such as smartphones, to intelligent vehicles (both terrestrial and aerial), and Internet of Things (IoT) devices. Each of these devices is associated with a different Quality of Service (QoS) requirements. Consumer devices often need the enhanced Mobile Broadband (eMBB) services, for which high throughput is a crucial requirement. On the other hand, the Vehicle to Everything (V2X) communications require Ultra Reliable Low Latency (URLLC) services, e.g., to formulate and maintain a platoon of transport vehicles following each other in a bumper-to-bumper distance to generate fuel savings [2]. In this case, any violation of the latency requirements can significantly decrease the observed fuel savings, or even cause a traffic accident. In contrast, the IoT devices are associated with a Massive Machine-Type Communications (mMTC). In this case, each individual device usually has relaxed requirements for the both transmission rate, and latency, but the network have to deal with tens of thousands of such devices. In addition, the IoT devices are usually of low hardware complexity, e.g., to enable long life on the battery. Unfortunately, this makes them potentially easy to be hacked and utilized to perform attacks on the 5G/6G network infrastructure, e.g. Denial of Service (DoS) [3]. One of the key technologies to meet both eMBB, URLLC, and mMTC transmission requirements is a so-called Massive Multiple-Input Multiple-Output (MMIMO) technology [4]. The main idea behind the MMIMO is to utilize large antenna arrays to formulate narrow beams steered directly toward the User Equipments (UEs). This can significantly improve the Spectral Efficiency (SE) due to the array gain, interference reduction, and spatial multiplexing. Moreover, the MMIMO can also improve network security, e.g., by mitigating eavesdropping [5]. However, the benefits of the MMIMO systems come at the cost of, e.g., more complicated signal processing, or hardware required by each transceiver chain to operate [6]. In the extreme case of fully digital MMIMO, each antenna is associated with a dedicated transceiver chain. This enables accurate beamforming, but requires more hardware and computational power to calculate precoder weights or estimate radio channels. The complexity of the signal processing stage even increases while introducing the concept of User-Centric Cell-Free MMIMO (UCCF MMIMO), where each UE can be potentially simultaneously served by multiple synchronised MMIMO Base Stations (BSs) [7]. This approach can provide UEs with a unified QoS, by e.g., coordinated interference management, and increased power of received signal, especially at the cell-edge. As a result, both the traditional MMIMO as well as the 6G UCCF MMIMO networks require more hardware and computational power, potentially consuming a

large amount of energy [8]. From this perspective, improvement of the Energy Efficiency (EE) in 5G and 6G wireless networks becomes a significant challenge, and as a result, EE is usually listed as one of the key Key Performance Indicator (KPI)s along with the SE [9].

Although there are multiple approaches to optimize both the SE and EE of the contemporary 5G and the future 6G network, there is an innovative trend to utilize location information for this purpose [10]. Historically, location information was introduced to the mobile network in the 1990's aiming at meeting the Federal Communications Commission (FCC) of United States (U.S.) requirements for the localization of the emergency calls [11]. However, with the development of the new network generations, location-based services started to be offered to the mobile network users, like navigation, mapping, or geo-marketing. Most importantly, for 5G and 6G networks, localization is expected to also be utilized for the optimization of the network itself, in terms of both SE and EE. One of the key concepts related to the utilization of location information in mobile networks is the so-called Radio Environment Map (REM) [12]. The concept of REM originates from Cognitive Radio (CR). In detail, the idea was to extend standard network architecture with a geolocation database containing, e.g., the characteristics of spectrum use or local law regulations. This was to allow for the dynamic use of licensed spectrum when there was no activity by the spectrum owner. However, the idea of REM can be extended beyond the CR use case to contain any kind of location-dependent data, which can be used to improve both network SE and EE, e.g., QoS maps, coverage related parameters, traffic density maps, or users density maps. This concept is sometimes referred to as Radio Service Map (RSM) [13]. However, deployment of REMs or RSMs requires proper architecture and interfaces, e.g., to fetch and store the data from mobile devices along with some mechanisms for network reconfiguration. Currently, mobile networks, more specifically the Radio Access Networks (RANs), are provided by a single vendor with limited options to deploy third-party algorithms, e.g., REM-based. To overcome this issue, in recent years concept of the Open RAN is gaining more interest from the Mobile Network Operator (MNO)s [14]. The Open RAN comes with the disaggregated BS deployment into the virtual Open RAN Centralized Unit (O-CU), virtual Open RAN Distributed Unit (O-DU), and physical Open RAN Radio Unit (O-RU), enabling multi-vendor composition of the mobile network hardware stack. Most importantly it extends the RAN with a RAN Intelligent Controller (RIC), where dedicated third-party algorithms (e.g., REM-based) can be installed in a form of the xApps and rApps. The xApps and rApps are aimed at the control loop of between 10 ms and 1 s, and above 1 s, namely Near Real-Time (Near-RT) and Non Real-Time (Non-RT) control loop, respectively. RIC provides xApps and rApps with data from RAN and enables RAN control through

the set of dedicated interfaces [15]. This makes Open RAN a promising candidate for the real-world implementation of the innovative algorithms aiming at SE and EE improvement of mobile networks on the basis of various information stored in REM.

The 5G/6G REM potentially deployed within the Open RAN architecture is expected to be filled with multiple types of location-dependent data associated with various services like eMBB, URLLC, mMTC, or V2X. This data formulates a multi-dimensional set following a non-trivial time, frequency, and spatial patterns. Moreover, a contemporary 5G and future 6G networks are expected to be built uppon multiple functional blocks supporting, e.g., MMIMO beamforming, radio resource scheduling, traffic steering, or network slicing [16]. The state-of-the-art approach to network optimization would be to provide a mathematical system model, define the optimization problem, and find the solution based on analytical methods. While for some cases it is an adequate approach, usually it is related to some assumption, e.g., by assuming MMIMO radio channel to perfectly follow Rayleigh distribution [17], or by assuming a single-carrier network instead of the Orthogonal Frequency Division Multiple Access (OFDMA) being a state-of-the-art for the 4G/5G and most probably also 6G networks [18]. On the other hand, while following the accurate and close-to-reality system model, both the formulation of the optimization problem and its optimal solution become very difficult. From this perspective, it seems reasonable to focus on the Machine Learning (ML) methods, which can process the real network data in order to, e.g., find hidden patterns, or predict the network behavior based on the multi-dimensional input data [19]. Moreover, dealing with a complex system such as wireless 5G/6G networks, it is usually hard to predict how a certain action would affect network KPIs before it happens, e.g., if switching on a certain BS would provide high EE gain while maintaining sufficient QoS. From this perspective, a sub-class of ML techniques, namely Reinforcement Learning (RL), is of high interests [20]. The idea of RL is to learn on how to act through the continuous interaction with the environment and observation of the outcome. In this case, even a very complicated wireless network can be optimized by treating it as a black-box, and observing actions and their corresponding outcome. From this perspective, the concept of REM is closely related to the ML, i.e., the REM provides storage for a variety of location-dependent data, which can be processed using ML methods in order to increase network SE or EE. Taking into account the importance of REM and ML, for the development of 5G and 6G networks, this dissertation has the following research hypothesis:

**The usage of information stored in Radio Environment Maps can improve spectral and energy efficiency of wireless networks, especially those using massive MIMO, by utilizing machine learning.**

This research claim will be proven by referencing the 16 original publications,

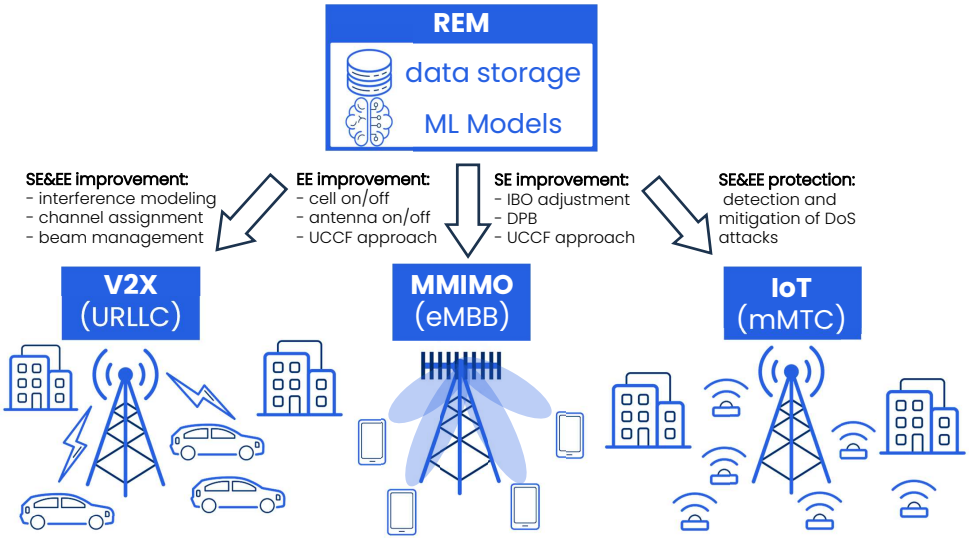


Figure 1: PhD candidate contribution to the SE and EE improvement of the 5G and beyond networks.

in most of which the PhD candidate is the main author, presenting various aspects of utilization of REM and ML for improving SE and EE of wireless networks. The general overview of the dissertation contribution is depicted in Fig. 1. The publications provide a variety of solutions for the improvement of wireless network SE and EE within three main use cases relevant to 5G and 6G:

- The first use case is V2X communications representing mainly the URLLC services. As a first consideration, the dissertation proposes a modeling of the localization error, for Global Navigation Satellite System (GNSS)-based positioning, being crucial for deployment and testing of REM solutions. Then, original algorithms have been proposed to utilize REM and ML for interference modeling and channel assignment, aiming at communications between the vehicles in the platoon based on Dynamic Spectrum Access (DSA). If the channels of proper capacity are provided (SE is improved), vehicles can move closer to each other, providing fuel savings, i.e., increasing EE. The proposed interference models are based on the real In-phase/Quadrature (IQ) samples captured during the field measurement campaign. Finally, REM and ML are utilized in the Open RAN architecture in the context of V2X communication in MMIMO network, to improve the SE by intelligent beam management. The contribution of the PhD candidate to the V2X communications use case

with respect to the publication list covers four original solutions, and can be summarized as follows:

  - **Modeling of Real Time Kinematics (RTK) Localization Error for REM [P14]:**
    * Developed a novel, simulation-compatible model of RTK localization error, essential for high-accuracy REMs.
    * Demonstrated how satellite geometry impacts localization accuracy.
  - **REM-Based Frequency Selection for Platoon Communications [P5]:**
    * Proposed Gaussian Mixture Model (GMM)-based REMs to model complex interference patterns.
    * Developed a frequency channel assignment algorithm using Dijkstra's method for minimizing channel switching.
  - **Federated Learning (FL) for Interference Modeling [P15]:**
    * Extended REM creation to multiple cooperating platoons using FL.
    * Demonstrated improvement in interference modeling accuracy and training time with FL approach.
  - **REM-Based Beam Management in Open RAN ([P1], [P13]):**
    * Introduced beam management based on mobility patterns and beam power maps stored in REM.
    * Developed a Policy Iteration algorithm to optimize beam switching decisions.
    * Proposed a deployment framework within Open RAN using Near-RT xApps.

- The second use case is focused purely on the MMIMO systems oriented on providing eMBB services. Within this use case, the dissertation proposes original algorithms utilizing REM and ML in order to improve EE by intelligent switching on/off either entire cells or individual antenna elements on the basis of user spatial distribution. Regarding the SE, the dissertation proposes to utilize REM and ML to adjust the operation point of the Power Amplifier (PA) for the MMIMO BS to balance the tradeoff between received power and introduced nonlinear distortion. Also, there is proposed a solution named Dynamic Point Blanking (DPB) where, based on the spatial distribution of users, some cells are dynamically muted to reduce interference. Next, for this use case, both EE and SE can be improved by introducing the concept of User-Centric Cell-Free (UCCF) MMIMO. The dissertation also demonstrates

how the concept of Open RAN can be utilized for this purpose. Unlike many state-of-the-art works, all algorithms proposed for the MMIMO use case are evaluated under an accurate 3D Ray-Tracing-based radio channel model proper for MMIMO, as well as the detailed system-level model exploiting, e.g., various precoding algorithms, Modulation and Coding Scheme (MCS) selection, and dedicated radio resource scheduler in time, frequency, and spatial domain. The contribution of the PhD candidate to the MMIMO communications use case with respect to the publication list covers five original solutions, and can be summarized as follows:

- **REM and RL-based Cell On/Off Switching [P6], [P7], [P8]:**
  - Developed REM and RL-based methods to decide BS activation pattern based on user spatial distribution, to improve EE.
  - Tested various metrics for multi-user localization pattern matching for efficient REM usage and faster RL convergence.
  - Demonstrated up to 70% EE improvement in realistic simulation environments based on 3D ray tracing radio channel model.
- **REM and RL-based Intelligent Antenna Selection [P9], [P11]**:
  - Proposed a two-stage model: first selecting the number of antennas, then choosing specific ones based on channel properties.
  - Adapted the algorithm for Open RAN via rApp deployment and Deep Reinforcement Learning (DRL) models.
  - Proposed rApp improving EE performance compared to the baseline algorithm by $\sim$24.8%.
- **REM and RL-based Input Back-Off (IBO) Optimization ([P10]):**
  - Introduced the Contextual Bandit-Based IBO Optimization (COBBIO) algorithm to adjust PA's IBO dynamically using DRL.
  - Balanced desired signal strength with nonlinear distortion to improve throughput.
- **REM and RL-based Interference Coordination via DPB [P16]:**
  - Used REM and RL to mute specific cells dynamically, reducing interference and enhancing cell-edge users SE.
- **UCCF MMIMO for High SE and EE of 6G Networks [P4], [P12]:**
  - Proposed the utilization of Open RAN xApps and rApps for control of UCCF MMIMO network.
  - Developed scheduling and Access Point (AP) association strategies to improve both SE and EE of UCCF MMIMO network.

    - Used realistic 3D ray tracing and nonlinear modeling to validate performance of the UCCF MMIMO network.

- The third use case is oriented on IoT devices and themMTC service. In this context, the REM and ML can be used to protect the low-hardware-complexity IoT devices from the DoS attacks in the RAN domain. Usually, the DoS reduces the network SE, as it is unable to provide services for legitimate users. However, while considering the IoT devices, it also significantly affects their EE by draining their batteries. Within this context, the dissertation presents a dedicated algorithm for the Signaling Storm Detection (SSD) compliant with the Open RAN architecture. The proposed SSD algorithm is not only validated in terms of the simulation studies but also deployed in the real-world testbed based on the Amarisoft 5G BS. The contribution of the PhD candidate to the IoT use case with respect to the publication list can be summarized as follows:
  - **KPI Profile-based Signaling Storm Detection [P1], [P2], [P3]:**
    - Developed an Open RAN-compatible SSD algorithm to protect industrial IoT devices from DoS attacks.
    - Validated performance in both simulation and a real testbed (Amarisoft 5G BS).
    - Highlighted dual impact: maintaining SE and preserving device battery life EE.

The remaining part of the dissertation is organized as follows: Chapter 2 describes the solutions proposed by the PhD candidate within V2X communication use case. Chapter 3 presents the contribution of the PhD candidate to the MMIMO use case. The Chapter 4 touches upon the PhD candidate solutions for IoT use case. The dissertation is concluded in Chapter 5.

# 2 V2X Communications Use Case

This Chapter present the contribution of the dissertation to the V2X use case, classified as an URLLC service. It is started with a brief overview of the background and related work related to this use case. Then four original solutions are described with respect to the publication list:

- Modeling of RTK Localization Error for REM **[P14]**
- REM-based Frequency Selection For Platoon Communications **[P4]**
- Federated Learning-based Interference Modeling **[P15]**
- REM-based Beam Management in Open RAN **[P1]**, **[P13]**

## 2.1 Background and Related Work

The number of vehicles on the roads has been growing over recent years. This causes traffic congestion, but also increases air pollution and fuel consumption. One of the recent solutions to this problem is the so-called *platoon-based driving* [21]. The idea is that, the vehicles would follow each other at a distance of a few meters, enabling EE improvement in terms of fuel savings. The key challenge in the *platoon-based driving* is the coordination of the speed, and acceleration between the vehicles. The studies have shown that it is most beneficial to rely on wireless communications for that purpose [22], i.e., on V2X communications, or more specifically, the Vehicle to Vehicle (V2V) communications, exploiting direct radio link between vehicles in the platoon. In this context, the V2X communications require the URLLC service to provide a stable connection, low latency, and required throughput (usually relatively small, e.g., 3 Mbit/s). Although there is a frequency band between 5.850-5.925 GHz, and 5.855-5.925 GHz dedicated for the V2X, studies show that it will not be sufficient to provide low enough latency, and high reliability for a growing number of vehicles [23]. From this perspective, it seems reasonable to find an alternative frequency band that can be utilized for inter-platoon communications. One common idea is to utilize unlicensed bands like 2.4 GHz or follow the DSA approach, that is, to utilize licenced bands like TV White Space (TVWS) in a way which would not negatively impact the QoS of the licensed users. **The major challenge from this perspective is to propose a method to assess the quality of the radio channels, in order to meet the requirements of the platoon communications.** The existing solutions to this problem utilize REM in a relatively stable radio environment, e.g., [24]. However, it will be shown that REM along with ML can be used to provide information about more sophisticated and dynamic interference patterns. Moreover, efficient creation of such a model can require multiple platoons

to cooperate in collecting data and training the ML model. Such an approach can be realized using the FL concept [25].

On the other hand, the V2X communication related to URLLC service can be provided by a cellular network utilizing a MMIMO technology, spectrally optimized for this purpose. This is sometimes reffered to as a Cellular Vehicle to Everything (C-V2X). One of the approaches to the MMIMO is to utilize a set of predefined beams, namely Grid of Beams (GoB) [26]. From the V2X perspective, each beam covers a relatively small area, and a high-speed vehicle should quickly switch between the consecutive beams along it's route. This is especially important from the perspective of the URLLC, where each connection reestablishment procedure would cause significant delay. To achieve this, under the challenging urban radio environment, and high-speed users, it is not sufficient to rely on the state-of-the-art algorithms utilizing channel state reports and receive power threshold like [27]. **Instead, the challenge is to propose an intelligent beam management algorithm, capable of predicting the beam sequence for the high-speed users**. This can be efficiently realized using the Open RAN architecture, providing the framework to host REM, ML models, and most importantly open interfaces for both data collection, and control actions.

## 2.2 Proposed Solution 1: Modeling of RTK Localization Error for REM

One of the key enablers of REM is the high-accuracy location information. Under the open-sky conditions for both the 5G and future 6G networks, the most common method is GNSS localization [28]. In detail, the centimeter-level localization can be provided by the RTK, which utilizes GNSS signals together with a ground reference station to eliminate both propagation and synchronization errors. As a basis for the next studies utilizing localization, the PhD candidate proposed a novel method of localization error modeling of RTK **[P14]**. The proposed method is based on the satellite geometry and the results of the measurements done in related works. Most importantly, it is suitable for the system-level simulation of wireless networks, e.g., 5G or 6G. The detail contribution of the PhD candidate in the proposed solution can be summarized as follows:

- At the moment of writing **[P14]**, the RTK was not a commonly known localization method for the community of mobile network researchers. Therefore, in **[P14]**, the PhD candidate provided a tutorial-like foundation of the RTK, to highlight the advantage of the phase measurements of the GNSS signals over the commonly used code-based measurements. Also, the process of eliminating the propagation and synchronization errors for location estimation was

explained with highlighting the importance of the reference station measurements. Finally, the impact of the satellite constellation was discussed.

- The novel key contribution proposed by the PhD candidate in **[P14]** is the model of the localization error introduced by the RTK (see Fig. 20 in **[P14]**). Unlike the model proposed in [29], which is tailored to the particular location, the proposed solution simulates the Global Positioning System (GPS) satellite constellation. As such, it can be used to provide a model of the localization error at any location and time. More specifically, the covariance matrix based on visible satellites is computed. Then it is fed into the autoregressive model, modeling the Gauss-Markov process, to obtain samples of the localization error properly time-correlated.

- Finally, in **[P14]**, the PhD candidate implemented the proposed model, verified it through the simulation studies, and compared it against the analytical formula. The studies exploited three distant locations and two motion patterns: static and dynamic UE, respectively. The analysis of variance (see Fig. 13 and Fig. 14 in **[P14]**) proved that the visible satellite constellation has a significant impact on the variance, and that the analytical formula can be used to estimate variance instead of the full simulation. To analyze the time correlation, a PhD candidate used the ANalysis Of VAriance (ANOVA) statistical test. The result (see Table 3 in **[P14]**) was that the null hypothesis stating that correlation time over the day and geographical location have the same mean value cannot be rejected. The simulation studies proved the correctness of the model, which can be used in system-level simulations of the 5G and 6G systems.

## 2.3 Proposed Solution 2: REM-based Frequency Selection For Platoon Communications

To facilitate high-quality intra-platoon communications, the PhD candidate proposed a REM-based Frequency Selection described in **[P4]**. The main idea is to extend the platoon of vehicles with a REM entity, as depicted in Fig. 2 in **[P4]**. The REM contains the location-dependent interference model built based on the measurement sample provided by the platoon along with its localizaiton, and provides intelligent mechanisms to indicate a platoon with a proper radio channel. The detail contribution of the PhD candidate to the proposed solution can be summarized as follows:

- While the state-of-the-art approach to REM is to contain the pair of location-interference power, this approach is efficient only if interference sources are

stable over time, and frequency, e.g., TVWS. In the case of a 2.4 GHz band, there are various interference sources of different transmission bandwidth and random transmission intervals, e.g., WiFi or Bluetooth. This results in sophisticated multi-modal distributions of interference. The novel proposition to deal with them is to utilize a GMM, i.e., to represent the Probability Density Function (PDF) of interference as a weighted sum of multiple Gaussian densities. Moreover, the proposed GMM is based on the mathematical considerations taking into account the wideband frequency-specific characteristics of interference. The proposed GMM with related location information is stored in REM. The proposed interference modeling method and tuning of GMM parameters are depicted in Fig. 6 and Fig. 7 of **[P4]**, respectively. It is worth mentioning that the utilized interference samples in the 2.4 GHz band were collected during a field measurement campaign on the S11 road between Poznań and Kórnik.

- By default, each new location encountered by the platoon is associated with a new GMM. This can result in high memory usage. However, often the similar locations are associated with a similar interference pattern and as a result, similar GMM stored in REM, e.g., because some of the interference sources can be stationary like WiFi APs. From this perspective, it is beneficial to reduce the REM size, while maintaining good quality of information about the radio environment. Therefore, the second novel proposition is to adapt the unsupervised learning clustering algorithm: Density Based Spatial Clustering of Applications with Noise (DBSCAN), which clusters the REM entries based on both the Kolmogorov–Smirnov (KS) statistical and geographical distances. The main idea of this approach is to cluster together areas with similar interference distributions being geographically close to each other. This is important from the perspective of, e.g., channel assignment based on the location information. The results of the clustering based on the IQ samples collected during the field measurements are depicted in Fig. 8, Fig. 9, and Fig. 10 in **[P4]**, respectively. The results indicated that to provide efficient clustering of GMM being in close geographical neighborhood, it is best to utilize a geographical distance threshold of 400 m, and KS distance threshold of about 0.012. Such a setting enables reduction of REM size by about 7%.

- Based on the GMM in REM, a novel channel assignment mechanism based on the adaptation of the state-of-the-art Dijkstra algorithm is proposed to minimize the number of channel reselections over the platoon route while keeping the outage probability below a service-specific threshold. To achieve this, first, a mathematical modeling of the outage probability, proper for the multi-

carrier system, was done (see Sec. II of **[P5]**). The resultant mathematical model provides a relationship between the outage probability and the interference distribution represented in REM by the GMM. Moreover, the utilization of the Dijkstra algorithm requires the definition of the graph. The novel proposition of the PhD candidate is to build a graph, where nodes represent radio channels providing sufficient outage probability in consecutive locations along the platoon route, and edges stand for the cost of switching the radio channel. The proposed algorithm is verified using the computer simulations utilizing real-world IQ samples collected during the field measurements on the S11 road between Poznań and Kórnik. The results are presented in Fig. 13 and Fig. 14 in **[P4]**. The key observation is that the proposed channel assignment method provides the least number of channel reselections, compared to the state-of-the-art solutions, i.e., 4 vs up to 24. Moreover, it never exceeds the required outage probability.

## 2.4 Proposed Solution 3: Federated Learning-based Interference Modeling

The REM-based frequency selection for platoon communications from **[P4]** was considering a single platoon. This idea can be extended to utilize multiple platoons contributing to the creation of GMM models in REM. A naive approach to this problem would be to follow the centralised training, i.e., send all the interference samples collected by the multiple platoons at the same location, use them for training of the single GMM model, and distribute the model back to the platoons. However, this would create a significant communications overhead related to the transmission of training data. On the other hand, the FL approach allows for reducing this overhead by training GMM models locally within each platoon, and sending to the central node only the resultant parameters of the GMM models. The central node then synthesizes them into the updated model and distributes them back to the platoons. Therefore, the Phd candidate had a leading contribution in the proposition of the FL-based Interference Modeling described in **[P15]**. The proposed FL-based extension to the idea from previous work is depicted in Fig. 4 in **[P15]**. The main concept is to introduce a hierarchical structure of REM, namely local REM, and global REM. Each platoon is equipped with a local REM. The platoon trains the GMM models in local REM and utilizes them for channel assignment. However, periodically, the local REMs send their models to the global REM, which utilizes FL algorithms to synthesize them into updated models. These updated models are then distributed back to the platoons, and the cycle repeats. The detailed contribution of the PhD candidate to the proposed solution can be summarized as follows:

- Proposition of the novel FL-based interference modeling, based on the adjustment of the state-of-the-art FL algorithm to the GMM. First, the dedicated algorithm is proposed to update the local REM in a cyclic manner based on the newly collected interference sample. Second, a novel solution for updating the global REM is proposed. The algorithm of the global REM update is an extension to the state-of-the-art *FedAvg* algorithm [25]. While the *FedAvg* is design to deal with Deep Neural Network (DNN) by averaging weights of multiple DNNs to obtain the global model, the approach proposed by the PhD candidate is designed to deal with GMM models.

- To demonstrate the multiple platoons contributing to the training of both local REMs and global REM, a large amount of data is required. It would be very difficult to obtain, store, and process such a data volume. Thus, the PhD candidate developed a simulation framework to generate interference samples related to the WiFi transmission from multiple sources in a 2.4 GHz bandwidth. This allowed for reproducing the sophisticated multi-modal distributions observed in a real-world setting during previous studies **[P4]**. Two scenarios were considered: single platoon and multiple platoons. In the case of a single platoon, the results are depicted in Fig. 8 and Fig. 9 in **[P15]** respectively. The key outcome is that the platoon should collect about 4096 samples to create a new GMM and perform a local REM update. Also, to obtain stable results, a large enough averaging should be applied. In the case of multiple platoons, the results are depicted in Fig. 10. The interesting observation is that utilization of FL with 7 platoons contributing to the training provides about a 4.5-fold reduction in Root Mean Square Error (RMSE) of outage probability estimation, compared to the scenario with only 1 platoon training its model.

## 2.5 Proposed Solution 4: REM-based Beam Management in Open RAN Architecture

The problem of ubiquitous connectivity for high-speed C-V2X users served by MMIMO BS, using GoB configuration (exploiting a set of predefined beams) is addressed by the PhD candidate in **[P13]** and extended in Sec. IV-A of **[P1]**. The work **[P13]** proposes an intelligent beam management algorithm, capable of predicting the beam sequence for the high-speed URLLC users based on the RL and REM. The main idea is to utilize REM, which contains location-dependent information about the received power reported by previous UEs, related to each MMIMO beam, along with the UE mobility pattern map with statistics of, e.g., network users speed and azimuth orientation (see Fig. 3 in **[P13]** for details). These studies were extended in

**[P1]** with the evaluation of the impact of various GNSS-based localization methods on the algorithm performance. Both **[P1]** and **[P13]** discuss the compatibility of the proposed solution with the Open RAN architecture, showing how the proposed algorithm can be deployed, but also which crucial parameters are missing in the Open RAN specifications. The detailed contribution of the PhD candidate to the proposed solution can be summarized as follows:

- Although the high-speed C-V2X users requiring URLLC service are challenging, e.g., from the perspective of the connection reliability, they are often characterized by a relatively predictable mobility pattern. For example, often cars follow the same roads with a possibility of changing their direction limited to the road architecture. The trains and other rail vehicles are even more predictable. Taking into account these considerations, in **[P13]** the PhD candidate proposed a novel REM architecture, containing the UE mobility Pattern Map, where the probability distribution of user (vehicle) speed and direction is stored for each location. On the other hand, the proposed REM contains the map of the location-dependent received power associated with each beam of the predefined GoB codebook.

- The PhD candidate assumed that the UE mobility pattern stored in REM follows the Markov property, i.e., the probability distribution of next UE speed and direction depends only on the present speed, direction, and location. From this perspective, the beam selection along the UE route can be formulated as an Markov Decision Process (MDP), i.e., the UE moves over the cell area and sequential decisions are made by BS on its association with a certain beam. While having enough data in REM, both mobility and received power maps provide sufficient information about the network, the PhD candidate proposed to utilize a policy iteration algorithm to deal with the MDP. The unique feature of the proposed solution is that it allows for a balance between two optimization goals: minimization of beam reselections (crucial for the URLLC services), and receive power maximization (potentially of high importance for eMBB services). The simulation studies in **[P13]** show that utilization of the proposed REM-based beam management algorithm, focused on minimization of beam reselections, allows for reducing the number of beam failures by about 2.18 times, compared to the baseline approach as depicted in Fig. 5 in **[P13]**. Also, while the proposed REM-based beam management algorithm is focused on the maximization of received power, the gain of about 23% compared to the baseline approach can be observed for the cell-edge users (see Fig. 6 in **[P13]**).

- In the work **[P13]** the perfect location information was assumed. However,

to access REM data UE will report its position using state-of-the-art methods. To complement simulation studies PhD candidate investigated the impact of the GNSS-based localization methods on the proposed REM-based beam management. The considered methods were: RTK of about 1 cm localization error (modelled as proposed in **[P14]**), Differential Global Positioning System (DGPS) of about 1 m localization error, and standard GPS of about 6 m error. The results presented in Fig. 4 in **[P1]** show that REM requires location information of relatively high quality, i.e., for the RTK, and DGPS, the number of beam failures was outperforming the baseline approach. However, while standard GPS was used, it was not the case.

- The intelligent algorithms utilizing REM require access to the network data and the possibility to change the configuration of RAN components. This can be realized in a standardized and unified way, while following the Open RAN architecture. From this perspective in **[P1]** and **[P13]**, the PhD candidate proposed the implementation of the REM-based beam management in the Open RAN architecture (see Fig. 3 in **[P1]**). The main idea is to follow the hierarchical architecture utilizing Non-RT RIC for the extensive offline computations required to create REM based on the long-term network KPIs and perform policy iteration optimization. It is proposed that the procedure of the beam management itself is realized by the Beam Mobility Management xApp (BMM-xApp) residing in the Near-RT RIC. The BMM-xApp receives the REM along with the proper policies and UE location from the Non-RT RIC. Based on this information, the BMM-xApp can make fast decisions on beam, management, interacting directly with the BS (in the Open RAN nomenclature named as E2 Node). However, the Open RAN specifications are still extended. Therefore, in **[P1]** the PhD candidate identified a few aspects, which requires further standardization effort, e.g., unified definition of the data format to exchange UE location information, data format to exchange ML modules between Near-RT and Non-RT RICs, or specific actions on the E2 interface (between Near-RT RIC and E2 Node) enabling the control over the beam management for the xApp.

# 3 MMIMO Communications Use Case

This Chapter present the contribution of the dissertation to the MMIMO use case, considering eMBB service. It starts with a brief overview of the background and related work. Then, five original solutions are described:

- REM and RL-based Cell On/Off Switching **[P7],[P6], [P8]**
- REM and RL-based Intelligent Antenna Selection **[P9], [P11]**
- REM and RL-based IBO Optimization **[P10]**
- REM and RL-based Interference Coordination **[P16]**
- UCCF MMIMO for High SE and EE of 6G Networks **[P12], [P4]**

## 3.1 Background and Related Work

To fulfil the growing throughput demand of the eMBB users, 5G and 6G networks are expected to utilize the MMIMO technique. The MMIMO enables achieving high SE by deployment of tens or even hundreds of antennas at each BS [30]. While following the digital precoding schema, each antenna is associated with a dedicated transceiver chain. Depending on the selected precoder, this allows for SE improvement through, e.g., Signal-to-Noise Ratio (SNR) maximization, interference cancellation, or spatial multiplexing. However, the high SE gains come at the cost of an increased power consumption, i.e., each antenna at MMIMO BS is associated with a dedicated transceiver chain [31]. Moreover, the 5G system will typically be a Heterogeneous Network (HetNet), i.e., a network composed of overlapping cells of various sizes, with BSs equipped with antenna arrays [6]. Although HetNet can provide large spectral efficiency benefits, increased energy consumption is expected. On the other hand, state-of-the-art research works show that many of the BSs in the network are underutilized within some periods [32], [33]. **Therefore, the challenge is to propose an intelligent solution to scale the active network resource, in order to increase EE of the MMIMO network, while not decreasing users' QoS.** This can be done at different levels. One approach is to switch on/off the entire BSs, e.g., [34]. While this approach allows for saving the most energy, it should be applied carefully, because it is related to some transition time, and should not result in a lack of coverage in some areas. More flexible approach, yet resulting in relatively smaller EE gains, is to dynamically adjust the number of active antennas on MMIMO BS to the current traffic demand, e.g., [35]. However, the related works in the topic of cell on/off switching do not consider MMIMO BSs at all, e.g.,[36],

[37]. The key drawback of state-of-the-art cell on/off switching and antenna selection algorithms considering MMIMO (e.g., [35], [38], [39]), is that the authors often assume a simplified system model, e.g., uncorrelated radio channels for MMIMO, single-carrier systems, while 5G and 6G are expected to utilize OFDMA or lack a time-frequency-space scheduler. Moreover, in the case of dynamic adjustment of the number of active antennas, the state-of-the-art works (e.g., [40]) assume that each antenna element contributes equally to the overall array gain, which is usually not the case in real propagation environments [41]. Thus, there is a demand for the intelligent algorithms evaluated under the close-to-reality system model. While such systems usually are hard to model and optimize using an analytical approach an ML, or specifically RL algorithms augmented with REM can be beneficial. Although some RL solutions were proposed for EE improvement of 5G networks (e.g., [42], [43]), they miss MMIMO and consider a simplified system model. Last but not least, it is important to envision how the REM-based, EE-oriented algorithms can be deployed in the real network. In this context, one of the key enablers of EE in future networks is the Open RAN architecture [44]. With its open interfaces, Open RAN can be used to monitor the necessary network KPIs and perform control actions such as cell on/off switching or adjustment of the number of active antennas (also named RF channel reconfiguration) [45].

However, not only can the EE of the MMIMO network providing eMBB service be improved. The contemporary and future MMIMO networks are deployed considering multiple building blocks, e.g., interference management, user-to-cell association, power adjustment, or radio resource scheduling. This creates a significant challenge in the management of such a network. But at the same time, it provides multiple degrees of freedom for network optimization aimed at SE. **Therefore, there is a demand for intelligent algorithms to manage MMIMO networks in order to increase their SE**. While starting the SE optimization from a cell-level, the operation point of the PA can be of high interest. While operating close to its maximum output power the PA generates strong out-of-band distortion, but also the strongest wanted signal. Initially, e.g., in [46], the nonlinear distortion was claimed to follow omnidirectional characteristics, which can be overcome in MMIMO systems through the beamforming. In contrast, in [47] it has been shown that under some radio conditions (e.g., line-of-sight), the nonlinear distortion can be steered in the same direction as wanted signal, achieving the same array gain. From this perspective, the proper adjustment of operation point of the PA is important in the MMIMO systems. This is typically measured in terms of the IBO being the ratio between the input saturation power of the PA and the average power of the input signal. This allows for balancing the tradeoff between the wanted signal power and the power of the generated nonlinear distortion. One analytical solution

is proposed in [48]. While this solution can be adapted to some configurations of MMIMO systems, e.g., using analog beamforming, the authors assumed a simplified system model, e.g., a flat fading channel. This is not the case in real-world scenarios, where the radio channel is rich in reflections and diffractions, making it frequency-selective. Moreover, the authors of [48] do not consider layered signal processing in a real BS composed of, e.g., scheduling, and utilization of a fixed set of Modulation and Coding Schemes (MCS), that affect the throughput achievable by the network users. Similarly, to EE optimization under the realistic system model, IBO can be adjusted in an intelligent manner, using the RL approach.

Another possibility to significantly improve SE of the MMIMO network is to take advantage of the cooperation between BSs. This idea was already introduced in Long-Term Evolution Advanced (LTE-A) networks as Coordinated Multi-Point (CoMP) [49]. In the literature, the most explored CoMP techniques are Joint Transmission (JT) to UE from several BSs and Dynamic Point Selection (DPS) allowing for almost instant handover of UE between BSs [50]. On the other hand, the much less investigated CoMP scheme is a so-called Dynamic Point Blanking (DPB). The idea of DPB is to mute particular BSs in frequency and time, e.g., to reduce interference, and improve the cell-edge users throughput [51]. The challenge is to properly choose the muting pattern that is appropriate for given network conditions, e.g., based on the spatial distribution of users in a cell using the combination of REM and RL.

However, the future 6G networks are expected to provide even more flexibility in the coordination of the transmission from multiple MMIMO BSs to the individual UEs. This approach is named UCCF MMIMO, and its main idea is to provide UE with a coordinated transmission from multiple APs, which are coordinated by the Central Processing Unit (CPU) [52]. This approach results in placing the UE in the middle of its virtual cell, increasing its throughput and QoS. Moreover, eliminating the problem of cell-edge users, characteristic for the legacy networks, where UE is typically served by a single BS providing the highest Received Signal Strength (RSS). Also, UCCF MMIMO can potentially improve the EE over the legacy approach, as a result of the increased number of degrees of freedom. One of the key challenges in a UCCF MMIMO network is to determine which APs should serve a specific user, e.g., distant APs might provide a marginal contribution to user throughput while increasing signaling overhead, and "wasting" allocated power. The procedure of AP selection is known as the Serving Cluster Formulation (SCF). However, to determine the quality of the SCF, one requires a reliable system model, proper for the 6G system, e.g., taking into account spatial-time-frequency resource scheduling, an accurate radio channel model, MCS selection, or nonlinear PA characteristics. Unfortunately, most of the state-of-the-art works neglect the impact of the nonlinear

distortion, and rely on some simplification in a system model, e.g., utilize Shannon law instead of MCSs [53], or an independent, identically distributed Rayleigh channel [54]. Proper modeling of such systems is crucial for the development of ML and REM-based solutions to manage UCCF MMIMO future 6G networks. Also, for the practical implementation of this novel network architecture, an Open RAN approach might be reasonable with its disaggregated and virtualized nature.

## 3.2 Proposed Solution 1: REM and RL-based Cell On/Off Switching

To improve the EE of the MMIMO network offering the eMBB services, the PhD candidate proposed a REM and RL-based solution aimed at Cell On/Off Switching. The general proposed concept is demonstrated in Fig. 2 in **[P6]**, and is an extension of the initial PhD candidate idea from **[P7]**. Under the assumption that the 5G and beyond networks will have access to the precise location of the users (e.g., using RTK), the novel proposition is to utilize this data to determine which MMIMO BSs should be active to provide high QoS for a given UE set. In detail, REM stores the information about the set of UE locations, and for each set of locations, an EE achieved under various sets of active BSs (see Fig. 3 in **[P6]**). The REM utilizes the RL to determine which BSs can be switched off for a particular set of UE locations. One of the challenges in this case is how to measure the similarity between a spatial distribution of UEs and REM entries. This was investigated by the PhD candidate in **[P8]** by comparing the impact of similarity measures on the REM and RL-based cell on/off switching algorithm, in terms of EE. The detailed contribution of the PhD candidate to the proposed solution can be summarized as follows:

- While the state-of-the-art solutions to the cell on/off switching based on the RL usually do not consider the MMIMO networks, the PhD candidate proposed a REM-based approach dedicated to this type of wireless systems. The idea was introduced in **[P7]** and much extended in **[P6]**. While the state-of-the-art REMs were dedicated to a single tuple of location-received signal strength, the PhD candidate proposed a novel REM structure to map a set of UE locations on the dedicated set of active BSs. The PhD candidate also proposed an RL algorithm to efficiently manage the process of cell on/off switching based on data in REM. The RL loop consists of recognition of current UE locations (state), decision on which BS should be active (action), and capturing the network EE (reward). After receiving the reward, a cycle repeats. In this context, the PhD candidate proposed a modified (e.g., compared to the 3GPP specifications) EE definition, i.e., EE is defined as a ratio between median user throughput and average power consumption. Most interestingly, while

the median throughput-based EE is used as a goal function, the proposed scheme also improves the UE throughput itself. It is observed both in terms of median and cell-edge UEs.

- In **[P6]** the PhD candidate proposed an extension to the state-of-the-art RL framework, dedicated to REM-based cell on/off switching, aiming reduction of training time. Based on the average received signal strength reported by the UEs, it is possible to exclude from the action space these sets of active BSs, which results in a lack of network coverage of certain UEs. Next, the PhD candidate proposed a REM-based Exploration Algorithm (REM-EA). Compared to the state-of-the-art methods, where a set of active BSs is determined separately for different sets UE locations, in the proposed REM-EA algorithm, knowledge from each REM entry is used to determine the set of active BSs. This is based on the idea that similar spatial distributions of UE location should be associated with a similar optimal set of active BSs.

- The state-of-the-art works covering the topic of cell on/off switching usually utilize a simplified system model, e.g., single carrier systems, lack of time-frequency-space radio resource allocation, or an uncorrelated Rayleigh radio channel model. In contrast, the PhD candidate developped an advanced simulator of the MMIMO network including radio channel model based on the 3D ray tracing software, with 3D models of buildings, dedicated module for UE to BS association, a time-frequency-space radio resource scheduler, Maximum Ratio Transmission (MRT), Regularized Zero-Forcing (RZF), and Zero-Forcing (ZF) precoders, OFDMA with multiple Resource Block (RB)s, and 15 MCS. The utilization of such a detailed system model justifies the need for ML methods, as the formulation of the optimization problem taking into account all building blocks, even if possible, results in a very complicated formulation. The proposed model is used in **[P7][P6][P8]**. And serves as a base for considerations toward antenna selection, IBO optimization, or UCCF MMIMO networks, presented in the following sections.

- Using the developed simulator of MMIMO network, the PhD candidate evaluated the proposed REM and RL-based solution to cell on/off switching, and compared it against the baseline algorithms. The initial results from **[P7]** (see Fig. 3 therein) indicated an about 44% improvement of the EE over the scenario without EE optimization. The superiority of the proposed solution against the state-of-the-art SWitching on/off-based Energy Saving (SWES) [34] algorithm was proven in **[P6]**, indicating the 70% EE improvement. However, please note that the considered scenarios were different, so the results cannot be compared 1-to-1. Also, the simulation studies in **[P6]**

demonstrated that the proposed REM-EA allows for speeding up RL training time by over 50% compared to the state-of-the-art RL Upper Confidence Bound (UCB) algorithm. See Fig. 14 in **[P6]** as a representative example. Finally, the PhD candidate evaluated the impact of the REM spatial resolution (quantization of UE locations) on the performance of the proposed cell on/off switching algorithm. The results depicted in Fig. 15 and Fig. 16 in **[P6]** led to the conclusion that if the quantization of UE locations of 5 m is used, the REM size can be reduced by half, while not decreasing significantly the resultant EE.

- The REM may already contain a number of entries with several UE locations and related sets of active BSs. It seems beneficial to match the currently observed UE locations with those in REM if they are similar enough so that existing knowledge can be directly used instead of performing the training procedure from scratch. However, for this purpose, an adequate similarity measure between two sets of UE locations is needed. In this context, in **[P8]** the PhD candidate evaluated four distance metrics, proper for measuring the similarities between sets of points, e.g., x-y locations. In detail, they are: Hausdorff distance (the greatest distance from a point in one set to the closest point in the other set), mean distance (being the distance between two mean points computed for each set), average distance (being the average of distances between every pair of points from two sets), and sum of minimums distance (found by measuring the closest distances between points of the two sets in both directions and then averaging them). Each distance metric is incorporated into the proposed REM and RL cell on/off switching algorithm and evaluated using the proposed simulation framework. The metrics were evaluated using almost perfect RTK localization, and standard GPS with accuracy of a few meters. The results presented in Fig. 5 in **[P8]** indicate that the sum of minimums distance is characterized by the highest EE, i.e., the gain of 56% and 48% over the scenario without cell on/off switching was indicated for RTK and GPS localization, respectively.

## 3.3 Proposed Solution 2: REM and RL-based Intelligent Antenna Selection

Sometimes, the UE traffic demand is too high to switch off the entire cell, but too low to take full advantage of tens or hundreds of active antennas. In this case, the MMIMO systems can be scaled down to increase their EE by switching some of the transceiver chains off. In **[P9]**, the PhD candidate proposed a novel solution to this problem, i.e., REM and RL-based Intelligent Antenna Selection. The high-level

concept is depicted in Fig. 1 therein. The proposed solution follows a similar concept to the one oriented on the cell on/off switching. The REM aims at mapping between the set of UE locations and the set of active antennas using the RL approach. To improve the computational efficiency, this process is divided into two parts: the Active Antenna Number Computational Block and the Antenna Selection Block. Based on the UE positions, the former determines how many antennas are needed, while the latter indicates which particular antennas should be switched on/off. The growing interest in Open RAN networks enables practical realizations of intelligent antenna selection. However, this requires a redesign of the algorithm to fit the specifications. From this perspective, in **[P11]**, the PhD candidate adjusted the proposed solution to fit the demands of the Open RAN network in the form of the RF Channel Reconfiguration rApp (RCR-rApp). The proposed rApp utilizes DRL, and follows strictly the capabilities of Open RAN interfaces in terms of the exposed KPIs. The detailed contribution of the PhD candidate to the REM and RL-based Intelligent Antenna Selection can be summarized as follows:

- In **[P9]**, the PhD candidate proposed a novel REM and RL-based Intelligent Antenna Selection. In some of the state-of-the-art works, it is assumed that each antenna element contributes equally to the overall array gain, and it is enough to determine the number of active antennas, i.e., it is not necessary to determine which antennas should be deactivated. This is usually the case under the simplified uncorrelated Rayleigh radio channel model, but not true in the real-world propagation environment, where, e.g., spatial correlation or shadowing of a specific propagation path can affect the contribution of individual antennas to the array gain. However, considering jointly how many antennas should be used, which exact antennas should be switched on/off, results in an enormous number of possible combinations. To overcome this problem PhD candidate proposed to split this problem into the Active Antenna Number Computation Block, being responsible for determining the number of active antennas (utilizing REM and RL for this purpose), and Antenna Selection Block, being responsible for selecting indicated number of active antennas based on some arbitrary rule, e.g., on the basis of the average channel gain, or spatial correlation.

- For the Active Antenna Number Computation block, PhD candidate proposed a REM structure, depicted in Fig. 2 in **[P9]**. Each REM entry is associated with a set of UE locations, and sub-entries related to the number of active antennas. For each sub-entry, a resultant EE (following the definition proposed in **[P6]**) and the number of visits are stored. The proposed REM is used by the RL agent to learn how many antennas are needed for a given set of UE locations

to maximize EE. Following the concept of information fusion, between REM entries proven in **[P6]**, the PhD candidate proposed the REM-Empowered Action Selection Algorithm (REASA). It is aiming to speed up RL training time by utilizing knowledge about EE from similar REM entries.

- Unlike the state-of-the-art works utilizing the simplified system model, the PhD extended the simulation environment from **[P6]** to include an antenna selection feature and utilized it to evaluate the proposed REM and RL-based Intelligent Antenna Selection algorithm, and compare it against the analytical baseline [17]. One of the key results is depicted in Fig. 6 in **[P9]**. The analytical solution obtained under the simplified system model indicates that, for the considered simulation experiments, on average, 13 antennas are needed, while the proposed REM and RL-based algorithm indicates on average 31 antennas. The results from Fig. 8 show that the analytical approach underestimates the number of active antennas, resulting in EE decreased by about 18% compared to the solution proposed by the PhD candidate. This demonstrates that solutions obtained under the simplified system model (e.g., uncorrelated Rayleigh radio channel model) are not valid under the close-to-reality conditions emulated by the 3D ray tracer and system model considering multiple building blocks like MCS, or space-frequency-time scheduler.

- In **[P11]**, the PhD candidate proposed how to push the proposed REM and RL-based Intelligent Antenna Selection toward the practical implementation in Open RAN network as RCR-rApp. In this case, the REM has a form of DNN utilized by the DRL agent. The input data is aligned with the data exposed over the Open RAN interfaces, and underlying Third Generation Partnership Project (3GPP) specifications. As UE location, understood as latitude and longitude, is not supported by the Open RAN interfaces, the PhD candidate proposed to reflect the spatial characteristics of users' distribution in a cell by capturing the number of users per beam. Therefore, the REM stores the information about the EE associated with a number of active antennas, cell load, power consumption of the cell, average user throughput, total number of users, and number of users associated with each beam (representing their angular spread over the cell). The simulation studies done in **[P11]** show the gain of about 24.8% for the proposed RCR-rApp over the scenario without EE optimization. This is close to the exhaustive search, resulting in 25% improvement in EE.

## 3.4 Proposed Solution 3: REM and RL-based IBO Optimization

While the proposed solutions in Sec. 3.2 and 3.3 aimed at EE improvement of the MMIMO network providing eMBB services, the solution proposed by the PhD candidate in **[P10]** touches upon the SE improvement. It is achieved on the cell-level by introducing REM and RL-based IBO Optimization in an analog MMIMO system. In detail, the PhD candidate proposed the COBBIO (see Fig. 2 in **[P10]**). An algorithm that adjusts the PA's operating point by finding a balance between wanted signal power and nonlinear distortion power in order to increase UE throughput. While the paper does not explicitly refer to REM, the utilized DRL agent, together with a replay buffer for storage of the results, can be implemented as REM. PhD candidate proposed to store the throughput obtained under different values of IBO labeled with an SNR-like metric related to the average channel gain and full transmit power. The detailed contribution of the PhD candidate to the REM and RL-based IBO optimization described in **[P10]** can be summarized as follows:

- In the context of the MMIMO networks, it is essential to investigate the nonlinear distortion generated by the PA. Especially, for the analog beamforming, it has been shown that distortions are beamformed together with the desired signal toward the allocated UE. The existing analytical solutions are not adequate, as they rely on the simplified system model, e.g. [48]. Taking into account the complexity of the contemporary 5G, and future 6G systems, the PhD candidate proposed COBBIO to adjust the IBO of users using the DRL approach, based on their radio conditions in an intelligent manner. This allows one to learn through interaction on how PAs operation point affects the resultant user throughput, affected also by the MCS and most importantly, frequency-selective fading.

- The PhD candidate proposed to formulate the IBO optimization Contextual Bandit problem defined by the state expressed as saturation SNR (theoretical SNR assuming average channel gain and presence of only white gaussian noise, neglecting nonlinear distortion), action defined as one of a few IBO with applied discretization to reduce action space. Finally the reward is a user throughput. The proposed COBBIO DRL agent interacts with an MMIMO network by selecting IBO and learns how to improve throughput. This approach makes the proposed COBBIO agnostic of the underlying system model, and capable of dealing with complicated systems, treating them as a black-box.

- PhD candidate evaluated the proposed solution against the analytical baseline [48]. For this purpose, the simulation environment initially proposed

in **[P6]** was extended with a proper model of nonlinear distortion, and an analog precoder, namely Equal Gain Transmission (EGT). The simulation studies considered 200 users generated using a 3D ray tracer radio channel. First, the PhD candidate performed a tuning of the DRL parameters, e.g., adjustment of batch size or number of neurons in hidden layers. Based on studies analyzing the batch size for a single Stochastic Gradient Descent (SGD) iteration, and the number of neurons per hidden layer (see Fig. 4 and Fig. 5 in **[P10]**), it was decided to follow a batch size of 2, and the number of neurons for each of the 3 hidden layers to 8. Next, the PhD candidate compared the proposed COBBIO algorithm against the analytical baseline [48]. The results from Fig. 6 indicate that compared to the proposed COBBIO, the baseline solution is characterized by an 8% degradation in median throughput, and 45% degradation for the cell-edge users (10th percentile throughput). This is related to the fact that the analytical baseline, based on the optimization under the flat radio channel, indicates a lower IBO to be used. In contrast, COBBIO proposed by the PhD candidate is trained directly on the network environment, and as a result selects higher values of IBO to mitigate nonlinear distortion at the cost of slightly lower power of the received signal (see comparison in Fig. 7).

## 3.5 Proposed Solution 4: REM and RL-based Interference Coordination

The SE improvement can be even higher while introducing coordination between cells in MMIMO network. From this perspective, an interesting but less explored field is DPB. In this approach, certain BSs are muted not only to achieve energy savings, but mainly to reduce interference. However, the muting cycles are very fast (order of single slots), and highly depend on the current spatial distribution of the users in the network. To properly select a muting pattern, in **[P16]** the PhD candidate proposed a REM and RL-based interference coordination. It extends the idea of mapping between the spatial distribution of UEs and the set of active BS presented in **[P6]** with the DRL agent (see Fig. 1 in **[P16]**). This approach enables better generalization of the knowledge obtained by the agent. Also, the optimization goal, or in the RL terminology: reward, is related to throughput not EE. The contribution of the PhD candidate to the REM and RL-based interference coordination, described in **[P16]** can be summarized as follows:

- The state-of-the-art solutions proposed for muting pattern selection in DPB mostly rely on the large-scale fading proper for single antenna BSs [51]. This approach can be insufficient to model a realistic 5G MMIMO HetNet. Thus,

the PhD candidate proposed a DRL framework for intelligent DPB based on the spatial distribution of users in a cell, stored in the REM, and processed by the DRL agent. The high-level idea is an extension of the proposed solution for EE in **[P6]**. However, the muting cycles are expected to be relatively short compared to the cell on/off switching. Moreover, the DNN has an input layer of fixed size, making it challenging to deal with different numbers of users in a cell and their location coordinates. To overcome this problem PhD candidate proposed to introduce initial clustering of the UE locations using the K-Means unsupervised learning algorithm, resulting in a fixed number of clusters, which can be fed into the DNN. Finally, for DPB, the optimization goal is to improve the throughput of the cell-edge users. From this perspective, the PhD candidate proposed to define reward in an RL problem as 10th percentile user throughput. Overall, the proposed DNN takes a number of UEs associated with each cluster resulting from the K-Means algorithm as input, and outputs the estimated throughput of the cell-edge users associated with each muting pattern.

- The REM and RL-based interference coordination was evaluated by the PhD candidate using the simulation environment proposed in **[P6]**. The results show that the solution proposed by the PhD candidate improves the cell-edge (10th percentile) user throughput by about 20.6% compared to the solution without DPB. This is almost as good result as exhaustive search, achieving 21.6% gain (see Fig. 4 in **[P16]**). In contrast, the state-of-the-art DPB algorithm even degraded the cell-edge users' throughput by about 52%. This is because it is based only on the large-scale fading coefficient, which is not enough to characterize MMIMO network. This demonstrates the need for intelligent DRL algorithms to deal with complicated 5G and 6G networks. Results from Fig. 5 in **[P16]** show that high cell-edge users throughput improvement is achieved with only 5% degradation of the average user throughput.

## 3.6 Proposed Solution 5: UCCF MMIMO for High SE and EE of 6G Networks

The CoMP methods like DPB enable coordination between BSs in MMIMO networks to improve their SE. However, CoMP exploited only a fixed cluster of cooperating BSs. In the context of 6G networks, this idea evolved toward the UCCF, where each UE can be served by a dedicated set of BSs (usually named APs in the UCCF networks terminology). Usually, UCCF MMIMO networks are evaluated under the simplified system model. Instead, to evaluate its potential for high network SE by utilization of REM and ML, in **[P12]** the PhD candidate proposed an

advanced simulation framework to model 6G UCCF MMIMO network. One of the conclusions from this work was that UCCF MMIMO networks can be efficiently implemented using the Open RAN architecture, allowing single/virtualized O-CU and O-DU to manage multiple O-RUs. Another observation was that, both SE and EE of the UCCF MMIMO network can be increased, while selecting the correct set of BSs (O-RUs), which should jointly serve a particular UE, i.e., SCF algorithm. The SCF in Open RAN architecture is discussed by the PhD candidate in **[P4]**. With the proposed architecture depicted in Fig. 1. With respect to the **[P12]** and **[P4]**, the detailed contribution of the PhD candidate to the UCCF MMIMO for increasing SE and EE of 6G Networks can be summarized as follows:

- Unlike state-of-the-art works studying the UCCF MMIMO networks utilizing simplified system models, e.g, single-carrier or based on the uncorrelated Rayleigh radio channel model, in **[P12]**, the PhD candidate proposed a realistic simulation environment. It is a system-level simulator of OFDMA-based UCCF MMIMO system, built of multiple functional blocks reflecting the signal processing stages of the real 5G and likely 6G network (see Fig. 2 in **[P12]**). In detail, the simulation environment proposed by the PhD candidate utilizes a realistic 3D ray-tracer to generate radio channel coefficients affected by the buildings and obstacles, as well as provides the uncorrelated Rayleigh radio channel for comparison. It enables testing of various SCF algorithms, and precoding algorithms, as well as supports a time-frequency-space radio resource scheduler adjusted by the PhD candidate to the needs of UCCF MMIMO network. For the calculation of the UE throughput, instead of the commonly used Shannon formula, the PhD candidate utilized an MCS assignment based on the effective SNR metric. Finally, a PhD candidate equipped the simulation environment with a module to simulate the impact of nonlinear transmitters PAs on the UCCF MMIMO network.

- Using the proposed environment, in **[P12]** the PhD candidate performed simulation experiments to evaluate the UCCF MMIMO network under both the realistic ray-tracer-based and uncorrelated Rayleigh radio channel models. The results are depicted in Fig. 7 in **[P12]**, illustrating the 10th, median, and 90th percentile of user throughput distribution related to varying numbers of O-RUs formulating a serving cluster. First observation is that the utilization of the UCCF MMIMO approach can improve the SE. Especially for the cell-edge users (10th percentile), the gain can be over 2-fold. The next observation was that, due to a lack of spatial correlation, the user throughput was much higher under the uncorrelated Rayleigh channel compared to the ray-tracer. From this perspective results obtained under the simplified radio channel model can

be too optimistic. Moreover, under the Rayleigh radio channel, the size of a serving cluster is underestimated, i.e., a serving cluster of 2 O-RUs is indicated as the best to provide the highest median throughput gain, while under the realistic ray-tracer radio channel model a cluster size of 3 O-RUs performs the best. The PhD candidate observed an even more negative impact on the evaluation of UCCF MMIMO network of the overly simplified radio channel model when introducing the nonlinear distortion. While setting the IBO of PAs to a relatively high value of 6 dB, for the uncorrelated Rayleigh radio channel, almost no throughput degradation was observed (see Fig. 8 in **[P12]**). In contrast, while utilizing a realistic ray-tracer radio channel model, for the same PAs operation point, the negative impact of nonlinear distortion could be observed (see Fig. 9 in **[P12]**). The overall conclusion is that to obtain reliable results of UCCF MMIMO network evaluation, the simplified system model should not be used. Instead, accurate system models like the one proposed by the PhD candidate should be considered.

- By continuing the studies on the UCCF MMIMO network, the PhD candidate figured out that the Open RAN architecture, due to its disaggregated and virtualized nature, is potentially a good choice for the practical deployment of UCCF MMIMO networks. Thus, in **[P4]** PhD candidate proposed an SCF based on the hierarchical cooperation between the xApp and rApp (see Fig. 1 in **[P4]**). In the proposed solution, the role of the xApp is to manage directly the process of SCF, based on the guidance from rApp. The rApp is proposed by the PhD candidate to host the computationally extensive modules of, e.g., REM and ML, which analyze the network KPIs in order to optimize the xApp performance.

- In **[P4]** the PhD candidate used the adjusted simulation environment proposed in **[P12]** in order to evaluate the SCF from the perspective of the EE. The results presented by the PhD candidate in Fig. 3 of **[P4]** indicate that utilization of the UCCF MMIMO architecture can provide up to 37% EE improvement over the state-of-the-art network centric architecture, where each UE is typically served by only one BS. This is because UCCF MMIMO network offers more degrees of freedom in network configuration, allowing the utilization of available radio resources in a more EE manner, i.e., the observed gain is the result of the joint transmission and interference coordination. Even higher EE improvement is expected while introducing additional energy saving algorithms like cell on/off switching or active antenna selection.

# 4 IoT Use Case

This Chapter presents the contribution of the dissertation to the IoT use case, considering the mMTC service. It starts with a brief overview of the background and related work related to this use case. The original solution is:

- KPI Profile-based Signaling Storm Detection **[P1][P3][P2]**

## 4.1 Background and Related Work

One of the significant groups of devices that are connected to 5G and beyond networks is the so-called Industrial IoT devices [55]. These are mostly stationary, low-data-rate devices, e.g., sensors used in the industry to report the temperature in the furnaces or liquid level in tanks. The main features of IoT devices used in the industry are low hardware complexity, resulting in low computational power and low cost. These allow for massive deployment of such devices in mobile networks that require mMTC service. From this perspective, there is a relatively high probability that some of them can be hacked and used to attack the network infrastructure. A possible attack scenario is the so-called Signaling Storm Attack (SSA), where the adversary utilizes standard mechanisms of the network Control Plane (CP) to cause DoS, e.g., flooding the network CP with invalid or repeated registration requests [56]. Even if these registration requests are rejected, they consume Core Network (CN) resources in the CP that are needed during the authorization process. This impacts the network SE, as the legitimate devices cannot fully utilize the radio resources occupied by the adversary. Moreover, such an attack can cause a negative impact on the EE. While the adversary occupies the control channel, legitimate devices would need to perform frequent retransmission, which can drain their batteries [57]. **It would be beneficial to identify adversary devices, and block them in the early stage of the registration process in the RAN to maintain high SE and EE of the IoT devices.** This can be hard to achieve in the state-of-the-art mobile networks, where both hardware and software are typically provided by a single vendor with only a limited possibility of affecting their configuration. In contrast, the concept of Open RAN enables interaction with RAN through dedicated interfaces, and interception of RAN protocol messages [58]. The O-RAN ALLIANCE identified SSA detection as one of the key problems to be resolved by the development of a dedicated xApp [59], though they did not provide a solution. It should utilize O-RAN interfaces to capture network messages and statistics to detect the abnormal activity of adversaries.

## 4.2 Proposed Solution: KPI Profile-based Signaling Storm Detection

In order to maintain both SE and EE of the IoT devices, in **[P3]** PhD candidate proposed an algorithm to detect and mitigate SSA. The proposed solution relies on the so-called KPI profile (see Fig. 2 in **[P3]**), which can be thought of as a specific case of REM. In detail, it contains the statistics of user connection requests sent within a specific day by the device associated with a given Timing Advance (TA). In this case, TA being the time delay between IoT device and BS is a representation of the position of the device that cannot be easily falsified by the malicious device. More specifically, the distance between IoT device and BS. The principle of the solution proposed by the PhD candidate is that, when the number of connection requests associated with a certain TA exceeds the statistics from KPI profile, the SSA is detected. To protect CN resources PhD candidate proposes to block incoming registration requests associated with this TA. The detailed contribution of the PhD candidate to the KPI profile-based SSA detection, with respect to **[P1][P3][P2]** can be summarized as follows:

- The implementation of SSA detection based on the KPI profile requires access to the messages exchanged between the IoT devices and RAN at the stage of registration, as well as the possibility to block certain connection requests. This can be efficiently done within the Open RAN architecture, providing a dedicated interface exposing such data and control capabilities to the third-party applications. From this perspective, in **[P3]** PhD candidate proposed to implement KPI profile-based SSD in the form of an SSD-xApp placed in Near-RT RIC, and interacting with the RAN with the use of an E2 interface. For the purpose of this implementation, a PhD candidate analyzed the protocol stack of 5G networks, with a focus on the registration and initial access procedures. The analysis led to the conclusion that the malicious network registration requests, causing SSA, can be blocked after exchanging only 3 messages between the adversary IoT device and RAN (see Fig. 1 in **[P3]**). The PhD candidate proposed that the SSD-xApp would use the E2 interface to capture the copy of *Msg2: Random Access Response* containing TA. Then SSD-xApp compares the current statistics of registration requests with a long-term KPI profile to decide on the presence of SSA. If the attack is detected SSD-xApp utilizes the E2 interface to block the incoming registration request from the device with a particular TA at the stage of RAN, to prevent excessive usage of the CN computational resources. For this solution, one of the key principles is that the considered IoT devices are stationary deployed, i.e., associated with a relatively stable TA, which is typical, e.g., in an industry

sensor network.

- To validate the proposed solution the PhD candidate first built a dedicated simulation framework. One of the SSD-xApp algorithm design parameters is the threshold to report attack, i.e., how much the values of KPI profile must be exceeded to indicate SSA. This was a subject of simulation studies done by the Phd candidate in **[P3]**. The results presented in Fig. 3 therein illustrate the probability of the SSA detection, and false alarm. From the perspective of the network management, it is essential to keep the probability of false alarm low, even at the cost of a small degradation of probability of detection, i.e., a small SSA would not be very harmful to the network, compared to the unnecessary rejection of registration requests caused by the false alarms. The results obtained under the scenario with 5 adversaries performing 3 attacks per day (each consisting of 100 registration requests) show that the properly selected threshold can provide a probability of false alarm as low as about 1.5%, while offering the probability of detection at the level of 92%.

- In practice, the TA, which is used by the PhD candidate to distinguish between the adversary and legitimate IoT devices, is quantized by the nature of the 5G protocol. As such, it is associated with some spatial resolution dependent on the utilized sub-carrier spacing. According to the 3GPP specifications for 5G system, the possible values are: 15, 30, 60, 120, and 240 kHz. This results in a spatial resolution ranging from about 5 m for the 240 kHz to about 78 m for the 15 kHz. As a result, sometimes TA of the legitimate devices can overlap with TA of the adversary. In such a case, the SSD-xApp can reject registration requests from the legitimate devices along with those coming from the adversary device. Taking this into account in **[P1]**, the PhD candidate extended the simulation studies to investigate the impact of the TA resolution on the SSD-xApp. The results depicted in Fig. 6 therein indicate that for the subcarrier spacing above 60 kHz, below 20% of registration requests coming from the legitimate devices are being rejected during SSA due to their TA overlapping with adversary TA. In contrast, when the lowest sub-carrier spacing of 15 kHz is selected, over 60% of the registration requests associated with legitimate devices are rejected. This shows that the proposed solution can have different performance while considering the practical limitations of a real 5G network. While rejection of registration requests from some of the legitimate devices can be seen as a drawback of the proposed method, it is significantly less harmful to the network than a serious DoS causing unavailability of the CN service. Moreover, recall that rejection happens only to the new registration requests; the devices already connected to this cell remain unaffected.

- While in **[P1]** and **[P3]** the SSD-xApp proposed by the PhD candidate was evaluated in terms of computer simulations, the next step is to test it against the real 5G network. This was done by the PhD candidate in **[P2]**. The SSD-xApp was deployed at the quasi-RIC platform being communicating with the Amarisoft 5G BS, i.e., exposing the required input data to the SSD-xApp using the Amarisoft Application Programming Interface (API), as it would be the E2 interface. For the evaluation under a real hardware testbed, the PhD candidate used Amarisoft 5G BS utilizing USRP B210 Software-Defined Radio (SDR) as an O-RU. The IoT devices were emulated by the Samsung A52s smartphones, one for the legitimate device, and one for the adversary (see Fig. 2 in **[P2]**). First part of the deployment is creation of the KPI profile. The critical observation is that even if there is only one legitimate, stationary IoT device, the KPI profile contains statistics for several TAs, as a result of channel changes or variance in the TA estimation procedure. This reflects properties of the real network, where TA varies over time. Based on the obtained KPI profile the SSD-xApp was tested by the PhD candidate in terms of the probability of SSA detection and probability of false alarm with respect to different thresholds (similarly to what was tested in **[P3]** using simulations). The results are depicted in Fig. 6 in **[P2]**. It can be seen that the SSD-xApp proposed by the PhD candidate can reduce the probability of false alarm below 0.5%, while offering about 68% probability of SSA detection. This is a good result, as it allows for to detection and mitigation of most of the SSA, but at the same time does not disrupt network operation under a non-disturbed period.

# 5 Summary

The contemporary 5G and future 6G networks are expected to utilize more and more advanced signal processing techniques and configuration options to offer a variety of services to mobile network users in various scenarios, e.g. URLLC service for V2X communications, eMBB service utilizing MMIMO techniques, or mMTC for IoT devices. The fundamental challenge is to properly manage such networks in order to provide high SE and EE. Within this dissertation, the PhD candidate demonstrates how to address these challenges with the use of REMs and ML techniques. In detail, PhD candidate demonstrates how REMs, originally conceived within the domain of Cognitive Radio, can be extended to store multidimensional, location-dependent data, e.g., interference distributions, user mobility, or QoS metrics. While analytical optimization methods require simplifications in system modeling, SE and EE of a realistic 5G/6G network utilizing, e.g., MMIMO, can be successfully optimized with the use of ML techniques. Within the dissertation, the PhD candidate demonstrated how a variety of ML techniques, including RL and FL, can be used to make REMs actionable. These methods enable data-driven decision making in network applications such as cell/antenna activation, beam management, interference modeling for DSA, or PA operation point adjustment. A recurring theme in this work is the practical feasibility of the proposed algorithms. The PhD candidate explored Open RAN architecture as a flexible deployment platform for the proposed REM and ML-based algorithms, leveraging xApps in Near-RT RIC, and rApps in Non-RT RIC for real-time and non-real-time management, respectively. The Ph.D. candidate identifies and addresses specific architectural integration paths and gaps in current standardization in the context of proposed solutions.

In detail, the PhD candidate proposed 10 original solutions demonstrating that location-aware, REM-enhanced ML techniques can significantly improve the SE and EE of next-generation wireless networks. The solutions cover three use cases: V2X Communications (URLLC service), MMIMO communications (eMBB service), and IoT (mMTC service). They are based on 16 original publications, in which, in most cases, the PhD candidate had a leading contribution. These works are published in a top international journals and proceedings of international conferences of high reputation like, e.g., Institute of Electrical and Electronics Engineers (IEEE) Transactions on Intelligent Transportation Systems, IEEE Journal on Selected Areas in Communications, IEEE Communications Magazine, IEEE Access, IEEE International Conference on Computer Communications (INFOCOM), IEEE International Conference on Communications (ICC). Overall, this shows a significant contribution of the PhD candidate to the state-of-the-art know-how and development of the wireless communications scientific area.

Therefore, the dissertation confirms the research claim formulated by the PhD candidate in Chapter 1: **The usage of information stored in Radio Environment Maps can improve spectral and energy efficiency of wireless networks, especially those using massive MIMO, by utilizing machine learning.**

# 6 References

[1] W. Saad, M. Bennis, and M. Chen, "A Vision of 6G Wireless Systems: Applications, Trends, Technologies, and Open Research Problems," *IEEE Network*, vol. 34, no. 3, pp. 134–142, 2020. DOI: 10.1109/MNET.001.1900287.

[2] P. Sroka and A. Kliks, "Towards edge intelligence in the automotive scenario: A discourse on architecture for database-supported autonomous platooning," *Journal of Communications and Networks*, vol. 24, no. 2, pp. 192–208, 2022. DOI: 10.23919/JCN.2022.000005.

[3] F. Guo, F. R. Yu, H. Zhang, X. Li, H. Ji, and V. C. M. Leung, "Enabling Massive IoT Toward 6G: A Comprehensive Survey," *IEEE Internet of Things Journal*, vol. 8, no. 15, pp. 11 891–11 915, 2021. DOI: 10.1109/JIOT.2021.3063686.

[4] M. Alsabah, M. A. Naser, B. M. Mahmmod, *et al.*, "6G Wireless Communications Networks: A Comprehensive Survey," *IEEE Access*, vol. 9, pp. 148 191–148 243, 2021. DOI: 10.1109/ACCESS.2021.3124812.

[5] R. Zi, J. Liu, L. Gu, and X. Ge, "Enabling Security and High Energy Efficiency in the Internet of Things With Massive MIMO Hybrid Precoding," *IEEE Internet of Things Journal*, vol. 6, no. 5, pp. 8615–8625, 2019. DOI: 10.1109/JIOT.2019.2921630.

[6] K. N. R. S. V. Prasad, E. Hossain, and V. K. Bhargava, "Energy Efficiency in Massive MIMO-Based 5G Networks: Opportunities and Challenges," *IEEE Wireless Communications*, vol. 24, no. 3, pp. 86–94, 2017. DOI: 10.1109/MWC.2016.1500374WC.

[7] E. Björnson and L. Sanguinetti, "Scalable Cell-Free Massive MIMO Systems," *IEEE Transactions on Communications*, vol. 68, no. 7, pp. 4247–4261, 2020. DOI: 10.1109/TCOMM.2020.2987311.

[8] H. Q. Ngo, L.-N. Tran, T. Q. Duong, M. Matthaiou, and E. G. Larsson, "On the Total Energy Efficiency of Cell-Free Massive MIMO," *IEEE Transactions on Green Communications and Networking*, vol. 2, no. 1, pp. 25–39, 2018. DOI: 10.1109/TGCN.2017.2770215.

[9] M. Giordani, M. Polese, M. Mezzavilla, S. Rangan, and M. Zorzi, "Toward 6G Networks: Use Cases and Technologies," *IEEE Communications Magazine*, vol. 58, no. 3, pp. 55–61, 2020. DOI: 10.1109/MCOM.001.1900411.

[10] S. E. Trevlakis, A.-A. A. Boulogeorgos, D. Pliatsios, *et al.*, "Localization as a Key Enabler of 6G Wireless Systems: A Comprehensive Survey and an Outlook," *IEEE Open Journal of the Communications Society*, vol. 4, pp. 2733–2801, 2023. DOI: 10.1109/OJCOMS.2023.3324952.

[11] J. A. del Peral-Rosado, R. Raulefs, J. A. López-Salcedo, and G. Seco-Granados, "Survey of Cellular Mobile Radio Localization Methods: From 1G to 5G," *IEEE Communications Surveys & Tutorials*, vol. 20, no. 2, pp. 1124–1148, 2018. DOI: 10.1109/COMST.2017.2785181.

[12] H. B. Yilmaz, T. Tugcu, F. Alagöz, and S. Bayhan, "Radio environment map as enabler for practical cognitive radio networks," *IEEE Communications Magazine*, vol. 51, no. 12, pp. 162–169, 2013. DOI: 10.1109/MCOM.2013.6685772.

[13] P. Tengkvist, G. P. Koudouridis, C. Qvarfordt, M. Dryjanski, and M. Cellier, "Multi-dimensional radio service maps for position-based self-organized networks," in *2017 IEEE 22nd International Workshop on Computer Aided Modeling and Design of Communication Links and Networks (CAMAD)*, 2017, pp. 1–6. DOI: 10.1109/CAMAD.2017.8031530.

[14] A. S. Abdalla, P. S. Upadhyaya, V. K. Shah, and V. Marojevic, "Toward Next Generation Open Radio Access Networks: What O-RAN Can and Cannot Do!" *IEEE Network*, vol. 36, no. 6, pp. 206–213, 2022. DOI: 10.1109/MNET.108.2100659.

[15] O-RAN ALLIANCE WG1, "O-RAN Architecture Description, v.13.0," O-RAN ALLIANCE, TS, Feb. 2025.

[16] H. X. Nguyen, K. Sun, D. To, Q.-T. Vien, and T. A. Le, "Digital Twin for O-RAN Toward 6G," *IEEE Communications Magazine*, vol. 63, no. 3, pp. 174–181, 2025. DOI: 10.1109/MCOM.003.2400016.

[17] E. Björnson, L. Sanguinetti, J. Hoydis, and M. Debbah, "Optimal Design of Energy-Efficient Multi-User MIMO Systems: Is Massive MIMO the Answer?" *IEEE Transactions on Wireless Communications*, vol. 14, no. 6, pp. 3059–3075, 2015. DOI: 10.1109/TWC.2015.2400437.

[18] E. Björnson, E. G. Larsson, and M. Debbah, "Massive MIMO for Maximal Spectral Efficiency: How Many Users and Pilots Should Be Allocated?" *IEEE Transactions on Wireless Communications*, vol. 15, no. 2, pp. 1293–1308, 2016. DOI: 10.1109/TWC.2015.2488634.

[19] N. Kato, B. Mao, F. Tang, Y. Kawamoto, and J. Liu, "Ten Challenges in Advancing Machine Learning Technologies toward 6G," *IEEE Wireless Communications*, vol. 27, no. 3, pp. 96–103, 2020. DOI: 10.1109/MWC.001.1900476.

[20] R. S. Sutton and A. G. Barto, *Reinforcement Learning: An Introduction*. Cambridge, MA, USA: A Bradford Book, 2018, ISBN: 0262039249.

[21] R. Hall and C. Chin, “"vehicle sorting for platoon formation: Impacts on highway entry and throughput",” *Transportation Research Part C: Emerging Technologies*, vol. 13, no. 5, pp. 405–420, 2005, ISSN: 0968-090X. DOI: https://doi.org/10.1016/j.trc.2004.09.001. [Online]. Available: http://www.sciencedirect.com/science/article/pii/S0968090X06000040.

[22] L. Xu, L. Y. Wang, G. Yin, and H. Zhang, “Communication Information Structures and Contents for Enhanced Safety of Highway Vehicle Platoons,” *IEEE Transactions on Vehicular Technology*, vol. 63, no. 9, pp. 4206–4220, 2014.

[23] R. Reddy G and R. R, “"An Empirical study on MAC layer in IEEE 802.11p/WAVE based Vehicular Ad hoc Networks",” *Procedia Computer Science*, vol. 143, pp. 720–727, 2018, 8th International Conference on Advances in Computing & Communications (ICACC-2018), ISSN: 1877-0509. DOI: https://doi.org/10.1016/j.procs.2018.10.443. [Online]. Available: http://www.sciencedirect.com/science/article/pii/S1877050918321410.

[24] M. Sybis, P. Kryszkiewicz, and P. Sroka, “On the Context-Aware, Dynamic Spectrum Access for Robust Intraplatoon Communications,” *Mobile Information Systems*, vol. 2018, pp. 1–16, Jun. 2018. DOI: 10.1155/2018/3483298.

[25] J. Konečný, H. B. McMahan, D. Ramage, and P. Richtárik, “Federated Optimization: Distributed Machine Learning for On-Device Intelligence,” *CoRR*, vol. abs/1610.02527, 2016. arXiv: 1610.02527. [Online]. Available: http://arxiv.org/abs/1610.02527.

[26] Y.-N. R. Li, B. Gao, X. Zhang, and K. Huang, “Beam Management in Millimeter-Wave Communications for 5G and Beyond,” *IEEE Access*, vol. 8, pp. 13 282–13 293, 2020. DOI: 10.1109/ACCESS.2019.2963514.

[27] F. Abinader, C. Rom, K. Pedersen, S. Hailu, and N. Kolehmainen, “System-Level Analysis of mmWave 5G Systems with Different Multi-Panel Antenna Device Models,” in *2021 IEEE 93rd Vehicular Technology Conference*, 2021, pp. 1–6. DOI: 10.1109/VTC2021-Spring51267.2021.9449044.

[28] M. Hoffmann and H. Bogucka, “Localization techniques for 5g radio environment maps,” in *Cognitive Radio-Oriented Wireless Networks*, A. Kliks, P. Kryszkiewicz, F. Bader, *et al.*, Eds., Cham: Springer International Publishing, 2019, pp. 232–246, ISBN: 978-3-030-25748-4.

[29] J. Hwang, H. Yun, Y. Suh, J. Cho, and D. Lee, "Development of an rtk-gps positioning application with an improved position error model for smartphones," *Sensors*, vol. 12, no. 10, pp. 12 988–13 001, 2012, ISSN: 1424-8220. DOI: 10.3390/s121012988. [Online]. Available: https://www.mdpi.com/1424-8220/12/10/12988.

[30] H. Tataria, M. Shafi, A. F. Molisch, M. Dohler, H. Sjöland, and F. Tufvesson, "6G Wireless Systems: Vision, Requirements, Challenges, Insights, and Opportunities," *Proceedings of the IEEE*, vol. 109, no. 7, pp. 1166–1199, 2021. DOI: 10.1109/JPROC.2021.3061701.

[31] E. Björnson, J. Hoydis, and L. Sanguinetti, "Massive MIMO Networks: Spectral, Energy, and Hardware Efficiency," *Foundations and Trends® in Signal Processing*, vol. 11, no. 3-4, pp. 154–655, 2017, ISSN: 1932-8346. DOI: 10.1561/2000000093. [Online]. Available: http://dx.doi.org/10.1561/2000000093.

[32] Y. Jin, N. Duffield, A. Gerber, *et al.*, "Characterizing data usage patterns in a large cellular network," in *Proceedings of the 2012 ACM SIGCOMM workshop on Cellular networks: operations, challenges, and future design*, 2012, pp. 7–12.

[33] M. Z. Shafiq, L. Ji, A. X. Liu, and J. Wang, "Characterizing and modeling internet traffic dynamics of cellular devices," *ACM SIGMETRICS Performance Evaluation Review*, vol. 39, no. 1, pp. 265–276, 2011.

[34] E. Oh, K. Son, and B. Krishnamachari, "Dynamic Base Station Switching-On/Off Strategies for Green Cellular Networks," *IEEE Transactions on Wireless Communications*, vol. 12, no. 5, pp. 2126–2136, May 2013, ISSN: 1558-2248. DOI: 10.1109/TWC.2013.032013.120494.

[35] Z. Zheng, J. Zhang, X. Wu, D. Liu, and L. Tian, "Zero-Forcing Precoding in the Measured Massive MIMO Downlink: How Many Antennas Are Needed?" *International Journal of Antennas and Propagation*, vol. 2019, pp. 1–10, Apr. 2019. DOI: 10.1155/2019/3518691.

[36] F. Han, S. Zhao, L. Zhang, and J. Wu, "Survey of Strategies for Switching Off Base Stations in Heterogeneous Networks for Greener 5G Systems," *IEEE Access*, vol. 4, pp. 4959–4973, 2016, ISSN: 2169-3536. DOI: 10.1109/ACCESS.2016.2598813.

[37] A. A. Abdulkafi, T. S. Kiong, D. Chieng, A. Ting, and J. Koh, "Energy Efficiency Improvements in Heterogeneous Network Through Traffic Load Balancing and Sleep Mode Mechanisms," *Wireless Personal Communications*, vol. 75, no. 4, pp. 2151–2164, Apr. 2014, ISSN: 1572-834X. DOI: 10.1007/s11277-013-

1460-x. [Online]. Available: https://doi.org/10.1007/s11277-013-1460-x.

[38] E. Björnson, L. Sanguinetti, J. Hoydis, and M. Debbah, "Optimal Design of Energy-Efficient Multi-User MIMO Systems: Is Massive MIMO the Answer?" *IEEE Transactions on Wireless Communications*, vol. 14, no. 6, pp. 3059–3075, 2015. DOI: 10.1109/TWC.2015.2400437.

[39] K. Senel, E. Björnson, and E. G. Larsson, "Joint Transmit and Circuit Power Minimization in Massive MIMO With Downlink SINR Constraints: When to Turn on Massive MIMO?" *IEEE Transactions on Wireless Communications*, vol. 18, no. 3, pp. 1834–1846, 2019. DOI: 10.1109/TWC.2019.2897655.

[40] J. Hoydis, S. ten Brink, and M. Debbah, "Massive MIMO in the UL/DL of Cellular Networks: How Many Antennas Do We Need?" *IEEE Journal on Selected Areas in Communications*, vol. 31, no. 2, pp. 160–171, 2013. DOI: 10.1109/JSAC.2013.130205.

[41] X. Gao, O. Edfors, F. Tufvesson, and E. G. Larsson, "Massive MIMO in Real Propagation Environments: Do All Antennas Contribute Equally?" *IEEE Transactions on Communications*, vol. 63, no. 11, pp. 3917–3928, 2015. DOI: 10.1109/TCOMM.2015.2462350.

[42] N. Islam, A. Alazab, and M. Alazab, "A Reinforcement Learning Based Algorithm Towards Energy Efficient 5G Multi-Tier Network," in *2019 Cybersecurity and Cyberforensics Conference (CCC)*, 2019, pp. 96–101.

[43] J. YE and Y. J. Zhang, "DRAG: Deep reinforcement learning based base station activation in heterogeneous networks," *IEEE Transactions on Mobile Computing*, pp. 1–1, 2019.

[44] A. I. Abubakar, O. Onireti, Y. Sambo, L. Zhang, G. K. Ragesh, and M. Ali Imran, "Energy Efficiency of Open Radio Access Network: A Survey," in *2023 IEEE 97th Vehicular Technology Conference (VTC2023-Spring)*, 2023, pp. 1–7. DOI: 10.1109/VTC2023-Spring57618.2023.10200477.

[45] O-RAN ALLIANCE WG1, "O-RAN Network Energy Savings Use Cases Technical Report 1.0," TR, Mar. 2023.

[46] E. Björnson, J. Hoydis, M. Kountouris, and M. Debbah, "Massive MIMO Systems With Non-Ideal Hardware: Energy Efficiency, Estimation, and Capacity Limits," *IEEE Transactions on Information Theory*, vol. 60, no. 11, pp. 7112–7139, 2014. DOI: 10.1109/TIT.2014.2354403.

[47] E. G. Larsson and L. Van Der Perre, "Out-of-Band Radiation From Antenna Arrays Clarified," *IEEE Wireless Communications Letters*, vol. 7, no. 4, pp. 610–613, 2018. DOI: 10.1109/LWC.2018.2802519.

[48] C. H. Azolini Tavares, J. C. Marinello Filho, C. M. Panazio, and T. Abrão, "Input Back-Off Optimization in OFDM Systems Under Ideal Pre-Distorters," *IEEE Wireless Communications Letters*, vol. 5, no. 5, pp. 464–467, 2016. DOI: 10.1109/LWC.2016.2585556.

[49] E. Dahlman, S. Parkvall, and J. Sköld, "Chapter 4 - LTE—An Overview," in *5G NR: the Next Generation Wireless Access Technology*, E. Dahlman, S. Parkvall, and J. Sköld, Eds., Academic Press, 2018, pp. 39–55, ISBN: 978-0-12-814323-0. DOI: https://doi.org/10.1016/B978-0-12-814323-0.00004-1. [Online]. Available: https://www.sciencedirect.com/science/article/pii/B9780128143230000041.

[50] S. Bassoy, H. Farooq, M. A. Imran, and A. Imran, "Coordinated Multi-Point Clustering Schemes: A Survey," *IEEE Communications Surveys Tutorials*, vol. 19, no. 2, pp. 743–764, 2017. DOI: 10.1109/COMST.2017.2662212.

[51] H. Wang, X. Tao, and P. Zhang, "Adaptive Modulation for Dynamic Point Selection/Dynamic Point Blanking," *IEEE Communications Letters*, vol. 19, no. 3, pp. 343–346, 2015. DOI: 10.1109/LCOMM.2015.2391259.

[52] O. T. Demir, E. Bjornson, and L. Sanguinetti. 2021.

[53] J. Zheng, J. Zhang, E. Björnson, Z. Li, and B. Ai, "Cell-Free Massive MIMO-OFDM for High-Speed Train Communications," *IEEE Journal on Selected Areas in Communications*, vol. 40, no. 10, pp. 2823–2839, 2022. DOI: 10.1109/JSAC.2022.3196088.

[54] H. A. Ammar, R. Adve, S. Shahbazpanahi, G. Boudreau, and K. V. Srinivas, "Downlink Resource Allocation in Multiuser Cell-Free MIMO Networks With User-Centric Clustering," *IEEE Transactions on Wireless Communications*, vol. 21, no. 3, pp. 1482–1497, 2022. DOI: 10.1109/TWC.2021.3104456.

[55] E. Sisinni, A. Saifullah, S. Han, U. Jennehag, and M. Gidlund, "Industrial Internet of Things: Challenges, Opportunities, and Directions," *IEEE Transactions on Industrial Informatics*, vol. 14, no. 11, pp. 4724–4734, 2018. DOI: 10.1109/TII.2018.2852491.

[56] J. Cao, M. Ma, H. Li, *et al.*, "A Survey on Security Aspects for 3GPP 5G Networks," *IEEE Comm. Surveys & Tutorials*, vol. 22, no. 1, pp. 170–195, 2020. DOI: 10.1109/COMST.2019.2951818.

[57] E. Bout, V. Loscri, and A. Gallais, "HARPAGON: An Energy Management Framework for Attacks in IoT Networks," *IEEE Internet of Things Journal*, vol. 9, no. 20, pp. 19 959–19 970, 2022. DOI: 10.1109/JIOT.2022.3172849.

[58] M. Dryjański, Ł. Kułacz, and A. Kliks, "Toward Modular and Flexible Open RAN Implementations in 6G Networks: Traffic Steering Use Case and O-RAN xApps," *Sensors*, vol. 21, no. 24, p. 8173, 2021.

[59] O-RAN ALLIANCE WG1, "Use Cases Detailed Specification, v.9.0," Tech. Rep., Oct. 2022. [Online]. Available: `https://orandownloadsweb.azurewebsites.net/specifications`.

# 7 Publications Reprint

## 7.1 Publication [P1]

M. Hoffmann, S. Janji, A. Samorzewski, L. Kułacz, C. Adamczyk, M. Dryjański, P. Kryszkiewicz, A. Kliks, and H. Bogucka, "Open RAN xApps Design and Evaluation: Lessons Learnt and Identified Challenges," *IEEE Journal on Selected Areas in Communications*, vol. 42, no. 2, pp. 473–486, 2024.

MNiSW Points: 200

Number of citations:

- according to Web of Science: 13
- according to Google Scholar: 38

mgr inż. Marcin Hoffmann
Instytut Radiokomunikacji, Politechnika Poznańska
ul. Polanka 3, 60-965 Poznań

Poznań, 30 sierpnia 2024 r.

# OŚWIADCZENIE W SPRAWIE AUTORSTWA PRACY

Oświadczam, że w pracy:

*M. Hoffmann et al., "Open RAN xApps Design and Evaluation: Lessons Learnt and Identified Challenges" IEEE Journal on Selected Areas in Communications, tom 42, numer 2, strony 473-486, luty 2024*

mój udział polegał na:

- Zaproponowaniu i zbadaniu dwóch algorytmów zgodnych z architekturą otwartej sieci dostępowej O-RAN. Pierwszy algorytm polegał na wykorzystaniu Mapy Środowiska Radiowego do inteligentnego przydzielania użytkownikom wiązek w sieci M-MIMO. Drugi wykorzystywał uczenie maszynowe i historyczne dane z sieci do wykrywania ataków typu ang. Signaling Storm.
- Przeprowadzeniu symulacji komputerowych dla obu zaproponowanych algorytmów
- Współautorstwie tekstu artykułu, oraz koordynacji uwzględnia uwag recenzentów w tekście artykułu

Mój procentowy udział w powstanie pracy szacuję na: 20%

.....

Podpis

dr hab. inż. Paweł Kryszkiewicz, prof. PP
Instytut Radiokomunikacji, Politechnika Poznańska
ul. Polanka 3, 60-965 Poznań

Poznań, 30 sierpnia 2024 r.

# OŚWIADCZENIE W SPRAWIE AUTORSTWA PRACY

Oświadczam, że w pracy:

*M. Hoffmann et al., "Open RAN xApps Design and Evaluation: Lessons Learnt and Identified Challenges" IEEE Journal on Selected Areas in Communications, tom 42, numer 2, strony 473-486, luty 2024*

mój udział polegał na:

- Koordynacja wkładów w rozdziale 4
- Korekta tekstu

Mój procentowy udział w powstanie pracy szacuję na: 5%

Podpis

mgr inż. Salim Janji
Instytut Radiokomunikacji, Politechnika Poznańska
ul. Polanka 3, 60-965 Poznań

Poznań, 30th of August 2024 r.

# AUTHROSHIP AND ENGAGEMENT DECLARATION

Hereby, I declare that regarding the publication underneath:

*M. Hoffmann et al., "Open RAN xApps Design and Evaluation: Lessons Learnt and Identified Challenges," in IEEE Journal on Selected Areas in Communications, vol. 42, no. 2, pp. 473-486, Feb. 2024*

My contribution was the following:

- Performing a literature review of materials describing open-source projects implementing RAN software, RAN Intelligent Controller (RICs), Service Management and Orchestration (SMO), core network (CN), and RAN simulators.
- Creating a theoretical comparison of functionalities and an interoperability analysis of four major open-source projects (OSC, OAI, ONF, OAIC).
- Writing section III: O-RAN DEPLOYMENTS - OPEN-SOURCE PLATFORMS COMPARISONS

I assess my contribution to this paper to be around: 15%

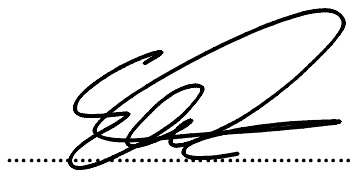

.....

Signature

dr inż. Łukasz Kułacz
Instytut Radiokomunikacji, Politechnika Poznańska
ul. Polanka 3, 60-965 Poznań

Poznań, 30 sierpnia 2024 r.

# OŚWIADCZENIE W SPRAWIE AUTORSTWA PRACY

Oświadczam, że w pracy:

*M. Hoffmann et al., "Open RAN xApps Design and Evaluation: Lessons Learnt and Identified Challenges" IEEE Journal on Selected Areas in Communications, tom 42, numer 2, strony 473-486, luty 2024*

mój udział polegał na:

- Implementacji części rozwiązań (TS-xApp)
- Instalacji, konfiguracji i testowaniu części platform (ONF)
- Redagowaniu fragmentów artykułu

Mój procentowy udział w powstanie pracy szacuję na: 15%

Kułacz Kułacz

Podpis

mgr inż. Adam Samorzewski
Instytut Radiokomunikacji, Politechnika Poznańska
ul. Polanka 3, 60-965 Poznań

Poznań, 30 sierpnia 2024 r.

# OŚWIADCZENIE W SPRAWIE AUTORSTWA PRACY

Oświadczam, że w pracy:

*M. Hoffmann et al., "Open RAN xApps Design and Evaluation: Lessons Learnt and Identified Challenges" IEEE Journal on Selected Areas in Communications, tom 42, numer 2, strony 473-486, luty 2024*

mój udział polegał na:

- opracowaniu kodu aplikacji xApp dla systemu O-RAN, a konkretnie *Traffic Steering xApp* oraz *QoS-based Resource Allocation xApp*,
- przygotowaniu tekstu dla rozdziału V (pt. *xApp Implementation-Driven Conclusions*) oraz częściowej edycji tekstu dla rozdziału VI (pt. *Challenges for O-RAN/Incentives to O-RAN Triggered Research*).

Mój procentowy udział w powstanie pracy szacuję na: 15%

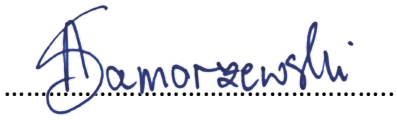

.....

Podpis

dr inż. Marcin Dryjański
Instytut Radiokomunikacji, Politechnika Poznańska
ul. Polanka 3, 60-965 Poznań

Poznań, 30 sierpnia 2024 r.

# OŚWIADCZENIE W SPRAWIE AUTORSTWA PRACY

Oświadczam, że w pracy:

*M. Hoffmann et al., "Open RAN xApps Design and Evaluation: Lessons Learnt and Identified Challenges" IEEE Journal on Selected Areas in Communications, tom 42, numer 2, strony 473-486, luty 2024*

mój udział polegał na:

- Przygotowaniu treści oraz rysunków do rozdziału II „O-RAN ARCHITECTURE, RIC AND USE CASES"
- Współpracy przy treści do rozdziału VI „CHALLENGES FOR O-RAN/INCENTIVES TO O-RAN TRIGGERED RESEARCH"
- Współpracy przy tworzeniu koncepcji publikacji
- Przeglądzie całego artykułu

Mój procentowy udział w powstanie pracy szacuję na: 15%

.....

Podpis

dr hab. inż. Adrian Kliks, prof. PP
Instytut Radiokomunikacji, Politechnika Poznańska
ul. Polanka 3, 60-965 Poznań

Poznań, 30 sierpnia 2024 r.

# OŚWIADCZENIE W SPRAWIE AUTORSTWA PRACY

Oświadczam, że w pracy:

*M. Hoffmann et al., "Open RAN xApps Design and Evaluation: Lessons Learnt and Identified Challenges" IEEE Journal on Selected Areas in Communications, tom 42, numer 2, strony 473-486, luty 2024*

mój udział polegał na:

- Współ-koordynowaniu pracy nad artykułem
- Udziale w dyskusjach merytorycznych
- Pisaniu fragmentów tekstu
- Pracy edycyjnej
- Pracy nad poprawkami do artykułu zgłoszonymi przez recenzentów

Mój procentowy udział w powstanie pracy szacuję na: 5%

Adrian Kliks

.....

Podpis

prof. dr hab. inż. Hanna Bogucka
Instytut Radiokomunikacji, Politechnika Poznańska
ul. Polanka 3, 60-965 Poznań

Poznań, 30 sierpnia 2024 r.

# OŚWIADCZENIE W SPRAWIE AUTORSTWA PRACY

Oświadczam, że w pracy:

*M. Hoffmann et al., "Open RAN xApps Design and Evaluation: Lessons Learnt and Identified Challenges" IEEE Journal on Selected Areas in Communications, tom 42, numer 2, strony 473-486, luty 2024*

mój udział polegał na:

- Pisaniu fragmentów tekstu
- Pracy edycyjnej
- Pracy nad poprawkami do artykułu zgłoszonymi przez recenzentów

Mój procentowy udział w powstanie pracy szacuję na: 5%

H. Bogucka

.....

Podpis

mgr inż. Cezary Adamczyk
Instytut Radiokomunikacji, Politechnika Poznańska
ul. Polanka 3, 60-965 Poznań

Poznań, 2 września 2024 r.

# OŚWIADCZENIE W SPRAWIE AUTORSTWA PRACY

Oświadczam, że w pracy:

*M. Hoffmann et al., "Open RAN xApps Design and Evaluation: Lessons Learnt and Identified Challenges" IEEE Journal on Selected Areas in Communications, tom 42, numer 2, strony 473-486, luty 2024*

mój udział polegał na:

- opisaniu problemu wykrywania i rozwiązywania konfliktów sterowania aplikacji xApp w sieciach O-RAN.

Mój procentowy udział w powstanie pracy szacuję na: 5%


.....

Podpis

# Open RAN xApps Design and Evaluation: Lessons Learnt and Identified Challenges

Marcin Hoffmann, *Graduate Student Member, IEEE*, Salim Janji, *Graduate Student Member, IEEE*, Adam Samorzewski, *Graduate Student Member, IEEE*, Łukasz Kułacz, *Member, IEEE*, Cezary Adamczyk, Marcin Dryjański, *Senior Member, IEEE*, Pawel Kryszkiewicz, *Senior Member, IEEE*, Adrian Kliks, *Senior Member, IEEE*, and Hanna Bogucka, *Senior Member, IEEE*

***Abstract*— The concept of open radio access networks (RAN) creates numerous opportunities for developing new technology and economy branches. At the same time, a flexible and modular approach in the disaggregated RAN entails the need for careful design of the overall RAN architecture and the implementation and deployment process of new applications. It is assumed that dedicated and specialized software companies may deliver the latter. A joint effort must be guaranteed among different sectors (industry, academia, and standardization bodies) to make the whole process efficient, safe, and reliable. Here, one of the critical driving forces origins from the open-source community that often stimulates the development of a specific technology. In this paper, we address the challenges that have to be faced by third-party application developers in the context of Open RAN. Based on many implemented applications (called xApps or rApps), we compare various available solutions. We pose the most critical issues that must be tackled in the near future to stimulate the progress in open RAN development further. In particular, we compare available open platforms for xApp development and testing. We present the details of implementing four selected applications describing the problems encountered. The paper is split into two logical parts - first, we identify the key ambiguities related to the development of new xApps, which address more complicated use cases like beam management. In the second part, we present the challenges associated with detailed software implementation in existing open platforms. In the first case, we show that dedicated beam mobility management xApp can reduce beam switches and keep beam failures low. However, it requires access to detailed localization information. Similarly, the signaling storm detection xApp provides expected performance under the assumption that there is access to detailed information on, e.g., time advance resolution parameter. We conclude here that several aspects still need to be well-defined to allow smooth software implementation; these include the rules for data reporting in time, parameters available in service models, and localization features. Concerning the second logical part, related to low-level implementation, we compare the numerical results of the traffic steering and quality-of-service-based resource allocation xApps and draw conclusions related to implementation and testing. In particular, we point out problems associated with the simulator, the software, and conflicts inside. Finally, we identify the key challenges which should be treated as incentives for joint academia-industry cooperation in the field of Open RAN. Thus, the paper presents the lesson learned during the first years of xApp development.**

***Index Terms*— Open RAN, 5G, 6G, xApp, ML.**

## I. Introduction

DISAGGREGATION, openness, flexibility, and modality are the new paradigms attributed to the next generation of wireless communication networks. Contrary to the traditional and prevalent approach to the radio access network (RAN) design, where most of the RAN elements are provided by one vendor and are hidden in the *black-box*, the concept of the Open RAN assumes that potentially multiple players provide dedicated RAN modules. Such a modular approach allows operators to modify and improve only selected network functionalities instead of completely replacing the black-boxed software. It is the network operator who decides what functions in the network should be activated or deactivated, which should be improved, kept unchanged, or uninstalled. These modifications can be done by adequately manipulating the installed software modules. This, in turn, opens the possibility for incremental system modifications following the concept of continuous integration and continuous development (CI/CD). The standardization activities related to Open RAN, which are led by the O-RAN ALLIANCE [1] emphasize the trend towards open and modular RAN. The set of standards released by this organization specifies the overall Open RAN architecture, requirements, and functionalities. In particular, new and open interfaces have been proposed to incentivize xApp/rApp providers to implement and deliver new algorithms dealing with specific aspects of wireless communications. However, along with the numerous and evident benefits of opening and disaggregating the RAN, significant challenges are related to the practical implementation of such a vibrant concept. First, the way for implementation and deployment of new xApps/rApps has to be unified and automated so

Manuscript received 22 December 2022; revised 2 August 2023; accepted 7 September 2023. Date of publication 28 November 2023; date of current version 17 January 2024. This work was in part by the National Centre for Research and Development in Poland within the 5GStar Project on "Advanced Methods and Techniques for Identification and Counteracting Cyberattacks on 5G Access Network and Applications under Grant CYBERSECIDENT/487845/IV/NCBR/2021. *(Corresponding author: Marcin Hoffmann.)*

Marcin Hoffmann, Salim Janji, Adam Samorzewski, Łukasz Kułacz, Pawel Kryszkiewicz, Adrian Kliks, and Hanna Bogucka are with the Rimedo Labs, 61-131 Poznań, Poland, and also with the Institute of Radiocommunications, Poznan University of Technology, 60-965 Poznań, Poland (e-mail: marcin.hoffmann@put.poznan.pl).

Cezary Adamczyk is with the Institute of Radiocommunications, Poznan University of Technology, 60-965 Poznań, Poland.

Marcin Dryjański is with the Rimedo Labs, 61-131 Poznań, Poland.

Color versions of one or more figures in this article are available at https://doi.org/10.1109/JSAC.2023.3336190.

Digital Object Identifier 10.1109/JSAC.2023.3336190

that every interested software provider may deliver valuable contributions to the community. Next, opening the RAN part to numerous, often external providers causes various security issues which must be tackled carefully. Also, the coexistence of applications from different xApp/rApp providers may lead to potential consistency and confluence problems and prospective conflicts. These topics are now the subject of both academic and industrial debate. However, despite all the efforts put into the foundation of an open and disaggregated RAN environment, the technology is still in its early stage of development. Although precisely specified in O-RAN ALLIANCE standards, the architecture is still modified and being adjusted to address new challenges and reply to the recent findings. Moreover, practical implementations also need more trusted simulation environments, commonly agreed ways for providing new software modules, methods of testing, and performance benchmarking.

These problems are particularly important from the perspective of the above-mentioned xApp/rApp providers, who still have limited possibilities of delivering new applications. When new xApp/rApp is being implemented, it has to be first simulated reliably and comprehensively, it has to be tested against numerous threats and risks, and the whole process has to be automated. Nowadays, it is not the case. This paper addresses this niche by presenting the observations gained in the years of xApp/rApp design and implementation. By implementing some xApps/rApps of different kinds, types, and scopes of functionalities, we are able to discuss the current state of the development art from the perspective of the xApp/rApp provider. We present our lessons learned and gained experience to identify key challenges, standardization, and research directions. To avoid the promotion of any commercial solutions and to promote open science, we concentrate on the Open RAN applications prepared with the openly available software and mutually compare the achieved results.

The paper is structured as follows - it contains four logical sections. First, a concise review of what O-RAN is is provided; next, the existing implementation frameworks are discussed and compared; third, we present four original xApp implementation results, discussing their performance and drawing conclusions about the whole design process. Its novelty, both comparative and scientific, can be summarized as follows:

- we present in detail four xApps, illustrating the message exchange between the particular O-RAN blocks; the proposed new methods solve particular research challenges related to wireless networks while preserving full compliance with the O-RAN standard requirements;
- we provide a detailed comparison of currently available software platforms and discuss their pros and cons; the comparison shall be the basis for the selection of open platforms for performing new research in the O-RAN domain,
- we provide an analysis of the identified O-RAN architectural ambiguities based on the challenges that have been faced during the implementation of the xApps,
- analogously, we share our synthetic observations in the context of current limitations related to xApp implementation; both ambiguities and limitations constitute the true research challenges for future O-RAN solutions.

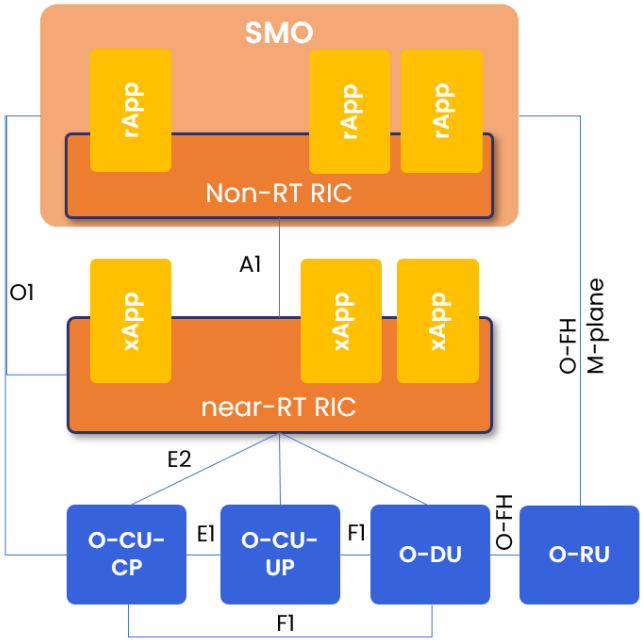


Fig. 1. O-RAN architecture, as defined by O-RAN ALLIANCE.

To precisely reflect the above topics, this paper is split into seven chapters, where the following section recaps the O-RAN architecture, RAN Intelligent Controller, and proposed use cases. Chapter 3 overviews the open-source platform for xApp development and testing. Next, Chapters 4 and 5 present the ways of four xApp implementations and draw conclusions related to architecture ambiguities and practical implementation, respectively. Chapter 6 discusses the key research challenges. The whole work is summarized in Chapter 7.

## II. O-RAN Architecture, RIC and Use Cases

**O-RAN ALLIANCE** [1] is the main standardization body specifying the O-RAN reference architecture, interfaces, deployment scenarios, use cases, etc. In addition to this, it also leads official plugfests, provides an open-source implementation of the O-RAN stack, and interoperability and testing of the O-RAN solutions. This chapter provides an overview of the O-RAN architecture defined by O-RAN ALLIANCE, focusing on the **RAN Intelligent Controller (RIC)** along with xApps.

### A. O-RAN Architecture

The O-RAN architecture is defined in [2] and builds upon 3GPP RAN standards towards openness and intelligence by adopting RAN splits, new interfaces, RICs, and Service Management and Orchestration (SMO) (see Figure 1). It adopts split 2 (also referred to as higher-layer split, HLS) between PDCP and RLC protocols within the New Radio (NR) air interface stack; and split 7.2x (also referred to as lower-layer split, LLS) within the PHY layer. The corresponding elements

of O-RAN are called **O-RAN Central Unit (O-CU)**, **O-RAN Distributed Unit (O-DU)**, and **O-RAN Radio Unit (O-RU)**.

O-CU is further split into the control plane (O-CU-CP), which covers Radio Resource Control (RRC) with Packet Data Convergence Protocol-Control Plane (PDCP-C) protocols, and the user plane (O-CU-UP) covering and Service Data Adaptation Protocol (SDAP) with PDCP-User Plane (PDCP-U). O-DU, in turn, encompasses Radio Link Control (RLC), Medium Access Control (MAC), and a high-physical layer, including the MAC scheduler. Finally, O-RU includes low-physical layer functionality like Orthogonal Frequency Division Multiple Access (OFDMA) processing, beamforming, and Radio Frequency (RF) front end.

An essential element introduced in O-RAN is the RAN Intelligent Controller (RIC), a separated-out entity from the processing units that allow access to RRM functions. RIC is split onto **Non-Real-Time RIC (Non-RT RIC)** and **Near-Real-Time RIC (Near-RT RIC)**. The former works in the timescale of above 1 s, is used for non-real-time radio resource management, higher layer procedure optimization, and policy optimization in RAN, and enables the artificial intelligence (AI) and machine learning (ML) workflow for RAN components. In addition, it provides policy-based guidance for the applications in Near-RT RIC and delivers Enrichment Information (EI) for the Near-RT RIC's applications. Near-RT RIC, on the contrary, is part of the RAN to enable control and optimization of algorithms for radio resource management, and it works with the control loop in a timescale of longer than 10 ms and shorter than 1 s utilizing the use-case specific applications called xApps.

O-RAN ALLIANCE also specifies new interfaces, including Open Fronthaul (OFH), which connects O-DU to O-RU, E2, and A1 serving as control loop connections, and O1, O2, OFH M-plane - i.e. management interfaces. O-CU-CP, O-CU-UP, and O-DU are called "E2 Nodes" in the O-RAN architecture. This is because they are connected via the E2 interface to the Near-RT RIC, by which their functionality can be controlled through external applications, i.e., the abovementioned xApps.

Among the mentioned interfaces, E2 and A1 are considered important in this paper, namely:

- **E2 interface**, which creates a closed loop within the RAN domain, is used to send the RIC control and policy toward E2 Nodes and to obtain the feedback from E2 Nodes to the Near-RT RIC.
- **A1 interface**, which provides policies, EI, and ML models towards Near-RT RIC and gets the policy feedback back to the Non-RT RIC.

### *B. O-RAN Near-RT RIC, xApps and Use Cases*

Near-RT RIC is a software platform allowing the xApps to control the RAN. This is supported by the RAN and UE databases storing the network state, along with xApp management, security, and conflict mitigation functions. It enables near real-time control optimization of the E2 Nodes via actions sent over the E2 interface, including CONTROL, INSERT, POLICY, and REPORT services [2]. The detailed description of Near-Real-Time RIC is defined in [3].

E2 Nodes mentioned above expose parameters and functionalities towards RIC through the E2 interface, which xApps and rApps can use to tune the behavior of the radio network. Examples of xApps are mobility, interference or beamforming management, traffic steering, load balancing, slice control, admission control, signaling anomaly detection, etc.

In this paper, we focus on xApps which are applications run at the Near-RT RIC. An xApp provides information to the Near-RT RIC about the data types it consumes and about outputs it produces. Such an application is independent of the Near-RT RIC and may be developed by a third-party provider. It controls a specific RAN functionality exposed by the E2 Node using the E2 service models (E2SM). The current service models include KPM (Key Performance Measurements), RC (RAN Control), NI (Network Interface), and CCC (Cell Configuration and Control) [3].

To summarize, Near-RT RIC is one of the critical elements in the O-RAN architecture, which allows feeding intelligence into the operations of the RAN. It creates a platform on which the software providers could build per-use case RRM algorithms to allow the optimization of radio resources for specific scenarios, also known as use cases, which are covered in the following subsection. The use cases, based on which xApps and rApps are developed, are defined in [4] and are based on the requirements of O-RAN ALLIANCE members. Those requirements also come as input to the O-RAN ALLIANCE's standardization in the form of priorities from Telecom Infra Project, an organization that brings together several operators. TIP's OpenRAN program supports the development of disaggregated and interoperable RAN solutions based on service provider requirements [5]. Specifically, within the RRM part, TIP defines the RAN Intelligence and Automation subgroup (RIA), aiming to develop and deploy AI-based xApps for use cases like RRM, SON, Massive MIMO, etc.

The current set of O-RAN ALLIANCE use cases, as specified in [4] covers 23 items and includes, among others: V2X HO management, UAV radio resource allocation, QoE optimization, traffic steering, Massive MIMO BF optimization, RAN sharing, QoS-based resource optimization, RAN slice SLA assurance, Dynamic Spectrum Sharing, indoor positioning, signaling storm protection, congestion protection, energy saving, etc.

Based on the use case definition and description defined by O-RAN WG1, other working groups define parameters and procedures to create a normative way for interoperable interfaces to allow interworking between vendors. Examples include parameters and new service models at the E2 interface or policy definitions for those use cases at the A1 interface.

## III. O-RAN Deployments—Open-Source Platforms Comparisons

To date, several open-source projects are used to implement Open RAN systems. Such platforms may provide the entire stack, including RAN software, RICs, SMO, or a subset of those components. This section presents several platforms and briefly describes the modules they provide. Since a complete end-to-end deployment or simulation of 5G systems requires implementing both the RAN and Core Network (CN) domains,

we also mention the 5G CN implementation that each project leverages in its platform while discarding any LTE Evolved Packet Core (EPC) implementations. We also highlight a few differences between them and conclude with an evaluation of each platform based on the documentation they provide and the hands-on experience gained while testing some of these projects.

### A. OpenAirInterface (OAI) [6]

OpenAirInterface (OAI) Software ALLIANCE (OSA) was established in 2014 by the non-profit organization EURECOM. Among others, OAI provides the following projects.

*1) OAI 5G CN and EPC CN:* these projects provide 5G standalone (SA) CN and 5G Non-standalone (NSA) CN network functions (NFs) implementations, respectively.

*2) OAI 5G RAN:* this OAI project implements software for NSA and SA gNB, eNB, 5G NSA and SA UE, and LTE UE.

*3) OAI's MOSAIC5G:* this project develops control and orchestration frameworks on top of OAI's RAN and CN modules, allowing for monitoring and controlling of the network. It includes Trirematrics and FlexCN platforms in its roadmap that provide SMO and CN control modules and a FlexRIC software we introduce below.

*a) E2 agent and FlexRIC:* FlexRIC provides an SDK that can implement a multi-vendor O-RAN compliant RT RIC that is specialized for a particular service (e.g., slice control, traffic control, etc.) with built-in service models (SMs) and support for the creation of further SMs [7]. OAI's FlexRIC design is meant to be extensible and compact with minimum overhead. Furthermore, unlike RICs provided by other projects, it follows an event-driven rather than poll-driven approach. The main modules contain an agent library that deploys E2-compatible agents in a base station and a server library that manages agents' connections, stores network information in the radio network information base (RNIB), and handles E2SM subscriptions. These subscriptions can be established by iApps, which are controller internal applications that either implement a specific control logic or expose E2SM subscriptions to xApps deployed on external controllers through different interfaces.

The agent library is radio access technology (RAT) and vendor-neutral, allowing multi-RAT and multi-vendor deployments. Agents can also connect to multiple controllers through the server library, which provides isolation between them. Furthermore, a virtualization layer with an agent can be implemented on top of a server deployment which allows recursive agent-server layers. This is beneficial in cases where we want to abstract out RAT heterogeneity or delegate control to multiple controllers per slice using different SMs.

### B. O-RAN Software Community (OSC) [8]

OSC is founded by O-RAN and Linux Foundation, and it aims to provide software that is fully O-RAN compliant. The project generally encompasses all O-RAN-related components, RAN elements, and interfaces. We present some OSC projects below.

*1) O-DU:* This project is composed of two sub-projects. *O-DU* Low focuses on the baseband PHY reference design, including three interfaces: L1/Fronthaul;*O-DU Low*/*O-DU High*, and *O-DU Low*/accelerator. *O-DU High*, is responsible for implementing L2 blocks for 5G NR SA mode that include NR MAC, NR Scheduler, and NR RLC layers. *O-DU High* also provides *DU APP*, which configures and manages all O-DU operations, and interfaces with external entities (e.g., O-CU, RIC, etc.). Finally, it implements an O1 module to handle O1 communication.

*2) O-CU: O-CU* was supposed to provide O-CU UP. However, it seems the project was disbanded, and instead, OSC uses a binary test stub provided by Radisys for end-to-end testing.

*3) Near-RT RIC:* This project provides an initial RIC platform to support xApps with limited support for O1, A1, and E2 interfaces.

*4) Non-RT RIC:* In the context of Non-RT RIC, OSC provides a Non-RT RIC Control Panel, which provides administrative and operator functions through A1, like policy management and Near-RT RICs setup. Also, an A1 Simulator module is implemented, which terminates the A1 interface and allows testing of the Non-RT RIC without deploying Near-RT RICs. To support management functions, an SMO project implements O1 and O1/VES interfaces responsible for the configuration, management, and report handling of NFs. Finally, and OAM project provides administrative and operator functions for O-RAN components.

### C. Open Networking Foundation (ONF) [9]

ONF was established as a project to develop software-defined networking (SDN) technologies, and currently, it is driven by operators and a community of developers. ONF developed its SD-RAN project, which provides a Near-RT RIC adapted to O-RAN specifications in its latest version at the time of writing this paper. Besides the Near-RT RIC, which is called *$\mu$ONOS-RIC* due to its implementation being based on ONF's *ONOS* platform, SD-RAN provides open-source components for the control and user planes of CU and DU, a RAN simulator, and xApps development SDK. The CU/DU modules are derived from OAI's 5G RAN project (see III-A.2). SD-RAN leverages a microservice approach that is compatible with O-RAN specifications

### D. Open AI Cellular (OAIC) [10]

Founded by USA National Science Foundation, OAIC uses OSC's Near-RT RIC (see III-B.3) on top of srsRAN [11], which provides components for implementing a complete end-to-end 4G and 5G NSA networks. For E2 implementation, OAIC leverages POWDER's E2 agents [12] in their architecture. Moreover, OAIC provides OAIC-T, an open-source AI cellular testing framework for testing xApps. It consists of a server that establishes the simulation environment according to input from configuration files and the actors that perform the test actions received from the server. Each actor contains an AI core component, and it can communicate with xApps or rApps under test and srsUEs to generate radio testing signals. Within

its framework, srsRAN provides srsUE to deploy 4G/5G UEs using ZeroMQ, srsENB as an eNB implementation with 5G NSA support, and srsEPC as a lightweight implementation of LTE EPC. At the same time, it lacks an implementation of 5G CN (they advertise using Open5GS [13] for 5G CN).

### *E. OpenRAN Gym [14], [15], [16]*

Combining several software frameworks, OpenRAN Gym allows data acquisition of RAN performance indicators from emulators or testbeds and RAN control to test O-RAN-compliant solutions powered by AI/ML. The platform encompasses the following.

- Open experimental wireless platforms for acquiring RAN data and testing solutions (e.g., Colosseum, which is the world's largest wireless network emulator, Arena testbed, etc.),
- RAN software implementations using srsRAN or OAI stacks,
- SCOPE framework, which is used for data collection and control of RAN during run-time which also adds further networking and control functionalities (e.g., slicing) to the RAN software, and
- ColO-RAN provides a lightweight RIC adapted from OSC's RIC, allowing xApps/rApps to monitor KPMs and control the RAN.

Using these tools, solutions can be validated on the Colosseum emulator, for example, and then ported to heterogeneous testbeds seamlessly as described in [14]

### *F. Comparison of Platforms and Their Compatibility*

Table I lists the perceived differences between the implementation options. Furthermore, in Fig. 2, we present the components used in currently available solutions and their combinations, and we also include other open-source CN projects not mentioned in our earlier discussion, which are compatible with some RAN implementations.

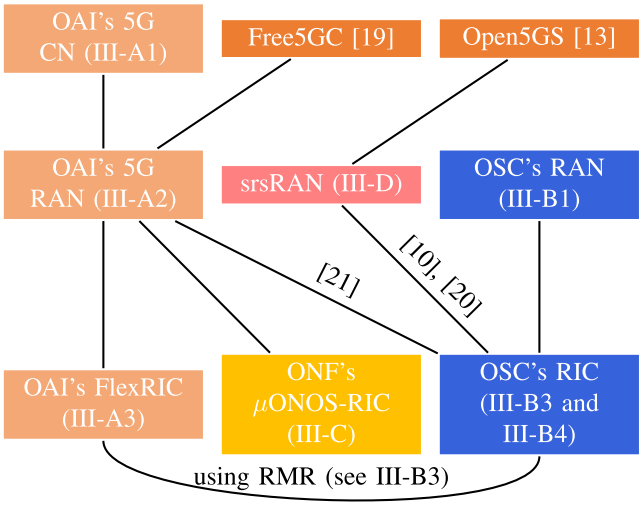


Fig. 2. Projects for building and testing a complete end-to-end 5G system with Open RAN functionalities and their compatibility. Starting from the top, the first row lists 5G CN projects, the second row mentions 5G RAN implementations, and the last row lists RIC implementations. Colors indicate the vendor: OAI (light orange); OSC (blue); ONF (yellow); srsRAN (red), and other vendors (dark orange).

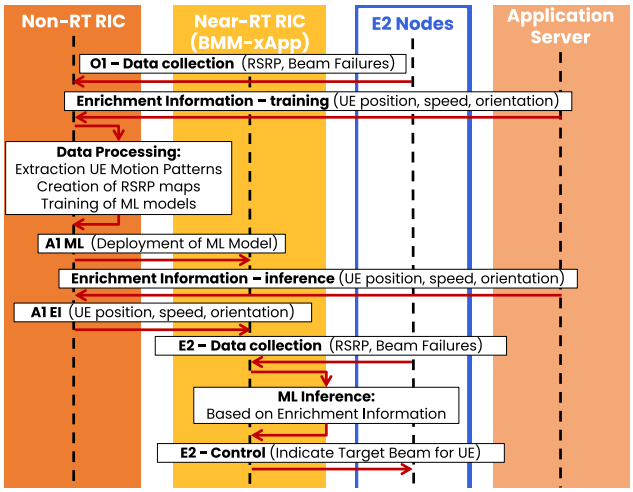


Fig. 3. The information flow between the BMM-xApp, and other O-RAN entities.

## IV. xApp Implementation-Driven Ambiguities Related to O-RAN Architecture

While standardization bodies define how the O-RAN architecture should be implemented to address various applications, some ambiguities are observed while working on specific use cases. Here we focus on Beam Mobility Management (BMM-xApp) and Signaling Storm Detection xApps (SSD-xApp). The use cases related to those xApps are analyzed within O-RAN ALLIANCE's documents.

### *A. Example RRM xApp - Beam Mobility Management*

One of the key technologies used in 5G NR is a Grid of Beams (GoB) beamforming. A UE is assigned to a specific beam (out of a static set) based on the downlink measurements of Reference Signal Received Power (RSRP). The measurements are typically carried using the Synchronization Signal Block (SSB), i.e., every 20 ms [22]. SSBs transmission for all beams lasts 5 ms. In this case, the main challenge is to deal with radio-link failures due to rapid changes in the radio environment when the UE moves fast. To avoid such situations, there is a need for AI/ML-assisted algorithms that utilize context information, e.g., UE location, to infer future target beams, possibly minimizing the number of beam reselections [23].

The challenge discussed above is addressed by the use case "AI/ML-assisted Beam Selection Optimization" from O-RAN ALLIANCE [23]. Its definition could be more specific, although O-RAN ALLIANCE specified utilized entities (e.g., Near-RT RIC) and interfaces (e.g., O1 and A1-ML). Below, we propose the remaining elements of the solution to the challenge mentioned above using the ML algorithm and data collected from E2 nodes. The information flow between the BMM-xApp, and other O-RAN entities is depicted in Fig. 3. The central concept of this development is to perform the most extensive computations related to data analysis and

TABLE I
COMPARISON OF EACH PLATFORM'S OPEN-SOURCE IMPLEMENTATIONS AND EXEMPLAR XAPPS

| | **OAI** | **OSC** | **ONF** | **OAIC** |
|---|---|---|---|---|
| CN | • OAI CN | • No CN or EPC | • OMEC CN | • LTE EPC |
| RAN | • Better CPU and memory utilization than srsRAN [17]<br>• Multiple UE simulation<br>• MOSAIC5G E2 agents<br>• No O1 interface implementation | • Radisys CU lacks integration with open-source CU and RU implementations<br>• DU and DU App<br>• O1 interface | • Leverages OAI's RAN modules<br>• ONF's own RAN simulator with more features and capability to simulate a large number of UEs | • Easier to modify [17]<br>• POWDER [12] E2 agents within srsRAN stack<br>• Single UE simulation<br>• No F1 interface for CU/DU split<br>• No O1 interface |
| RIC | • Better CPU, memory utilization, and latency than OSC's RIC [7]<br>• Recursive agent library for the abstraction of underlying topology<br>• iApps have less overhead than xApps | • Completely O-RAN compliant<br>• All O-RAN components including Non-RT RIC<br>• Requires more resources due to containerization and microservice structure | • $\mu$ONOS-RIC using ONOS modules<br>• Code used in previous SDN activities and is therefore reliable<br>• Good documentation<br>• Latest version is fully O-RAN compliant | • Uses OSC's RIC |
| xApps | • Key performance metrics (KPMs) monitoring, slice monitoring and control, and traffic controller | • Anomaly detection, HelloWorld xApp, HW-go xApp, KPM monitoring, QoE predictor, RIC APP ML, RIC Measurement Campaign xApp, traffic steering, and GS-lite stream processing engine [18] | • onos-kpimon (KPM monitoring), onos-rsm (slice management), onos-mho (mobile handover for mobility management), onos-mlb (load balancing between cells), onos-pci (for managing PCI resources) | • Besides the xApps provided by OSC, OAIC introduced their own KPI monitor and slice control xApps |
| Lang.<br>Lic. | • *C/C++*<br>• OAIPL1.1 | • *Python*, *Go* , and *C/C++*<br>• ALV2 mostly besides CCLA4I | • *Go*<br>• ALV2 | • *C/C++*<br>• GAGPLV3 |

training of the ML model in the Non-RT RIC. The Near-RT RIC receives the pre-trained ML model and uses it to infer UE target beams. First, the O1 interface is configured to provide Non-RT RIC with users' RSRP measurements and beam failure statistics from E2 nodes. The beam failure statistics are used to monitor ML model accuracy, i.e., when the observed number of beam failures increases, the ML model re-training is triggered. RSRP measurements are used to create an RSRP map for each beam, following the Radio Environment Map (REM) concept [24]. For this purpose, EI, specifically: the position, speed, and orientation of each user, is obtained from the Application Server (specifically - the location server). The obtained data are being processed in the Non-RT RIC. First, the location information is analyzed to extract the UE Motion Patterns. They are, e.g., histograms that represent the probability of future UE speed and orientation while in a particular location. A representative example can be a vehicular scenario. When users encounter a road intersection, most turn right, while only a few turn left. Next, the RSRP map is created, i.e., for each beam associated with a considered BS, the spatial distribution of RSRP is created by aligning location information from the external Application Server, and RSRP collected from E2 Nodes. The alignment can be done by comparing the data if these are accurately timestamped. These RSRP maps capture specific radio environment characteristics, e.g., obstacles in a particular location can block some beams. Both UE Motion Patterns and RSRP maps represent the radio environment and are used to train ML models. The ML models can be trained according to different optimization goals, e.g., minimizing beam reselections while maintaining users' QoS or maximizing SNR. Reinforcement Learning (RL) can be used as it learns through interaction with the environment (wireless network) [25]. After the training, the obtained ML model is transferred to Near-RT RIC via the A1 ML interface and deployed in the BMM-xApp to make inferences on target beams for UEs. To provide input to the deployed ML model, EI (precisely: location information) must be sent from the external Application Server to the BMM-xApp. This is done in a two-stage manner: first, EI is sent to the Non-RT RIC, and next, it is forwarded to the Near-RT RIC through the A1-EI. In addition, the E2 interface is configured to collect information about the RSRP and beam failures. First, the UE's localization is used in the ML inference performed by BMM-xApp, i.e., the target beam is selected. Secondly,

the BMM-xApp monitors beam failures to validate the ML model performance. If too many beam failures occur, it is a signal that the ML model is outdated. In such a case BMM-xApp can temporarily switch to the *emergency* mode in which some analytical beam management procedure based on RSRP reports is performed (e.g., [26]) until a new ML model is provided from the Non-RT RIC.

Recalling that this use-case is at its early stage of specification in O-RAN ALLIANCE, still, some implementation ambiguities are observed:

- **Location information** is currently not discussed within the O-RAN specifications; it is only mentioned as a specific type of EI message. However, it could be used by many xApps, and some of its aspects should be discussed within O-RAN ALLIANCE workgroups. The localization server should, at minimum, provide the following:
  - *Localization technique* that was used to obtain the location information; (There are many localization techniques of significantly different accuracy, e.g., an accuracy of 10 meters characterizes standard Global Navigational Satellite System (GNSS) receiver, while Real Time Kinematics (RTK) introduces only a centimeter-level error.)
  - *Available measurements* that can be provided together with the user's position, e.g., user's speed and bearing;
  - *Report time-intervals*; (If the location information is provided only once per second, the performance of BMM-xApp could be degraded as beam management can be triggered every 20 ms [22].)
  - *Delay* associated with passing the UE's localization information, which is required by Near-RT RIC, and transferred via Non-RT RIC as shown in Fig. 3. (Note that the recently introduced Y1 interface between Near-RT RIC and the Application Server can significantly lower this delay.)
- **Alignment of reported data in time**, i.e., precise timestamping of both RSRP and location information at the moment of measurement is crucial, e.g., for high-speed users who can travel a few meters during the time between the position was obtained, and the EI was received in Non-RT RIC.
- **ML Modules**
  - *Deployment of ML Modules within O-RAN architecture* should be clarified. At the current stage of standardization, there are several options in SMO and Non-RT RIC architecture where ML model training can be performed. For example, training can be performed either by a vendor-dependent module, dedicated rApp, within the rApp, or even outside of the Non-RT RIC and SMO.
  - *A1 interface* specifications, at their current state, do not explicitly define ML Model service operations [27].
- **E2 interface** lacks actions related to beam management [28], i.e., at this stage, it is unclear how BMM-xApp would enforce switching a particular user to the given beam.

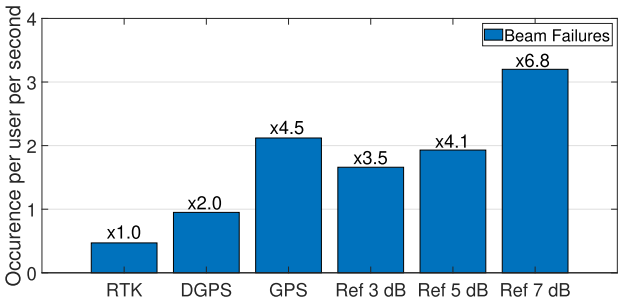


Fig. 4. Number of beam failures per user, per second versus the utilized localization technique.

To highlight the importance of the quality of location information for the BMM-xAPP relying on the REM, we have performed computer simulation studies in the scenario described in detail in [29]. The scenario considers a single Massive MIMO BS, operating at mmWaves frequency band, that supports eight beams. Within this cell, we have placed 300 UEs moving along a street, with a speed of 25 m/s, to reflect the road scenario. We have tested the BMM-xApp following the optimization goal of minimization of beam reselections while avoiding beam failures (situations when, for a given UE, the target beam has 8 dB higher RSRP than the current/source beam) under three localization techniques: RTK, Differential Global Navigation Satellite System (DGPS), and standard GPS. The standard deviations of their corresponding localization error are as follows [30]: 1 cm, 1 m, 6 m, for RTK, DGPS, and GPS, respectively. We have compared the BMM-xApp against the *Ref* beam management algorithm that relies on the static power margin [26], i.e., reselection happens for a given UE, when the target beam has RSRP higher by the margin over the current/source beam's RSRP. We have considered margins of 3, 5, and 7 dB, respectively. The resultant number of beam failures per user per second is depicted in Fig. 4. RTK provides almost perfect location information, but some beam failures occur due to channel variations. However, when additionally localization accuracy is degraded, more beam failures arise, i.e., compared to the RTK, it is about 2.0 and 4.5 times more beam failures while utilizing DGPS and GPS, respectively. Comparing the BMM-xApp that uses RTK against the *Ref* approach based on the static margin, it can be seen that number of beam failures is 3.5, 4.1, and 6.8 times higher for power margins of 3, 5, and 7 dB respectively. The BMM-xApp that utilizes slightly less accurate DGPS also outperforms *Ref*. However, when only standard GPS is available for the BMM-xApp, the accuracy of location information is not good enough, and the number of observed beam failures is worse than in the case of *Ref* with a power margin of 3 dB, and 5 dB. Thus, the information about the supported localization technique would be necessary for designing robust xApps.

### *B. Example Security xApp - Signalling Storm Detection*

The signaling storm attack is aimed at causing Denial of Service (DoS) in a network by occupying radio resources in a CP by an adversary or malfunctioning device [31]. Such

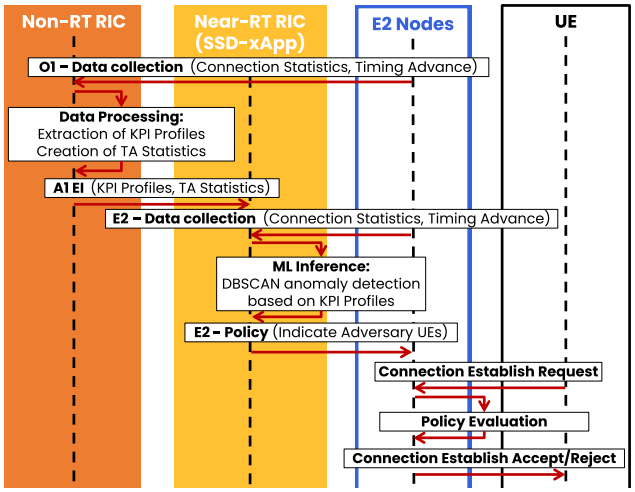


Fig. 5. The information flow between the SSD-xApp, and other O-RAN entities.

devices can persistently send control messages like registration requests that will be rejected after validation in the CN or can intentionally disconnect from the network after a successful registration. Such behavior is hazardous in the Internet of Things (IoT) networks. The IoT devices have low complexity and can be relatively easily hacked by adversaries to flood networks with CP messages, e.g., adversaries can install on the IoT device software that will constantly restart the device triggering the registration procedure. It is essential to notice that such a device will be authorized to connect to the network, and as such hard to be detected [32]. From this perspective, it is essential to equip 5G networks with an intelligent mechanism that can detect the signaling storm as close to its origin as possible, possibly at the stage of RAN. After detection, further communications with malfunctioning devices should stop to prevent flooding the CN with CP messages.

This xApp addresses a use case following requirements of O-RAN Signalling Storm Protection from [4] with a slight modification: here, both attack detection and mitigation are integrated into a single SSD-xApp to reduce the amount of communication overhead. The O-RAN ALLIANCE specifies the high-level roles of the O-RAN entities and utilized interfaces for this use case. As the other details, e.g., ML method and data exchanged with the E2 node, are missing, we propose our solution below, keeping it fully compliant with O-RAN specification. The SSD-xApp utilizes the Timing Advance (TA) parameter being computed and exchanged at the early stage of the device's registration procedure (i.e., Msg2: Random Access Response [33]). As this indirectly characterizes the distance electromagnetic wave travels between the UE and the BS, it is difficult to be falsified. As such, it can filter malfunctioning devices, creating an increased number of connection-establishment requests without interrupting CN functions, e.g., device authentication. The information flow between the SSD-xApp and other O-RAN entities is depicted in Fig. 5. It starts with configuring the O1 interface to provide Non-RT RIC with connection statistics, including registration requests, RRC connection establishment requests, etc., and related TAs extracted from Msg2. This data is processed within the Non-RT RIC to produce the so-called Key Performance Indicator (KPI) Profiles [34]. The KPI Profiles are the long-term statistics of a given KPI, e.g., the mean and standard deviation of the number of connection-establishment requests over the day. In addition, TA related to connection statistics is analyzed, e.g., in the form of histograms. The A1-EI is used to send KPI Profiles and TA statistics observed over a long period in Non-RT RIC to the SSD-xApp residing in Near-RT RIC. This step should repeat periodically, e.g., twice a day, or on an event basis, e.g., when a high number of new UEs is deployed in a factory. The SSD-xApp obtains from E2 nodes temporal information about the connection statistics (e.g., number of connection-establish requests over the last 5 minutes) and related TAs. Next, the SSD-xApp compares the long-term KPI Profile with temporal connection statistics computing the so-called anomaly values. It utilizes the unsupervised learning clustering algorithm Density-Based Spatial Clustering of Applications with Noise (DBSCAN) to detect the abnormal activity of users in the network, i.e., signaling storm. When the signaling storm is detected, the SSD-xApp analyses statistics of TA to produce a policy that will filter out connection establishment requests related to users associated with those TAs. The formulated policy is sent to the E2 Nodes via the E2 interface. Based on that policy, the E2 Node can accept or reject the connection-establish requests sent by the UEs by comparing their TAs with blacklisted TAs defined in the policy.

As with the BMM-xApp, also here some implementation ambiguities can be mentioned:

- **Resolution of TA** relies on the network configuration. A low resolution of TA will increase the number of devices having the same TA and potentially blocked. From this perspective, it might be useful to provide the xApp with some extra historical information about the UE context from the CN registers, to distinguish an adversary from a legitimate user, e.g., historical channel state information, network identifiers, etc.
- **Non-RT RIC** architecture is not specified in terms of storage processing of EI [35]. Regarding the KPI Profiles utilized by the SSD-xApp, it is unclear whether there would be some dedicated vendor-dependent Non-RT RIC module for processing and storing such xApp-provider-defined EI or whether some rApp would realize this functionality.
- **E2 interface** policy service is not clearly defined within the O-RAN specifications [28]. It might happen that E2 Nodes would not support rejecting connection establish requests based on the TA parameter.

To highlight the importance of the ambiguities mentioned above, we have studied the potential impact of the TA resolution on the number of legitimate users being rejected from the network when adversary activity is detected. We are considering a simulation setup described in our previous work [36]: a single cell of IIoT network of a 2 km radius, with 100 randomly located, stationary legitimate IIoT sensors and five adversaries. Intervals between legitimate users' connection requests follow the exponential distribution with a

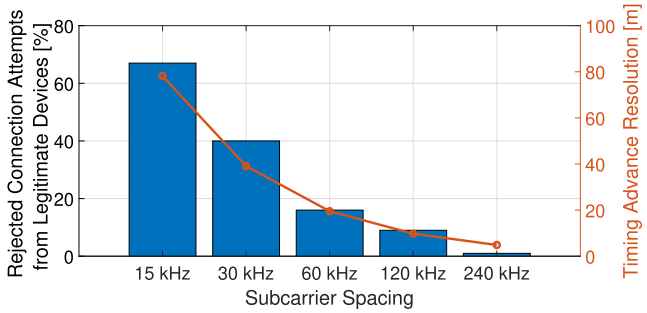


Fig. 6. The ratio of rejected connection attempts from legitimate devices, and calculated TA resolution versus the subcarrier spacing.

rate parameter equal to 5 per hour. Each adversary performs, on average three attacks per day consisting of 100 consecutive connection requests sent within the intervals of 5 s. Because the TA resolution is a function of the utilized subcarrier spacing, we have considered values proper for a 5G system: 15, 30, 60, 120, and 240 kHz, respectively. As we see in Fig. 6 the percentage of rejected connection attempts from legitimate devices drops with the subcarrier spacing, as a result of increasing TA resolution. It can be seen that for high values of subcarrier spacing, detection of adversary almost doesn't affect the performance of legitimate users, i.e., all their connection attempts are accepted. This is because of high TA resolution for subcarrier spacing of 240 kHz, i.e., about 5 m. On the other hand, while utilizing low subcarrier spacing of 15 kHz the spatial resolution of TA is significantly decreased to about 78 m. As a result, more than 60% of legitimate devices are rejected from the network because their TA is the same as the TA of the detected adversary.

## V. xApp Implementation-Driven Conclusions

Contrary to the prior chapter, where we focused on the ambiguity related to xApp development, here we concentrate on issues related to the detailed application implementation on selected open RIC platforms. For comparison, we have chosen two xApps - Traffic Steering xApp (TS-xApp) and QoS-Based Resource Allocator xApp (QRA-xApp), which consider use-cases standardized by the O-RAN ALLIANCE specifications [4].

The xApps have been deployed within the environment running on the virtual machine with the Ubuntu operating system (OS). It is based on the architecture packed in Kubernetes pods and Docker images. To ensure proper implementation of the xApps, the following virtual hardware requirements are obligated: a) processor with at least 2 cores, b) Random Access Memory (RAM) with the size of min. 8 GB, c) Read-Only Memory (ROM) with a minimum size of 50 GB, d) Ubuntu OS version 20.04.5 LTS.

### A. Traffic Steering xApp

TS-xApp addresses the use case #5: O-RAN Traffic Steering from [4]. It allows the dynamic switching of mobile users between cells available in the access network. The purpose of such a mechanism is to manage the current mobile traffic

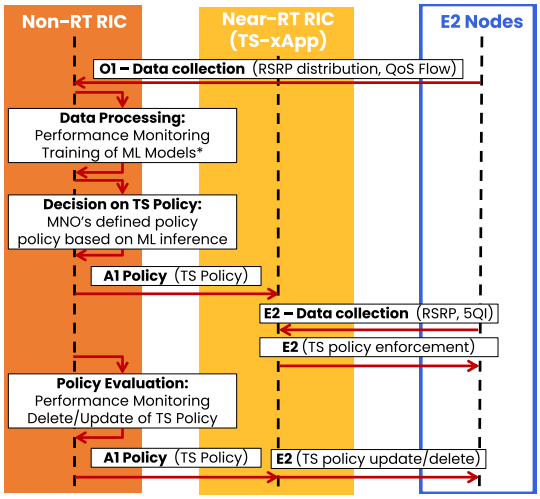


Fig. 7. The information flow between the TS-xApp, and other O-RAN entities.

to ensure the radio system's high performance. Depending on actual needs, the MNO can realize various TS targets such as guaranteeing equal traffic load for all nodes (load balancing), separating users with different Quality-of-Service (QoS) demands (service-based association), supporting the reduction of energy consumption, and many others.

In the TS xApp, the user association is performed through the E2 Interface using an O-RAN-defined handover control mechanism. The decisions about switching users among cells are made based on the RSRP distribution reports received through the E2 Interface and policies that the Non-RT RIC sends through the A1 interface. The rules, which indicate preferred and forbidden cells for a particular UE, can be found inside these policies. The preferences can be oriented to users assigned to a specific slice (slice-oriented approach) or having strictly specified identification (user-centric approach). The A1 policies are exchanged between Non-RT RIC and TS xApp in the form of JavaScript Object Notation (JSON) files, which are prepared according to the schema of the "Traffic Steering Preferences" type standardized by the O-RAN ALLIANCE [4], [37]. The information flow is depicted in Fig. 7.

TS-xApp has been integrated with the SD-RAN environment provided by the ONF; it can handle connections with the $\mu$ONOS RIC components of the SD-RAN. Furthermore, it can interpret the received E2 and A1 messages correctly and suggest (to RIC) performing adequate handover operations, the results of which are reflected in the RAN Simulator. The source code of the xApp can be found in [38]. In Tab. II, the results for the TS xApp performance are presented. The considered, intentionally-simple scenario consisted of two single-cell base stations and a single UE terminal moving between the coverage areas of both BSs. Within the tests, three different UE-oriented policies were enforced. Those policies indicated the preferences for connection handling with the user by a particular cell - PREFER, AVOID, and FORBID. The UE recognized cells marked in a policy with these labels as cells by which the UE should, should not, and must not be served, respectively. Thus, referring to Tab. II, it can be

TABLE II

ASSOCIATION OF THE UE WITHIN THE NETWORK BY THE TS XAPP ACCORDING TO DIFFERENT POLICIES

| POLICY NAME | USER ASSOCIATION TIME PART [%] | | | |
|---|---|---|---|---|
| | ENFORCED FOR 1st CELL | | ENFORCED FOR 2nd CELL | |
| | 1st CELL | 2nd CELL | 1st CELL | 2nd CELL |
| NONE | 50 | 50 | 50 | 50 |
| PREFER | 75 | 25 | 25 | 75 |
| AVOID | 25 | 75 | 75 | 25 |
| FORBID | 0 | 100 | 100 | 0 |

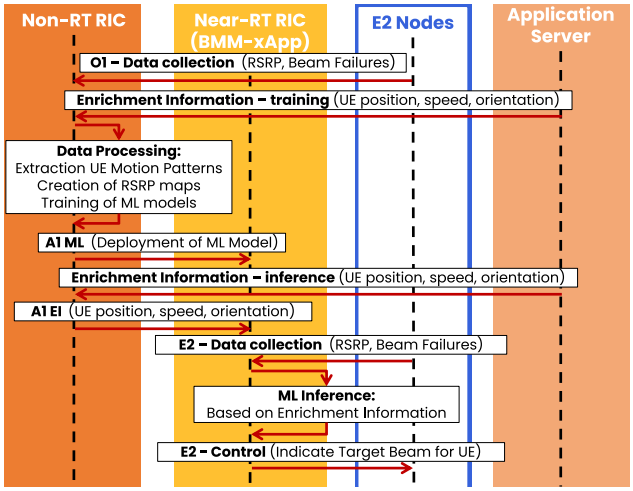


Fig. 8. The information flow between the QRA-xApp, and other O-RAN entities.

observed that when the connection between the user and cell is marked with the PREFER label, this link is handled for 75% of the observation time. The AVOID mark causes the opposite result – the UE is served by such a cell for 25% of the observation time. Next, the FORBID label resulted in not serving the user by a given cell. Finally, in the case where no policy was enforced for the TS xApp, the UE was associated with a cell based on the RSRP report. Thus, it was noticed the user was served for 50% of the observation time by one cell and 50% by another. Please note that the whole TS algorithm could be complemented with other functionalities, such as load balancing between the base station. Thus, for a given service-based user association, the TS should keep the balance between the cell load to optimize the usage of resources. However, to achieve this, the policies shall be generated flexibly, reflecting both operator needs and the current state of the network.

### B. QoS-Based Resource Allocation xApp

QRA-xApp addresses use case no. 8: O-RAN QoS Based Resource Optimization from [4]. It is responsible for splitting radio resources in the form of Physical Resource Blocks (PRBs) among available slices within the network. With the QRA xApp, the MNOs can manipulate the radio resources allocated by the scheduler to manage the networks' performance by allocating more PRBs for high-performance slices (e.g., Mobile Broadband - MBB) and simultaneously reducing the number of resources for slices demanding low data rate (e.g., Voice services).

TABLE III

RADIO RESOURCE ALLOCATION FOR DIFFERENT SCHEMAS WITHIN THE QRA XAPP

| UE ID | 5QI | BANDWIDTH PART [%] | | |
|---|---|---|---|---|
| | | EQUAL | PREFER-3 | RESERVE |
| 1 | 1 | 12.5 | 6.25 | 5 |
| 2 | 2 | 12.5 | 6.25 | 10 |
| 3 | 4 | 25 | 12.5 | 40 |
| 4 | 2 | 12.5 | 6.25 | 10 |
| 5 | 3 | 25 | 62.5 | 30 |
| 6 | 1 | 12.5 | 6.25 | 5 |

This allocation of radio resources is done to meet the SLA targets defined inside policies (passed to xApp in the form of JSON files by the Non-RT RIC through the A1 Interface) by basing on measurement reports received through the E2 Interface for a particular slice served by some gNB. The SLA targets are specified in the A1 policy file as a throughput rate expressed in [bps], which can be translated to the number of needed PRBs (and vice versa) by taking into account current propagation conditions for a slice (e.g., SNR/RSRP distribution, number of active UEs, service/slice types, etc.). This group of SLA targets specified inside A1 policies consists of UE- or slice-oriented parameters such as Guaranteed and Maximum Throughput per Slice, Maximum Throughput per UE, Maximum Number of UEs per Slice, etc. The O-RAN ALLIANCE has defined the used shape of A1 policies as the schema of policy type called "SLA Target" [4], [37]. Fig. 8 depicts the information flow between the involved entities.

QRA-xApp, similarly to TS-xApp, has been integrated and tested using the ONF's SD-RAN environment. The QRA xApp connects to the SD-RAN's $\mu$ONOS RIC components. Thanks to the correct interpretation of received E2 and A1 messages, the xApp performs adequate resource-allocation-related operations, the results of which (delivered via RIC to E2 nodes) could be visible in real-time mode in the form of terminal logs.

In Tab. III, the results for the QRA xApp are presented. The considered scenario consisted of two single-cell base stations and six UEs moving simultaneously between the locations in the coverage of each BSs. Each user served within the network could belong to a different slice. All UEs connected to a specific network cell and using the same service type (denoted by the 5G QoS Identifier – 5QI) were grouped in a particular slice. Within the tests, four service types (5QI equal to 1, 2, 3, or 4) and three different schemas of radio resource allocation (EQUAL, PREFER-X, and RESERVE) have been taken into account. According to the EQUAL approach, all available PRBs were divided among existing slices equally. Next, the PREFER-X schema (where X is the number indicating the service type, i.e., the 5QI, of a particular slice – 1, 2, 3, or 4) shares all the resources among the slices in the ratio of 5:1 for ones with "preferred" service type (5QI) to the rest of them. Finally, the RESERVE approach divides all PRBs within the cell among available slices in the ratio of 5X, where X is the number that indicates the service type of a given slice (5QI). Thus, for our scenario with four different service types (1, 2,

TABLE IV
CHALLENGES FACED DURING xAPP DEVELOPMENT AND TESTING

| Aspect | Challenges |
|---|---|
| Simulator | • Available RAN simulators do not provide complete functionality needed to test different specific practical scenarios (e.g., different network size, base station capabilities, network operation duration, etc.) |
| Conflicts | • Absence of conflict mitigation units prevents testing the operation of multiple xApps working simultaneously<br>• Multiple A1 policies that could be turned on simultaneously should be verified against each other beforehand |
| SDK/API | • Standard compliance: base stations or simulators do not provide the functions or parameters needed for complete O-RAN functionality implementation<br>• Abstraction of O-RAN messages that implement certain functionalities (e.g., RSRP monitoring, handover control, etc.) would simplify xApp development process<br>• Interoperability between components like simulators and RICs<br>• Exemplar xApps should be provided and they should cover the functionality of the platform as much as possible |

3, and 4), the ratio of sharing the resources for RESERVE schema equals 5:10:15:20.

In Table IV, we summarize the challenges faced during the development, deployment, and testing of xApps using different platforms.

## VI. CHALLENGES FOR O-RAN/INCENTIVES TO O-RAN TRIGGERED RESEARCH

Following the discussion on xApp/rApp implementation and deployment issues, we try to identify the key challenges that appear on the Open RAN development path in this section.

### A. Challenge A: The Need for Intelligent Conflict Management

Intelligent RAN control functions enabled in the Near-RT RIC with the introduction of xApps allow flexibility in adapting network operation characteristics. While implementing a single application, there is no need for any mechanism responsible for conflict management; what is necessary is only the subscription functionality so that the particular xApp or rApp can request access to specific parameters or metrics through standardized service models. On the other hand, having multiple xApps/rApps, developed by various third-party providers, working simultaneously in RICs will inevitably lead to conflicts between control actions affecting the E2 Nodes finally. Thus, incorporating two (or more) xApps/rApps immediately entails the need for stable and precise solutions for conflict management [39]. The xApp/rApp developer has to be aware of the applied policy in case of any prospective conflicts - whether any priority or hierarchy between the applications shall be used and how it may impact the functioning of the application. Based on our implementation experience, it is one of the key challenges that must be effectively solved to enable reliable xApp provisioning.

### B. Challenge B: Security

Another critical point that was immediately observable during the implementation of the xApps/rApps is related broadly to Open rAN security - both on the architectural side and from the perspective of xApp/rApp delivery by the third party. When discussing the security of an O-RAN architecture, one should note that the attack surface is expanded compared to the standard radio segment of a mobile communication network. This surface contains “traditional” attacks related to the omnipresent radio transmission medium, cyberattacks related to virtualization (softwarization) of RAN functions, i.e., attacks on xApps, rApps, and edge Artificial Intelligence (AI) algorithms residing in O-RAN and Multi-access Edge Computing entity (MEC), as well as attacks related to O-RAN interfaces.

The O-RAN specification and *openness* of the radio interface poses challenges for the entire network security. Inadequately defined and poorly secured O-RAN applications and interfaces (including the front-haul interface, O1, O2, A1, and E2) can potentially be targets of attacks. Attackers can utilize these new open interfaces to attack the system, which could lead to a denial of service, data tampering, or data leaking, all of which indirectly impact the system’s security. Each O-RAN interface and function may be subject to different threats, and each threat will have a particular impact; thus, for each threat, specific security measures and solutions must be used for all aspects and assets [40]. Finally, AI and ML algorithms residing at the network edge (a consequence of the ML-as-a-Service paradigm for 5G/6G networks) become a target of a new type of attack - attacks on AL/ML. These threats can be classified as (i) *poisoning attacks* manipulating the data or the learning algorithm in the model training phase, (ii) *evasion attacks* aiming at the inference stage (test phase) based on the previously learned model, and (iii) *inference attacks* aiming at recovering the training data or their labels, discovering the model architecture and its parameters [41].

At the same time, O-RAN architecture can increase security in radio access networks because it allows for running xApps in Near-RT RIC, which can be developed to continuously monitor and analyze security threats and protect RAN from malicious and illegal access to network segments. It makes it possible to detect threats much faster before they affect the operation of the entire network. xApps can be developed for specific types of threats in a given network that can be detected closer to their occurrence. AI/ML algorithms can also be designed to improve security, e.g., by detecting various anomalies in radio traffic. Future research should aim to develop such xApps for O-RAN security despite expanded surface attacks.

### C. Challenge C: The Need for Complete Automation and Testing Procedures

Another challenge raised immediately during the implementation of all the applications discussed above is the stringent need for broad automation of the xApp/rApp delivery, testing, and deployment process. As the applications can be tested, verified, and installed manually at the current stage, it is impossible to keep this stage in the future. Thus, based on the gained experience, one of the key challenges at the current stage of O-RAN development is the lack of automation related to testing and installing the xApps/rApps on the RIC platforms. The template-based approach for xApp and rApp development is discussed in [42]. A general automated, distributed, and AI-enabled testing framework has been presented in [43], to test AI models deployed in O-RAN.

This currently requires manual integration of the application every time a new one is to be deployed. There is no unified way to smoothly introduce new/upgraded xApps to the system, which consumes the resources of both the providers and the operators/customers. The xApp providers utilize the resources for this purpose instead of focusing on developing and improving the algorithms. At the same time, the customer/receiver needs to use more time to check that the xApp performs according to its design manually.

### D. Challenge D: Portability

Yet another topic that yields currently cumbersome tasks is the portability of xApps/rApps between RIC platforms. What has been heavily experienced is that having the same core algorithm requires significant manual integration work to deploy it as an xApp on one RIC, with a more or less similar amount of work, when putting the same algorithm onto xApp for a different RIC. There are several reasons influencing this situation. First, the various commercial and open-source RIC platforms have different maturity levels, where each focuses on another aspect. Second, the standardization of the RICs and E2 and A1 interfaces still needs to mature enough to have a clear implementation guide for the vendors. And finally, there is a lack of a standard for SDK/API/CDK such that the xApp/rApp could be ported from one RIC to another with minimal intervention to the packaging of the xApp.

Due to the above, when having an algorithm, the xApp developer needs first to get up to speed with the RIC platform and accompanied SDK to surround the xApp with the proper interfacing. There is yet another aspect to it, which is not directly related to the RIC platform itself but to the corresponding E2 nodes, which it works with. It relates to integrating the RIC with the particular RAN software, which may utilize a different set of, e.g., E2 service models or other versions of the same E2 service model. In such a setup, the xApp may only get some of the required parameters from the E2 node, which the RIC platform works with. This requires modification in the xApp itself so that the algorithm takes into account either fewer parameters or different parameters compared to a different RIC-CU-DU constellation.

### E. Challenge E: Ambiguity in Implementation - Processing Resources Optimization

Finally, from the perspective of xApp/rApp functionality design and testing, the final challenge is related to the ambiguity in implementation. While the O-RAN ALLIANCE defines use cases with examples of messages exchanged between nodes, the xApp/rApp developers should have freedom of implementation limited only by the interface specification. Only in this case long-term development and improvement of applications are possible. It will resemble a market where various products (applications) can compete and the most suitable (for a given network) solution can be implemented. For example, the BMM-xApp, as described in Sec. IV-A, can be implemented using both the ML modules in Non-RT RIC and xApp in Near-RT RIC. However, similar results, i.e., a decision of a beam reselection sent to gNB, can be obtained by a single rApp, xApp, or a combination of rApp and xApp. The various solutions may use different sets of measurements for learning purposes. The problem becomes even more significant while considering a use case not considered by the O-RAN specification. To implement such an xApp/rApp, developers must have sufficient freedom. This shows that the set of parameters exposed on interfaces should be as broad as possible. On the other hand, each Application should be constantly monitored for the amount and type of information exchanged on the interfaces. Additionally, a responsible RIC (directly or indirectly, first to get support from SMO) should take care of the computational and storage resources required by a given application. If unlimited freedom is given to developers, the application may poorly scale with, e.g., the number of UEs or operation time. The application should be *killed* if the limit is reached and reported to the community and developers.

## VII. Conclusion

Open RAN as the technology is still in one of its initial phases of development. Much effort is put toward a precise and adequate definition of various standards, reflecting different aspects of the Open RAN community. Moreover, from a scientific perspective, numerous projects and activities have recently started that target many vivid and essential problems related to the fair functioning of the complete open system. However, the process should also consider the experience gained during initial implementation experiments and deployments. In this paper, we have described the lessons learned during the practical implementation of some xApps, selected based on the indications from the O-RAN ALLIANCE documents. It has been shown that from the perspective of xApp/rApp algorithmic design, the overall architecture still has a bit of ambiguity. It limits the scope of perspective investigation of the proposed solutions. Next, in-detail implementation of the selected applications led to identifying the key modifications and adjustments that could improve the impact of the open-source RIC platforms. Finally, the overall discussion on the xApp development and deployment process allowed us to identify precisely five key challenges that must be handled in the near future. As these challenges impact various aspects of the open RAN concept, it is evident that joint efforts from

academia, standardization body, and industry are necessary. We claim that with tight cooperation between these three sectors, the further development of the open, disaggregated, flexible, and modular radio access networks will be expanded.

## REFERENCES


[1] *O-RAN ALLIANCE*. Accessed: Oct. 8, 2023. [Online]. Available: https://www.o-ran.org

[2] *O-Ran Architecture Description, V.8.0*, O-RAN ALLIANCE WG, O-RAN ALLIANCE e.V., Alfter, Germany, Mar. 2023.

[3] *Near-Real-Time Ran Intelligent Controller Near-RT RIC Architecture, V.2.1*, O-RAN ALLIANCE WG3, O-RAN ALLIANCE e.V., Alfter, Germany, 2022.

[4] *Use Cases Detailed Specification, V.8.0*, O-RAN ALLIANCE WG1, O-RAN ALLIANCE e.V., Alfter, Germany, Jul. 2022.

[5] Telecom Infra Project, *Open RAN Project Website*, 501(c)(6) Non-Profit, USA, 2022.

[6] *OpenAirInterface—5G Software Alliance for Democratising Wireless Innovation*. Accessed: Sep. 21, 2022. [Online]. Available: https://openairinterface.org/

[7] R. Schmidt, M. Irazabal, and N. Nikaein, "FlexRIC: An SDK for next-generation SD-RANs," in *Proc. 17th Int. Conf. Emerg. Netw. EXperiments Technol.*, Dec. 2021, pp. 411–425, doi: 10.1145/3485983.3494870.

[8] *O-RAN Software Community*. Accessed: Sep. 13, 2022. [Online]. Available: https://o-ran-sc.org/

[9] *Open Networking Foundation*. Accessed: Oct. 6, 2022. [Online]. Available: https://opennetworking.org/

[10] *Open AI Cellular (OAIC)*. Accessed: Nov. 8, 2022. [Online]. Available: https://www.openaicellular.org

[11] *srsRAN—Your Own Mobile Network*. Accessed: Nov. 23, 2022. [Online]. Available: https://www.srslte.com/

[12] J. Breen et al., "POWDER: Platform for open wireless data-driven experimental research," in *Proc. 14th Int. Workshop Wireless Netw. Testbeds, Experim. Eval. Characterization*. New York, NY, USA: Association for Computing Machinery, Sep. 2020, pp. 17–24.

[13] S. Lee. *Open5GS*. Accessed: Jun. 2, 2022. [Online]. Available: https://open5gs.org/open5gs/

[14] L. Bonati, M. Polese, S. D'Oro, S. Basagni, and T. Melodia, "Open-RAN gym: AI/ML development, data collection, and testing for O-RAN on PAWR platforms," *Comput. Netw.*, vol. 220, Jan. 2023, Art. no. 109502.

[15] L. Bonati, M. Polese, S. D'Oro, S. Basagni, and T. Melodia, "OpenRAN gym: An open toolbox for data collection and experimentation with AI in O-RAN," in *Proc. IEEE Wireless Commun. Netw. Conf. (WCNC)*, Apr. 2022, pp. 518–523.

[16] M. Polese, L. Bonati, S. D'Oro, S. Basagni, and T. Melodia, "ColO-RAN: Developing machine learning-based xApps for open RAN closed-loop control on programmable experimental platforms," *IEEE Trans. Mobile Comput.*, vol. 22, no. 10, pp. 5787–5800, Oct. 2023.

[17] F. Gringoli, P. Patras, C. Donato, P. Serrano, and Y. Grunenberger, "Performance assessment of open software platforms for 5G prototyping," *IEEE Wireless Commun.*, vol. 25, no. 5, pp. 10–15, Oct. 2018.

[18] *RIC Applications (RICAPP)—RIC Applications—Confluence*. Accessed: Sep. 18, 2022. [Online]. Available: https://wiki.o-ran-sc.org/pages/viewpage.action?pageId=1179662

[19] *Free5GC*. Accessed: Sep. 24, 2022. [Online]. Available: https://www.free5gc.org/

[20] D. Johnson, D. Maas, and J. Van Der Merwe, "NexRAN: Closed-loop RAN slicing in POWDER—A top-to-bottom open-source open-RAN use case," in *Proc. 15th ACM Workshop Wireless Network Testbeds, Exp. Eval. Characterization*. New York, NY, USA: Association for Computing Machinery, 2022, pp. 17–23.

[21] *O-RAN Alliance—Virtual Exhibition*. Accessed: Oct. 16, 2022. [Online]. Available: https://www.virtualexhibition.o-ran.org/classic/generation/2021/category/intelligent-ran-control-demonstrations/sub/intelligent-control/140

[22] C. N. Barati, S. Dutta, S. Rangan, and A. Sabharwal, "Energy and latency of beamforming architectures for initial access in mmWave wireless networks," *J. Indian Inst. Sci.*, vol. 100, no. 2, pp. 281–302, Apr. 2020.

[23] *Massive MIMO Use Cases, Technical Report, V.1.0*, O-RAN ALLIANCE WG1, O-RAN ALLIANCE e.V., Alfter, Germany, Jul. 2022.

[24] J. Perez-Romero et al., "On the use of radio environment maps for interference management in heterogeneous networks," *IEEE Commun. Mag.*, vol. 53, no. 8, pp. 184–191, Aug. 2015.

[25] H. Lee, Y. Jang, J. Song, and H. Yeon, "O-RAN AI/ML workflow implementation of personalized network optimization via reinforcement learning," in *Proc. IEEE Globecom Workshops (GC Wkshps)*, Dec. 2021, pp. 1–6.

[26] F. Abinader, C. Rom, K. Pedersen, S. Hailu, and N. Kolehmainen, "System-level analysis of mmWave 5G systems with different multi-panel antenna device models," in *Proc. IEEE 93rd Veh. Technol. Conf. (VTC-Spring)*, Apr. 2021, pp. 1–6.

[27] *A1 Interface: Application Protocol, V.3.02*, O-RAN ALLIANCE WG2, O-RAN ALLIANCE e.V., Alfter, Germany, Jul. 2022.

[28] *Near-Real-Time Ran Intelligent Controller E2 Service Model (E2SM), Ran Control, V.1.03*, O-RAN ALLIANCE WG3, O-RAN ALLIANCE e.V., Alfter, Germany, Oct. 2022.

[29] M. Hoffmann and P. Kryszkiewicz, "Beam management driven by radio environment maps in O-RAN architecture," in *Proc. IEEE Int. Conf. Commun. Workshops (ICC Workshops)*, May 2023, pp. 1–6.

[30] P. Misra and P. Enge, *Global Position Systems: Signals, Measurements and Performance*. Lincoln, MA, USA: Ganga-Jamuna Press, 2006.

[31] F. Francois, O. H. Abdelrahman, and E. Gelenbe, "Impact of signaling storms on energy consumption and latency of LTE user equipment," in *Proc. IEEE IEEE 17th Int. Conf. High Perform. Comput. Commun., 7th Int. Symp. Cyberspace Saf. Secur., IEEE 12th Int. Conf. Embedded Softw. Syst.*, Aug. 2015, pp. 1248–1255.

[32] M. Pavloski, "Detecting and mitigating storm attacks in mobile access to the cloud," in *Proc. IEEE Int. Conf. Fog Comput. (ICFC)*, Jun. 2019, pp. 53–58.

[33] *Technical Specification Group Radio Access Network; NR; Medium Access Control (MAC) Protocol Specification (Release 17)*, document TS 38.214, V.17.2.0, 3GPP, Sep. 2022.

[34] L. Bodrog, M. Kajo, S. Kocsis, and B. Schultz, "A robust algorithm for anomaly detection in mobile networks," in *Proc. IEEE 27th Annu. Int. Symp. Pers., Indoor, Mobile Radio Commun. (PIMRC)*, Sep. 2016, pp. 1–6.

[35] *Non-RT RIC Architecture, V.2.0*, O-RAN ALLIANCE WG2, O-RAN ALLIANCE e.V., Alfter, Germany, Jul. 2022.

[36] M. Hoffmann and P. Kryszkiewicz, "Signaling storm detection in IIoT network based on the open RAN architecture," in *Proc. IEEE Conf. Comput. Commun. Workshops (INFOCOM WKSHPS)*, Hoboken, NJ, USA, 2023, pp. 1–2. [Online]. Available: https://ieeexplore.ieee.org/document/10226043, doi: 10.1109/INFOCOMWKSHPS57453.2023.10226043.

[37] *A1 Interface: Type Definitions, V.4.0*, O-RAN ALLIANCE WG2, O-RAN ALLIANCE e.V., Alfter, Germany, Oct. 2022.

[38] *Rimedo Labs Traffic Steering xApp*. Accessed: Sep. 25, 2022. [Online]. Available: https://github.com/RIMEDO-Labs/rimedo-ts

[39] C. Adamczyk and A. Kliks, "Conflict mitigation framework and conflict detection in O-RAN near-RT RIC," *IEEE Commun. Mag.*, early access, May 18, 2023, doi: 10.1109/MCOM.018.2200752.

[40] C. T. Shen et al., "Security threat analysis and treatment strategy for ORAN," in *Proc. 24th Int. Conf. Adv. Commun. Technol. (ICACT)*, Feb. 2022, pp. 417–422.

[41] C. Benzaïd and T. Taleb, "AI for beyond 5G networks: A cyber-security defense or offense enabler?" *IEEE Netw.*, vol. 34, no. 6, pp. 140–147, Nov. 2020.

[42] A. Kliks, M. Dryjanski, V. Ram, L. Wong, and P. Harvey, "Towards autonomous open radio access networks," *ITU J. Future Evolving Technol.*, vol. 4, no. 2, pp. 251–268, 2023.

[43] B. Tang, V. K. Shah, V. Marojevic, and J. H. Reed, "AI testing framework for next-G O-RAN networks: Requirements, design, and research opportunities," *IEEE Wireless Commun.*, vol. 30, no. 1, pp. 70–77, Feb. 2023.


**Marcin Hoffmann** (Graduate Student Member, IEEE) received the M.Sc. degree (Hons.) in electronics and telecommunication from the Poznań University of Technology in 2019, where he is currently pursuing the Ph.D. degree with the Institute of Radiocommunications. He is also a Senior Research and Development Engineer with the Rimedo Labs working on O-RAN software development solutions. His research interests are the utilization of machine learning and location-dependent information for the purpose of network management.

**Salim Janji** (Graduate Student Member, IEEE) received the B.Sc. degree in electrical engineering from the University of Balamand in 2017 and the M.Sc. degree in electronics and telecommunications from the Institute of Radiocommunications in 2020. He is currently pursuing the Ph.D. degree with PUT focusing on UAV base stations. He is also a Teaching Assistant. He is also a Research and Development Engineer with the Rimedo Labs. Besides UAV base stations, his research interests include reinforcement learning in wireless networks, reconfigurable intelligent surfaces (RIS), and O-RAN.

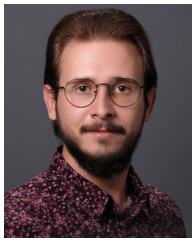

**Adam Samorzewski** (Graduate Student Member, IEEE) received the master's degree in electronics and telecommunications from the Poznan University of Technology, where he is currently pursuing the Ph.D. degree. He is currently a Research and Development Engineer with the Rimedo Labs developing software for O-RAN systems. His research interests include sustainable radio resource management in wireless systems supplied by renewable energy sources, wireless systems, radio resource management, and energy saving.

**Łukasz Kułacz** (Member, IEEE) received the Ph.D. degree in telecommunications from the Poznan University of Technology (PUT), Poland, in 2022. He is currently a Research and Teaching Assistant with the Institute of Radiocommunications, PUT. He is also a Senior Research and Development Engineer and the Technical Team Leader with the Rimedo Labs. He is involved in both, national, and international research projects. His research interests include the software-defined radio and utilization of context information for radio network operation improvement, in particular in the radio resource allocation process improvement.

**Cezary Adamczyk** is currently pursuing the Ph.D. degree with the Poznan University of Technology, conducting research in the field of radio resource optimization in open RAN, currently focusing on mitigation of conflicts between control decisions. He is also a Specification Engineer at one of the world's leading RAN provider, working on the development of O-RAN Alliance standards for the Open Fronthaul interface and their integration into the company's products.

**Marcin Dryjański** (Senior Member, IEEE) received the Ph.D. degree (Hons.) from the Poznan University of Technology in September 2019. Over the past 15 years, he was a Research and Development Engineer and a Consultant, a Technical Trainer, the Technical Leader, and an Advisor. He has been involved in 5G design since 2012, when he was the Work-Package Leader in the FP7 5GNOW Project. Currently, he is the CEO and a Principal Consultant with the Rimedo Labs. He is the coauthor of many articles on 5G and LTE-advanced pro and open RAN.

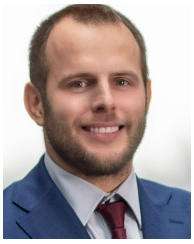

**Pawel Kryszkiewicz** (Senior Member, IEEE) received the M.Sc. and Ph.D. degrees (Hons.) in telecommunications from the Poznan University of Technology (PUT), Poland, in 2010 and 2015, respectively. He is currently an Associate Professor with the Institute of Radiocommunications, PUT. He was involved in a number of international research projects. His main fields of interests are multicarrier signal design for green communications and problems related to the practical implementation of massive MIMO systems.

**Adrian Kliks** (Senior Member, IEEE) received the Postdoctoral degree in technical computer science and telecommunications in February 2019. He is currently an Associate Professor with the Poznan University of Technology and has taken part in numerous industrial and commissioned projects. He leads OPUS projects on V2X communication and RISes. In 2014 and 2016, he was the IEEE Membership Development/Web Visibility Chair of the EMEA Area. Since 2019, he has been the Editor-in-Chief of the *Journal of Telecommunications and Information Technology* of the Institute of Communications. A Vice Chair of the IEEE VTS Polish Chapter. He is the Co-Founder of the PUT spin-off company—Rimedo Labs.

**Hanna Bogucka** (Senior Member, IEEE) is currently a Professor with the Institute of Radiocommunications, PUT. She is involved in research in wireless cognitive and green communication. She is a member of the Polish Academy of Sciences. She also serves as the Member-at-Large of the IEEE Communications Society Board of Governors and Europe Regional Chair for the IEEE ComSoc Fog/Edge Industry Community.

## 7.2 Publication [P2]

H. Bogucka, M. Hoffmann, P. Kryszkiewicz and L. Kulacz, "An Open-RAN Testbed for Detecting and Mitigating Radio-Access Anomalies," in *IEEE Communications Magazine*, early access, 2025.

MNiSW Points: 200

mgr inż. Marcin Hoffmann
Instytut Radiokomunikacji, Politechnika Poznańska
ul. Polanka 3, 60-965 Poznań

Poznań, 9 stycznia 2025 r.

# OŚWIADCZENIE W SPRAWIE AUTORSTWA PRACY

Oświadczam, że w pracy:

*H. Bogucka, M. Hoffmann, P. Kryszkiewicz and L. Kulacz, "An Open-RAN Testbed for Detecting and Mitigating Radio-Access Anomalies," in IEEE Communications Magazine,* Early Access 2025.

mój udział polegał na:

- Zaproponowaniu i integracji algorytmu wykrywania ataków typu ang. signaling storm z siecią 5G amarisoft. Algorytm bazuje na tworzeniu tzw. profilu KPI modelującym charakterystykę ruchu w sieci w celu wykrywania anomalii - ataków.
- Współautorstwo tekstu pierwszej wersji artykułu.
- Przeprowadzeniu eksperymentów z użyciem sieci 5G Amarisoft i smartfonów 5G, oraz opracowaniu wyników

Mój procentowy udział w powstanie pracy szacuję na: 30%

.....

Podpis

dr hab. inż. Paweł Kryszkiewicz, prof. PP
Instytut Radiokomunikacji, Politechnika Poznańska
ul. Polanka 3, 60-965 Poznań

Poznań, 14 sierpnia 2025 r.

# OŚWIADCZENIE W SPRAWIE AUTORSTWA PRACY

Oświadczam, że w pracy:

*H. Bogucka, M. Hoffmann, P. Kryszkiewicz and L. Kulacz, "An Open-RAN Testbed for Detecting and Mitigating Radio-Access Anomalies," in IEEE Communications Magazine,* Early Access 2025.

mój udział polegał na:

- Zaproponowanie algorytmu wykrywania i przeciwdziałania zakłóceniom, przeprowadzenie testów, analiza danych i ich wizualizacja
- Napisanie rodziału „Jamming detection and mitigation xApp”
- Udział w tworzeniu układu pomiarowego
- Poprawki merytoryczne i językowe w całym artykule
- Udział w przygotowaniu poprawek do artykułu w procesie recenzji

Mój procentowy udział w powstanie pracy szacuję na: 30%

Podpis

dr inż. Łukasz Kułacz
Instytut Radiokomunikacji, Politechnika Poznańska
ul. Polanka 3, 60-965 Poznań

Poznań, 14 sierpnia 2025 r.

# OŚWIADCZENIE W SPRAWIE AUTORSTWA PRACY

Oświadczam, że w pracy:

*H. Bogucka, M. Hoffmann, P. Kryszkiewicz and L. Kulacz, "An Open-RAN Testbed for Detecting and Mitigating Radio-Access Anomalies," in IEEE Communications Magazine,* Early Access 2025.

mój udział polegał na:

- Opracowaniu oprogramowania umożliwiającego przeprowadzenie eksperymentu
- Integracji algorytmów detekcji i mitygacji zagrożeń

Mój procentowy udział w powstanie pracy szacuję na: 15%

Kułacz Łukasz

Podpis

prof. dr hab. inż. Hanna Bogucka
Instytut Radiokomunikacji, Politechnika Poznańska
ul. Polanka 3, 60-965 Poznań

Poznań, 14 sierpnia 2025 r.

# OŚWIADCZENIE W SPRAWIE AUTORSTWA PRACY

Oświadczam, że w pracy:

*H. Bogucka, M. Hoffmann, P. Kryszkiewicz and L. Kulacz, "An Open-RAN Testbed for Detecting and Mitigating Radio-Access Anomalies," in IEEE Communications Magazine,* Early Access 2025.

mój udział polegał na:

- przygotowaniu treści czterech sekcji,
- integracji wkładu współautorów oraz
- edycji artykułu.

Mój procentowy udział w powstanie pracy szacuję na: 25%

H. Bogucka

.....

Podpis

# An Open-RAN Testbed for Detecting and Mitigating Radio-Access Anomalies

Hanna Bogucka, Marcin Hoffmann, Paweł Kryszkiewicz, Łukasz Kułacz

## Abstract

This article presents the open radio access network (O-RAN) testbed for secure radio access. We discuss radio-originating attack detection and mitigation methods based on anomaly detection and how they can be implemented as specialized applications (xApps) in this testbed. We also present results of the methods applied in real-world scenarios and implementations.

## Introduction

The traditional way of providing the Radio Access Network (RAN) is a black (closed) box supplied by a single vendor. The Open-RAN (O-RAN) concept is based on two ideas: the disaggregation of RAN functionality from the underlying hardware (introduced in the Fifth Generation (5G) radio specifications by 3GPP) and the definition of functional RAN modules with interfaces [1]. The disaggregation and modularity of O-RAN allow for an open ecosystem for vendors, software developers, and system integrators.

In 5G RAN, the functions of the base station are split into entities with open interfaces: a centralized unit (CU) with a separated User-Plane (CU-UP) having N3 interface with User Plane Function (UPF) and Control-Plane (CU-CP) having N2 interface with Access and Mobility Function (AMF), a distributed unit (DU), and a remote radio unit (RU). With the O-RAN approach, different vendors can develop those entities due to the open interfaces, including Open Front-Haul (O-FH). Moreover, the RAN Intelligent Controllers (RICs) are a new component that allows the provision of Artificial Intelligence (AI)-based management for radio network automation.

Figure 1 presents the O-RAN architecture. The white modules (including functionalities and interfaces) are open versions of the 3GPP specified nodes DU, CU-CP, CU-UP, and RU, which are evolved by O-RAN to support open interfaces with new services. In contrast, orange blocks and interfaces are specified by the O-RAN Alliance. The "O-"prefix (in O-CU, O-DU, O-RU) stands for "open." At least one O-CU-CP, one O-CU-UP, and one O-DU comprise the E2 node. RICs are Non-Real-Time RIC (Non-RT RIC) and Near-Real-Time RIC (Near-RT RIC). Non-RT RIC is a software platform for applications called rApps for high-level RAN optimization in a *non-real-time control loop* (with a latency of one second or more). It allows RAN configuration and management and provides enrichment information and guidance via policies and Machine Learning (ML) models to the Near-RT RIC via the A1 interface. Near-RT RIC is a software platform for a set of xApps, which are applications running in a *near real-time control loop*, that is, in a time scale longer than ten milliseconds and shorter than one second. It enables near-RT control and optimization of RAN elements and resources via fine-grained data collection and actions over the E2 interface [2]. Service and Management Orchestration (SMO) entity supports the orchestration of O-RAN components, including Non-RT RIC. Finally, O-Cloud is a cloud computing platform comprising a collection of physical infrastructure nodes that meet O-RAN requirements to host the relevant O-RAN functions (Near-RT RIC, O-CU-CP, O-CU-UP, and O-DU), the supporting software components (such as Operating System, Virtual Machine Monitor, Container Runtime, etc.) and the management and orchestration functions. Details of O-RAN blocks and interfaces can be found in [1].

The O-RAN concept poses a challenge to its security. Inadequately defined and poorly secured O-RAN interfaces and applications may be vulnerable to cyberattacks. Moreover, in a decentralized approach to information processing, security management becomes difficult as significant parts of the network can be attacked anywhere at any time. These security issues result from O-RAN'sO-RAN's novel features: *openness* and *intelligence*. However, these same features of O-RAN create opportunities for detection and response to attacks. The transparency of new open interfaces increases scrutiny of vulnerabilities and failures.

O-RAN security challenges and solutions have been overviewed and discussed in several recent papers (e.g., [2–5]), MNOs'MNOs' documents (e.g., [6]), and governmental statements (e.g., [7]). Importantly, all stakeholders agree that O-RAN brings more competition to implementing security solutions usable with equipment from any O-RAN-compliant vendor. O-RAN RICs provide a framework to enhance security, resilience, and adaptability. Embedded intelligence allows for monitoring and analysis of security threats and protects RAN from malicious and illegal access to network segments. It makes it possible to detect

ISSN: 0163-6804
Digital Object Identifier: 10.1109/MCOM.003.2400513

*The authors are with Poznan University of Technology, Poland, and also with RIMEDO Labs, Poland. Hanna Bogucka is corresponding author.*

threats before they affect the operation of the entire network. Significantly, xApps and rApps can be developed for specific types of threats in a network, which can be detected and eliminated closer to the place of their occurrence.

This article discusses the security opportunities the O-RAN architecture brings. We present an O-RAN testbed with xApps for anomaly detection in the radio segment, near-real-time reactions, and defense against attacks launched. To our knowledge, the proposed algorithms are pioneers in the field of O-RAN. Unlike the simulation studies, the implementation of such algorithms on real hardware is limited first to what O-RAN specification supports and second to what a particular platform supports in terms of input/output data.

The following section discusses the attack surface in the radio segment, mitigation methods, and O-RAN security opportunities. Then we present our O-RAN testbed implementing xApps for anomaly detection and mitigation methods. After that we present xApps developed for jamming and signaling storm detection and mitigation, respectively, as well as their measured performance in our testbed implementations. We conclude the article in the final section.

## O-RAN for Radio-Access Security

Virtualization, functional disaggregation, and open interfaces in O-RAN inevitably extend the threat surface. The Security Focus Group (SFG) working group (WG11) within the O-RAN Alliance has identified six groups of threat surfaces (causes of attack vulnerabilities) for O-RAN [8]. Four of these groups are related to O-RAN's openness, virtualization, disaggregation, and intelligence. The other two are the consequences of accessibility in the supply chain and provided software (SW). Apart from the threat surfaces mentioned, [8] identifies eight threat categories, depending on the goals of attacks. Noticeably, some threats would appear in standard RANs, computer networks, or cloud services, not exclusively in O-RAN. This article focuses on radio-segment security threats, particularly those detected as anomalies, that is, causing signals or observations to deviate from standard or expected ones, making them inconsistent with the rest.

### Attacks on the Radio Segment and Anomalies

The radio interface is inherently exposed to attacks related to the omnipresent transmission medium. A standard way to assess risks is based on their threat to *confidentiality*, *integrity*, and *availability* of transferred information.

*Confidentiality* in RAN can be compromised by eavesdropping, data decryption and detection capabilities, and traffic analysis. The *integrity* of information is lost when an adversary intercepts and tampers with it in a way that tricks the recipient into behaving differently. *Spoofing* (disguising a communication or user identity) or Man in the Middle (MITM) attacks (intercepting messages and changing their content) are typically considered attacks in RANs. Finally, the information *availability* may be compromised by attacks that interrupt connections or exhaust network resources and cause traffic congestion. Threats in this category typically considered in RANs are jamming (which injects unwanted signals into the

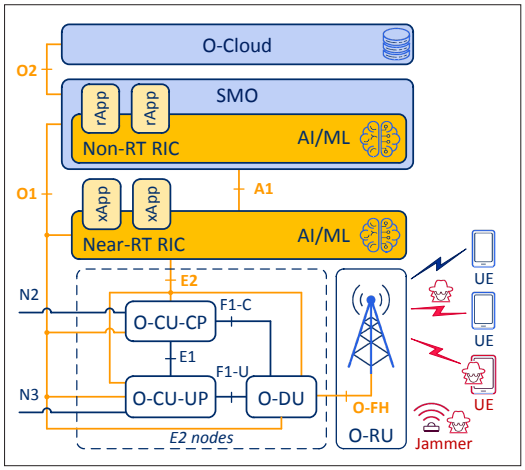


FIGURE 1. O-RAN architecture and radio attacks.

communication or control channels), Signaling Storm (SS) (seizing resources for signaling in the control plane), or Denial of Service (DoS) (aimed at massive requests for network resources, either in the control or user plane). Note that according to MITRE FiGHT (5G Hierarchy of Threats) knowledge base, SS is a subcategory of a DoS attack; that is, if launched in the random-access channel, its consequence might be a denial of access to a network for legitimate users. The literature (e.g., [9]) extensively describes radio attacks and appropriate countermeasures. As shown in Fig. 1, they can be launched at UE, in a radio link, or in an external radio source. In what follows, we discuss the O-RAN security testbed and the two common radio attacks: jamming and SS.

Jamming may be of different kinds [10]:

- *Regular*, when jammers do not follow any medium access control protocol
- D*elusive*, when jammers inject a legitimate sequence of bits in a communication channel
- *Random*, when jammers conserve their energy by alternating between active and idle states
- *Responsive*, when jammers transmit only if the legitimate transmitter is active
- *Go-next*, when a jammer targets one frequency channel at a time and follows frequency hops of the legitimate transmitter
- *Control-channel jamming*, when a jammer targets the control message exchanges.

In general, jamming acts like noise, keyed noise, or interference; therefore, it can be detected if it deteriorates the reception quality. However, there are no means to remove it from the useful signal. Mitigating its negative effects involves adapting to the deteriorated radio conditions. Smart (delusive) jamming mimics legitimate transmission (e.g., 5G) and is harder to detect, but it requires specialized equipment and adequate transmission power (as in the victim system). Such a jammer can be treated like a spoofing device.

The latter type of anomaly attack considered, SS, can be prevalent since it is relatively easy to launch using a cheap, authorized device, such as a prepaid phone. In [11], models for SSs and existing detection and mitigation solutions are presented, although this article focuses on Radio Resource Control (RRC). In general, the methods counteracting the SS attack aim at detecting and breaking suspicious connections or blocking

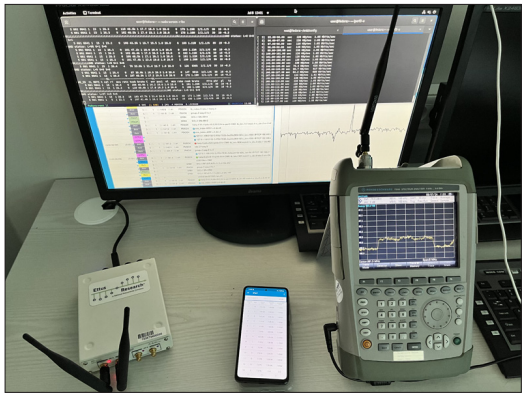

FIGURE 2. O-RAN testbed setup: Amarisoft CU/DU, USRP B210 O-RU (jammer or O-RU), Samsung A52s 5G UE (legitimate or launching SS), and spectrum analyzer.

access to the signaling channels.

### O-RAN Opportunities for Anomaly Detection/Mitigation

An essential element in introducing O-RAN security is the inclusion of the security subsystem in the Near-RT RIC architecture. Its primary task is to prevent malicious xApps from affecting the O-RAN performance and data leaks. Additionally, mechanisms to mitigate conflicts between xApps should be a security practice for O-RAN.

Regarding attack detection and defense in the radio segment, O-RAN architecture has vast potential, mainly thanks to the specialized xApps and rApps that protect RAN against attacks. They can be easily installed and updated as new threats occur and new solutions and countermeasures are elaborated. Moreover, xApps and rApps address the zero-trust model by continuously monitoring, detecting, and reacting to threats, including anomalies in the radio traffic [12].

## O-RAN Security Testbed and Real-World Experiments

As said above, O-RAN architecture supports system security through Near-RT RIC and Non-RT RIC and specialized xApps and rApps designed to detect and eliminate threats promptly before they impact the network. Below, we present a testbed to run and evaluate security xApps for ML-based anomaly detection. The example scenarios and xApps are chosen to illustrate attacks, their detection, and mitigation in selected representative scenarios: jamming in Ultra-Reliable, Low Latency Communication (URLLC) and SS in massive Machine-Type Communication (mMTC). The selection of these use cases will be justified in the following sections. Figure 1 presents the general scenario for our setup, and Fig. 2 shows the equipment used for monitoring the attacks and mitigation applications. Here, we consider just a one-cell scenario since the detection and mitigation methods presented here operate in a single cell or even a single link.

Our O-RAN testbed is built on the Amarisoft software platform, which provides CU/DU functionality. The O-RU is realized by attaching a USRP B210 to the Amarisoft CU/DU through the USB 3.0 cable, emulating O-FH. Connected UE (5G smartphone — Samsung A52s) transmits data with the *iperf* program (a tool for data stream generation and performance measurement).

Near-RT RIC enables the deployment of dedicated xApps that protect RAN against jamming and a signaling storm. Its operation is emulated by the *wrapper* to Amarisoft Application Programming Interface (API), that is, the Python code that acts as an intermediary abstraction layer between xApps in Near-RT RIC and Amarisoft CU/DU, which is an E2 node.

An E2 interface application protocol called E2AP is specified over SCTP/IP as the transport protocol [1, 2]. On top of E2AP, application-specific controls and events are conveyed through E2 service models (E2SM). The RIC services, named *REPORT*, *INSERT*, *CONTROL*, *POLICY*, and *QUERY*, are provided on O-CU-CP, O-CU-UP, and O-DU for xApps to access messages and measurements and enable control of these entities from the Near-RT RIC. Different data types are grouped for each RIC service as a so-called style.

In our testbed, a dedicated application between Amarisoft CU/DU and xApps, which represents the E2 interface, has been developed based on the WebSocket and utilizes Amarisoft API for the CONTROL and REPORT services. The RIC services (both REPORT and CONTROL) are provided to the xApps. Our Near-RT RIC platform supports the following E2SM styles and data defined by the O-RAN Alliance WG3 [13].

Finally, in our experiments, the transmit power of all devices (legitimate and attacking) was 10 mW, the center frequency in the downlink (DL) was set to 881.5 MHz, in the uplink (UL) to 836.5 MHz, and the system bandwidth to 5 MHz.

## Jamming Detection and Mitigation xApp

The 5G system is quite robust against interference caused by jammers in the long run. While the jamming signal increases the noise floor at the receiver, the MCS adaptation or retransmissions prevent the link from failing. An update of MCS (after the signal-to-noise ratio change is reported) may take several milliseconds, and similarly, a retransmission delay may not be acceptable for URLLC. In addition, jamming can be easy and inexpensive to launch with low-cost software-defined-radio (SDR) equipment, making it more likely to occur. Utilizing SDR, our testbed was jammed with white noise in a continuous or keyed manner (repeatable sequence of 100 ms of jamming and 100 ms of no jamming). This resulted in increased packet latency (measured via ping command). The non-jamming scenario allows 95 percent of packets to reach the destination and return in less than 40 ms (recall that the utilized testbed is not optimized for latency). The permanent jamming increased this time to 80 ms. The worst performance was observed under keyed jamming, requiring a 200 ms time budget as a result of packet retransmissions. Thus, detecting jamming is crucial for URLLC and is to be carried out in Near-RT RIC for delay minimization.

### Jamming Detection

In [14], we proposed a jamming detection method based on the analysis of the *Channel State Information* and *Reference Signal Received Power* reports by UE in DL. Here, we present a better-performing method based on the statistics of correct transport block reception messages: the ACK/NACK messages for each transport block in

DL and available in E2 nodes. In the experiment, it has been observed that the ACK message statistics were significantly altered by jamming. This can be justified by the anomalous nature of the distortion created by a jammer, not taken into account while designing the radio interface. On the other hand, the typical radio communication effects, such as shadowing or inter-cell interference, are considered for network design, preventing multiple NACK messages from occurring.

The message exchange between E2 Nodes, UE, and Jamming Detection (and mitigation) xApp (JD-xApp) is shown in Fig. 3. First, UE sends ACK/NACK messages via PUCCH (Physical Uplink Control Channel) or PUSCH (Physical Uplink Shared Channel) to E2 nodes. Next, these reports are sent to the JD-xApp over the E2 interface. Several methods can be used to analyze such a dataset for an anomaly. We propose to analyze the mean Block Error Rate (BLER) over the last transmitted $N$ blocks. If BLER is above the threshold β, we assume that jamming occurs, preventing RAN from correct MCS selection.

Note that the long observation window N (high number of ACK/NACK reports) makes the algorithm more robust against false alarms but also less efficient in short-term jamming detection. If β is too low, a small increase in mean BLER (caused by varying channel conditions) is detected as jamming. Most importantly, JD-xApp should calibrate β and $N$ in each E2 node, as various schedulers can maintain various mean BLER levels. The calibration of β and $N$ can be done by collecting ACK/NACK measurements while the network is operating without a jamming signal. The non-jammed state can be confirmed by some other measurements, such as using a spectrum analyzer. Based on this dataset, various values of β and $N$ can be tested, calculating the probability of a false alarm ($P_{fa}$). Multiple (β, $N$) pairs are available for the selected values of $P_{fa}$. One should be selected based on the below discussion.

Our measurements show that the longer the observation window $N$, while maintaining such β value to keep $P_{fa}$ constant (based on previous calibration), the higher the probability of detection ($P_d$) of jamming. Moreover, the keyed jamming is more challenging to detect. The measurements were carried out for varying UE positions in the radius of 1–15 m. In our indoor environment, the power (transmitted from gNodeB or jammer) was attenuated in the range of 30–55 dB. These mobility dynamics do not allow for performance evaluation for one specific value of Signal-to-Jamming power Ratio (SJR). For jamming received with higher power (e.g., SJR around 0 dB), the negative impact on the 5G link performance is higher, but it is easier to detect. Low-power jamming (e.g., SJR around 20 dB) is difficult to detect but causes hardly any harm to the link quality. In the test scenario, $P_d$ exceeds 50 percent for both jamming types while $N$ = 10000.

The proposed jamming detection requires a very limited set of information, that is, ACK/NACK messages. Extending its capabilities, for example, to estimate jammer location, can be possible only if the required information is available at a given O-RAN interface, for example, UE location. As for the utilized testbed, the algorithm's extension is limited by the set of reports provided by Amarisoft.

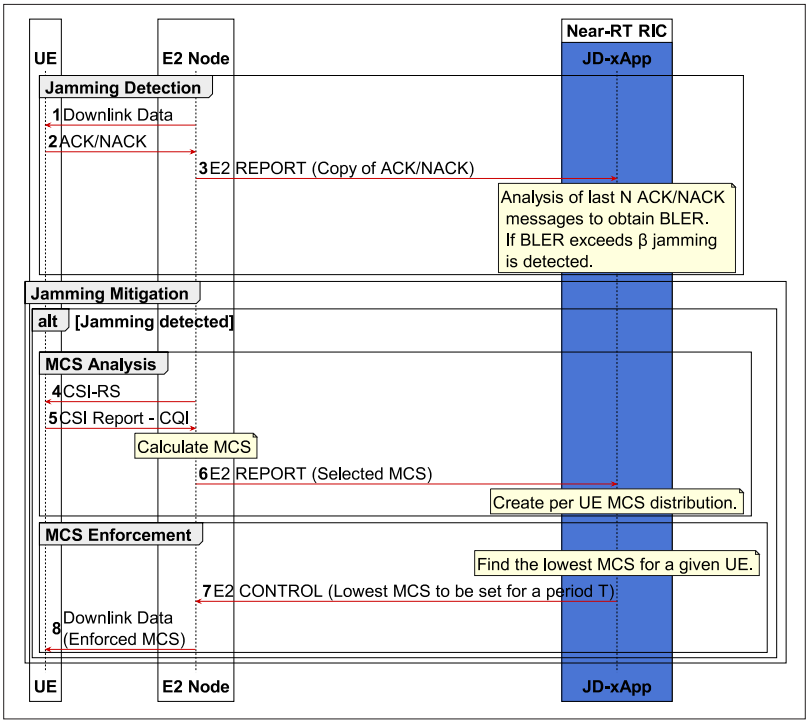


FIGURE 3. UML sequence diagram for jamming detection and mitigation.

## Jamming Mitigation

Mitigation of jamming is a difficult task as straightforward solutions, such as transmit power increase or carrier frequency reconfiguration, are difficult when multiple cells must be coordinated while limiting inter-cell interference and maintaining continuous service provision. On the other hand, a 5G network can adapt to some interference or jamming present in a wireless channel using channel state measurements and MCS selection. However, standard link-adaptation mechanisms can be too slow, especially for a keyed jamming, causing link failures.

In our testbed, it is proposed that the MCS distribution for a given UE be analyzed when the jamming is present and that minimal observed MCS be assigned. While reduced, MCS can result in higher resource utilization, decreasing the number of UEs to be served in parallel; if the proposed scheme is not employed, potentially all the URLLC devices connected can have too high transmission latency, preventing their application from being performed successfully.

The JD-xApp must subscribe to the DL MCS values assigned to a given UE by the E2 node. Its distribution over some time is estimated within JD-xApp. If jamming is detected, JD-xApp sends a proper policy via the E2 interface, preventing the scheduler from assigning the jammed UE higher MCS than the one specified in the policy.

In our experiment, the MCS of transmission to jammed UE was set to 1 to obtain maximal protection against jamming. The jamming mitigation performance can be assessed by observing packet round trip time (using the ping command). The

Cumulative Distribution Function (CDF) of the packet delay in the absence and the presence of two types of jamming, as well as in the case when JD-xApp is applied, is shown in Fig. 4. One can observe that jamming causes a *heavy tail* of this distribution if some transport blocks are received with an error requiring retransmission. Jamming

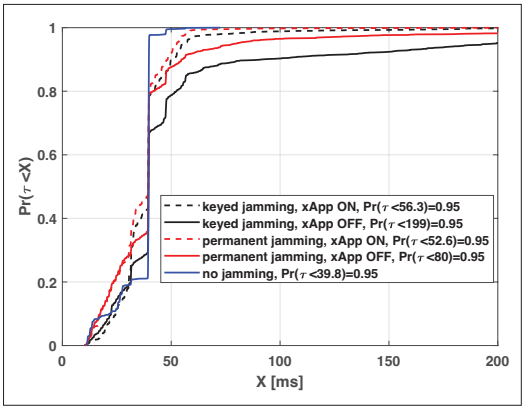


FIGURE 4. CDF of packet delay (by ping tool) with/without jamming and with/without jamming mitigation xApp.

detection and mitigation xApp allows for reducing the time budget required for 95 percent of packets to around 56 ms for both permanent and keyed jamming. This is a nearly 35 percent reduction, from 80 ms to 52.6 ms, in the case of permanent jamming, and a nearly fourfold reduction, from 199 ms to 56.3 ms, in the case of keyed jamming. While there is a slight difference between both jamming types when mitigation xApp is on, this seems to be statistically negligible. This proves that our jamming mitigation xApp is highly effective in our testbed environment. Both jamming detection and mitigation should work effectively for various jammer distance and transmission power configurations as long as the observed SJR is within the useful range of all MCSs.

## SS Detection and Mitigation xApp

O-RAN architecture allows for the protection of resources caused by SSs in the access channels of an mMTC network. Typically, SS can be launched by hacked mMTC devices. The connected devices usually have fixed locations and can be identified during initial access based on their Timing Advance (TA) parameter, that is, propagation delay time between UE and gNodeB. For the TA parameter to be useful, the devices must be stationary, for example, as in the network of sensors. This allows selective blocking of a malicious device that constantly sends connection requests aiming at flooding the Core Network (CN) control plane. Thus, SS detection is automatically the mitigation technique; that is, the detected source of the attack is consequently eliminated.

In [15], we have proposed a dedicated SS detection xApp (SSD-xApp) for this application scenario. The SSD-xApp is placed in a Near-RT RIC and utilizes O-RAN interfaces to capture and analyze control plane messages exchanged between gNodeB (or an E2 node) and UE to protect CN resources by rejecting connection requests from the signaling storm attack. The related UML sequence diagram is depicted in Fig. 5.

First, the SSD-xApp must build a Key Performance Indicator (KPI) profile that contains, per TA statistics, the mean and standard deviation of the number of UE connection attempts observed during consecutive time intervals for each TA. Whenever UE sends a connection-establish request, the Random Access Response (RAR) using the E2 interface is transferred from gNodeB to SSD-xApp to create the KPI profile.

After the training phase, the SSD-xApp goes to the inference phase. Again, it utilizes the E2 interface to capture RAR from the E2 Node, but now, it uses the KPI profile to detect potential threats. The so-called anomaly value is calculated as the (estimated) *standard score* of the number of connection requests associated with a particular TA for a given period, that is, the currently observed number of connection requests minus the mean divided by the standard deviation of the number of connection requests estimated in the training phase (and available in the KPI profile). If the calculated anomaly value exceeds the threshold $\gamma$ (maximal allowed estimated *standard score*) for a particular TA, the SSD xApp formulates a policy to reject connection-establish requests from UEs of this TA. Note that the same TA may be reported for several UEs, and applying security policy may occasionally result in the rejection of some legitimate requests.

Building on the idea presented in [15] (simulated with 100 mMTC devices and five adversaries), we tested the proposed SSD-xApp in the real-world O-RAN testbed described above. One smartphone was used as a legitimate stationery mMTC device that sent connection-establish requests three times per minute. Another smartphone emulated the adversary mMTC device, launching 15 signaling storm attacks per hour; one attack composed of 12 connection establish requests sent in 2 s intervals. The first part of the SSD-xApp evaluation aimed to create the KPI profile. It was built in one hour and contained the average number and the standard deviation of connection-establish requests sent by the legitimate mMTC device within one minute.

The critical observation after obtaining the measurement-based KPI profile is that even if there is only one legitimate stationary mMTC device, the KPI profile contains statistics for three TAs. This reflects the properties of a network where TA varies over time. After obtaining a reliable KPI profile, we examined the SSD-xApp running under different anomaly threshold $\gamma$. The SSD-xApp continuously tracks the connection-establish requests from the last minute, calculates anomaly values, and performs SS detection. Each evaluation was 1 hour long to provide statistically reliable results. The results are depicted in Fig. 6. Note that the selection of anomaly threshold $\gamma$ is crucial for balancing the probability of detection ($P_d$), the probability of false alarm ($P_{fa}$), and the probability of the rejection of legitimate UE along with an attacker. In the case of mMTC traffic, keeping low $P_{fa}$ and not deteriorating transmission quality is crucial. Thus, $P_d$ can be "sacrificed" (selected lower) within a reasonable range.

It can be seen in Fig. 6 that the SSD-xApp can keep $P_d$ around 68 percent while reducing $P_{fa}$ below 0.5 percent for $\gamma = 1$. As in the case of mMTC traffic, low $P_{fa}$ is of high importance, and the $P_d$ at the level of 68 percent is a good result, that is, it allows the detection and blocking of most of the SS attacks. On the other hand, it is beneficial not to disturb network operation when less intensive signaling storms occur, as they will not cause access denial.

## Conclusions

An O-RAN platform with its xApps running in Near-RT RIC can be used to monitor, analyze, and

eliminate threats, providing a higher level of security. As demonstrated, dedicated xApps can be developed to protect the network against anomalies such as jamming or signaling storms in the example URLLC and mMTC use cases, although their application is not limited to these examined scenarios. The presented jamming detection and mitigation xApp, in the URLLC scenario, allows for reducing the required packet latency level for 95 percent of packets for both permanent and keyed jamming. The SS detection and mitigation xApp in the mMTC scenario results in a sufficient probability of detection while reducing the probability of false alarms below 0.5 percent.

A challenge for future research is to develop JD-xApp for smart jamming and a more sophisticated jamming signal, such as a synchronization signal. It should also involve a quantitative evaluation of JD with respect to the signal-to-jamming power ratio. Moreover, the utilization of early-stage registration messages to detect SS caused by the moving adversary and the impact of E2 message delay on the SSD-xApp performance are topics for prospective studies.

## Acknowledgment

This work was funded by the National Centre for Research and Development in Poland within the 5GStar project CYBERSECIDENT/487845/IV/NCBR/2021 on "Advanced methods and techniques for identification and counteracting cyber-attacks on 5G access network and applications."

## References

[1] O-RAN WG1, "O-RAN Architecture Description," June 2024, https://orandownloadsweb. azurewebsites.net/specifications.
[2] M. Hoffmann *et al.*, "Open RAN xApp. Design and Evaluation: Lessons Learnt and Identified Challenges," *IEEE J. Sel. Areas Commun.*, vol. 42, no. 2, Feb. 2024, pp. 473–86.
[3] M. Polese *et al.*, "Understanding O-RAN: Architecture, Interfaces, Algorithms, Security, and Research Challenges," *IEEE Commun. Surveys & Tutorials*, 2023, vol. 25, no. 2, pp. 1376–1411
[4] M. Liyanagea *et al.*, "Open RAN Security: Challenges and Opportunities," *J. Netw. Comput. Appl.*, vol. 214, C, May 2023.
[5] J. Green *et al.*, "Implementing and Evaluating Security in O-RAN: Interfaces, Intelligence, and Platforms," *IEEE Network*, vol. 29, July 2024.
[6] Open RAN MoU Signatories: "Open RAN Technical Priorities Focus on Security," 2023.
[7] National Security Agency and Cybersecurity and Infrastructure Security Agency (USA) "Open Radio Access Network Security Considerations," Sept. 15, 2022.
[8] O-RAN Alliance WG 11, "O-RAN Security Threat Modeling and Remediation Analysis 6.0," O-RAN.WG11.O-RAN-Threat-Model-v04.00, 2023.
[9] J. Cao *et al.*, "A Survey on Security Aspects for 3GPP 5G Networks," *IEEE Commun. Surv. Tut.*, vol. 22, no. 1, 1st Qtr. 2020, pp. 170–95.
[10] Y. Arjoune *et al.*, "Smart Jamming Attacks in 5G New Radio: A Review," *Proc. Annual Comp. and Comm. Workshop and Conf.*, Las Vegas, NV, USA, 2020, pp. 1010–15.
[11] A. Tabiban *et al.*, "Signaling Storm in O-RAN: Challenges and Research Opportunities," *IEEE Commun. Mag.*, vol. 62, no. 6, June 2024, pp. 58–64.
[12] O-RAN Alliance, "Zero Trust Architecture for Secure O-RAN," white paper, May 2024.
[13] O-RAN Alliance WG3, "O-RAN E2 Service Model (E2SM), RAN Control 6.0" O-RAN.WG3.E2SM-RC-R003-v06.00, 2024.

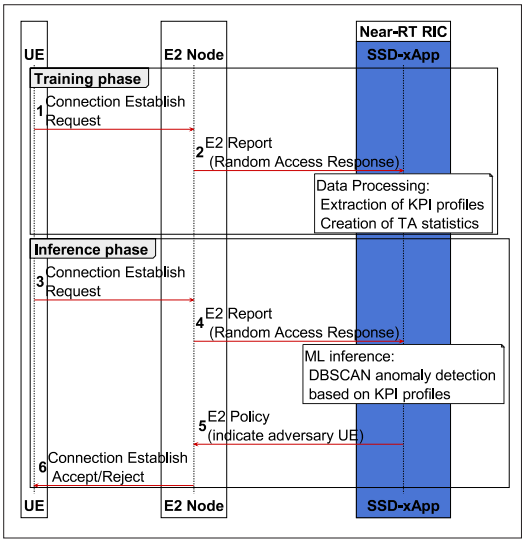


FIGURE 5. UML sequence diagram for signaling storm detection and mitigation.

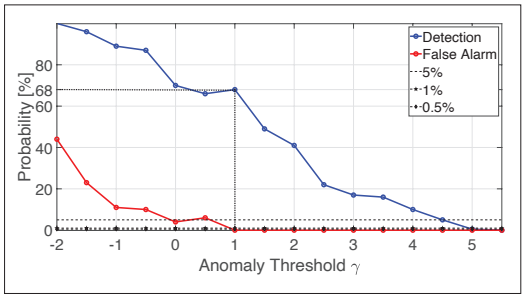


FIGURE 6. Probability of detection $P_d$ and false alarm $P_{fa}$ vs. anomaly threshold $\gamma$.

[14] P. Kryszkiewicz and M. Hoffmann "Open RAN for Detection of a Jamming Attack in a 5G Network," *IEEE VTC*, Spring 2023.
[15] M. Hoffmann et al., "Signaling Storm Detection in IIoT Network based on the Open RAN Architecture," *Proc. IEEE INFOCOM 2023 Workshops*, Hoboken, NJ, USA, 2023, pp. 1–2.

## Biographies

Hanna Bogucka is a professor at the Institute of Radiocommunications at PUT and the co-founder of RIMEDO Labs. She is involved in research in wireless cognitive and green communication. She is a member of the Polish Academy of Sciences. She also serves as the Member-at-Large of the IEEE Communications Society BoG.

Marcin Hoffmann is a Senior R&D engineer at Rimedo Labs working on O-RAN software development solutions. He is also a Ph.D. candidate at PUT. His research includes utilizing machine learning for 5G/6G network management.

Paweł Kryszkiewicz is an associate professor at the Institute of Radiocommunications, PUT. He is also the co-founder and Technical Director of RIMEDO Labs. He is a Fulbright Alumnus of the Worcester Polytechnic Institute, MA, and the author of over 100 publications on multicarrier systems, dynamic spectrum access, and O-RAN.

Łukasz Kułacz is an assistant professor at the Institute of Radiocommunications. His main fields of interest are Open RAN implementations and radio resource management.

## 7.3 Publication [P3]

M. Hoffmann and P. Kryszkiewicz, "Signaling Storm Detection in IIoT Network based on the Open RAN Architecture," in *IEEE INFOCOM 2023 - IEEE Conference on Computer Communications Workshops (INFOCOM WKSHPS)*, pp. 1–2, 2023.

MNiSW Points: 200

Number of citations:

- according to Web of Science: 6
- according to Google Scholar: 28

mgr inż. Marcin Hoffmann
Instytut Radiokomunikacji, Politechnika Poznańska
ul. Polanka 3, 60-965 Poznań

Poznań, 9 stycznia 2025 r.

# OŚWIADCZENIE W SPRAWIE AUTORSTWA PRACY

Oświadczam, że w pracy:

*M. Hoffmann, P. Kryszkiewicz,* "Signaling Storm Detection in IIoT Network based on the Open RAN Architecture," *IEEE INFOCOM 2023 - IEEE Conference on Computer Communications Workshops (INFOCOM WKSHPS), Hoboken, NJ, USA 1, strony 1-2, sierpień 2023*

mój udział polegał na:

- Zaproponowaniu algorytmu wykrywania ataków typu signaling storm w bezprzewodowej sieci 5G obsługującej urządzenia IIoT (Industrial Internet of Things), zgodnego z architekturą otwartej sieci dostępowej O-RAN.
- Przygotowaniu w całości tekstu pierwszej wersji artykułu.
- Przeprowadzeniu symulacji komputerowych i opracowaniu wyników

Mój procentowy udział w powstanie pracy szacuję na: 85%

.....

Podpis

dr hab. inż. Paweł Kryszkiewicz, prof. PP
Instytut Radiokomunikacji, Politechnika Poznańska
ul. Polanka 3, 60-965 Poznań

Poznań, 9 stycznia 2024 r.

# OŚWIADCZENIE W SPRAWIE AUTORSTWA PRACY

Oświadczam, że w pracy:

*M. Hoffmann, P. Kryszkiewicz, "*Signaling Storm Detection in IIoT Network based on the Open RAN Architecture," *IEEE INFOCOM 2023 - IEEE Conference on Computer Communications Workshops (INFOCOM WKSHPS), Hoboken, NJ, USA 1, strony 1-2, sierpień 2023*

mój udział polegał na:

- Dyskusji z głównym autorem struktury pracy, wykorzystanej metodologii, a także uzyskanych wyników
- Korekcie tekstu

Mój procentowy udział w powstanie pracy szacuję na: 15%

Podpis

IEEE INFOCOM 2023 - IEEE Conference on Computer Communications Workshops (INFOCOM WKSHPS) | 978-1-6654-9427-4/23/$31.00 ©2023 IEEE | DOI: 10.1109/INFOCOMWKSHPS57453.2023.10226043

# Signaling Storm Detection in IIoT Network based on the Open RAN Architecture

Marcin Hoffmann
*Rimedo Labs*
*Institute of Radiocommunications*
*Poznan University of Technology*
Poznan, Poland

Pawel Kryszkiewicz
*Rimedo Labs*
*Institute of Radiocommunications*
*Poznan University of Technology*
Poznan, Poland

***Abstract*—The Industrial Internet of Things devices due to their low cost and complexity are exposed to being hacked and utilized to attack the network infrastructure causing a so-called Signaling Storm. In this paper, we propose to utilize the Open Radio Access Network (O-RAN) architecture, to monitor the control plane messages in order to detect the activity of adversaries at its early stage.**

## I. Introduction

One of the significant groups of devices being connected to the 5G and beyond networks is the so-called Industrial Internet of Things (IIoT) devices [1]. These are mostly stationary deployed sensors used in the industry, e.g., to report the temperature in the furnaces. The main features of IIoT devices are low hardware complexity resulting in low computational power and low cost. While there can be hundreds of IIoT devices from various vendors in a single network there is a relatively high probability that some of them can be hacked and used to attack the network infrastructure. A possible attack scenario is the so-called Signaling Storm Attack (SSA), where the adversary utilizes standard mechanisms of the network Control Plane (CP) to cause Denial of Service (DoS), e.g., flooding the network CP with invalid or repeated registration requests [2]. Even if these registration requests are rejected they consume Core Network (CN) resources in the CP that are needed during the authorization process. It would be beneficial to somehow identify adversary devices in the early stage of the registration process in the Radio Access Network (RAN) to protect CN resources. This can be hard to achieve in state-of-the-art mobile networks, where both hardware and software are provided typically by a single vendor with only a limited possibility of affecting their configuration. On the opposite, the concept of Open RAN (O-RAN) enables interaction with RAN through the dedicated interfaces, and interception of RAN protocol messages [3]. The O-RAN ALLIANCE identified SSA detection as one of the key problems to be resolved by the development of a dedicated xApp [4]. It should utilize O-RAN interfaces to capture network messages and statistics to detect the abnormal activity of adversaries.

In this paper, we propose a xApp to detect the abnormal activity of IIoT devices at the beginning of their registration procedure. The xApp uses O-RAN interfaces to intercept CP messages to learn the required long-term network statistics. These are used to detect the abnormal activity of adversaries.

This work has been funded by the Polish Ministry of Education and Science within task no. 0312/SBAD/8161, in 2022, and by the National Centre for Research and Development in Poland within project no. CYBERSECIDENT/487845/IV/NCBR/2021

## II. Signaling Storm Detection in O-RAN

In order to detect the SSA it is crucial for the xApp to subscribe to messages that are exchanged between the IIoT device and the 5G NodeB (gNB) at the very beginning of the registration procedure. These messages are depicted in Fig. 1 based on the 5G New Radio (NR) specification [5]. First, the IIoT device sends Msg1, which contains the random access preamble. After the successful reception of Msg1, the gNB responds to the IIoT device with a Msg2: Random Access Response. The Msg2 contains the Timing Advance (TA) command, which is the time offset related to the signal propagation time between the gNB and IIoT devices. As the IIoT devices are in most cases stationary the TA is constant for them and proportional to the distance to the gNB. While the identifier of the IIoT device, e.g., Cell Radio Network Temporary Identifier (C-RNTI) does not have to remain the same between the consecutive registration attempts, during initial access the adversary IIoT devices can be filtered using their specific TA parameters. With the use of O-RAN interfaces, the Msg2 can be copied and transferred to the SSA detection xApp for statistical analysis. Following the general framework, from [6], the so-called Key Performance Indicator (KPI) Profiles, are formulated. The statistics in the KPI Profiles are computed within the consecutive time intervals $T$, e.g., every 5 minutes. They contain the long-term statistics of RRC Setup Requests (RSRs) associated with observed values of TA, i.e., mean number $\mu_{t,i}$ and standard deviation $\sigma_{t,i}$, where $i$ denotes TA index and $t$ denotes the time of a day period $(t-T;t)$ for which statistics are calculated. An example of such a KPI Profile is depicted in 2. During the network operation, the number of RSRs is constantly monitored for each


978-1-6654-9427-4/23/$31.00 ©2023 IEEE

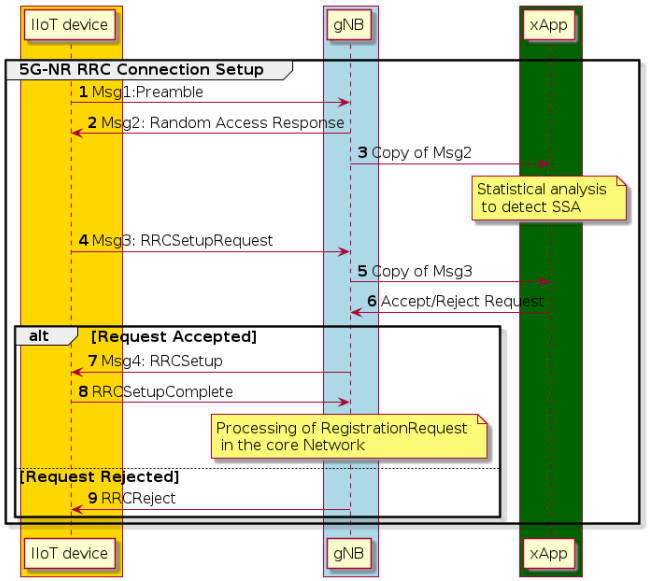


Fig. 1. CP messages exchanged between IIoT device, gNB, and SSA detection xApp.

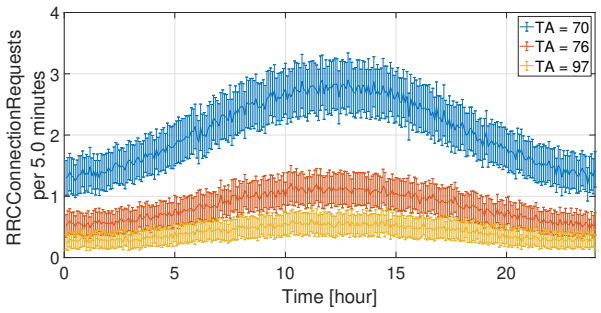


Fig. 2. Example of KPI profile with a mean and standard deviation of the number of RSRs associated with a given TA per 5 minutes.

observed TA. It is compared against the values from the KPI Profile to compute the so-called anomaly value [6]:

$$a(t,i) = \frac{X(t,i) - \mu_{t,i}}{\sigma_{t,i}}, \tag{1}$$

where $X(t,i)$ is the number of RSRs observed during time-period $t$ with $i$-th TA. If anomaly value $a(t,i)$ exceeds the threshold $\gamma$ the SSA is being detected. Based on the detection result the SSA detection xApp indicates the gNB to either accept the RSR and proceed with the registration or reject it. It can be also a general policy send from the xApp, e.g., *Reject all requests of TA=77.*

## III. Simulation Results

The proposed SSA detection algorithm was verified through computer simulations. We have considered a single cell of a 5G-IIoT network of 2 km radius with 100 legitimate IIoT devices and 5 adversaries. The legitimate IIoT devices send RSR following the exponential distribution with a mean rate parameter of 5 RSRs per hour. The rate is changing over the daytime resembling a sinusoidal function: it is increased and decreased by 35% at noon, and midnight respectively. Each adversary starts its SSA following the exponential distribution of rate equal to 3 attacks per day. Each attack consists of 100 consecutive RSRs sent within the interval of 5 seconds. In the simulation, we have assumed that the KPI profiles are already computed for the network without adversaries. We have compared the SSA detection for different thresholds of anomaly detection $\gamma$ for 20-day-long simulations. The resultant probability of false alarm and SSA detection is depicted in Fig. 3. It can be seen that for the low value of $\gamma$ both the probability of detection and the false alarm is very close to 1.0. The probability of a false alarm can be decreased to 1.5% by setting $\gamma = 6.5$ at the cost of the probability of detection degradation to 92%. The proposed method allows to balance both probabilities by setting a proper threshold $\gamma$ depending on the network's operator requirements.

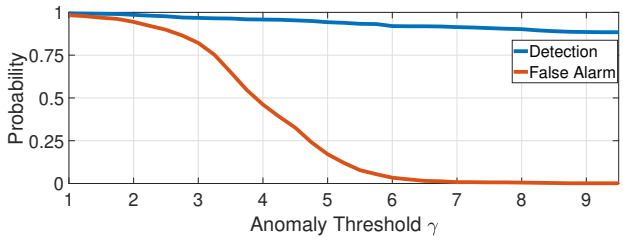


Fig. 3. Probabilities of SSA detection and false alarm for the proposed xApp as a function of threshold parameter $\gamma$.

## IV. Conclusion

The utilization of O-RAN architecture enables the detection of SSA at an early stage of the adversary registration process. By properly setting the threshold parameter the proposed SSA detection algorithm can offer high detection probability while causing only a few false alarms.

## References

[1] E. Sisinni, A. Saifullah, S. Han, U. Jennehag, and M. Gidlund, "Industrial internet of things: Challenges, opportunities, and directions," *IEEE Transactions on Industrial Informatics*, vol. 14, no. 11, pp. 4724–4734, 2018.

[2] J. Cao, M. Ma, H. Li, R. Ma, Y. Sun, P. Yu, and L. Xiong, "A survey on security aspects for 3gpp 5g networks," *IEEE Comm. Surveys & Tutorials*, vol. 22, no. 1, pp. 170–195, 2020.

[3] M. Dryjański, Ł. Kułacz, and A. Kliks, "Toward Modular and Flexible Open RAN Implementations in 6G Networks: Traffic Steering Use Case and O-RAN xApps," *Sensors*, vol. 21, no. 24, p. 8173, 2021.

[4] O-RAN ALLIANCE WG1, "Use cases detailed specification, v.9.0," Tech. Rep., 10 2022. [Online]. Available: https://orandownloadsweb.azurewebsites.net/specifications

[5] 3GPP, "Technical Specification Group Radio Access Network; NR; Medium Access Control (MAC) protocol specification (Release 17) ," TS 38.214 v.17.2.0, Sep. 2022.

[6] L. Bodrog, M. Kajo, S. Kocsis, and B. Schultz, "A robust algorithm for anomaly detection in mobile networks," in *2016 IEEE 27th Annual International Symposium on Personal, Indoor, and Mobile Radio Communications (PIMRC)*, 2016, pp. 1–6.

## 7.4 Publication [P4]

M. Hoffmann and P. Kryszkiewicz, "O-RAN for Energy-Efficient Serving Cluster Formulation in User-Centric Cell-Free MMIMO," in *IEEE INFOCOM 2024 - IEEE Conference on Computer Communications Workshops (INFOCOM WKSHPS)*, pp. 1–2, 2024.

MNiSW Points: 200

Number of citations:

- according to Web of Science: 1
- according to Google Scholar: 1

mgr inż. Marcin Hoffmann
Instytut Radiokomunikacji, Politechnika Poznańska
ul. Polanka 3, 60-965 Poznań

Poznań, 9 stycznia 2025 r.

# OŚWIADCZENIE W SPRAWIE AUTORSTWA PRACY

Oświadczam, że w pracy:

*M. Hoffmann and P. Kryszkiewicz, "O-RAN for Energy-Efficient Serving Cluster Formulation in User-Centric Cell-Free MMIMO," IEEE INFOCOM 2024 - IEEE Conference on Computer Communications Workshops (INFOCOM WKSHPS), Vancouver, BC, Canada, 2024, pp. 1-2.*

mój udział polegał na:

- Zaproponowaniu algorytmu hierarchicznego algorytmu formowania klastrów obsługujących w sieci Massive MIMO zorientowanej na użytkownika, zgodnego z architekturą otwartej sieci dostępowej O-RAN. Algorytm ma na celu zwiększenie efektywności energetycznej.
- Przygotowaniu w całości tekstu pierwszej wersji artykułu.
- Przeprowadzeniu symulacji komputerowych i opracowaniu wyników

Mój procentowy udział w powstanie pracy szacuję na: 85%

Hoffmann

.....

Podpis

dr hab. inż. Paweł Kryszkiewicz, prof. PP
Instytut Radiokomunikacji, Politechnika Poznańska
ul. Polanka 3, 60-965 Poznań

Poznań, 9 stycznia 2025 r.

# OŚWIADCZENIE W SPRAWIE AUTORSTWA PRACY

Oświadczam, że w pracy:

*M. Hoffmann and P. Kryszkiewicz, "O-RAN for Energy-Efficient Serving Cluster Formulation in User-Centric Cell-Free MMIMO," IEEE INFOCOM 2024 - IEEE Conference on Computer Communications Workshops (INFOCOM WKSHPS), Vancouver, BC, Canada, 2024, pp. 1-2.*

mój udział polegał na:

- Dyskusji z głównym autorem struktury pracy, wykorzystanej metodologii, a także uzyskanych wyników
- Korekcie tekstu

Mój procentowy udział w powstanie pracy szacuję na: 15%

Podpis

IEEE INFOCOM 2024 - IEEE Conference on Computer Communications Workshops (INFOCOM WKSHPS) | 979-8-3503-8447-5/24/$31.00 ©2024 IEEE | DOI: 10.1109/INFOCOMWKSHPS61880.2024.10620770

# O-RAN for Energy-Efficient Serving Cluster Formulation in User-Centric Cell-Free MMIMO

Marcin Hoffmann
*Institute of Radiocommunications*
*Poznan University of Technology*
Poznan, Poland

Pawel Kryszkiewicz
*Institute of Radiocommunications*
*Poznan University of Technology*
Poznan, Poland

***Abstract*—The 6G Massive Multiple-Input Multiple-Output (MMIMO) networks can follow the so-called User-Centric Cell-Free (UCCF) architecture, where a single user is served by multiple Access Points (APs) coordinated by the Central Processing Unit (CPU). In this paper, we propose how O-RAN functionalities, i.e., rApp-xApp pair, can be used for energy-efficient Serving Cluster Formulation (SCF). Simulation studies show up to 37% gain in Energy Efficiency (EE) of the proposed solution over the state-of-the-art Network-Centric (NC) designs.**

## I. Introduction

The UCCF MMIMO is an emerging technology for future 6G networks [1]. Unlike the state-of-the-art NC approach, where a given user is typically served by one Base Station (BS), the UCCF MMIMO network is to provide the user with a coordinated transmission from multiple APs, that are coordinated by the CPU. This approach allows to significantly improve the network Spectral Efficiency (SE) and to provide users with equalized Quality of Service (QoS). Moreover, the UCCF network design can potentially improve the EE over the NC approach, as a result of the increased number of degrees of freedom. One of the key challenges in a UCCF MMIMO network is to determine which APs should serve a specific user, e.g., distant APs might provide a marginal contribution to user throughput while increasing signaling overhead, and "wasting" allocated power. The procedure of AP selection is known as the SCF. It has been shown that the practical implementation of the UCCF MMIMO network can follow the Open Radio Access Network (O-RAN) architecture [2]. By utilizing the 7.2 split, the E2 Node (here O-RAN Distributed Unit) can serve as CPU and control transmission from multiple O-RAN Radio Units (O-RUs). The control of an O-RAN network is possible with the use of so-call xApps, and rApps that are deployed within Near Real-Time RAN intelligent Controller (Near-RT RIC), and Non-RT RIC, respectively. The former works within the control loop of time scale between 10 ms and 1 s while the latter above 1 s. While the SCF through the dedicated xApp has been proposed in [3], the authors did not consider the participation of Non-RT RIC and were focused on the SE and throughput, not EE. Moreover, the numerical analysis assumes a simple radio channel model and most importantly a narrowband, single-carrier system, while real 5G, and plausibly 6G, networks utilize Orthogonal Frequency Division Multiple Access (OFDMA).

The presented work was funded by the Polish National Science Centre, project no. 2022/45/N/ST7/01930.

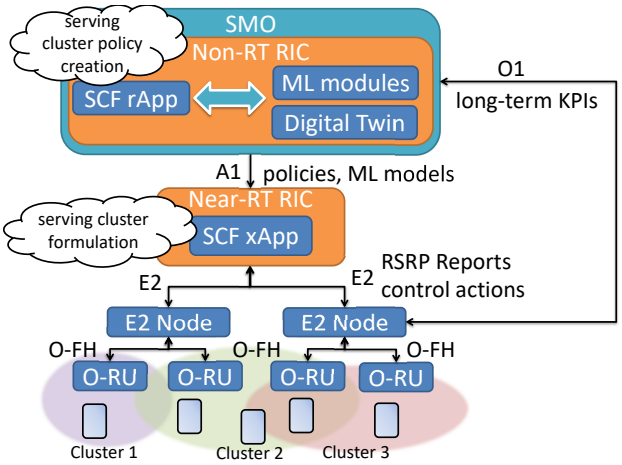


Fig. 1. The concept of rApp-xApp cooperation for EE-oriented SCF in O-RAN UCCF MMIMO network.

In this paper, we propose EE-oriented SCF that involves cooperation between rApp in Non-RT RIC and xApp in Near-RT RIC. The simulation studies are performed with the use of an advanced OFDMA-based UCCF MMIMO network simulator utilizing 3D Ray Tracing software.

## II. xApp/rApp for EE-oriented SCF

The concept of rApp-xApp cooperation for EE-oriented SCF in O-RAN UCCF MMIMO network is depicted in Fig. 1. The SCF rApp placed in the Non-RT RIC is responsible for creating policies for SCF that contain, e.g., the number of O-RUs that should formulate a serving cluster, or SCF algorithm to be utilized, out of the set available in the xApp. These are communicated to the SCF xApp through the A1 interface, possibly together with pre-trained ML models. To formulate these policies SCF rApp utilizes 3GPP-compliant KPIs measured over the O1 interface [4], e.g., UL/DL throughput distribution, and power consumption. Potentially rApp can also


979-8-3503-8447-5/24/$31.00 ©2024 IEEE

use information from ML models or Digtial Twin-based simulations deployed within the Non-RT RIC. On the other hand, the SCF xApp is responsible directly for SCF according to the A1 policies produced by rApp, and user Reference Signal Received Power (RSRP) measurements. Both control actions - SCF, and input data - RSRP reports are obtained by the E2 interface that connects Near-RT RIC with E2 Nodes (O-DUs). The E2 Nodes are further responsible for the configuration of O-RUs to create the desired serving clusters, e.g., synchronization of multi-point MMIMO transmission, channel estimation, and sharing of user data. However, enabling these features requires standardization effort both within the A1 and E2 interface, to enable new policy types and E2 Service Models (SMs) proper for the UCCF MMIMO network.

To test the validity of the proposed approach an SCF based on the reported RSRPs is proposed. The serving cluster is formulated separately for each UE by selecting the $N$ O-RUs of the highest RSRPs. The $N$ is provided by the SCF rApp through A1 policy and refers to Serving Cluster Size (SCS). After the serving cluster is formulated the SCF rApp can monitor both per-user EE based on UL/DL throughput distribution and O-RU's power consumption, or RAN EE by dividing the total UL/DL throughput by the total power consumption. Such measurements can be used to train the ML model or to adjust Digital Twin (DT) to support SCF rApp with the formulation of policies that improve EE.

## III. Simulation Results

The proposed xApp-rApp pair SCF algorithm is evaluated within an advanced network simulator of the OFDMA-based UCCF MMIMO network described in [5] that utilizes Wireless InSite 3D Ray Tracer, and dedicated radio resource scheduler. We assume that there is a single E2 Node responsible for radio resource scheduling that coordinates transmission from O-RUs. We consider 1 macro O-RU of transmit power equal to 46 dBm, equipped with 128 antennas, and 5 micro O-RUs of transmit power equal to 30 dBm, equipped with 32 antennas. The network utilizes 25 MHz bandwidth around a center frequency of 3.6 GHz. The Zero-Forcing (ZF) precoding is used independently within each O-RU. The results are obtained after 15 independent simulation runs, each emulating 500 ms of network operation, considering 20 randomly placed UEs. In Fig. 2 a distribution of per-user EE is shown for varying SCS. The size equal to 1 corresponds to the NC approach. It can be seen that utilization of the UCCF approach provides per-user EE gains over the NC approach in at least 70% of cases. Also for growing SCS the distribution of per-user EE becomes more uniform. However, for SCS $>$ 3 EE of about 60% of users starts to degrade compared to the SCS $=$ 3. A similar tendency can be observed in the RAN EE depicted in Fig. 3. The highest EE is related to the SCS $=$ 3. It provides gains of about 37% over the NC approach. For higher SCS the

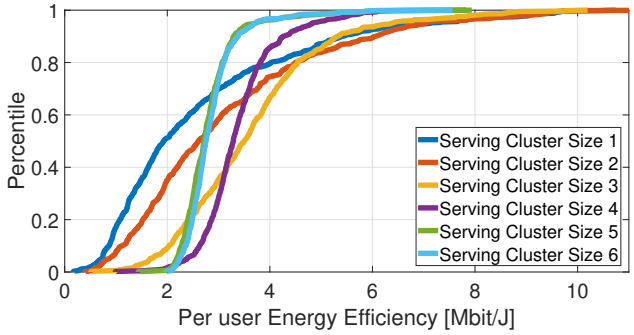


Fig. 2. Distribution of per-user EE for varying Serving Cluster Size.

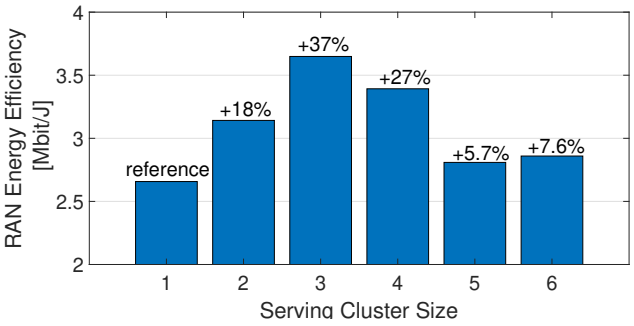


Fig. 3. RAN EE for varying serving cluster size.

EE gains degrade. The reason can be that while increasing the number of SCS too much, users are being served by some distant O-RUs. These O-RUs are "wasting" transmit power to overcome large path loss.

## IV. Conclusion

We have shown the utilization of the proposed SCF xApp and rApp can provide significant EE gains in the O-RAN-based UCCF MMIMO network over the NC approach. However, to maximize gains, the SCS must be carefully chosen by SCF rApp based on the network state. In the future, this work can be extended by the utilization of DT or O-RU's micro sleep controlled by SCF xApp.

## References

[1] I. F. Akyildiz, A. Kak, and S. Nie, "6G and Beyond: The Future of Wireless Communications Systems," *IEEE Access*, vol. 8, pp. 133 995–134 030, 2020.

[2] V. Ranjbar, A. Girycki, M. A. Rahman, S. Pollin, M. Moonen, and E. Vinogradov, "Cell-Free mMIMO Support in the O-RAN Architecture: A PHY Layer Perspective for 5G and Beyond Networks," *IEEE Communications Standards Magazine*, vol. 6, no. 1, pp. 28–34, 2022.

[3] R. Beerten, A. Girycki, and S. Pollin, "User Centric Cell-Free Massive MIMO in the O-RAN Architecture: Signalling and Algorithm Integration," in *2022 IEEE Conference on Standards for Communications and Networking (CSCN)*, 2022, pp. 181–187.

[4] "Management and orchestration; 5G performance measurements," 3GPP, TS 28.552 v.18.2.0, Mar. 2023.

[5] M. Hoffmann and P. Kryszkiewicz, "Evaluation of User-Centric Cell-Free Massive Multiple-Input Multiple-Output Networks Considering Realistic Channels and Frontend Nonlinear Distortion," *Applied Sciences*, vol. 14, no. 5, 2024. [Online]. Available: https://www.mdpi.com/2076-3417/14/5/1684

## 7.5 Publication [P5]

M. Hoffmann, P. Kryszkiewicz, and A. Kliks, "Frequency selection for platoon communications in secondary spectrum using radio environment maps," *IEEE Transactions on Intelligent Transportation Systems*, vol. 23, no. 3, pp. 2637– 2650, 2022.

MNiSW Points: 140

Number of citations:

- according to Web of Science: 9
- according to Google Scholar: 12

mgr inż. Marcin Hoffmann
Instytut Radiokomunikacji, Politechnika Poznańska
ul. Polanka 3, 60-965 Poznań

Poznań, 20 maja 2022 r.

# OŚWIADCZENIE W SPRAWIE AUTORSTWA PRACY

Oświadczam, że w pracy:

*M. Hoffmann, P. Kryszkiewicz, A. Kliks, "Frequency Selection for Platoon Communications in Secondary Spectrum Using Radio Environment Maps," IEEE Transactions on Intelligent Transportation Systems, tom 23, nr 3, str. 2637-2650, marzec 2022*

mój udział polegał na:

- Zaproponowaniu modelowania rozkładu interferencji w kanale radiowym z użyciem tzw. Gaussian Mixture Model
- Adaptacji algorytmu DBSCAN (ang. Density-Based Spatial Clustering of Applications with Noise) do grupowania nieodleglych lokacji charakteryzujących się podobnym rozkładem interferencji.
- Implementacji i adaptacji algorytmu Dijkstry do procesu wyboru kanałów radiowych na trasie konwoju w celu minimalizacji liczby przełączeń.
- Analizie danych pomiarowych z użyciem zaproponowanych rozwiązań
- Opracowaniu wyników
- Przygotowaniu pierwszej wersji

Mój procentowy udział w powstanie pracy szacuję na: 70%

Marcin Hoffmann

Podpis

dr hab. inż. Paweł Kryszkiewicz, prof. PP
Instytut Radiokomunikacji, Politechnika Poznańska
ul. Polanka 3, 60-965 Poznań

Poznań, 21 sierpnia 2025 r.

# OŚWIADCZENIE W SPRAWIE AUTORSTWA PRACY

Oświadczam, że w pracy:

*M. Hoffmann, P. Kryszkiewicz, A. Kliks, "Frequency Selection for Platoon Communications in Secondary Spectrum Using Radio Environment Maps," IEEE Transactions on Intelligent Transportation Systems, tom 23, nr 3, str. 2637-2650, marzec 2022*

mój udział polegał na:

- Koordynacji prac badawczych
- Definicji problemu i miary zagregowanej interferencji wykorzystującej pojemność kanału radiowego
- Propozycji algorytmu grafowego dla minimalizacji liczby przełączeń kanału radiowego
- Zbudowaniu układu pomiarowego i przeprowadzeniu pomiarów sygnału zakłócającego (wraz z trzecim autorem)
- Dyskusji ze współautorami uzyskanych wyników i metod ich prezentacji
- Iteracyjnym nanoszeniu poprawek na tekst; dyskusji uwag ze współautorami

Mój procentowy udział w powstanie pracy szacuję na: 20%

Podpis

dr hab. inż. Adrian Kliks, prof. PP
Instytut Radiokomunikacji, Politechnika Poznańska
ul. Polanka 3, 60-965 Poznań

Poznań, 20 maja 2022 r.

# OŚWIADCZENIE W SPRAWIE AUTORSTWA PRACY

Oświadczam, że w pracy:

*M. Hoffmann, P. Kryszkiewicz, A. Kliks, "Frequency Selection for Platoon Communications in Secondary Spectrum Using Radio Environment Maps," IEEE Transactions on Intelligent Transportation Systems, tom 23, nr 3, str. 2637-2650, marzec 2022*

mój udział polegał na:

- zdefiniowaniu problemu badawczego i dyskusjach merytorycznych na temat sposobów jego rozwiązania
- pisaniu fragmentów tekstu oraz sprawdzaniu pracy.

Mój procentowy udział w powstanie pracy szacuję na: 10%

Adrian Kliks

Podpis

# Frequency Selection for Platoon Communications in Secondary Spectrum Using Radio Environment Maps

Marcin Hoffmann, *Graduate Student Member, IEEE*, Pawel Kryszkiewicz, *Senior Member, IEEE*, and Adrian Kliks, *Senior Member, IEEE*

***Abstract*— Platoon-based driving is an idea that vehicles follow each other at a close distance, in order to increase road throughput and fuel savings. This requires reliable wireless communications to adjust the speeds of vehicles. Although there is a dedicated frequency band for vehicle-to-vehicle (V2V) communications, studies have shown that it is too congested to provide reliable transmission for the platoons. Additional spectrum resources, i.e., secondary spectrum channels, can be utilized when these are not occupied by other users. Characteristics of interference in these channels are usually location-dependent and can be stored in the so-called Radio Environment Maps (REMs). This paper aims to design REM, in order to support the selection of secondary spectrum channel for intra-platoon communications. We propose to assess the channel's quality in terms of outage probability computed, with the use of estimated interference distributions stored in REM. A frequency selection algorithm that minimizes the number of channel switches along the planned platoon route is proposed. Additionally, the REM creation procedure is shown that reduces the number of database entries using (Density-Based Spatial Clustering of Applications with Noise) DBSCAN algorithm. The proposals are tested using real IQ samples captured on a real road. Application of the DBSCAN clustering to the constructed REM provided 7% reduction in its size. Utilization of the proposed channel selection algorithm resulted in a 35 times reduction of channel switches concerning channel assignment performed independently in every location.**

***Index Terms*— Radio environment map, V2V, Gaussian mixture model, interference modeling.**

## I. Introduction

THE number of vehicles on the roads consistently grew, through recent years, causing increasing traffic congestion. This implies not only time delays but also energy wastes and pollution. An obvious solution to improve road throughput is to deploy additional infrastructure, e.g., by building new roads or extending the number of lanes of existing ones. However, this solution is first time-consuming, secondly expensive, and finally, it is not always possible to expand vehicular infrastructure e.g., to build additional lane under urban conditions. On the other hand, there is an idea to deal with the mentioned issues by changing the driving pattern into the so-called *platoon*-based [1]. *Platoon*-based driving pattern assumes that a group of vehicles will follow each other, while maintaining short inter-vehicles distance, e.g., few meters [2]. The first vehicle in the platoon is the platoon-leader. It is typically responsible for the management, and coordination of platoon behavior, e.g., adjusting speed, or inter-vehicle distance. However, also distributed solutions are under consideration [3]. There are several benefits from the deployment of the *Platoon*-based driving. First, short inter-vehicle spaces improve the road capacity that is also related to the reduction of traffic congestion [4]. Secondly, vehicles following the platoon leader save fuel, implying the reduction of carbon footprint [5]. The shorter the inter-vehicle distance, the higher the expected fuel savings. However, very short inter-vehicle distance requires precise and error-free coordination of vehicles in order to prevent collisions.

This is one of the key challenges in *platoon*-based driving, i.e., to ensure safety for vehicles. Each car within the platoon must be able to adapt its speed to the platoon leader, including sudden breakings, while maintaining short inter-vehicles distance. Studies have shown that for this purpose it is more beneficial to rely on the short-range wireless communications sending, e.g., a message about breaking, than on direct measurements from distance sensors [6]. The short-range wireless communication between vehicles within the platoon can be realized using, e.g., Dedicated Short-Range communications (DSRC). The DSRC physical and medium-access layers are described in IEEE 802.11p, and Wireless Access in Vehicular Environment (WAVE) standards [7]. WAVE operates in the dedicated frequency band: 5.850-5.925 GHz, and 5.855-5.925 GHz in the USA, and Europe, respectively. This is one of the Unlicensed National Information Infrastructure (U-NII) bands. However, studies have shown that with a growing number of vehicles utilizing DSRC this amount of spectrum will not be sufficient to provide low enough latency, and high reliability [8], [9]. Moreover, similar issues could be identified while considering platoon communications based on the cellular technologies e.g. Cellular Vehicle-to-Everything (C-V2X) [10]. The reason for this is the limited capacity of the wireless channel. While the intra-platoon spectrum access

Manuscript received January 30, 2021; revised June 7, 2021 and November 12, 2021; accepted December 14, 2021. Date of publication December 24, 2021; date of current version March 9, 2022. This work was supported by the National Science Centre in Poland under Project 2018/29/B/ST7/01241. The Associate Editor for this article was T.-H. Kim. *(Corresponding author: Marcin Hoffmann.)*

The authors are with the Institute of Radiocommunications, Poznań University of Technology, 61-131 Poznań, Poland (e-mail: marcin.ro.hoffmann@doctorate.put.poznan.pl).

Digital Object Identifier 10.1109/TITS.2021.3136681

could be designed in an orthogonal, collision-free manner, the orthogonality between transmissions of various platoons and vehicles cannot be guaranteed. Even if different platoons use the same waveform, for which orthogonality can be obtained, it will not be achieved as a result of the lack of coordination, e.g., in general, different platoons are not time-synchronized and can start transmissions in the same time instance. This lack of orthogonality results in inter-platoon interference, which reduces wireless channel capacity and causes communication delays. These delays may further lead to, e.g., instability in platoon formation, or reduced cyber security [11]–[13]. This would further imply larger inter-vehicle distances, that will significantly reduce the *platoon*-based driving benefits, e.g. fuel saves.

From this perspective, it seems reasonable to find an alternative frequency band that can be utilized for inter-platoon communications. Because vehicles within the platoon already formulate a small network, the whole communication can be synchronously offloaded to the less occupied frequency band. Such a procedure cannot be easily applied for general V2V communications, because it would require special synchronization mechanisms. One solution is to offload the platoon communications into the unlicensed band, e.g., 2.4 GHz, where no protection of other users' transmission is necessary. Although this approach seems not to be appropriate in the urban areas, where wireless access points density is large, it looks promising to be utilized under highway conditions [14]. In [15] a so-called Cognitive Anypath Vehicular Protocol (CoRoute) was proposed, in order to utilize instantaneous channel state information, and neighboring vehicles positions for opportunistic vehicular communication over 2.4 $GHz$ industrial, scientific, and medical (ISM) band. Authors of [16] focus on the coexistence of V2X and Vehicular ad-Hoc network (VANET) systems in the unlicensed band, proposing a spectrum sensing scheme, vehicle interference models, and resource allocation algorithm. However, these works do not consider location-dependent interference characteristics.

Another idea is to look for the additional spectrum resources in the millimeter-waves band [17], [18]. However, in such high frequencies radio channel, the achievable range is very limited, which decreases the connection reliability. Reliability, that is crucial for platoon stability.

On the other hand, although almost all of the frequency bands below 3 GHz are assigned to a variety of wireless systems, they are not fully utilized in practice [19]. Therefore, there is a possibility to exploit additional spectrum resources in the moments when these are not occupied by Primary Users (PUs), i.e., wireless systems that are licensed to transmit in a given band. This scheme is known in the literature as Dynamic Spectrum Access (DSA) [20]. DSA can further benefit from the information about the surrounding radio environment e.g., interference. It has been shown that this kind of information is in most cases related to the location, which makes an opportunity to create intelligent geolocation databases, known as the Radio Environment Maps (REMs) [21]. One example of REMs application is a storage of information about the unoccupied television channels: so-called TV White Spaces (TVWS) [22]–[24]. It is applicable because the terrestrial TV signal is stable over time, and location, i.e., location of the terrestrial TV transmitters along with their transmission power and channels assignment remains constant over a long-time period.

Most importantly, the DSA, e.g., TVWS, is a well-suited solution for intra-platoon communications. The main reason is the low potential of interference caused by a platoon to other services. This is caused by relatively small transmission range, rapid changes of platoon position and other wireless services typically distanced from the road sites. Various REM architectures and implementation challenges for the purpose of DSA in platoon communications using TVWS had been described in [25]. In [26] authors proposed an algorithm to exploit TVWS data stored in REM, to apply DSA in V2X communications. While the above-mentioned REM applications assume relatively stable spectrum conditions and fixed PU types, REM can be used to represent more sophisticated cases as well, e.g., for scenarios with time-varying radio conditions and heterogeneous PUs. However, in this case, the PUs-originating interference has to be monitored and modeled to allow for the required reliability of intra-platoon communications.

The aim of this work is to propose a REM-based method of selecting alternative frequencies, where intra-platoon communications can be transferred. The main focus is put on the assessment of the radio channels quality under complex interference patterns. We expect that offloading intra-platoon communications to the high-quality channel, e.g., of low outage probability, will improve the general performance of control algorithms e.g. Cooperative Adaptive Cruise Control (CACC). While the platoon control mechanisms are out of the scope of this paper, the proposed, advanced models of interference can be applied to improve platoon stability and safety modeling done in [13] and [12]. The final goal of this paper is an optimal frequency assignment to the platoon. The REM contains location-dependent information about interference in a given frequency band. Various radio bands can be characterized by various interference patterns, varying over time. We propose to characterize interference at a given channel and location as a random variable, and REM to store proper interference distribution parameters. This solution allows for higher accuracy than typically used single-number interference characterization, e.g., by its mean power [25]–[27]. As the interference distribution at a given location will be estimated using a limited number of sensing reports, its accuracy can be insufficient. On the other hand, the interference properties in the neighboring locations should be closely correlated. As a result, some interference distributions in adjacent locations should be merged in order to increase accuracy. At the same time, REM size can be reduced. For this purpose, we propose to modify a Density-Based Spatial Clustering of Applications with Noise (DBSCAN) algorithm. The proposed modification aims to incorporate both geographical neighborhood and interference distribution similarities in the clustering procedure. Moreover, we propose a channel quality assessment method utilizing the interference distributions stored in REM. This channel quality assessment

method is necessary to assign reliable enough channel for platoon communications. We propose to assign a wireless channel to the platoon by minimizing the number of frequency switches along the planned route while providing sufficiently low channel capacity outage. An optimal solution is proposed utilizing the well-known Dijkstra algorithm [28]. The test field for validation of our proposal is the 2.4 GHz band. This part of radio frequencies is occupied by a variety of systems, e.g. WiFi, Bluetooth, ZigBee, providing various and non-regular interference patterns. Through the analysis of real data captured in the 2.4 GHz band during the measurement campaign, we will show that these interference patterns can be accurately represented using Gaussian Mixture Model (GMM).

The main contribution of the paper are:

- We propose an outage probability as a metric for channel quality assessment. The advantage of this metric over, e.g., latency is universality. Moreover, it can be obtained relatively easily, and irrespective of the transmission scheme, and medium access algorithms used. State-of-the-art solutions, e.g., [29], rely on creating location-dependent Signal-to-Interference-and-Noise-Ratio (SINR) maps. This approach makes those maps valid only for devices of equal transmission power and does not reflect the influence of narrowband interference on the signal. In our solution, we separate interference distribution from other parameters, e.g., pathloss and transmission power. This enables flexibility of providing frequency band to the platoon on the basis of platoon-specific requested transmission parameters.
- We propose to train Gaussian Mixture Models (GMMs) in order to model interference distribution in secondary spectrum channels. State-of-the-art Radio Environment Maps usually are designed so as they contain pairs of location-mean interference power [25]–[27]. This approach is sufficient while modeling interference from relatively stable sources, e.g., terrestrial television stations. However, such a model cannot be applied to scenarios where many interference sources of various transmission schemes operate simultaneously. Under such conditions more advanced models are necessary, i.e., the proposed GMMs.
- We propose to utilize the DBSCAN clustering algorithm in order to reduce REM size. Among other state-of-the-art clustering algorithms, DBSCAN has an ability to take into the account both close geographical distance between REM entries and similarities between interference distributions. Prior work related to the topic of REMs did not consider such an approach [25]–[27]. The procedure of DBSCAN clustering can be thought of as a process reverse to kriging [30]. Instead of interpolating between REM points, we propose to create clusters (areas) where interference follows the same distribution.
- We propose to use the Dijkstra algorithm to reduce the number of channel switches along the planned platoon route. We represent the problem of minimization of channel switches as a graph, where nodes refer to locations and edges represent available radio channels. A similar approach was proposed for the planning of UAV path [29]. However, in our case due to the nature of the platoon's route, the computational complexity is much lower. Another state-of-the-art channel assignment algorithms [31], [32] aim at lowering the number of channel switches in the vehicular communication scenario but without forecasting the whole platoon route. As a result, they will not guarantee the performance of our, Dijkstra-based algorithm.

The rest of the paper is organized as follows: Sec. II describes REM deployment, channel assessment method, minimization of channel switches along the platoon route using Dijkstra algorithm, and adaptation of DBSCAN algorithm to enable REM size reduction. The field measurement campaign setup, together with recorded data distribution analysis is provided in Sec. III. Evaluation of REM algorithms using the measurement data is described in Sec. IV. Conclusions are formulated in Sec. V.

## II. Radio Channel Quality Assessment Utilizing Radio Environment Maps

In this paper, an autonomous platoon consisting of $N_{\mathrm{v}}$ vehicles is considered, as it is depicted in Fig. 1. The platoon is claimed to travel over the route denoted as set of $\mathcal{L}$ geographical locations $\mathcal{X} = \{\mathbf{x}_l\}_{l=1}^{\mathcal{L}}$, where $\mathbf{x}_l$ denotes vector of earth-centered earth-fixed (ECEF) geographical coordinates related to platoon location $l$. The route covers mostly highway areas. However, urban, and suburban areas can appear at the beginning and end of the route. The first vehicle is the platoon leader responsible for the management and behavior of the platoon. This functionality is done by sending proper information to the following $N_{\mathrm{v}}-1$ vehicles through a wireless channel. To ensure short inter-vehicle distance necessary for providing e.g. fuel saves, the wireless transmission must satisfy requirements on channel capacity $C_{\mathrm{th}}$, and reliability expressed e.g. as the maximum allowable probability of link capacity being below $C_{\mathrm{th}}$ denoted as $\mathcal{P}_{max}$. These requirements must be ensured for transmission between the platoon leader, and every other vehicle in the platoon. The resultant maximum transmission range is the distance between the platoon leader and $N_{\mathrm{v}}$-th vehicle, denoted as $d$. Although there is a dedicated frequency band for V2V communications around 5.9 GHz, the studies have shown that it will be highly occupied and transmission requirements for reliability would not be satisfied [25]. Thus, the intra-platoon communication is realized in terms of DSA, by utilization of one of the unoccupied secondary spectrum channels, denoted as channel $i$. A major challenge is to choose a secondary spectrum channel $i$ from the set of available secondary spectrum channels $\mathcal{I}$ satisfying both $C_{\mathrm{th}}$, and $\mathcal{P}_{max}$ in each of the consecutive platoon locations $\mathcal{X}$. Although platoon can perform spectrum sensing, it is more beneficial to rely on past knowledge about the radio environment. It allows to e.g., characterize long term interference patterns over secondary spectrum channels $\mathcal{I}$ at given location $\mathbf{x}_l$, and plan future channel switching along the whole platoon route. We propose to create an intelligent database of location-dependent information about the radio environment i.e., REM. REM aims to assess the quality of secondary

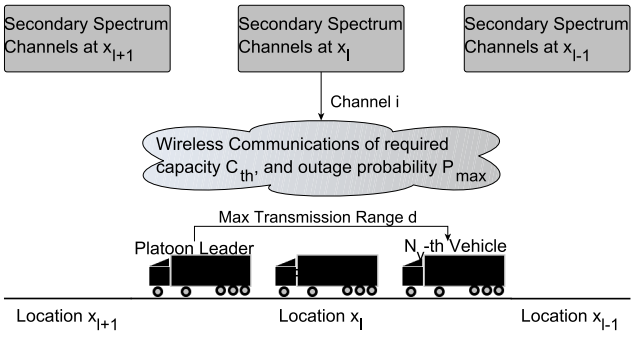


Fig. 1. Illustration of the intra-platoon communication, with the use of the secondary spectrum channels.

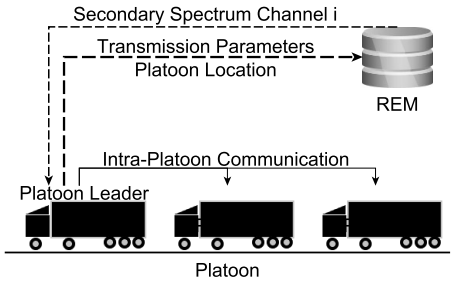


Fig. 2. Concept of REM utilization for platoon communications.

spectrum channels available in consecutive locations, based on past knowledge about interference distributions. The remaining part of this section will describe general REM architecture, algorithms for channel quality assessment and assignment, and method for reduction of REM size.

### A. REM for Platoon Communication

The general aim of the REMs is to provide the network with location-dependent data describing the radio environment, to, e.g., enable DSA. However, REM is not only the database. It provides intelligent mechanisms of location-dependent data acquisition, processing, and storage. The high-level REM architecture consists of the so-called Measurement Capable Devices (MCDs) providing the data, REM storage and acquisition unit, and REM manager responsible for proper data processing in order to handle communication with REM users [33].

For the purpose of intra-platoon communications, REM manager, storage, and acquisition units can be deployed as an extension to the existing cellular network infrastructure. Then, data exchange between the platoon leader and REM can be realized with the use of roadside units. The platoon can act both as an MCD, and REM user. When platoon acts as MCD it provides REM with batches of interference samples tagged with its geographical coordinates. These raw interference samples are processed by the REM manager unit to obtain their statistical models. Finally, model parameters, are saved in the REM storage unit. When platoon acts as a REM user it requests the REM manager to assign secondary spectrum channel $i \in \mathcal{I}$ for intra-platoon communications at location $\mathbf{x}_l$ based on transmission parameters given by the platoon leader, and interference model parameters saved in REM. The high-level idea of this procedure is depicted in Fig. 2. The platoon leader sends to REM information about its location and desired transmission parameters. REM determines which secondary spectrum channel is the best for intra-platoon communication, and sends index $i$ of this channel to the platoon leader. To enable optimization of secondary spectrum channel assignment along the whole platoon route, we consider centralized REM architecture. However, the major research issue related to the procedure of selection of secondary spectrum channel is the assessment of the available radio resources, possibly located at various frequency bands.

### B. Outage Probability Estimation

To assign a frequency band to a given platoon, a channel quality assessment method is necessary. The most effective approach from the perspective of platoon stability is to use the latency as a metric [34]. However, in general case its estimation is not straightforward, i.e., the latency depends on the used radio access technology and medium access protocol. Moreover to accurately estimate the latency the distribution of the incoming packets should be known. Instead, a reasonable comparison between radio channels, irrespective of the particular system properties, e.g., utilized coder or modulation, can be done on the basis of capacity being the upper bound estimate of the real system throughput. Such an approach is legitimated by the literature, e.g., to compare various frequency bands, in the context of Dynamic Spectrum Access [35], or for the purpose of communications with unmanned aerial vehicles [29]. However, in Sec. II-C, we will show that there exists a relation between the radio channel capacity and latency. We decided to compute the capacity of a single channel as a sum over the capacities of component narrow frequency sub-channels. The first motivation is that various interference sources can have various frequency-specific emission characteristics. The second reason is that many contemporary systems utilize multi-carrier communication based on the Orthogonal-Frequency-Division-Multiplexing (OFDM), e.g., 802.11p, Digital Video Broadcasting- Terrestrial (DVB-T), 5G. Thus Shannon capacity between most distanced cars within the platoon, at location $\mathbf{x}_l$, can be computed as follows:

$$c^{(i,\mathbf{x}_l)} = \mathrm{B} \sum_{k \in \mathcal{K}} \log_2 \left( 1 + \frac{P_{tx}^{(i,\mathbf{x}_l)} \cdot L(d)^{(i,\mathbf{x}_l)}}{\sigma_{\mathrm{n}}^2 + I_k^{(i,\mathbf{x}_l)}} \right), \qquad (1)$$

where, $i$ stands for the secondary spectrum channel index, $\mathcal{K}$ is the set of active sub-channels used in intra-platoon communications, B is the sub-channels spacing, $P_{tx}^{(i,\mathbf{x}_l)}$ is the transmitter power per sub-channel (maximum power reported by the platoon leader), $\sigma_{\mathrm{n}}^2$ is the noise power over sub-channel band, $I_k^{(i,\mathbf{x}_l)}$ stands for the interference power on sub-carrier $k$, and $L(d)^{(i,\mathbf{x}_l)}$ is distance $d$ dependent channel gain (including TX and RX antenna gains). Typically radio channel gain randomly varies over frequency, and time. There are several empirical models of this phenomenon proposed for the evaluation of V2V communications [36]. However, measurement studies have shown that when vehicles follow each other at close distance, e.g., below 200 m, there would be

mainly Line-Of-Sight (LOS) propagation between them [37]. While there exists an advanced radio channel model, utilizing geometry of the surrounding scatters [38], this will be not useful for this application. The platoon would not have such detailed information about e.g., the location of buildings and other vehicles. Thus, less complex, yet well-established distance-dependent models can be used, e.g., two slope pathloss model [39]. Although channel impulse response will influence a single sub-channel, its influence should be averaged when considering the whole band. Moreover, the channel response variations caused by fast fading cannot be estimated before transmission occurs in the channel. On the other hand, the interference $I_k^{(i,\mathbf{x}_l)}$ from primary systems can significantly vary over locations and frequencies affecting capacity. As a result, we propose to make an assumption about the flat channel, to focus on the interference impact on the channel capacity.

Crucial for the platooning purpose is the reliable, transmission of the messages containing information about platoon leader velocity and acceleration. The low communication reliability and high latency can significantly decrease the benefits from platoon driving pattern, or in the worst cause a platoon crash. However, the required capacity is relatively low, e.g., using 802.11p safety messages are transmitted using minimal supported bit-rate [40]. However, the platoon requires that the capacity is available, e.g., it is more important to provide often the minimum required channel capacity, than high instantaneous channel capacity rarely. As such channel outage probability is of higher importance than ergodic or maximal channel capacity. Due to the randomly changing interference, the capacity $c^{(i,\mathbf{x}_l)}$ becomes a random variable. As a result the probability of capacity being below a certain threshold is of high importance. Such situation occurs when the temporal signal-to-interference ratio (SINR) is very low. Thus it is reasonable to use the Shannon formula simplification for low SINR [41]: $\log_2\left(1+\frac{P_{tx}^{(i,\mathbf{x}_l)}\cdot L(d)^{(i,\mathbf{x}_l)}}{\sigma_{\mathrm{n}}^2+I_k^{(i,\mathbf{x}_l)}}\right)\approx\frac{1}{\ln 2}\cdot\left(\frac{P_{tx}^{(i,\mathbf{x}_l)}\cdot L(d)^{(i,\mathbf{x}_l)}}{\sigma_{\mathrm{n}}^2+I_k^{(i,\mathbf{x}_l)}}\right)$. This allows for the following transformation of (1):

$$c^{(i,\mathbf{x}_l)}\approx\frac{\mathrm{B}\cdot P_{tx}^{(i,\mathbf{x}_l)}\cdot L(d)^{(i,\mathbf{x}_l)}}{\ln 2}\cdot\sum_{k\in\mathcal{K}}\frac{1}{\hat{I}_k^{(i,\mathbf{x}_l)}},\tag{2}$$

where $\hat{I}_k^{(i,\mathbf{x}_l)}=\sigma_{\mathrm{n}}^2+I_k^{(i,\mathbf{x}_l)}$. Now the outage probability formula is given as:

$$\mathcal{P}_{out}^{(i,\mathbf{x}_l)}=\mathcal{P}\left(\sum_{k\in\mathcal{K}}\frac{1}{\hat{I}_k^{(i,\mathbf{x}_l)}}<\frac{\ln 2\cdot C_{\mathrm{th}}}{\mathrm{B}\cdot P_{tx}^{(i,\mathbf{x}_l)}\cdot L(d)^{(i,\mathbf{x}_l)}}\right),\tag{3}$$

where $C_{\mathrm{th}}$ is the minimum required link capacity that supports the safe operation of the platoon. It can bee seen that due to the Shannon formula simplification for low SINR, the outage probability is only a function of single random variable, i.e., cumulative interference power $\sum_{k\in\mathcal{K}}\frac{1}{\hat{I}_k^{(i,\mathbf{x}_l)}}$. Moreover, the interference distribution in a particular location can be characterized in terms of one instead of $\mathcal{K}$-dimensional distribution. This will much simplify the data representation in REM. The interference in wireless communications usually follows the log-normal distribution [42]. Following this phenomenon, it seems reasonable to take the logarithm of (3). As a result, we expect to deal with Gaussian-like distributions instead of log-normal, which are much more complex to model. Both sides of (3) are always positive, thus logarithm of both sides can be found as:

$$\mathcal{P}\left(\chi^{(i,\mathbf{x}_l)}<\ln\frac{\ln 2\cdot C_{\mathrm{th}}}{\mathrm{B}\cdot P_{tx}^{(i,\mathbf{x}_l)}\cdot L(d)^{(i,\mathbf{x}_l)}}\right),\tag{4}$$

where $\chi^{(i,\mathbf{x}_l)}=\ln\sum_{k\in\mathcal{K}}\frac{1}{\hat{I}_k^{(i,\mathbf{x}_l)}}$ is the interference power distribution related to the frequency channel $i$, and location $\mathbf{x}_l$. Now the outage probability, can be computed, using the distribution of $\chi^{(i,\mathbf{x}_l)}$, which characterizes interference, and some constants provided by the platoon leader, i.e., its transceiver bandwidth, maximal transmit power and minimum required link capacity. The $\chi^{(i,\mathbf{x}_l)}$ distribution parameters related to geographical locations are envisioned to be stored in REM. The modeling of $\chi^{(i,\mathbf{x}_l)}$ on the basis of field measurements will be described in Sec. III-B.

### C. Relation Between Outage Probability and Latency

Although in this paper the outage probability is considered as a MAC-independent channel quality assessment metric, it can be mapped to the transmission latency, if necessary. Since there is usually no acknowledgment procedure in V2V communications when sending safety messages, and some Listen-before-talk procedure is used (e.g., in IEEE 802.11p standard), it can be expected that a delay occurs when the channel is busy. In the idealized model the channel is busy if its instantaneous capacity is lower than the capacity required for the transmission $C_{\mathrm{th}}$. At such time instance the achieved data rate equals zero. On the other hand, if the channel capacity exceeds required threshold, the data rate is fixed as a result of a single modulation-coding scheme used for broadcast messages and equals for the perfect system $C_{\mathrm{th}}$. This allows to calculate mean data rate in a channel as $(1-\mathcal{P}(c^{(i,\mathbf{x}_l)}<C_{\mathrm{th}}))C_{\mathrm{th}}$. This is the upper bound of the mean data rate that can be achieved in this channel. From this perspective, we can formulate the lower bound of the latency as a function of outage probability, and under the assumption of fixed packet size $D$. The formula is given by:

$$\tau^{(i,\mathbf{x}_l)}\geq\frac{D}{(1-\mathcal{P}(c^{(i,\mathbf{x}_l)}<C_{\mathrm{th}}))C_{\mathrm{th}}}.\tag{5}$$

A similar way of modeling latency is used in some works focused on the control algorithms, e.g., [34], [43]. Observe that the actual mean delay $\tau^{(i,\mathbf{x}_l)}$ will be probably higher as a result of radio access technology not achieving channel capacity and because of limitations of the Medium Access Control scheme. We propose to observe the outage probability, a well-established metric, irrespective of various possible transmission technologies of the platoon and the neighboring wireless systems.

### D. Radio Channel Assignment

Using (4) the outage probability related to every channel $i$ in each location $\mathbf{x}_l$ belonging to the platoon route can

be estimated. The most straightforward channel selection assumes selection of the channel related to the lowest outage probability:

$$\hat{i}^{(\mathbf{x}_l)} = \arg\min_{i} \mathcal{P}\left(\chi^{(i,\mathbf{x}_l)} < \ln \frac{\ln 2 \cdot C_{\text{th}}}{\mathrm{B} \cdot P_{tx}^{(i,\mathbf{x}_l)} \cdot L(d)^{(i,\mathbf{x}_l)}}\right). \quad (6)$$

However, such an approach can result in frequent channel switching. In the worst-case channel will be switched in every new location. This is not encouraged from the perspective of connection stability. In practical implementations, it is enough to ensure the outage probability being below the given threshold $\mathcal{P}_{\max}$. Thus we can define a channel assignment as the optimization problem, where the target is to minimize the number of channel switches along the platoon route, subject to outage probability being below the required value:

$$\min_{i^{(\mathbf{x}_r)}} \sum_{l=1}^{\mathcal{L}-1} s(i^{(\mathbf{x}_l)}, i^{(\mathbf{x}_{l+1})}),$$
$$s.t.\ \mathcal{P}(c^{(i^{(\mathbf{x}_l)},\mathbf{x}_l)} < C_{\text{th}}) \leq \mathcal{P}_{\max} \quad (7)$$

where $l$ is the index representing consecutive platoon locations, and $\mathcal{L}$ is the total number of locations along the platoon route, and $s(i^{(\mathbf{x}_r)}, i^{(\mathbf{x}_{r+1})})$ is the cost of a single channel switch, defined as follows:

$$s(i^{(\mathbf{x}_l)}, i^{(\mathbf{x}_{l+1})}) = \begin{cases} 1, & \text{if, } i^{(\mathbf{x}_l)} \neq i^{(\mathbf{x}_{l+1})} \\ 0, & \text{if } i^{(\mathbf{x}_l)} = i^{(\mathbf{x}_{l+1})}. \end{cases} \quad (8)$$

We propose to solve the optimization problem (7) by using graph theorem. The graph representation of channel assignment is depicted in Fig. 3. The example graph is constructed assuming 3 channels and 5 locations. Nodes represent radio channels providing sufficient outage probability, in consecutive locations. Graph edges stand for the channel switching cost. Following (8), the cost is equal to 1, when channel switching occurs, and 0 otherwise. Additionally, two nodes "START", and "END" are introduced with edge costs equal to 0. The optimization problem can be now solved in terms of finding the shortest path between "START" and "END" nodes. Because all graph edges are non-negative, the optimal solution to the problem of finding the shortest path can be computed using Dijkstra algorithm [28]. The problem can be alternatively expressed as a linear programming problem. While linear programming belongs to a class of convex optimization, the Dijkstra algorithm provides global optimum [44].

The worst-case computational complexity of the Dijkstra algorithm on any directed graph is [45]:

$$O(E + V \log V), \quad (9)$$

where $E$ denotes the total number of edges and $V$ the number of vertices. The worst-case number of vertices is calculated considering that in each location, out of $\mathcal{L}$ along the platoon route, there are $\mathcal{I}$ possible wireless channels. While each of these location-channel pairs constitutes a vertex, the total number of vertices can be calculated as:

$$V = \mathcal{L} \cdot \mathcal{I} \quad (10)$$

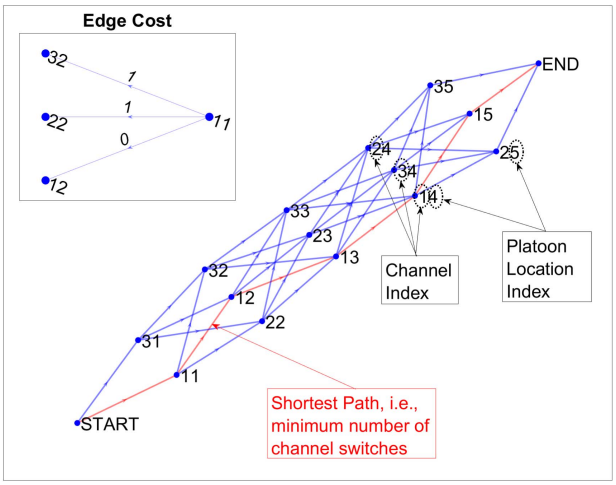


Fig. 3. Example of a graph representation of channel switching problem. There are 3 channels, and 5 platoon locations. Nodes represent available radio channels in the secondary spectrum.

From each of these vertices, $\mathcal{I}$ edges start, being connected to the maximum of $\mathcal{I}$ possible channels in the next location. The worst-case number of edges is the number of vertices $V$ multiplied by the maximum number of available radio channels $\mathcal{I}$ giving:

$$E = V \cdot \mathcal{I} = \mathcal{L} \cdot \mathcal{I}^2. \quad (11)$$

The resultant worst-case computational complexity of the Dijkstra algorithm is given by:

$$O(E + V \log V) = O\left(\mathcal{L} \cdot \mathcal{I}^2 + \mathcal{L} \cdot \mathcal{I} \log \mathcal{L} \cdot \mathcal{I}\right). \quad (12)$$

The channel assignment scheme computed in REM with the use of Dijkstra algorithm can be sent to the platoon leader. If the platoon route changes or there is a significant interference distribution change, the calculations have to be repeated.

### *E. Reduction of REM Size*

One could imagine that there will be potentially a lot of data, obtained over many locations in REM. On the other hand, there is a possibility that there exists a spatial correlation between them, i.e., the interference $\chi^{(i,\mathbf{x}_l)}$ follows the same distribution over neighbouring geographical locations. The challenge is to choose a clustering algorithm proper for REM data. Successful clustering will be able to increase the statistical correctness of the interference distribution estimates and decrease the REM size, i.e., the amount of data that has to be processed. It should be able to deal both with distance in terms of distribution, and geographical position, i.e., the aim is to connect geographically close points, where $\chi^{(i,\mathbf{x}_l)}$ follows the same distribution. One simple and popular clustering algorithm is the so-called K-means [46]. The major drawback of this method is that it requires a-priori the number of clusters to be created. A method that overcomes this issue is, e.g., hierarchical clustering [47]. However, this method cannot simultaneously deal with two distance measures. The solution, where both numbers of clusters is not fixed, and there is a possibility

of incorporating both geographical distance and distribution similarity measure is the so-called Density-Based Spatial Clustering of Applications with Noise (DBSCAN) [48]. Originally DBSCAN, has two parameters: neighbourhood radius $\epsilon$, defining maximum radius used for neighbourhood search, and $N_p$ being the minimum number of points to formulate a cluster. However, there is a possibility to define a more complex function for neighbourhood determination. In order to cluster REM entries being both in geographically close distance, and characterized with similar $\chi^{(i,\mathbf{x}_l)}$ distributions, we propose to define neighbourhood radius for geographical distance $\epsilon_g$, and neighbourhood radius for distribution similarity $\epsilon_{KS}$. The geographical distance between two points is computed in terms of Euclidean distance, which is proper when using ECEF coordinates:

$$d_g(\mathbf{x}_l, \mathbf{x}_{l'}) = ||\mathbf{x}_l - \mathbf{x}_{l'}||, \tag{13}$$

where $||\cdot||$ denotes an Euclidean norm, and $\mathbf{x}_l$ vector of ECEF geographical coordinates related to REM entries $l$, and $l'$ respectively. The neighborhood radius for geographical distance $\epsilon_g$ must be obtained based on empirical studies. The similarity measure between interference distributions is defined in terms of Kologomorov-Smirnoff distance [49]:

$$d_{\mathrm{KS}}(i, \mathbf{x}_l, \mathbf{x}_{l'}) = \sup_z |F(z)^{(i,\mathbf{x}_l)} - F(z)^{(i,\mathbf{x}_{l'})}|, \tag{14}$$

where $F(z)^{(i,\mathbf{x}_l)}$ denotes the cumulative distribution function of $\chi_i^{(i,\mathbf{x}_l)}$. The neighbourhood radius can be computed on the basis of critical value $c(\alpha)$ related to the significance level $\alpha$:

$$\epsilon_{KS} = c(\alpha) \cdot \sqrt{\frac{n+m}{n \cdot m}}, \tag{15}$$

where $n$ and $m$ are the number of data samples used to estimate $F(z)^{(i,\mathbf{x}_l)}$ and $F(z)^{(i,\mathbf{x}_{l'})}$, respectively. Precomputed values of $c(\alpha)$, proper for Kolmogorov distribution can be found in tables [50]. Let us introduce two auxiliary logic formulas: $Q_g(\mathbf{x}_l, \mathbf{x}_{l'}) : d_g(\mathbf{x}_l, \mathbf{x}_{l'}) < \epsilon_g$, and $Q_{KS}(\mathbf{x}_l, \mathbf{x}_{l'}) : \forall i,\ d_{\mathrm{KS}}(i, \mathbf{x}_l, \mathbf{x}_{l'}) < \epsilon_{KS}$. Finally, the function that determines if two data points in REM can be classified as neighbors during DBSCAN procedure can be formulated as:

$$f(\mathbf{x}_l, \mathbf{x}_{l'}) = \begin{cases} 1, & \text{if } Q_g(\mathbf{x}_l, \mathbf{x}_{l'}) \wedge Q_{KS}(\mathbf{x}_l, \mathbf{x}_{l'}) \\ 0, & \text{otherwise.} \end{cases} \tag{16}$$

Using the above equation as an alternative distance function, DBSCAN can be performed to cluster the REM data. The $\epsilon_g$ must be obtained based on empirical study. It is reasonable to start from a low $\epsilon_g$ value and increase it and observe, e.g., maximum distance to the nearest neighborhood over all clusters. The REM entries within a single cluster share similar $\chi^{(i,\mathbf{x}_l)}$ distribution over all channels $i$, and are geographically close to each other. These REM entries can be merged, to reduce REM size. One important property of DBSCAN is that a particular group of points, i.e., REM entries, can remain without cluster assignment. REM entry without cluster assignment cannot be merged to another, because it is either characterized with unique $\chi^{(i,\mathbf{x}_l)}$ distribution, or too geographically distanced from other REM entries.

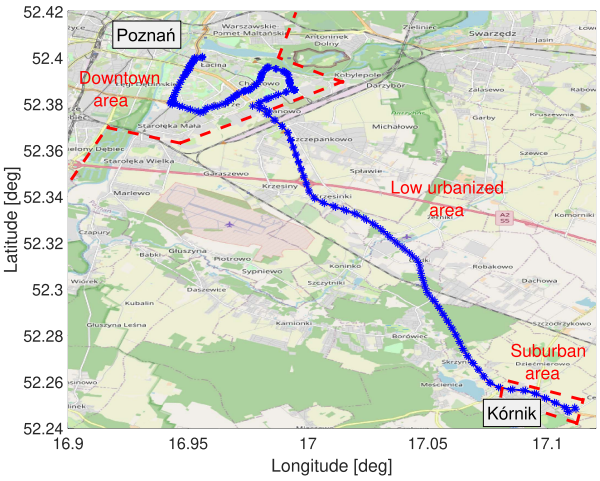


Fig. 4. Measurement campaign route between Poznań, and Kórnik, mostly along the S11 speedway.

## III. Measurement Campaign

To assess the proposed methods with realistic input data field measurements were conducted. We have arbitrarily selected three non-overlapping WiFi™ channels of center frequencies 2.412 GHz, 2.437 GHz, and 2.462 GHz, i.e., channel numbered widely as 1, 6, and 11. The 2.4 GHz band is treated as the *worst case* scenario with a high number of interference sources of various types. The data has been collected along the route between Poznań, and Kórnik in Poland, as depicted in Fig. 4. The route has been traveled from Poznań to Kórnik and back. The major part of the route was a two-lane speedway S11 placed mostly in the low urbanized area. However, the few first kilometers of the measurement campaign are carried in Poznan downtown. The last part of the measurements is carried close to Kórnik representing a small town or suburban scenario. As such the measurements should be representative of all main types of propagation environments.

### A. Measurement Setup

The measurement data were collected in terms of in-phase and quadrature (IQ) received signal samples collected using the Rhode&Schwarz FSL6 spectrum analyzer. There was an omnidirectional antenna PCTEL LPBMLPVMB/LTE of 3 dBi gain, installed on the rooftop of the car, and attached to the spectrum analyzer. The spectrum analyzer was configured to obtain maximal sensitivity (turned on preamplifier and 0 dB input attenuation) resulting in about -84 dBm of thermal noise (measured over 20 MHz bandwidth) reported with the sampling frequency of 20 Msps. Also, there was a U-Blox GPS receiver reporting car position every second with the use of messages defined by the National Marine Electronics Association (NMEA) protocol. Both GPS module and spectrum analyzer are plugged into the laptop using USB, and Ethernet connections, respectively. The whole setup was controlled by the Matlab software, including data capturing, and time stamping both the IQ samples from spectrum analyzer and position from GPS receiver. The power supply was provided from the car 12 V socket.

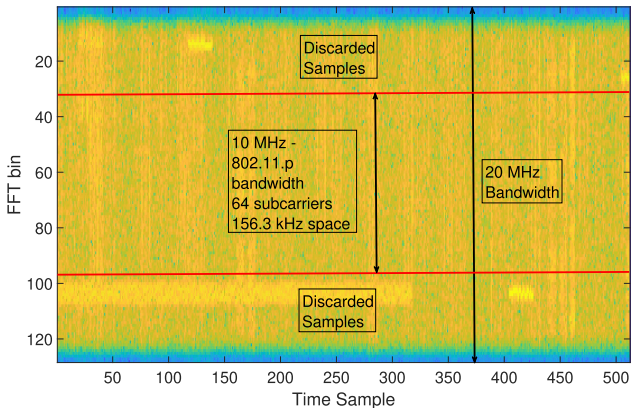


Fig. 5. Example of a spectrogram for the received signal. Samples at both frequency edges are discarded to keep coherence with 802.11p bandwidth and to not consider distortions caused by spectrum analyzer frequency characteristics.

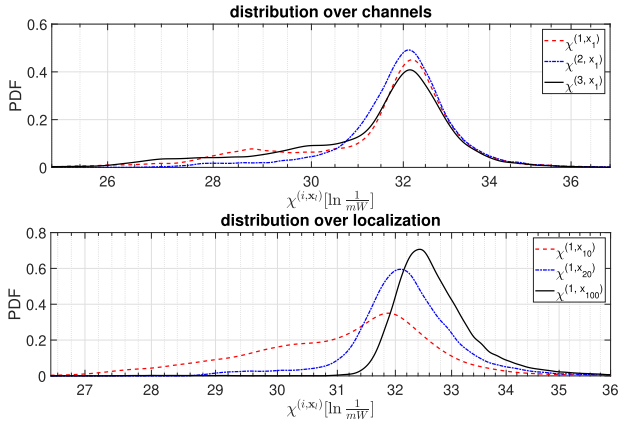


Fig. 6. Probability Density Function of $\chi^{(i,\mathbf{x}_l)}$ over three WiFi channels in a single location, and over a single WiFi channel in three locations.

The spectrum analyzer collects 65536 IQ samples in one frequency channel at one measurement. Next, the center frequency is sequentially switched between the chosen WiFi channels: 1st, 6th, and 11th. Each IQ sample vector is tagged with a geographical position and time. In most cases, the sensing in each channel is repeated approximately every 250 ms. However, after 50 observations the laptop saves the observed samples as a file to the hard drive. This introduces around 6.5 seconds of stoppage in the data collection. There were 248 files with measurement data captured in total along the route.

### *B. Data Analysis*

To extract the interference and noise power ($\hat{I}_k^{(i,\mathbf{x}_l)}$) related to each of the sub-carriers a Discrete Fourier Transform (DFT) was applied to the collected IQ samples. While the samples were collected with a sampling rate of 20 MHz, DFT of 128 points was used. This results in the same subcarrier spacing as in the IEEE 802.11p standard. As IEEE 802.11p uses 10 MHz of bandwidth with 64 subcarriers, only the middle 64 subcarriers are considered for further processing. This allows discarding subcarriers belonging to a roll-off frequency range of the spectrum analyzer. An example of a spectrogram with the bandwidth of interest marked is depicted in Fig. 5. The measurement data processed with the use of the 128 point DFT is available online [51].

As was already mentioned captured data is organized in files, containing vectors of IQ samples. These vectors of IQ samples can be seen as the batches of data measured by the platoon at a certain location and send to REM for further processing. Measurement data having the same geographical position tag reported via NMEA messages are used to formulate one REM entry. Examples of the estimated probability density functions (PDFs) of $\chi^{(i,\mathbf{x}_l)}$ over various WiFi channels and locations are depicted in Fig. 6. The first observation is that the distributions vary over channels, thus outage probability also will vary. As a result, there would exist a channel being the best for opportunistic transmission in a particular location. Second observation is that the $\chi^{(i,\mathbf{x}_l)}$ distribution varies over locations. This justifies the idea of REM and the spatial divisions of data. Final observation is that $\chi^{(i,\mathbf{x}_l)}$ follow non trivial distributions. In some cases these have multimodal distributions, i.e., having more than a single peak. In other cases $\chi^{(i,\mathbf{x}_l)}$ distribution is characterized with non-regular tails. This can be justified by the nature of interference generated from many sources with varying characteristics. If there was only a single interference source, there would be only one peak in PDF of $\chi^{(i,\mathbf{x}_l)}$. However, if there are several sources of temporal interference having different transmission characteristics, then multiple peaks are expected to occur in $\chi^{(i,\mathbf{x}_l)}$ PDF, representing different configurations of interference sources. Under some channels, and locations there might be one most common configuration of interference sources, then instead of clearly visible multiple peaks, the distribution tails are shaped in a non-trivial way. This is expected in the 2.4 GHz band where many communication systems operate simultaneously, e.g., WiFi and Bluetooth. Such a non-trivial, e.g., multimodal distributions can be efficiently modeled using the so-called Gaussian Mixture Model (GMM) [52]. GMM represents the random variable PDF as the weighted sum of $J$ component Gaussian densities. In our case modeling of the one-dimensional distribution of $\chi^{(i,\mathbf{x}_l)}$ is considered:

$$p(\chi^{(i,\mathbf{x}_l)}) = \sum_{j=1}^{J} w_j \mathcal{N}(\chi^{(i,\mathbf{x}_l)} | \mu_j, \sigma_j), \tag{17}$$

where $p(\chi^{(i,\mathbf{x}_l)})$ denotes the distribution of $\chi^{(i,\mathbf{x}_l)}$, $w_j$ is the $j$-th mixture component weight, i.e., the probability that $\chi^{(i,\mathbf{x}_l)}$ comes from the $j$-th mixture component, $\mathcal{N}(\chi^{(i,\mathbf{x}_l)} | \mu_j, \sigma_j)$ is the conditional Gaussian distribution of $\chi^{(i,\mathbf{x}_l)}$, i.e., Gaussian distribution of $\chi^{(i,\mathbf{x}_l)}$, under assumption that it comes from the $j$-th mixture component. Finally $\mu_j$ is the mean, and $\sigma_j$ is the standard deviation of $j$-th mixture component. GMM can be then represented in this case by the vector of weights $\mathbf{w}$, the vector of components means $\mu$, and vector of standard deviations $\sigma$. Such a model seems adequate for being stored in REM, as it represents the distribution with only a few parameters instead of, e.g., histogram, direct PDF, or raw interference samples. A common approach to obtain estimates of distribution parameters is the so-called maximum

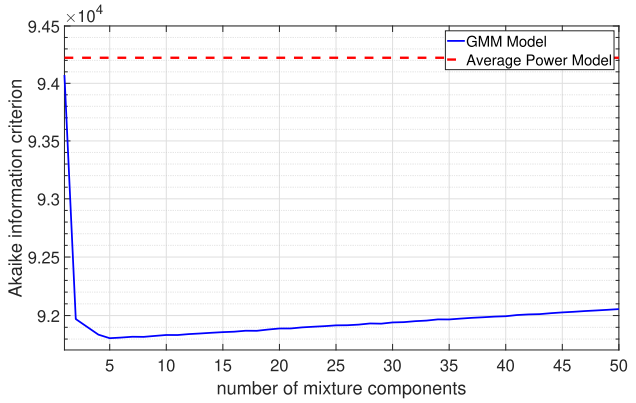


Fig. 7. Example of AIC related to fitting GMM to measurement data, while varying number of components $J$.

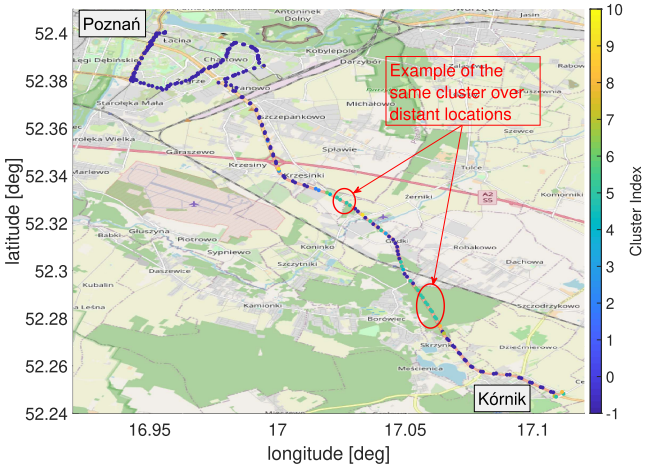


Fig. 8. Results of REM entries clustering using DBCAN, for $N_p = 2$, $\epsilon_{KS} = 0.12$, and $\epsilon_g = \infty$. The points marked with index $-1$ could not be clustered.

likelihood (ML) estimation. However, in the case of GMM the log-likelihood function is nonlinear, i.e., the logarithm of the sum over exponential functions [52]. There is no closed-form ML GMM parameter estimator. However, there is an iterative algorithm called expectation-maximization (EM), which can be utilized [53].

One of the challenges related to the modeling distribution with GMM is obtaining the proper number of components, i.e., high enough to reflect accurately interference distribution but low enough not to introduce overfitting. To ensure this, GMM fits are evaluated in terms of Akaike Information Criterion (AIC), which is the function of model log-likelihood, and the number of parameters [54]:

$$\mathrm{AIC}_J = \omega_J - 2\ln\hat{L}, \tag{18}$$

where $\omega_J$ is the number of parameters of GMM with $J$ components, and $\hat{L}$ is the maximum of likelihood function related to GMM having $J$ components. In the case of GMM modeling one-dimensional distribution of $\chi^{(i,\mathbf{x}_l)}$, $\omega_J$ equals $3J$. We have fitted GMM to measurement data, using various number of mixture components $J$. For each model the corresponding $\mathrm{AIC}_J$ was computed. In addition AIC related to the model exploiting only average value of $\chi^{(i,\mathbf{x}_l)}$ is computed. This model stands for the state-of-the-art approach in REM [25]–[27]. A representative result, obtained by fitting interference distribution from a single measured samples file, is depicted in Fig. 7. The lower $\mathrm{AIC}_J$ value is the better, i.e., the best balance between GMM accuracy and number of parameters is provided. It can be seen that GMM model significantly outperforms the state-of-the-art average power model for any considered number of mixture components. Between the GMM models, the one consisting of 5 components offers the lowest value of AIC. Based on these measurements we decided to model $\chi^{(i,\mathbf{x}_l)}$ as 5 component GMM for all REM entries The obtained GMM parameters would be then stored in REM, for the purpose of channel assignment (see Sec. II-D).

In fully deployed REM we can expect that newly collected interference samples should result in the update of the GMM parameters stored in REM, e.g., newer samples are more important than the old ones as the interference characteristics can evolve in time. This can affect both the number of mixture components $J$, and mixture component parameters: $w_j$, $\mu_j$, and $\sigma_j$. One method for adaptive adjusting number of mixture components, and recursive update of $w_j$, $\mu_j$, and $\sigma_j$, utilizing exponential averaging had been described in [55]. However, application and in-depth verification of this approach would require a much larger data set. We leave it open for future research.

### C. DBSCAN Clustering

The REM constructed, according to the interference modeling procedure described in the previous subsection is claimed to contain some redundant data. I.e., some of the GMMs parameters describing $\chi^{(i,\mathbf{x}_l)}$ are expected to be very similar. To reduce those similarities REM size reduction algorithm using DBSCAN (see Sec. II-E) is launched on the REM.

The DBSCAN-based algorithm takes three arguments: $N_p$ minimum number of points to formulate cluster, neighbourhood radius for geographical distance $\epsilon_g$ and distribution similarity $\epsilon_{KS}$. We set $N_p = 2$, because it is the lowest supported value, which results in the highest opportunity for finding similar REM entries. The value of $\epsilon_{KS}$ is computed using (15). Each distribution was obtained using the same number of samples: $n = m = 25600$, i.e., there were 50 vectors of measurement data utilized to create a single REM entry, after 128-point DFT each vector has a time resolution of 512 samples. We took commonly used in statistic $c(\alpha = 0.05) = 1.358$. The resultant neighbourhood radius for distribution similarity is $\epsilon_{KS} = 0.012$. Initially the neighbourhood radius for geographical distance would be set to be very large in order to evaluate only similarities between distributions. The result of DBSCAN performed on the REM data is depicted in Fig. 8. There, are 10 clusters created, that are allowed to achieve about 12 % reduction of the REM size. It can be seen that more REM entries can be clustered together in the low urbanized area. However, there are REM entries having the same $\chi^{(i,\mathbf{x}_l)}$ distributions but quite distant to each other, e.g., the maximum distance to the nearest neighbor (NN) within the same cluster is about 5 km. This is a negative phenomenon in terms of REM entries merging as the intuition

is that more distant points should create separate areas. This justifies the introduction of the second neighborhood radius $\epsilon_{\mathrm{g}}$. We have examined several $\epsilon_{\mathrm{g}}$ values. The resultant maximum distance to NN within-cluster is depicted in Fig. 9. Results are compared to the maximum distance between consecutive REM entries marked with the dashed line. It can be observed that slightly above the threshold of 400 m, the maximum distance to NN within-cluster exceeds the maximum distance between original REM entries. The geographical neighborhood radius $\epsilon_{\mathrm{g}}$ is set to the value of 400 m. The results of DBSCAN clustering obtained for $\epsilon_{\mathrm{g}} = 400$ m, are depicted in Fig. 10. It can be seen that only REM entries being in the close geographical neighborhood can be grouped. The biggest area covered with a single cluster is the forest area, while in the more urbanized regions no clusters could be identified. The DBSCAN provides about 7% REM size reduction. This value is less than, 12% reported previously, due to constraint on grouping together only REM entries being within close geographical distance. Although this gain is moderate, we can expect that gains will increase while measurement density rises. Moreover, as the 2.4 GHz band of consideration presents the most varying interference conditions, it is expected that in another band more homogeneous interference sources will result in higher REM size reduction.

## IV. Evaluation of the REM-Based Channel Assignment

In order to evaluate the proposed REM-based channel assignment method, a 10-truck platoon is considered, traveling from Poznań to Kórnik and back, as it is depicted in Fig. 4. To obtain numerical results, a well-established, two slope path loss model is used [39]. Through analysis of measurement data authors of the model observed that path loss exponent is rapidly changing after distance between two vehicles $d$ exceeds the critical value $d_{\mathrm{c}}$. The received signal strength (RSS) observed by the receiver at distance $d$ from the transmitter is given by:

$$P(d) = \begin{cases} P(d_0) - 10\gamma_1 \log_{10}(\dfrac{d}{d_0}) + X_{\sigma_1} & \text{if } d_0 \le d \le d_{\mathrm{c}} \\ P(d_0) - 10\gamma_1 \log_{10}(\dfrac{d_{\mathrm{c}}}{d_0}) & \text{if } d > d_{\mathrm{c}} \\ \quad -10\gamma_2 \log_{10}(\dfrac{d}{d_{\mathrm{c}}}) + X_{\sigma_2}, & \end{cases} \tag{19}$$

where $\gamma_1$ and $\gamma_2$ are path loss exponents, $X_{\sigma_1}$, and $X_{\sigma_2}$ are zero-mean Gaussian distributed random variables that model the effect of shadowing, and $P(d_0)$ is the RSS at the reference distance $d_0$. We assume the $P(d_0)$ is computed with the use of the Free Space Loss model, for the reference distance of $d_0 = 1$ m.

The set of parameters used by the platoon is presented in Tab. I. The maximal inter-vehicles distance in a single platoon is set to 200 m. It is an approximate length of a 10-truck platoon. Transmitted power per subcarrier $\mathrm{P_{tx}}$ value is the maximum allowed in 2.4 GHz band [56]. This includes antenna gains. The number of sub-carriers and sub-carrier spacing follows the 802.11p standard [7]. Finally, 3 Mbit/s is set to be the desired capacity $C_{\mathrm{th}}$. It is the lowest supported bitrate in 802.11p, claimed to be used for emergency messages [40]. The radio channel parameters are $d_{\mathrm{c}} = 100$ m, $\gamma_1 = 2$, $\gamma_2 = 4$, $\sigma_1 = 5.6$ dB, and $\sigma_2 = 8.4$ dB. These are proper for the considered 2-lane street scenario [39].

Now the algorithm, where the channel providing the lowest outage probability is chosen for platoon communication in

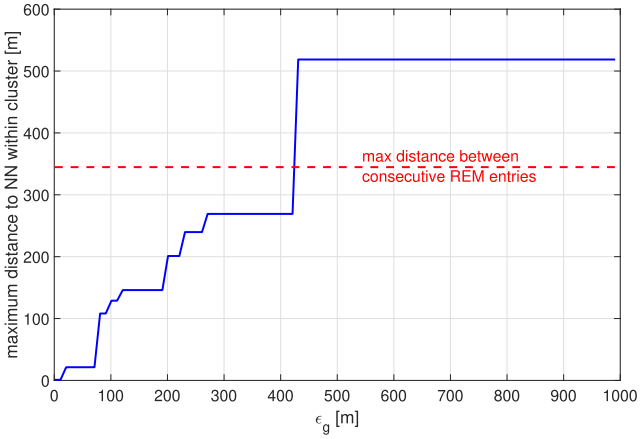


Fig. 9. Dependency between the geographical neighborhood radius $\epsilon_g$, and maximum NN over all clusters. Neighbourhood radius for distribution similarity is $\epsilon_{\mathrm{KS}} = 0.012$.

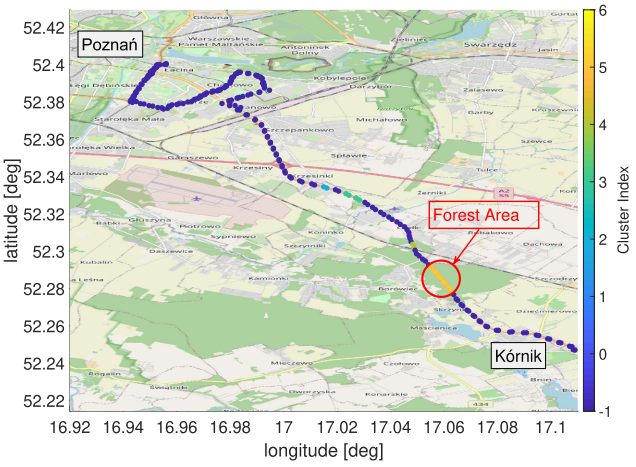


Fig. 10. Results of REM entries clustering using DBCAN, for $\mathrm{N_p} = 2$, $\epsilon_{\mathrm{KS}} = 0.12$, and $\epsilon_{\mathrm{g}} = 400$ m. The points marked with index $-1$ could not be clustered.

TABLE I
Platoon Configuration and Radio Parameters

| Parameter | Value |
|---|---|
| frequency $f$ | 2.4 GHz |
| distance $d$ | 200 m |
| sub-carrier spacing B | 156.3 kHz |
| number of used sub-carriers $\mathrm{N_f}$ | 48 |
| transmitted power per sub-carrier $\mathrm{P_{tx}}$ | 20 dBm $-10\log_{10}(\mathrm{N_f})$ |
| desired capacity $C_{\mathrm{th}}$ | 3 Mbit/s |
| critical distance $d_{\mathrm{c}}$ | 100 m |
| path loss exponent $\gamma_1$ | 2 |
| path loss exponent $\gamma_2$ | 4 |
| $X_{\sigma_1}$ standard deviation $\sigma_1$ | 5.6 dB |
| $X_{\sigma_2}$ standard deviation $\sigma_2$ | 8.4 dB |

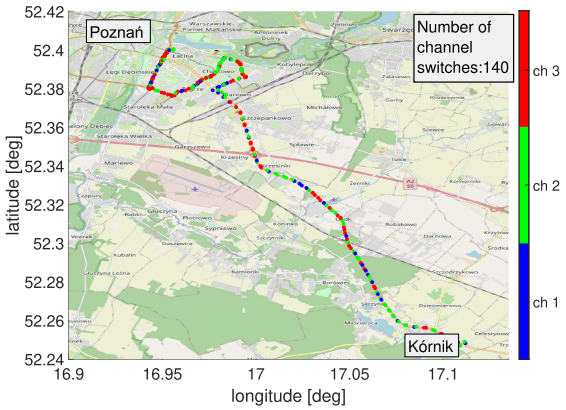


Fig. 11. Results of channel assignment performed independently in every platoon location using (6).

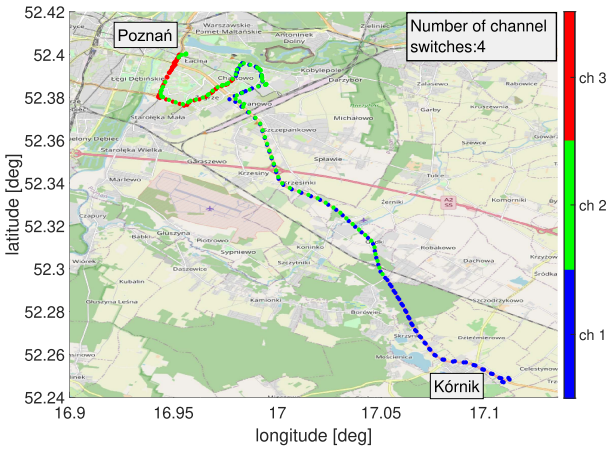


Fig. 12. Results of channel assignment based on the Dijkstra algorithm.

every location according to (6) is evaluated. The assigned channels are depicted on the map and as a function of distance from start in Fig. 11 and Fig. 13, respectively. It can be easily observed, that this scheme encourages frequent channel switching The channel is changed 140 times along the route. As it was mentioned in Sec. II-D, the number of channel switches can be reduced, as it is necessary only to provide a sufficient level of outage probability. Following the acceptable bit error rate in [40], we set maximum allowed outage probability to: $\mathcal{P}_{\max} = 10^{-4}$. With the use of this value, the channel assignment along the planned platoon route has been optimized using the Dijkstra algorithm (see Sec. II-D). The obtained results are depicted in Fig. 12, and Fig. 13, respectively. With the use of the Dijkstra algorithm, the number of channel switches has been drastically decreased. Instead of 140 there are only 4 channel switches along the route, which stands for almost 35 times reduction.

Finally, we have compared the proposed solutions against two state-of-the-art algorithms aimed at dynamic channel selection for vehicular communications. First algorithm follows bumblebees behaviour [32]. This will be called a *Bumblebee* algorithm here. The algorithm observes the mean interference power variation in the chosen channel over time. If the mean interference power observed in the current location is 15% greater than the one observed in the previous location, the channel is switched to the best one, i.e., of the lowest mean interference power. The 15% cost should prevent frequent channel switching. The second state-of-the-art algorithm utilizes machine learning techniques in order to obtain statistics of channel occupancy [31]. We will refer to this algorithm as *Learning-Based*. Similar to the proposed approach, *Learning-Based* algorithm utilizes a location-dependent database. However, instead of direct modeling of channel characteristics, channel occupancy is translated onto the reward. The authors of [31] assumed the arbitrary values of the reward 3 for the free channel and $-3$ for the busy channel. In every platoon location, channel statistics are an exponential average of the reward. We have trained the *Learning-Based* algorithm with the use of our measurement data, and under the assumption that the channel is busy when $\mathcal{P}_{\max}$ is exceeded.

Comparison between channels selected along the platoon road, by the proposed algorithm based on equation (6), proposed application of Dijkstra algorithm, *Bumblebee* algorithm, and *Learning-Based* algorithm is depicted in Fig. 13. The most important information that can be observed is that both *Bumblebee* algorithm (yellow stars) and *Learning-Based* algorithm (green circles) sometimes chose channels that exceed the allowable level of outage probability $\mathcal{P}_{\max}$, i.e., 6, and 12 times respectively. It is due to modeling inaccuracies. *Bumblebee* utilizes mean interference power to assess the quality of radio channel and *Learning-Based* algorithm stores an exponential average of the reward, not interference distribution itself. Instead, the proposed Dijkstra algorithm utilizes REM, storing information about interference distribution that prevents the outage for selected channels from exceeding $\mathcal{P}_{\max}$. Furthermore, it can be seen that both *Bumblebee*, and *Learning-Based* algorithms do not switch channels as often as in the case of channel assignment based on (6). This relation is clearly visible in Fig. 14. In the case of *Bumblebee*, and *Learning-Based* algorithm channel switching occurs 24, and 18 times, respectively. However, when the Dijkstra algorithm is used the platoon switches channel only 4 times. It stands for the 6 times reduction in relation to the *Bumblebee* algorithm and 4.5 times reduction in relation to the *Learning-Based* algorithm. It is because the Dijkstra algorithm optimizes the channel switching globally along the whole route using knowledge from REM. The *Bumblebee* algorithm utilizes only locally available sensing samples. Although *Learning-Based* algorithm also utilizes a database with location-dependent data, the channel selection algorithm is designed so as it does not take into account the dependencies between consecutive locations like our solution does.

Finally, Fig. 15 shows a lower bound of latency computed using (5) along the platoon road, for the packet size $D = 400$ bytes [8]. It can be observed that in most of the locations latency is on the level of 1.067 ms. This is because in those locations outage probability is close to 0, and a fixed throughput equal to channel capacity $C_{\text{th}}$ is assumed in (5). Although in the locations where outage probability is the highest the lower bound latency increases by up to 35 $\mu$s (by 3%), in practice delays are expected to be much longer, e.g., due to the specific medium access algorithm. Still, this 3% increase can have a non-negligible, negative impact on

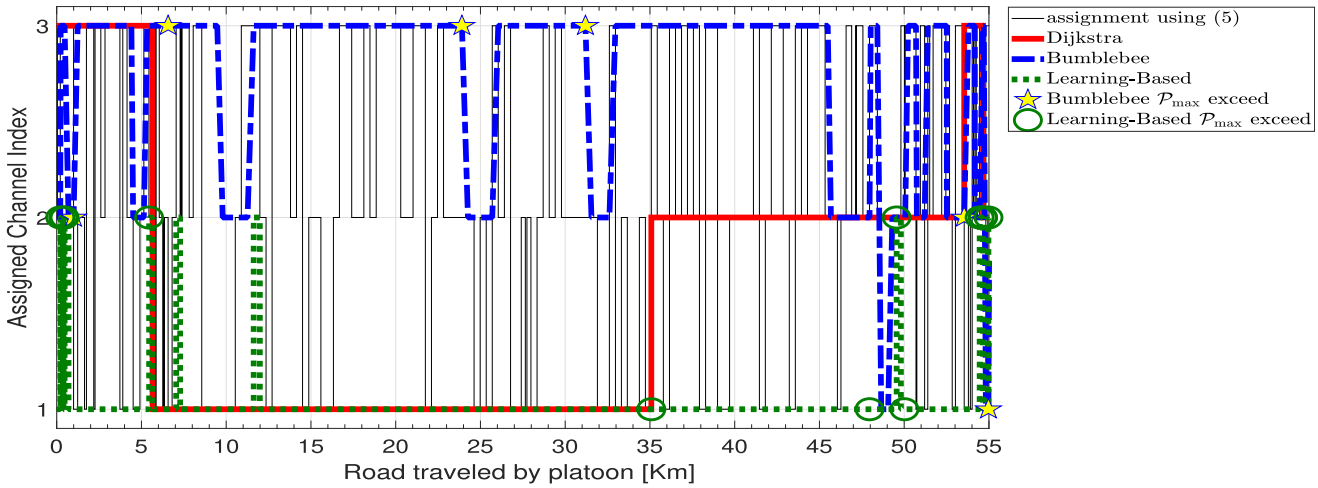


Fig. 13. Results of the channel assignment along the platoon road.

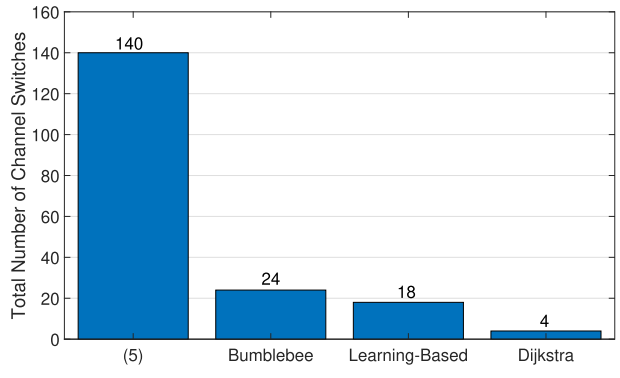


Fig. 14. Total number of channel switches along the platoon road.

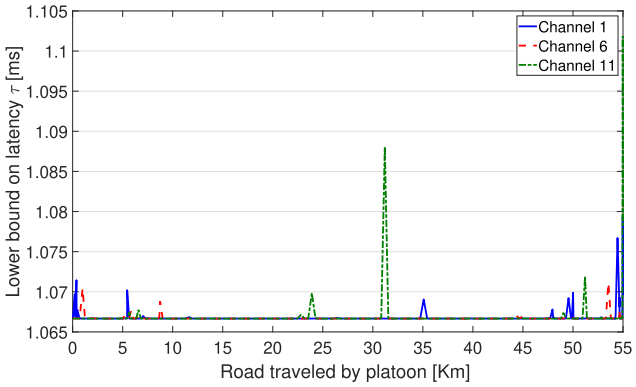


Fig. 15. Lower bound of latency along the platoon road for packet size $D = 400$ bytes.

the platoon control system. In Fig. 16 there is a comparison of the lower bound of latency between the proposed Dijkstra algorithm, and two state-of-the-art solutions: *Bumblebee* algorithm and *Learning-Based* algorithm. We can see that the proposed algorithm is characterized by the lowest lower bound of latency oscillating around the level of 1.0667 ms, and not exceeding the level of 1.0671 ms. The highest peaks could be observed for the Bumblebee algorithm, it is caused by the modeling inaccuracies, i.e., channel selection based on the mean interference power. The performance of *Learning-Based*

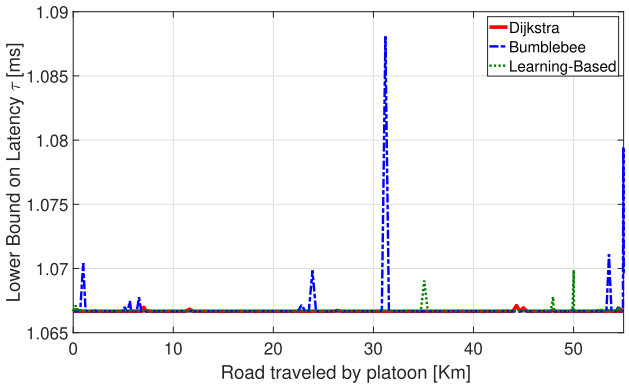


Fig. 16. Lower bound of latency along the platoon road for different channel selection algorithms, and packet size of $D = 400$ bytes.

algorithm is in-between these two algorithm mentioned above. Still some latency peaks can be observed. This is because *Learning-Based* algorithm utilizes better model of channel characteristic than *Bumblebee* algorithm, but not as good as the proposed GMM model.

## V. Conclusion

In this paper, we have presented the design of REM with aim of selecting a proper secondary spectrum channel for intra-platoon communications. This included a method for assessment of available secondary spectrum channels quality, application of Dijkstra algorithm for frequency selection in order to reduce the number of channel switches along the platoon route, and utilization of DBSCAN for the purpose of REM size reduction.

The observed non-trivial distributions of interference can be effectively modeled with GMM of 5 components as proved using AIC. This GMM interference model can be effectively used to construct REM. The size of REM can be reduced by grouping REM entries of similar interference distributions, and being in close geographical distance. It can be done using the proposed modification to the DBSCAN algorithm, and provide the reduction of REM size of about 7%. Finally, the

assignment of the secondary spectrum channel independently in every platoon location results in a high number of channel switches. The proposed, Dijkstra algorithm-based method reduces the number of channel switches about 35 times.

In the future, additional measurement campaigns are necessary, e.g., to observe how GMM parameters are changing over the daytime. Having more data captured over different daytime, algorithms for recursive GMM updates can be evaluated. Also, interference distribution should be evaluated under other frequency bands potentially promising for opportunistic intra-platoon communication e.g., TVWS, WiFi™ 5 GHz band. Finally, an advanced network simulator can be developed to study the proposed REM algorithms under realistic conditions, where also interference from other platoons will be taken into the account.

## REFERENCES


[1] R. Hall and C. Chin, "Vehicle sorting for platoon formation: Impacts on highway entry and throughput," *Transp. Res. C, Emerg. Technol.*, vol. 13, nos. 5–6, pp. 405–420, 2005. [Online]. Available: http://www.sciencedirect.com/science/article/pii/S0968090X06000040

[2] D. Jia, K. Lu, J. Wang, X. Zhang, and X. Shen, "A survey on platoon-based vehicular cyber-physical systems," *IEEE Commun. Surveys Tuts.*, vol. 18, no. 1, pp. 263–284, 1st Quart., 2016.

[3] H. Zheng, J. Wu, W. Wu, and R. R. Negenborn, "Cooperative distributed predictive control for collision-free vehicle platoons," *IET Intell. Transp. Syst.*, vol. 13, no. 5, pp. 816–824, May 2019.

[4] B. van Arem, C. J. G. van Driel, and R. Visser, "The impact of cooperative adaptive cruise control on traffic-flow characteristics," *IEEE Trans. Intell. Transp. Syst.*, vol. 7, no. 4, pp. 429–436, Dec. 2006.

[5] E. Chan, "Overview of the SARTRE platooning project: Technology leadership brief," in *Proc. SAE Converg., SAE Int.*, Oct. 2012. [Online]. Available: https://www.sae.org/publications/technical-papers/content/2012-01-9019/, doi: 10.4271/2012-01-9019.

[6] L. Xu, L. Y. Wang, G. Yin, and H. Zhang, "Communication information structures and contents for enhanced safety of highway vehicle platoons," *IEEE Trans. Veh. Technol.*, vol. 63, no. 9, pp. 4206–4220, Nov. 2014.

[7] A. M. S. Abdelgader and W. U. Lenan, "The physical layer of the IEEE 802.11 p WAVE communication standard: The specifications and challenges," in *Proc. World Congr. Eng. Comput. Sci.* 2014, pp. 1–8.

[8] R. G. Rajeswar and R. Ramanathan, "An empirical study on MAC layer in IEEE 802.11 p/WAVE based vehicular ad hoc networks," *Proc. Comput. Sci.*, vol. 143, pp. 720–727, Jan. 2018. [Online]. Available: http://www.sciencedirect.com/science/article/pii/S1877050918321410

[9] A. Bohm, M. Jonsson, and E. Uhlemann, "Performance comparison of a platooning application using the IEEE 802.11p MAC on the control channel and a centralized MAC on a service channel," in *Proc. IEEE 9th Int. Conf. Wireless Mobile Comput., Netw. Commun. (WiMob)*, Oct. 2013, pp. 545–552.

[10] P. Wang, B. Di, H. Zhang, K. Bian, and L. Song, "Platoon cooperation in cellular V2X networks for 5G and beyond," *IEEE Trans. Wireless Commun.*, vol. 18, no. 8, pp. 3919–3932, Aug. 2019.

[11] F. de Oliveira Souza, L. A. B. Torres, L. A. Mozelli, and A. A. Neto, "Stability and formation error of homogeneous vehicular platoons with communication time delays," *IEEE Trans. Intell. Transp. Syst.*, vol. 21, no. 10, pp. 4338–4349, Oct. 2020.

[12] Y. A. Harfouch, S. Yuan, and S. Baldi, "An adaptive switched control approach to heterogeneous platooning with intervehicle communication losses," *IEEE Trans. Control Netw. Syst.*, vol. 5, no. 3, pp. 1434–1444, Sep. 2018.

[13] M. H. Basiri, M. Pirani, N. L. Azad, and S. Fischmeister, "Security of vehicle platooning: A game-theoretic approach," *IEEE Access*, vol. 7, pp. 185565–185579, 2019.

[14] A. J. Ghandour, K. Fawaz, H. Artail, M. D. Felice, and L. Bononi, "Improving vehicular safety message delivery through the implementation of a cognitive vehicular network," *Ad Hoc Netw.*, vol. 11, no. 8, pp. 2408–2422, Nov. 2013. [Online]. Available: http://www.sciencedirect.com/science/article/pii/S1570870513001285

[15] W. Kim, M. Gerla, S. Y. Oh, K. Lee, and A. Kassle, "CoRoute: A new cognitive anypath vehicular routing protocol," in *Proc. 7th Int. Wireless Commun. Mobile Comput. Conf.*, Jul. 2011, pp. 766–771.

[16] P. Wang, B. Di, H. Zhang, K. Bian, and L. Song, "Cellular V2X communications in unlicensed spectrum: Harmonious coexistence with VANET in 5G systems," *IEEE Trans. Wireless Commun.*, vol. 17, no. 8, pp. 5212–5224, Aug. 2018.

[17] J. Choi, V. Va, N. Gonzalez-Prelcic, R. Daniels, C. R. Bhat, and R. W. Heath, "Millimeter-wave vehicular communication to support massive automotive sensing," *IEEE Commun. Mag.*, vol. 54, no. 12, pp. 160–167, Dec. 2016.

[18] M. Giordani, A. Zanella, and M. Zorzi, "Millimeter wave communication in vehicular networks: Challenges and opportunities," in *Proc. 6th Int. Conf. Mod. Circuits Syst. Technol. (MOCAST)*, May 2017, pp. 1–6.

[19] A. Kliks, P. Kryszkiewicz, J. Perez-Romero, A. Umbert, and F. Casadevall, "Spectrum occupancy in big cities—Comparative study—Measurement campaigns in Barcelona and Poznań," in *Proc. 10th Int. Symp. Wireless Commun. Syst. (ISWCS)*, Aug. 2013, pp. 1–5.

[20] Q. Zhao and B. M. Sadler, "A survey of dynamic spectrum access," *IEEE Signal Process. Mag.*, vol. 24, no. 3, pp. 79–89, May 2007.

[21] H. B. Yilmaz, T. Tugcu, F. Alagöz, and S. Bayhan, "Radio environment map as enabler for practical cognitive radio networks," *IEEE Commun. Mag.*, vol. 51, no. 12, pp. 162–169, Dec. 2013.

[22] A. Kliks, P. Kryszkiewicz, A. Umbert, J. Pérez-Romero, F. Casadevall, and L. Kulacz, "Application of radio environment maps for dynamic broadband access in TV bands in urban areas," *IEEE Access*, vol. 5, pp. 19842–19863, 2017.

[23] L. Yin, J. Li, S. Yin, and S. Li, "Cognitive spectrum handoff game in the TV white space with radio environment map," in *Proc. IEEE 14th Int. Conf. Commun. Technol.*, Nov. 2012, pp. 369–373.

[24] J. van de Beek *et al.*, "REM-enabled opportunistic LTE in the TV band," in *Proc. IEEE Int. Symp. Dyn. Spectr. Access Netw.*, Oct. 2012, pp. 272–273.

[25] M. Sybis, P. Kryszkiewicz, and P. Sroka, "On the context-aware, dynamic spectrum access for robust intraplatoon communications," *Mobile Inf. Syst.*, vol. 2018, pp. 1–16, Jun. 2018.

[26] P. Sroka, P. Kryszkiewicz, and A. Kliks, "Radio environment maps for dynamic frequency selection in V2X communications," in *Proc. IEEE 91st Veh. Technol. Conf. (VTC-Spring)*, May 2020, pp. 1–6.

[27] K. Katagiri, K. Sato, and T. Fujii, "Crowdsourcing-assisted radio environment database for V2V communication," *Sensors*, vol. 18, no. 4, p. 1183, Apr. 2018. [Online]. Available: https://www.mdpi.com/1424-8220/18/4/1183

[28] K. Mehlhorn and P. Sanders, *Shortest Paths*. Berlin, Germany: Springer, 2008, pp. 191–215, doi: 10.1007/978-3-540-77978-0_10.

[29] S. Zhang and R. Zhang, "Radio map based path planning for cellular-connected UAV," in *Proc. IEEE Global Commun. Conf. (GLOBECOM)*, Dec. 2019, pp. 1–6.

[30] S. Roger, C. Botella, J. J. Pérez-Solano, and J. Perez, "Application of radio environment map reconstruction techniques to platoon-based cellular V2X communications," *Sensors*, vol. 20, no. 9, p. 2440, Apr. 2020. [Online]. Available: https://www.mdpi.com/1424-8220/20/9/2440

[31] S. Chen, R. Vuyyuru, O. Altintas, and A. M. Wyglinski, "On optimizing vehicular dynamic spectrum access networks: Automation and learning in mobile wireless environments," in *Proc. IEEE Veh. Netw. Conf. (VNC)*, Nov. 2011, pp. 39–46.

[32] K. S. Gill, B. Aygun, K. N. Heath, R. J. Gegear, E. F. Ryder, and A. M. Wyglinski, "Memory matters: Bumblebee behavioral models for vehicle-to-vehicle communications," *IEEE Access*, vol. 6, pp. 25437–25447, 2018.

[33] J. Perez-Romero *et al.*, "On the use of radio environment maps for interference management in heterogeneous networks," *IEEE Commun. Mag.*, vol. 53, no. 8, pp. 184–191, Aug. 2015.

[34] T. Zeng, O. Semiari, W. Saad, and M. Bennis, "Joint communication and control for wireless autonomous vehicular platoon systems," *IEEE Trans. Commun.*, vol. 67, no. 11, pp. 7907–7922, Nov. 2019.

[35] I. F. Akyildiz, W.-Y. Lee, M. C. Vuran, and S. Mohanty, "A survey on spectrum management in cognitive radio networks," *IEEE Commun. Mag.*, vol. 46, no. 4, pp. 40–48, Apr. 2008.

[36] G. Acosta-Marum and M.-A. Ingram, "Six time- and frequency-selective empirical channel models for vehicular wireless LANs," *IEEE Veh. Technol. Mag.*, vol. 2, no. 4, pp. 4–11, Dec. 2007.

[37] M. G. Nilsson, C. Gustafson, T. Abbas, and F. Tufvesson, "A measurement-based multilink shadowing model for V2V network simulations of highway scenarios," *IEEE Trans. Veh. Technol.*, vol. 66, no. 10, pp. 8632–8643, Oct. 2017.

[38] M. Boban, J. Barros, and O. K. Tonguz, "Geometry-based vehicle-to-vehicle channel modeling for large-scale simulation," *IEEE Trans. Veh. Technol.*, vol. 63, no. 9, pp. 4146–4164, Nov. 2014.
[39] L. Cheng, B. E. Henty, D. D. Stancil, F. Bai, and P. Mudalige, "Mobile vehicle-to-vehicle narrow-band channel measurement and characterization of the 5.9 GHz dedicated short range communication (DSRC) frequency band," *IEEE J. Sel. Areas Commun.*, vol. 25, no. 8, pp. 1501–1516, Oct. 2007.
[40] C. Campolo, A. Molinaro, A. Vinel, and Y. Zhang, "Modeling event-driven safety messages delivery in IEEE 802.11 p/WAVE vehicular networks," *IEEE Commun. Lett.*, vol. 17, no. 12, pp. 2392–2395, Dec. 2013.
[41] D. Tse and P. Viswanath, *Fundamentals of Wireless Communication*. Cambridge, MA, USA: Cambridge Univ. Press, 2005.
[42] P. Cardieri and T. S. Rappaport, "Statistical analysis of co-channel interference in wireless communications systems," *Wireless Commun. Mobile Comput.*, vol. 1, no. 1, pp. 111–121, 2001.
[43] T. Zeng, O. Semiari, M. Chen, W. Saad, and M. Bennis, "Federated learning on the road: Autonomous controller design for connected and autonomous vehicles," 2021, *arXiv:2102.03401*.
[44] S. Boyd and L. Vandenberghe, *Convex Optimization*. Cambridge, U.K.: Cambridge Univ. Press, 2004.
[45] M. Barbehenn, "A note on the complexity of Dijkstra's algorithm for graphs with weighted vertices," *IEEE Trans. Comput.*, vol. 47, no. 2, p. 263, Feb. 1998.
[46] D. Arthur and S. Vassilvitskii, "K-means++: The advantages of careful seeding," in *Proc. 18th Annu. ACM-SIAM Symp. Discrete Algorithms*. Philadelphia, PA, USA: Society for Industrial and Applied Mathematics, 2007, pp. 1027–1035.
[47] S. C. Johnson, "Hierarchical clustering schemes," *Psychometrika*, vol. 32, no. 3, pp. 241–254, 1967.
[48] M. Ester, H.-P. Kriegel, J. Sander, and X. Xu, "A density-based algorithm for discovering clusters in large spatial databases with noise," in *Proc. 2nd Int. Conf. Knowl. Discovery Data Mining*, Palo Alto, CA, USA, 1996, pp. 226–231.
[49] F. J. Massey, Jr., "The Kolmogorov-Smirnov test for goodness of fit," *J. Amer. Statist. Assoc.*, vol. 46, no. 253, pp. 68–78, 1951. [Online]. Available: http://www.jstor.org/stable/2280095
[50] E. Calixto, "Chapter 1—Lifetime data analysis," in *Gas and Oil Reliability Engineering*, 2nd ed. E. Calixto, Ed. Boston, MA, USA: Gulf Professional Publishing, 2016, pp. 1–92. [Online]. Available: http://www.sciencedirect.com/science/article/pii/B9780128054277000014
[51] *WLAN Road Measurement Data*. Accessed: Nov. 9, 2021. [Online]. Available: http://v2x.et.put.poznan.pl
[52] C. M. Bishop, *Pattern Recognition and Machine Learning* (Information Science and Statistics). Berlin, Germany: Springer, 2006.
[53] A. P. Dempster, N. M. Laird, and D. B. Rubin, "Maximum likelihood from incomplete data via the *EM* algorithm," *J. Roy. Stat. Soc. B, Methodol.*, vol. 39, no. 1, pp. 1–38, Jan. 1977. [Online]. Available: http://www.jstor.org/stable/2984875
[54] H. Akaike, "A new look at the statistical model identification," *IEEE Trans. Autom. Control*, vol. AC-19, no. 6, pp. 716–723, Dec. 1974.
[55] Z. Zivkovic, "Improved adaptive Gaussian mixture model for background subtraction," in *Proc. 17th Int. Conf. Pattern Recognit.*, vol. 2, 2004, pp. 28–31.
[56] E. Vangeel, *Wideband Transmission Systems; Data Transmission Equipment Operating in the 2,4 GHz Band; Harmonised Standard for Access to Radio Spectrum HS Wideband Transmission Systems 2,4 GHz*, Standard EN 300 328, ETSI, Sophia Antipolis, France, 2019. [Online]. Available: https://www.etsi.org/deliver/etsi-en/300300-300399/300328/02.02.02-60/en-300328v020202p.pdf

**Marcin Hoffmann** (Graduate Student Member, IEEE) received the M.Sc. degree (Hons.) in electronics and telecommunication from the Poznań University of Technology in 2019, where he is currently pursuing the Ph.D. degree with the Institute of Radiocommunications. He is gaining scientific experience by being involved in both national and international research projects. His main fields of interest are utilization of machine learning and location-dependent information for the purpose of network management.

**Pawel Kryszkiewicz** (Senior Member, IEEE) received the M.Sc. and Ph.D. degrees (Hons.) in telecommunications from the Poznań University of Technology (PUT), Poland, in 2010 and 2015, respectively. He is currently an Assistant Professor with the Institute of Radiocommunciations, PUT. He was involved in a number of national and international research projects. His main fields of interest are problems concerning the physical layer of the dynamic spectrum access systems, multicarrier signal design for green communications, and problems related to practical implementation of massive MIMO systems.

**Adrian Kliks** (Senior Member, IEEE) is currently an Associate Professor with the Institute of Radiocommunications, Poznań University of Technology, Poland. His research interests include new waveforms for wireless systems applying either nonorthogonal or noncontiguous multicarrier schemes, cognitive radio, advanced spectrum management, deployment and resource management in small cells, and network virtualization.

## 7.6 Publication [P6]

M. Hoffmann, P. Kryszkiewicz, and A. Kliks, "Increasing energy efficiency of massive-MIMO network via base stations switching using reinforcement learning and radio environment maps," *Computer Communications*, vol. 169, pp. 232–242, 2021.

MNiSW Points: 140

Number of citations:

- according to Web of Science: 20
- according to Google Scholar: 33

mgr inż. Marcin Hoffmann
Instytut Radiokomunikacji, Politechnika Poznańska
ul. Polanka 3, 60-965 Poznań

Poznań, 10 kwietnia 2021 r.

# OŚWIADCZENIE W SPRAWIE AUTORSTWA PRACY

Oświadczam, że w pracy:

*M. Hoffmann, P. Kryszkiewicz, A. Kliks, "Increasing energy efficiency of Massive-MIMO network via base stations switching using reinforcement learning and radio environment maps" Computer Communications, tom 169, marzec 2021*

mój udział polegał na:

- Opracowaniu koncepcji wykorzystania uczenia ze wzmocnieniem i mapy środowiska radiowego do poprawy efektywności energetycznej sieci M-MIMO
- Opracowaniu algorytmów przyspieszających zbieżność uczenia, poprzez analityczne heurystyki, na bazie sugestii i koncepcji P. Kryszkiewicza
- Implementacji oraz integracji zaproponowanych algorytmów z symulatorem
- Przeprowadzeniu eksperymentów symulacyjnych
- Przygotowaniu w całości pierwszej wersji tekstu artykułu

Mój procentowy udział w powstanie pracy szacuję na: 70%

.....

Podpis

dr hab. inż. Paweł Kryszkiewicz, prof. PP
Instytut Radiokomunikacji, Politechnika Poznańska
ul. Polanka 3, 60-965 Poznań

Poznań, 21 sierpnia 2025 r.

# OŚWIADCZENIE W SPRAWIE AUTORSTWA PRACY

Oświadczam, że w pracy:

*M. Hoffmann, P. Kryszkiewicz, A. Kliks, "Increasing energy efficiency of Massive-MIMO network via base stations switching using reinforcement learning and radio environment maps" Computer Communications, tom 169, marzec 2021*

mój udział polegał na:

- Koordynacji prac badawczych
- Dyskusji z pierwszym autorem napotkanych problemów w tym: metod reprezentacji uzyskanej wiedzy powstałej w procesie uczenia maszynowego w geolokacyjnej bazie danych
- Udział w implementacji środowiska symulacyjnego (np. moduł prekodowania i alokacji użytkowników)
- Zaproponowanie metody zmniejszenia przestrzeni stanów ASR
- Dyskusji ze współautorami uzyskanych wyników i metod ich prezentacji/porównania
- Strukturyzacji artykułu
- Iteracyjnym nanoszeniu poprawek na tekst; dyskusji uwag ze współautorami

Mój procentowy udział w powstanie pracy szacuję na: 20%

Podpis

dr hab. inż. Adrian Kliks, prof. PP
Instytut Radiokomunikacji, Politechnika Poznańska
ul. Polanka 3, 60-965 Poznań

Poznań, 10 kwietnia 2021 r.

# OŚWIADCZENIE W SPRAWIE AUTORSTWA PRACY

Oświadczam, że w pracy:

*M. Hoffmann, P. Kryszkiewicz, A. Kliks, "Increasing energy efficiency of Massive-MIMO network via base stations switching using reinforcement learning and radio environment maps" Computer Communications, tom 169, marzec 2021*

mój udział polegał na:

- Uczestniczeniu w dyskusjach nad uzyskiwanymi wynikami
- Współredagowaniu tekstu pracy.

Mój procentowy udział w powstanie pracy szacuję na: 10%

Adrian Kliks

.....

Podpis

Computer Communications 169 (2021) 232–242

Contents lists available at ScienceDirect

Computer Communications

journal homepage: www.elsevier.com/locate/comcom

# Increasing energy efficiency of Massive-MIMO network via base stations switching using reinforcement learning and radio environment maps

Marcin Hoffmann, Paweł Kryszkiewicz *, Adrian Kliks

*Institute of Radiocommunications, Poznań University of Technology, Poznań, Poland*

ARTICLE INFO

*Keywords:*
Massive MIMO
Radio Environment Map
Base station switching on/off
Reinforcement learning
Energy efficiency

ABSTRACT

Energy Efficiency (EE) is of high importance while considering Massive Multiple-Input Multiple-Output (M-MIMO) networks where base stations (BSs) are equipped with an antenna array composed of up to hundreds of elements. M-MIMO transmission, although highly spectrally efficient, results in high energy consumption growing with the number of antennas. This paper investigates EE improvement through switching on/off underutilized BSs. It is proposed to use the location-aware approach, where data about an optimal active BSs set is stored in a Radio Environment Map (REM). For efficient acquisition, processing and utilization of the REM data, reinforcement learning (RL) algorithms are used. State-of-the-art exploration/exploitation methods including $\epsilon$-greedy, Upper Confidence Bound (UCB), and Gradient Bandit are evaluated. Then analytical action filtering, and an REM-based Exploration Algorithm (REM-EA) are proposed to improve the RL convergence time. Algorithms are evaluated using an advanced, system-level simulator of an M-MIMO Heterogeneous Network (HetNet) utilizing an accurate 3D-ray-tracing radio channel model. The proposed RL-based BSs switching algorithm is proven to provide 70% gains in EE over a state-of-the-art algorithm using an analytical heuristic. Moreover, the proposed action filtering and REM-EA can reduce RL convergence time in relation to the best-performing state-of-the-art exploration method by 60% and 83%, respectively.

## 1. Introduction

In the last decades we could observe a huge growth in the deployment of mobile telecommunication networks. It is caused by an increasing number of mobile devices: smartphones, tablets, but also Internet-of-Things (IoT) devices. With the increased number of mobile devices, and rapidly growing network infrastructure, energy-efficiency (EE) became a major field of research aiming at reducing operators' costs and carbon emissions [1]. EE becomes even more challenging, when considering the 5G Massive Multiple-Input Multiple-Output (M-MIMO) network utilizing large antenna arrays [2]. Although M-MIMO enables reduction of the transmitted power, through high effective antenna gain obtained using beamforming, it is not always enough to compensate the power consumed by hardware components e.g., transceivers chains, filters, modulators [3]. Moreover, the 5G system will be typically a heterogeneous network (HetNet), i.e., a network composed of overlapping cells of various sizes, with each Base Station (BS) equipped with an antenna array [4]. Although HetNet can provide large spectral-efficiency benefits, increased energy consumption is expected.

The energy consumption decrease is acceptable only if the Quality of Service (QoS) for the end users is not degraded significantly. However, it has been shown that traffic load in a telecommunication network varies over time [5,6]. As such, many of the BSs are underutilized within some time periods. There are several ways of adjusting BSs configuration to this phenomenon and reducing the energy consumption. First, the antennas and related transceiver chains receiving the least amount of power can be switched off [7]. Secondly, some energy savings can be provided by reducing the resolution of analog-to-digital converters, by up to one bit [8]. Thirdly, energy consumption can be decreased, when hybrid analog–digital precoding is used [9]. But the highest reduction of the consumed power can be achieved by switching off underutilized BSs.

There are several base station on/off switching algorithms proposed in the literature [10,11]. Some of them obtain a subset of active BSs through optimization methods. Others propose analytical heuristics, considering the traffic load, or a number of User Equipments (UEs) served by each BS. Another approach is to observe the performance of a chosen active BSs set, gather knowledge and make an *a posteriori* decision about the optimal active BSs set. This can be achieved by utilizing a subclass of machine learning (ML) algorithms, called reinforcement learning (RL) [12]. There are a few works where RL is considered for providing energy savings in wireless networks [13–15]. The idea of the existing RL-based BS-switching algorithms relies mostly on the utilization of explicit traffic load or user association information.

* Corresponding author.
*E-mail addresses:* marcin.ro.hoffmann@doctorate.put.poznan.pl (M. Hoffmann), pawel.kryszkiewicz@put.poznan.pl (P. Kryszkiewicz), adrian.kliks@put.poznan.pl (A. Kliks).

https://doi.org/10.1016/j.comcom.2021.01.012
Received 2 July 2020; Received in revised form 22 November 2020; Accepted 7 January 2021
Available online 28 January 2021

However, in an M-MIMO network simple network models do not suffice. High-level information about UE influence on a system's EE cannot be accurate enough. This is the result of significantly varying channel conditions depending on UE location. Fortunately, 5G comes with improved localization techniques [16], enabling the so-called location-aware communications [17]. Accurate localization allows to tag the measurement of various radio link parameters with UE coordinates. Such location-dependent information can be stored in the so-called Radio Environment Map (REM) [18]. REM is an intelligent unit attached to the existing network infrastructure responsible for the acquisition, storage, and processing of location-dependent information with the aim to improve network performance.

In this paper, the 5G M-MIMO network is subject to EE maximization while keeping high QoS for the users. Although in the early stages of 5G rather hybrid antenna arrays, i.e., a limited number of digital transceiver chains combined with an analog processing network, would be deployed in order to reduce the implementation cost, we are considering full digital architecture. This is proper for fully developed 5G networks pointing toward 6G [19,20]. The EE can be changed by the activation/deactivation of BSs. The considered network is highly complex, including an advanced radio channel model (3D ray tracing-based), realistic channel estimation inducing errors, user-to-BS association, scheduling, and precoding algorithms. This precludes simple, yet accurate problem formulation in order to utilize standard optimization methods. Instead, Reinforcement Learning (RL) has been used, where the active BS set can be changed to observe *a posteriori* changes in M-MIMO network QoS metrics. The high influence of UEs location on M-MIMO network performance is exploited by the utilization of REM for storing RL states. This allows the network to preserve the learned active BSs set for each UE distribution pattern. In order to increase the convergence speed of the proposed algorithm (as in a real network, BS deactivation is a serious operation possibly disconnecting some UEs from the network), analytical possible action filtering is implemented, i.e., a reduction of the possible set of active BSs to be considered in RL. In addition, an information fusion function is proposed in order to utilize in a given network state (i.e., for a certain UEs location pattern) information about past network performance in the adjacent states, i.e., REM-based Exploration Algorithm (REM-EA). The *distance* between the states will be specified using Haussdorf distance. This helps to improve learning convergence even further, while not deteriorating the final EE of the system.

The paper is organized as follows: In Section 2 an overview of the related works is presented. The considered system is described in Section 3, while Section 4 presents an idea of REM, and describes REM deployment in the considered M-MIMO HetNet. The RL concept adopted to BS switching in M-MIMO HetNet and the proposed REM-based algorithms are described in Section 5. The simulation environment and results are presented in Section 6. Finally, the conclusions are formulated in Section 7.

## 2. Related work

A vast number of algorithms providing energy savings by switching off underutilized BSs can be found in the literature. A major group of the proposed solutions comprise algorithms based on simplified network models and optimization heuristics [10]. One of the prospective ideas is to turn off pico or femto BSs having no or just a few UEs in their coverage area to serve [21]. A more advanced approach relies on switching off BSs on the basis of a traffic load threshold [22]. Another solution, is based on switching off a particular BS only if another BS has enough available radio resources to take over the additional load [23]. However, the authors of these articles did not consider M-MIMO BSs, and utilized simple radio channel models. Thus, the proposed analytical heuristics are inadequate to be implemented under the real radio conditions. The authors of [24] proposed a distributed solution for energy-efficient BS switching based on the game theory. Although there is M-MIMO considered, the antenna array is claimed to be deployed only at the macro BS (MBS), while small BSs are equipped with single antennas only. The utilized spectral efficiency estimate for MBS is simplified, i.e, it neglects inter-UE interference, and assumes that every UE can be served using an independent spatial beam. Finally, not very accurate radio channel model is assumed. It consists only of the pathloss and Rayleigh fading, not considering, e.g., spatial correlation affecting M-MIMO performance.

On the other hand, there are several algorithms utilizing reinforcement learning for providing an EE gain through BS switching. In [13], there is an actor-critic algorithm utilized to switch off BSs, so as to minimize the overall system power consumption. The action selection is done on the basis of a stochastic policy following Boltzmann distribution, while environment state is defined as the total traffic load per BS. A more advanced solution takes into account not only power consumption, but also latency, and the number of served UEs [25]. Additionally, the authors utilize Boltzmann distribution-based action selection, though with the so-called Q-learning algorithm. The authors of [14] proposed a three-state (i.e., active, stand-by, and sleep) Markov Decision Process for BS, and a Value Iteration RL framework to minimize network power consumption. Also there is the BS switching algorithm, utilizing the so-called Deep Reinforcement Learning, i.e., RL learning boosted with the use of a deep neural network [15]. The cost function including power consumption, QoS, and switching cost is minimized on the basis of the input traffic load estimates and active BSs set.

The major issue of all mentioned RL algorithms is the lack of M-MIMO consideration in the system model. Secondly, similarly to the analytical heuristic methods, the RL algorithms are evaluated using simple radio channel models, e.g., considering only the pathloss component and Rayleigh fading. Although algorithms were accurately studied in terms of their final performance, less effort was put into the evaluation of their convergence time. Fast convergence is crucial not only for minimizing BS hardware expenditure, but also for reducing QoS degradation related to the learning process, i.e., trying actions that degrade QoS to obtain *a posteriori* knowledge.

In this paper, we propose to utilize the knowledge about UE location in the M-MIMO network instead of explicit traffic load information used in the recent works. We will show that this approach can simplify the full RL problem to the so-called *Associative Search*. In contrast to the majority of the mentioned works, in this paper the convergence of state-of-the-art RL exploration methods will be extensively studied. In addition, an analytical action filtering algorithm is proposed to speed up RL convergence. Moreover, the proposed REM-EA utilizes the similarities between UEs position sets, using data stored in REM, to further improve RL convergence. The gains of the proposed algorithms over the existing exploration strategies are proven through computer simulations. In comparison to the other recent works, in this paper, an advanced system level simulator is implemented that utilizes a realistic 3D-ray-tracing radio channel model. Following the studies were models considering regular deployment of BSs were claimed as inaccurate in practice, we decided to evaluate the proposed algorithms using the realistic *Madrid Grid Model*, used previously in, e.g., METIS project [26]. It would be beneficial to study random BS locations, as proposed in many contemporary works, e.g., [27], but the complexity of the simulated system prevents us from such considerations. Maybe this would be possible in the future for a simplified system model.

## 3. System description

In this paper we consider switching BSs on/off in a single, two-tier HetNet. The network consists of a MBS, and several pico BSs (PBSs). All BSs in the system share the same radio frequency resources, and utilize Orthogonal Frequency Division Multiple Access (OFDM). All BSs in the HetNet are equipped with large antenna arrays exploiting from tens up to hundreds of antenna elements. The number of antenna

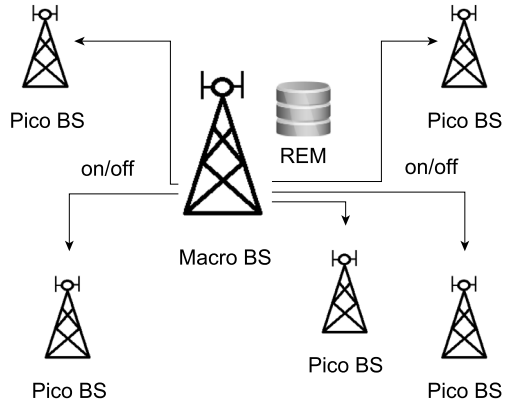


**Fig. 1.** Scheme of the considered M-MIMO HetNet.

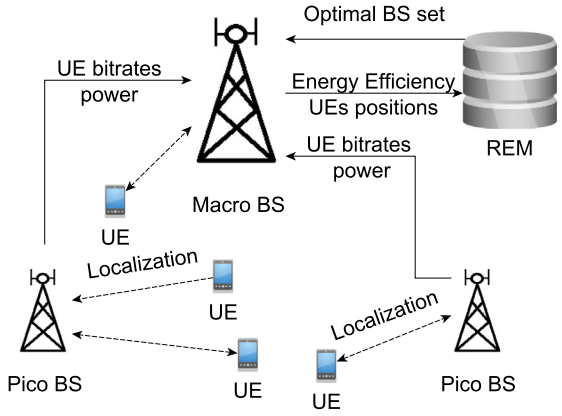


**Fig. 2.** Scheme of REM deployment in the considered M-MIMO HetNet.

elements, and array design can vary between the consecutive BSs. We assume that the MBS is not considered for switching off as it provides a general coverage in the cell and performs the centralized management functions. Commonly, the utilized radio access technologies have a fixed set of Modulation-Coding Schemes (MCS) with the associated minimum Received Signal Strength (RSS) that allows then to serve a given UE. This approach is followed in this paper. The process of switching BSs on/off is also centralized and managed from the MBS, where REM and RL algorithms are deployed, as depicted in Fig. 1.

The REM deployed in the Macro BS has access to all control information available in the BSs, e.g., UE bitrates, UE to BS association, channel estimates, power consumption. In this paper, downlink bitrates will be of interest. This information is then utilized to formulate REM entries necessary for the RL base station switching algorithms.

### 3.1. Power modeling

There are several BS power consumption models proposed for the LTE system [28,29]. Unfortunately they are not adequate for M-MIMO evaluation. M-MIMO utilizes tens or hundreds of antennas per BS, which is much more than the maximum of 8 antenna elements available in LTE-A [30]. Therefore, in this work, the model for the evaluation of M-MIMO BS energy consumption proposed in [3] is used. Mainly, the power consumption of all $N_{\mathrm{BS}}$ BSs is composed of 3 components: effective transmitted power (ETP), transceivers chains power, and fixed power. ETP stands for the energy consumption related to the total radiated power $P_{\mathrm{tx},b}$ by BS $b$ and power amplifier efficiency $\eta$. It is given by:

$$P_{\mathrm{ETP},b} = \frac{P_{\mathrm{tx},b}}{\eta}. \tag{1}$$

The transceivers chain power in the $b$th BS is denoted as $P_{\mathrm{tc},b}$. It describes the power consumed by the hardware utilized by every single antenna (such as modulators, filters, etc.) and a local oscillator (LO). It can be computed as:

$$P_{\mathrm{tc},b} = M_b P_{\widehat{\mathrm{TC}}} + P_{\mathrm{LO}}, \tag{2}$$

where $M_b$ stands for the number of antennas deployed at BS $b$, $P_{\widehat{\mathrm{TC}}}$ models the amount of power consumed by the single transceiver chain, and $P_{\mathrm{LO}}$ is the power necessary for the LO to work.

The last component, fixed power $P_{\mathrm{fix}}$ denotes the power necessary for, e.g., baseband signal processing, in each BS.

In this paper, by switching off the BSs we put them in the stand-by-mode, where the utilization of hardware resources is much reduced. In consequence, a BS operating in the stand-by-mode consumes in total power $P_{\mathrm{off}}$. Moreover, it is assumed that such a BS can be switched on rapidly, e.g., within 30 $\mu s$ [31]. Such a short switching time enables immediate changes in the active BSs set. Deeper sleep/switch off, although more energy efficient, will require much more time for transition between on/off states, and due to that, it is not considered in our paper.

The overall system power consumption $P_{\mathrm{tot}}$ is given by:

$$P_{\mathrm{tot}} = \sum_{b=1}^{N_{\mathrm{BS}}} P_{\mathrm{tot},b}, \tag{3}$$

where

$$P_{\mathrm{tot},b} = \begin{cases} P_{\mathrm{ETP},b} + P_{\mathrm{fix}} + P_{\mathrm{tc},b}, & \text{for active BS} \\ P_{\mathrm{off}}, & \text{for BS in stand-by-mode} \end{cases} \tag{4}$$

## 4. Radio environment map

The idea of acquisition of location-aware data in order to improve network performance comes from cognitive radio [32]. There is a concept of the Radio Environment Map (REM) proposed to gather location-dependent information about the surrounding radio environment to enable opportunistic transmission for secondary users [33]. Although REM generally stores interference power or received signal strength values, the idea can be easily extended to include any context information that can be useful for network operation. As a result, REMs can store location-aware data about e.g., UEs velocity or network traffic load, and as such are sometimes called Radio Service Maps [18]. In this paper, REM stores information processed by the learning procedure that include UEs positions and achievable EE depending on the active BSs set.

### 4.1. REM deployment

The deployment of REM in the considered M-MIMO HetNet is depicted in Fig. 2. We assume that a so-called REM agent is installed on the MBS. The first objective of the REM agent is to process the data provided by the UEs and BSs, and store them in REM. Secondly, the REM agent optimizes the current active BSs set according to the proper algorithm, and using REM data. UEs provide their locations measured with state-of-the-art localization methods, e.g., using highly accurate satellite navigation [34]. Each BS calculates the associated UEs bitrates and its power consumption. The REM agent calculates the network EE metric based on these inputs and stores it characterized by the given UEs position set. On the basis of the previous measurements, and according to the chosen learning algorithm, the REM agent chooses the next active BSs set.

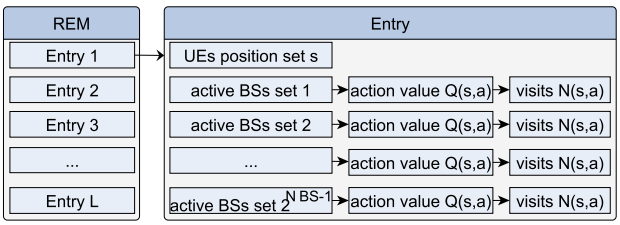


**Fig. 3.** Data structure in REM. While MBS is not considered for switching off, there are $2^{N_{\text{BS}}-1}$ possible active BSs sets.

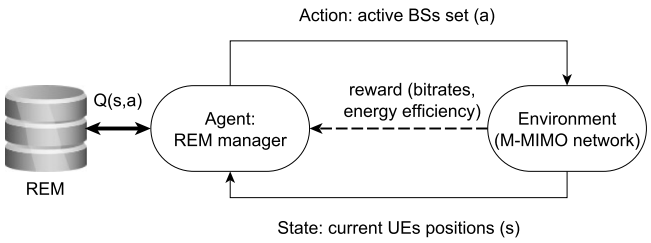


**Fig. 4.** Diagram of REM learning with the use of RL.

### 4.2. REM data structure

The structure of an REM database is presented in Fig. 3. Each entry is identified on the basis of the UEs positions set $\mathbf{s}$, being in fact a vector of the UEs coordinates on the Cartesian plane, rounded to fit a square grid. The length of the considered grid square side is denoted as $g$. In order to evaluate the similarity between different UEs position sets $\mathbf{s}$, the so-called Hausdorff distance (HD) metric is used [35]. The main reason to choose HD is its ability to compare data sets having a different number of measurements, i.e., UEs in our case. Suppose there have been $N_{\text{UE}}$ UEs present in the network at positions $\mathbf{s}_{\text{REM}} = \{s_{\text{REM},1}, s_{\text{REM},2}, \dots, s_{\text{REM},N_{\text{UE}}}\}$ with $s_{\text{REM},n}$ being the position of $n$th UE. The HD to the current position set of $N_{\text{UE}'}$ UEs $\mathbf{s}_0 = \{s_{0,1}, s_{0,2}, \dots, s_{0,N_{\text{UE}'}}\}$ is given by [36]:

$$d_h(\mathbf{s}_{\text{REM}}, \mathbf{s}_0) = \max(hd(\mathbf{s}_{\text{REM}}, \mathbf{s}_0), hd(\mathbf{s}_0, \mathbf{s}_{\text{REM}})), \tag{5}$$

$$hd(\mathbf{s}_{\text{REM}}, \mathbf{s}_0) = \max_{s_{\text{REM}} \in \mathbf{s}_{\text{REM}}} \{ \min_{s_0 \in \mathbf{s}_0} (d_e(s_{\text{REM}}, s_0)) \}, \tag{6}$$

$$hd(\mathbf{s}_0, \mathbf{s}_{\text{REM}}) = \max_{s_0 \in \mathbf{s}_0} \{ \min_{s_{\text{REM}} \in \mathbf{s}_{\text{REM}}} (d_e(s_0, s_{\text{REM}})) \}, \tag{7}$$

where $d_e(\cdot,\cdot)$ stands for Euclidean distance. On the basis of $d_h(\mathbf{s}_{\text{REM}}, \mathbf{s}_0)$, a decision is made if the new UEs position set is recognized as one of the REM entries or not. The UEs position set is recognized as an existing REM entry if $d_h(\mathbf{s}_{\text{REM}}, \mathbf{s}_0) < g$. Otherwise, a new entry is created and labeled with a new UEs position set $\mathbf{s}_0$. In Fig. 3 it is assumed $L$ distinct UEs positions sets exist in the REM.

In addition to the UEs position set, every REM entry contains so-called, action values $Q(\mathbf{s}, \mathbf{a})$. These are metrics on how a particular active BSs set $\mathbf{a}$ is preferred, while a given UEs position set $\mathbf{s}$ is encountered. The methods of calculation and utilization of $Q(\mathbf{s}, \mathbf{a})$ are described in Section 5. Finally, variable $N(\mathbf{s}, \mathbf{a})$ is stored for a given UEs location set $\mathbf{s}$ and a given active BSs set $\mathbf{a}$, presenting the number of times action $\mathbf{a}$ was taken in state $\mathbf{s}$.

## 5. Reinforcement learning

An efficient way to utilize REM data is to implement some RL algorithms. In RL the so-called agent learns through interaction with the so-called environment by taking appropriate actions and receiving the so-called reward [37]. The RL scheme utilized for increasing the energy efficiency of the considered M-MIMO HetNet by BSs switching is depicted in Fig. 4.

The consecutive elements of the RL framework will now be described in detail:

- **State** $\mathbf{s} \in \mathcal{S}$ is defined as the set of UEs coordinates rounded to fit the square grid of size $g$. States are recognized using the HD metric defined by (5). $\mathcal{S}$ is a set of all historical UEs positions stored in REM.
- **Action** $\mathbf{a} \in \mathcal{A}$ is a binary vector of $N_{\text{BS}}$ elements. Each vector element represents one BS, and its value 1 or 0 represents its activity or sleep mode, respectively. All possible actions are denoted by set $\mathcal{A}$. As MBS will not be considered for switching off, i.e., the element of $\mathbf{a}$ representing MBS always equals 1, the size of action space $N_{\text{a}}$ grows exponentially with the number of PBSs in the HetNet: $N_{\text{a}} = 2^{N_{\text{BS}}-1}$. However, it will be shown that $N_{\text{a}}$ can be reduced using simple analytical estimations.
- **Reward** $r(\mathbf{s}, \mathbf{a})$ depends on EE and the number of served UEs. Commonly, the EE metric is computed by dividing the average UE bitrate (over all considered UEs in the network) by the average system power consumption [38]. In order to increase fairness, e.g., bitrate for cell-edge users, it is proposed to use median downlink user bitrate instead:

$$EE(\mathbf{s}, \mathbf{a}) = \frac{c_{50}(\mathbf{s}, \mathbf{a})}{P_{\text{avg}}(\mathbf{s}, \mathbf{a})}, \tag{8}$$

where $c_{50}(\mathbf{s}, \mathbf{a})$ is the median UE bitrate measured in state $\mathbf{s}$ while exploiting action $\mathbf{a}$, and $P_{\text{avg}}(\mathbf{s}, \mathbf{a})$ is the average power consumed by all BSs computed with (3). In addition, reward $r(\mathbf{s}, \mathbf{a})$ depends on the number of currently served UEs. On the basis of the channel estimates it can be deduced how many UEs can be served if all BSs were active $N_{\text{UE}}(\mathbf{s}, \mathbf{1})$, and compare it against $N_{\text{UE}}(\mathbf{s}, \mathbf{a})$, being the number of UEs served in state $\mathbf{s}$ while taking action $\mathbf{a}$. Reward $r(\mathbf{s}, \mathbf{a})$ is thus given by:

$$r(\mathbf{s}, \mathbf{a}) = \begin{cases} EE(\mathbf{s}, \mathbf{a}) & \text{if } N_{\text{UE}}(\mathbf{s}, \mathbf{a}) \geq N_{\text{UE}}(\mathbf{s}, \mathbf{1}) \\ 0 & otherwise. \end{cases} \tag{9}$$

This constraint causes that the active BSs set with the number of served UEs smaller than in a fully active network obtains a reward equal to 0.
- **Environment** is the considered M-MIMO HetNet. The environment respond with reward $r(\mathbf{s}, \mathbf{a})$ (as a result of transmission after previous action) and a new state $\mathbf{s}$ (as a result of UEs movement). An important observation is that modifications of the environment state, i.e., UEs position sets, are not influenced by the chosen actions, i.e., active BSs sets. This fact will be later used to simplify the RL problem.
- **Agent** is the REM manager. Its goal is to maximize the overall future reward returned by the environment, by learning the environment through taking actions $\mathbf{a}$. We will use the so-called Q-learning algorithm, because it ensures convergence to the optimal solution, while requiring only simple updates of action values $Q(\mathbf{s}, \mathbf{a})$ stored in REM [12].

In Q-learning, every action $\mathbf{a}$ in state $\mathbf{s}$ can be characterized by an action-value $Q(\mathbf{s}, \mathbf{a})$ being the *profit* of taking this action. Action values are updated according to the following rule:

$$Q(\mathbf{s}, \mathbf{a}) \leftarrow Q(\mathbf{s}, \mathbf{a}) + \alpha \cdot [r(\mathbf{s}, \mathbf{a}) + \xi \cdot \max_{\mathbf{a}' \in \mathcal{A}} Q(\mathbf{s}', \mathbf{a}') - Q(\mathbf{s}, \mathbf{a})], \tag{10}$$

where $\alpha$ is a step-size parameter, $\xi \in \langle 0, 1 \rangle$ is the discount-factor determining how much the action-value from future state $Q(\mathbf{s}', \mathbf{a}')$ should affect the current action value $Q(\mathbf{s}, \mathbf{a})$. As it was already mentioned, in the considered system all states are independent from the actions, i.e., UEs motion is not affected by the active BSs set. As a result, we can represent our problem as a set of independent optimization tasks in each state. However, solving them still requires RL to interact with the environment. Such a simplified RL problem is known in the literature as *Associative*

*Search*, or *Contextual Bandit* [12]. We decided to describe it equivalently as "myopic" Q-learning, with the discount-factor set to zero: $\xi = 0$. Thus, the update of the action values is simply a $1-\alpha$ filter:

$$Q(\mathbf{s},\mathbf{a}) \leftarrow (1-\alpha)\cdot Q(\mathbf{s},\mathbf{a}) + \alpha \cdot r(\mathbf{s},\mathbf{a}). \tag{11}$$

Therefore, in this particular case, $Q(\mathbf{s},\mathbf{a})$ can be found as the forecasted reward for taking action $\mathbf{a}$ in state $\mathbf{s}$.

### 5.1. Exploration strategies

One of the RL challenges is to properly balance the time spent by the algorithm on exploiting the current knowledge, and exploring new actions. There are several exploration-exploitation strategies, widely used in order to manage action selection on the basis of action values $Q(\mathbf{s},\mathbf{a})$.

#### 5.1.1. $\epsilon$-Greedy

The simplest approach is the so-called $\epsilon$-greedy [39]. The algorithm is driven by the $\epsilon \in \langle 0;1\rangle$ parameter, being the probability of exploration. Encountering state $\mathbf{s}$, action $\mathbf{a}_t = \arg\max_{\mathbf{a}\in\mathcal{A}} Q(\mathbf{s},\mathbf{a})$, i.e., a greedy action, is chosen with probability of $1-\epsilon$. With the probability of $\epsilon$, a random action $\mathbf{a}_t \in \mathcal{A}$ is chosen. It seems reasonable to first focus more on the exploration, while later on the exploitation. Therefore, it is proposed that $\epsilon$ be calculated using:

$$\epsilon = \frac{1}{\sqrt[\beta]{\sum_{\mathbf{a}\in\mathcal{A}} N(\mathbf{s},\mathbf{a})}}, \tag{12}$$

where $N(\mathbf{s},\mathbf{a})$ was defined in Section 4.2 and $\beta$ is the weighting factor allowing for balance between exploitation and exploration.

#### 5.1.2. Upper Confidence Bound

The Upper Confidence Bound (UCB) is a more advanced exploration strategy [12]. Its advantage is that it does not utilize randomness. Action $\mathbf{a_t}$ is selected on the basis of action value $Q(\mathbf{s},\mathbf{a})$, the number of visits in state $\mathbf{s}$, i.e., $\sum_{\mathbf{k}\in\mathcal{A}} N(\mathbf{s},\mathbf{k})$, and the number of times that a particular action was selected $N(\mathbf{s},\mathbf{a})$:

$$\mathbf{a_t} = \arg\max_{\mathbf{a}\in\mathcal{A}} \left\{ Q(\mathbf{s},\mathbf{a}) + c\cdot\sqrt{\frac{\ln\sum_{\mathbf{k}\in\mathcal{A}} N(\mathbf{s},\mathbf{k})}{N(\mathbf{s},\mathbf{a})}} \right\}, \tag{13}$$

where $c$ is an arbitrary constant weighting the exploration-exploitation strategies. If $c$ is high, then the algorithm would often choose rarely explored actions. On the other hand, the lower the $c$, the more greedy the algorithm becomes.

Both UCB and $\epsilon$-greedy algorithms can benefit from the so-called *optimistic initialization*, i.e., setting the initial values of $Q(\mathbf{s},\mathbf{a})$ to a high one. The algorithm is then forced to test every action at least once. If the set of possible actions is large, it prolongs the convergence of the algorithm until all actions are tested at least once.

#### 5.1.3. Gradient Bandit

The Gradient Bandit (GB), in contrast to the $\epsilon$-greedy and UCB algorithms, relies not on the direct reward values but on relations between them, by obtaining a probability distribution of taking each action [12]. The probability of taking action $\mathbf{a}$ follows the so-called soft-max distribution:

$$P\{\mathbf{a}_t = \mathbf{a}\} = \frac{e^{Q(\mathbf{s},\mathbf{a})}}{\sum_{\mathbf{k}\in\mathcal{A}} e^{Q(\mathbf{s},\mathbf{k})}} = \pi(\mathbf{a}). \tag{14}$$

The formula for updating the action value is slightly different from (11):

$$\begin{cases} Q(\mathbf{s},\mathbf{a}_t) \leftarrow Q(\mathbf{s},\mathbf{a}_t) + \alpha_{\mathrm{gb}}\{r(\mathbf{s},\mathbf{a}_t) - \hat{r(\mathbf{s})}\}\{1-\pi(\mathbf{a}_t)\}, & \text{and} \\ Q(\mathbf{s},\mathbf{a}) \leftarrow Q(\mathbf{s},\mathbf{a}) - \alpha_{\mathrm{gb}}\{r(\mathbf{s},\mathbf{a}) - \hat{r(\mathbf{s})}\}\cdot\pi(\mathbf{a}), & \text{for } \mathbf{a}\neq\mathbf{a}_t, \end{cases} \tag{15}$$

where $\alpha_{\mathrm{gb}}$ is the step-size parameter, and $\hat{r(\mathbf{s})}$ is the average reward received in state $\mathbf{s}$ in the previous visits. The main idea is that if the chosen action provides a higher reward, then the probability of its exploitation increases. The *optimistic initialization* in the case of GB does not work, because the action values are relative to each other in this case.

### 5.2. Proposed action space reduction (ASR) method

Frequent switching BSs on/off is not encouraged by wireless network operators and users. Operators are afraid of destabilizing or damaging the hardware installed on BSs. Users do not want to get poor Quality of Experience (QoE). Therefore, it is reasonable to reduce the RL convergence time, e.g., by *a priori* removal of actions that cannot be optimal in a given state. It is proposed that the actions which result in zero-reward be excluded. Suppose that there is a UE that receives a strong enough signal (to be served) from only a single BS. This BS should be explicitly prevented from being switched off to preserve the required QoS, i.e., not limiting the number of connected UEs.

Due to the channel hardening property of the M-MIMO, the average channel gain is relatively stable despite the slight variations of every single radio channel [3]. Thus on the basis of channel estimates in state $\mathbf{s}$ we can *a priori* estimate the number of UEs having RSS above the threshold required for communication with minimum quality with any of the active BSs set (action) $N_{\mathrm{ue}}(\mathbf{s},\mathbf{a})$:

$$N_{\mathrm{ue}}(\mathbf{s},\mathbf{a}) = \sum_{s_i\in\mathbf{s}} f(s_i,\mathbf{a}), \tag{16}$$

where $s_i$ denotes the localization of UE $i$, and $f(s_i,\mathbf{a})$ determines if UE $i$ can be served by the network while considering action $\mathbf{a}$:

$$f(s_i,\mathbf{a}) = \begin{cases} 1 & \text{if UE } i \text{ can be served,} \\ 0 & \text{otherwise,} \end{cases} \tag{17}$$

Using the above equations, the number of served users $N_{\mathrm{ue}}(\mathbf{s},\mathbf{a})$ related to each action $\mathbf{a}\in\mathcal{A}$ can be estimated before making the decision about BSs switching. Every action that results in a reduction of the number of served users in comparison to the maximal number $\max_{\mathbf{a}\in\mathcal{A}}\{N_{\mathrm{ue}}(\mathbf{s},\mathbf{a})\}$ (over all actions) is excluded from the action space (never explored), i.e., BSs crucial for providing the minimal QoS are explicitly prevented from being switched off. As a result of ASR a smaller action space $\grave{\mathcal{A}}$ is obtained and used in the algorithms instead of $\mathcal{A}$, i.e., $\mathbf{a}\in\grave{\mathcal{A}}$.

### 5.3. REM-based exploration algorithm (REM-EA)

Although we concluded that the transitions between states are not influenced by actions, we can expect that a similar optimal active BSs set, i.e., action $\mathbf{a}$, should be chosen in the similar states, i.e., similar UEs position sets. On the basis of promising initial results and observations of the UCB algorithm, our second proposal is to modify it so as to exploit the knowledge from all REM entries, i.e., states, but properly weighted. Most importantly, this is executed with reduced action space, i.e., after using ASR. Let us define $\mathbf{s}_0$ as the currently visited state and $\mathbf{s}_l$ as another state related to REM entry $l$. The REM-EA is then given as:

$$\mathbf{a}_t = \arg\max_{\mathbf{a}\in\grave{\mathcal{A}}} \left\{ \hat{Q}(\mathbf{a}) + c\cdot\sqrt{\frac{\ln\sum_{\mathbf{k}\in\grave{\mathcal{A}}}\hat{N}(\mathbf{k})}{\hat{N}(\mathbf{a})}} \right\}, \tag{18}$$

where:

$$\hat{Q}(\mathbf{a}) = \frac{Q(\mathbf{s}_0,\mathbf{a}) + \sum_{\mathbf{s}\in S\setminus\mathbf{s}_0, Q(\mathbf{s},\mathbf{a})\neq 0} \frac{Q(\mathbf{s},\mathbf{a})}{d_h(\mathbf{s}_0,\mathbf{s})^\gamma}}{1 + \sum_{\mathbf{s}\in S\setminus\mathbf{s}_0, Q(\mathbf{s},\mathbf{a})\neq 0} \frac{1}{d_h(\mathbf{s}_0,\mathbf{s})^\gamma}}, \tag{19}$$

$$\hat{N}(\mathbf{a}) = \frac{N(\mathbf{s}_0,\mathbf{a}) + \sum_{\mathbf{s}\in S\setminus\mathbf{s}_0} \frac{N(\mathbf{s},\mathbf{a})}{d_h(\mathbf{s}_0,\mathbf{s})^\gamma}}{1 + \sum_{\mathbf{s}\in S\setminus\mathbf{s}_0} \frac{1}{d_h(\mathbf{s}_0,\mathbf{s})^\gamma}}, \tag{20}$$

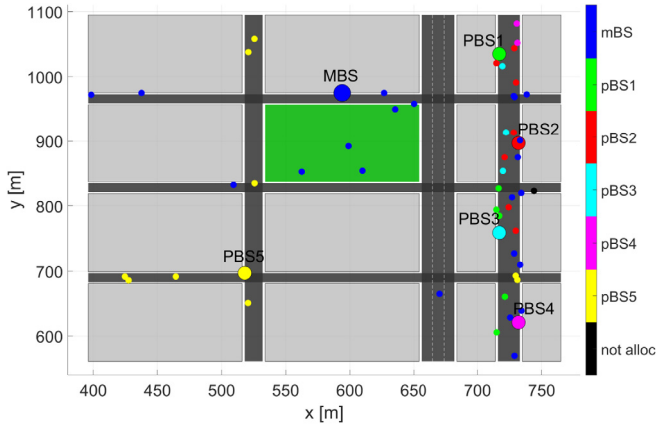


**Fig. 5.** Deployment of the BSs (big dots) in the considered M-MIMO HetNet, and UEs initial positions (small dots — color-coded is association of a UE to a BS).

and $d_h(\mathbf{s}_0, \mathbf{s})$ is the HD between the UE position set $\mathbf{s}_0$ and $\mathbf{s}$ (5), and $\gamma$ is an arbitrary constant. The larger the $\gamma$, the smaller the impact on the current action selection more distanced REM entries have. It will be shown in the computer simulation that the proposed reasoning based on spatial (in states space) correlation, i.e., REM-EA, can provide further improvement for RL convergence, due to the efficient utilization of REM data.

## 6. Simulation results

The algorithms described in the previous sections are evaluated in terms of computer simulations using a realistic, 3D-ray-tracing radio channel model. We consider a system level simulation of a single, two-tier M-MIMO HetNet composed of an MBS and a set of PBSs. Each resembles a 5G system by using proper configuration, e.g., OFDM with numerology, slots and subframes, channel estimation using uplink pilots, Modulation And Coding Schemes and effective SINR mapping. The M-MIMO uses a Regularized Zero Forcing precoder [3]. The downlink traffic is used for the optimization of HetNet EE and presented using various statistics in later sections.

### 6.1. Simulation environment

The implemented simulator consists of several functional blocks that will be briefly described in the next subsections.

#### 6.1.1. Base station deployment

The HetNet is deployed in an urban scenario following the *Madrid Grid Model*, which exploits various challenging regions: a park, narrow street canyons, and a promenade [26]. There are in total 6 BSs in the considered system, i.e., 1 MBS and 5 PBSs. The BSs are deployed on the basis of initial coverage simulations as it is shown in Fig. 5. The MBS is placed in the central part of the map near the park, and provides general coverage. PBSs 1 to 4 are located along the promenade, aiming at the improvement of network capacity in the most crowded area. PBS 5 is placed in the street canyon to extend the network coverage in the place where MBS coverage is insufficient. Both the MBS and PBSs are equipped with rectangular antenna arrays. The MBS exploits a single 128-element panel arranged in a 16 × 8 rectangle, i.e., having 16 columns and 8 rows.

Each PBS is equipped with two 2 × 8 (2 columns, 8 rows) rectangular panels pointing in opposite directions. The MBS antenna array is deployed 2.5 m above the rooftop at the total height of 45 m. The PBS antenna arrays are claimed to be installed on street lamps 5 m above the ground.

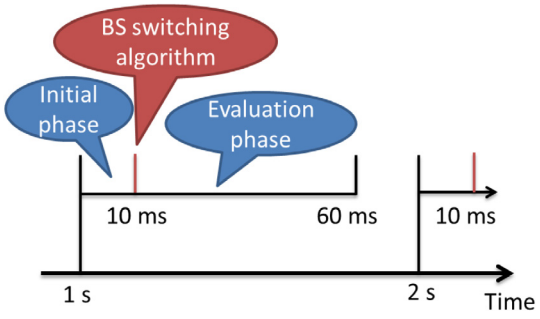


**Fig. 6.** Channel generation scheme.

#### 6.1.2. UE to BS association

In the considered network, the UE-to-BS association is centralized using the Dynamic Point Selection (DPS) concept. It is performed every 10 ms. In order to reduce the system complexity, and focus only on BSs switching, a simple UE-to-BS association based on the Received Signal Strength (RSS) is used. RSS from a given UE is summarized over all antennas available at a given BS. The UEs are not associated with any BS, if their highest (over BSs) average (over antennas) RSS is below the threshold $P_{th} = -120$ dBm. This threshold is based on minimal MCS requirements according to the parameters specified in Section 6.1.4.

There are 50 UEs generated, and their initial positions are depicted in Fig. 5. They are generated so that the most crowded area is the promenade in the right part of the considered map. However, some UEs are located in the park and in the street canyons as well. The UEs move with the speed of 1.5 $\frac{\text{m}}{\text{s}}$.

#### 6.1.3. Traffic model

In this paper, the data stream to each UE follows the *full-buffer* model, i.e., even a single UE associated to a BS utilizes all of its time–frequency resources. As a result, the traffic load in the considered M-MIMO HetNet is always maximal, creating the most challenging scenario for EE improvement.

#### 6.1.4. Scheduler, precoder

For users associated to a given BS, the scheduling and precoding is executed every timeslot. The scheduler is based on the design proposed in [40]. For each Resource Block (RB), independent initial allocation is performed. Associated UEs are sorted according to their proportionality fairness metric, i.e., the ratio of potential rate and past rate. The considered M-MIMO utilizes Regularized Zero Forcing Precoder that allows many UE layers to be allocated in parallel to the same time–frequency resources. However, the scheduler rejects a new UE whose channel is too correlated with already allocated UEs (based on the channel correlation coefficient) and stops adding layers when the total estimated bitrate decreases. The SINR values estimated for each RB allocated to a given UE are used for MCS selection. This utilizes Exponential Effective SINR mapping and 15 MCSs with proper coefficients defined in [41,42].

#### 6.1.5. Channel generation

The 3D ray-tracing model is claimed to be the most accurate and realistic for the evaluation of the M-MIMO network [43]. The cost of the utilization of a 3D ray-tracing model is the long time of channel generation, large amount of required storage, and long simulation time itself. To overcome these limitations, and allow the simulation of relatively long UEs paths, we propose to generate the radio channel coefficients in several short batches, as it is depicted in Fig. 6. The channel is generated and system-level simulations are carried out only over each batch period.

There are 15 batches generated, each lasting 60 ms. There is a 1 s time gap between the consecutive batches. It is to allow the UEs

**Table 1**
Simulation system parameters.

| Parameter | Value |
|---|---|
| Simulation time | 15 s |
| Time slot duration | 0.5 ms |
| Number of UEs | 50 |
| Channel realizations | 10 |
| UEs speed | $1.5\frac{\text{m}}{\text{s}}$ |
| Number of PBSs | 5 |
| Central frequency | 3.55 GHz |
| Bandwidth | 300 MHz |
| Subcarrier spacing | 30 kHz |
| Number of MBS antennas | 128 ($16 \times 8$) |
| Number of PBS antennas | 32 ($2 \times 2 \times 8$) |
| RSS threshold $P_{\text{th}}$ | −120 dBm |
| REM grid size $g$ | 3 m |

**Table 2**
Power model parameters.

| Parameter | Value |
|---|---|
| MBS transmitted power $P_{\text{tx,MBS}}$ | 46 dBm |
| PBS transmitted power $P_{\text{tx,PBS}}$ | 30 dBm |
| Amplifier efficiency $\eta$ | 0.5 [3] |
| Transceiver chain power $P_{\widetilde{\text{TC}}}$ | 0.4 W [3] |
| Local oscillator power $P_{\text{LO}}$ | 0.2 W [3] |
| BS fix power $P_{\text{fix}}$ | 10 W [3] |
| BS stand-by power $P_{\text{off}}$ | 10 W [31] |

to change their positions significantly, which can result in a different optimal active BSs set. First, 10 ms of each batch is for initiating the simulator, e.g., to obtain initial UE rates or interference statistics, then the BS switching algorithm is launched and the obtained active BSs set (action) is evaluated during the last 50 ms. The statistics are obtained based on the last 50 ms of each batch. To provide some changes and randomness in the radio environment, there are 10 different channels generated with the same UEs paths but different locations of scatterers in the environment, e.g., persons. In addition, channel variation is boosted by Gaussian channel estimation error generated independently for each simulation iteration, following the model described in [44].

### 6.2. Simulation setup

The main parameters of the simulation environment are presented in Table 1. Every simulation is performed using the same setup by default. Any slight changes will be explicitly described in the text.

The parameters related to the Power consumption model from Section 3.1 are presented in Table 2.

### 6.3. Benefits of the REM solution

The first simulation experiment is performed in order to show the maximum potential benefits of the utilization of REM, compared to the existing solution based on analytical heuristics. The existing analytical heuristic is the so-called switching on/off-based energy saving (SWES) algorithm [23]. The SWES algorithm has been adopted to the *full-buffer* UE traffic model. Originally, SWES switches off BSs according to their traffic load. We modified SWES to switch BSs on/off on the basis of the median user bitrate obtained with the Shannon formula. A BS can be switched off if the initial median user bitrate is degraded by no more than 5%.

To obtain the REM solution, we temporarily switched off the radio environment variations, i.e., channel estimation error, and exploited only single channel realization. Then, having an invariable radio environment, the REM was learned using an exhaustive search.

The resultant energy savings are depicted in Fig. 7. It can be observed that the REM solution performs better than the SWES algorithm, increasing the overall power savings to 19%. But not only the power saving are higher due to the utilization of REM solution. In Fig. 8 it is shown that the median user bitrate is about 50 Mbps higher when utilizing REM in relation to the SWES algorithm. At the same time, SWES provides a median user bitrate gain of about 13 Mbps over a scenario without EE optimization. The bitrate gains are caused by reduced interference related to switching off some of the BSs, which remains consistent with the previous research findings [27]. The interference changes are hard to be analytically estimated, thus SWES switches off the sub-optimal set of BSs. Taking into the account the gains from energy savings and median user bitrate, the overall system EE is 70% higher when utilizing REM in comparison to the SWES algorithm. Moreover, EE obtained with the REM solution is 136% higher in relation to the scenario without EE optimization.

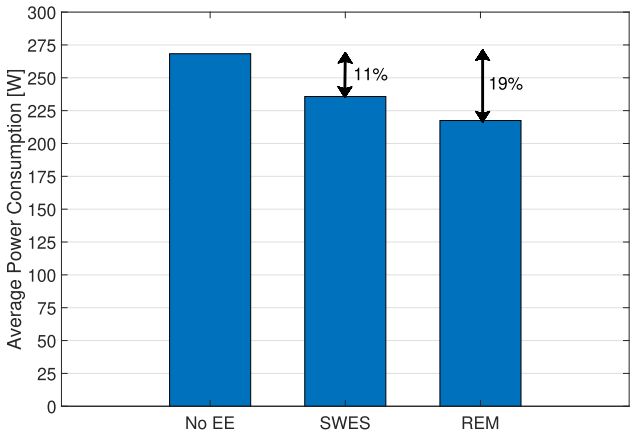


**Fig. 7.** Achievable energy savings, while there is no EE optimization (no ee), for SWES algorithm, and REM, respectively.

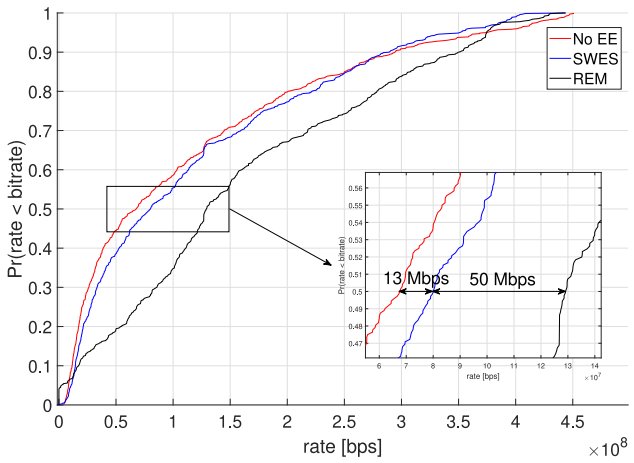


**Fig. 8.** Empirical Cumulative Distribution Function of UEs bitrates, while there is no EE optimization (no ee), for SWES algorithm and REM respectively.

### 6.4. State-of-the-art exploration algorithms

We have shown that REM can provide the network with much better solution than SWES. The challenge, is however, to efficiently learn, i.e., minimize, the number of times a given action has to be tested in a given state $\mathbf{s}$ before stabilizing at one solution, hopefully, the best one. Moreover, the utilized RL has to be able to adapt to changing radio environment conditions. First, the state-of-the-art exploration strategies: $\epsilon$-greedy (Section 5.1.1), UCB (Section 5.1.2), and Gradient Bandit (Section 5.1.3) are studied to obtain the best parameters for fair comparison and application of the improvements proposed in Sections 5.2 and 5.3.

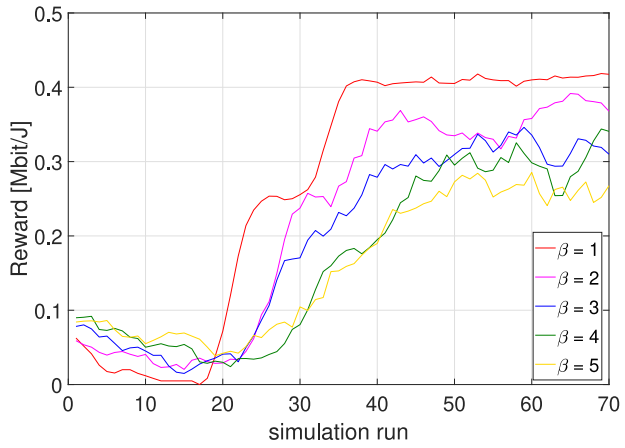


**Fig. 9.** Convergence of the $\epsilon$-greedy exploration method. There is a 5-tap moving average applied over simulation runs.

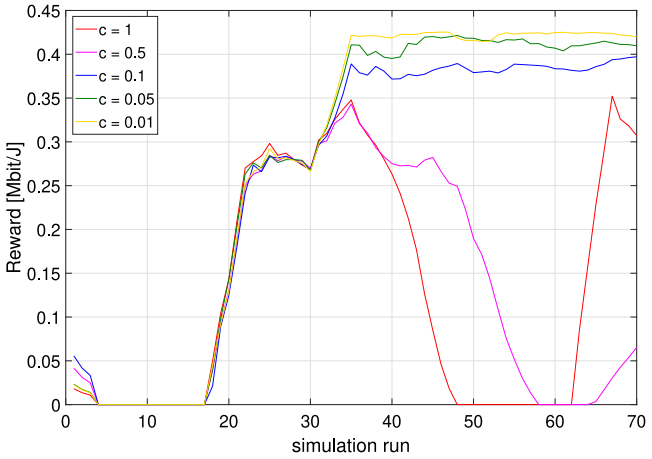


**Fig. 10.** Convergence of the UCB exploration method. There is a 5-tap moving average applied over simulation runs.

#### 6.4.1. $\epsilon$-Greedy

Fig. 9 depicts a convergence of the $\epsilon$-greedy exploration method. It can be seen that the lower the $\beta$ parameter, the faster the convergence is. Low $\beta = 1$, being the optimal value, indicates that it is profitable for the algorithm to perform greedily. For a higher $\beta$ value, the algorithm spends too much time on the exploration of random actions, which are often related to a low reward.

#### 6.4.2. UCB

A similar tendency can be observed in the convergence of the UCB algorithm depicted in Fig. 10. The $c$ parameter in (13) provides a balance between executing a greedy action and exploring less known actions. For high $c$, the actions providing a low reward are chosen too often. We can see that in the case of UCB also the algorithm performs better when it is focused mainly on the greedy action exploitation. The chosen value of $c$ equals 0.01.

#### 6.4.3. Gradient Bandit

The Gradient Bandit algorithm performs on the basis of the probability distribution of taking particular actions. Action probability increases when the reward is higher than the average reward. As we can see in Fig. 11, the algorithm has a tendency to run into the suboptimal solution. However, the fastest convergence could be observed for $\alpha_{GB} = 20$.

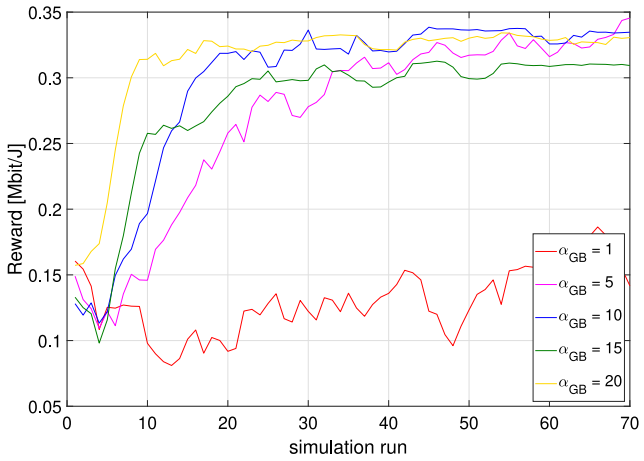


**Fig. 11.** Convergence of the Gradient Bandit exploration method. There is a 5-tap moving average applied over simulation runs.

**Table 3**
Mean reward obtained in the last 30 simulation runs, for $\epsilon$-greedy, UCB, and Gradient Bandit exploration algorithms.

| $\epsilon$-greedy | | UCB | | Gradient Bandit | |
|---|---|---|---|---|---|
| $\beta$ | EE ($\frac{Mbit}{J}$) | c | EE ($\frac{Mbit}{J}$) | $\alpha_{GB}$ | EE ($\frac{Mbit}{J}$) |
| 1 | 0.41 | 1 | 0.14 | 1 | 0.14 |
| 2 | 0.35 | 0.5 | 0.11 | 5 | 0.32 |
| 3 | 0.31 | 0.1 | 0.38 | 10 | 0.33 |
| 4 | 0.28 | 0.05 | 0.41 | 15 | 0.30 |
| 5 | 0.26 | 0.01 | 0.41 | 20 | 0.33 |

#### 6.4.4. Comparison and application of ASR

Additionally, all of the three exploration methods are evaluated in terms of the mean of the reward obtained on the basis of the last 30 simulation runs. The results are presented in Table 3. It can be observed that Gradient Bandit does not converge to the solution providing a maximal reward visible in the $\epsilon$-greedy and UCB methods. The comparison of the algorithms' convergence for the best previously obtained parameters is depicted in Fig. 12. The fastest convergence can be observed for the Gradient Bandit algorithm, however it stabilizes at a suboptimal solution. The $\epsilon$-greedy and UCB perform similarly, with the slight advantage on the side of UCB. These converge after about 35 simulation runs. The broken line in Fig. 12 depicts the result of the ASR (Section 5.2) applied to the considered RL algorithms. It can be seen that in the case of UCB the convergence can be reduced from about 35 to about 15 simulation runs, i.e., about 2.3 times. This improvement is obtained thanks to reduction of actions space. In the next section it will be shown that the convergence speed can be further increased using knowledge from another REM entries (different states).

### 6.5. Performance of REM-EA

Finally, the REM-EA from Section 5.3 is evaluated, to show that it is beneficial for the RL algorithms to utilize information stored in REM for various states (UEs positions) to build a knowledge about the current state. REM-EA is based on the UCB as it has been proved in the previous sections to provide the best results. The same constant $c = 0.01$ is used for REM-EA. However, REM-EA has in addition a parameter $\gamma$ weighting the impact of distanced REM information (in state sense) on the action being chosen in the current state. The results of REM-EA for various $\gamma$ values are presented in Fig. 13. The results are compared against the UCB algorithm with ASR applied. For high $\gamma$ values, REM-EA does not exploit the knowledge from similar REM entries and tends to perform as the pure UCB algorithm. However, for low $\gamma$ values the impact of neighboring states is too high, which results

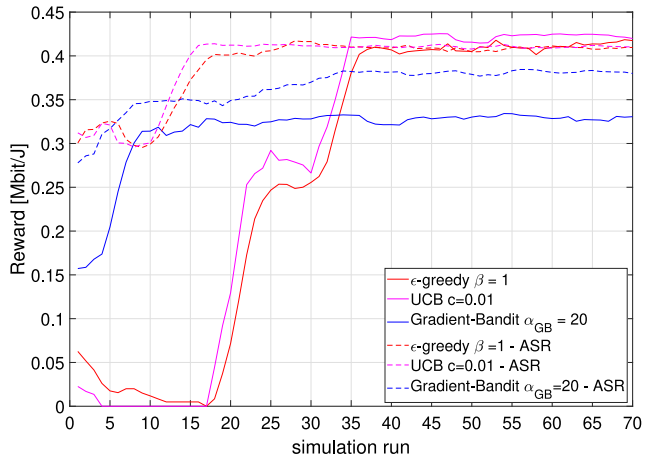


**Fig. 12.** Comparison of the state-of-the-art exploration methods (solid lines), and improvement using ASR (broken lines). There is a 5-tap moving average applied over simulation runs.

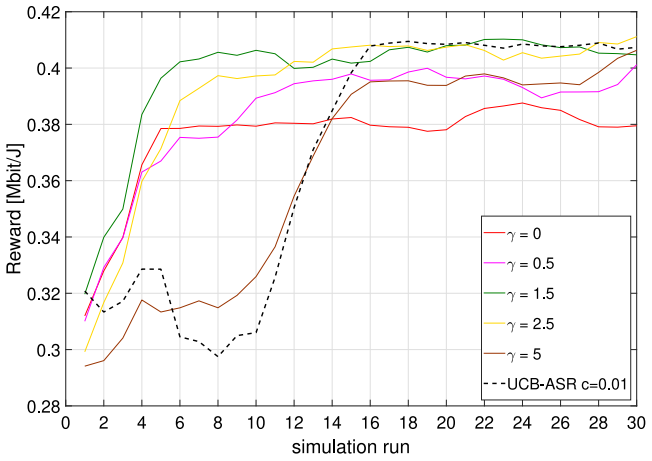


**Fig. 13.** REM-EA convergence over different $\gamma$ values. There is a 5-tap moving average applied over simulation runs.

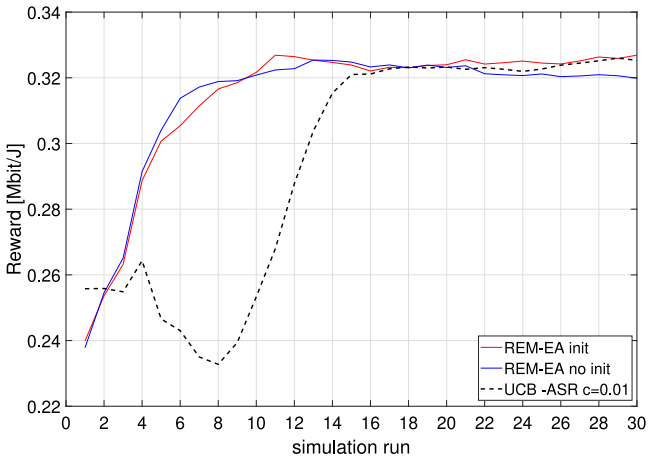


**Fig. 14.** Convergence of REM-EA while there are entries in REM (REM-EA init), REM-EA starting form empty REM (REAM-EA no init) and UCB, under a scenario with 45 UEs. For $c = 0.01$, and $\gamma = 1.5$. There is a 5-tap moving average applied over simulation runs.

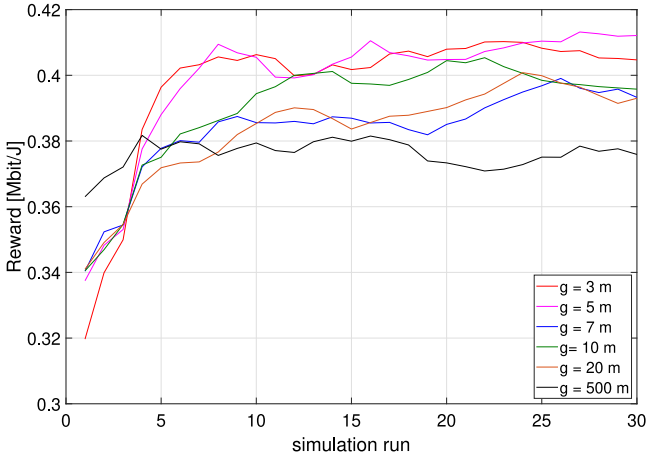


**Fig. 15.** REM-EA convergence over various square grid size $g$ for $\gamma = 1$, and $c = 0.01$. There is a 5-tap moving average applied over simulation runs.

in reaching only a sub-optimal solution. The optimal $\gamma$ value providing the proper weighting of REM data seems to be 1.5. The application of the REM-EA can speed up the convergence to about 6 simulation runs, i.e., in the considered network the proposed algorithm requires 6 passes of UEs, each lasting 15 s, to obtain enough knowledge to find an energy-efficient BSs activity pattern. It is a convergence time reduction by about 60% in relation to the UCB with ASR, and about 83% in relation to the pure UCB, while remaining the same optimal solution. Obviously, this is an example of starting from an empty REM, i.e., worst case scenario. If there is some knowledge gathered in the REM the EE solution is claimed to be obtained much faster than in 6 simulation runs. However, REM already containing a huge number of entries would be required to prove this.

To evaluate how REM-EA performs while REM already has some entries and unknown state appears, a single channel realization exploiting 45 instead of 50 UEs is considered. Each of UEs locations, together with the radio channel coefficients are independently randomly generated, with the same spatial density. The REM-EA algorithm has been run in three cases: with initial knowledge from the previous simulations, without knowledge, and compared against the UCB-ASR method. The results are depicted in Fig. 14. The most crucial is the result for the REM-EA init approach. Its performance is very similar to running REM-EA without previous knowledge. It seems that previous knowledge saved in REM is too distanced (in terms of HD) to boost convergence. Most importantly, the previous knowledge degrades neither the convergence speed nor the maximal reward. Still, the convergence time is over 50% faster in comparison to the UCB algorithm. REM-EA can adopt to the new environment conditions without performance degradation.

### 6.6. Square grid size analysis

We propose in Section 4 to use a square grid of size $g$ in our REM, to store the REM entries labeled with UEs position set **s**. While previously relatively high accuracy was used, i.e., $g = 3$ m, this can result in a significant REM size. Now, coarser grid sizes $g$, resulting in the reduction of the number of REM entries, are evaluated. It can be seen in Fig. 15 that lowering the grid resolution does not increase the RL convergence. However, larger grid size (above $g = 5$ m) results in reduced maximal reward value. This is caused by the smaller flexibility of BSs switching, i.e., for a coarser grid significantly different UEs propagation conditions require a single BSs activity pattern to be chosen. Fig. 16 presents the number of REM entries related to each grid resolution. The conclusion is that there is a trade-off between the number of REM states and REAM-EA performance. There can be found a grid resolution, e.g., $g = 5$ m, which can provide both a high reward and minimized REM size, i.e., a reduction by almost 50% in comparison to a system with $g = 3$ m.

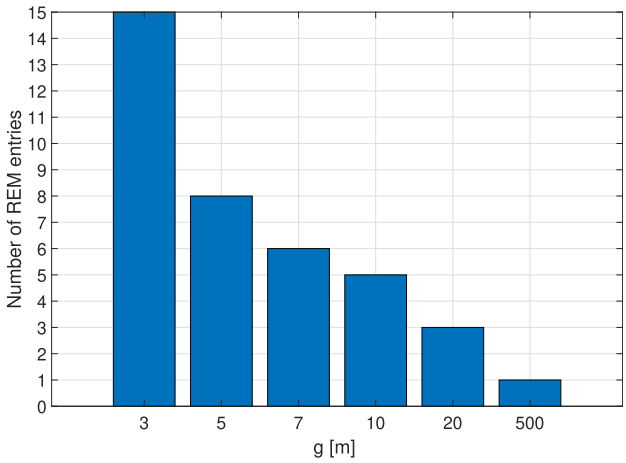


**Fig. 16.** The number of REM entries over various square grid size $g$.

## 7. Conclusions

This paper proposes location-dependent data for providing EE gains in the M-MIMO HetNet. The underutilized BSs are switched off on the basis of the data stored in REM. First, the design of the REM and its deployment in the HetNet is proposed. Secondly, RL is proposed to manage the data acquisition and utilization process, using state-of-the-art exploration algorithms, i.e., $\epsilon$-greedy, UCB, and Gradient Bandit. Finally, two algorithms are proposed to speed up the RL convergence time. In ASR the number of served UEs is estimated on the basis of an analytical formula that allows the reduction of the action space. The second proposed algorithm is REM-EA. The data from the whole REM are utilized to obtain a proper active BSs set in the current state. The algorithms were extensively evaluated using an advanced M-MIMO HetNet simulator, and a realistic 3D-ray-tracing radio channel model. It has been proven that REM-based solution performs better then the state-of-the-art SWES algorithm. Further studies have shown that the state-of-the-art RL exploration algorithms' convergence benefits first, from the analytical estimations, i.e., ASR, and secondly, from the utilization of the similarities between the states stored in REM, i.e., REM-EA.

In the future, the current study can be extended to include higher-mobility UEs or possibly vehicles. Although in the article the problem was formulated as *Associative Search*, where the reward, i.e., EE, can be maximized in each state independently, it may be worth considering the dependency between the consecutive states in the future. Such a dependency can occur while taking into account the fact that frequent BS on/off switching increases the hardware expenditure [45]. One interesting further study is to incorporate both the costs of energy and those related to potential hardware replacement in the reward function. The aim of the agent would then be to minimize the operator cost, and balance the savings from EE BS switching, and expenditures related to hardware performance degradation. In that case, it would also be necessary to study the impact of the learning factor on the long-term Q-learning performance. Finally, studies on the reduction of REM size without performance degradation are important from the point of view of algorithm implementation in a real network. This can be achieved, e.g., by utilizing deep neural networks, but requires long simulation runs and varying UEs paths to first populate the REM.

## CRediT authorship contribution statement

**Marcin Hoffmann:** Conceptualization, Software, Investigation, Writing - original draft. **Paweł Kryszkiewicz:** Supervision, Project administration, Validation, Writing - original draft, Writing - review & editing. **Adrian Kliks:** Supervision, Writing - review & editing.

## Declaration of competing interest

The authors declare that they have no known competing financial interests or personal relationships that could have appeared to influence the work reported in this paper.

## Acknowledgment

The presented work has been funded by the Polish Ministry of Science and Higher Education subvention within the task "Cognitive and sustainable communication systems" in 2020. The simulations have been based on the QCM simulator from Huawei Technologies Sweden Research Center.

## References

[1] Z. Hasan, H. Boostanimehr, V.K. Bhargava, Green cellular networks: A survey, some research issues and challenges, IEEE Commun. Surv. Tutor. 13 (4) (2011) 524–540.

[2] E. Larsson, O. Edfors, F. Tufvesson, T.L. Marzetta, Massive MIMO for next generation wireless systems, IEEE Commun. Mag. 52 (2) (2014) 186–195, http://dx.doi.org/10.1109/MCOM.2014.6736761.

[3] E. Björnson, J. Hoydis, L. Sanguinetti, Massive MIMO networks: Spectral, energy, and hardware efficiency, Found Trends® Signal Process 11 (3–4) (2017) 154–655, http://dx.doi.org/10.1561/2000000093.

[4] K.R.S.V. Prasad, E. Hossain, V.K. Bhargava, Energy efficiency in massive MIMO-based 5g networks: Opportunities and challenges, IEEE Wirel. Commun. 24 (3) (2017) 86–94, http://dx.doi.org/10.1109/MWC.2016.1500374WC.

[5] Y. Jin, N. Duffield, A. Gerber, P. Haffner, W.-L. Hsu, G. Jacobson, S. Sen, S. Venkataraman, Z.-L. Zhang, Characterizing data usage patterns in a large cellular network, in: Proceedings of the 2012 ACM SIGCOMM Workshop on Cellular Networks: Operations, Challenges, and Future Design, 2012, pp. 7–12.

[6] M.Z. Shafiq, L. Ji, A.X. Liu, J. Wang, Characterizing and modeling internet traffic dynamics of cellular devices, ACM SIGMETRICS Perform. Eval. Rev. 39 (1) (2011) 265–276.

[7] X. Gao, O. Edfors, F. Tufvesson, E.G. Larsson, Massive MIMO in real propagation environments: Do all antennas contribute equally? IEEE Trans. Commun. 63 (11) (2015) 3917–3928.

[8] C. Mollén, J. Choi, E.G. Larsson, R.W. Heath, Uplink performance of wideband massive MIMO with one-bit ADCs, IEEE Trans. Wireless Commun. 16 (1) (2017) 87–100.

[9] R. Zi, X. Ge, J. Thompson, C. Wang, H. Wang, T. Han, Energy efficiency optimization of 5G radio frequency chain systems, IEEE J. Sel. Areas Commun. 34 (4) (2016) 758–771, http://dx.doi.org/10.1109/JSAC.2016.2544579.

[10] F. Han, S. Zhao, L. Zhang, J. Wu, Survey of strategies for switching off base stations in heterogeneous networks for Greener 5G systems, IEEE Access 4 (2016) 4959–4973, http://dx.doi.org/10.1109/ACCESS.2016.2598813.

[11] J. Wu, Y. Zhang, M. Zukerman, E.K. Yung, Energy-efficient base-stations sleep-mode techniques in green cellular networks: A survey, IEEE Commun. Surv. Tutor. 17 (2) (2015) 803–826.

[12] R.S. Sutton, A.G. Barto, Reinforcement Learning: An Introduction, A Bradford Book, Cambridge, MA, USA, 2018.

[13] S. Sharma, S.J. Darak, A. Srivastava, Transfer reinforcement learning based framework for energy savings in cellular base station network, in: 2019 URSI Asia-Pacific Radio Science Conference, AP-RASC, 2019, pp. 1–4.

[14] N. Islam, A. Alazab, M. Alazab, A reinforcement learning based algorithm towards energy efficient 5G multi-tier network, in: 2019 Cybersecurity and Cyberforensics Conference, CCC, 2019, pp. 96–101.

[15] J. Ye, Y.J. Zhang, DRAG: Deep reinforcement learning based base station activation in heterogeneous networks, IEEE Trans. Mob. Comput. (2019) 1–1.

[16] M. Hoffmann, P. Kryszkiewicz, G. Koudouridis, Modeling of real time kinematics localization error for use in 5G networks, EURASIP J. Wireless Commun. Networking 2020 (2020) http://dx.doi.org/10.1186/s13638-020-1641-8.

[17] R.D. Taranto, S. Muppirisetty, R. Raulefs, D. Slock, T. Svensson, H. Wymeersch, Location-aware communications for 5G networks: How location information can improve scalability, latency, and robustness of 5G, IEEE Signal Process. Mag. 31 (6) (2014) 102–112.

[18] P. Tengkvist, G.P. Koudouridis, C. Qvarfordt, M. Dryjanski, M. Cellier, Multi-dimensional radio service maps for position-based self-organized networks, in: 2017 IEEE 22nd International Workshop on Computer Aided Modeling and Design of Communication Links and Networks (CAMAD), 2017, pp. 1–6, http://dx.doi.org/10.1109/CAMAD.2017.8031530.

[19] N. Rajatheva, I. Atzeni, E. Bjornson, A. Bourdoux, S. Buzzi, J.-B. Dore, S. Erkucuk, M. Fuentes, K. Guan, Y. Hu, X. Huang, J. Hulkkonen, J.M. Jornet, M. Katz, R. Nilsson, E. Panayirci, K. Rabie, N. Rajapaksha, M. Salehi, H. Sarieddeen, T. Svensson, O. Tervo, A. Tolli, Q. Wu, W. Xu, White paper on broadband connectivity in 6G, 2020, arXiv http://hdl.handle.net/10754/662965.

[20] C. Guo, W. Hong, L. Tian, Y. Yu, Design and pattern measurement of a sub-6GHz 64-channel full digital massive MIMO system, in: 2019 IEEE MTT-S International Wireless Symposium, IWS, 2019, pp. 1–3, http://dx.doi.org/10.1109/IEEE-IWS.2019.8803969.

[21] C. Liu, B. Natarajan, H. Xia, Small cell base station sleep strategies for energy efficiency, IEEE Trans. Veh. Technol. 65 (3) (2016) 1652–1661, http://dx.doi.org/10.1109/TVT.2015.2413382.

[22] A.A. Abdulkafi, T.S. Kiong, D. Chieng, A. Ting, J. Koh, Energy efficiency improvements in heterogeneous network through traffic load balancing and sleep mode mechanisms, Wirel. Pers. Commun. 75 (4) (2014) 2151–2164, https://doi.org/10.1007/s11277-013-1460-x.

[23] E. Oh, K. Son, B. Krishnamachari, Dynamic base station switching-on/off strategies for green cellular networks, IEEE Trans. Wireless Commun. 12 (5) (2013) 2126–2136, http://dx.doi.org/10.1109/TWC.2013.032013.120494.

[24] M. Feng, S. Mao, T. Jiang, BOOST: Base station on-off switching strategy for Green Massive MIMO HetNets, IEEE Trans. Wireless Commun. 16 (11) (2017) 7319–7332.

[25] L. Wang, X. Feng, X. Gan, J. Liu, H. Yu, Small cell switch policy: A reinforcement learning approach, in: 2014 Sixth International Conference on Wireless Communications and Signal Processing (WCSP), 2014, pp. 1–6.

[26] METIS, Deliverable D6.1, Simulation guidelines, Version: v1.0, Mobile and wireless communications Enablers for the Twenty-twenty Information, 2013.

[27] X. Ge, B. Yang, J. Ye, G. Mao, C. Wang, T. Han, Spatial spectrum and energy efficiency of random cellular networks, IEEE Trans. Commun. 63 (3) (2015) 1019–1030, http://dx.doi.org/10.1109/TCOMM.2015.2394386.

[28] H. Holtkamp, G. Auer, V. Giannini, H. Haas, A parameterized base station power model, IEEE Commun. Lett. 17 (11) (2013) 2033–2035.

[29] A. Capone, S. D'Elia, I. Filippini, A.E.C. Redondi, M. Zangani, Modeling energy consumption of mobile radio networks: An operator perspective, IEEE Wirel. Commun. 24 (4) (2017) 120–126.

[30] J. Lee, J.-K. Han, J.C. Zhang, MIMO technologies in 3GPP LTE and LTE-advanced, EURASIP J. Wireless Commun. Netw. 2009 (2009) https://doi.org/10.1155/2009/302092.

[31] P. Frenger, P. Moberg, J. Malmodin, Y. Jading, I. Godor, Reducing energy consumption in LTE with Cell DTX, in: 2011 IEEE 73rd Vehicular Technology Conference (VTC Spring), 2011, pp. 1–5.

[32] S. Sodagari, A secure radio environment map database to share spectrum, IEEE J. Sel. Top. Sign. Proces. 9 (7) (2015) 1298–1305.

[33] A. Kliks, P. Kryszkiewicz, A. Umbert, J. PéRez-Romero, F. Casadevall, L. Kułacz, Application of radio environment maps for dynamic broadband access in TV bands in urban areas, IEEE Access 5 (2017) 19842–19863.

[34] M. Fortunato, J. Critchley-Marrows, M. Siutkowska, M.L. Ivanovici, E. Benedetti, W. Roberts, Enabling high accuracy dynamic applications in urban environments using PPP and RTK on android multi-frequency and multi-GNSS smartphones, in: 2019 European Navigation Conference, ENC, 2019, pp. 1–9.

[35] D. Huttenlocher, G.A. Klanderman, W.J. Rucklidge, Comparing images using the hausdorff distance, IEEE Trans. Pattern Anal. Mach. Intell. 15 (9) (1993) 850–863, http://dx.doi.org/10.1109/34.232073.

[36] K. Sim, M. Nia, C. Tso, T. Kho, Chapter 34 - brain ventricle detection using hausdorff distance, in: Q.N. Tran, H.R. Arabnia (Eds.), Emerging Trends in Applications and Infrastructures for Computational Biology, Bioinformatics, and Systems Biology, in: Emerging Trends in Computer Science and Applied Computing, Morgan Kaufmann, Boston, 2016, pp. 523–531, http://dx.doi.org/10.1016/B978-0-12-804203-8.00034-1, http://www.sciencedirect.com/science/article/pii/B9780128042038000341.

[37] S. Whiteson, Reinforcement learning, in: Adaptive Representations for Reinforcement Learning, Springer Berlin Heidelberg, Berlin, Heidelberg, 2010, pp. 7–15.

[38] S. Tombaz, K.W. Sung, J. Zander, On metrics and models for energy-efficient design of wireless access networks, IEEE Wirel. Commun. Lett. 3 (6) (2014) 649–652.

[39] A. Tijsma, M.M. Drugan, M.A. Wiering, Comparing exploration strategies for Q-learning in random stochastic mazes, in: 2016 IEEE Symposium Series on Computational Intelligence (SSCI), 2016, pp. 1–8.

[40] T. Yoo, A. Goldsmith, On the optimality of multiantenna broadcast scheduling using zero-forcing beamforming, IEEE J. Sel. Areas Commun. 24 (3) (2006) 528–541.

[41] B. Bossy, P. Kryszkiewicz, H. Bogucka, Optimization of energy efficiency in the downlink LTE transmission, in: 2017 IEEE International Conference on Communications, ICC, 2017, pp. 1–6.

[42] Z. Hanzaz, H.D. Schotten, Performance evaluation of Link to system interface for long term evolution system, in: 2011 7th International Wireless Communications and Mobile Computing Conference, 2011, pp. 2168–2173.

[43] S. Zhang, A. Doufexi, A. Nix, Evaluating realistic performance gains of massive multi-user MIMO system in urban city deployments, in: 2016 23rd International Conference on Telecommunications, ICT, 2016, pp. 1–6.

[44] A. Serra Pagès, J. Olmos, M. Lema, Modelling channel estimation error in LTE link level simulations, 2012, IC1004 TD(12)03067.

[45] L. Chiaraviglio, P. Wiatr, P. Monti, J. Chen, J. Lorincz, F. Idzikowski, M. Listanti, L. Wosinska, Is green networking beneficial in terms of device lifetime? IEEE Commun. Mag. 53 (5) (2015) 232–240, http://dx.doi.org/10.1109/MCOM.2015.7105670.

## 7.7 Publication [P7]

M. Hoffmann, A. Kliks, P. Kryszkiewicz, and G. P. Koudouridis, "A Reinforcement Learning Approach for Base Station On/Off Switching in Heterogeneous M-MIMO Networks," in *2020 IEEE 21st International Symposium on "A World of Wireless, Mobile and Multimedia Networks" (WoWMoM)*, pp. 170–172, 2020.

MNiSW Points: 140

Number of citations:

- according to Web of Science: 6
- according to Google Scholar: 7

mgr inż. Marcin Hoffmann
Instytut Radiokomunikacji, Politechnika Poznańska
ul. Polanka 3, 60-965 Poznań

Poznań, 10 kwietnia 2021 r.

# OŚWIADCZENIE W SPRAWIE AUTORSTWA PRACY

Oświadczam, że w pracy:

*M. Hoffmann, A. Kliks, P. Kryszkiewicz, G. P. Koudouridis, "A Reinforcement Learning Approach for Base Station On/Off Switching in Heterogeneous M-MIMO Networks," IEEE International Symposium on "A World of Wireless, Mobile and Multimedia Networks" (WoWMoM), Cork, Irlandia, 31 sierpnia- 3 września 2020r.*

mój udział polegał na:

- Opracowaniu koncepcji wykorzystania uczenia ze wzmocnieniem i mapy środowiska radiowego do poprawy efektywności energetycznej sieci M-MIMO
- Implementacji oraz integracji zaproponowanych algorytmów z symulatorem
- Przeprowadzeniu eksperymentów symulacyjnych
- Przygotowaniu w całości pierwszej wersji tekstu artykułu

Mój procentowy udział w powstanie pracy szacuję na: 70%

.....

Podpis

dr hab. inż. Paweł Kryszkiewicz, prof. PP
Instytut Radiokomunikacji, Politechnika Poznańska
ul. Polanka 3, 60-965 Poznań

Poznań, 21 sierpnia 2025 r.

# OŚWIADCZENIE W SPRAWIE AUTORSTWA PRACY

Oświadczam, że w pracy:

*M. Hoffmann, A. Kliks, P. Kryszkiewicz, G. P. Koudouridis, "A Reinforcement Learning Approach for Base Station On/Off Switching in Heterogeneous M-MIMO Networks," IEEE International Symposium on "A World of Wireless, Mobile and Multimedia Networks" (WoWMoM), Cork, Irlandia, 31 sierpnia- 3 września 2020r.*

mój udział polegał na:

- Koordynacji prac badawczych
- Dyskusji z pierwszym autorem napotkanych problemów w tym: metod reprezentacji uzyskanej wiedzy powstałej w procesie uczenia maszynowego w geolokacyjnej bazie danych
- Dyskusji ze współautorami uzyskanych wyników i metod ich prezentacji/porównania
- Strukturyzacji artykułu
- Iteracyjnym nanoszeniu poprawek na tekst; dyskusji uwag ze współautorami

Mój procentowy udział w powstanie pracy szacuję na: 15%

Podpis

Dr hab. inż. Adrian Kliks, prof. PP
Instytut Radiokomunikacji, Politechnika Poznańska
ul. Polanka 3, 60-965 Poznań

Poznań, 10 kwietnia 2021 r.

# OŚWIADCZENIE W SPRAWIE AUTORSTWA PRACY

Oświadczam, że w pracy:

*M. Hoffmann, A. Kliks, P. Kryszkiewicz, G. P. Koudouridis, "A Reinforcement Learning Approach for Base Station On/Off Switching in Heterogeneous M-MIMO Networks," IEEE International Symposium on "A World of Wireless, Mobile and Multimedia Networks" (WoWMoM), Cork, Irlandia, 31 sierpnia- 3 września 2020r.*

mój udział polegał na:

- Uczestniczeniu w dyskusjach naukowych dotyczących rozwiązania problemu włączania i wyłączania stacji bazowych, w tym na propozycji zastosowania wybranych metod uczenia maszynowego
- Sprawdzeniu parokrotnym tekstu publikacji przed jej wysłaniem.

Mój procentowy udział w powstanie pracy szacuję na: 10%

Adrian Kliks

Podpis

Georgios P. Koudouridis, PhD
Huawei Technologies,
164 40 Stockholm,
Sweden

Stockholm, 13th of April 2021

# AUTHORSHIP AND ENGAGEMENT DECLARATION

Hereby, I declare that regarding the publication underneath:

> *M. Hoffmann, A. Kliks, P. Kryszkiewicz and G. P. Koudouridis, "A Reinforcement Learning Approach for Base Station On/Off Switching in Heterogeneous M-MIMO Networks," IEEE International Symposium on "A World of Wireless, Mobile and Multimedia Networks" (WoWMoM), Cork, Ireland, 31st August- 3rd September 2020,*

my contribution was the following:

- Discussing the research work objectives and the material, and quality reviewing/writing text of the overall article.

I assess my contribution to this paper to be around 5%.

With kind regards,

signature

2020 IEEE 21st International Symposium on "A World of Wireless, Mobile and Multimedia Networks" (WoWMoM)

# Poster: A Reinforcement Learning Approach for Base Station On/Off Switching in Heterogeneous M-MIMO Networks

Marcin Hoffmann*, Adrian Kliks*, Paweł Kryszkiewicz*, and Georgios P. Koudouridis†
*Institute of Radiocommunications, Poznań University of Technology, Poznań, Poland
†Wireless Systems Lab., Huawei Technologies, Stockholm, Sweden
marcin.ro.hoffmann@doctorate.put.poznan.pl, adrian.kliks@put.poznan.pl,
pawel.kryszkiewicz@put.poznan.pl, George.Koudouridis@huawei.com

***Abstract*—The introduction of large antenna arrays facilitating massive multiple-input-multiple output (M-MIMO), and the addition of a tier of pico and femto base stations (BS), implementing an heterogeneous network, provides means to improve network throughput and capacity in 5G networks. However, the addition of antennas and BSs implies additional hardware and is associated with higher energy consumption. Improving the energy efficiency (EE) while reducing the power consumption of such heterogeneous M-MIMO dense networks can be performed by switching off base stations that have few users to serve and redistribute those users among the active neighboring base stations. One promising solution to intelligently map user spatial distribution to the optimal set of active BSs is by utilizing radio service maps (RSM). In this paper we propose a novel approach that effectively switches off base stations by combining reinforcement learning with RSM data. The proposed approach is evaluated through computer simulations using a 3D ray tracing model. The simulation results show the benefits of RSM and machine learning use for the improvements in EE of the considered heterogeneous M-MIMO networks.**

***Index Terms*—massive MIMO, heterogeneous networks, energy efficiency, machine learning**

## I. Introduction

Massive Multiple Input Multiple Output technique is considered as one of the technical enablers in achieving high throughput in 5G networks and beyond. It assumes presence of the massive antenna arrays in the base stations (BSs), i.e., exploiting the number of antenna elements much greater than one [1]. This allows for precise delivery of location-dependent services due to the great possibility of forming very narrow beams. In addition, M-MIMO can be combined with the heterogeneous networks concept, i.e., deployment of M-MIMO pico or femto BSs [2]. Although large antenna arrays utilized in M-MIMO greatly improve the spectral efficiency of a mobile network, they are associated with high energy consumption due to computationally intensive signal processing and additional hardware, e.g., modulators, filters, etc. [3].

This work was supported by Huawei Technologies, Sweden, and by the Polish Ministry of Science and Higher Education subvention within the task "Cognitive and sustainable communication systems" in 2020.

In this context, reducing the power consumption seems to be one of major research problems when dense M-MIMO networks are deployed. Vast literature on energy saving in cellular heterogenous networks offers various solutions to this problem [4], [5]. Some algorithms switch off BSs on the basis of the number of user equipment's (UE) being in their coverage area, while others are taking into the account various traffic load metrics. There is also a solution utilizing Reinforcement Learning (RL), but it is not considering M-MIMO neither 3D ray tracing channel model [6]. The channel model reflects only the pathloss.

This paper aims at showing how location-dependent information being stored, acquired and processed by the so called Radio Service Map (RSM) can be used to determine an optimal set of candidate active BSs for a specific UE positions pattern. The selection of BSs that are switched off in order to improve energy efficiency (EE) and reduce energy consumption is performed by means of machine learning based on a Reinforcement Learning (RL) scheme. The proposed approach is evaluated by means of advanced simulations for a heterogeneous M-MIMO network setup, utilizing accurate 3D ray tracing radio channel model.

## II. Radio Service Map

The concept of RSM is to provide a network with a mechanism to acquire, store and process relevant context information [7]. In general, an RSM entry consists of a measured value, such as the received signal strength, along with the location of the measured value [8]. RSM can contain various types of context information, e.g., radio data, UEs velocity data, traffic load data. The acquired data is processed and distributed with the aim to improve the network performance.

In this paper RSM will be used for pico BSs switching on/off, with the aim to provide an EE improvement under QoS constraints. RSM designed for this application contains the information about the network performance metrics over different UE spatial distributions, and active BS sets. A proposed structure of the RSM storage database is depicted in Fig. 1. Each RSM entry is labeled with UE coordinates set, and network performance metrics related to all possible active BS

978-1-7281-7374-0/20/$31.00 ©2020 IEEE
DOI 10.1109/WoWMoM49955.2020.00038

sets. UE coordinates are rounded to a grid of a 2 m resolution. In our case the metrics are the cell-edge (10th percentile), and median UE bitrates, the average system EE and the number of UEs being out of the network coverage. The RSM is claimed to acquire necessary data from the macro BS.

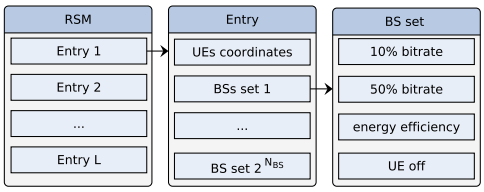


Fig. 1. Proposed RSM data structure.

## III. Reinforcement Learning Scheme

In RL a so-called agent interacts with the observed environment at discrete time intervals. The agent receives states from the environment and takes actions according to its policy. The environment responds with a so-called reward [9].

In our application, an environment state $s$ is defined as the vector of UEs positions rounded to a 2 m grid. To measure the similarity between the current set of UE coordinates and the RSM entries, the algorithm utilizes the Haussdorf distance, i.e., the longest of distances between a point from one data set and the closest point from another data set [10]. The agent is the RSM manager, who takes actions on the basis of the data from the RSM. The action $i$ is defined as the set of active BSs. Usually environment responds with a single reward value, however in this case the proposed reward is defined by the bit-rate for the worst 10% of the users $r_{10}(s,i)$, the median user bit-rate $r_{50}(s,i)$, the average system EE $EE(s,i)$, and the number of UEs being out of the network range $ue_{\text{off}}(s,i)$. The objective of the agent is to maximize EE defined by:

$$EE(s,i) = \frac{r_{\text{avg}}(s,i)}{P_{\text{avg}}(s,i)}, \tag{1}$$

where $r_{\text{avg}}(s,i)$ is the average system bitrate, and $P_{\text{avg}}(s,i)$ is the average BSs consumed power computed with the model described in [1]. However there are some additional QoS constraints:

$$\begin{aligned} r_{10}(s,i) &\geq k \cdot r_{10}(s,\text{ref}), \\ r_{50}(s,i) &\geq k \cdot r_{50}(s,\text{ref}), \\ ue_{\text{off}}(s,i) &\leq ue_{\text{off}}(s,\text{ref}), \end{aligned} \tag{2}$$

where $k \in [0;1]$ is an arbitrary constant, and ref stands for the set with all BSs active. These guarantee that the throughput of cell-edge users (10th percentile) and median users is not deteriorated significantly. Moreover, the number of connected UEs cannot be lower than in the reference scenario.

In the considered RL scheme it is easy to notice that the set of active BSs is independent from UE positions. This allows to simplify full RL problem to the so called *Associative Search*, where every state is treated independently [9]. For each system state $s$ (UEs positions) the action $i$ (set of active BS) can be chosen independently maximizing overall reward.

If the actual state of the environment $s$ observed by the agent is new, then all BSs are set to be active, so as to gain reference results. Otherwise, the algorithm can either explore random active BSs set, with a probability of 1-$\epsilon$, or exploit the BSs set providing the highest EE under (2) constraints, with a probability of $\epsilon$. This approach is well known as the $\epsilon$-greedy strategy [9]. During the first visits in the given state, the algorithm is focused on exploration, while later on it performs actions on the basis of the obtained knowledge. To ensure this the following heuristic formula is used for obtaining the exploitation probability $\epsilon$, given by:

$$\epsilon = \frac{1}{\sqrt[3]{n(s)}}, \tag{3}$$

where $n(s)$ stands for the number of past visits at the environment state $s$.

## IV. Illustrative Simulation Results

The BS switching algorithm proposed in Sec. III, is evaluated and compared against SWitching-on/off based Energy Saving (SWES) algorithm [5] based on simulations using a 3D ray tracing channel model. SWES algorithm, originally proposed for LTE system switches off BSs on the basis of their mobile traffic load. It is based on the analytical heuristics utilizing neither machine learning nor databases.

The simulation scenario considers a M-MIMO heterogeneous network consisting of a single macro BS (mBS) equipped with a 128-element antenna array, and five pico BSs (pBSs) equipped with 32-element antenna arrays. The BSs locations (bigger dots) are depicted in Fig. 2, including initial UE positions (smaller dots). There are 60 UEs moving with the speed of 1.5 m/s. It should be noticed that mBS is not considered for switching off.

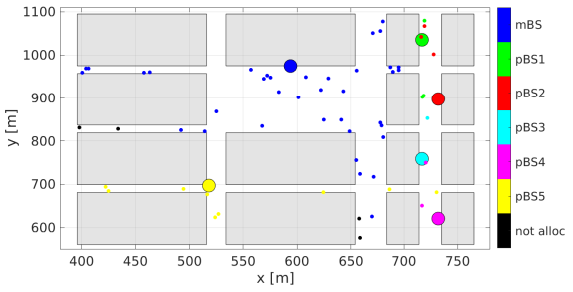


Fig. 2. BS deployment and initial UE positions

All of the BSs radiate fixed amount of power: mBS 46, and pBS 30 dBm respectively. Each UE follows *full buffer* traffic model, that results in the highest network load. This implies some changes in the SWES algorithm. Instead of switching off BSs on the basis of traffic load metrics, the BSs are switched off so as to minimize power consumption under QoS constraints (2). The utilized simulation environment is a full

OFDM-based system level simulator utilizing M-MIMO with the Regularized Zero Forcing (RZF) precoder, Dynamic Point Selection and 15 Modulation and Coding Schemes (MCS).

Radio channel coefficients are generated using a realistic 3D ray tracing model. This process is computationally complex and lasts relatively long, i.e., it takes $\sim 5$ minutes to generate a single channel realization. Following that fact simulation is performed in 60-ms time blocks. The statistics obtained during first 10 ms in each block are discarded from the final results. After each block the simulation time is shifted by 1 s to enforce visible differences in the UE positions and reduce the required simulation time. Four time blocks are considered. In order to allow RSM to learn, the simulation was run 120 times, repeating the UEs move pattern.

Fig. 3 illustrates the increase of system EE as the number of iterations of the learning process increases. At the beginning more effort is put into exploration, resulting in lower performance. In some of the cases EE is high, however, QoS constraints (2), are not fulfilled, requiring a given BS pattern to be abandoned. A short term abuse of the constraints is possible, allowing the system to obtain realistic performance statistics, that is possible only when a given BS pattern is tested. After some visits in the particular environment states, RSM contains some knowledge that can be exploited. This results in up to 44%, and 30% EE improvement over the scenario without BSs switching off for the proposed RSM-based method and SWES algorithm, respectively.

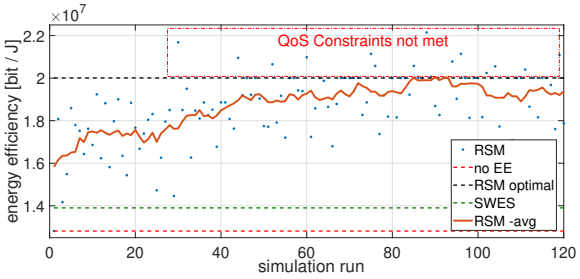


Fig. 3. Achievable EE in consecutive simulation runs. *RSM -avg* refers to the smoothing *RSM* results with the use of a 10-sample moving average.

Cumulative Distribution Function (CDF) of UE achievable bitrates together with an average consumed power for each BS is shown in Fig. 4 considering the best active BSs set obtained by RL and stored in the RSM, SWES algorithm, and a scenario without BSs switching. While the proposed RSM-based algorithm provides gain both for 10th percentile and median UE rate over both compared approaches, the average BSs power consumption is reduced approx. 15%, and 10% in relation to the scenario without BSs switching, and SWES algorithm, respectively.

## V. Conclusions

In this paper utilization of RSM is proposed for the improvement of heterogeneous M-MIMO network EE. An RL scheme is proposed to find the optimal set of BSs to be

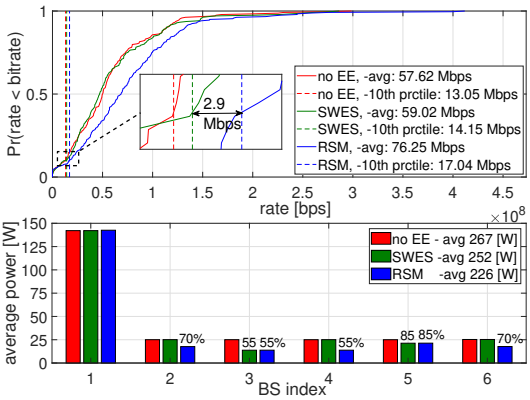


Fig. 4. Cumulative Distribution Function (CDF) of UE achievable bitrates, and power consumed by BSs.

deactivated. The gathered knowledge is stored in the RSM. The illustrative results show that the proposed solution can significantly improve the achievable EE in the system, by both power reduction and bitrate increase.

In the future, the proposed algorithm will be studied more comprehensively, including longer simulations or different UE motion scenarios. Also more complex exploration algorithms can be implemented instead of an $\epsilon$-greedy, e.g., so called Upper Confidence Bound (UCB), or based on genetic algorithms.

## References


[1] E. Björnson, J. Hoydis, and L. Sanguinetti, "Massive MIMO Networks: Spectral, Energy, and Hardware Efficiency," *Foundations and Trends® in Signal Processing*, vol. 11, no. 3-4, pp. 154–655, 2017. [Online]. Available: http://dx.doi.org/10.1561/2000000093

[2] K. N. R. S. V. Prasad, E. Hossain, and V. K. Bhargava, "Energy Efficiency in Massive MIMO-Based 5G Networks: Opportunities and Challenges," *IEEE Wireless Communications*, vol. 24, no. 3, pp. 86–94, June 2017.

[3] E. G. Larsson, O. Edfors, F. Tufvesson, and T. L. Marzetta, "Massive MIMO for next generation wireless systems," *IEEE Communications Magazine*, vol. 52, no. 2, pp. 186–195, February 2014.

[4] F. Han, S. Zhao, L. Zhang, and J. Wu, "Survey of strategies for switching off base stations in heterogeneous networks for greener 5g systems," *IEEE Access*, vol. 4, pp. 4959–4973, 2016.

[5] E. Oh, K. Son, and B. Krishnamachari, "Dynamic base station switching-on/off strategies for green cellular networks," *IEEE Transactions on Wireless Communications*, vol. 12, no. 5, pp. 2126–2136, May 2013.

[6] S. Sharma, S. J. Darak, and A. Srivastava, "Transfer reinforcement learning based framework for energy savings in cellular base station network," in *2019 URSI Asia-Pacific Radio Science Conference (AP-RASC)*, March 2019, pp. 1–4.

[7] P. Tengkvist, G. P. Koudouridis, C. Qvarfordt, M. Dryjanski, and M. Cellier, "Multi-dimensional radio service maps for position-based self-organized networks," in *2017 IEEE 22nd International Workshop on Computer Aided Modeling and Design of Communication Links and Networks (CAMAD)*, June 2017, pp. 1–6.

[8] J. Perez-Romero, A. Zalonis, L. Boukhatem, A. Kliks, K. Koutlia, N. Dimitriou, and R. Kurda, "On the use of radio environment maps for interference management in heterogeneous networks," *IEEE Communications Magazine*, vol. 53, no. 8, pp. 184–191, August 2015.

[9] R. S. Sutton and A. G. Barto, *Reinforcement Learning: An Introduction*. Cambridge, MA, USA: A Bradford Book, 2018.

[10] D. P. Huttenlocher, G. A. Klanderman, and W. J. Rucklidge, "Comparing images using the Hausdorff distance," *IEEE Transactions on Pattern Analysis and Machine Intelligence*, vol. 15, no. 9, pp. 850–863, Sep. 1993.

## 7.8 Publication [P8]

M. Hoffmann and P. Kryszkiewicz, "Similarity Measures for Location- Dependent MMIMO, 5G Base Stations On/Off Switching Using Radio Environment Map," in *2021 IEEE 22nd International Symposium on a World of Wireless, Mobile and Multimedia Networks (WoWMoM)*, pp. 286–291, 2021.

MNiSW Points: 140

mgr inż. Marcin Hoffmann
Instytut Radiokomunikacji, Politechnika Poznańska
ul. Polanka 3, 60-965 Poznań

Poznań, 20 maja 2022 r.

# OŚWIADCZENIE W SPRAWIE AUTORSTWA PRACY

Oświadczam, że w pracy:

*M. Hoffmann, P. Kryszkiewicz "Similarity Measures for Location-Dependent MMIMO, 5G Base Stations On/Off Switching Using Radio Environment Map", IEEE International Symposium on a World of Wireless, Mobile and Multimedia Networks, IEEE WOWMOM, Piza, Włochy, czerwiec 2021*

mój udział polegał na:

- Rozszerzeniu zaproponowanego we wcześniejszych pracach rozwiązania polegającego na inteligentnym włączaniu/wyłączaniu stacji bazowych w celu zwiększenie efektywności energetycznej sieci MMIMO, o niezbadane dotąd metryki odległości pomiędzy zbiorami położeń użytkowników.
- Przeprowadzeniu symulacji komputerowych.
- Zebraniu i analizie wyników eksperymentów symulacyjnych.
- Przygotowaniu pierwszej wersji artykułu.

Mój procentowy udział w powstanie pracy szacuję na: 80%

Marcin Hoffmann

Podpis

dr hab. inż. Paweł Kryszkiewicz, prof. PP
Instytut Radiokomunikacji, Politechnika Poznańska
ul. Polanka 3, 60-965 Poznań

Poznań, 21 sierpnia 2025 r.

# OŚWIADCZENIE W SPRAWIE AUTORSTWA PRACY

Oświadczam, że w pracy:

*M. Hoffmann, P. Kryszkiewicz "Similarity Measures for Location-Dependent MMIMO, 5G Base Stations On/Off Switching Using Radio Environment Map", IEEE International Symposium on a World of Wireless, Mobile and Multimedia Networks, IEEE WOWMOM, Piza, Włochy, czerwiec 2021*

mój udział polegał na:

- Koordynacji prac badawczych
- Propozycji problemu badawczego i dyskusji z pierwszym autorem uzyskanych wyników i napotkanych problemów
- Sugestii metod prezentacji wyników i porównania metod.
- Strukturyzacji artykułu
- Iteracyjnym nanoszeniu poprawek na tekst; dyskusji uwag ze współautorem

Mój procentowy udział w powstanie pracy szacuję na: 20%

Podpis

2021 IEEE 22nd International Symposium on a World of Wireless, Mobile and Multimedia Networks (WoWMoM)

2021 IEEE 22nd International Symposium on a World of Wireless, Mobile and Multimedia Networks (WoWMoM) | 978-1-6654-2263-5/20/$31.00 ©2021 IEEE | DOI: 10.1109/WoWMoM51794.2021.00053

# Similarity Measures for Location-Dependent MMIMO, 5G Base Stations On/Off Switching Using Radio Environment Map

Marcin Hoffmann
*Institute of Radiocommunications*
*Poznań University of Technology*
Poznań, Poland
marcin.ro.hoffmann@doctorate.put.poznan.pl

Paweł Kryszkiewicz
*Institute of Radiocommunications*
*Poznań University of Technology*
Poznań, Poland
pawel.kryszkiewicz@put.poznan.pl

***Abstract*—The Massive Multiple-Input Multiple-Output (MMIMO) technique together with Heterogeneous Network (Het-Net) deployment enables high throughput of 5G and beyond networks. However, a high number of antennas and a high number of Base Stations (BSs) can result in significant power consumption. Previous studies have shown that the energy efficiency (EE) of such a network can be effectively increased by turning off some BSs depending on User Equipments (UEs) positions. Such mapping is obtained by using Reinforcement Learning. Its results are stored in a so-called Radio Environment Map (REM). However, in a real network, the number of UEs' positions patterns would go to infinity. This paper aims to determine how to match the current set of UEs' positions to the most similar pattern, i.e., providing the same optimal active BSs set, saved in REM. We compare several state-of-the-art distance metrics using a computer simulator: an accurate 3D-Ray-Tracing model of the radio channel and an advanced system-level simulator of MMIMO Het-Net. The results have shown that the so-called Sum of Minimums Distance provides the best matching between REM data and UEs' positions, enabling up to 56% EE improvement over the scenario without EE optimization.**

***Index Terms*—Distance Metrics, Massive MIMO, Radio Environment Map, Base Stations Switching, Energy Efficiency**

## I. Introduction

Key enablers for achieving high network throughput in 5G and beyond, are Massive Multiple-Input Multiple-Output (MMIMO), and Heterogeneous Network (Het-Net) design [1]. MMIMO provides throughput gain by utilizing large antenna arrays transmitting energy directly to the user equipment (UE), i.e., beamforming. Het-Net stands for the idea where an additional tier of small (e.g., pico) Base Stations (BSs) is densely deployed close to the UEs. It results in macro BS traffic being offloaded and increases network capacity. Although the deployment of both Het-Net and MMIMO can effectively reduce the transmit power in the network, it is not always enough to compensate energy consumption related to additional hardware [2]. Thus, the improvement of 5G and future 6G networks' energy efficiency (EE) is of high importance [3]. Research has shown that many of the currently deployed BSs are underutilized over long periods of time [4]. The problem would arise even more while considering the dense deployment of pico BSs. Some of those underutilized BSs can be temporally switched off without affecting UEs' Quality of Service (QoS) in order to improve network EE. There are a number of algorithms relying on standard optimization methods proposed in the literature to solve this problem [5]. However, in most cases, they suffer from simplistic modeling of a wireless network. Proper modeling is even more difficult when MMIMO is used. It is because a MMIMO network consists of several complex functional blocks including precoding, user scheduling, channel estimation, and user-to-BS assignment. As a result, the behavior of the system is hard to predict efficiently. Thus, it is more beneficial to utilize one of the machine learning approaches, e.g., Reinforcement Learning (RL). In RL, a so-called agent interacts with the network and observes the outcome, e.g., EE related to a given set of active BSs. Some algorithms utilizing RL to provide EE gains through BSs on/off switching have already been proposed [6], [7]. These RL algorithms switch BSs on/off based on bitrates reported by UEs, i.e., the state is defined as a set of UEs bitrates. Because the set of active BSs affects future UEs bitrates this implies a complex sequence of states.

However, 5G networks are expected to come with accurate localization techniques [8]. In our previous papers, we have presented the idea of utilizing RL for BSs on/off switching based on UEs' positions to improve network EE [9], [10]. We proposed to create a Radio Environment Map (REM), which provides the network with information about an optimal, in terms of EE, set of active BSs related to the current set of UEs' positions. This idea evolved from the earlier works, where REM was used, e.g., to enable opportunistic transmission in licensed frequency bands [11]. Originally an entry in REM is created as a tuple of a localization tag, and measured radio link parameter, e.g., Received Signal Strength (RSS). However,

The simulations were based on the QCM simulator from Huawei Technologies Sweden Research Center. The presented work was funded by the Polish Ministry of Science and Higher Education subvention within the task "New methods of increasing energy and spectral efficiency and localization awareness for mobile systems" in 2020.

978-1-6654-2263-5/21/$31.00 ©2021 IEEE
DOI 10.1109/WoWMoM51794.2021.00053

the idea can easily be extended to fill REM with any kind of location-dependent data that can be beneficial in terms of network performance [12]. The proposed mapping between the set of UEs' positions, and active BSs is beneficial in terms of RL application. Because an active BSs set does not affect UEs motion, EE can be optimized independently for every set of UEs' positions. Thus, the full RL problem is simplified to the so-called Contextual Bandit problem. The main focus of [9], [10] was on the learning procedure and improvement of its speed, i.e., how to design learning so that a minimal number of iterations is required to achieve optimal EE. Thus the algorithm started from an empty REM and the same UEs motion pattern was considered all the time. In a real network, the number of different UEs' positions patterns would go to infinity. As such REM has to be equipped with a similarity measure that allows merging different patterns, reducing the REM size but also improving the convergence speed.

While [9], [10] focused mainly on learning from a time perspective, this paper proposes learning optimization from a spatial perspective. Here it is assumed that REM contains some location-dependent knowledge from previous users' patterns and learning. The data in REM is tagged with a set of UEs' locations, and the research issue addressed in this paper is if a new set of UEs positions could be matched to one of the already existing REM entries, and which one should it be. This procedure aims to improve network EE, without the necessity to perform a long learning phase. Several state-of-the-art distance metrics are compared in terms of computer simulations, in order to select the one which efficiently utilizes gains from historical knowledge stored in REM. An advanced system-level simulator of a MMIMO network and a realistic 3D-Ray-Tracing radio channel model are used for this purpose. Moreover, distance metrics are evaluated with two localization methods: almost perfect Real Time Kinematics (RTK), and much less accurate standard Global Positioning System (GPS).

The paper is organized as follows: The system model is presented in Sec. II. REM and related RL procedures are described in Sec. III. The considered distance metrics are presented in Sec. IV. The results of computer simulations are discussed in Sec. V. The paper is concluded in Sec. VI.

## II. System Model

In this section, a brief description of the considered system, power modeling, and EE definition is introduced. For more details, we refer the reader to our previous paper [10].

### A. Network Architecture

In this paper, we consider a MMIMO Het-Net consisting of one Macro BS (MBS), and $N_{\mathrm{BS}} - 1$ Pico BSs (PBSs). The Het-Net is considered to be deployed under urban conditions. MBS and PBSs share a common frequency band and utilize Orthogonal Frequency Division Multiple Access (OFDMA). All BSs support MMIMO, and are equipped with $m \times n$ (columns $\times$ rows) rectangular antenna arrays, exploiting up to above a hundred antenna elements. There are $N_{\mathrm{UE}}$ UEs randomly distributed over the network, moving with speed $v$. The position of the $i$-th UE is reported by standard cellular localization techniques utilizing either RTK or a standard GPS system, as described in 3GPP TS.38.305. The coordinates of the $i$-th UE are given in Cartesian coordinates as $\mathbf{x}_i = [x_i \ y_i]$. We assume that UE can be served by the network when its RSS is above a given threshold $P_{th}$ for at least one of the BSs. The MBS is expected to manage the process of location-dependent PBSs switching on/off and is not considered for being switched off. The process of PBSs switching on/off is performed with the use of positions reported by UEs and REM data. To enable easy exchange of information, REM is expected to be deployed on the MBS. The general aim of REM-based PBSs on/off switching procedure is to improve network EE.

### B. Power Model

To assess network EE, it is crucial to know how much power this network consumes. When considering the MMIMO network, a proper power consumption model must be chosen. It is because of the significant contribution of hardware to the total amount of energy consumption in MMIMO BSs. Such a proper model was found in [13]. We decided to use three major power consumption model components [9], [10]:

- **Effective Transmitted Power (ETP)** $P_{\mathrm{ETP},b}$ being the total power $P_{\mathrm{tx},b}$ radiated by the BS $b$, and affected by amplifier efficiency $\eta$:

$$P_{\mathrm{ETP},b} = \frac{P_{\mathrm{tx},b}}{\eta}. \tag{1}$$

- **Transceiver Chains Power (TCP)** $P_{\mathrm{TC},b}$, being the power consumed by the local oscillator $P_{\mathrm{LO}}$, and hardware $P_{\hat{\mathrm{TC}}}$ related to each of BS $b$ antennas $M_b$:

$$P_{\mathrm{TC},b} = M_b \cdot P_{\hat{\mathrm{TC}}} + P_{\mathrm{LO}}. \tag{2}$$

- **Fix Power** $P_{\mathrm{fix}}$, is the constant amount of power necessary for, e.g., back-haul signaling and baseband signal processing.

By switching BSs off we mean putting them into the stand-by mode in fact. In standby mode, most of the BS hardware components are switched off in order consume only the minimal amount of power denoted as $P_{\mathrm{off}}$. BS in the standby mode can be activated almost immediately, e.g., within 30 $\mu$s [14]. The total amount of power consumed by the system is given as:

$$P_{tot} = \sum_{b=1}^{N_{\mathrm{BS}}} P_{tot,b}, \tag{3}$$

where

$$P_{tot,b} = \begin{cases} P_{\mathrm{ETP},b} + P_{\mathrm{TC},b} + P_{\mathrm{fix}}, & \text{for active BS,} \\ P_{\mathrm{off}}, & \text{for BS in stand-by mode.} \end{cases} \tag{4}$$

### C. Energy Efficiency Definitions

Among several definitions of EE proposed in the literature, the most common is that EE is the ratio between the average UE bitrate and the average power consumed by the network [15]. We propose a similar EE definition, yet using a median of UE bitrate $c_{50}$ instead of average:

$$EE = \frac{c_{50}}{P_{\text{avg}}}, \tag{5}$$

where $P_{\text{avg}}$ is the average power consumption computed according to (3). This definition of EE provides more fairness and protects UEs with poor radio conditions. The procedure of REM-based BSs on/off switching aims at the maximization of EE given as above over different sets of UEs' positions. However, there is also an additional QoS constraint. Switching off BS cannot cause disconnecting UEs from the network.

## III. Radio Environment Map & Reinforce Learning for MMIMO network EE optimization

The data stored in REM is organized in entries, and the procedure of EE optimization is performed independently within each entry. A REM entry is tagged with a set of UEs positions, i.e., $\mathcal{S}_l : \{\mathbf{x}_i\}_{i=1}^{N_{\text{UE}}}$ for the $l$-th REM entry. Instead of a single measured value, as in most state-of-the-art REM implementations, our REM entry contains information about network performance for each of $2^{N_{\text{BS}}-1}$ possible on/off configurations of PBSs. The resultant data structure of REM is depicted in Fig. 1. The presented REM data structure is designed to support RL, thus related nomenclature is used in Fig. 1, e.g., $Q(\mathcal{S}_l, \mathbf{a})$ being the so-called action value.

### A. Reinforcement Learning

The general idea of RL is that a so-called agent obtains knowledge about the environment through interaction in discrete time intervals, and observation of outcome, i.e., reward [16]. At the beginning of each interval, the RL agent recognizes the environment state, which is a set of current UEs positions $\mathcal{S}_l$. Later on, the agent interacts with the environment, i.e., it makes an action denoted as $\mathbf{a}$. In our case, action $\mathbf{a}$ represents a set of active PBSs. There are several algorithms of obtaining action $\mathbf{a}$, usually in order to balance exploration and exploitation, e.g., $\epsilon$-greedy, Upper Confidence Bound. Some of these algorithms utilize knowledge about the number of times a particular action was chosen in the past $N(\mathcal{S}_l, \mathbf{a})$, which is stored in REM. At the end of the time interval, the environment responds with a reward which is related to EE definition (5):

$$r(\mathcal{S}_l, \mathbf{a}) = \begin{cases} EE(\mathcal{S}_l, \mathbf{a}), & \text{if } N_{\text{UE}}(\mathcal{S}_l, \mathbf{a}) = N_{\text{UE}}(\mathcal{S}_l, \mathbf{1}), \\ 0, & \text{otherwise}, \end{cases} \tag{6}$$

where $N_{\text{UE}}(\mathcal{S}_l, \mathbf{a})$ denotes number of UEs connected to network under active PBS set $\mathbf{a}$, and $N_{\text{UE}}(\mathcal{S}_l, \mathbf{1})$ denotes number of UEs that would be connected to network if all PBSs were active, i.e., under action $\mathbf{1}$. Finally, reward value is utilized to update so-called action values $Q(\mathcal{S}_l, \mathbf{a})$ that are stored in REM. Action values are the measure of profitability of choosing particular action being in state $\mathcal{S}_l$, in order to maximize expected reward, i.e, EE. There are also several update rules of action values available, e.g., Q-learning [16].

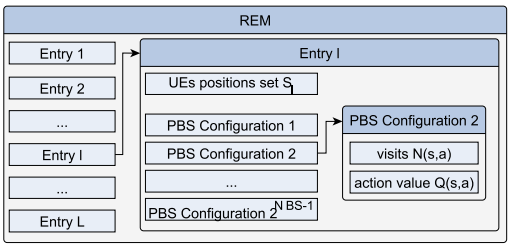


Fig. 1. Data structure in REM. While MBS is not considered for switching off, there are $2^{N_{\text{BS}}-1}$ possible active BSs sets.

### B. Utilization of REM data by RL

The procedure of REM construction with the use of RL is presented in detail in [9], [10]. In this paper, we assume that we have REM already filled with $L$ entries, i.e., for L different UEs location patterns the learning was already performed. The current set of UEs positions is denoted as $\mathcal{S}_{\tilde{l}}$. Our target is to specify such a distance metric that finds a REM entry characterized by a set of UEs positions $\mathcal{S}_l$ most similar (in the sense of the optimal set of active PBSs) to $\mathcal{S}_{\tilde{l}}$:

$$\hat{l} = \arg\min_{l} d_f(\mathcal{S}_l, \mathcal{S}_{\tilde{l}}), \tag{7}$$

where $d_f(\mathcal{S}_l, \mathcal{S}_{\tilde{l}})$ denotes the distance between $\mathcal{S}_l$ and $\mathcal{S}_{\tilde{l}}$ computed according to metric $f$. After obtaining the most similar REM entry $\hat{l}$, first, a procedure of Action Space Reduction (ASR) is launched, aiming at the rejection of all PBSs configurations that result in serving fewer UEs, than a configuration with all PBSs turned on [10]. The remaining PBSs configurations formulate action space $\tilde{\mathcal{A}}$. Finally, a greedy action is selected:

$$\mathbf{a}_t = \arg\max_{\mathbf{a} \in \tilde{\mathcal{A}}} Q(\mathcal{S}_{\tilde{l}}, \mathbf{a}) \tag{8}$$

## IV. Distance Metrics

It is expected that the result of (7) highly depends on the chosen distance metric $d_f(\cdot, \cdot)$. During our previous studies, we have arbitrarily chosen the Hausdorff Distance for this purpose. However, the Hausdorff Distance is reported as very sensitive to changes in a single UE position, even when the overall structure in the set of UEs' positions remains very similar [17]. Fortunately, there are several other metrics proposed in the literature [18]. We decided to compare four distance metrics in total, being in our opinion the most intuitive and suitable for our problem, e.g., enabling the comparison of two position sets with a different number of UEs.

### A. Hausdorff Distance

The idea of the Hausdorff Distance is that first, for each UE position $\mathbf{x}_n$ in set $\mathcal{S}_l$, a Euclidean Distance to the closest UE position $\mathbf{x}_m$ in set $\mathcal{S}_{\tilde{l}}$ is computed. Then the maximum value

of these distances is taken. Next, the procedure is repeated in reversed order, and the max of the two resultant values is taken. Mathematically, it can be defined as:

$$d_{hd}(\mathcal{S}_l, \mathcal{S}_{\bar{l}}) = \max\left[hd(\mathcal{S}_l, \mathcal{S}_{\bar{l}}), hd(\mathcal{S}_{\bar{l}}, \mathcal{S}_l)\right], \tag{9}$$

where:

$$hd(\mathcal{S}_a, \mathcal{S}_b) = \max_{\mathbf{x}_i \in \mathcal{S}_a}\{\min_{\mathbf{x}_j \in \mathcal{S}_b} \delta(\mathbf{x}_i, \mathbf{x}_j)\}, \tag{10}$$

and $\delta(\cdot,\cdot)$ denotes a Euclidean Distance between two points. From (10) it can be observed that a change in the position of a single UE can have a significant impact on the Hausdorff Distance.

### B. Mean Distance

A distance metric that can reduce the impact of a single UE on its outcome is the so-called Mean Distance. The idea is that first, a mean point is computed for each set of UEs' positions. Secondly, a Euclidean Distance is computed between these means:

$$d_{mean}(\mathcal{S}_l, \mathcal{S}_{\bar{l}}) = \delta\left(\frac{\sum_{\mathbf{x}_i \in \mathcal{S}_l} \mathbf{x}_i}{|\mathcal{S}_l|}, \frac{\sum_{\mathbf{x}_j \in \mathcal{S}_{\bar{l}}} \mathbf{x}_j}{|\mathcal{S}_{\bar{l}}|}\right) \tag{11}$$

where $|\mathcal{S}_l|$, and $|\mathcal{S}_{\bar{l}}|$ stands for the number of elements in sets $\mathcal{S}_l$, and $\mathcal{S}_{\bar{l}}$ respectively.

### C. Average Distance

A similar approach is used in a metric called Average Distance. However, first, a Euclidean Distance is computed between every pair of points. Secondly, these distances are averaged:

$$d_{avg}(\mathcal{S}_l, \mathcal{S}_{\bar{l}}) = \frac{1}{|\mathcal{S}_l||\mathcal{S}_{\bar{l}}|} \cdot \sum_{\mathbf{x}_i \in \mathcal{S}_l, \mathbf{x}_j \in \mathcal{S}_{\bar{l}}} \delta(\mathbf{x}_i, \mathbf{x}_j) \tag{12}$$

### D. Sum of Minimums Distance

The slightly different idea lies under the Sum of Minimums Distance. First, for each UE position $\mathbf{x}_n$ from set $\mathcal{S}_l$ closest position from set $\mathcal{S}_{\bar{l}}$ is found, and a related Euclidean Distance is computed. These distances are then summed. The same procedure is applied in opposite direction. The Sum of Minimums results in large distance values in relation to the remaining distance metrics considered in this paper, thus we decided to replace the sum with average. The final Sum of Minimums Formula is given by:

$$d_{som}(\mathcal{S}_l, \mathcal{S}_{\bar{l}}) = \frac{1}{2}\left(\frac{\sum_{\mathbf{x}_i \in \mathcal{S}_l} \min_{\mathbf{x}_j \in \mathcal{S}_{\bar{l}}} \delta(\mathbf{x}_i, \mathbf{x}_j)}{|\mathcal{S}_l|} + \right.$$
$$\left. + \frac{\sum_{\mathbf{x}_j \in \mathcal{S}_{\bar{l}}} \min_{\mathbf{x}_i \in \mathcal{S}_l} \delta(\mathbf{x}_j, \mathbf{x}_i)}{|\mathcal{S}_{\bar{l}}|} + \right) \tag{13}$$

This distance metric can be thought of as a balance between the effect of extreme change in a single UE position, and the general structure of UEs' positions. It is similar to the Hausdorff Distance, yet in (9) max is replaced with average here.

## V. Simulation Results

For the purpose of evaluation of the distance metrics given in the previous section, a system-level simulator of MMIMO HetNet described in Sec. II-A is implemented. The simulator is described shortly below. A more detailed description can be found in [10].

The simulation area, deployment of BSs, and one of the evaluated sets of UEs positions are depicted in Fig. 2. There

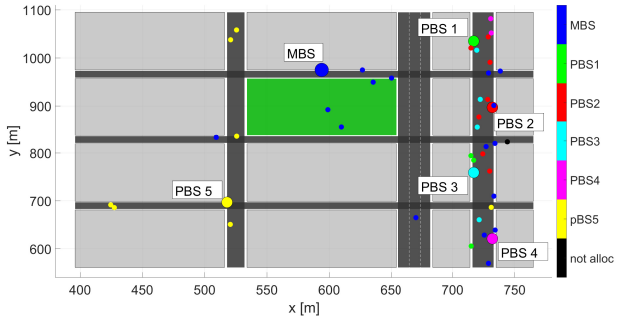


Fig. 2. Deployment of the BSs (larger dots), together with one of the evaluated set of UEs positions (smaller dots).

are 5 PBSs and a single MBS. They are equipped with full-digital antenna arrays, which is proper for advanced 5G and beyond networks [19]. The antenna array installed at MBS consists of 128 elements arranged in 16 columns, and 8 rows. Each of the PBSs is equipped with two antenna arrays of 16 elements, having 2 columns and 8 rows. These antenna arrays are pointing in opposite directions. In each set of UEs positions, there would be 40 UEs moving with the speed of 1.5 m/s in random directions.

The considered MMIMO HetNet is OFDM-based, and exploits 15 Modulation and Coding Schemes (MCSs). UEs are assigned to BSs with the use of the Dynamic Point Selection (DPS) performed every 10 ms. This procedure can be finished within a single time slot [20]. We assume that each UE is served by the BS providing the highest RSS. If RSS observed by the UE is below the required threshold $P_{th}$ to every BS, it cannot be served by the network. For every UE connected to one of the active BSs, a procedure of scheduling and precoding is performed. The scheduler is designed to provide fairness, as described in [21]. The so-called Regularized-Zero-Forcing (RZF) precoder is used to enable the simultaneous allocation of the same time-frequency resources to various UEs. The BSs always allocates all radio resources to connected UEs, i.e., data stream follows the *full-buffer* rule.

Radio channel coefficients are generated using 3D-Ray-Tracer, following the same procedure as in our previous papers. To provide significant changes in UEs' positions over the simulation period, the radio channel is generated in 15 batches lasting 60 ms, with 1 s long gaps between them. This procedure is introduced to reduce simulation time as explained in [10]. The remaining simulation parameters, including e.g., power model, are summarized in Tab. I.

TABLE I
SIMULATION PARAMETERS

| Parameter | Value |
|---|---|
| Simulation Time | 15 s |
| Time Slot Duration | 0.5 ms |
| Number of UEs $N_{\mathrm{UE}}$ | 40 |
| UEs Speed $v$ | $1.5\frac{m}{s}$ |
| Number of PBSs $N_{\mathrm{BS}}-1$ | 5 |
| Central Frequency | 3.55 GHz |
| Bandwidth | 300 MHz |
| Subcarrier Spacing | 30 kHz |
| Number of MBS Antennas | 128 ($16\times 8$) |
| Number of PBS Antennas | 32 ($2\times 2\times 8$) |
| Precoder Type | RZF |
| RSS threshold $P_{\mathrm{th}}$ | -120 dBm |
| MBS Transmitted Power $P_{\mathrm{tx,MBS}}$ | 46 dBm |
| PBS Transmitted Power $P_{\mathrm{tx,PBS}}$ | 30 dBm |
| Amplifier Efficiency $\eta$ | 0.5 [13] |
| Transceiver Chain Power $P_{\widetilde{\mathrm{TC}}}$ | 0.4 W [13] |
| Local Oscillator Power $P_{\mathrm{LO}}$ | 0.2 W [13] |
| BS Fix Power $P_{\mathrm{fix}}$ | 10 W [13] |
| BS Stand-By Power $P_{\mathrm{off}}$ | 10 W [14] |

### A. Design of the Experiment

This paper aims to compare four distance metrics, and their ability to match different sets of UEs' positions resulting in the same optimal RL action, i.e., set of active PBSs. To achieve this, we have generated a radio channel for 50 UEs. At first, a single subgroup of 40 UEs is chosen, and 30 simulation runs are performed repeating their motion pattern to learn, i.e., build REM with reliable knowledge. At this phase, UEs' positions are claimed to be accurately reported using RTK. For the REM-learning purpose, we used the ASR algorithm described in [10]. As a result of those 30 initial simulation runs, a REM of 15 entries is created. Next, 45 simulation runs were performed. Each simulation run was related to a new, random subgroup of 40 UEs out of 50 initially generated. After determination of the closest REM entry, using metrics defined in Sec. IV, a greedy action was chosen (8), i.e., the configuration of PBSs which provided the highest EE in the past. The procedure was repeated for each distance metric. We ensured distance metrics are evaluated under identical unknown sets of UEs' positions by setting a constant random generator seed. Most importantly, this procedure was designed to test REM and its metrics, not the RL scheme. The experiment was conducted for two accuracy levels of positions reported by the UEs: RTK, having the error standard deviation $\sigma = 1$ cm, and standard GPS receiver, with error standard deviation of $\sigma = 6$ m [8].

### B. Results Under RTK Localization Error

The first results were obtained under RTK localization error, which in practice stands for almost perfect localization accuracy. The distribution of average EE achieved over 45 randomly obtained sets of UEs is depicted in Fig. 3 in terms of Cumulative Distribution Function (CDF). At first, it can be observed that in all cases where historical knowledge from other sets of UEs positions stored in REM is utilized, network

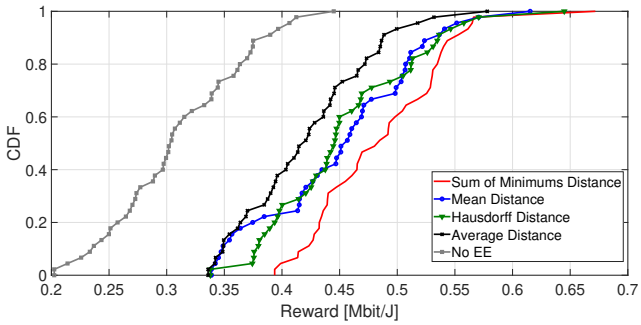


Fig. 3. CDF of average EE achieved over randomly obtained sets of UEs positions, while using RTK for as a localization technique.

EE is improved over the No EE scenario where all PBs are active. The second major observation is that Sum of Minimums Distance (13) outperforms other distance metrics. Similarly, when REM utilizes the Average Distance (12) it always provides the least EE gain. Between these two cases there are the Hausdorff Distance (9) and Mean Distance (11). They seem to perform similarly. The same hierarchy of distance metrics is visible when considering results averaged over all tested sets of UEs positions depicted in Fig. 5. A REM-based solution utilizing the Sum of Minimums Distance provides a $56\%$ improvement over a No EE scenario, while the one utilizing Average Distance gives only $36\%$.

The reason why the Sum of Minimums is the best, is because it balances sensitivity to a single UE movement and the overall structure of UEs' positions. On the other hand, Average Distance utilizes distances between every pair of UEs' positions and averages them. In this case, the result can be much affected by large distances between UEs being, e.g., on the opposite sides of the cell, yet close to other users.

### C. Results Under GPS Localization Error

A standalone GPS receiver is characterized by much poorer accuracy than RTK, i.e., standard deviation equals 6 m instead of 1 cm [8]. In Fig. 4, there is a CDF of achievable EE over 45 random sets of UEs positions, reported with Gaussian-distributed error introduced by GPS [22]. The relations between the performance of REM under different distance metrics are similar to the case utilizing RTK. However, now Mean Distance is better than Hausdorff Distance. It may be caused by the ability of Mean Distance to suppress localization error while computing the mean points of each set. At some points, it is even better than Sum of Minimums. As it could be expected, the overall performance of REM is worse as a result of a less accurate localization method. However, differences are not very big. It can be seen in Fig. 5 that in the worst case of Average Distance, average EE gains over No EE scenario obtained using GPS are equal to $32\%$ instead of $36\%$ obtained using RTK. When considering the utilization of Sum of Minimums Distance average EE gains are reduced from $56\%$ to $48\%$. Nevertheless, results show that there is still a

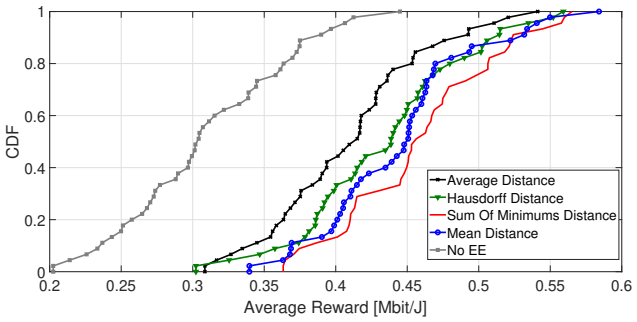


Fig. 4. CDF of average EE achieved over randomly obtained sets of UEs positions, while using GPS as a localization technique.

significant improvement in network EE while using historical knowledge from REM together with localization provided by GPS.

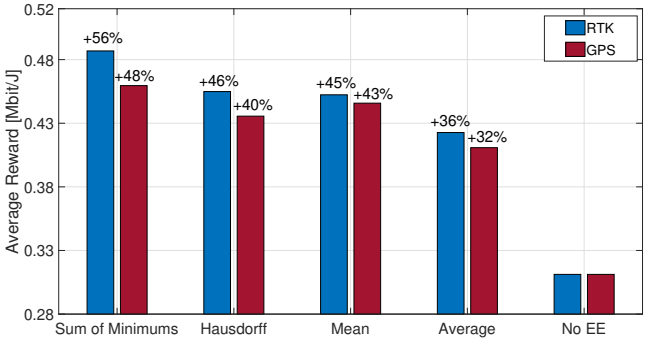


Fig. 5. EE averaged over randomly obtained sets of UEs positions, in relation to the scenario without EE optimization–no EE.

## VI. Conclusions

In this paper, we have compared 4 distance metrics in order to find out which one provides the best utilization of knowledge about the EE-maximizing set of active BSs stored in REM. The results have shown that the highest EE gains over a No EE scenario (all PBs are active) could be observed when the Sum of Minimums Distance was used. The EE is $56\%$, and $48\%$ higher than in the reference scenario while utilizing RTK and GPS as a localization technique, respectively.

## References


[1] A. Dogra, R. K. Jha, and S. Jain, "A Survey on beyond 5G network with the advent of 6G: Architecture and Emerging Technologies," *IEEE Access*, pp. 1–1, 2020.

[2] E. Björnson, L. Sanguinetti, J. Hoydis, and M. Debbah, "Optimal design of energy-efficient multi-user mimo systems: Is massive mimo the answer?" *IEEE Transactions on Wireless Communications*, vol. 14, no. 6, pp. 3059–3075, 2015.

[3] Y. L. Lee, D. Qin, L. C. Wang, and G. H. Sim, "6G Massive Radio Access Networks: Key Applications, Requirements and Challenges," *IEEE Open Journal of Vehicular Technology*, pp. 1–1, 2020.

[4] Y. Jin, N. Duffield, A. Gerber, P. Haffner, W.-L. Hsu, G. Jacobson, S. Sen, S. Venkataraman, and Z.-L. Zhang, "Characterizing Data Usage Patterns in a Large Cellular Network," in *Proceedings of the 2012 ACM SIGCOMM Workshop on Cellular Networks: Operations, Challenges, and Future Design*, ser. CellNet '12. New York, NY, USA: Association for Computing Machinery, 2012, p. 7–12. [Online]. Available: https://doi.org/10.1145/2342468.2342471

[5] F. Han, S. Zhao, L. Zhang, and J. Wu, "Survey of Strategies for Switching Off Base Stations in Heterogeneous Networks for Greener 5G Systems," *IEEE Access*, vol. 4, pp. 4959–4973, 2016.

[6] S. Sharma, S. J. Darak, and A. Srivastava, "Transfer Reinforcement Learning based Framework for Energy Savings in Cellular Base Station Network," in *2019 URSI Asia-Pacific Radio Science Conference (AP-RASC)*, 2019, pp. 1–4.

[7] N. Islam, A. Alazab, and M. Alazab, "A Reinforcement Learning Based Algorithm Towards Energy Efficient 5G Multi-Tier Network," in *2019 Cybersecurity and Cyberforensics Conference (CCC)*, 2019, pp. 96–101.

[8] M. Hoffmann, P. Kryszkiewicz, and G. Koudouridis, "Modeling of Real Time Kinematics localization error for use in 5G networks," *EURASIP Journal on Wireless Communications and Networking*, vol. 2020, 01 2020.

[9] M. Hoffmann, A. Kliks, P. Kryszkiewicz, and G. P. Koudouridis, "A Reinforcement Learning Approach for Base Station On/Off Switching in Heterogeneous M-MIMO Networks," in *2020 IEEE 21st International Symposium on "A World of Wireless, Mobile and Multimedia Networks" (WoWMoM)*, 2020, pp. 170–172.

[10] M. Hoffmann, P. Kryszkiewicz, and A. Kliks, "Increasing energy efficiency of massive-mimo network via base stations switching using reinforcement learning and radio environment maps," *Computer Communications*, 2021. [Online]. Available: http://www.sciencedirect.com/science/article/pii/S0140366421000335

[11] A. Kliks, P. Kryszkiewicz, A. Umbert, J. PéRez-Romero, F. Casadevall, and L. Kułacz, "Application of Radio Environment Maps for Dynamic Broadband Access in TV Bands in Urban Areas," *IEEE Access*, vol. 5, pp. 19 842–19 863, 2017.

[12] P. Tengkvist, G. P. Koudouridis, C. Qvarfordt, M. Dryjanski, and M. Cellier, "Multi-dimensional radio service maps for position-based self-organized networks," in *2017 IEEE 22nd International Workshop on Computer Aided Modeling and Design of Communication Links and Networks (CAMAD)*, 2017, pp. 1–6.

[13] E. Björnson, J. Hoydis, and L. Sanguinetti, "Massive MIMO networks: Spectral, energy, and hardware efficiency," *Foundations and Trends® in Signal Processing*, vol. 11, no. 3-4, pp. 154–655, 2017. [Online]. Available: http://dx.doi.org/10.1561/2000000093

[14] P. Frenger, P. Moberg, J. Malmodin, Y. Jading, and I. Godor, "Reducing Energy Consumption in LTE with Cell DTX," in *2011 IEEE 73rd Vehicular Technology Conference (VTC Spring)*, 2011, pp. 1–5.

[15] S. Tombaz, K. W. Sung, and J. Zander, "On Metrics and Models for Energy-Efficient Design of Wireless Access Networks," *IEEE Wireless Communications Letters*, vol. 3, no. 6, pp. 649–652, 2014.

[16] R. S. Sutton and A. G. Barto, *Reinforcement Learning: An Introduction*, 2nd ed. The MIT Press, 2018. [Online]. Available: http://incompleteideas.net/book/the-book-2nd.html

[17] T. Eiter and H. Mannila, "Distance measures for point sets and their computation," *Acta Informatica*, vol. 34, 02 1999.

[18] M. Sherif and A.-C. Ngonga Ngomo, "A systematic survey of point set distance measures for link discovery," *Semantic Web*, vol. 9, pp. 1–16, 11 2017.

[19] N. Rajatheva, I. Atzeni, E. Bjornson, A. Bourdoux, S. Buzzi, J.-B. Dore, S. Erkucuk, M. Fuentes, K. Guan, Y. Hu, X. Huang, J. Hulkkonen, J. M. Jornet, M. Katz, R. Nilsson, E. Panayirci, K. Rabie, N. Rajapaksha, M. Salehi, H. Sarieddeen, T. Svensson, O. Tervo, A. Tolli, Q. Wu, and W. Xu, "White Paper on Broadband Connectivity in 6G," 2020. [Online]. Available: http://hdl.handle.net/10754/662965

[20] R. Agrawal, A. Bedekar, R. Gupta, S. Kalyanasundaram, H. Kroener, and B. Natarajan, "Dynamic point selection for lte-advanced: Algorithms and performance," in *2014 IEEE Wireless Communications and Networking Conference (WCNC)*, 2014, pp. 1392–1397.

[21] Taesang Yoo and A. Goldsmith, "On the optimality of multiantenna broadcast scheduling using zero-forcing beamforming," *IEEE Journal on Selected Areas in Communications*, vol. 24, no. 3, pp. 528–541, 2006.

[22] P. Misra and P. Enge, *Global positioning system: signals, measurements, and performance*. Ganga-Jamuna Press, 2006. [Online]. Available: https://books.google.pl/books?id=pv5MAQAAIAAJ

## 7.9 Publication [P9]

M. Hoffmann and P. Kryszkiewicz, "Reinforcement Learning for Energy-Efficient 5G Massive MIMO: Intelligent Antenna Switching," *IEEE Access*, vol. 9, pp. 130329–130339, 2021.

MNiSW Points: 100

Number of citations:

- according to Web of Science: 13
- according to Google Scholar: 26

mgr inż. Marcin Hoffmann
Instytut Radiokomunikacji, Politechnika Poznańska
ul. Polanka 3, 60-965 Poznań

Poznań, 20 maja 2022 r.

# OŚWIADCZENIE W SPRAWIE AUTORSTWA PRACY

Oświadczam, że w pracy:

*M. Hoffmann, P. Kryszkiewicz, "Reinforcement Learning for Energy-Efficient 5G Massive MIMO: Intelligent Antenna Switching," IEEE Access, tom 9, str. 130329-130339, wrzesień 2021*

mój udział polegał na:

- Zaproponowaniu algorytmu inteligentnego przełączania anten bazującego na informacji o położeniu użytkowników w sieci. Algorytm składa się z dwóch etapów: etapu dobrania liczby aktywnych anten do warunków w sieci, oraz etapu wyboru podzbioru aktywnych anten spośród wszystkich znajdujących się w macierzy.
- Przeprowadzeniu symulacji komputerowych.
- Opracowaniu i analizie wyników eksperymentów symulacyjnych
- Napisaniu pierwszej wersji artykułu.

Mój procentowy udział w powstanie pracy szacuję na: 80%

Marcin Hoffmann

Podpis

dr hab. inż. Paweł Kryszkiewicz, prof. PP
Instytut Radiokomunikacji, Politechnika Poznańska
ul. Polanka 3, 60-965 Poznań

Poznań, 21 sierpnia 2025 r.

# OŚWIADCZENIE W SPRAWIE AUTORSTWA PRACY

Oświadczam, że w pracy:

*M. Hoffmann, P. Kryszkiewicz, "Reinforcement Learning for Energy-Efficient 5G Massive MIMO: Intelligent Antenna Switching," IEEE Access, tom 9, str. 130329-130339, wrzesień 2021*

mój udział polegał na:

- Koordynacji prac badawczych
- Dyskusji z pierwszym autorem struktury zaproponowanego systemu i napotkanych problemów
- Udział w implementacji środowiska symulacyjnego (np. moduł prekodowania i alokacji użytkowników)
- Dyskusji ze współautorem uzyskanych wyników i metod ich prezentacji/porównania
- Strukturyzacji artykułu
- Iteracyjnym nanoszeniu poprawek na tekst; dyskusji uwag ze współautorem

Mój procentowy udział w powstanie pracy szacuję na: 20%

Podpis

IEEE Access
Multidisciplinary ⋮ Rapid Review ⋮ Open Access Journal

Received August 23, 2021, accepted September 14, 2021, date of publication September 16, 2021,
date of current version September 28, 2021.

*Digital Object Identifier 10.1109/ACCESS.2021.3113461*

# Reinforcement Learning for Energy-Efficient 5G Massive MIMO: Intelligent Antenna Switching

**MARCIN HOFFMANN, (Graduate Student Member, IEEE), AND PAWEL KRYSZKIEWICZ, (Senior Member, IEEE)**
Institute of Radiocommunications, Poznań University of Technology, Polanka, 61-131 Poznań, Poland

Corresponding author: Marcin Hoffmann (marcin.ro.hoffmann@doctorate.put.poznan.pl)

This work was supported by the Polish Ministry of Science and Higher Education subvention within the task "New methods of increasing energy and spectral efficiency and localization awareness for mobile systems", in 2020, under Grant 0312/SBAD/8158.

**ABSTRACT** To provide users with high throughputs, the fifth generation (5G) and beyond networks are expected to utilize the Massive Multiple-Input Multiple-Output technology (MMIMO), i.e., large antenna arrays. However, additional antennas require the installation of dedicated hardware. As a result the power consumption of a 5G MMIMO network grows. This implies, e.g., higher operator costs. From this angle, the improvement of Energy Efficiency (EE) is identified as one of the key challenges for the 5G and beyond networks. EE can be improved through intelligent antenna switching, i.e., disabling some of the antennas installed at a 5G MMIMO Base Station (BS) when there are few User Equipments (UEs) within the cell area. To improve EE in this scenario we propose to utilize a sub-class of Machine Learning techniques named Reinforcement Learning (RL). Because 5G and beyond networks are expected to come with accurate UE localization, the proposed RL algorithm is based on UE location information stored in an intelligent database named a Radio Environment Map (REM). Two approaches are proposed: first EE is maximized independently for every set of UEs' positions. After that the process of learning is accelerated by exploiting similarities between data in REM, i.e., REM-Empowered Action Selection Algorithm (REASA) is proposed. The proposed RL algorithms are evaluated with the use of a realistic simulator of the 5G MMIMO network utilizing an accurate 3D-Ray-Tracing radio channel model. The utilization of RL provides about 18.5% EE gains over algorithms based on standard optimization methods. Moreover, when REASA is used the process of learning can be accomplished approximately two times faster.

**INDEX TERMS** Reinforcement learning, massive MIMO, energy efficiency, radio environment maps, 5G, machine learning, wireless communication.

## I. INTRODUCTION

Mobile network throughput can be significantly increased by the utilization of the Massive Multiple-Input Multiple-Output (MMIMO) technology [1]. The idea of MMIMO is to equip a Base Station (BS) with an antenna array of a high number of elements, i.e., much greater than 1 [2]. The large number of antenna elements allows the system to, e.g., increase the amount of the wanted signal's power being received by the User Equipment (UE). It can be achieved through proper weighting of the signal transmitted from each of the BS antennas, i.e., beamforming. However, the underlying cost of improved network throughput is reduced Energy Efficiency (EE). This phenomenon is mainly related to the increased power consumption caused by additional hardware related to each of the BS antennas [3]. As high power consumption affects network operators' costs and contributes to the world's carbon footprint, EE optimization is identified as one of the key challenges for fifth generation (5G) and beyond networks [4], [5]. There are several possibilities to improve EE of the MMIMO network. The highest gains are expected to be obtained by switching off underutilized BSs. Several algorithms have already been reported in the literature [6]. A representative example of those techniques is an algorithm that switches off a BS if its traffic can be offloaded to the neighboring cells [7]. However, some research has shown that frequent BS on/off switching can reduce the lifetime of BSs, and cause high replacement costs [8]. On the other hand,

The associate editor coordinating the review of this manuscript and approving it for publication was Miguel López-Benítez.

it has been shown that energy consumption scales nearly linearly with the number of active BS antennas, e.g., during the following studies [9], [10]. This number can be adjusted to the network state, e.g., the number of connected UEs. It has been shown that not all antennas contribute equally to the overall array gain. Therefore, a proper antenna selection algorithm should be used to obtain a subset of active antennas, to, e.g., improve EE [11]. While this problem is difficult to be fully specified and solved, because of its complexity, several heuristic metrics have been proposed to reduce its computational complexity. The simplest one is to select antennas characterized by the highest mean channel gains to all served UEs [12]–[14]. A more advanced solution additionally takes into the account spatial channel response correlations within the antenna array installed at the BS [15], [16]. Another approach is to use a channel gain-based antenna selection algorithm as an initial solution and then run a bio-inspired optimization algorithm [17]. On the other hand it has been shown that greedy algorithms can be successfully used for the purpose of antenna selection [18]. Finally antenna selection can be realized with the use of a machine learning techniques [19], [20]. However, machine learning-based antenna selection requires large training sets. Moreover learning of the models is very time-consuming when compared against e.g. channel gain-based algorithms.

The major drawback of the above mentioned papers is that they do not provide a good answer to the question: How many antennas do we need? Most of them only propose the order in which the antennas should be deactivated, i.e., an antenna selection algorithm. Though there are some papers where closed-form expressions are obtained for the number of active antennas that maximize MMIMO network EE [21]–[23]. However, the authors assume that every antenna contributes equally to the array gain, and simple Shannon formula-based throughput estimation is used. For real radio conditions, the network throughput is typically lower than a Shannon formula-based one. As a result of this inaccuracy, the obtained number of active antennas is misestimated, and the resultant EE is not optimal. One should also notice that, it is not a trivial task to use standard optimization methods to improve MMIMO network EE under real conditions. Mainly because the MMIMO system is too complex to obtain its accurate analytical model including: precoder, scheduler, intra-cell interference and realistic radio channel model.

Taking into account the limitations of the standard optimization methods, our proposal is to use machine learning for intelligent antenna switching in a complex MMIMO system. The solution is divided into two parts. First, antennas are sorted, e.g., based on their mean channel gains. Next, the optimal number of active antennas which maximize EE under a given pattern of UE positions is obtained using Reinforcement Learning (RL). The process of RL requires memory to store the results of learning, and necessary parameters. For this purpose, MMIMO BS is expected to be equipped with an intelligent database of location-dependent data known as a Radio Environment Map (REM) [24]. Although state of the art REMs were designed to store value-location tuples, we propose to map a set of all connected UE positions onto the number of active antennas. A similar representation has been used in the context of base station switching in [25]. We propose to learn how many antennas are needed through interaction with the MMIMO network, i.e., using RL. The high-level idea of RL application is that for a given set of UE positions, various numbers of active antennas would be tested, and their resultant EE would be observed, in order to learn how to act in the future. In RL there is a problem of balancing gaining new knowledge (exploration), and exploitation of the current knowledge. At first, we utilize for this purpose a state-of-the-art algorithm named Upper-Confidence-Bound [26]. Then, we show that the utilization of similarities between UE positions saved in REM, can accelerate the learning phase. It shows that a combination of RL with REM produces a synergy effect. For the evaluation purpose, an advanced system-level simulator of the MMIMO network is used, together with an accurate 3D-Ray-Tracing radio channel model. While the paper focuses on downlink transmission only, being the most important factor to obtain high EE for a given network operator, the proposed method can easily be extended for uplink transmission.

The main contributions of this paper are as follows:

- Comparison between the optimal number of active antennas indicated by an algorithm based on standard optimization methods [21], [22], [27], and the optimal number of active antennas based on the observation of EE in a realistic simulator based on a 3D-Ray-Tracing radio channel model.
- Proposal of an algorithm combining REM, and RL schemes to map the network state (specified by UE position pattern) to the number of active antennas maximizing EE.
- Exploiting the similarities between sets of UE positions saved in REM in order to accelerate the learning phase.

The paper is organized as follows: Sec. II provides the reader with an overview of the system model. In Sec. III presents an intelligent antenna switching algorithm, including a description of the antenna selection algorithm and two approaches to active antenna number computation: state-of-the-art, and REM based. The proposed RL scheme aimed at providing REM with information about the optimal number of active antennas is described in Sec. IV. In Sec. V, the results of computer simulations are presented. The paper is concluded in Sec. VI. To improve readability all acronyms are listed in Tab. 1.

## II. SYSTEM MODEL

This paper aims at maximization of EE through Intelligent Antenna Switching, while considering downlink in a single MMIMO cell. In the cell there is one BS equipped with $M$ antennas arranged in a rectangular array, and serving $K$ single-antenna UEs. The BS total transmission power does not depend on the number of active antennas, and

**TABLE 1. List of abbreviations.**

| Acronym | Full term(s) |
|---|---|
| AANCB | Active Antenna Number Computation Block |
| ASB | Antenna Selection Block |
| BS | Base Station |
| ETP | Effective Trnasmitted Power |
| EE | Energy Efficiency |
| 5G | fifth generation |
| MMIMO | Massive Multiple-Input Multiple-Output |
| MRC | Maximum Ration Combining |
| OFDMA | Orthogonal Frequency-Division Multiple Access |
| REM | Radio Environment Map |
| RTK | Real Time Kinematics |
| RL | Reinforcement Learning |
| REASA | REM-Empowered Action Selection Algorithm |
| RB | Resource Block |
| TCP | Transciever Chains Power |
| UCB | Upper Confidence Bound |
| UE | User Equipment |
| ZF | Zero-Frocing |

has a constant value of $P_{\mathrm{T}}$ for fair comparison. A downlink in the considered MMIMO cell is based on Orthogonal Frequency-Division Multiple Access (OFDMA), where the available spectrum is divided into $N_{\mathrm{rb}}$ Resource Blocks (RBs). UEs are capable to report their positions with the use of standard cellular network mechanisms. They are claimed to utilize high accuracy satellite navigation available in 5G and beyond networks, e.g., Real Time Kinematics (RTK), providing cm-level accuracy [28], [29]. Less accurate location information is expected to decrease the performance of the proposed algorithms but can be an interesting subject of future studies similar to [30]. The process of intelligent antenna switching consists of the two stages, and requires two additional functional blocks to be installed at the BS: Active Antenna Number Computation Block (AANCB) and Antenna Selection Block (ASB), as depicted in Fig. 1. AANCB is responsible for providing information about the number of active antennas $\hat{m}$ (out of all available $M$) to the MMIMO BS, e.g., on the basis of current positions of UEs. Later on, ASB selects $\hat{m}$ active antennas indicated by AANCB, according to a given selection metric. AANCB and ASB cooperate to improve EE of the considered MMIMO cell.

### A. POWER CONSUMPTION MODEL

Although there are several definitions of EE in the literature, all of them consist of the term related to the throughput and the term related to the power consumption. Thus before the problem of the EE optimization can be formulated, first, a power consumption model proper for the MMIMO BS must be defined. There are already several power consumption models proposed, for a single-antenna BS, or a MIMO BS [31], [32]. These are not adequate for MMIMO, where BSs are equipped with possibly above hundred-element antenna arrays. A popular model of MMIMO BS power consumption can be found in [2]. Similarly as in our previous work, we will consider three components having major impact on power consumption [25]:

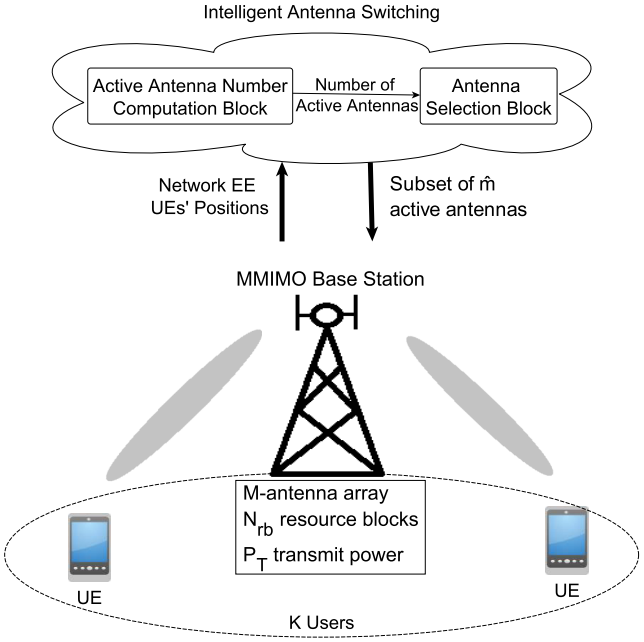


**FIGURE 1. The concept of Intelligent Antenna Switching realized by extending the MMIMO BS by Active Antenna Number Computation Block, and Antenna Selection Block.**

- **Effective Transmitted Power (ETP)** $P_{\mathrm{ETP}}$ is the total power $P_{\mathrm{T}}$ transmitted by the MMIMO BS, taking into the account the power amplifier efficiency $\eta$:

$$P_{\mathrm{ETP}} = \frac{P_{\mathrm{T}}}{\eta}. \tag{1}$$

- **Transceiver Chains Power (TCP)** $P_{\mathrm{TCP}}(m)$, is the power consumed by the local oscillator $P_{\mathrm{LO}}$, and $m$ active transceiver chains (equivalent to the number of active antennas), each of power consumption $P_{\hat{\mathrm{TCP}}}$:

$$P_{\mathrm{TCP}}(m) = m \cdot P_{\hat{\mathrm{TCP}}} + P_{\mathrm{LO}}. \tag{2}$$

- **Fixed Power** $P_{\mathrm{fix}}$, is the constant amount of power consumed by the BSs for, e.g., backbone communication or processing of signaling information.

The overall power consumption of the considered MMIMO BS is given by:

$$P_{\mathrm{tot}}(m) = P_{\mathrm{ETP}} + P_{\mathrm{TCP}}(m) + P_{\mathrm{fix}}. \tag{3}$$

### B. PROBLEM FORMULATION

Having a power consumption model proper for MMIMO BS, a definition of EE can be introduced, and optimization problem can be formulated. Several definitions of EE can be found in the literature [33]. The most commonly used is the one, where EE is given by the ratio of average network throughput, and average network power consumption. We proposed a slight modification to this definition [25]:

$$EE(\mathbf{s}, m) = \frac{c_{50}(\mathbf{s}, m)}{P_{\mathrm{tot}}(m)}, \tag{4}$$

where $\mathbf{s}$ denotes the set of UE positions, i.e., state, $m$ is the number of active antennas, $P_{\text{tot}}(m)$ is the power consumption related to $m$ active antennas, computed according to (3), and $c_{50}(\mathbf{s}, m)$ stands for the median user bitrate related to the set of UEs at positions $\mathbf{s}$, and $m$ active antennas. In the original definition of EE, users having high bitrates contribute much to the average network EE. Instead, our proposition improves the fairness by protecting users characterized by poor radio conditions. The optimization problem addressed in this paper is to maximize EE (4) independently for all visited states, i.e., sets of UE positions $\mathbf{s}$. In every state $\mathbf{s}$, the optimization is achieved by adapting the number of active antennas $\hat{m}$, so as to maximize EE (4):

$$\max_{m} EE(\mathbf{s}, m), \forall \mathbf{s} \in \mathcal{S}, \tag{5}$$

where $\mathcal{S}$ denotes a set of all considered states.

## III. INTELLIGENT ANTENNA SWITCHING ALGORITHM

To obtain the subset of active antennas we propose to extend the MMIMO BS by two additional functional blocks creating together the Intelligent Antenna Switching Algorithm, i.e., AANCB and ASB. Our aim is to split the process between AANCB deciding on the number of active antennas, and ASB, responsible for obtaining the exact subset of active antennas. The motivation behind this split is to reduce the computational complexity. Without ASB, there would be $2^M$ possible configurations of active antennas to be evaluated. With the introduction of ASB there are only $M$ possible numbers of active antennas to be selected.

### A. ANTENNA SELECTION BLOCK

The aim of ASB is to select a subset of $\hat{m}$ active antennas from all $M$ antennas installed at the MMIMO BS. This procedure is known as the antenna selection algorithm. In this paper we assumed to arbitrarily choose the antenna selection algorithm that will be used by ASB. To focus on learning REM with a proper number of active antennas, rather than the improvement of the antenna selection algorithm, a state-of-the-art solution based on average channel gains has been chosen [11]. The $\hat{m}$ antennas having the highest channel gain averaged over K users, and $N_{\text{rb}}$ RBs, have been chosen to be active. This algorithm is both intuitive and characterized by simple implementation.

### B. ACTIVE ANTENNA NUMBER COMPUTATION BLOCK

The aim of AANCB is to compute the number of active antennas that will maximize the EE of a MMIMO cell under a given set of UE positions $\mathbf{s}$. The computed number of active antennas is passed to ASB to obtain the exact subset of active antennas. Two versions of AANCB will be described: a state-of-the-art solution based on analytical computations, and a REM-based idea.

#### 1) STATE-OF-THE-ART SOLUTION

The MMIMO network EE has been optimized under the Zero-Forcing (ZF) precoding scheme [21], [22], [27], and the Maximum Ratio Combining (MRC) precoding scheme [34], [35]. The focus of this paper is on a more complex ZF precoder (see Sec. V). The number of active antennas therein is adapted to the number of users connected to MMIMO BS. While the UE position has a significant impact on wireless channel characteristics, it is not taken into account in the state-of-the-art papers. Although the authors obtained closed form expressions for the number of antennas, their simulation scenarios, EE definition and power models slightly differ from the ones presented in this paper. Thus, these expressions can't be directly implemented. Instead, we will adapt them to the considered definition of EE (4). The bitrate of the UE located at position $s$ can be calculated as a function of the number of active antennas $m$, using an approximation proper for the ZF precoder [27]:

$$\hat{c}(s, m) = B \cdot \log\left(1 + \frac{(m - K)P_{\text{T}}\beta(s)}{K\sigma^2}\right), \tag{6}$$

where $\beta(s)$ is a mean channel gain between a user located at position $s$ and the BS, averaged over all antennas and RBs, $B$ is the system bandwidth, and $\sigma^2$ is the power of the white Gaussian noise at the user's receiver. Using the above formula, a median user bitrate $\hat{c}_{50}(\mathbf{s}, m)$ can be estimated in the function of active antennas $m$:

$$\hat{c}_{50}(\mathbf{s}, m) = median\left[\{\hat{c}(s, m)\} s \in \mathbf{s}\right]. \tag{7}$$

Then, the number of active antennas $\hat{m}$ related to the set of UE positions $\mathbf{s}$ can be computed by solving:

$$\hat{m} = \arg\max_{m} \left\{\frac{\hat{c}_{50}(\mathbf{s}, m)}{P_{\text{tot}}(m)}\right\}. \tag{8}$$

Because obtaining a closed form expression of this equation is out of this paper's scope, numerical methods will be used.

#### 2) REM-BASED SOLUTION

The state-of-the-art solution assumes that only the number of UEs connected to MMIMO BS and their path losses should be taken into account while computing the number of active antennas. However, $K$ users can create various spatial patterns, resulting in different radio conditions, e.g., their channels can be more or less correlated or follow various non-Rayleigh distributions. Such properties of realistic MMIMO channels has been confirmed by measurements, e.g., [36]. Thus, we propose to optimize the number of active antennas separately within each set of UE positions. For this purpose an intelligent database called REM is employed at the MMIMO BS. The aim of REM is to store and process information related to the given set of UE positions, e.g., power consumption, bitrates, number of active antennas. As a long-term result of machine learning, REM provides MMIMO BS with information about the optimal number of active antennas, maximizing EE for a given set of UE positions.

The data stored in REM is organized in entries, as depicted in Fig. 2. Every new set of UE positions $\mathbf{s}$ creates an unique REM entry, labeled with $\mathbf{s}$. Besides the set of UE positions,

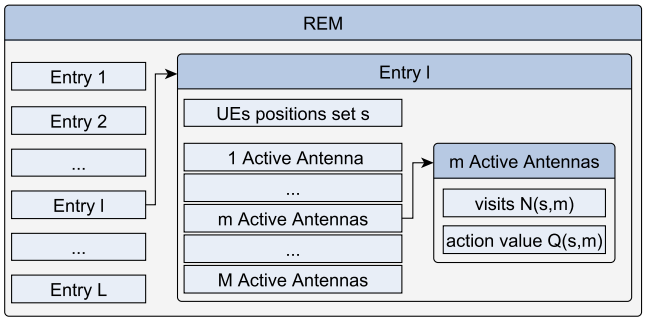


**FIGURE 2.** The structure of data stored in REM.

each REM entry contains, for each considered number of active antennas $m$, the so-called action value $Q(\mathbf{s}, m)$ used by RL, and computed on the basis of $EE(\mathbf{s}, m)$ observed previously. These variables will be described in detail in the next section. Finally, information about the number of times a particular number of active antennas has been tested $N(\mathbf{s}, m)$, is stored in each REM entry as well.

## IV. REINFORCEMENT LEARNING SCHEME

The solution proposed in this paper is to provide the network with an optimal number of active antennas, maximizing EE, separately for each set of UE positions. This information is to be stored in REM. However, REM must first get this knowledge. An effective approach to this task is to use RL, where the process of learning is based on interaction, i.e., a so called agent interacts with an environment in discrete time steps, by taking so-called actions, and observing their outcome-reward [26]. This procedure is depicted in Fig. 3 in the context of filling REM with information about the most energy efficient number of active antennas. The main elements of an RL scheme can be described as follows:

- **Environment** is a single cell in the MMIMO network equipped with $M$ antennas and serving $K$ UEs, as described in Sec. II.
- **A State s** is the set of UE positions. First, the currently reported set of UE positions is compared against REM entries. If the reported set of UE positions cannot be found in REM, a new entry is created.
- **An Action** $m$ is the considered number of active antennas, $m \in \{1, \ldots, M\}$ being the output of AANCB. The exact configuration of active antennas is obtained by ASB, as described in Sec. III-A.
- **A Reward** $r(\mathbf{s}, m)$ in this case is EE computed according to (4). The reward is obtained after an observation period called *step*, when a given action $m$ is under evaluation. The step duration has to be long enough for an average instantaneous EE metric variation caused by short-term changes in scheduling and channel coefficients.
- **An Agent** is a REM unit deployed at MMIMO BS as AANCB. It is responsible for taking actions $m$ according to the environment state $\mathbf{s}$, and updating action preferences on the basis of observed reward $r(\mathbf{s}, m)$.

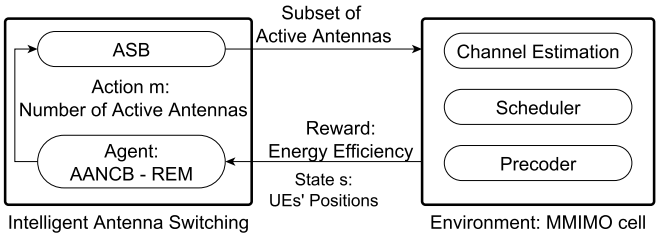


**FIGURE 3.** The RL scheme for training REM.

### A. ACTION VALUES UPDATE RULE

In REM there is information about potential EE related to each possible action $m$ (the number of active antennas) in state $\mathbf{s}$, based on previous experience. In RL it is known as an action value $Q(\mathbf{s}, m)$. Each time an agent receives a reward, the related action value is updated. In general, the action values depend both on the reward obtained after the current step and the action values of the next state. However, in the considered model the movement of UEs does not depend on the number of active antennas, i.e., the action does not affect the future state. This case is known in the literature as the problem of *Contextual Bandit* or *Associative Search* [26]. As a result it is enough to use the reward observed after performing the current action. Thus, the update rule is a simple exponential average of rewards observed after each visit in state $\mathbf{s}$ taking action $m$:

$$Q(\mathbf{s}, m) \leftarrow (1 - \alpha) \cdot Q(\mathbf{s}, m) + \alpha \cdot r(\mathbf{s}, m), \tag{9}$$

where $\alpha \in [0, 1]$ is a step size parameter.

### B. UPPER CONFIDENCE BOUND SELECTION ALGORITHM

One of the challenges related to RL is the so-called exploration-exploitation problem, i.e., the problem of how much time should an agent spend on learning the environment by taking fewer explored actions in contrast to exploiting previously obtained knowledge by taking the best known action. There are several algorithms designed to balance exploration and exploitation, e.g., $\epsilon$-greedy, soft-max distribution, Upper Confidence Bound (UCB) [37]. Due to the so-called channel hardening property of MMIMO systems, the radio signal after the procedure of precoding is almost immune to small-scale fading [38]. Thus, from the perspective of UE, achievable bitrates should be relatively stable, i.e, affected mainly by slow-varying large-scale fading. Due to that fact, we decided to utilize the UCB algorithm, because it is not utilizing randomness for action selection, i.e, the algorithm is not blindly exploring actions that are expected to result in low reward. Action selection, following UCB algorithm, is given as follows [26]:

$$\hat{m} = \arg \max_{1 \le m < M} \left\{ Q(\mathbf{s}, m) + c \cdot \sqrt{\frac{\ln \sum_{k=1}^{M} N(\mathbf{s}, k)}{N(\mathbf{s}, m)}} \right\}, \tag{10}$$

where $N(\mathbf{s}, m)$ stands for the number of times action $m$ was selected in state $\mathbf{s}$, term $\sum_{k=1}^{M} N(\mathbf{s}, k)$ is the total number of

visits in state $s$, and $c$ is an arbitrary constant. The overall idea of UCB is to promote potentially promising actions that have been rarely selected. It is achieved through the introduction of the term $c \cdot \sqrt{\frac{\ln \sum_{k=1}^{M} N(\mathbf{s},k)}{N(\mathbf{s},m)}}$ in (10). This term grows for uncertain $Q(\mathbf{s}, m)$ estimates, i.e., obtained with a low number of measurements. It is smaller for the actions that are selected often [26]. To control the balance between exploration and exploitation the constant $c$ is introduced. For a high value of $c$ algorithms tend to be more focused on exploration, while for low values of $c$, on exploitation. In the extreme case of $c = 0$, UCB becomes a greedy algorithm focused only on exploitation.

Additionally, in every state $\mathbf{s}$, the UCB algorithm is forced to take each action at least once, even when $c$ is set to zero. This behavior is called optimistic initialization [26]. It is obtained by initially setting $Q(\mathbf{s}, m)$ to very large values. After the first reward is observed the update rule is $Q(\mathbf{s}, m) \leftarrow r(\mathbf{s}, m)$ instead of (9), that is used for next rewards.

### C. REM-EMPOWERED ACTION SELECTION ALGORITHM

In the case of the UCB algorithm, the EE optimization is strictly following the *Associative Search* rule, i.e., no information about other states is used. However, it can be expected that similar sets of UE positions would result in a similar number of antennas that should be active. Such a phenomenon was observed during our previous studies, exploiting the problem of BSs switching [25]. Therein, we have taken advantage of these similarities between states (REM entries) to speed up the process of learning. Thus, in this paper we propose an approach named REM-Empowered Action Selection Algorithm (REASA) for the purpose of active antenna selection. We expect that due to utilization of the similarities between REM entries REASA can achieve the same end level of EE as in the case of UCB, but requiring less time. REASA is designed as an extension of the UCB algorithm. In the case of UCB action selection is based on one action value related to the current state, while REASA uses action values $Q(\mathbf{s}, m)$ from all states averaged proportionally to the distance to the current state. Suppose that $\{\mathbf{s}_l\}_{l=1}^{L}$ denotes states saved in REM, and $\mathbf{s}_\mathrm{i}$ is the currently reported set of UE positions. REASA is given by:

$$\hat{m} = \arg \max_{1 \le m < M} \left\{ \hat{Q}(\mathbf{s}_\mathrm{i}, m) + c \cdot \sqrt{\frac{\ln \sum_{k=1}^{M} \hat{N}(\mathbf{s}_\mathrm{i}, k)}{\hat{N}(\mathbf{s}_\mathrm{i}, m)}} \right\}, \tag{11}$$

where:

$$\hat{Q}(\mathbf{s}_\mathrm{i}, m) = \frac{Q(\mathbf{s}_\mathrm{i}, m) + \sum_{l=1, l\neq \mathrm{i}, Q(\mathbf{s}_l, m)\neq 0}^{L} \frac{Q(\mathbf{s}_l, m)}{d_h(\mathbf{s}_\mathrm{i}, \mathbf{s}_l)^\gamma}}{1 + \sum_{l=1, l\neq \mathrm{i}, Q(\mathbf{s}_l, m)\neq 0}^{L} \frac{1}{d_h(\mathbf{s}_\mathrm{i}, \mathbf{s}_l)^\gamma}}, \tag{12}$$

$$\hat{N}(\mathbf{s}_\mathrm{i}, m) = \frac{N(\mathbf{s}_\mathrm{i}, m) + \sum_{l=1, l\neq \mathrm{i}}^{L} \frac{N(\mathbf{s}_l, m)}{d_h(\mathbf{s}_\mathrm{i}, \mathbf{s}_l)^\gamma}}{1 + \sum_{l=1, l\neq \mathrm{i}}^{L} \frac{1}{d_h(\mathbf{s}_\mathrm{i}, \mathbf{s}_l)^\gamma}}, \tag{13}$$

$\gamma$ is an arbitrary constant that scales the impact of more distant REM entries on the current action selection, and $d_h(\mathbf{s}_\mathrm{i}, \mathbf{s}_l)$ is the Hausdorff Distance between $\mathbf{s}_\mathrm{i}$ and $\mathbf{s}_l$. It is computed according to [39]:

$$d_h(\mathbf{s}_\mathrm{i}, \mathbf{s}_l) = \max\{h(\mathbf{s}_\mathrm{i}, \mathbf{s}_l), h(\mathbf{s}_\mathrm{l}, \mathbf{s}_i)\}, \tag{14}$$

where:

$$h(\mathbf{s}_\mathrm{a}, \mathbf{s}_b) = \max_{\mathbf{x}_k \in \mathbf{s}_a} \{\min_{\mathbf{x}_j \in \mathbf{s}_b} \delta(\mathbf{x}_k, \mathbf{x}_j)\}, \tag{15}$$

and $\delta(\cdot, \cdot)$ denotes a Euclidean Distance between two points on the Cartesian plane: $\mathbf{x}_k$ and $\mathbf{x}_j$. Each of these points represents the coordinates of a single UE. One should note that the Hausdorff Distance is used, as it is a state-of-the-art measure of similarity between two sets of points of possibly different sizes, used e.g., for the purpose of image processing [39]. However, the performance of other distance metrics should be compared in the future, similarly to [30]. Comparing to the UCB, tuning parameters of REASA may be more challenging because there is an additional parameter: $\gamma$.

The procedure of RL-based Intelligent Antenna Switching using either UCB or REASA action selection is summarized as Algorithm 1.

**Algorithm 1** RL-Based Intelligent Antenna Selection

**Require:** Sequence of states $\mathcal{S}$
**for each:** $\mathbf{s} \in \mathcal{S}$
1: **if** $\mathbf{s}$ not in REM **then** create new entry
2: **end if**
3: obtain action $\hat{m}$ (number of active antennas) using UCB eq. (10) or REASA eq. (11)
4: increment $N(\mathbf{s}, \hat{m})$
5: select $\hat{m}$ active antennas using ASB (as described in Sec. III-A)
6: wait till new reward $r(\mathbf{s}, \hat{m})$ is obtained
7: **if** $N(\mathbf{s}, \hat{m}) == 1$ **then** $Q(\mathbf{s}, \hat{m}) \leftarrow r(\mathbf{s}, \hat{m})$
8: **else** update action value $Q(\mathbf{s}, \hat{m})$ according to eq. (9)
9: **end if**

## V. SIMULATIONS RESULTS

The algorithms aimed at increasing the EE of a MMIMO network by switching off selected antennas, are evaluated in this section. For this purpose an advanced system-level simulator of a 5G-like, OFDMA-based MMIMO cell described in Sec. II is used. The cell covers mainly a park area surrounded by approximately 45 m tall buildings, according to the *Madrid Grid Model* [40]. The simulation parameters are presented in Tab. 2. The multi-stage system-level simulator used in this manuscript includes, e.g., channel estimation using Sounding Reference Signals, user scheduling with the proportional fair rule and ZF precoding, as presented in detail in [25]. We are considering a medium range BS, of transmit power equal to 38 dBm [41]. The BS is equipped with a rectangular antenna array of 128 elements placed in 8 rows and 16 columns. The available bandwidth equals 300 MHz

**TABLE 2. Simulation Parameters.**

| Parameter | Value |
|---|---|
| Simulated Time | 15 s |
| Time Slot Duration | 0.5 ms |
| Number of UEs $N_{\mathrm{UE}}$ | 40 |
| UEs Speed $v$ | $1.5\frac{m}{s}$ |
| Central Frequency | 3.55 GHz |
| Bandwidth | 300 MHz |
| Subcarrier Spacing | 30 kHz |
| Number of RBs $N_{\mathrm{rb}}$ | 272 |
| Number of BS Antennas $M$ | 128 ($16 \times 8$) |
| Precoder Type | ZF |
| Transmitted Power $P_{\mathrm{T}}$ | 38 dBm [41] |
| Amplifier Efficiency $\eta$ | 0.5 [2] |
| Transceiver Chain Power $P_{\widehat{\mathrm{TC}}}$ | 0.4 W [2] |
| Local Oscillator Power $P_{\mathrm{LO}}$ | 0.2 W [2] |
| BS Fixed Power $P_{\mathrm{fix}}$ | 10 W [2] |

around the center frequency of 3.55 GHz. Every 0.5 ms the scheduling algorithm allocates all 272 RBs to users connected to the MMIMO BS. Resource allocation is done independently for each RB following the proportional fair rule, i.e., the ratio between potential and past bitrate [42]. Beamforming is realized with the use of the so-called Zero-Forcing (ZF) precoding, aiming at the suppression of intra-cell interference [10]. There are 7 UEs in the cell moving with the speed of 1.5 m/s. Their initial positions are drawn from a uniform distribution. The location of the BS (larger dot) together with a single realization of UEs' initial positions (smaller dots) is depicted in Fig. 4. This is a low traffic scenario, that can be observed e.g., during night time. This scenario is expected to allow for a significant number of transmission chains to be deactivated, significantly increasing EE. The coefficients of radio channels are generated with the use of a realistic 3D-Ray-Tracing model [43]. The channel model individually tracks propagation paths between the UE antenna and each of the BS's antennas. Up to two reflections of each ray are considered (to limit computational complexity), but with many scattering rays possible. To produce accurate coefficients of the radio channel, 3D-Ray-Tracer takes into account the urban scenario, including reflections from the buildings and other obstacles, e.g., randomly distributed and moving pedestrians. To mimic the radio channel estimation error, a zero-mean Gaussian-distributed random variable is added to the real channel coefficients [44].

### A. TERMINOLOGY

The process of evaluation of the EE-improving algorithms consists of performing RL for several sets of initial UE positions. For each set of initial UE's positions, these users and their movement is observed over some time period. To clarify the design of the simulation experiment the following terminology is introduced:

- **A Step** is a time period of 60 ms when one cycle of RL is performed. First, initial 10 ms are discarded from statistics as a start-up phase, allowing, e.g., the scheduler to stabilize. After these 10 ms, the state is identified and the agent takes an action (decides on the number of active antennas) using values of $Q(\mathbf{s}, m)$ and $N(\mathbf{s}, m)$ stored in REM. After the remaining 50 ms the EE of the network is reported as a reward. While the computer simulator utilizing the Ray-Tracing-based channel is highly computationally complex, after these 60 ms, a time shift of 1 s is introduced and another step begins, starting from the recognition of a new state. This allows us to observe significant changes in UEs positions in a reasonable simulation time.
- **An Episode** is a sequence of several steps with the same UE path. During every episode, the same set of states is visited. From the network perspective the UE pattern and their path being the same as at some time in the past means that a given episode repeats. To assess algorithms in terms of learning speed, the average EE obtained during consecutive episodes would be observed. After many repetitions of a single episode, the UCB algorithm should focus on exploitation. In this case the mean EE over a single episode shows the average EE over UE paths (over all visited states).
- **An Experiment** consists of a constant number of episodes. Different experiments are characterized by different initial positions of the UEs. The presented results would often be averaged over several experiments, to average simulation results over different possible positions of UEs in the cell.
- **Ref** stands for the state-of-the art algorithm determining the number of active antennas, defined in Sec. III-B1.
- **No EE** denotes a scenario, where there is no EE optimization, i.e., all $M$ antennas are active.
- **REM-UCB** denotes the algorithm of learning REM with the use of UCB described in Sec. IV-B
- **REASA** is the algorithm of learning REM, utilizing similarities between REM entries from Sec. IV-C

The dependencies between Experiment, Episode and Step, are summarized in Fig. 5.

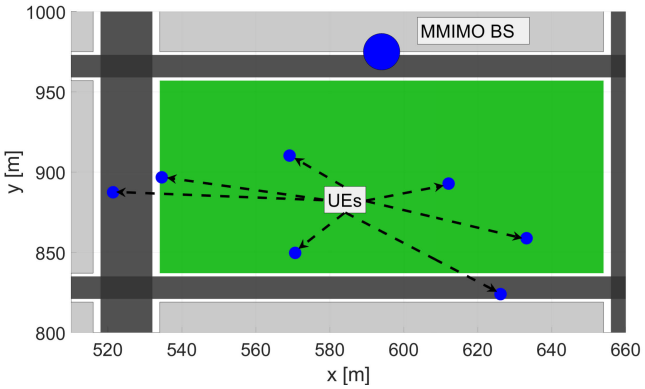


**FIGURE 4. Deployment of MMIMO BS, together with a single realization of UEs' initial positions.**

### B. HOW MANY ANTENNAS ARE NEEDED?

The aim of the first simulations is to show that the optimal number of active antennas obtained for the full system model

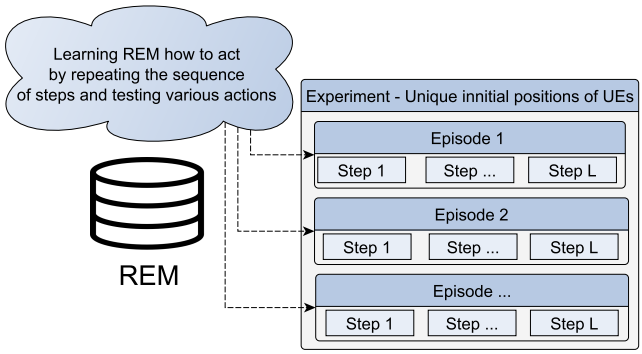


**FIGURE 5.** Diagram of dependencies between Experiments, Episodes and Steps.

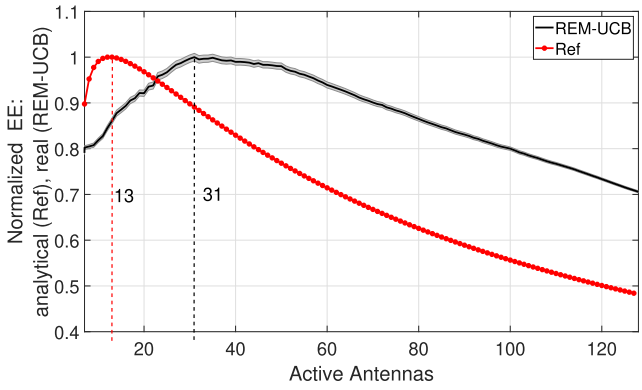


**FIGURE 6.** Comparison of normalized EE: analytical (ref), and real (REM-UCB), on the basis of 50 experiments. Shaded area around REM-UCB denotes a 95% confidence interval.

with the REM-UCB algorithm is different than obtained for simplified modeling with the Ref algorithm. For this purpose 50 experiments are conducted assuming perfect channel knowledge to make environment invariable. For such conditions, the number of episodes required to obtain knowledge about every action is equal to the number of antennas $M = 128$. Therefore, the number of episodes is set to the value of 128, making REM-UCB only to explore all possible actions, i.e., an exhaustive search is performed. Each episode consists of 1 step, i.e., 50 different random patterns of UE positions are tested. This allows us to estimate the average EE for 7 UEs randomly distributed in a cell. Fig. 6 presents the reward related to each action, averaged over all experiments, and normalized by the highest value. The red line refers to the Ref algorithm, while the black one to REM-UCB. The shaded area around REM-UCB marks the 95% confidence interval for a mean estimate. It can be seen that the Ref algorithm on average chooses a lower number of active antennas than REM-UCB, i.e., 13 against 31. It is because the Ref algorithm utilizes a simplified system model. It assumes that all antennas contribute equally to BS throughput, and that all users can be simultaneously served by the BS. In practice, due to channel correlations, some UEs cannot be served using the same time-frequency resources. Due to the antenna array geometry and correlations between antennas, they do not contribute equally to the throughput. That is why the

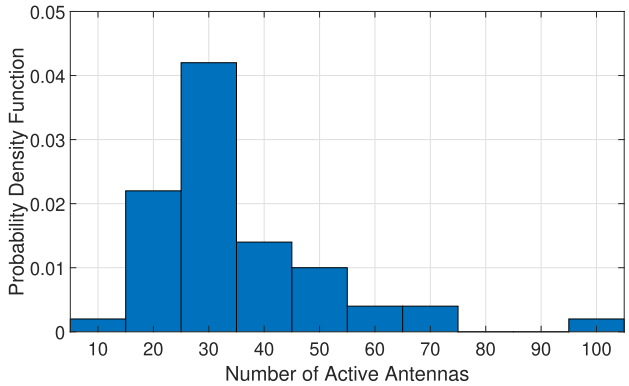


**FIGURE 7.** Probability Density Function of the optimal number of active antennas over 50 experiments obtained using the REM-UCB algorithm.

average optimal number of active antennas obtained through direct observations of EE via REM-UCB is larger. However, the results depicted in Fig. 6 are averaged over experiments related to different sets of UE positions. For each set of UE positions, a different number of active antennas can be optimal. In Fig. 7 a probability density function is shown for the optimal number of active antennas obtained for a full system model, over considered 50 experiments. It can be seen that, although the average optimal number of active antennas is around 30 (exactly 31 while considering Fig. 6), different patterns of UE positions can result in an optimal number of active antennas as low as 10, or as high as 100. This result justifies the deployment of REM, where the number of active antennas can be optimized independently for different patterns of UE positions.

### C. EVALUATION OF REM-UCB

The previous observations have shown that the number of active antennas indicated by the Ref algorithm is typically underestimated, and that the optimal number of active antennas should be adjusted to the particular pattern of UE positions. For this purpose, a REM-UCB learning algorithm is utilized. To evaluate the phase of learning, 10 experiments were conducted. Each experiment exploits 160 episodes. Because REM-UCB utilizes the so-called optimistic initialization, the Q-values have initially very big values to enforce checking each action at least once, as explained at the end of Sec. IV-B. Thus the 128 initial episodes are necessary to evaluate every possible action in each visited state once, while the remaining 32 episodes provide an evaluation of the algorithm performance under different values of $c$ parameter, after initial "exploration" is finalized. Every episode consists of 15 steps. The resultant average reward-EE obtained after each episode and averaged over experiments is depicted in Fig. 8. We can see that during the initial 128 episodes, when each possible action is tested, the reward first increases and after about 40 episodes starts to decrease. The first reason is related to the implementation, i.e., actions are tested starting from one to all active antennas over initial 128 episodes. Maximum can be observed because both having too many and not enough active antennas causes poor EE. After every

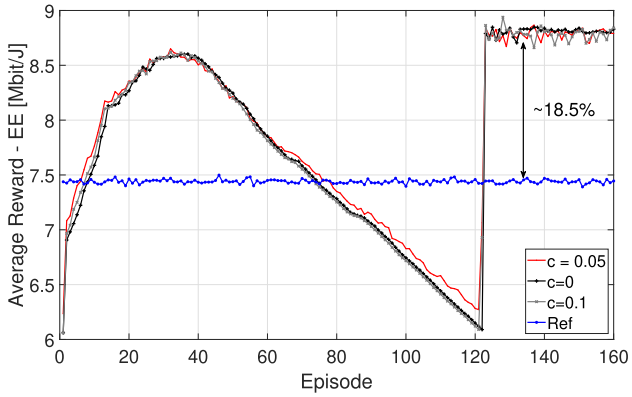


**FIGURE 8.** Average reward (EE) obtained with the use of REM-UCB, after each episode, and averaged over 10 experiments.

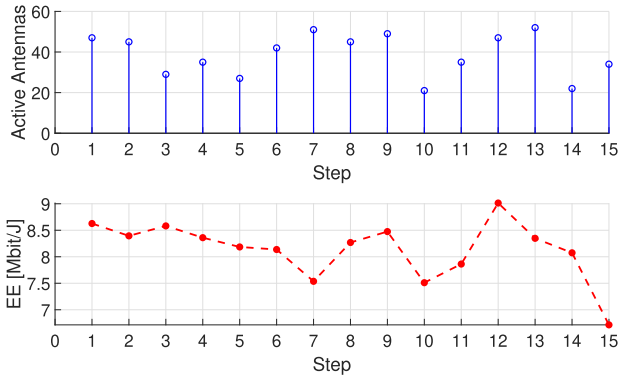


**FIGURE 9.** Optimal number of active antennas and related EE in the consecutive steps of Experiment 1.

action is taken at least once the algorithm is no longer forced to take unprofitable actions. As a result, after about 120-th episode reward rapidly grows, and remains relatively stable and provides about 18.5% EE improvement over the Ref algorithm. During the last 32 episodes, the least fluctuations are observed, when $c = 0$. In this case, the algorithm performs greedily, i.e., it exploits the current knowledge by always taking the best known action. This is caused by the fact that in the considered scenario all UEs have a line-of-sight connection to the BSs, and thus related radio channels are stable, even though the channel estimation error is introduced.

To highlight the fact that every set of UE positions can be potentially related to a different number of active antennas, we have plotted the optimal number of antennas and EE related to each step in Experiment 1. The results are depicted in Fig. 9. It can be seen that the optimal number of active antennas varies from about 20 to about 50 between steps. Similarly the related EE depends on the UE positions.

EE is defined as the ratio of the median-user bitrate and mean power consumption as shown in (4). Fig. 10 depicts separately power consumption and median-user bitrate obtained with the use of Ref algorithm, REM-UCB, and under No EE scenario. Results are averaged over the last 32 episodes, i.e., the period when reward becomes stable. REM-UCB results are obtained for $c = 0$. It can be seen that both power

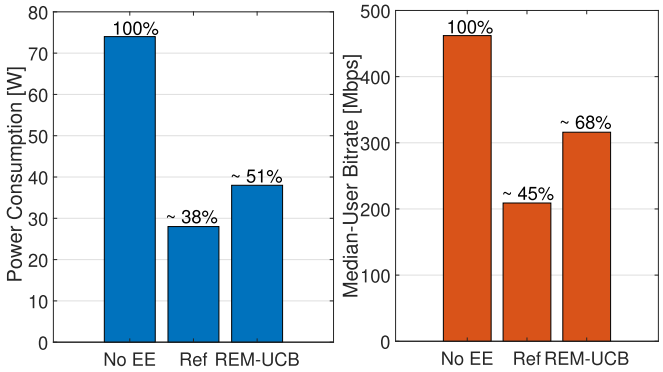


**FIGURE 10.** Power Consumption and Median-User Bitrate averaged over the last 32 episodes. REM-UCB results obtained for $c = 0$.

consumption and median-user bitrate are decreased as a result of the Intelligent Antenna Switching in comparison to the No EE scenario. In the case of the Ref algorithm, higher power savings are observed, comparing to the REM-UCB: about 38% of No EE scenario power consumption against about 51%. However, the Ref algorithm can achieve median-user bitrate only as high as about 45% of bitrate achieved under the No EE scenario, while REM-UCB achieves about 68%. That is why the resultant EE achieved by REM-UCB is better than the Ref algorithm.

### D. EVALUATION OF REASA

Although the REM-UCB algorithm provides REM with the optimal number of active antennas for a given set of UE positions, we hope that the learning phase can be speed up, i.e., EE gains provided by REM-UCB after about 120 episodes can be reached faster. The speed-up can be achieved by the utilization of similarities between the patterns of UE positions, i.e., a similar pattern of UE positions would probably be related to a similar optimal number of active antennas. This idea is implemented in the REASA algorithm described in Sec. IV-C. We have evaluated the REASA algorithm under the same scenario as REM-UCB: 10 experiments, each consisting of 160 episodes exploiting 15 steps. In addition, the REM is from the beginning filled with 50 entries. These entries had been obtained during simulations reported in Sec. V-B. Most importantly, the experiments generated here are independent from those reported in Sec. V-B, i.e., UE positions and paths are not repeated. The resultant average reward-EE obtained after each episode and averaged over experiments is depicted in Fig. 11. As it can be observed, due to the utilization of REASA together with REM possessing initial knowledge about past experiments, EE can be improved almost instantly for a completely new UE positions pattern. The drawback of the utilization of $c = 0$ in the case of REASA is that the algorithm tends to permanently exploit sub-optimal solutions. However, these solutions are much better than Ref. The quality of the sub-optimal solution depends on the $\gamma$ constant. The higher the $\gamma$, the smaller the impact of similar REM entries on current action selection. The best sub-optimal solution is observed for $\gamma = 1.5$.

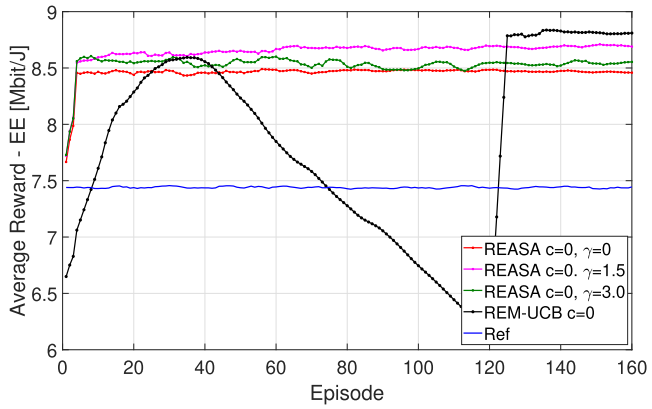


**FIGURE 11.** Average reward (EE) obtained with the use of REASA, after each episode, and averaged over 10 experiments.In order to smooth the plot, a moving average of reward over 10 consecutive episodes is applied.

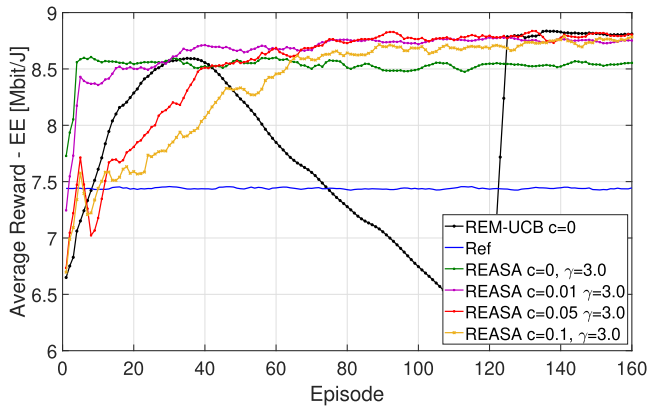


**FIGURE 12.** The impact of the $c$ constant on the REASA algorithm, for the $\gamma$ parameter equal to 3.0.In order to smooth the plot, a moving average of the reward over 10 consecutive episodes is applied.

The same level of EE as for REM-UCB can be achieved by REASA by making the algorithm less greedy (increasing $c$), and proper balancing of the impact of similarities on the current action, i.e., tuning the $\gamma$ parameter. Although $\gamma = 1.5$ gave the best sub-optimal result, the optimal solution couldn't be achieved for this value of $\gamma$ by increasing the constant $c$. Thus, we decided to slightly reduce the impact of similar REM entries on the current action by setting $\gamma = 3.0$. The performance of REASA under $\gamma = 3.0$, and varying constant $c$ is depicted in Fig. 12. It can be seen that constant $c$ must be properly chosen. Too low value of $c$ favors a sub-optimal solution because of excessive exploitation, i.e., $c = 0$ (green line), $c = 0.01$ (purple line). On the other hand, too high value of the $c$ constant results in too frequent exploration of the sub-optimal actions. As a result, the performance is slightly worse than the performance of REM-UCB. The best results were observed for $c$ equal to 0.05. Most importantly, this value of $c$ guarantees convergence to a solution as good as the one observed for REM-UCB algorithm. However, due to the utilization of similarities between REM entries, the procedure of learning REM can be reduced from about 120 episodes to only about 60. This shows that the proposed REASA can reduce the required learning phase at least twofold. These results are promising from the perspective of potential practical implementations of a long time of network operation. In this case, similar states should occur very often. Then, REASA is expected to provide an even higher speed-up of the learning phase in relation to the REM-UCB.

## VI. CONCLUSION

The results have shown that, state of the art optimization of EE, in the case of MMIMO BS, based on analytical formulas, does not provide an optimal solution under realistic conditions. It is because of some simplified assumptions, e.g., that every antenna contributes equally to the resultant array gain. Instead we propose to extend the network with a REM unit, and utilize an RL scheme, to provide mapping between patterns of UE positions and the number of active antennas. The results have shown that this approach can increase EE by 18.5% compared to the reference algorithm. Moreover, by exploiting the similarities between REM entries, the learning phase can be significantly reduced, i.e., when the REASA algorithm is used instead of the REM-UCB method.

In the future more focus can be put on the selection and improvement of the antenna selection algorithm itself. More advanced metrics can be used to asses network and user bitrates, e.g., by taking into the account the correlations between radio channels. Finally studies similar to [30] can be performed to compare the performance of REASA under an alternative distance metric, e.g., the Sum of Minimums.

## ACKNOWLEDGMENT

The simulations were based on the QCM simulator from Huawei Technologies Sweden Research Center.

## REFERENCES

[1] E. G. Larsson, O. Edfors, F. Tufvesson, and T. L. Marzetta, "Massive MIMO for next generation wireless systems," *IEEE Commun. Mag.*, vol. 52, no. 2, pp. 186–195, Feb. 2014.
[2] E. Björnson, J. Hoydis, and L. Sanguinetti, *Massive MIMO Networks: Spectral, Energy, and Hardware Efficiency*, vol. 11, nos. 3–4. Foundations and Trends in Signal Processing, 2017, pp. 154–655, doi: 10.1561/2000000093.
[3] K. N. R. S. V. Prasad, E. Hossain, and V. K. Bhargava, "Energy efficiency in massive MIMO-based 5G networks: Opportunities and challenges," *IEEE Wireless Commun.*, vol. 24, no. 3, pp. 86–94, Jun. 2017.
[4] M. Masoudi *et al.*, "Green mobile networks for 5G and beyond," *IEEE Access*, vol. 7, pp. 107270–107299, 2019.
[5] S. Buzzi, C.-L. I, T. E. Klein, H. V. Poor, C. Yang, and A. Zappone, "A survey of energy-efficient techniques for 5G networks and challenges ahead," *IEEE J. Sel. Areas Commun.*, vol. 34, no. 4, pp. 697–709, Apr. 2016.
[6] F. Han, S. Zhao, L. Zhang, and J. Wu, "Survey of strategies for switching off base stations in heterogeneous networks for greener 5G systems," *IEEE Access*, vol. 4, pp. 4959–4973, 2016.
[7] E. Oh, K. Son, and B. Krishnamachari, "Dynamic base station switching-on/off strategies for green cellular networks," *IEEE Trans. Wireless Commun.*, vol. 12, no. 5, pp. 2126–2136, May 2013.
[8] L. Chiaraviglio, P. Wiatr, P. Monti, J. Chen, J. Lorincz, F. Idzikowski, M. Listanti, and L. Wosinska, "Is green networking beneficial in terms of device lifetime?" *IEEE Commun. Mag.*, vol. 53, no. 5, pp. 232–240, May 2015.
[9] S. Cui, A. J. Goldsmith, and A. Bahai, "Energy-efficiency of MIMO and cooperative MIMO techniques in sensor networks," *IEEE J. Sel. Areas Commun.*, vol. 22, no. 6, pp. 1089–1098, Aug. 2004.

[10] E. Björnson, M. Bengtsson, and B. Ottersten, "Optimal multiuser transmit beamforming: A difficult problem with a simple solution structure [lecture notes]," *IEEE Signal Process. Mag.*, vol. 31, no. 4, pp. 142–148, Jul. 2014.

[11] X. Gao, O. Edfors, F. Tufvesson, and E. G. Larsson, "Massive MIMO in real propagation environments: Do all antennas contribute equally?" *IEEE Trans. Commun.*, vol. 63, no. 11, pp. 3917–3928, Nov. 2015.

[12] C. Jiang and L. J. Cimini, "Antenna selection for energy-efficient MIMO transmission," *IEEE Wireless Commun. Lett.*, vol. 1, no. 6, pp. 577–580, Dec. 2012.

[13] Z. Chen, J. Yuan, and B. Vucetic, "Analysis of transmit antenna selection/maximal-ratio combining in Rayleigh fading channels," *IEEE Trans. Veh. Technol.*, vol. 54, no. 4, pp. 1312–1321, Jul. 2005.

[14] E. Kurniawan, A. Madhukumar, and F. Chin, "Antenna selection technique for MIMO-OFDM systems over frequency selective Rayleigh fading channel," *IET Commun.*, vol. 1, pp. 458–463, Jul. 2007.

[15] T.-H. Tai, H.-J. Chen, W.-H. Chung, and T.-S. Lee, "Energy efficient norm-and-correlation-based antenna selection algorithm in spatially correlated massive multi-user MIMO systems," in *Proc. IEEE Int. Workshop Signal Process. Syst. (SiPS)*, Oct. 2017, pp. 1–5.

[16] A. F. Molisch, M. Z. Win, Y.-S. Choi, and J. H. Winters, "Capacity of MIMO systems with antenna selection," *IEEE Trans. Wireless Commun.*, vol. 4, no. 4, pp. 1759–1772, Jul. 2005.

[17] J. C. Marinello, T. Abrão, A. Amiri, E. de Carvalho, and P. Popovski, "Antenna selection for improving energy efficiency in XL-MIMO systems," *IEEE Trans. Veh. Technol.*, vol. 69, no. 11, pp. 13305–13318, Nov. 2020.

[18] M. O. K. Mendonca, P. S. R. Diniz, T. N. Ferreira, and L. Lovisolo, "Antenna selection in massive MIMO based on greedy algorithms," *IEEE Trans. Wireless Commun.*, vol. 19, no. 3, pp. 1868–1881, Mar. 2020.

[19] X. Chai, H. Gao, J. Sun, X. Su, T. Lv, and J. Zeng, "Reinforcement learning based antenna selection in user-centric massive MIMO," in *Proc. IEEE 91st Veh. Technol. Conf. (VTC-Spring)*, May 2020, pp. 1–6.

[20] W. Yu, T. Wang, and S. Wang, "Multi-label learning based antenna selection in massive MIMO systems," *IEEE Trans. Veh. Technol.*, vol. 70, no. 7, pp. 7255–7260, Jul. 2021.

[21] Z. Zheng, J. Zhang, X. Wu, D. Liu, and L. Tian, "Zero-forcing precoding in the measured massive MIMO downlink: How many antennas are needed?" *Int. J. Antennas Propag.*, vol. 2019, pp. 1–10, Apr. 2019.

[22] K. Senel, E. Björnson, and E. G. Larsson, "Joint transmit and circuit power minimization in massive MIMO with downlink SINR constraints: When to turn on massive MIMO?" *IEEE Trans. Wireless Commun.*, vol. 18, no. 3, pp. 1834–1846, Mar. 2019.

[23] J. Hoydis, S. T. Brink, and M. Debbah, "Massive MIMO in the UL/DL of cellular networks: How many antennas do we need?" *IEEE J. Sel. Areas Commun.*, vol. 31, no. 2, pp. 160–171, Feb. 2013.

[24] J. Van De Beek, T. Cai, S. Grimoud, B. Sayrac, P. Mahonen, J. Nasreddine, and J. Riihijarvi, "How a layered REM architecture brings cognition to today's mobile networks," *IEEE Wireless Commun.*, vol. 19, no. 4, pp. 17–24, Aug. 2012.

[25] M. Hoffmann, P. Kryszkiewicz, and A. Kliks, "Increasing energy efficiency of massive-MIMO network via base stations switching using reinforcement learning and radio environment maps," *Comput. Commun.*, vol. 169, pp. 232–242, Mar. 2021. [Online]. Available: https://www.sciencedirect.com/science/article/pii/S0140366421000335

[26] R. S. Sutton and A. G. Barto, *Reinforcement Learning: An Introduction*. Cambridge, MA, USA: A Bradford Book, 2018.

[27] E. Björnson, L. Sanguinetti, J. Hoydis, and M. Debbah, "Optimal design of energy-efficient multi-user MIMO systems: Is massive MIMO the answer?" *IEEE Trans. Wireless Commun.*, vol. 14, no. 6, pp. 3059–3075, Oct. 2015.

[28] M. Hoffmann, P. Kryszkiewicz, and G. P. Koudouridis, "Modeling of real time kinematics localization error for use in 5G networks," *EURASIP J. Wireless Commun. Netw.*, vol. 2020, no. 1, pp. 1–19, Dec. 2020.

[29] H. Viswanathan and P. E. Mogensen, "Communications in the 6G era," *IEEE Access*, vol. 8, pp. 57063–57074, 2020.

[30] M. Hoffmann and P. Kryszkiewicz, "Similarity measures for location-dependent MMIMO, 5G base stations on/off switching using radio environment map," 2021, *arXiv:2105.01948*. [Online]. Available: http://arxiv.org/abs/2105.01948

[31] H. Holtkamp, G. Auer, V. Giannini, and H. Haas, "A parameterized base station power model," *IEEE Commun. Lett.*, vol. 17, no. 11, pp. 2033–2035, Nov. 2013.

[32] A. Capone, S. D'Elia, I. Filippini, A. E. C. Redondi, and M. Zangani, "Modeling energy consumption of mobile radio networks: An operator perspective," *IEEE Wireless Commun.*, vol. 24, no. 4, pp. 120–126, Aug. 2017.

[33] S. Tombaz, K. W. Sung, and J. Zander, "On metrics and models for energy-efficient design of wireless access networks," *IEEE Wireless Commun. Lett.*, vol. 3, no. 6, pp. 649–652, Dec. 2014.

[34] S. Mukherjee and S. K. Mohammed, "On the energy-spectral efficiency trade-off of the MRC receiver in massive MIMO systems with transceiver power consumption," 2014, *arXiv:1404.3010*. [Online]. Available: http://arxiv.org/abs/1404.3010

[35] U. Amin, S. Anwar, W. Khan, and S. I. Khan, "Energy efficiency analysis of single-cell massive MIMO under pilot contamination," in *Proc. 13th Int. Bhurban Conf. Appl. Sci. Technol. (IBCAST)*, Jan. 2016, pp. 704–709.

[36] S. Payami and F. Tufvesson, "Channel measurements and analysis for very large array systems at 2.6 GHz," in *Proc. 6th Eur. Conf. Antennas Propag. (EUCAP)*, Mar. 2012, pp. 433–437.

[37] A. D. Tijsma, M. M. Drugan, and M. A. Wiering, "Comparing exploration strategies for *Q*-learning in random stochastic mazes," in *Proc. IEEE Symp. Ser. Comput. Intell. (SSCI)*, Dec. 2016, pp. 1–8.

[38] A. O. Martínez, J. Ø. Nielsen, E. De Carvalho, and P. Popovski, "An experimental study of massive MIMO properties in 5G scenarios," *IEEE Trans. Antennas Propag.*, vol. 66, no. 12, pp. 7206–7215, Dec. 2018.

[39] D. P. Huttenlocher, G. A. Klanderman, and W. J. Rucklidge, "Comparing images using the Hausdorff distance," *IEEE Trans. Pattern Anal. Mach. Intell.*, vol. 15, no. 9, pp. 850–863, Sep. 1993.

[40] *Deliverable D6.1, Simulation Guidelines, Version: V1.0 Ed. Mobile and Wireless Communications Enablers for the Twenty-Twenty Information*, METIS, Sweden, 2013.

[41] *Base Station (BS) Radio Transmission and Reception*, document TR 38.104, Version 15.9.0, 3GPP, Apr. 2020.

[42] T. Yoo and A. Goldsmith, "On the optimality of multiantenna broadcast scheduling using zero-forcing beamforming," *IEEE J. Sel. Areas Commun*, vol. 24, no. 3, pp. 528–541, Mar. 2006.

[43] Qamcom. *Qamcom/QCM*. Accessed: Mar. 10, 2021. [Online]. Available: https://github.om/qamcom/QCM

[44] A. S. Pagès, J. Olmos, and M. Lema, "Modelling channel estimation error in LTE link level simulations," Eur. Cooperat. Sci. Technol., COST IC1004 Cooperat. Radio Commun. Green Smart Environ., 3rd Sci. Meeting, Barcelona, Spain, Feb. 2012.

**MARCIN HOFFMANN** (Graduate Student Member, IEEE) received the M.Sc. degree (Hons.) in electronics and telecommunication from Poznań University of Technology, in 2019, where he is currently pursuing the Ph.D. degree with the Institute of Radiocommunications. He is gaining scientific experience by being involved in both national and international research projects. His research interests include utilization of machine learning and location-dependent information for the purpose of network management.

**PAWEL KRYSZKIEWICZ** (Senior Member, IEEE) received the M.Sc. and Ph.D. degrees (Hons.) in telecommunications from Poznań University of Technology (PUT), Poland, in 2010 and 2015, respectively. He is currently an Assistant Professor with the Institute of Radiocommunciations, PUT. He was involved in a number of national and international research projects. His research interests include the problems concerning the physical layer of the dynamic spectrum access systems, multi-carrier signal design for green communications, and problems related to practical implementation of massive MIMO systems.

## 7.10 Publication [P10]

M. Hoffmann and P. Kryszkiewicz, "Contextual Bandit-Based Amplifier IBO Optimization in Massive MIMO Network," *IEEE Access*, vol. 11, pp. 127035– 127042, 2023.

MNiSW Points: 100

Number of citations:

- according to Web of Science: 1
- according to Google Scholar: 1

mgr inż. Marcin Hoffmann
Instytut Radiokomunikacji, Politechnika Poznańska
ul. Polanka 3, 60-965 Poznań

Poznań, 9 stycznia 2025 r.

# OŚWIADCZENIE W SPRAWIE AUTORSTWA PRACY

Oświadczam, że w pracy:

*M. Hoffmann, P. Kryszkiewicz,* "Contextual Bandit-Based Amplifier IBO Optimization in Massive MIMO Network," *IEEE Access, tom 11, strony 127035-127042, listopad 2023*

mój udział polegał na:

- Zaproponowaniu algorytm inteligentnego doboru punktu pracy wzmacniacza w systemie M-MIMO uwzględniającym zniekształcenia nieliniowe generowane przez wzmacniacz mocy. Zaproponowany algorytm wykorzystuje uczenie przez interakcję w celu zwiększenia przepływności osiąganych przez użytkowników sieci.
- Przygotowaniu tekstu artykułu
- Przeprowadzeniu symulacji komputerowych i opracowaniu wyników
- Dyskusjach i poprawkach artykułu na podstawie recenzji

Mój procentowy udział w powstanie pracy szacuję na: 80%

.....

Podpis

dr hab. inż. Paweł Kryszkiewicz, prof. PP
Instytut Radiokomunikacji, Politechnika Poznańska
ul. Polanka 3, 60-965 Poznań

Poznań, 9 stycznia 2024 r.

# OŚWIADCZENIE W SPRAWIE AUTORSTWA PRACY

Oświadczam, że w pracy:

*M. Hoffmann, P. Kryszkiewicz,* "Contextual Bandit-Based Amplifier IBO Optimization in Massive MIMO Network," *IEEE Access, tom 11, strony 127035-127042, listopad 2023*

mój udział polegał na:

- Koordynacji prac badawczych
- Propozycja tematyki badawczej i zaprezentowanie modelu matematycznego nieliniowości
- Dyskusji ze współautorami uzyskanych wyników i metod ich prezentacji/porównania
- Iteracyjnym nanoszeniu poprawek na tekst; dyskusji uwag ze współautorem

Mój procentowy udział w powstanie pracy szacuję na: 20%

Podpis

IEEE Access
Multidisciplinary ⋮ Rapid Review ⋮ Open Access Journal

Received 22 August 2023, accepted 1 November 2023, date of publication 9 November 2023, date of current version 16 November 2023.

*Digital Object Identifier 10.1109/ACCESS.2023.3331740*

RESEARCH ARTICLE

# Contextual Bandit-Based Amplifier IBO Optimization in Massive MIMO Network

**MARCIN HOFFMANN, (Graduate Student Member, IEEE), AND PAWEL KRYSZKIEWICZ, (Senior Member, IEEE)**
Institute of Radiocommunications, Poznań University of Technology, 60-965 Poznan, Poland
Corresponding author: Marcin Hoffmann (marcin.hoffmann@put.poznan.pl)

This work was supported by the Polish National Science Centre under Project 2021/41/B/ST7/00136.

**ABSTRACT** Massive Multiple-Input Multiple-Output (MMIMO) is one of the 5G key enablers. Though, most of the works consider MMIMO under assumptions of ideal hardware. It has been shown that Power Amplifiers (PAs) introduce nonlinear distortion while operating close to their saturation power. Moreover, these distortions are in some cases beamformed toward the user, preventing antenna array gain from solving this problem. One of the possible solutions is an adaptive adjustment of the PA operating point, measured by Input Back off (IBO), to find a balance between wanted signal power and nonlinear distortion power. This work proposes a Contextual Bandit-Based IBO Optimization (COBBIO) algorithm to find rate-maximizing IBO for a given user's radio conditions using learning through interaction. The proposed solution is tested in a realistic analog beamforming MMIMO cell simulator with multiple functional blocks, e.g., precoder, user scheduler, and utilizing an accurate 3D Ray-Tracing radio channel model. COBBIO provides throughput gains both over fixed-IBO schemes and state-of-the-art analytical IBO adjustment algorithms. The highest gains were observed for the so-called cell-edge users, where up to 83% improvement over the state-of-the-art algorithm was observed for the proposed COBBIO algorithm.

**INDEX TERMS** Massive MIMO, 5G, machine learning, nonlinear distortion, input back-off (IBO).

## I. INTRODUCTION

The Massive Multiple-Input Multiple-Output (MMIMO) technology is a key enabler for achieving high user throughputs in 5G, and presumably 6G networks [1]. However, the phenomena related to hardware impairments in MMIMO still require attention. In [2] the influence of nonlinear PA on the out-of-band radiation of an MMIMO transmitter has been analyzed. Unlike previous studies, e.g., [3], it shows that the nonlinear distortion can achieve a similar array gain as the wanted signal. Therefore, this problem needs proper countermeasures, e.g., nonlinearity-minimizing precoders [4]. Moreover, the nonlinear distortion problem statement and some of its solutions, common for Orthogonal Frequency Division Multiplexing (OFDM) systems, can be applied directly to MMIMO OFDM systems, e.g., iterative, nonlinearity-aware reception [5], [6]. Another approach to decrease the impact of nonlinear distortion on the OFDM system is to reduce the Peak-to-Average Power Ratio (PAPR), e.g., with the use of the dedicated waveforms designed using Machine Learning (ML) models [7]. The drawback of this approach is that utilization of a new waveform requires redesigning network protocols for both Base Station (BS) and User Equipment (UE). However, this problem can be addressed from the transceiver control perspective, by adjustment of the PA operation point, measured by the Input-Back-Off (IBO) being the ratio between the input saturation power of the PA and the average power of the input signal. In state-of-the-art systems, the PA's IBO is fixed to make Error Vector Magnitude (EVM) or spectral emission mask at the transmitter output compliant with the standard. However, by changing IBO the relation between wanted signal power, distortion power, and the thermal noise at the receiver can be balanced, as such optimizing the network's performance. Most importantly, the adjustment of IBO does not require changes in the 5G network protocols enabling

The associate editor coordinating the review of this manuscript and approving it for publication was Adnan Kavak.

its adoption in the existing networks. Moreover, while the IBO modification can increase adjacent channel emission the coexistence ability can be restored by proper filtering [5].

In [8] the Signal-To-Noise-and-Distortion Ratio (SNDR) of an OFDM link is maximized by the PA IBO adjustment at BS which utilizes OFDM. While this solution can be adapted to some configurations of MMIMO systems, e.g., analog beamforming, the authors assumed a simplified system model, e.g., flat fading channel. This is not the case in real-world scenarios, where the radio channel is rich in reflections, and diffractions, making it frequency selective. Moreover, the authors of [8] do not consider layered signal processing in a real BS composed of, e.g., scheduling, and utilization of a fixed set of Modulation and Coding Schemes (MCS), that affect the throughput achievable by the network users.

While accurate mathematical modeling of a 5G MMIMO system may be difficult, its analytical optimization may be even harder. We propose to utilize ML, which is considered one of the key enablers for intelligent 6G networks [1]. In detail, we propose a COntextual Bandit-Based amplifier IBO Optimization (COBBIO) algorithm. Contextual bandit is a sub-class of the Reinforcement Learning (RL) algorithms, where the aim of the agent is to learn what actions should be taken within the current context in order to maximize reward [9], i.e., how to adjust the value of IBO dynamically, with respect to the radio channel conditions, so as to maximize user throughput. The proposed COBBIO algorithm utilizes a Deep Q Network (DQN) model, which unlike the state-of-the-art IBO optimization method [8] is trained directly on the network data making it aware of the frequency-selective radio channel, and multi-stage signal processing used inside the BS [10]. The proposed COBBIO algorithm is built on top of the contextual bandit framework that defines internal algorithms for data capture, model training, and providing a balance between exploitation and exploration. The superiority of the proposed solution is justified by an advanced, analog beamforming MMIMO BS simulation using a 3D Ray-Tracing radio channel model. One should notice that considered analog beamforming is the worst-case scenario from the perspective of nonlinear distortion, i.e., the same MMIMO array gain is applied to both the wanted signal and distortion term [6].

The paper is organized as follows: the system model is described in Sec. II. The proposed method of IBO optimization, i.e., the COBBIO algorithm based on the contextual bandit is described in Sec. III. The simulation environment is described in IV. The results are presented and discussed in Sec. V. Conclusions are formulated in Sec. VI.

## II. SYSTEM MODEL

A downlink in a single MMIMO cell is considered utilizing $M$ transmit antennas and $N_{\text{rb}}$ Resource Blocks (RBs) with the block diagram depicted in Fig. 1. First, a user scheduler decides on the allocation of the radio resources. Its decisions are passed to the so-called 5G Distributed Unit (DU), which is responsible for the physical layer processing of the user's

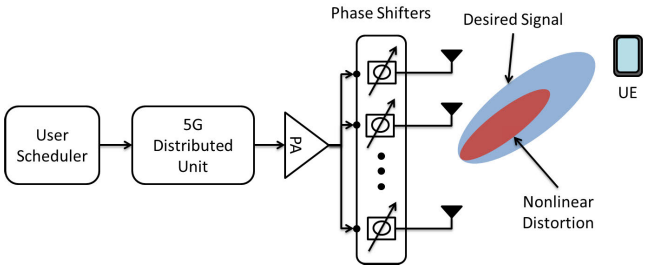


**FIGURE 1.** System model.

data, e.g., bit-symbol mapping and coding according to given Modulation and Coding Schemes (MCSs), channel estimation, and OFDM multiplexing. The output signal is then fed into the Power Amplifier (PA). The PA nonlinear effects are reflected by the soft limiter model where the output OFDM sample $\hat{s}(n)$ at $n$-th time instance is related to the input OFDM sample $s(n)$ by [8]:

$$\hat{s}(n) = \begin{cases} s(n), & \text{for } |s(n)| < A_{\text{sat}}, \\ A_{\text{sat}} \cdot e^{j \arg\{s(n)\}}, & \text{for } |s(n)| \geq A_{\text{sat}}, \end{cases} \tag{1}$$

where $A_{\text{sat}}$ is the PA saturation voltage. The IBO ($\gamma^2$) is given by:

$$\gamma^2 = \frac{A_{\text{sat}}^2}{P_{\text{in}}} = \frac{A_{\text{sat}}^2}{\mathbb{E}\{|s(n)|^2\}}, \tag{2}$$

where $P_{\text{in}}$ denotes the average power of input signal $s(n)$. It has been shown in [8] that the PA output can be decomposed as

$$\hat{s}(n) = \alpha s(n) + d(n), \tag{3}$$

where

$$\alpha = 1 - e^{-\gamma^2} + \frac{\sqrt{\pi}}{2}\gamma \cdot \text{erfc}(\gamma) \in \langle 0; 1 \rangle \tag{4}$$

is the wanted signal scaling factor and $d(n)$ is nonlinear distortion sample uncorrelated with signal $s(n)$ of power

$$\sigma_d^2 = \frac{A_{\text{sat}}^2}{\gamma^2}\left(1 - \alpha^2 - e^{-\gamma^2}\right). \tag{5}$$

If for a given PA the mean power of $s(n)$ is increased, decreasing $\gamma$, the higher wanted signal power at the receiver is expected at the cost of increased $\sigma_d^2$. Next, the signal from the PA output is equally divided between $M$ antenna elements. Here, an analog beamformer is considered which utilizes $M$ phase shifters to steer the beam in the direction of the user. Although such a solution allows simultaneously serving only one user, it has the advantage of low hardware and signal processing complexity [11]. While the same precoding is applied to both the wanted signal and distortion the same radiation pattern will be obtained for both signals, resulting in the worst-case scenario, i.e., the MMIMO array gain will not increase the signal-to-distortion ratio [12], independently from the wireless channel properties. The array-channel gain $G_l$ of signal $\hat{s}(n)$ at the resource block $l$ can be calculated

as $G_l = \sum_{m=0}^{M} h_{m,l} w_m$, where $h_{m,l}$ is a complex channel coefficient between the single antenna user, and $m$-th antenna of the BS at RB $l$, and $w_m = \frac{1}{\sqrt{M}} e^{j\varphi_m}$ is the beamforming coefficient for $m$-th antenna. The highest Signal-to-Noise Ratio (SNR) can be obtained using the considered PA for transmitting a single carrier of amplitude $A_{\text{sat}}$ with perfect beamformer, i.e., $\varphi_m = -\arg\{h_{m,l}\}$, resulting in $G_l = \frac{1}{\sqrt{M}} \sum_{m=0}^{M} |h_{m,l}|$. In this case the SNR equals $G_l^2 A_{\text{sat}}^2 / \sigma_n^2$, where the $\sigma_n^2$ denotes the power of Additive White Gaussian Noise (AWGN). However, as there are multiple frequencies $l$ to be used we average this metric over all RBs obtaining the saturation SNR

$$\text{SNR}_{\text{sat}} = \frac{A_{\text{sat}}^2}{\sigma_n^2} \cdot \frac{1}{N_{\text{rb}} M} \sum_{l=0}^{N_{\text{rb}}} \left( \sum_{m=0}^{M} |h_{m,l}| \right)^2. \tag{6}$$

This is an adaptation of $\text{SNR}_{\text{sat}}$ metric used for Single Input Single Output (SISO) wireless channel description in [8] to an MMIMO system.

Authors of [8] assume the wireless channel is frequency flat over the whole OFDM band resulting in a constant gain in the whole band, i.e., $\forall l G_l = G$. In such a system signal-to-noise-plus-distortion ratio (SNDR) is given by:

$$\text{SNDR} = \frac{G\alpha^2 P_{in}}{G\sigma_d^2 + \sigma_n^2}. \tag{7}$$

While this assumption allowed to propose an analytical formula for the *optimal* IBO, it is suboptimal in a frequency-selective channel. Moreover, the practical 5G system has some limitations, e.g., due to the MCS selection mechanism at some point increasing SNDR would not provide further user-throughput improvement. This is not considered in [8].

## III. FRAMEWORK FOR CONTEXTUAL BANDIT-BASED IBO OPTIMIZATION

In this work, we propose to extend the MMIMO BS with the dedicated IBO optimization module, where the proposed COBBIO algorithm is deployed. Our objective is to adjust IBO ($\gamma^2$) for a currently scheduled user so as to maximize its throughput. The system model described in Sec. II consists of many functional blocks like user scheduler, analog precoder, MCS selection, and most importantly it is affected by the nonlinear distortion, that is steered toward UE together with a desired signal. Such a complex system is hard to be modeled analytically and optimized with the use of standard optimization methods. Instead, we propose to utilize ML techniques. The considered problem can be classified as the so-called contextual bandit problem [9], i.e., within the context of a currently scheduled user our objective is to select IBO, which will result in the highest throughput.

### A. CONTEXTUAL BANDIT FRAMEWORK

The framework for the proposed COBBIO algorithm is depicted in Fig. 2. It is similar to a RL framework in that it involves an agent interacting with the environment by taking proper actions based on the observed states and received rewards. The difference is that there is no dependency between the consecutive states, i.e., the contextual bandit agent may focus only on the maximization of the reward in the current state. The components that constitute the contextual bandit framework for the proposed COBBIO algorithm are defined as follows:

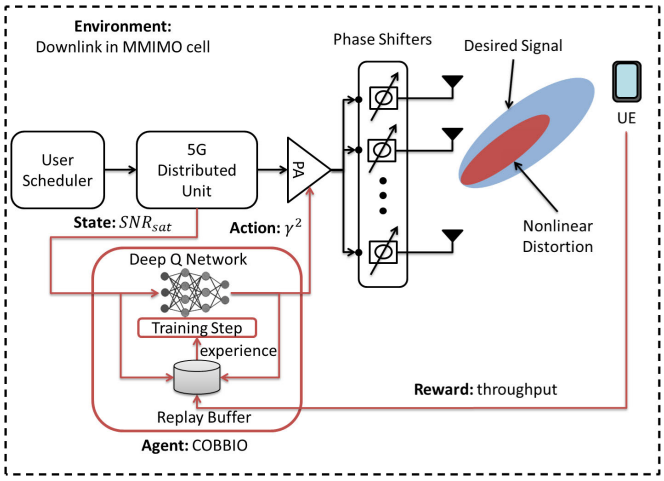


**FIGURE 2.** Contextual bandit based IBO optimization.

- **Environment** is a downlink in the MMIMO cell, i.e., our system model described in Sec. II.
- **State** is defined as the $SNR_{\text{sat}}$ computed according to (6). Due to the averaging over the RBs, this metric would be relatively stable, and good for the characterization of the user's radio conditions. It's important to note that $SNR_{\text{sat}}$ is a continuous variable, making the RL state space continuous as well.
- **Action** is defined as the IBO ($\gamma^2$), and is also continuous. Both the wanted signal power and distortion power change monotonically in the function of $\gamma^2$. Thus the problem of continuous action space can be resolved by discretization as proposed in [13]. As a result, action is one of the fixed IBO levels ranging from $\gamma^2_{\text{min}}$ to $\gamma^2_{\text{max}}$ with the equal step of $\gamma^2_{\text{step}}$.
- **Reward** is defined as the throughput that was achieved by the currently scheduled UE. In Fig. 2 the throughput is reported by the UE to visualize the contextual bandit cycle. In practice, such a value is available at the 5G DU.
- **Agent** is the proposed COBBIO algorithm. It recognizes the state ($SNR_{\text{sat}}$) and performs an action, i.e., selects the value of IBO ($\gamma^2$). A detailed description of the agent's internal algorithms is provided in the following sections.

### B. DEEP Q NETWORK

The aim of the agent is to select the IBO ($\gamma^2$) that provides the highest user throughput, based on the $SNR_{\text{sat}}$. In other words, the agent must approximate the so-called Q-function to determine the expected reward associated with each action (IBO value). For a problem that has a continuous state space and discrete action space, a common approach is to

utilize a dedicated artificial neural network, i.e., the so-called DQN [14]. The DQN takes the state ($SNR_{sat}$) as an input and outputs the Q-values. In the case of the contextual bandit, where the agent is focused only on the maximization of the reward in the current state, the Q-values are directly the expected reward (user throughput) associated with each action ($\gamma^2$). It has been proven that a 3-layer neural network can approximate any discontinuous function [15]. Thus we propose the DQN architecture to consist of an input layer of size 1, 3 hidden dense layers of size $K$, followed by the so-called rectified linear unit (ReLU), which introduces a following nonlinear function between input and output $g(x) = \max\{0, x\}$, and an output layer of size equal to the number of actions. As can be seen in Fig. 2, the training of DQN is incorporated at the end of the contextual bandit cycle. After the agent receives the reward, the experience sample that is defined as state, action, and reward tuple is put into the so-called Replay Buffer, a cyclic buffer data structure of size $J$. Then a batch of $L$ experience samples is taken from the Replay Buffer and used to perform a single Stochastic Gradient Descent (SGD) step to update the weights of DQN [16]. The $L$ samples are selected from the Replay Buffer according to the Combined Experience Replay (CER) [17]. CER is a low-complexity algorithm that takes the latest observed experience sample and randomly selects the remaining $L-1$ experience samples from the Replay Buffer. The SGD optimizes the DQN weights so as to minimize the Mean Absolute Error (MAE) between the received rewards, and DQN output, i.e., estimated Q-values.

### C. ACTION SELECTION

One of the challenges in solving the Contextual Bandit problem is the balance between exploration and exploitation, i.e., how much time an agent should spend on exploring new actions, and when it should act greedy by selecting the best-known action (the one associated with the highest Q-value). In our previous work, we have shown that Upper Confidence Bound (UCB) provides good exploration-exploitation balance, and fast convergence [18]. However, UCB is not proper for dealing with continuous state space as it requires storing a number of visits in each state. We propose to utilize a well-known $\epsilon$-greedy strategy [9], i.e., with the probability of $\epsilon$ agent selects the random action, and with the probability of $1-\epsilon$ selects the greedy (best-known) action, associated with the highest Q-value. It is expected that the agent would spend more time on exploration during the first phases of training, and after getting enough experience would turn into the exploitation of current knowledge. We propose to start with an $\epsilon = 1.0$ and decay it according to the following rule:

$$\epsilon \leftarrow \max\left(\epsilon_{\min}, \epsilon - \frac{\delta_\epsilon}{N_a}\right), \tag{8}$$

where $\epsilon_{\min}$ is the minimal arbitrary chosen probability of exploration, $\delta_\epsilon$ is the decay step, and $N_a$ is the total number of actions that the agent has already taken.

## IV. SIMULATION ENVIRONMENT

To evaluate the proposed IBO optimization module based on the deep contextual bandit framework, we have developed an advanced simulator of the MMIMO 5G cell. In this section, the utilized 5G network simulator is described together with its parameters. Moreover, the utilized 3D Ray-Tracing channel model is presented that has been used to generate accurate and realistic radio channel coefficients.

We are considering a downlink in a single MMIMO cell, which operates at the center frequency of 3.6 GHz, i.e., within the 3GPP n78 band [19]. The available bandwidth is equal to the 25 MHz and is divided between $N_{\text{rb}} = 69$ resource blocks, including a guardband. The MMIMO BS is equipped with a rectangular antenna array of $M = 128$ elements (8 vertical $\times$ 16 horizontal). The saturation power of PA $A^2_{\text{sat}}$ is equal to the 38 dBm, which corresponds to the 3GPP *Medium Range BS*. The transmit power is divided equally between the resource blocks. The power of thermal noise is $-174$ dBm/Hz. The MMIMO cell utilizes the following algorithms for the purpose of downlink transmission:

- **User Scheduler:** we utilize a Round Robin user scheduler. This ensures the same sequence of scheduled users during each simulation in order to provide a fair comparison between the proposed IBO optimization algorithm and baseline solutions.
- **Precoder:** we utilize the so-called Equal Gain Transmission (EGT) precoder [20]. The EGT is a phase-only precoder, proper for analog systems, and ensures that equal power is being allocated per antenna.
- **MCS Selection:** we consider MCSs selection algorithm that is based on the SNR estimates obtained at the stage of user scheduling and precoding, i.e., one of the 15 MCSs is assigned to the scheduled user based on the Exponential Effective SNR (EES) mapping, as defined in [21] and [22]. The minimal required EES is $-6.28$ dB, while the highest, 15th MCS is assigned when the estimated EES is above 20.13 dB.

While evaluating the algorithms oriented on the optimization of the MMIMO network it is of high importance to utilize realistic radio channel models. Measurement studies show that the commonly used i.i.d. Rayleigh channel model significantly differs from the real propagation environment [23]. Thus, to obtain radio channel coefficients between the BS and users, we utilize the realistic Wireless InSite™ 3D Ray-Tracer. It is configured to consider 15 reflections and 1 diffraction between the MMIMO BS's antennas and each of the single-antenna users. We have defined the 3D urban scenario that follows the well-established Madrid Grid test environment [24]. The deployment of a MMIMO BS, and example placement of users is depicted in Fig. 3. The MMIMO BS is deployed 2.5 m above the rooftop of the central building, i.e., at a height of 45 m, with a 5 deg downtilt. The users are uniformly distributed over the cell area to create a heterogenous radio environment that includes both Line of Sight (LOS) conditions in a park area (green square), and Non-Line of Sight (NLOS) in the narrow streets between

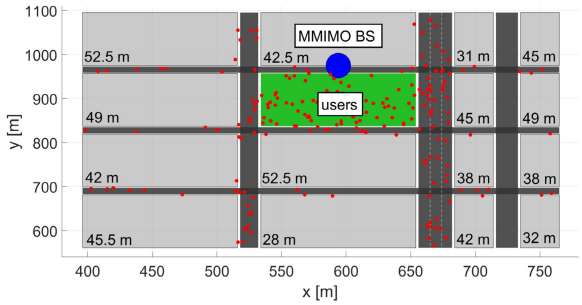


**FIGURE 3.** Deployment of the MMIMO BS (blue dot) and example placement of the users (red dots). Values on grey rectangles, e.g., 52.5 m, denote building heights.

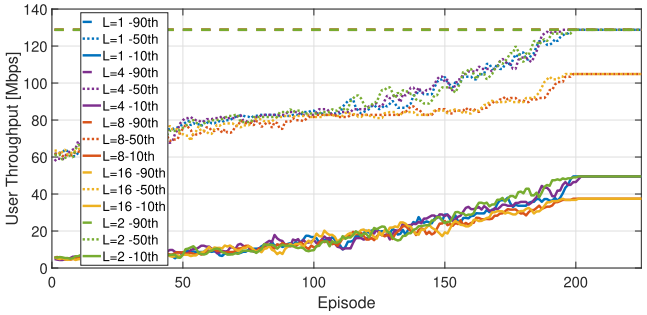


**FIGURE 4.** 90th, 50th, and 10th percentiles of user throughput distribution in the function of training epoch, for number of neurons per layer $K = 128$, and varying experience samples $L$.

**TABLE 1.** Simulation parameters.

| Parameter | Value |
|---|---|
| Center Frequency | 3.6 GHz |
| Bandwidth | 25 MHz |
| Number of Resource Blocks $N_{\text{rb}}$ | 69 |
| Number of Antennas $M$ | 128 (8 vertical, 16 horizontal) |
| Saturation Power $A^2_{\text{sat}}$ | 38 dBm |
| Thermal noise | $-174$ dBm/Hz |
| Analog precoder | Equal Gain Transmission [20] |
| User Scheduler | Round Robin |
| Urban model | Madrid Grid [24] |
| Radio channel model | Wireless InSite$^{\text{TM}}$ Ray-Tracer |

the relatively high buildings of tens of meters. The simulation parameters are summarized in Table 1.

We compare the proposed COBBIO algorithm against the baseline algorithm (''Reference''), that maximizes the SNDR given by (7). The baseline algorithm approximates optimal IBO $\hat{\gamma}^2$ based on the $SNR_{\text{sat}}$ according to the following equation [8]:

$$\hat{\gamma}^2 = 5.975 \cdot e^{0.00943 \cdot \text{SNR}_{\text{sat}}} - 12.79 \cdot e^{-0.0775 \cdot \text{SNR}_{\text{sat}}} [\text{dB}]. \tag{9}$$

Besides the baseline algorithm, we also consider two schemes of constant IBO (''Fixed IBO''): $\gamma^2 = 0$ dB, and $\gamma^2 = 6$ dB respectively.

## V. RESULTS

The simulation environment described in the previous section is utilized to evaluate the proposed COBBIO algorithm in terms of computer simulations. Regarding the RL terminology that is also valid for the contextual bandit, the simulation experiments consist of episodes. Each episode is a sequence of steps, i.e., a sequence of contexts (states) that the agent recognizes to take proper action and observe the reward. In this simulation, the experiment step is a single time slot. Within the time slot, IBO is adjusted based on the $SNR_{\text{sat}}$, and user throughput is observed as a reward. However, firstly, COBBIO's hyperparameters must be obtained. Some of them can be selected based on state-of-the-art knowledge about the RL and 5G MMIMO networks, while others must be obtained through simulation studies. The action space (discretized values of IBO) ranges from $\gamma^2_{\text{min}} = 0$ dB, to $\gamma^2_{\text{min}} = 9$ dB with a step of $\gamma^2_{\text{step}} = 1$ dB. The motivation for such a range is that low values of IBO, e.g., $\gamma^2_{\text{min}}$ below 0 dB produce large nonlinear distortion that causes significant QoS degradation. On the other hand high values of IBO $\gamma^2_{\text{min}}$, e.g., above 9 dB can result in the poor energy efficiency of a PA, without additional QoS improvement [25]. The studies on CER have shown that the size of a Replay Buffer equal to $J = 1000$ is a good choice [17]. Our target is to train the agent to select greedy actions that will maximize the throughput of a currently scheduled user, thus the minimal probability of exploration is $\epsilon_{\text{min}} = 0$. While implementing this solution in a real 5G network, one may consider setting the probability of exploration $\epsilon_{\text{min}}$ to a non-zero value, to deal with changes in a radio environment. The training step takes only a one-time slot (0.5 ms for a 5G OFDM network under the assumption of 30 kHz subcarrier spacing). The convergence time is not crucial in this case, i.e., collecting 1000 data samples takes only 5 seconds. Thus we have set a relatively large epsilon decay step of $\delta_\epsilon = 1000$.

To adjust the number of experience samples $L$ to be taken from Replay Buffer for a single SGD step, we have set a large number of neurons in hidden layers: $K = 128$ and tested different values of $L$ for 200 pedestrian users randomly placed over the cell area, and moving with the speed of 1.5 m/s. We have conducted 225 episodes of online training, within every episode each user was scheduled once so there were 200 steps taken by the agent . The 90th, 50th, and 10th percentiles of user throughput distribution in the function of training episode, for $K = 128$ neurons per layer, and varying number of experience samples $L$ are depicted in Fig. 4. The first observation is that users with the best radio conditions (90th percentile) reach the maximum throughput all the time. The throughput achieved by 50th and 10th percentile users stabilize after about 225 episodes. It can be seen that for $L > 4$ performance of COBBIO starts to degrade for the 50th and 10th percentile of users. One of the hypothesis for such a behavior is that during SGD the loss and related gradient are computed over a bigger set of samples. This reduces the noise, and increases the stability of learning, but for arbitrary non-convex functions, SGD with large batch size can stuck in local optimum [26]. In such a case some instability related

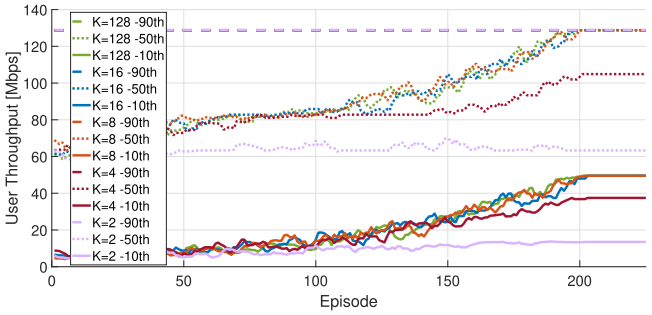


**FIGURE 5.** 90th, 50th, and 10th percentiles of user throughput distribution in the function of training episode, for experience samples $L = 2$, and a varying number of neurons per layer $K$.

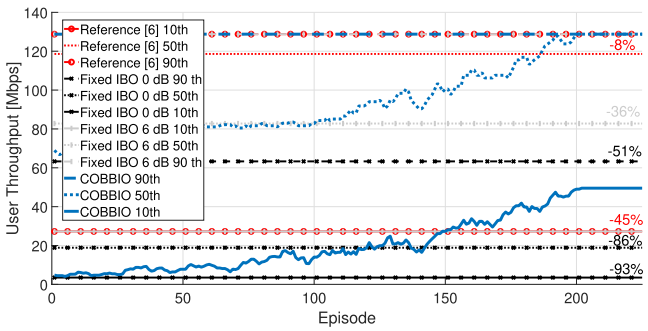


**FIGURE 6.** Comparison of 90th, 50th and 10th percentiles of user throughput distribution between the proposed COBBIO algorithm ($L = 2$, $K = 8$), reference algorithm and fixed IBO schemes ($\gamma^2 = 0$ dB, and $\gamma^2 = 6$ dB).

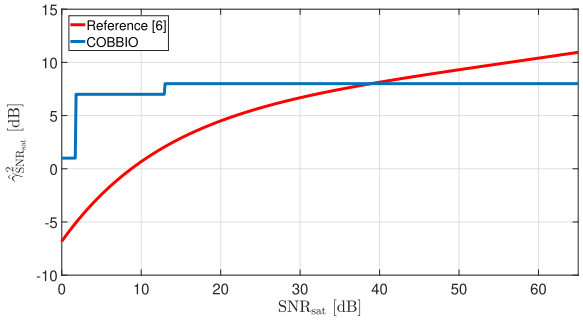


**FIGURE 7.** Comparison of selected IBO in the function of $SNR_{sat}$ between the reference algorithm, and the proposed COBBIO algorithm.

to small batch size can potentially help to search for global optimum. Based on the observation of the results we have selected the $L = 2$, because of the best convergence for 10th percentile users, i.e., the most challenging group of users that suffer the worst radio conditions.

After tuning the number of experience samples to $L = 2$ our target is to tune the number of neurons in the hidden layers $K$. For this purpose, we have utilized the same setup of online training as for adjusting the number of experience samples $L$. The results in terms of 90th, 50th, and 10th percentiles of user throughput distribution are depicted in Fig. 5. It can be seen that for the number of neurons in hidden layer $K$ equal to 2 and 4 the performance of COBBIO is significantly degraded. However, the number of neurons per hidden layer can be lowered to $K = 8$ without decreasing the COBBIO's performance in terms of user throughput. On the other hand, a lower number of DQN parameters reduces the prediction time and required memory. The final architecture of the DQN can be summarized as follows: input layer of size 1, followed by the three hidden layers of size $K = 8$, and an output layer of size 9, i.e., the number of actions that the agent can take. This DQN has a total number of 241 trainable parameters.

After tuning the hyperparameters we have compared the COBBIO algorithm against the two fixed IBO schemes of $\gamma^2 = 0$ dB, and $\gamma^2 = 6$ dB, and reference algorithm based on [8]. The scenario was the same as for the adjustment of $L$ and $K$. The results in terms of 90th, 50th, and 10th percentiles of user throughput distribution are depicted in Fig. 6. It can be seen that the 90th percentile is deteriorated by 51% for fixed IBO of $\gamma^2 = 0$ dB, compared to the remaining algorithms. This is caused by the high nonlinear distortion. In the case of the 50th percentile the proposed COBBIO algorithm has the best performance, i.e., the reference algorithm, fixed IBO of $\gamma^2 = 6$ dB fixed IBO of $\gamma^2 = 0$ dB are characterized by the median user throughput decreased by 8%, 36%, and 86% respectively, in relation to the COBBIO algorithm. A similar tendency is observed for the 10th percentile user throughput, where compared to COBBIO the 45% degradation is observed for the reference algorithm and fixed IBO of $\gamma^2 = 6$ dB, and 93% for $\gamma^2 = 0$ dB. This shows the benefits of learning through interaction that allows one to select proper IBO after approximately 200 training episodes.

The comparison of IBO selected by the reference algorithm [8] and the proposed COBBIO algorithm in a function of $\text{SNR}_{\text{sat}}$ is presented in Fig. 7. We can see that the theoretical IBO values computed according to [8] do not align with the actions taken by the COBBIO. Most importantly for the low values of $\text{SNR}_{\text{sat}}$ (e.g., below 20 dB), the theoretical optimum is up to several dBs lower than the IBO values that are selected by the COBBIO. Within the next few paragraphs, we will show that this is the result of the simplified system model assumed by the authors of [8], i.e., mostly by the flat radio channel. On the other hand for $\text{SNR}_{\text{sat}} > 40$ dB the theoretical optimal IBO values are much bigger than the ones selected by the COBBIO. It is because the practical system has an upper bound of the reasonable SNDR to be achieved related to the maximal possible MCS. In such a case it is not necessary to increase further IBO in order to reduce nonlinear distortion power.

For further investigations we compared the previously trained COBBIO ($K = 8$, $L = 2$) against the reference algorithm, and fixed IBO schemes under the new set of states (contexts, related to a newly generated set of UEs), independent from those used previously to tune the hyperparameters. From Fig. 7 it can be seen that the biggest difference between the value of IBO indicated by the reference algorithm, and the proposed COBBIO algorithm was observed for the

relatively low values of $SNR_{sat} < 40$. These values of IBO correspond mainly to the 10th and 50th percentile of user throughput distribution depicted in Fig. 6, for which the highest benefits of utilizing COBBIO were observed. To focus on these challenging cases, 1620 pedestrian users are randomly placed over the cell area such that their path loss is at least 100 dB. Later on they are moving with the speed of 1.5 m/s. In such a scenario the proposed prediction of IBO is the most beneficial, i.e., its results are significantly different than the results of the reference algorithm. Following the Round Robin scheduling strategy, each user receives in total 6 time slots of 0.5 ms duration, with the first allocation being neglected while obtaining statistics, i.e., average user rate, Capacity Effective SINR Mapping (CESM) [27], and wideband SNDR calculated according to the (7). The statistics are aggregated over the 81 simulation runs. As a result, there are 1620 values of each metric taken for statistical analysis.

In Fig. 8 there is a comparison between the Cumulative Distribution Function (CDF) of the wideband SNDR distribution among users for all tested IBO adjustment solutions. It can be seen that the reference algorithm provides the best wideband SNDR. Such a result could be expected because wideband SNDR is exactly what has been optimized by the authors of [8]. However, the real radio environment is not characterized by a flat wideband channel. One of the statistics that includes channel frequency-selectivity is CESM which relies on per-RB Shannon capacity. The CDFs of CESM are shown in Fig. 9. The fixed IBO scheme of $\gamma^2 = 0$ dB is characterized by the worst CESM resulting from too high distortion power. The second fixed IBO scheme of $\gamma^2 = 6$ dB outperforms the previous one, the reference algorithm, and sometimes even slightly the proposed COBBIO algorithm (recall the COBBIO maximizes rate, not CESM). Recalling Fig. 7 the IBO of 6 dB is good for users that suffer poor radio conditions. However, this does not allow users under better channel conditions to achieve CESM higher than around 27 dB, limiting potentially their rate. On the other hand, the reference algorithm, due to the assumption of a flat radio channel, obtains in many cases CESM lower than the other solutions. This shows that the wideband SNDR optimization is not optimal in a frequency-selective channel. Finally, the COBBIO algorithm is designed to maximize each user rate that is reflected by relatively high CESM values. The main advantage of this approach is that it is trained through interaction on real-network data considering, e.g., a limited set of MCS and frequency-selective radio channels. It is visible that the reference solution obtains higher CESM for around 10% of best channel users. This is caused by the limited MCS set, i.e., the COBBIO algorithm achieves for these users maximal MCS and does not need to increase CESM any further.

Finally, in Fig. 10 the users' throughput is shown. All considered schemes are compared in terms of the 10th percentile (cell-edge users throughput), median, and 90th percentile of user throughput distribution. The COBBIO

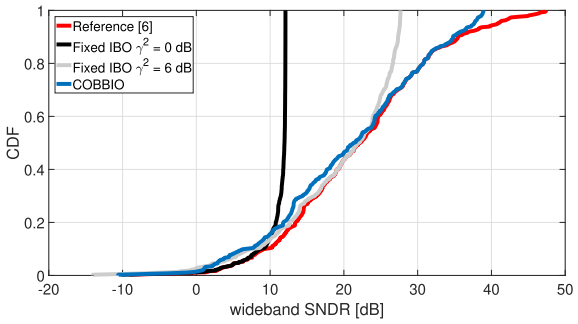


**FIGURE 8.** CDF of the wideband SNDR calculated using (7) for the fixed IBO schemes ($\gamma^2 = 0$ dB, and $\gamma^2 = 6$ dB), reference algorithm, and the proposed COBBIO algorithm.

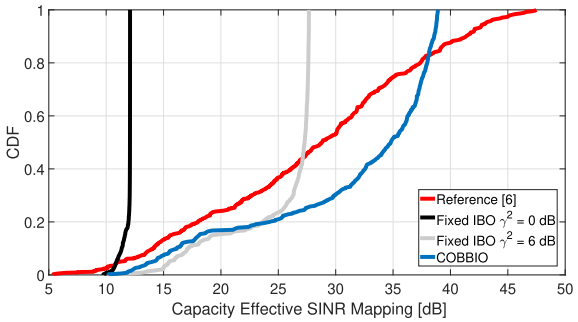


**FIGURE 9.** CDF of CESM obtained for the fixed IBO schemes ($\gamma^2 = 0$ dB, and $\gamma^2 = 6$ dB), reference algorithm, and the proposed COBBIO algorithm.

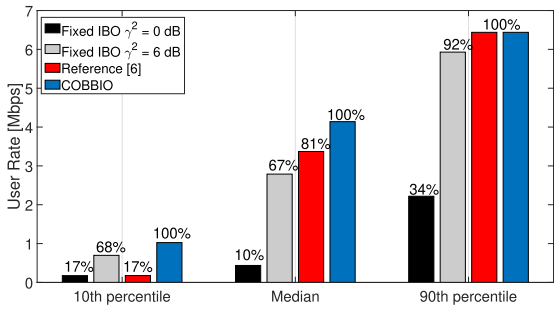


**FIGURE 10.** Statistics of user-rates: 10th percentile, median, and 90th percentile, computed for the reference algorithm, COBBIO algorithm, and fixed IBO schemes, of $\gamma^2 = 0$ dB, and $\gamma^2 = 6$ dB.

algorithm provides the best user throughputs for all considered percentiles. While the reference solution is the closest in terms of performance for the median and 90th percentile, it is significantly outperformed by the 10th percentile achieving only 17% of the COBBIO's throughput. For the worst-case users (10th percentile) the fixed IBO of $\gamma^2 = 6$ dB achieves the user's rate closest to the ML-based solution. Still, the achievable throughput is lower by around 32%.

## VI. CONCLUSION

The management of contemporary 5G and future 6G networks should take into account the nonlinear distortion generated by the PAs. We have shown utilizing an accurate 3D Ray-tracing radio channel model that adjustment of PA IBO based on the proposed COBBIO algorithm can

significantly improve throughput in an MMIMO 5G network. This is not achievable with state-of-the-art analytical IBO adjustment solutions nor with the fixed IBO solutions, that are contemporarily used to guarantee a given EVM at the transmitter output.

## ACKNOWLEDGMENT

For the purpose of open access, the author has applied a CC-BY public copyright license to any author accepted manuscript (AAM) version arising from this submission.

## REFERENCES

[1] I. F. Akyildiz, A. Kak, and S. Nie, "6G and beyond: The future of wireless communications systems," *IEEE Access*, vol. 8, pp. 133995–134030, 2020.
[2] E. G. Larsson and L. Van Der Perre, "Out-of-band radiation from antenna arrays clarified," *IEEE Wireless Commun. Lett.*, vol. 7, no. 4, pp. 610–613, Aug. 2018.
[3] E. Björnson, J. Hoydis, M. Kountouris, and M. Debbah, "Massive MIMO systems with non-ideal hardware: Energy efficiency, estimation, and capacity limits," *IEEE Trans. Inf. Theory*, vol. 60, no. 11, pp. 7112–7139, Nov. 2014.
[4] F. Rottenberg, G. Callebaut, and L. Van der Perre, "The Z3RO family of precoders cancelling nonlinear power amplification distortion in large array systems," *IEEE Trans. Wireless Commun.*, vol. 22, no. 3, pp. 2036–2047, Mar. 2023.
[5] Y. Sun and H. Ochiai, "Performance analysis and comparison of clipped and filtered OFDM systems with iterative distortion recovery techniques," *IEEE Trans. Wireless Commun.*, vol. 20, no. 11, pp. 7389–7403, Nov. 2021.
[6] M. Wachowiak and P. Kryszkiewicz, "Clipping noise cancellation receiver for the downlink of massive MIMO OFDM system," *IEEE Trans. Commun.*, vol. 71, no. 10, pp. 6061–6073, Oct. 2023.
[7] Y. Huleihel, E. Ben-Dror, and H. H. Permuter, "Low PAPR waveform design for OFDM systems based on convolutional autoencoder," in *Proc. IEEE Int. Conf. Adv. Netw. Telecommun. Syst. (ANTS)*, Dec. 2020, pp. 1–6.
[8] C. H. A. Tavares, J. C. M. Filho, C. M. Panazio, and T. Abrão, "Input back-off optimization in OFDM systems under ideal pre-distorters," *IEEE Wireless Commun. Lett.*, vol. 5, no. 5, pp. 464–467, Oct. 2016.
[9] R. S. Sutton and A. G. Barto, *Reinforcement Learning: An Introduction*. Cambridge, MA, USA: A Bradford Book, 2018.
[10] W. Yu, F. Sohrabi, and T. Jiang, "Role of deep learning in wireless communications," *IEEE BITS Inf. Theory Mag.*, vol. 2, no. 2, pp. 56–72, Nov. 2022.
[11] E. Bjornson, L. Van der Perre, S. Buzzi, and E. G. Larsson, "Massive MIMO in sub-6 GHz and mmWave: Physical, practical, and use-case differences," *IEEE Wireless Commun.*, vol. 26, no. 2, pp. 100–108, Apr. 2019.
[12] C. Mollen, E. G. Larsson, U. Gustavsson, T. Eriksson, and R. W. Heath, "Out-of-band radiation from large antenna arrays," *IEEE Commun. Mag.*, vol. 56, no. 4, pp. 196–203, Apr. 2018.
[13] Y. Tang and S. Agrawal, "Discretizing continuous action space for on-policy optimization," in *Proc. 34th AAAI Conf. Artif. Intell., (AAAI), 32nd Innov. Appl. Artif. Intell. Conf., (IAAI), 10th AAAI Symp. Educ. Adv. Artif. Intell., (EAAI)*, New York, NY, USA: AAAI Press, Feb. 2020, pp. 5981–5988, doi: 10.1609/aaai.v34i04.6059.
[14] F. R. Yu and Y. He, *Reinforcement Learning and Deep Reinforcement Learning*. Cham, Switzerland: Springer, 2019, pp. 15–19.
[15] V. E. Ismailov, "A three layer neural network can represent any multivariate function," *J. Math. Anal. Appl.*, vol. 523, no. 1, Jul. 2023, Art. no. 127096. [Online]. Available: https://www.sciencedirect.com/science/article/pii/S0022247X23000999
[16] N. Ketkar, *Stochastic Gradient Descent*. Berkeley, CA, USA: Apress, 2017, pp. 113–132.
[17] S. Zhang and R. S. Sutton, "A deeper look at experience replay," in *Proc. Deep Reinforcement Learn. Symp. (NIPS)*, 2017. [Online]. Available: https://sites.google.com/view/deeprl-symposium-nips2017/home and https://arxiv.org/abs/1712.01275
[18] M. Hoffmann and P. Kryszkiewicz, "Reinforcement learning for energy-efficient 5G massive MIMO: Intelligent antenna switching," *IEEE Access*, vol. 9, pp. 130329–130339, 2021.
[19] *Base Station (BS) Radio Transmission and Reception (Release 18)*, Standard 3GPP, TS 38.104 v.18.2.0, 3GPP, Jun. 2023.
[20] S. Zhang, R. Zhang, and T. J. Lim, "Massive MIMO with per-antenna power constraint," in *Proc. IEEE Global Conf. Signal Inf. Process. (GlobalSIP)*, Dec. 2014, pp. 642–646.
[21] Z. Hanzaz and H. D. Schotten, "Performance evaluation of link to system interface for long term evolution system," in *Proc. 7th Int. Wireless Commun. Mobile Comput. Conf.*, Jul. 2011, pp. 2168–2173.
[22] B. Bossy, P. Kryszkiewicz, and H. Bogucka, "Optimization of energy efficiency in the downlink LTE transmission," in *Proc. IEEE Int. Conf. Commun. (ICC)*, May 2017, pp. 1–6.
[23] S. Willhammar, J. Flordelis, L. Van Der Perre, and F. Tufvesson, "Channel hardening in massive MIMO: Model parameters and experimental assessment," *IEEE Open J. Commun. Soc.*, vol. 1, pp. 501–512, 2020.
[24] *Deliverable D6.1, Simulation Guidelines v1.0*, document ICT-317669-METIS/D6.1, METIS, Mobile and Wireless Communications Enablers for the Twenty-Twenty Information, 2013.
[25] P. Kryszkiewicz, "Efficiency maximization for battery-powered OFDM transmitter via amplifier operating point adjustment," *Sensors*, vol. 23, no. 1, p. 474, Jan. 2023. [Online]. Available: https://www.mdpi.com/1424-8220/23/1/474
[26] T. Takase, S. Oyama, and M. Kurihara, "Why does large batch training result in poor generalization? A comprehensive explanation and a better strategy from the viewpoint of stochastic optimization," *Neural Comput.*, vol. 30, no. 7, pp. 2005–2023, Jul. 2018, doi: 10.1162/neco_a_01089.
[27] Z. Hanzaz and H. D. Schotten, "Analysis of effective SINR mapping models for MIMO OFDM in LTE system," in *Proc. 9th Int. Wireless Commun. Mobile Comput. Conf. (IWCMC)*, Jul. 2013, pp. 1509–1515.

**MARCIN HOFFMANN** (Graduate Student Member, IEEE) received the M.Sc. degree (Hons.) in electronics and telecommunication from the Poznań University of Technology, in 2019, where he is currently pursuing the Ph.D. degree with the Institute of Radiocommunications. He is also gaining scientific experience by being involved in both national and international research projects. His research interests include the utilization of machine learning and location-dependent information for the purpose of network management.

**PAWEL KRYSZKIEWICZ** (Senior Member, IEEE) received the M.Sc. and Ph.D. degrees (Hons.) in telecommunications from the Poznań University of Technology (PUT), Poland, in 2010 and 2015, respectively. He is currently an Associate Professor with the Institute of Radiocommunications, PUT. He was involved in a number of international research projects. His research interests include multicarrier signal design for green communications and problems related to the practical implementation of massive MIMO systems.

## 7.11 Publication [P11]

M. Hoffmann and M. Dryjański, "Energy Efficiency in Open RAN: RF Channel Reconfiguration Use Case," *IEEE Access*, vol. 12, pp. 118493–118501, 2024.

MNiSW Points: 100

Number of citations:

- according to Web of Science: 1
- according to Google Scholar: 5

mgr inż. Marcin Hoffmann
Instytut Radiokomunikacji, Politechnika Poznańska
ul. Polanka 3, 60-965 Poznań

Poznań, 3 września 2024 r.

# OŚWIADCZENIE W SPRAWIE AUTORSTWA PRACY

Oświadczam, że w pracy:

*M. Hoffmann, M. Dryjański, "Energy Efficiency in Open RAN: RF Channel Reconfiguration Use Case," IEEE Access, tom 12, strony 118493-118501, sierpień 2024*

mój udział polegał na:

- Zaproponowaniu algorytmu wyłączania anten w formie rAppa zgodnego z architekturą O-RAN i wykorzystującego głębokie uczenie ze wzmocnieniem do optymalizacji efektywności energetycznej sieci Massive MIMO
- Współudziale w przygotowaniu tekstu artykułu
- Przeprowadzeniu symulacji komputerowych i opracowaniu wyników
- Dyskusjach i poprawkach artykułu na podstawie recenzji

Mój procentowy udział w powstanie pracy szacuję na: 60%

.....

Podpis

dr inż. Marcin Dryjański
Rimedo Labs
ul. Polanka 3, 61-131 Poznań

Poznań, 3 września 2024 r.

# OŚWIADCZENIE W SPRAWIE AUTORSTWA PRACY

Oświadczam, że w pracy:

*M. Hoffmann, M. Dryjański, "Energy Efficiency in Open RAN: RF Channel Reconfiguration Use Case," IEEE Access, tom 12, strony 118493-118501, sierpień 2024*

mój udział polegał na:

- Przygotowaniu treści do rozdziałów: *II. HOW TO INCREASE EE IN O-RAN?, III B. COOPERATION WITH xApps/NEAR RT CONTROL LOOP, IV B. CHALLENGES,*
- Współtworzeniu treści do rozdziałów: *I. INTRODUCTION, III. OPEN RAN rAPPS FOR INCREASING NETWORK ENERGY EFFICIENCY, VI. CONCLUSION*
- Współpracy przy tworzeniu koncepcji artykułu
- Dyskusje i poprawki po recenzjach
- Przeglądzie artykułu

Mój procentowy udział w powstanie pracy szacuję na: 40%

Dryjański

.....

Podpis

IEEE Access
Multidisciplinary ⋮ Rapid Review ⋮ Open Access Journal

Received 5 August 2024, accepted 19 August 2024, date of publication 26 August 2024, date of current version 3 September 2024.

*Digital Object Identifier 10.1109/ACCESS.2024.3449700*

RESEARCH ARTICLE

# Energy Efficiency in Open RAN: RF Channel Reconfiguration Use Case

**MARCIN HOFFMANN[1,2], (Member, IEEE), AND MARCIN DRYJAŃSKI[1], (Senior Member, IEEE)**

[1]Rimedo Labs, 61-131 Poznan, Poland
[2]Institute of Radiocommunications, Poznan University of Technology, 60-965 Poznan, Poland

Corresponding author: Marcin Hoffmann (marcin.hoffmann@put.poznan.pl)

This work was supported in part by the Polish Ministry of Education and Science in terms of Publication Fee and Computer Simulations under Grant 0312/SBAD/8167, and in part by the Rimedo Labs own budget in terms of algorithm design.

**ABSTRACT** Recently, energy efficiency (EE) has been pointed out as one of the key requirements within mobile networks. The development of intelligent algorithms providing Radio Access Networks (RAN) with EE features is possible when having access to the Key Performance Indicators (KPIs), and proper control actions, e.g., cell on/off switching, or Radio Frequency (RF) channel reconfiguration. These features together with a Machine Learning (ML) framework are available in the O-RAN architecture. This paper provides an overview of the EE framework according to the use cases specified by the O-RAN ALLIANCE. It is followed by the implementation of the Energy Saving rApp (ES-rApp). The rApp utilizes Deep Q-Learning (DQL) to increase EE through intelligent RF channel reconfiguration. Simulation results show up to a 24.8% EE gain over the static RF Channel Configuration (RCC).

**INDEX TERMS** Open RAN, 5G, energy efficiency, RAN intelligent controller, deep Q-learning, massive MIMO.

## I. INTRODUCTION

Recently, Energy Efficiency (EE) has become one of the key topics within RAN [1]. It is currently on the industry and research agendas. As high user throughput is targeted within 5G and beyond networks, an increasing number of energy-consuming hardware is deployed. Moreover, energy-efficient RAN must offer a high Quality-of-Service (QoS) to the network users. The Possibility of dynamically controlling the used resources and hardware by adapting its usage to the actual traffic demand, would bring significant benefits to the Mobile Network Operators (MNOs). In this perspective, Energy Saving (ES) mechanisms play a crucial role. They are involved in all layers and domains within RAN, from energy-efficient hardware, through the cloud, software stack, and orchestration [2]. Significant efforts have been put in during the standardization phase of 5G New Radio (NR) by 3GPP within Release-18 onwards to provide MNOs with unified ES mechanisms [3]. The most recent example related to beyond 5G standardization which relates significantly to energy consumption is Integrated Sensing and Communications (ISAC) [4]. This is motivated by the fact that ISAC utilizes dedicated hardware to perform both functionalities, e.g., M-MIMO downlink communications, and radar [5].

Energy savings come at the cost of less available resources, which may impact the overall performance of the system. Thus, the optimization goal is typically defined taking both of these into account. For this purpose, EE is usually defined as a ratio between the average user throughput and average power consumption. EE monitoring can help MNOs balance the user throughput-power consumption tradeoff to lower energy costs or reduce carbon footprint. However, to enable intelligent and case-dependent EE optimization, algorithms need access to network interfaces, both for monitoring and control purposes. There are various options possible to improve ES in RAN, e.g., using legacy RAN built on physical hardware. They are, however, of low efficiency due to the

The associate editor coordinating the review of this manuscript and approving it for publication was Adamu Murtala Zungeru.

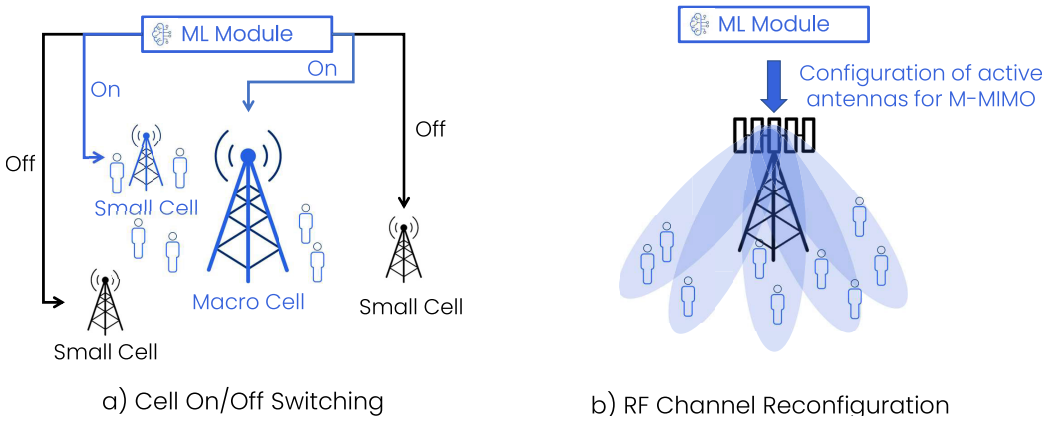


**FIGURE 1.** O-RAN use cases aimed at providing energy savings a) COOS b) RCR.

dedicated capacity allocated and powered on all the time, and limited management capabilities offered by incumbent RAN vendors. As an alternative, the Open RAN concept fits here better with virtual components, open interfaces, and unified native intelligence enabling multi-vendor competition and programmability [6]. A specific and industry-wide adopted realization of Open RAN is defined by O-RAN ALLIANCE and referred to as O-RAN. In the O-RAN standardization and development effort, EE is one of the key requirements, namely, the O-RAN ALLIANCE is currently providing means to support ES topics [7], e.g., with the use of centralized ES policies.

The key aspect of O-RAN is to embed native intelligence, through the use of a RAN Intelligent Controller (RIC), which is standardized in two flavors, namely a Non-Real Time RIC (Non-RT RIC) and Near-Real Time RIC (Near-RT RIC), which operate in timescales of above 1 s, and between 10 ms and 1 s respectively [8]. Both RICs serve as platforms for the so-called RIC applications, which can be developed either by the RIC vendors themselves or by third parties: rApps for Non-RT RIC, and xApps for the Near-RT RIC. xApps and rApps can utilize ML algorithms and fit well for addressing the ES aspects, e.g., xApps for symbol-level micro sleeps, and rApps for algorithms that perform hardware reconfiguration, like scaling down the antenna array.

In the literature, there are some works on the O-RAN architecture with a focus on the utilization of ML algorithms. For example, in [6] a Deep Reinforcement Learning (DRL) agent is proposed for resource allocation, and in [9], ML is utilized to predict Service-Level Agreement violation. However, both works do not cover the topic of EE. EE, in turn, is mentioned in [10], however, not as a main topic, but as one of the many use cases. In that paper, it is achieved through the per Resource Block (RB) power allocation, which is not currently planned to be supported according to the O-RAN ALLIANCE specifications. The existing literature lacks an overview of EE use cases that are agreed upon in the O-RAN community as possible for implementation according to [11]. These use cases are, among others, Cell On/Off Switching (COOS), which is well investigated in the research community, and RF Channel Reconfiguration (RCR) in Massive Multiple-Input Multiple-Output (M-MIMO) scenarios, also known as antenna selection (see Fig. 1.)

The existing RCR algorithms rely widely on the ML techniques, e.g., [12]. However, these solutions require detailed Channel State Information (CSI), i.e., radio channel coefficients between the user and each of the Base Station's (BS's) antennas. Such physical layer data is not available according to the 3GPP, and O-RAN specifications, which makes those algorithms hard to implement in practice. On the other hand, there is an algorithm that utilizes deep learning to predict RCC based on the average channel gain and precoder weights [13]. Those weights are hard to be exposed in real-time by the BS while considering adaptive beamforming schemes like Zero Forcing, or Maximum Ratio Combining. Of course, they can be obtained for the Grid of Beams (GoB) beamforming, where a strictly specified set of weights is used, but as fixed values, they do not contribute to the ML model. Finally, RCR can be performed based on the cell load threshold as proposed in [14], but this approach offers neither flexibility nor high performance. Thus, in this paper, the authors propose an intelligent RCR that not only utilizes ML to optimize EE defined as the ratio between the user average throughput and average power consumption, but also takes as input features that are exposed by the BS according to the O-RAN ALLIANCE and 3GPP specifications [11], [15].

The aim of this paper is, first, to discuss the role of O-RAN in providing ES, and improving EE of the 5G and beyond networks concerning the O-RAN ALLIANCE and 3GPP. Secondly, to propose an ES-rApp that utilizes DRL to perform RCR aimed at the maximization of EE. The proposed ES-rApp utilizes input parameters that are aligned with the O-RAN ALLIANCE use-case definition, and exposed by the BS according to the 3GPP specifications. In addition, most of the current implementations for a particular use case are realized with a single xApp or rApp. Therefore, the third novelty presented in this paper

is the interworking of an xApp - rApp tandem. The rApp oversees their operation and controls the xApp's operation for fine-tuning the performance. In Sect. II authors discuss the role of O-RAN architecture in providing ES at the feature level, i.e., COOS, and RCR. It is followed up by an overview of the generalized O-RAN framework for the development of ES-rApps in Sect. III. Here, the authors also highlight the importance of cooperation between rApps and xApps, to support ES mechanisms. Based on the general framework, in Sect. IV, a detailed description of an O-RAN-compliant ES-rApp is provided. It is supported by numerical results showing the benefits of the solution presented in Sect. V. The paper is summarized in Sect. VI.

The contribution of the paper can be summarized as follows:

- We provide the description and discuss the role of O-RAN in the improvement of EE in the current 5G and future 6G networks based on both O-RAN ALLIANCE and 3GPP specifications.
- We propose an ES-rApp that unlike [12] and [13] is design in compliance with O-RAN ALLIANCE and 3GPP specifications. The proposed ES-rApp utilizes DRL for RCR, which allows for higher EE gains than the load-based solution [14].
- We propose a scheme of cooperation between the ES-rApp that performs RCR in a large timescale and BMM xApp that performs near-real-time user-to-beam association [8], [16].

## II. HOW TO INCREASE EE IN O-RAN?

As mentioned in the previous section, O-RAN enables the introduction of ES optimization algorithms through Non-RT and Near-RT RICs. More specifically, Non-RT RIC, along with rApps, belongs to the management plane, while Near-RT RIC serves as a platform for xApps, abstracting out part of the RAN and enabling direct control of BS entities. There are two control interfaces associated with those: A1, which operates between Non-RT RIC and Near-RT RIC, facilitating policy management, enrichment information transfer, and ML model updates; and E2, which connects Near-RT RIC with RAN nodes, serving as a control loop responsible for executing commands and gathering measurements from BS nodes (in O-RAN called E2 Nodes). The O1 interface is responsible for configuration and management. It connects the Service Management and Orchestration (SMO) system in which Non-RT RIC resides with RAN nodes [17]. Through the abovementioned framework and interfaces, O-RAN enables the development of use case-dependent xApps, and rApps aiming at the improvement of EE, e.g., by disabling some parts of RAN hardware during low traffic load. The decisions to switch off hardware to save energy are typically taken based on long-term trends and statistics. Therefore, ML-based schemes can significantly help in improving ES schemes by, e.g., predicting traffic changes before they happen. O-RAN specifications [11] provide the ES use cases that define general schemes and signaling flows that the algorithms (deployed as xApps and rApps) shall fit in.

Fig. 1-a shows the concept of COOS, where the idea is to shut down (or put in sleep mode) the whole cell. In the figure, pico/small cells serve as the capacity layer and are subject to switching off or on depending on the traffic needs. Note that COOS does not only concern pico/small cells - it refers to a "cell" generically. Therefore, it can be utilized in other scenarios, e.g., switching off/on a regular carrier, or a Component Carrier in the Carrier Aggregation scenario. The cells subject to switching off are capacity cells, while the coverage cell should always be on. The other O-RAN use case, presented in Fig. 1-b is defined as RCR, where instead of switching off/on the whole cell, the algorithm switches off/on some of the RF channels that correspond to the number of beams in a M-MIMO cell. If the traffic is low, the number of beams can be decreased, not lowering users' QoS.

In addition to the definition of use cases, O-RAN provides a framework for the operation of various algorithms. This is realized through the separation of concerns using Near-RT and Non-RT RIC, and standardized interfaces, like, O1, A1, and E2. When working with ES it is important to consider that those algorithms cannot work in a vacuum. The decision to switch off the whole or part of the BS needs to be coordinated with other features [18]. Such coordination and a holistic approach to ES help to avoid instability in the network.

## III. OPEN RAN rAPPS FOR INCREASING NETWORK ENERGY EFFICIENCY

The traffic load varies in the mobile network over the day, or even between different days of the week. It is related to the users' mobility and behavior, e.g., from Monday to Friday people work in city centers, thus usually BSs therein are highly loaded from morning till afternoon. On the other hand, a lot of people have their homes in the suburbs, thus BSs deployed therein remain almost empty until late afternoon. This creates an opportunity to either switch off entire cells or perform RCR to increase EE, which in O-RAN architecture can be implemented in the form of rApp or xApp. Considering the ES applications, one should note that the reconfiguration of the O-RAN Radio Unit (O-RU), by either switching on/off or changing the RCC requires some transition time, and sometimes even a restart of the device. Thus, we propose to implement ES algorithms in the form of an ES-rApp. The generalized framework for the deployment of the ES-rApp is depicted in Fig. 2. The rApp is hosted in a Non-RT RIC residing inside the SMO, along with a Collection and Control (CC) entity. They are used to provide the ES-rApp with data captured from E2 Nodes to perform control actions (e.g., switching off/on of cells, or reconfiguration of RF channels).

### A. INFORMATION FLOW AND RL FRAMEWORK

Fig. 2-a depicts the signaling flow (based on O-RAN documentation [11]) between Non-RT RIC, with an ES-rApp, and other O-RAN entities. At first, the ES-rApp

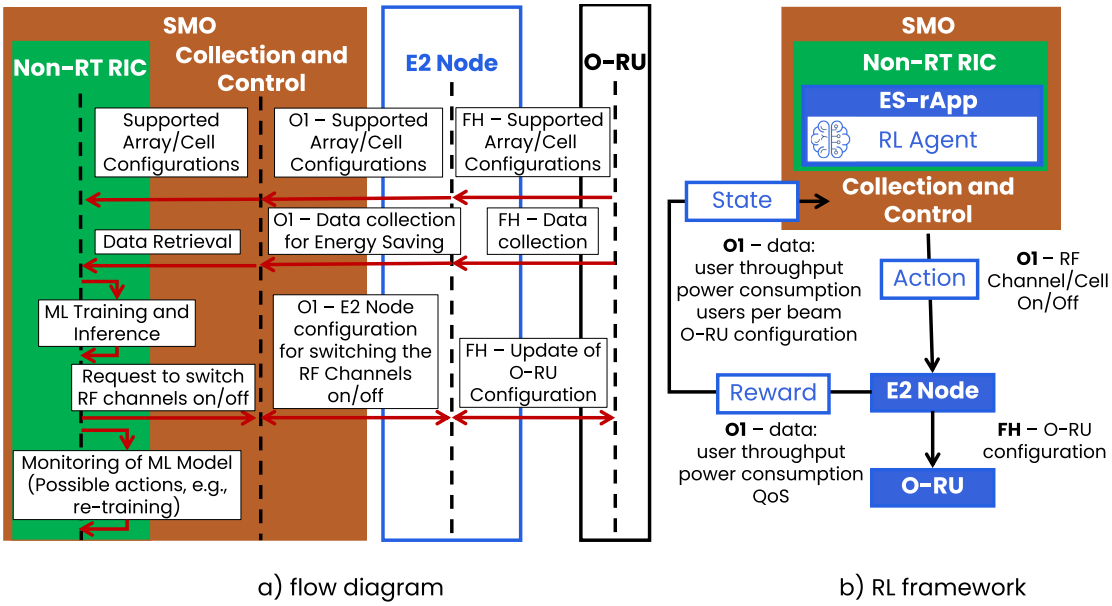


**FIGURE 2.** Information flow diagram (a) and corresponding RL framework (b) applicable to COOS and RCR O-RAN use-cases.

obtains information about supported configurations of O-RU, e.g., sleeping modes, and RCCs. This is done through the hierarchical connection utilizing the O1 interface between SMO and E2 Node (i.e., a BS node connected through the E2 interface to RIC), and the Open Fronthaul (O-FH) interface between E2 Node and O-RU. Next, the ES-rApp is configured to receive from E2 Node and O-RU, data compliant with the 3GPP specification [15]. The ES-rApp can monitor, e.g., cell load, power consumption, and user throughputs. The ES-rApp would then utilize the ML to process the collected data to dynamically switch off/on cells, or perform RCR. The resultant decision made by the ES-rApp is communicated to Non-RT RIC, which utilizes CC to change the configuration of O-RU via a cascade of O1, and O-FH. Both COOS and RCR affect the network performance. Thus, in the last stage, the ES-rApp utilizes a previously established O1 connection to evaluate network performance and retrain the ML model if needed.

The performance of the network after COOS or RCR actions is hard to predict based on analytical calculations. Thus, the ES-rApp must act in a trial-and-error manner, i.e., select O-RU configuration, observe the performance in terms of users' QoS or ES, and use this observation to update the ML model. This approach is known as RL, i.e., learning through interaction, which is proven to fit the O-RAN architecture [6]. To fulfill this requirement, the authors propose to use the RL framework as shown in Fig. 2-b. In this framework, a so-called agent (ES-rApp) interacts with the environment (E2 Nodes, O-RUs), by making actions (decisions on O-RU reconfigurations) based on the state (KPIs, e.g., cell-load), and observes the reward (KPIs, e.g., power consumption, user throughput), as depicted in Fig. 2-b. The whole process is cyclic, i.e., the agent recognizes the state, takes action and observes the reward. After multiple iterations, the rApp is trained on how to configure O-RU to maximize rewards, e.g., EE.

### B. COOPERATION WITH xApps/NEAR RT CONTROL LOOP

ES features should interact with other Radio Resource Management (RRM) algorithms. The decision to switch off some of the resources needs to be coordinated. Fig. 3 shows an example where a Beam Mobility Management xApp (BMM-xApp) operates within a near-RT control loop, and the ES-rApp operates within the non-RT control loop. The ES-rApp aims to intelligently adjust the configuration of the antenna array based on the network state, to maximize EE. The BMM-xApp is responsible for switching the users between beams based on the location information, to reduce

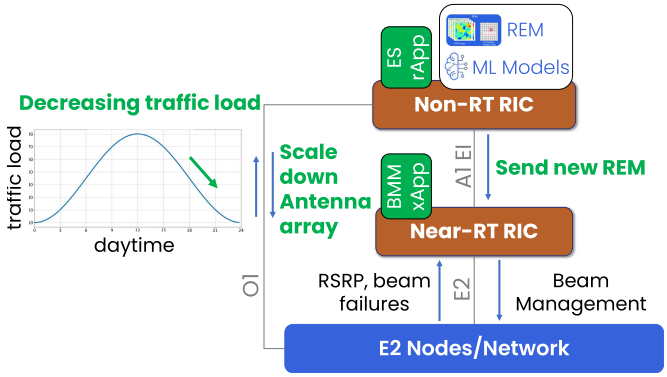


**FIGURE 3.** Cooperation between rApp and xApp.

the number of beam reselections and radio link failures [8], [16].

The ES-rApp and BMM-xApp cooperate hierarchically. The former performs the reconfiguration of the M-MIMO BS within relatively long intervals. BMM-xApp provides fast decisions on user-to-beam association and relies on the Radio Environment Map (REM), representing the spatial distribution of received power associated with each beam. When the ES-rApp changes the array configuration, the number and shape of beams also change. Thus, the BMM-xApp must be equipped with different sets of REMs proper for each available array configuration. When the ES-rApp decides to change the array configuration, an appropriate notification is sent to the BMM-xApp.

One should note that when there are multiple Apps in a single system, conflicts may occur. Beyond obvious ones, like two Apps concurring to change the same parameters, others, like different objectives set for two Apps, can be challenging, e.g., one App maximizes saved energy, while another maximizes user performance. If both work concurrently, they can constantly modify the network behavior, causing instabilities and making it difficult for both of them to converge. Such conflicts should then be considered on multiple levels, between two rApps, between two xApps, and between rApp and xApp [19]. One approach is to jointly design a set of Apps, so that they do not come into conflict by design, but rather work in a coordinated manner - which is the case here. The other is to design conflict resolution or mitigation functions, which are out of the scope of this paper.

## IV. IMPLEMENTATION OF ML-BASED ES-rApp

In the previous section, the general information flow and RL framework were introduced to provide an overview of the environment where the ES-rApp is deployed. In this section, we propose an implementation of an ES-rApp aiming at the maximization of EE through dynamic RCR, according to the input/output data, and architecture requirements defined in the O-RAN ALLIANCE use-case [11].

### A. DESIGN OF THE ES-rApp

As per Fig. 2, ES-rApp is deployed in Non-RT RIC. Its main goal is to perform an O-RU antenna array selection through the cascade of O1 and O-FH interfaces to maximize EE. The algorithm aims to adjust the number of ARCs, taking into account the dependencies between O-RU configuration, power consumption, user throughput, PRB utilization, and distribution of users over beams, provided to ES-rApp through the O1 interface. This approach allows the reconfiguration of O-RU to enable both high ES during low-load hours and preserve users' QoS during peak-load hours. The decisions of RCR may result in modifications of the maximum number of spatial streams, or the O-RU antenna Tx power, thus they should be made within the non-RT control loop. The ES-rApp fits in the RL framework discussed in Sec. III-A, i.e., it performs the following steps periodically: observes multiple KPIs (state $\mathbf{s}$), based on that, selects one of the RCCs (action $a$) and measures its performance in terms of EE (reward $r$). We propose the following detailed definitions of RL framework components:

- **An Environment** is a single cell of an O-RAN compliant network equipped with an M-MIMO antenna array.
- **An Agent** is the ES-rApp placed in the Non-RT RIC aiming at EE maximization through dynamic RCR. The agent both takes actions and monitors their performance with the use of the CC mechanism that provides the termination of O1 and O-FH.
- **An Action** is defined as one of the possible RCCs at O-RU and is enforced by the agent via O1 and O-FH. We assumed a discrete action space $\mathcal{A} = \{a_1, a_2, a_3\}$, where actions $a_1$, $a_2$, and $a_3$ corresponds with 100%, 50%, and 25% of Active RF Channels (ARCs) respectively. To compensate for beamforming gain variations related to scaling up/down the number of active antenna elements, a constant Tx power for the whole array is assumed.
- **A State s** is constituted as a tuple containing one-hot encoded current RCC (oneHotRCR) and several KPIs defined according to the 3GPP specifications [15]: mean PRB utilization over all M-MIMO layers within the whole cell (RRU.PrbTotSdmDl, scaled to range $0-1$), means power consumption per carrier (PEE.AvgPower, divided by the maximum power consumption measured under full cell load), average downlink (DL) user throughput per cell (DRB.UEThpDl, divided by $10^7$), the total number of users connected to the cell (RRC.ConnMean), and the number of users associated with each beam (L1M.SSBBeamRelatedUeNbr.<beam index>) reflecting their spatial distribution (in case of reduced number of beams caused by RCR values are zero-padded). In detail, $\mathbf{s}$ = (oneHotRCR, RRU.PrbTotSdmDl, PEE.AvgPower, DRB.UEThpDl, RRC.ConnMean, L1M.SSBBeamRelatedUeNbr.<min beam index>, $\cdots$ L1M.SSBBeamRelatedUeNbr.<max beam index> )
- **A Reward** is defined as EE, being the ratio between average DL user throughput, and average power consumption per carrier measured over an observation period, i.e., $r = \frac{\text{DRB.UEThpDl}}{\text{PEE.AvgPower}}$. The KPIs related to the computation of the reward are obtained through O1 and are compliant with [15].

The above definition of the RL framework components is based on the KPIs defined in 3GPP specifications, that are available in an O-RAN M-MIMO network through the O1 interface. This allows ES-rApp to be independent of any specific data models, e.g., power consumption. On the other hand, the proper KPIs can be generated through computer simulations to enable evaluation of the proposed ES-rApp.

To implement an RL agent inside ES-rApp, we utilize Deep Q-Network (DQN), which is adequate for dealing with discrete and finite action space. Therefore, DQN fits well

for selecting one of several RCCs by ES-rApp. It estimates the expected reward (EE) associated with each action (i.e., possible RCCs) in the observed state (see Fig. 4). Usually, consecutive states in RL affect each other. However, in the case of RCR, ES-rApp can select any possible configuration independently of the previous decisions, i.e., only based on observed KPIs (state). Thus, it is enough for ES-rApp to be focused on the maximization of EE separately in each state. This approach is known as myopic DQL. DQN is built of an input layer, two hidden layers and an output layer. The input layer takes the features according to the state definition, i.e., there are 7 + <number of beams> inputs. Each hidden layer is the so-called dense layer built of 256 neurons (the output of a single neuron from the former layer is provided as input to every neuron in the following layer) and is followed by the Rectified Linear Unit. The output layer has a size equal to the number of elements in the set representing the action space. In this case, $|\mathcal{A}| = 3$), and maps directly on EE expected to be achieved while selecting a particular action $a$ in a given state $\mathbf{s}$. Based on [20] the computational complexity of the utilized dense layer is $O(n \cdot m)$, where $m$ is the layer's input size, and $n$ is the layer's output size. In order to ensure stable network operation, the RCR is expected to be done by rApp within the timescale of minutes. This enables rApp to control multiple cells. However, evaluation of such scenarios is considered for future work.

### B. CHALLENGES

During the design of the ES-rApp, several challenges need to be taken into account:

#### 1) SWITCHING OFF RF CHANNELS

changes the properties of the antenna array that enforces whole O-RU reconfiguration, e.g., the number of supported beams, or the number of possible layers.

#### 2) THE RL ALGORITHM

must be supported with mechanisms that prevent testing of obviously wrong solutions, e.g., during busy hours, the configuration with 20% of ARCs should never be tested.

#### 3) THE rApp

must strictly cooperate with other xApps, e.g., with BMM-xApp. Changing the O-RU configuration usually requires its restart, and the users should be temporarily offloaded to other beams to ensure QoS fulfillment.

#### 4) SWITCHING OFF RF CHANNELS

results in fewer beams, thus the overall Tx power is decreased, which affects the coverage. Thus, the power of the remaining beams needs adjustment to compensate. One approach is to establish a constant total power for the whole antenna array, but in-depth studies are needed related to the power amplifiers' operation points and potential non-linear distortion.

**TABLE 1. Simulation parameters.**

| Parameter | Value |
|---|---|
| Carrier Frequency | 3.5 GHz |
| Bandwidth | 100 MHz |
| Number of Resource Blocks | 273 |
| Antenna height | 25 m |
| Cell radius | 500 m |
| Tx power | 55 dBm |
| Antenna array | rectangular $(8 \times 8)$ |
| Path loss model | 3GPP UMa [21] with spatial correlation [22] |
| Traffic model | sinusoidal (from 5 to 150 UEs) |
| Power consumption model | 3GPP power consumption model [3] |
| Full-load power consumption | 1120 W [11] |

## V. SIMULATION RESULTS

The proposed ES-rApp was verified in a python-based simulation environment developed by the authors, considering DL in an Urban Macrocell (UMa) of an O-RAN network according to the scenario definition and BS configuration in [3] and [21]. The UMa has a radius of 500 m and operates in the n78 band, utilizing 100 MHz bandwidth split into 273 RBs, at the carrier frequency of 3.5 GHz. BS is installed at a height of 25 m and transmits with a total Tx power of 55 dBm, it utilizes the GoB scheme, i.e., a fixed set of up to 32 predefined beams. The user is associated with a beam that provides the highest Rx power. The beam's Rx power is calculated based on the UMa path-loss model and array radiation pattern from the 3GPP specification [21]. In addition, a spatially correlated shadowing model is used independently for each beam, which models the presence of obstacles [22]). Within a single beam, radio resources are split equally between users, with a limit of 30 RBs per user. We assume that users do not have specified QoS requirements for radio resources. The number of ARCs can be scaled down to $8 \times 4$ (32 elements), or $8 \times 2$ (16 elements), which supports 16, and 8 beams respectively. According to the initial studies, in [11], the 64 antenna O-RU during full load consumes the power of 1120 W. This value changes with the traffic load and can be scaled down by reducing the number of ARCs. Based on the 3GPP power consumption model described in [3] the power consumption for such a 64 antenna O-RU is given by:

$$P_{\mathrm{dl}}[\mathrm{W}] = 630 \cdot s_{\mathrm{a}} + 360 \cdot s_{\mathrm{a}} \cdot s_{\mathrm{f}} + 220 + P_{\mathrm{tx}}, \qquad (1)$$

where $s_{\mathrm{a}}$ is the fraction of active antennas, $s_{\mathrm{f}}$ is the cell load, and $P_{\mathrm{tx}}$ is the Tx power. Simulation parameters are summarized in Table 1. The simulations are arranged in so-called episodes. An episode corresponds to one day and consists of 144 steps, i.e., the decision on RCR is made by the ES-rApp once every 10 minutes. Within a single episode the number of users in the cell changes according to the sinusoidal traffic profile, from 5 at midnight to 150 at noon. At every step, a number of users are randomly placed over the cell area, to reflect the real network where the spatial placement of users in a cell varies between days. Next the ES-rApp selects the RCC and observes the reward. Finally, a state-action-reward tuple is put into the database.

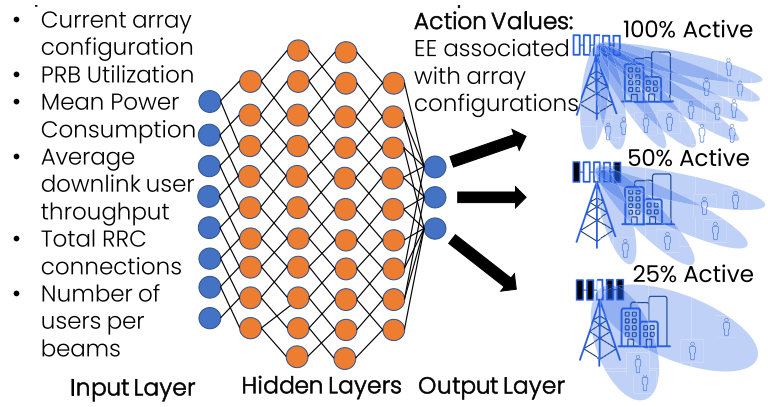


**FIGURE 4.** Input and output features of DQN utilized by the ES-rApp.

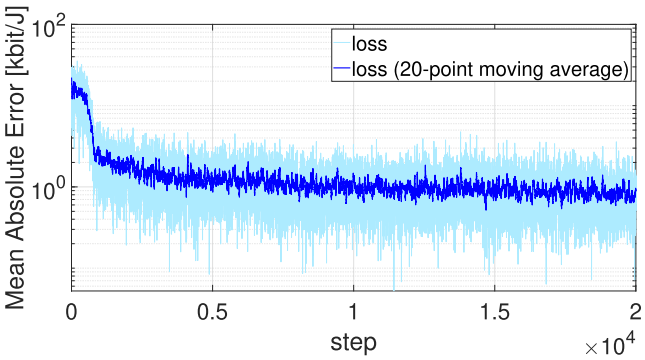


**FIGURE 5.** Offline training loss for ES-rApp, both raw and processed through a 20-point moving average.

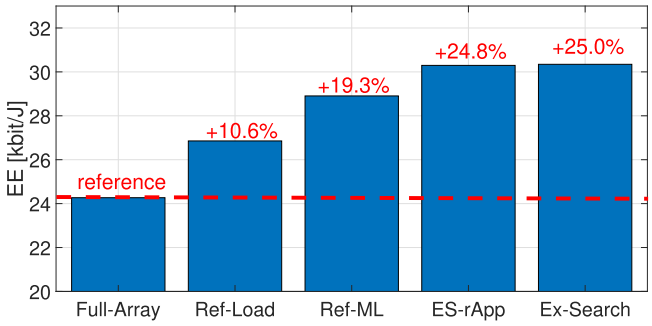


**FIGURE 6.** Energy Efficiency averaged over 50 days.

First, we captured the training data by exploring different RCCs over 15 days (episodes), which resulted in 2160 training samples. We used them to train the DQL agent offline, using batch size equal to 4, and Mean Absolute Error loss function. The training loss (both raw, and smothen with a 20-point moving average) is depicted in Fig. 5. It can be seen that after 20000 training steps (iterations of stochastic gradient descent), the mean absolute error of EE prediction stabilizes at the level of about 1 kbit/J.

After the training phase, we compared the proposed ES-rApp against two state-of-the-art algorithms: Ref-Load algorithm [14], which scales down the number of ARCs when PRB utilization is below 10%, and Ref-ML algorithm [13] selecting RCC based on the average channel gain and precoder weights. As Ref-ML originally has a constraint on the minimum user throughput, for a fair comparison, we set its goal to maximize EE, which already cares about users' QoS. In addition, we have evaluated a Full-Array scenario with 64 ARCs, serving as a reference level for EE gains, and Exhaustive Search Ex-Search that evaluates each possible RCC under identical placement of users, to select one providing the highest EE. The Ex-Search stands for the upper bound on EE gains. Before capturing the results, we trained both ES-rApp and Ref-ML with the use of the data captured during a 15-day-long simulation. Fig. 6 presents a comparison between EE averaged over 50 days achieved by each of the evaluated algorithms. All algorithms provide EE gains over Full-Array. A simple PRB threshold-based Ref-Load provides only a 10.6% EE gain. Thus, it is more beneficial to utilize ML-based methods that achieve 19.3% and 24.8% EE gains for Ref-ML and ES-rApp respectively. Here the set of input features plays a crucial role. The Ref-ML utilizes precoder weights as one of those. However, under GoB they are constant and do not contribute much to the model accuracy. On the other hand, the proposed ES-rApp utilizes a set of input features that is proper for GoB beamforming, e.g., the number of users per beam. As a result, it can improve EE by 24.8% compared to the Full-Array and performs close to the upper bound defined by the Ex-Search, i.e., the absolute difference in EE is only about 50 bit/J.

To better understand the resultant average EE, in Fig. 7, we compared its components: the power consumption and average user throughput achieved by the tested algorithms over the day. Ref-ML is characterized by the lowest power consumption of up to about 1.1 kW, compared to almost 1.4 kW consumed by Full-Array. However, it comes at the cost of poorer throughput during peak load hours. On the other hand, the Ref-Load algorithm preserves users' throughput but acts cautiously, and does not fully utilize the opportunity to increase EE. The proposed ES-rApp provides both high ES during low-load hours and high throughput

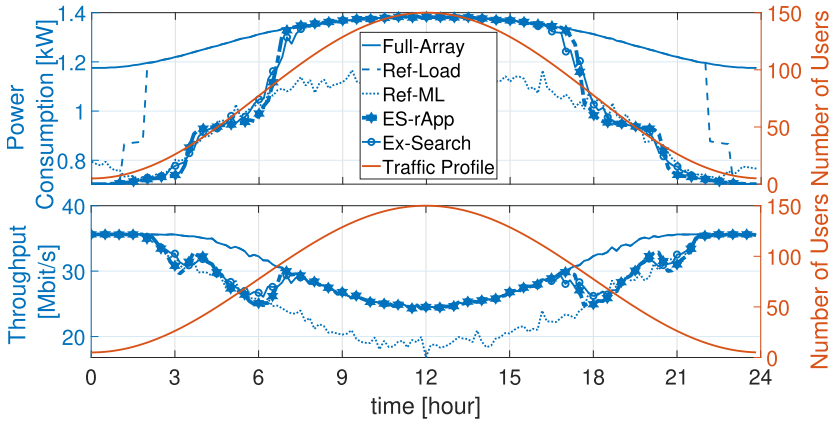


**FIGURE 7.** Traffic profile, power consumption (upper subplot), and average user throughput (lower subplot) achieved over the daytime. Results are averaged over 50 days.

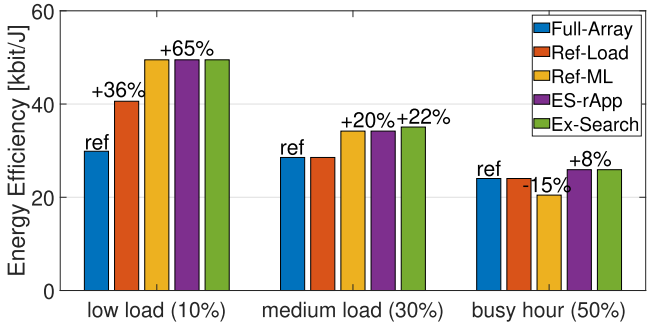


**FIGURE 8.** Relation between cell load and Energy Efficiency, based on the ETSI traffic profile [23]. Results are averaged over 50 days.

during peak load. Moreover, its RCR decisions are almost the same as the optimal ones derived by Ex-Search. Compared to Ref-Load, it is due to the utilization of ML, while compared to Ref-ML, due to the better selection of input features.

While, in Fig. 7 the network traffic is represented by the number of users it is beneficial to investigate the explicit relation between obtained EE and the cell load. In Fig. 8 there is a relation between achieved EE, and cell load for the proposed ES-rApp and reference algorithms. There are 3 load scenarios considered, according to the ETSI traffic profile [23]: low load, medium load, and busy hour that corresponds to the 10%, 30% and 50% of cell load respectively. The load is calculated for the Full-Array case in terms of mean PRB utilization over all M-MIMO layers within the whole cell (RRU.PrbTotSdmDl [15]). The results confirm the previous observations. The Ref-Load provides EE gains over Full-Array only under low load scenarios (about 36%) due to its cautious behavior. The Ref-ML provides EE gains over Full-Array compared to the proposed ES-rApp under low and medium load (about 65% and 20% respectively), while under busy hour tries to reduce the number of active antennas too much resulting in about 15% EE degradation compared to the Full-Array. Finally, the proposed ES-rApp achieves EE gains of 8% over the Full-Array also under busy hour load. Only under the medium load, EE obtained by the ES-rApp is lower than the one associated with an Ex-Search, i.e., 20% EE gain over the Full Array for ES-rApp versus 22% for the Ex-Search.

## VI. CONCLUSION

The O-RAN architecture acts as a key enabler for the implementation of ES features in 5G and beyond networks by providing a unified environment for the deployment of ES-oriented rApps and xApps. The environment includes interfaces for data CC, and ML features for model training, deployment, and inference. The O-RAN specifications provide a detailed description of ES use cases, including message flow between engaged entities and an ML framework. Based on all these, the authors have proposed an ES-rApp that performs RCR, using DQL to maximize EE. Due to the utilization of RL, ES-rApp can follow the hidden dependencies between O-RU configuration, power consumption, throughput, PRB utilization, and distribution of users over beams to intelligently scale up/down the number of ARCs. Such an intelligent reconfiguration of O-RU enables both high ES during low-load hours and preserving users' QoS during peak-load hours. The simulation results show up to 24.8% improvement in achieved EE while utilizing the proposed ES-rApp compared to the Full-Array. It also outperforms state-of-the-art algorithms: Ref-Load [14], and Ref-ML [13]. The future work aims at addressing aspects like scaling with a larger simulation environment (dozens of BSs); integration of the algorithm within a realistic setup using a commercial-grade RIC and RAN emulator; varying users' QoS profiles; or utilizing real-life traffic patterns and traffic demands. The other topic is to analyze multiple Apps working together to achieve energy saving in harmony within the hierarchy - i.e., a joint rApp/xApp operation. Finally, as the RIC framework should support various Apps from various vendors that achieve different goals, the authors see it as important to concern conflict mitigation.

## ACKNOWLEDGMENT

The research work related to Algorithm Design was founded by Rimedo Laboratories.

## REFERENCES

[1] S. Han, T. Xie, and I. Chih-Lin, "Greener physical layer technologies for 6G mobile communications," *IEEE Commun. Mag.*, vol. 59, no. 4, pp. 68–74, Apr. 2021.

[2] D. López-Pérez, A. De Domenico, N. Piovesan, G. Xinli, H. Bao, S. Qitao, and M. Debbah, "A survey on 5G radio access network energy efficiency: Massive MIMO, lean carrier design, sleep modes, and machine learning," *IEEE Commun. Surveys Tuts.*, vol. 24, no. 1, pp. 653–697, 1st Quart., 2022.

[3] *Study on Network Energy Savings for NR (Release 18)*, Standard TR 38.864 v.18.1.0, 3GPP, Mar. 2023.

[4] A. Kaushik, R. Singh, S. Dayarathna, R. Senanayake, M. Di Renzo, M. Dajer, H. Ji, Y. Kim, V. Sciancalepore, A. Zappone, and W. Shin, "Toward integrated sensing and communications for 6G: Key enabling technologies, standardization, and challenges," *IEEE Commun. Standards Mag.*, vol. 8, no. 2, pp. 52–59, Jun. 2024.

[5] A. Bazzi and M. Chafii, "On outage-based beamforming design for dual-functional radar-communication 6G systems," *IEEE Trans. Wireless Commun.*, vol. 22, no. 8, pp. 5598–5612, Jun. 2023.

[6] L. Bonati, S. D'Oro, M. Polese, S. Basagni, and T. Melodia, "Intelligence and learning in O-RAN for data-driven NextG cellular networks," *IEEE Commun. Mag.*, vol. 59, no. 10, pp. 21–27, Oct. 2021.

[7] "Open RAN technical priorities, focus on energy efficiency," Deutsche Telekom, Orange, Telefonica, TIM, Vodafone, Tech. Document O-RAN MoU, Jun. 2021. [Online]. Available: https://cdn.prod.website-files.com/60b1962ffda0a42f779c765b/60cd8e6f8dd92c298b891216_Open%2BRAN%2BTechnical%2BPriority%2BDocument%2B-%2BFinal%2BVersion.xlsx

[8] M. Hoffmann, S. Janji, A. Samorzewski, Ł. Kułacz, C. Adamczyk, M. Dryjański, P. Kryszkiewicz, A. Kliks, and H. Bogucka, "Open RAN xApps design and evaluation: Lessons learnt and identified challenges," *IEEE J. Sel. Areas Commun.*, vol. 42, no. 2, pp. 473–486, Feb. 2024.

[9] J. Thaliath, S. Niknam, S. Singh, R. Banerji, N. Saxena, H. S. Dhillon, J. H. Reed, A. K. Bashir, A. Bhat, and A. Roy, "Predictive closed-loop service automation in O-RAN based network slicing," *IEEE Commun. Standards Mag.*, vol. 6, no. 3, pp. 8–14, Sep. 2022.

[10] A. Giannopoulos, S. Spantideas, N. Kapsalis, P. Gkonis, L. Sarakis, C. Capsalis, M. Vecchio, and P. Trakadas, "Supporting intelligence in disaggregated open radio access networks: Architectural principles, AI/ML workflow, and use cases," *IEEE Access*, vol. 10, pp. 39580–39595, 2022.

[11] *O-RAN Network Energy Savings Use Cases Technical Report 1.0*, document TR O-RAN ALLIANCE WG1, Mar. 2023.

[12] B. Lin, F. Gao, S. Zhang, T. Zhou, and A. Alkhateeb, "Deep learning-based antenna selection and CSI extrapolation in massive MIMO systems," *IEEE Trans. Wireless Commun.*, vol. 20, no. 11, pp. 7669–7681, Nov. 2021.

[13] N. Rajapaksha, J. Mohammadi, S. Wesemann, T. Wild, and N. Rajatheva, "Minimizing energy consumption in MU-MIMO via antenna muting by neural networks with asymmetric loss," *IEEE Trans. Veh. Technol.*, vol. 73, no. 5, pp. 6600–6613, May 2024.

[14] P. Frenger and K. W. Helmersson, "Massive MIMO muting using dual-polarized and array-size invariant beamforming," in *Proc. IEEE 93rd Veh. Technol. Conf. (VTC-Spring)*, Apr. 2021, pp. 1–6.

[15] *Management and Orchestration; 5G Performance Measurements*, Standard 3GPP, TS 28.552 v.18.2.0, Mar. 2023.

[16] M. Hoffmann and P. Kryszkiewicz, "Beam management driven by radio environment maps in O-RAN architecture," in *Proc. IEEE Int. Conf. Commun. Workshops (ICC Workshops)*, Rome, Italy, 2023, pp. 54–59, doi: 10.1109/ICCWorkshops57953.2023.10283527.

[17] *O-RAN Architecture Description, v.8.0*, document O-RAN ALLIANCE, TS, O-RAN ALLIANCE WG1, Mar. 2023.

[18] M. Dryjanski and M. Szydelko, "A unified traffic steering framework for LTE radio access network coordination," *IEEE Commun. Mag.*, vol. 54, no. 7, pp. 84–92, Jul. 2016.

[19] C. Adamczyk and A. Kliks, "Conflict mitigation framework and conflict detection in O-RAN near-RT RIC," *IEEE Commun. Mag.*, vol. 61, no. 12, pp. 199–205, Dec. 2023, doi: 10.1109/MCOM.018.2200752.

[20] B. Shah and H. Bhavsar, "Time complexity in deep learning models," *Proc. Comput. Sci.*, vol. 215, pp. 202–210, Dec. 2022.

[21] *Study on Channel Model for Frequencies From 0.5 to 100 GHz (Release 17)*, Standard TS 38.901 v.17.0.0, 3GPP, Mar. 2022.

[22] C. Zhang, X. Chen, H. Yin, and G. Wei, "Two-dimensional shadow fading modeling on system level," in *Proc. IEEE 23rd Int. Symp. Pers., Indoor Mobile Radio Commun. (PIMRC)*, Sep. 2012, pp. 1671–1676.

[23] *Environmental Engineering (EE); Metrics and Measurement Method for Energy Efficiency of Wireless Access Network Equipment; Part 1: Power Consumption—Static Measurement Method*, Standard ETSI, ES 202 706-1, v1.7.1, ETSI, Aug. 2022.

**MARCIN HOFFMANN** (Member, IEEE) received the M.Sc. degree (Hons.) in electronics and telecommunication from Pozna University of Technology, in 2019, where he is currently pursuing the Ph.D. degree with the Institute of Radiocommunications. He is currently a Senior Research and Development Engineer with the Rimedo Laboratories working on O-RAN software development solutions and spectrum sharing-related projects. He is gaining scientific experience by being involved in both national and international research projects. In addition to that, he works on massive MIMO and advanced beamforming techniques. His scientific articles are published in top journals like IEEE JOURNAL ON SELECTED AREAS IN COMMUNICATIONS, IEEE TRANSACTIONS ON INTELLIGENT TRANSPORTATION SYSTEMS, and IEEE ACCESS. His research interests include the utilization of machine learning and location-dependent information for the purpose of network management.

**MARCIN DRYJAŃSKI** (Senior Member, IEEE) received the Ph.D. degree (Hons.) from Poznan University of Technology, in September 2019. Over the past 15 years, he was a Research and Development Engineer, a Consultant, a Technical Trainer, the Technical Leader, a Board Member, and an Advisor. He has been involved in 5G design, since 2012, where he was the Work-Package Leader of the FP7 5GNOW Project. Currently, he is the CEO and a Principal Consultant with the Rimedo Laboratories. He is the co-author of many articles on 5G, LTE-Advanced Pro and Open RAN and the co-author of the book *From LTE to LTE-Advanced Pro and 5G* (M. Rahnema, M. Dryjanski, Artech House, 2017).

## 7.12 Publication [P12]

M. Hoffmann and P. Kryszkiewicz, "Evaluation of User-Centric Cell-Free Massive Multiple-Input Multiple-Output Networks Considering Realistic Channels and Frontend Nonlinear Distortion," *Applied Sciences*, vol. 14, no. 5, p. 1684, 2024.

MNiSW Points: 100

Number of citations:

- according to Web of Science: 2
- according to Google Scholar: 7

mgr inż. Marcin Hoffmann
Instytut Radiokomunikacji, Politechnika Poznańska
ul. Polanka 3, 60-965 Poznań

Poznań, 9 stycznia 2025 r.

# OŚWIADCZENIE W SPRAWIE AUTORSTWA PRACY

Oświadczam, że w pracy:

*M. Hoffmann and P. Kryszkiewicz, "Beam Management Driven by Radio Environment Maps in O-RAN Architecture," 2023 IEEE International Conference on Communications Workshops (ICC Workshops), Rome, Italy, 2023, pp. 54-59*

mój udział polegał na:

- Zaproponowaniu zgodnego z architekturą otwartej sieci dostępowej O-RAN algorytmu wykorzystującego mapy środowiska radiowego, oraz uczenie ze wzmocnieniem do dynamicznego zarządzania wiązką w systemach wieloantenowych – Massive MIMO.
- Przygotowaniu w całości tekstu pierwszej wersji artykułu.
- Przeprowadzeniu symulacji komputerowych i opracowaniu wyników

Mój procentowy udział w powstanie pracy szacuję na: 75%

.....

Podpis

dr hab. inż. Paweł Kryszkiewicz, prof. PP
Instytut Radiokomunikacji, Politechnika Poznańska
ul. Polanka 3, 60-965 Poznań

Poznań, 21 sierpnia 2025 r.

# OŚWIADCZENIE W SPRAWIE AUTORSTWA PRACY

Oświadczam, że w pracy:

*M. Hoffmann and P. Kryszkiewicz, "Beam Management Driven by Radio Environment Maps in O-RAN Architecture," 2023 IEEE International Conference on Communications Workshops (ICC Workshops), Rome, Italy, 2023, pp. 54-59*

mój udział polegał na:

- Koordynacji prac badawczych
- Dyskusji z pierwszym autorem struktury zaproponowanego systemu i napotkanych problemów
- Dyskusji ze współautorem uzyskanych wyników i metod ich prezentacji/porównania
- Strukturyzacji artykułu
- Iteracyjnym nanoszeniu poprawek na tekst; dyskusji uwag ze współautorem

Mój procentowy udział w powstanie pracy szacuję na: 25%

Podpis

# Beam Management Driven by Radio Environment Maps in O-RAN Architecture

Marcin Hoffmann
*Rimedo Labs*
*Institute of Radiocommunications*
*Poznan University of Technology*
Poznan, Poland
0000-0002-4957-0173

Pawel Kryszkiewicz
*Rimedo Labs*
*Institute of Radiocommunications*
*Poznan University of Technology*
Poznan, Poland
0000-0001-9054-9416

2023 IEEE International Conference on Communications Workshops (ICC Workshops) | 979-8-3503-3307-7/23/$31.00 ©2023 IEEE | DOI: 10.1109/ICCWORKSHOPS57953.2023.10283527

***Abstract*—The Massive Multiple-Input Multiple-Output (M-MIMO) is considered as one of the key technologies in 5G, and future 6G networks. From the perspective of, e.g., channel estimation, especially for high-speed users it is easier to implement an M-MIMO network exploiting a static set of beams, i.e., Grid of Beams (GoB). While considering GoB it is important to properly assign users to the beams, i.e., to perform Beam Management (BM). BM can be enhanced by taking into account historical knowledge about the radio environment, e.g., to avoid radio link failures. The aim of this paper is to propose such a BM algorithm, that utilizes location-dependent data stored in a Radio Environment Map (REM). It utilizes received power maps, and user mobility patterns to optimize the BM process in terms of Reinforcement Learning (RL) by using the Policy Iteration method under different goal functions, e.g., maximization of received power or minimization of beam reselections while avoiding radio link failures. The proposed solution is compliant with the Open Radio Access Network (O-RAN) architecture, enabling its practical implementation. Simulation studies have shown that the proposed BM algorithm can significantly reduce the number of beam reselections or radio link failures compared to the baseline algorithm.**

***Index Terms*—Radio Environment Map, Open RAN, 5G networks, Massive MIMO, Beam Management**

## I. Introduction

Massive Multiple-Input Multiple-Output (M-MIMO) is considered one of the key enablers for achieving high user throughput in contemporary 5G, and future 6G networks [1]. The idea of M-MIMO is to equip Base Stations (BSs) with large antenna arrays, i.e., exploiting dozens or even hundreds of antennas. Through proper amplitude scaling and phase shifting of the signal being transmitted or received by each of BS's antennas the radiation pattern of the antenna array can be modified in a flexible manner [2]. This procedure is known as beamforming. Beamforming allows for, e.g., increasing received signal strength, or suppressing interference. Moreover, due to the application of beamforming, it is possible to simultaneously serve multiple User Equipments (UEs) using the same time-frequency resources, i.e., spatial domain multiple access. There are two main approaches to the practical implementation of the M-MIMO system, namely Grid of Beams (GoB) beamforming, and adaptive beamforming [3]. GoB beamforming in 5G relies on downlink measurements of the Reference Signal Received Power (RSRP), based typically on Synchronization Signal Blocks (SSBs) transmitted by BS [3]. On the opposite, adaptive beamforming requires accurate channel estimation, which in a time-division duplexing (TDD) system is based on the Sounding Reference Signal (SRS) transmitted by UE in the uplink. Although SRS-based beamforming allows achieving higher user throughputs, due to better knowledge about radio channel coefficients, it requires more complex signal processing and management of SRS signals transmitted by UEs in the neighboring cells. Moreover, SRS-based beamforming is inappropriate for high-speed UEs because the channel estimate becomes almost immediately outdated when UE moves [4]. From this perspective, GoB beamforming that utilizes a static set of beams, requiring UE to only indicate RSRP related to SSB, is much easier for practical implementations. GoB beamforming is indicated as a promising solution to be implemented in millimeter wave frequency bands [5].

GoB beamforming exploits a static set of beams covering the area of a cell. However, due to reflections, or shadowing, e.g., from surrounding buildings, RSRP related to a particular beam can follow an unobvious spatial distribution. Moreover, while considering high-speed UEs the RSRP can change rapidly, requiring fast beam reselections supported by the 5G control plane. Following the specifications of the 5G, BSs send SSB signals for all the covered beams in a 5 ms long burst. The burst repeats every 20 ms [6]. The most straightforward approach to BM would be to select a new beam after every SSB burst. However, while switching between beams within a single cell requires less Radio Resource Control (RRC) configuration than the inter-cell handover the signaling, and reconfiguration overhead still exists [7]. Some balance between beam reselections and signaling overhead should be found. From this perspective, Beam Management (BM) is indicated as one of the key challenges for GoB beamforming [8].

In [9], a baseline, 5G BM algorithm is proposed. Therein, the beam is switched when RSRP related to the best target beam is above the current source beam by some specified margin. Such an approach can prevent too frequent beam

The presented work has been funded by the Polish Ministry of Education and Science within the status activity task no. 0312/SBAD/8164.

reselections, but it is characterized by poor flexibility by a single margin parameter. To overcome these issues, especially in the context of high-speed UEs, some studies propose to utilize context information to support BM, e.g., UE location, speed, and bearing. The authors of [10] propose to train a so-called Deep Learning Agent that takes UE location, Signal-to-Noise-Ratio (SNR), mobility vectors, and current beam index, to predict if RSRP would fall below the desired level. Based on that prediction, the decision on beam switching is made. The drawback of the method is that the decision is greedy, i.e., no long-term optimization taking into account UE's expected route is applied. In [11], the authors proposed a stochastic geometry modeling of BM to maximize the area spectral efficiency. However, to formulate and resolve the optimization problem, some simplifications are assumed, e.g., with regard to the antenna array radiation pattern, BSs placement, and channel model. These can make the proposed solution impractical in real environments. Finally, there are some algorithms focused on the handovers in 4G-LTE networks utilizing the so-called Radio Environment Maps (REMs), e.g., [12]. The proposed REM stores RSRP-location pairs in the form of a map, to be used to predict the signal level for UE in the next time step, and decide on the eventual handover. However, the algorithm is designed to deal with handover between two BSs equipped with omnidirectional antennas. It is not adequate for BM in a 5G network utilizing GoB beamforming. In such a case, UE can be dynamically switched between up to tens of candidate beams. Last but not least, most authors of the BM algorithms do not consider what signals and Key Performance Indicators (KPIs) have to be exchanged in 5G networks. Moreover, there is no discussion on how their proposal can be implemented in a real network. The lack of such considerations can be justified by the fact that contemporary large-scale mobile networks are not appropriate for introducing novel, third-party ideas. There are limited possibilities for controlling Radio Access Network (RAN), e.g., by sending messages related to BM or receiving RSRP measurement reports. However, in recent years the idea of the so-called Open-Radio Access Network (O-RAN) is gaining more and more attention [13].

In this paper, we propose a REM-based BM adjusted for the O-RAN architecture. REM stores two types of location-dependent data: RSRP related to each beam at a given location, and a UE mobility map that describes the motion pattern of UEs in a probabilistic manner. Based on these two types of maps we define BM as a Markov Decision Process (MDP) that can be optimized with the use of the so-called Policy Iteration (PI) method from the family of RL algorithms, aimed at the maximization of a cumulative reward (related to the optimization goal) [14]. The process is flexible and allows the Mobile Network Operator (MNO) to define its optimization goals, e.g., maximization of RSRP, and minimization of beam reselections, while maintaining the desired RSRP. Most importantly, our solution is compliant with the O-RAN architecture enabling its practical implementation.

The paper is organized as follows: The system model is described in Sec. II. The required components placement in the O-RAN architecture is presented in Sec. III. The proposed REM-based BM algorithm is presented in Sec. IV. The simulation scenario is provided in Sec. V with results discussed in Sec. VI. The paper is concluded in Sec. VII.

## II. System Model

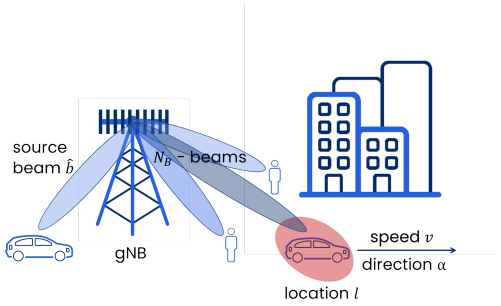


Fig. 1. System model

In this paper, we are considering a BM procedure in a single cell of a 5G network, as depicted in Fig. 1. In the cell, there is a single gNB equipped with an antenna array that supports $N_{\mathrm{B}}$ beams. The SSB signals related to those beams are transmitted every $T_{\mathrm{B}}$ ms. During each SSB burst, UE being in location $l$ can compute RSRP related to every beam $b$ denoted as $P_r(b,l)$. After each SSB burst, a decision can be made to switch UE between beams, indicated by the index of a target beam $b$. Following the definitions in [9] we assume that *radio link failure* is the situation when the used source beam $\hat{b}$ has RSRP $P_r(\hat{b},l)$ smaller by at least $\delta_{\mathrm{th}}$ than the strongest beam:

$$P_r(\hat{b},l) < \max_b \left(P_r(b,l)\right) - \delta_{\mathrm{th}}. \tag{1}$$

The considered cell implements the baseline BM procedure proper for the 5G network as defined in [9]. The beam is switched when RSRP related to the best target beam exceeds the RSRP of the source beam by at least $\delta_{\mathrm{ho}}$ (defined margin):

$$P_r(\hat{b},l) < \max_b \left(P_r(b,l)\right) - \delta_{\mathrm{ho}}. \tag{2}$$

While the RSRP measurement is available after the SSB burst, the baseline BM procedure suffers a delay of $T_{\mathrm{B}}$ ms.

## III. Proposed BM implementation in ORAN

The aim of O-RAN is to standardize interfaces between RAN components, allowing MNOs to deploy a network consisting of components provided by various vendors. Moreover, the architecture is extended by the RAN Intelligent Controller (RIC). RIC is a unit that is responsible for the reconfiguration of RAN, based on the data collected from RAN components, and processed with the use of Machine Learning (ML) techniques. It is assumed that the cell considered in this paper (see Sec. II) is compliant with the O-RAN architecture [15] depicted in Fig. 2. The BM functionality is deployed within RIC. RIC is split into two parts: Non-RT RIC, which operates

in the time-frame of above 1 s, and Near-RT RIC, which operates in near real-time, i.e., between 10 ms and 1 s [15]. The O-RAN specification defines the roles of both Non-RT RIC and Near-RT RIC in the case of BM [16]. Non-RT RIC is proper for, e.g., data capture and aggregation, training of ML models, and extensive computations. Depending on the implementation, Non-RT RIC modules can be either rApps or built-in vendor-dependent entities. On the other hand, Near-RT RIC hosts the so-called BM-xApp that performs near real-time actions in the network, i.e., reselects beams for UEs. The communication between Non-RT RIC and Near-RT RIC is performed through the A1 interface. The A1 interface provides mechanisms to, e.g., send ML models obtained in Non-RT RIC to Near-RT RIC to make inference. BM-xApp controls beam reselections through the E2 interface attached to gNB. The E2 interface can be used also to obtain feedback information about, e.g., *radio link failures*. On the other hand, the information from gNB can be obtained in Non-RT RIC via the O1 interface. It can be, e.g., RSRP reported by the users, and *radio link failure* statistics. The observed increased number of *radio link failures* can trigger an update of the ML model in Non-RT RIC. At the same time, BM-xApp in Near-RT RIC can trigger mechanisms to prevent Quality of Service (QoS) degradation, e.g., temporal utilization of the baseline switching algorithm until the ML model inference is completed in the changed radio environment. In addition, both Non-RT RIC and Near-RT RIC can use external services like a Localization Server. According to the O-RAN specification [16], the Localization Server provides information about user location captured from the external application layer to both Non-RT RIC and Near-RT RIC. We expect Non-RT RIC to contain a module dedicated to long-term analysis of user location information in order to extract, e.g., UE mobility patterns.

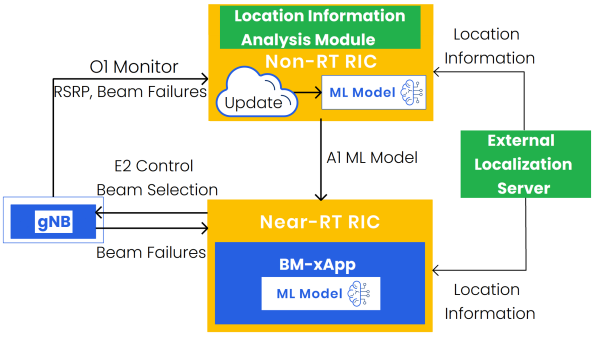


Fig. 2. Beam Management using the O-RAN architecture

## IV. REM-Based Beam Management

Following the O-RAN architecture, the proposed REM-based BM is split between Non-RT RIC and Near-RT RIC. The first part of this section describes the deployment of REM-based BM related to Non-RT RIC, while the latter one describes the Near-RT RIC part of REM-based BM.

### A. Non-RT RIC

Non-RT RIC operates in a time frame of above 1 s, thus it is appropriate for the implementation of REM-based BM functionality that requires extensive computations, and large memory. The first element of the proposed algorithm to be implemented in Non-RT RIC is REM. REM stores RSRP values for each location and beam as reported by UEs creating maps, as depicted in Fig. 3. The input RSRP data is provided to Non-RT RIC through the O1 interface and is associated with the UE location provided by the external Localization Server. Such a location-RSRP pair is used to update REM. REM is built on the basis of a square grid with a single tile having a size equal to $g$, e.g., $10m$. The reported RSRP values are averaged within each REM tile for a given beam. Besides the RSRP map, REM contains a map of UE mobility pattern over the cell area. The UE mobility pattern is given as the conditional probability $\mathcal{P}(v, a|l, \tilde{v}, \tilde{\alpha})$ of moving with speed $v$ in direction $\alpha$, while being in location $l$, and moving currently with the speed of $\tilde{v}$ in direction $\tilde{\alpha}$. While in many cases this model allows us to predict UEs future velocity with high reliability, e.g., for cars moving on a motorway with high probability, it can be used to model more difficult traffic situations as well, e.g., UEs on a junction turning left and right with 40% and 60% probability, respectively. This mobility map is obtained through a long-term analysis of the location information (position, speed, direction) provided by an external Localization Server in a dedicated Non-RT RIC module. These can be used to empirically estimate probabilities for the UEs mobility map. To reduce the amount of data being stored in REM, some quantization is necessary, e.g., position rounded to fit into one of REM's square tiles, direction split into 8 possible angles of 45 deg. resolution. Under some specific scenarios, e.g., a small cell dedicated for users inside high-speed vehicles traveling along the motorway, or while initializing the UE Mobility Pattern Map for a given tile, simple estimation, i.e., $v = \tilde{v}$ and $\alpha = \tilde{\alpha}$, can be sufficient.

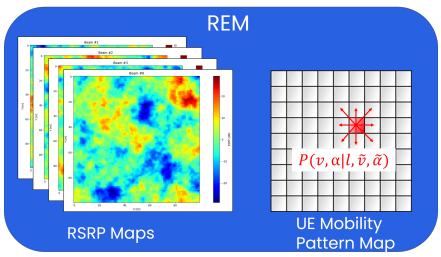


Fig. 3. Data stored in REM to be used for BM.

It can be seen that the definition of a UE mobility pattern specified by probability $\mathcal{P}(v, a|l, \tilde{v}, \tilde{\alpha})$ follows the Markov property, i.e., the next UE speed $v$ and direction $\alpha$ depends only on the present speed $\tilde{v}$, direction $\tilde{\alpha}$, and location $l$. We assume that these do not depend on the previous state. From this perspective, beam selection in REM-based BM can be formulated as the Markov Decision Process (MDP), where a

UE moves over the cell area, and sequential decisions are made by BS on its association with a certain beam. Based on the knowledge from REM these decisions can be assessed in terms of expected RSRP values at a given location. The algorithm iteratively learns, off-line the optimal beam assignment, in terms of a given goal function. The defined MDP consists of the following components:

- **Agent** is a UE that moves over the cell area following its mobility pattern $\mathcal{P}(v, \alpha|l, \tilde{v}, \tilde{\alpha})$. In each state $s$, the Agent takes one of the available actions $a$ on the basis of policy $\pi(s, a)$
- **Environment** is the considered cell. The cell (environment) is modeled through REM, namely the RSRPs related to particular SSBs at a given UE location $P_r(b, l)$, and UE's mobility pattern at a given location $\mathcal{P}(v, a|l, \tilde{v}, \tilde{\alpha})$.
- **State** $s$ is defined as the current UE speed $\tilde{v}$, direction $\tilde{\alpha}$, location $l$, and source beam $\hat{b}$.
- **Action** $a$ is the selection of one of the $N_{\mathrm{B}}$ target beams
- **Policy** $\pi(s, a)$ is the probability distribution of taking action $a$ in state $s$.
- **Reward** is defined so as to enable MNO balancing between the minimization of the number of beam reselections, and using the beams of the highest RRSP. Its formal definition is:

$$r(s, a) = \beta \cdot f_{\mathrm{BR}}(s, a) + (1 - \beta) \cdot f_{\mathrm{RSRP}}(s, a), \quad (3)$$

where $\beta \in [0, 1]$ is the design parameter to balance between the minimization of beam reselections, and RSRP maximization goals, respectively. $f_{\mathrm{BR}}(s, a)$ is defined as:

$$f_{\mathrm{BR}}(s, a) = \begin{cases} -1000 & \text{if (1) is true} \\ -1 & \text{if } a \neq \hat{b} \\ 0 & \text{otherwise,} \end{cases} \quad (4)$$

and $f_{\mathrm{RSRP}}(s, a)$ is given by:

$$f_{\mathrm{RSRP}}(s, a) = \begin{cases} 0 & \text{if } a = \arg\max_b \left(P_r(b, l)\right) \\ -1000 & \text{otherwise.} \end{cases} \quad (5)$$

In the case of $f_{\mathrm{BR}}(s, a)$, a high negative reward of $-1000$ is associated when an action causes a *radio link failure* (1). A small negative reward of $-1$ is given to the agent for switching the source beam $\hat{b}$ to another beam, and a reward equal to 0 is given when the beam is not switched. This function is maximized if the number of beam switches is minimized while not causing radio link failures. In the case of $f_{\mathrm{RSRP}}(s, a)$, reward equal to 0 is given to the agent for selecting the highest-RSRP beam. Other actions are associated with large negative rewards of $-1000$. The function is maximized if always the highest RSRP beam is selected. One should notice that $f_{\mathrm{BR}}(s, a)$, and $f_{\mathrm{RSRP}}(s, a)$ are only the representative examples of goal functions. The proposed solution can work with flexibly defined reward functions that will suit MNOs' specific needs.

By storing information about the environment dynamics (UE mobility patterns), and information about the rewards in states (to be computed from RSRP maps) in REM, we can obtain the optimal solution for MDP offline in Non-RT RIC using the so-called Policy Iteration (PI) algorithm [14]. The aim of the PI algorithm is to obtain the optimal policy, i.e., the policy that maximizes the so-called expected discounted reward. The PI algorithm starts from an arbitrary policy and consists of two alternating steps, namely *Policy Evaluation*, and *Policy Improvement*. The *Policy Evaluation* step aims at estimating the so-called *value function*, which stands for the expected return while being in state $s$ and following policy $\pi(s, a)$ thereafter. After the *Policy Evaluation* is finished, *Policy Improvement* begins. It modifies the policy toward the optimal one. The algorithm is finished when the policy is not changing anymore, i.e., it converged to the optimum.

### B. Near-RT RIC

Offline-computed optimal policies to be followed in each state $\pi^*(s, a)$ are transferred from Non-RT RIC to BM-xApp that is located in the near RT RIC, through a dedicated A1 ML interface (See Fig. 2). The aim of BM-xApp is to enforce those policies, i.e., to indicate gNB through the E2 interface, that a particular UE should be switched to another target beam. BM-xApp determines state $s$ of the UE on the basis of its current location $l$, speed $v$, and direction $\alpha$ obtained from the external Localization Server. The information in REM, and consequently the policies, are quantized in space, i.e., following the square grid of size $g$. Thus the UE location obtained from the external Localization Server is rounded to fit the closest (in terms of Euclidean distance) point in REM constituting input location $l$. BM-xApp also provides a mechanism to prevent QoS degradation. This might be the case when, e.g., data in REM becomes outdated, or some temporal high RSRP variation occurs. If a *radio link failure* is detected, BM-xApp arbitrary indicates through the E2 interface to gNB to switch this user to the new target beam providing the highest RSRP.

## V. Simulation Scenario

In this paper, we are considering BM in a single small cell covering an area of $500 \times 500$ m. A single gNB is deployed in the middle of the left edge, i.e., of x-y coordinates $(0, 250)$ m. The gNB is equipped with an $8 \times 8$ rectangular antenna array that is based on the *Micro Urban* scheme described in the 5G specification [17]. The gNB supports $N_{\mathrm{B}} = 16$ orthogonal beams. SSB burst period $T_{\mathrm{B}}$ equals 20 ms, which is a typical value reported in the literature [6], [10]. The antenna array is installed at the height of 10 m and transmits a signal with the TX power distributed to all beamforming antennas of 10 dBm/MHz. The radiation pattern is computed following the formulas from [17]. The gNB operates with a bandwidth of 100 MHz at the center frequency of 26 GHz. Due to the high path loss, this band is suitable for such a small area cell. To model the impact of the radio environment on RSRP related to each beam, e.g., the presence of some obstacles

that attenuate the signal, we have used a spatially correlated shadowing model independent for each beam [18]. We have set the correlation distance to 10 m. In order to ensure identical radio conditions for the evaluated algorithms, the same random seed is used to generate correlated shadowing before each simulation. The radio channel coefficients are affected by fast fading that is independent for each realization and follows the Rayleigh distribution. BM is especially challenging for high-speed users. Thus, we are considering the urban road scenario, where UEs are moving with the speed of $v = 25$ m/s. The road users can only move along the defined lanes, so in this scenario, the direction can be either $\alpha = 0$ (downward) or $\alpha = 180$ (upward). We assume that high-speed users utilize cm-level accuracy Real Time Kinematics localization, which is supported in mobile networks since LTE [19]. We are considering 300 UEs going through the cell downward. We set the margin for *radio link failure* to $\delta_{\text{th}} = 8$ dB [12]. The simulation parameters are summarized in Table I.

TABLE I
SIMULATION PARAMETERS

| **Parameter** | Value |
|---|---|
| cell size | $500 \times 500$ m |
| gNB placement (x,y) | $(0, 250)$ m |
| height of antenna array | 10 m |
| antenna array model | $8 \times 8$ *Micro Urban* [17] |
| number of beams $N_{\text{B}}$ | 8 |
| SSB-burst period $T_{\text{B}}$ | 20 ms |
| TX power | 10 dBm/MHz |
| center frequency | 26 GHz |
| correlation distance for shadowing | 10 m |
| number of users | 300 |
| user speed $v$ | 25 m/s |
| user direction $\alpha$ | $\{0, 180\}$ |
| margin for *radio link failure* $\delta_{\text{th}}$ | 8 dB |

## VI. SIMULATION RESULTS

The proposed REM-based BM is evaluated within the scenario described in Sec. V. At first, we populated the REM with RSRP data, so that it contains a statistically correct estimation of the mean RSRP value, over all available reports, for each beam within every square tile of size $g = 2$ m. Next, we created a UE mobility pattern map, based on the knowledge about the possible UE speed $v$ and directions $\alpha$. Having the necessary data collected, we ran the PI algorithm to obtain policies. We obtained two sets of policies: the first, are aimed at the minimization of beam reselections, while avoiding *radio link failures* (1) (BR-MIN). Second, aimed at RSRP maximization (RSRP-MAX). The corresponding $\beta$ values are 1, and 0 for BR-MIN, and RSRP-MAX, respectively. We compared the proposed solutions against the standard BM procedures in 5G (denoted as *Baseline*) with $\delta_{\text{ho}}$ values of $\{3, 5, 7\}$ dB. In Fig. 4 there is an illustration of RSRP-MAX, BR-MIN, and *Baseline* ($\delta_{\text{ho}} = 5$ dB) algorithms in the form of an RSRP vs. time plot for a single user. To smooth out the results, a 15-point moving average is applied. The RSRP-MAX algorithm provides the user with the highest RSRP based on

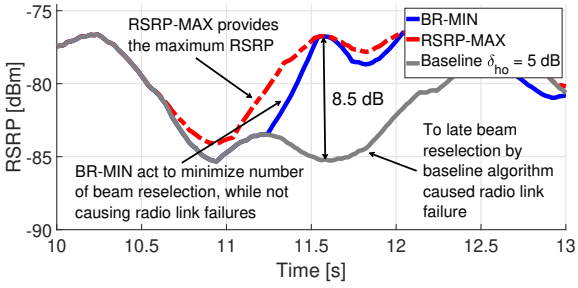


Fig. 4. Illustration of RSRP-MAX, BR-MIN, and *Baseline* ($\delta_{\text{ho}} = 5$ dB) algorithms. The results are obtained for a single user, and a 15-point moving average is applied to smooth the plot.

information in REM. On the opposite, the *Baseline* algorithm to prevent the ping-pong effect performs beam reselection when a better target beam, i.e., of RSRP above the current by at least 5 dB, is detected. It can be seen that for a high-speed user it causes *radio link failures*. It is due to its reactive character, i.e., beam reselection can be triggered only after a new RSRP measurement arrives, i.e., after $T_{\text{B}}$ ms. BR-MIN proactively minimizes the number of beam reselections. Due to the historical knowledge from REM, it is trained to perform beam reselection before the RSRP of the source beam significantly drops (and is reported), causing *radio link failure*.

To capture statistically significant KPIs related to the performance of the proposed REM-based BM, it is compared with the *Baseline* approach exploiting different values of $\delta_{\text{ho}}$. A 15 s long simulation has been performed for all the considered 300 UEs. The first comparison is aimed at the number of beam reselections, and the number of *radio link failures*. The results are presented in Fig. 5. The statistics are averaged over time and the number of UEs, i.e., the number of occurrences per user per second. It can be seen that when BM-xApp acts

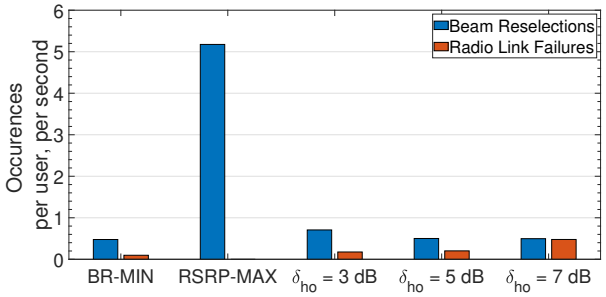


Fig. 5. Beam reselections and *radio link failures*. Averaged per user, per second.

according to the RSRP-MAX the number of beam reselections is the highest. It is reasonable, as the algorithm constantly follows the beam providing the highest RSRP. BM-xApp following the BR-MIN policy is characterized by about 29% reduction of the number of beam reselections compared to the *Baseline* algorithm with $\delta_{\text{ho}} = 3$ dB. For the remaining values of $\delta_{\text{ho}}$, the *Baseline* algorithm has similar beam reselection

performance, i.e., about 0.5 reselections per user per beam. However, the *Baseline* algorithm has much poorer statistics of *radio link failures*, i.e., 1.81, 2.08, and 4.91 times worse for $\delta_{\text{ho}} = 3, 5$, and 7 dB, respectively. It is because RSRP related to a particular beam can decay fast, especially when UE moves at a high speed. BM-xApp utilizes policies obtained from REM, thus it can predict the time of beam reselection to avoid QoS deterioration. However, due to fast fading, sometimes temporal channel variations can cause a *radio link failure*, even when the BR-MIN policy is used.

Another KPI to compare between BM-xApp and the *Baseline* algorithm is RSRP distribution. The Cumulative Distribution Function (CDF) of RSRPs observed by all of the UEs during the 15 s long simulation is depicted in Fig. 6. It can be seen that BM-xApp following the RSRP-MAX policy always chooses the beam with the highest RSRP. The highest gains can be observed for the so-called cell-edge users, i.e, the 10th percentile of the RSRP distribution. The RSRP-MAX algorithm improves RSRP of the cell-edge users by about 23% compared to the *Baseline* algorithm (for $\delta_{\text{ho}} = 3$ dB). On the other hand, when BM-xApp follows the BR-MIN policy, RSRP significantly drops. Although the RSRP distribution in the case of BM-xApp following the BR-MIN policy is similar to the *Baseline* algorithm for $\delta_{ho} = 7$ dB, it is important that, unlike with the *Baseline* algorithm, decisions made by BM-xApp rarely cause *radio link failures*.

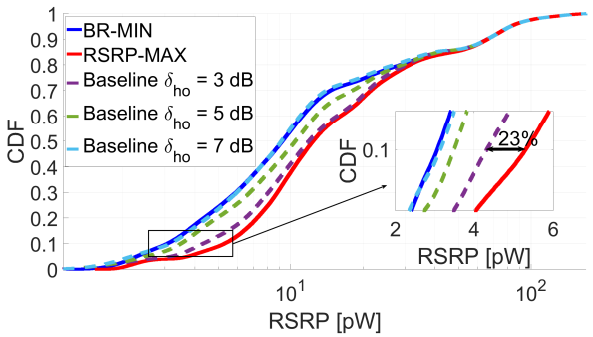


Fig. 6. Comparison of RSRP distributions related to the BM xApp, and the *Baseline* algorithms.

## VII. Conclusions

In this paper, we have proposed BM based on the information stored in REM. It is close to practical implementation because of using the O-RAN architecture. In the paper, we have clearly defined the role of Non-RT RIC, and Near-RT RIC, together with interfaces for their communications, in the context of the proposed BM. The BM xApp was tested for two policies, i.e., BR-MIN, and RSRP-MAX, against the baseline algorithm. Simulation studies have shown that following the BR-MIN policy can minimize the number of beam reselections, while preventing QoS degradation caused by rapid drops of RSRP, e.g., for high-speed UEs. While the *baseline* algorithm can obtain similar number of beams reselections it is penalized by 2.18 times more *radio link failure* events. On the other hand, the proposed BM following the RSRP-MAX policy provides users with maximum RSRP values. Most importantly, the proposed solution is flexible, i.e., goal functions can be redefined according to the MNOs' needs.

## References

[1] I. F. Akyildiz, A. Kak, and S. Nie, "6G and Beyond: The Future of Wireless Communications Systems," *IEEE Access*, vol. 8, pp. 133 995–134 030, 2020.

[2] A. Ehab, I. Mahamod, N. Rosdiadee, and A. Fadzilah, "Beamforming techniques for massive MIMO systems in 5G: overview, classification, and trends for future research," *Frontiers of Information Technology & Electronic Engineering*, vol. 18, no. 6, p. 753, 2017.

[3] K.-y. Lee, Y.-J. Song, and J.-S. Jang, "Adaptive Downlink Beamforming based on SRS for Channel Estimation using Coherence Bandwidth Characteristic in sub-6GHz 5G NR," in *2021 Wireless Telecommunications Symposium (WTS)*, 2021, pp. 1–5.

[4] A. Davydov, V. Sergeev, A. Putilin, B. Mondai, T. Hewavithana, A. Papathanassiou, and A. Sengupta, "Uplink Massive MIMO Functional Split for C-RAN System Under Rapid User Mobility Conditions," in *2021 IEEE 32nd Annual International Symposium on Personal, Indoor and Mobile Radio Communications*, 2021, pp. 1117–1121.

[5] M. Rebato, L. Rose, and M. Zorzi, "Performance Assessment of MIMO Precoding on Realistic mmWave Channels," in *2019 IEEE International Conference on Communications Workshops*, 2019, pp. 1–6.

[6] C. N. Barati, S. Dutta, S. Rangan, and A. Sabharwal, "Energy and latency of beamforming architectures for initial access in mmWave wireless networks," *Journal of the Indian Institute of Science*, vol. 100, no. 2, pp. 281–302, 2020.

[7] Y. Jo, J. Lim, and D. Hong, "Mobility Management Based on Beam-Level Measurement Report in 5G Massive MIMO Cellular Networks," *Electronics*, vol. 9, no. 5, 2020.

[8] Y.-N. R. Li, B. Gao, X. Zhang, and K. Huang, "Beam Management in Millimeter-Wave Communications for 5G and Beyond," *IEEE Access*, vol. 8, pp. 13 282–13 293, 2020.

[9] F. Abinader, C. Rom, K. Pedersen, S. Hailu, and N. Kolehmainen, "System-Level Analysis of mmWave 5G Systems with Different Multi-Panel Antenna Device Models," in *2021 IEEE 93rd Vehicular Technology Conference*, 2021, pp. 1–6.

[10] W. Na, B. Bae, S. Cho, and N. Kim, "Deep-learning Based Adaptive Beam Management Technique for Mobile High-speed 5G mmWave Networks," in *2019 IEEE 9th International Conference on Consumer Electronics*, 2019, pp. 149–151.

[11] S. S. Kalamkar, F. Baccelli, F. M. Abinader, A. S. M. Fani, and L. G. U. Garcia, "Beam Management in 5G: A Stochastic Geometry Analysis," *IEEE Transactions on Wireless Communications*, vol. 21, no. 4, pp. 2275–2290, 2022.

[12] C. Suarez-Rodriguez, B. A. Jayawickrama, Y. He, F. Bader, and M. Heimlich, "Performance analysis of REM-based handover algorithm for multi-tier cellular networks," in *IEEE International Symposium on Personal, Indoor, and Mobile Radio Communications*, 2017, pp. 1–6.

[13] L. Bonati, S. D'Oro, M. Polese, S. Basagni, and T. Melodia, "Intelligence and Learning in O-RAN for Data-Driven NextG Cellular Networks," *IEEE Comm. Magazine*, vol. 59, no. 10, pp. 21–27, 2021.

[14] R. S. Sutton and A. G. Barto, *Reinforcement learning: An introduction*. MIT press, 2018.

[15] M. Dryjański, Ł. Kułacz, and A. Kliks, "Toward Modular and Flexible Open RAN Implementations in 6G Networks: Traffic Steering Use Case and O-RAN xApps," *Sensors*, vol. 21, no. 24, p. 8173, 2021.

[16] O.-R. W. G. 1, "Massive MIMO Use Cases ," O-RAN Alliance, TR O-RAN.WG1.MMIMO-USE-CASES-TR-v.01.00, Jul. 2022.

[17] 3GPP, "Study on International Mobile Telecommunications (IMT) parameters for 6.425-7.025GHz, 7.025-7.125GHz and 10.0-10.5 GHz (Release 17) ," TS 38.921 v.17.1.0, Mar. 2022.

[18] C. Zhang, X. Chen, H. Yin, and G. Wei, "Two-dimensional shadow fading modeling on system level," in *2012 IEEE 23rd International Symposium on Personal, Indoor and Mobile Radio Communications*, 2012, pp. 1671–1676.

[19] M. Hoffmann, P. Kryszkiewicz, and G. P. Koudouridis, "Modeling of Real Time Kinematics Localization Error for Use in 5G Networks," *EURASIP J. Wirel. Commun. Netw.*, vol. 2020, no. 1, jan 2020.

## 7.13 Publication [P13]

M. Hoffmann and P. Kryszkiewicz, "Beam Management Driven by Radio Environment Maps in O-RAN Architecture," in *2023 IEEE International Conference on Communications Workshops (ICC Workshops)*, pp. 54–59, 2023.

MNiSW Points: 70

Number of citations:

- according to Web of Science: 4
- according to Google Scholar: 13

mgr inż. Marcin Hoffmann
Instytut Radiokomunikacji, Politechnika Poznańska
ul. Polanka 3, 60-965 Poznań

Poznań, 9 stycznia 2025 r.

# OŚWIADCZENIE W SPRAWIE AUTORSTWA PRACY

Oświadczam, że w pracy:

*Hoffmann, Marcin, and Paweł Kryszkiewicz. "Evaluation of User-Centric Cell-Free Massive Multiple-Input Multiple-Output Networks Considering Realistic Channels and Frontend Nonlinear Distortion." Applied Sciences (2076-3417) 14.5 (2024).*

mój udział polegał na:

- Zaproponowaniu zaawansowanego modelu sieci Massive MIMO zorientowanej na użytkownika wykorzystującego model kanału radiowego z trójwymiarowym śledzeniem promieni, oraz modelującego efekty nieliniowe we wzmacniaczu mocy.
- Implementację algorytmów odpowiedzialnych za tzw. formowanie klastrów obsługujących w sieci Massive MIMO zorientowanej na użytkownika
- Propozycję algorytmu przydziału zasobów w czasie, częstotliwości i przestrzeni dla sieci Massive MIMO zorientowanej na użytkownika, na podstawie istniejących rozwiązań.
- Przygotowaniu w całości tekstu pierwszej wersji artykułu.
- Przeprowadzeniu symulacji komputerowych i opracowaniu wyników

Mój procentowy udział w powstanie pracy szacuję na: 70%

.....

Podpis

dr hab. inż. Paweł Kryszkiewicz, prof. PP
Instytut Radiokomunikacji, Politechnika Poznańska
ul. Polanka 3, 60-965 Poznań

Poznań, 21 sierpnia 2025 r.

# OŚWIADCZENIE W SPRAWIE AUTORSTWA PRACY

Oświadczam, że w pracy:

*Hoffmann, Marcin, and Paweł Kryszkiewicz. "Evaluation of User-Centric Cell-Free Massive Multiple-Input Multiple-Output Networks Considering Realistic Channels and Frontend Nonlinear Distortion." Applied Sciences (2076-3417) 14.5 (2024).*

mój udział polegał na:

- Koordynacji prac badawczych
- Konsultacja tematyki badawczej i zaprezentowanie modelu matematycznego nieliniowości
- Dyskusji ze współautorem uzyskanych wyników i metod ich prezentacji/porównania
- Iteracyjnym nanoszeniu poprawek na tekst oraz zapis matematyczny; dyskusji uwag ze współautorem

Mój procentowy udział w powstanie pracy szacuję na: 30%

Podpis

applied sciences

MDPI

*Article*

# Evaluation of User-Centric Cell-Free Massive Multiple-Input Multiple-Output Networks Considering Realistic Channels and Frontend Nonlinear Distortion

**Marcin Hoffmann * and Paweł Kryszkiewicz**

Institute of Radiocommunications, Poznan University of Technology, 60-965 Poznan, Poland; pawel.kryszkiewicz@put.poznan.pl

* Correspondence: marcin.hoffmann@put.poznan.pl; Tel.: +48-501-872-860

**Abstract:** Future 6G networks are expected to utilize Massive Multiple-Input Multiple-Output (M-MIMO) and follow a user-centric cell-free (UCCF) architecture. In a UCCF M-MIMO network, the user can be potentially served by multiple surrounding Radio Units (RUs) and Distributed Units (DUs) controlled and coordinated by a single virtualized Centralized Unit (CU). Moreover, in an M-MIMO network, each transmit frontend is equipped with a Power Amplifier (PA), typically with nonlinear characteristics, that can have a significant impact on the throughput achieved by network users. This work evaluates a UCCF M-MIMO network within an advanced system-level simulator considering multicarrier transmission, using Orthogonal Frequency-Division Multiplexing (OFDM), realistic signal-processing steps, e.g., per resource block scheduling, and a nonlinear radio frontend. Moreover, both idealistic independent and identically distributed (i.i.d.) Rayleigh and 3D ray-tracing-based radio channels are evaluated. The results show that under the realistic radio channel, the novel user-centric network architecture can lead to an almost uniform distribution of user throughput and improve the rate of the users characterized by the worst radio conditions by over 3 times in comparison to a classical, network-centric design. At the same time, the nonlinear characteristics of the PA can cause significant degradation of the UCCF M-MIMO network's performance when operating close to its saturation power.

**Keywords:** massive MIMO; user-centric cell-free networks; OFDM; 3D ray tracing; nonlinear distortion



**Citation:** Hoffmann, M.; Kryszkiewicz, P. Evaluation of User-Centric Cell-Free Massive Multiple-Input Multiple-Output Networks Considering Realistic Channels and Frontend Nonlinear Distortion. *Appl. Sci.* **2024**, *14*, 1684. https://doi.org/10.3390/app14051684

Academic Editor: Mirosław Klinkowski

Received: 18 January 2024
Revised: 15 February 2024
Accepted: 16 February 2024
Published: 20 February 2024



## 1. Introduction

To meet the growing demands of mobile network users, it is not enough to utilize larger bandwidths or densify networks. In addition, advanced transmission techniques that increase spectral efficiency must be used. For currently deployed 5G networks and future 6G networks, such a technique is Massive Multiple-Input-Multiple-Output (M-MIMO) [1], which involves the use of multi-element antenna arrays that allow for the creation of narrow beams of radio signals directed toward individual users. This enables spatial multiplexing of users sharing the same time-frequency resources. Fifth-generation systems employing M-MIMO typically assume that the connection of one user is provided by a single base station (BS), which is referred to as a network-centric architecture. In such an architecture, radio signal coverage is uneven, with users closer to the BS receiving a much stronger signal than those farther away. As a result of this uneven Received Signal Strength (RSS) distribution, there is a significant disparity in throughput between users near the BS and those at the cell edge [2]. Therefore, for 6G systems, a novel, user-centric cell-free architecture combined with M-MIMO (UCCF M-MIMO) is being considered [3]. In a UCCF M-MIMO network, the concept of cells disappears, and following the so-called canonical definition in [4], the user can be served by all surrounding base stations. This effectively places the user in the center of a virtual cell, greatly reducing the throughput disparities

among different users. The deployment of UCCF M-MIMO is possible using the open Radio Access Network (RAN) architecture and related 7.2 split [5]. In detail, a UCCF M-MIMO network (or more specifically its part) based on open RAN architecture is constituted by a single virtualized Central Unit (CU), virtualized Distributed Unit (DU), and multiple physical Radio Units (RUs). The virtualized CU–DU coordinates the RUs and is jointly responsible for user scheduling and high physical layer functions, e.g., calculation of precoding weights and modulation and coding scheme (MCS) selection. The physical RUs distributed over the cell area perform low physical layer functions and Radio Frequency (RF) processing of the signal, e.g., modulation, FFT, and application of precoder weights. However, the canonical implementation of UCCF M-MIMO assumes that every user is being served by all RUs. This approach would require enormous computational resources, e.g., to estimate the radio channel coefficients between all RUs and all UEs, compute large matrices of precoding weights, and perform resource scheduling. As in practice, both the virtualized CU–DU and each of the physical RUs have limited computational resources, it is of high importance to ensure reasonable scaling of a UCCF M-MIMO network. Moreover, some RUs that are placed far away from the UE would provide minor performance benefits compared to the required signaling overhead and demand for computational resources. From this perspective, it is of high importance to limit the number of RUs that are serving a single UE to balance performance gains and the growing computational and signaling overhead. In UCCF M-MIMO, this is achieved through the formulation of so-called serving clusters [6]. Serving clusters are dynamically formulated by the centralized CU–DU using various algorithms, e.g., those based on RSS or advanced Machine Learning (ML) solutions, which are aimed at meeting different optimization goals, like load balancing, energy efficiency, or throughput maximization. The architecture of UCCF M-MIMO is summarized in Figure 1.

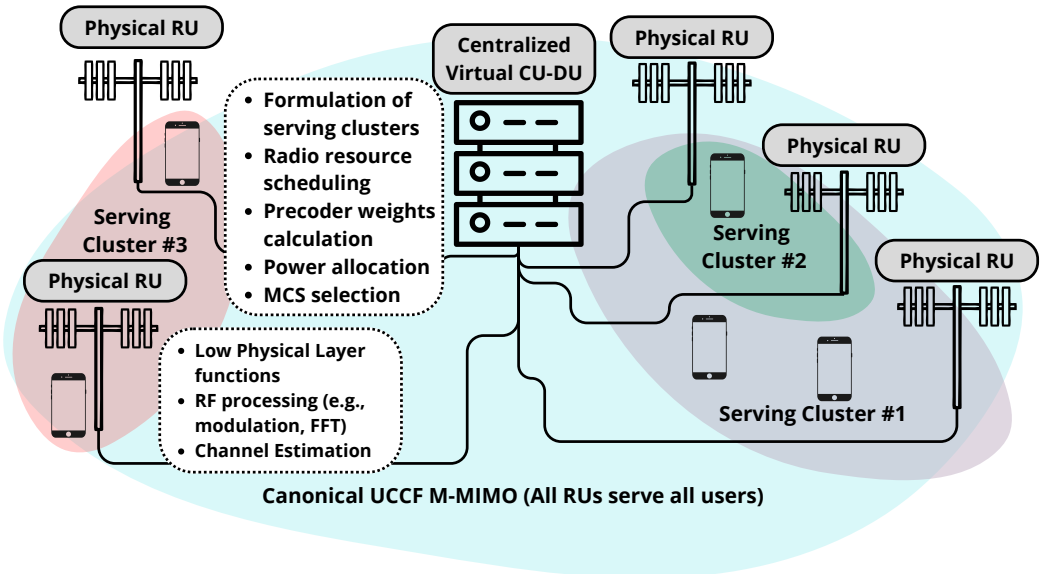


**Figure 1.** The concept and architecture of a UCCF M-MIMO network.

The user-centric cell-free M-MIMO network is an emerging topic regarding 6G, and numerous works focusing on simulation studies of such systems have already been published. However, most of them, even those coauthored by highly cited experts in the M-MIMO field like [4,7–10], utilize relatively simple system models. In most cases, these models involve single-carrier, narrowband transmission. In contrast, practical implementations of 5G/6G mobile networks utilize multi-tone modulations, typically Orthogonal Frequency-Division Multiple Access (OFDMA). Moreover, the time-frequency radio resources are often scheduled to users in 5G/6G networks as so-called resource blocks (RBs), which are also typically not considered in recent works. In addition, user throughput in practical 5G/6G communication systems depends on the selected modulation and coding scheme

(MCS), not the Shannon rate, as claimed in most recent works, e.g., [11]. Another point is the utilization of simple statistical models of radio channels that neglect the spatial correlations between users, which are crucial for M-MIMO. For example, the independent and identically distributed Rayleigh channel (which, in our work, is shown to be inadequate for simulations of M-MIMO systems), e.g., in [10]. Finally, most current works on both network-centric and UCCF M-MIMO networks neglect the impact of the typically nonlinear Power Amplifier (PA) on users' throughputs. However, it has been shown that in the worst-case scenario of Line-of-Sight (LoS) communication, the nonlinear distortion is steered toward scheduled users with the same precoding gain as the desired signal [12]. Also, when multiple users are scheduled, spatial intermodulations can occur, further affecting network performance [13]. Only the authors of [14] considered nonlinear distortion in the UCCF M-MIMO network but evaluated it under the Rayleigh channel, which we show is not appropriate for such an analysis. Therefore, there is a need to investigate M-MIMO systems with a user-centric architecture in an environment closely resembling a real network, including the use of OFDMA and a precise radio channel model based on 3D ray tracing. Furthermore, the multi-layer nature of future 6G systems, consisting of various functional blocks responsible for resource allocation, precoding, and the selection of modulation and coding schemes, should be considered. Finally, studies on the UCCF M-MIMO network should take into account the possible nonlinear distortion generated by Power Amplifiers (PAs) installed at M-MIMO RUs.

Compared to previous works, our contribution involves the proposition of an advanced simulation environment of an OFDMA-based UCCF M-MIMO network. This environment utilizes a realistic 3D ray-tracing radio channel model, radio resource allocation performed by a dedicated scheduler entity, throughput calculation based on the MCS, and, most importantly, a realistic model of a Power Amplifier (PA) that relies on the embedded link level to obtain a realistic impact of nonlinear distortion on the user throughput. This paper aims to provide the research community with an advanced system model that can be used to develop and test algorithms within an environment that is far closer to the real world compared to most other proposed system models [4,7–10]. The solution is described using mathematical formulas and algorithms for easy implementation by other researchers. Moreover, using the proposed advanced computer simulator, we examine the benefits of implementing a UCCF M-MIMO network architecture compared to the traditional network-centric architecture. This comparison is performed under an idealistic independent and identically distributed (i.i.d.) Rayleigh channel model and a realistic one obtained using ray-tracing software. Last but not least, we examine the UCCF M-MIMO network when utilizing nonlinear PAs. The simulation studies show that the results obtained under simplified models, e.g., under a Rayleigh channel or without nonlinear distortion, overestimate the achievable throughput compared to realistic 3D ray-tracing-based simulations. This is consistent with our observations during our previous studies [15], i.e., the antenna selection algorithm optimized under a simplified system model does not perform well under the more realistic one. In the following sections of this work, Section 2 presents the system model. The modeling of nonlinear distortion is described in Section 3. Section 4 provides a detailed description of the proposed simulation environment. The results of computer simulation studies are presented and discussed in Section 5. This paper concludes in Section 6.

## 2. System Model

In this paper, we consider a downlink in a UCCF M-MIMO network deployed according to the open RAN architecture with a centralized virtual CU–DU managing $N_{\mathrm{RU}}$ RUs. The RU of index $l$ is equipped with an M-MIMO antenna array of $M_l$ elements and has a total maximum radiation power of $P_l$. We assume a full-digital antenna array, i.e., each of the $M_l$ antennas is associated with a dedicated transceiver chain. At the end of the $m$-th transceiver chain, just before the antenna, there is a PA with a maximum output power (sometimes called saturation power) of $P_{\max,l} = \frac{P_l}{M_l}$. In the literature, there exists the

concept of hybrid beamforming, where a single transceiver chain is connected to several antennas to reduce implementation costs and computational complexity [16]. However, the full digital approach allows us to set precoder weights far more accurately, i.e., individually for each antenna. This enables us to achieve an upper bound of user throughput. While at the current stage of implementation of 5G systems hybrid beamforming is most likely to be practically used, future 6G systems can be expected to utilize more advanced solutions, e.g., due to more optimized hardware design.

The operation point of all PAs can be set to the $l$-th RU in terms of a so-called Input Back-Off (IBO) $\gamma_l$, which is the ratio between the input saturation power of the PA and the average power of the input signal. Lowering the operation point of the PA can avoid signal clipping and reduce the resultant nonlinear distortion, which is discussed in Section 3. In the case of a *perfect* PA, as considered typically in the literature, it is assumed that the average signal power at the PA output is equal to the saturation power. However, in this case, no nonlinear distortion will be modeled.

The considered UCCF M-MIMO network is OFDMA-based and utilizes bandwidth $B$ allocated at carrier frequency $f$. The bandwidth is split into $N_{\mathrm{rb}}$ resource blocks (RBs). Each of them exploits 12 OFDM subcarriers in the frequency domain and lasts one time slot of $T_{\mathrm{slot}}$. We assume that within a single RB of index $r$, the radio channel is flat. Thus, the vector of the complex radio channel coefficients between the $i$-th single-antenna User Equipment (UE) and the M-MIMO RU $l$ for RB $r$ is given by:

$$\mathbf{h}_{i,l,r} = \begin{bmatrix} h_{i,l,r,1} & h_{i,l,r,2} & \cdots & h_{i,l,r,M_l} \end{bmatrix}^T. \tag{1}$$

We assume that each radio channel coefficient already takes into account the antenna gain. The radio channel coefficients are estimated by the RUs and then transferred to the CU–DU for the purpose of centralized formulation of serving clusters, radio resource scheduling, calculation of precoder weights, power allocation, and MCS selection. To reduce the computational complexity of the considered UCCF M-MIMO system, we assume that the calculations of the precoder weights and power allocation are performed independently for each RU, as this allows for avoiding inversions of large matrices while utilizing a Zero-Forcing (ZF) precoder. As we are considering a multicarrier system, we also assume that both the precoder weights and power allocation are calculated independently for each RB $r$. As a result, RU $l$ transmits the following signal to UE $i$ at RB $r$ if scheduled:

$$\mathbf{X}_{i,l,r} = \sqrt{\frac{p_{i,l,r}}{12}} \delta_{i,r} \mathbf{D}_{i,l} \mathbf{A} \mathbf{w}_{i,l,r}^T \boldsymbol{\xi}_i, \tag{2}$$

where $p_{i,l,r}$ is the power allocated to UE $i$ by RU $l$ at RB $r$; $\mathbf{w}_{i,l,r}$ is the vertical vector of the precoder weights with a mean power equal to one; $\delta_{i,r}$ represents the result of radio resource scheduling ($\delta_{i,r} = 1$ if RB $r$ is allocated to UE $i$; otherwise, it is equal to zero); $\mathbf{D}_{i,l}$ is a matrix that is the result of serving cluster formulation, defined as $\mathbf{D}_{i,l} = \mathbf{I}_{M_l}$ if the $i$-th UE is being served by the $l$-th RU and otherwise, $\mathbf{D}_{i,l} = \mathbf{0}_{M_l}$; $\mathbf{A}_l$ is a diagonal matrix of size $M_l$, with each element $\alpha_{m,l}$ being the nonlinear attenuation of the desired signal for the $m$-th antenna of RU $l$ (see Section 3); and $\boldsymbol{\xi}_i$ is the vector of 12 downlink QAM symbols of UE $i$, i.e., one symbol per subcarrier. We can treat each element of $\boldsymbol{\xi}_i$ as an uncorrelated random variable of zero mean and a variance equal to one. Considering that there are $N_{\mathrm{UE}}$ users in total in the considered UCCF M-MIMO network, the total downlink signal received by UE $i$ at RB $r$ is given by:

$$\begin{aligned}\mathbf{y}_{i,r} &= \sum_{l=1}^{N_{\mathrm{RU}}}\sum_{k=1}^{N_{\mathrm{UE}}}\mathbf{h}_{i,l,r}^{H}\cdot\mathbf{X}_{k,l,r}+n_{i,r}+n_{\mathrm{dis},i}\\ &=\underbrace{\left(\sum_{l=1}^{N_{\mathrm{RU}}}\sqrt{\frac{p_{i,l,r}}{12}}\delta_{i,r}\mathbf{h}_{i,l,r}^{H}\mathbf{D}_{i,l}\mathbf{A}_{l}\mathbf{w}_{i,l,r}^{T}\right)\boldsymbol{\xi}_{i}}_{\text{Desired Signal}}+\\ &+\underbrace{\sum_{\substack{k=1\\k\neq i}}^{N_{\mathrm{UE}}}\left(\sum_{l=1}^{N_{\mathrm{RU}}}\sqrt{\frac{p_{k,l,r}}{12}}\delta_{k,r}\mathbf{h}_{i,l,r}^{H}\mathbf{D}_{k,l}\mathbf{A}_{l}\mathbf{w}_{k,l,r}^{T}\right)\boldsymbol{\xi}_{k}}_{\text{Inter-user interference}}+\underbrace{n_{i,r}}_{\text{Noise}}+\underbrace{n_{\mathrm{dis},i,r}}_{\text{Distortion}},\end{aligned}\tag{3}$$

where $n_{i,r}$ denotes the thermal noise, and $n_{\mathrm{dis},i,r}$ denotes the nonlinear distortion term that is the result of RU's PA characteristics, which is described in Section 3. It can be seen that both the desired signal and inter-user interference terms contain summation over all RUs. In this work, we consider that RUs are perfectly synchronized and connected with a backhaul of negligible latency. This is the best-case scenario in the context of a UCCF M-MIMO network, as it allows for the highest gains in the desired signal. Based on Equation (3), we can formulate the Signal-to-Interference-plus-Noise Ratio (SINR) for UE $i$ at RB $r$:

$$\mathrm{SINR}_{i,r}=\frac{\left|\sum_{l=1}^{N_{\mathrm{RU}}}\sqrt{p_{i,l,r}}\delta_{i,r}\mathbf{h}_{i,l,r}^{H}\mathbf{D}_{i,l}\mathbf{A}_{l}\mathbf{w}_{i,l,r}^{T}\right|^{2}}{\sum_{k=1}^{N_{\mathrm{UE}}}\left|\sum_{l=1}^{N_{\mathrm{RU}}}\sqrt{p_{k,l,r}}\delta_{k,r}\mathbf{h}_{i,l,r}^{H}\mathbf{D}_{k,l}\mathbf{A}_{l}\mathbf{w}_{k,l,r}^{T}\right|^{2}-\left|\sum_{l=1}^{N_{\mathrm{RU}}}\sqrt{p_{i,l,r}}\delta_{i,r}\mathbf{h}_{i,l,r}^{H}\mathbf{D}_{i,l}\mathbf{A}_{l}\mathbf{w}_{i,l,r}^{T}\right|^{2}+\sigma_{i,r}^{2}+\sigma_{\mathrm{dis},i,r}^{2}},\tag{4}$$

where $\sigma_{r}^{2}$, and $\sigma_{\mathrm{D},i,r}^{2}$ are the power of the thermal noise and nonlinear distortion per RB, respectively. As the radio channels between the users and precoder weights are known in the CU–DU at the stage of resource scheduling, the SINR can be relatively well approximated. Unfortunately, this is not the case when considering nonlinear distortion. However, the UE is capable of reporting interference levels that can be used to estimate the distortion terms, e.g., interference can be calculated based on Channel Quality Indicator (CQI) reports. Such an estimation is necessary to select the proper MCS by the CU–DU. We assume that a single MCS is allocated for each scheduled user. For this purpose, an effective signal quality metric must be obtained for all RBs allocated to this user, i.e., the so-called effective SINR. It has been shown in the literature that for the considered multicarrier OFDM system that is prone to frequency-selective fading of radio channels, the proper effective SINR metric is Exponential Effective SINR Mapping (EESM) [17]. The EESM for UE $i$ depends on the selected MCS and can be calculated as follows:

$$\mathrm{EESM}_{i,mcs}=-\beta_{mcs}\ln\left(\frac{1}{N_{\mathrm{rb}}}\sum_{r\in\mathcal{R}_{i}}\exp\left(-\frac{\mathrm{SINR}_{i,r}}{\beta_{mcs}}\right)\right),\tag{5}$$

where $\mathcal{R}_{i}$ is a set of indices of the RBs allocated to UE $i$, and $\beta_{mcs}$ serves as an approximate value to adjust for the selected modulation alphabet and coding rate. It will be adjusted by the CU–DU based on the selected MCS (see Section 4.4).

As in practice, both the virtualized CU–DU and each of the physical RUs have limited computational resources, it is of high importance to ensure reasonable scaling of the UCCF M-MIMO network. Following the definition in [3], the UCCF M-MIMO network is scalable when each of the following tasks has finite computational complexity and resource requirements concerning each RU as $N_{\mathrm{UE}}\to\infty$ in the whole network:

1. Signal processing for channel estimation.
2. Signal processing for data reception and transmission.
3. Fronthaul signaling for data and Channel State Information (CSI) sharing.
4. Power allocation optimization.

One of the possible solutions to meet scalability tasks 1-3 is to limit the number of users that a single RU can serve. Naturally, the single RU can only serve users that are within range of its reference signals. This limits the number of users for the channel estimation. Moreover, M-MIMO networks usually utilize a limited number of pilot sequences that put a boundary on the channel estimation computational resources, allowing them to meet scalability task 1. In the considered network, the result of serving cluster formulation is not directly related to signal processing for data reception and transmission. It can be that the RU serves many UEs but only a fraction of them currently have radio resources allocated. To set the maximum complexity of data reception and transmission in the considered UCCF M-MIMO network, we assume that there is a maximum number of Multi-User MIMO (MU-MIMO) layers that a single RU can create, i.e., a single RB can be allocated to a maximum of $N_{\mathrm{L}}$ users within a single RU. This allows us to meet the requirements of scalability task 2. With the fixed maximum number of MU-MIMO layers, the size of the precoding matrices will be limited, resulting in finite computational complexity of reception and transmission. As each of the RUs can support only a finite number of pilot sequences for channel estimation and MU-MIMO layers, the fronthaul signaling overhead (task 3) also has finite computational complexity. Finally, the computational complexity of power allocation optimization depends highly on the utilized algorithm. However, one can imagine low-complexity algorithms that can be applied independently for users served by each RU, e.g., an equal-power division that would offer finite computational complexity requirements, meeting scalability task 4.

## 3. PA Nonlinear Model

Most recent works focusing on M-MIMO networks neglect the impact of hardware impairments, such as the nonlinear characteristics of PAs. However, it has been shown that in the worst-case scenario, the distortion generated by the PAs installed at the M-MIMO's RU can be steered toward the UE with the same precoding gain as the desired signal. To model this phenomenon in this paper, we consider the so-called Rapp model of the PA [18].

As described in Section 2, every RU is equipped with a fully digital antenna array, meaning that there are $M_l$ transceiver chains and the same number of PAs installed at each RU. While the PA operates on a passband analog signal, our digital signal model creates equivalent distortions. Let us denote the $n$-th complex sample input to the PA from the $m$-th transceiver chain at the $l$-th RU as $\tilde{x}_{m,l}(n)$. This sample has already passed all stages of physical layer processing like precoding, modulation, and IFFT. The output complex sample $\tilde{y}_{m,l}(n)$ of the Rapp-modeled PA is a result of the following nonlinear transformation of the input signal sample $\tilde{x}_{m,l}(n)$ [18]:

$$\tilde{y}_{m,l}(n) = \frac{G\tilde{x}_{m,l}(n)}{1 + \left( \frac{\left|\tilde{x}_{m,l}(n)\right|^{2p}}{P^{p}_{\max,l}} \right)^{\frac{1}{2p}}}, \tag{6}$$

where $G$ is the amplifier gain (without loss of generality, $G = 1$ is assumed from now on); $P_{\max,l}$ is the saturation power at the output of each PA installed at RU $l$; and $p$ is the smoothing factor. The higher the $p$, the closer the PA's characteristic to the so-called soft limiter. Under the assumption that a complex Gaussian signal is transmitted (valid for OFDM signals [19]), based on the Bussgang theorem, the output sample of PA $\tilde{y}_{m,l}(n)$ can be decomposed into the desired signal sample $\tilde{x}_{m,l}(n)$ scaled by $\alpha_{m,l}$ and the nonlinear distortion sample $\tilde{n}_{\mathrm{dis},m,l}(n)$, which is uncorrelated with $\tilde{x}_{m,l}(n)$:

$$\tilde{y}_{m,l}(n) = \alpha_{m,l}\tilde{x}_{m,l}(n) + \tilde{n}_{\mathrm{dis},m,l}(n). \tag{7}$$

The scaling factor is given by:

$$\alpha_{m,l} = \frac{\mathbb{E}[\tilde{y}_{m,l}(n)\tilde{x}_{m,l}(n)^*]}{\mathbb{E}[\tilde{x}_{m,l}(n)\tilde{x}_{m,l}(n)^*]}, \tag{8}$$

where $\mathbb{E}[\,]$ denotes expectation and $^*$ is the complex conjugate. For the considered Rapp model of the PA, there is no closed-form expression to calculate $\alpha_{m,l}$. However, both the scaling factor $\alpha_{m,l}$ and the power of nonlinear distortion can be calculated numerically by simulating the processing of input samples by the Rapp model of the PA. Based on the output nonlinear distortion associated with each RU and taking into account the effect of the radio channel coefficients, one can estimate the power of nonlinear distortion $\sigma^2_{\text{dis},i,r}$ for the $i$-th UE within the band of the $r$-th RB:

$$\sigma^2_{\text{dis},i,r} = \mathbb{E}\left[\left|\sum_{l=1}^{N_{\text{RU}}}\sum_{m=1}^{M_l} h_{i,l,r,m}\mathcal{F}\{\tilde{n}_{\text{dis},m,l}(n)\}_r\right|^2\right], \tag{9}$$

where $\mathcal{F}\{\}_r$ denotes the Fourier transform at RB $r$. Similarly, one can estimate the values of $\alpha_{m,l}$ that constitute the diagonal matrix $\mathbf{A}_l$. Both $\mathbf{A}_l$, and $\sigma^2_{\text{dis},i,r}$ are necessary for the $\text{SINR}_{i,r}$ calculation in Equation (4).

## 4. Simulation Environment

Unlike the authors of the state-of-the-art works on UCCF M-MIMO networks [7–9], we propose an advanced simulation environment to evaluate the network's behavior. The main part of the simulation environment is the computer simulator, which consists of multiple functional blocks corresponding to the system model described in Section 2. The main loop of the proposed computer simulator for the UCCF M-MIMO network is depicted in Figure 2. Within one iteration of the simulation loop, a period of a single time slot is considered. The loop comprises six steps that are described in the following sections.

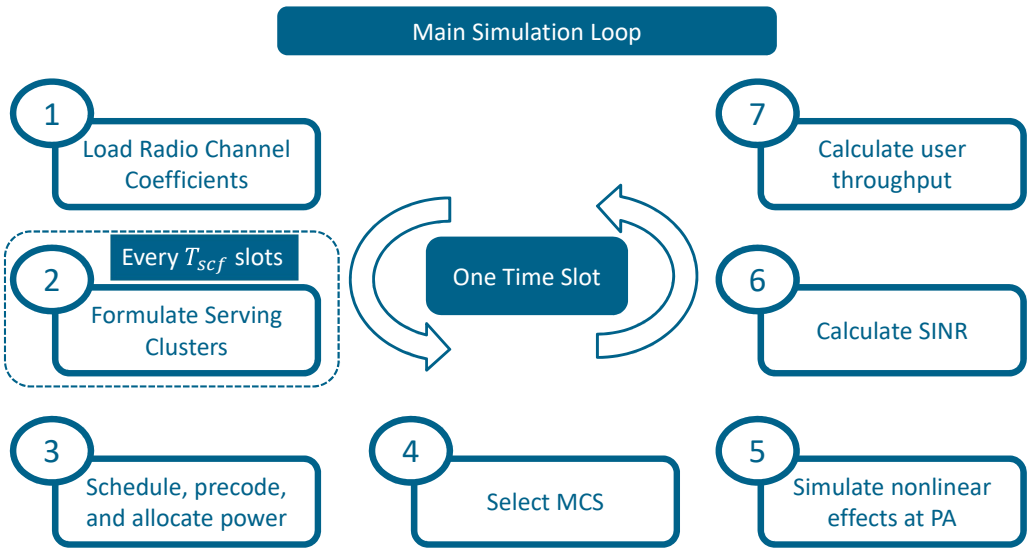


**Figure 2.** A block diagram of the main simulation loop.

### *4.1. Generation of Radio Channel Coefficients*

The simulation loop starts with the generation of the radio channel coefficients. There are two radio channel models implemented within the simulation environment. Both rely on the data from the Wireless InSite 3D ray-tracing software. The ray-tracing software can be controlled by setting different numbers of reflections and diffractions. The first option is to directly obtain the realistic radio channel coefficients from the 3D ray-tracer

output. This radio channel model closely reflects the reality of M-MIMO systems because it takes into account the spatial correlations between the radio channels of various users. The second option is to utilize the uncorrelated Rayleigh channel, commonly used in the literature. When this option is used, the radio channel coefficients are generated as uncorrelated complex Gaussian noise with a mean of zero and a variance equal to the average channel gain (including large-scale fading such as path loss) from the 3D ray-tracer output. It should be noted that the Rayleigh channel replaces the small-scale fading from the 3D ray-tracer output. The large-scale fading in both cases is a result of the ray-tracing simulations. This approach enables achieving comparable results between the two considered radio channel models. As such, the computational cost is nearly the same for both radio channels. However, as mentioned above, the channel is precomputed, thereby not increasing the computation time for a single simulator run. Potentially, by replacing the ray-tracing software from the simulation environment with a much simpler empirical large-scale fading model combined with the Rayleigh channel, the simulation time would be reduced at the cost of losing some of the close-to-reality properties of the considered radio environment.

### 4.2. Formulation of Serving Clusters

The second step of the simulation loop is the formulation of serving clusters. This procedure is run once every $T_{\text{scf}}$ time slots to enable stable radio resource scheduling, which relies on past user bitrates, i.e., the scheduler utilizes information about the past bitrates of users, and frequent reformulation of serving clusters could cause instability in radio resource allocation. We have implemented a state-of-the-art serving cluster formulation algorithm that takes as input the Reference Signal Received Powers (RSRPs) between the $i$-th UE and all RUs that are within the range of reference signals for this UE. The RSRP between the $i$-th UE and the $l$-th RU is denoted as $\gamma_{i,l}$ and defined as follows:

$$\gamma_{i,l} = \frac{P_l}{N_{\text{rb}}} \cdot \frac{\sum_{r=1}^{N_{\text{rb}}}, \sum_{m=1}^{M_l} |h_{i,l,r,m}|^2}{N_{\text{rb}} M_l} \tag{10}$$

where $\frac{P_l}{N_{\text{rb}}}$ is the transmit power per single RB. Based on this input, the serving cluster for the $i$-th UE is formulated by $J$ RUs characterized by the highest RSRP $\gamma_{i,l}$, i.e., for these RUs, $\mathbf{D}_{i,l} = \mathbf{I}_{M_l}$. For the remaining RUs, $\mathbf{D}_{i,l} = \mathbf{0}_{M_l}$. Such an approach is commonly used in related works on UCCF M-MIMO networks, e.g., [20], or with slight modifications introducing an RSRP threshold in [21].

### 4.3. Scheduling of Radio Resources, Precoding, and Power Allocation

We have implemented a centralized radio resource scheduling algorithm, which is placed within the CU–DU. It is based on the concept of a network-centric approach [22]. However, we have adapted it to the UCCF M-MIMO network architecture. The resulting procedure is presented in Algorithm 1. The scheduling algorithm takes as input the exponential average of UE past rates, inter-cluster interference observed by the UE, radio channel coefficients, and a threshold $\Delta$ in the range $< 0; 1)$ for the radio channel correlation coefficient, which signifies the minimum requirement for creating a new MU-MIMO layer. The implemented scheduling algorithm independently allocates each RB to users. The allocation is based on the Proportional Fairness (PF) metric, which is defined as the ratio between the maximum expected throughput at a given RB and the user's past rates. The calculation of the PF metric is performed in steps 2–5 of the scheduling algorithm, resulting in the sequence $\mathcal{K}$ containing the indices of the UEs (denoted as $k$), which are sorted according to their PF metrics. The user with the highest PF metric (first element of the sequence $\mathcal{K}$) is given the RB. However, due to the utilization of M-MIMO, the same time-frequency resources can be multiplexed in space. Thus, according to the PF metric, the next UEs are allocated, creating a set of $allocatedUEs$ with $N_{\text{L}}$ elements representing spatial layers. This procedure is described in steps 8–25 of the algorithm. Firstly, in step 10

the spatial correlation between all users within the *allocatedUEs* set is calculated, with the spatial correlation coefficient between the $i$-th and $k$-th UE at RB $r$ defined as:

$$\Theta_{r,i,k} = \left| \frac{\sum_{l=1}^{N_{\mathrm{RU}}} \mathbf{h}_{i,l,r} \mathbf{D}_{i,l} \cdot \mathbf{D}_{k,l} \mathbf{h}_{k,l,r}^{H}}{\sqrt{\sum_{l=1}^{N_{\mathrm{RU}}} \|\mathbf{h}_{i,l,r}\|^2 \cdot \sum_{l=1}^{N_{\mathrm{RU}}} \|\mathbf{h}_{k,l,r}\|^2}} \right|. \tag{11}$$

**Algorithm 1** Radio resource scheduling in a UCCF M-MIMO network

**Require:** past rate of each UE, inter-cluster interference calculated from the total past interference by each UE, radio channel coefficients, channel correlation threshold $\Delta$

1: **for** $r$ in 1 to $N_{\mathrm{rb}}$ **do**
2: compute the maximum wanted power for each UE using the *Desired Signal* term from (3), assuming that a single UE is scheduled, MRT precoder, and $p_{i,l,r} = \frac{P_l}{N_{\mathrm{rb}}}$
3: compute the maximum expected UE throughput for RB $r$ using the Shannon formula, with the SINR of each UE being the ratio of its maximum wanted power computed in step 2 and reported inter-cluster interference
4: compute the PF metric for each UE, being the ratio of its past rate and the current maximum expected throughput for RB $r$
5: create a sequence $\mathcal{K}$ containing the indices of UEs, sorted according to their PF metrics in descending order
6: $sumRate \leftarrow 0$
7: $allocatedUEs \leftarrow \varnothing$
8: **for** $k$ in $\mathcal{K}$ **do**
9: add $k$ to set of *allocatedUEs*
10: compute channel correlation coefficients between UEs being within the set of *allocatedUEs* using (11)
11: **if** any correlation coefficient exceeds $\Delta$ **then**
12: remove $k$ from set of *allocatedUEs*
13: **else**
14: set $\mathbf{D}_{k,l} = \mathbf{0}_{M_l}$ for all RUs that reached the maximum number of $N_{\mathrm{L}}$ spatial layers
15: compute precoding ZF vectors for *allocatedUEs*
16: allocate power equally between the *allocatedUEs*
17: compute the expected $\tilde{\mathrm{SINR}}_{i,r}$ of *allocatedUEs* using (4) and reported inter-cluster interference
18: compute *newSumRate* of *allocatedUEs* using the Shannon formula and expected SINR computed in the previous step
19: **if** $sumRate > newSumRate$ **then**
20: remove $k$ from set of *allocatedUEs*
21: **break**
22: **else**
23: $sumRate \leftarrow newSumRate$
24: $\delta_{k,r} \leftarrow 1$
25: **end if**
26: **end if**
27: **end for**
28: **end for**

If any of the computed channel correlation coefficients exceeds the threshold $\Delta$, the last added user is removed from the set of *allocatedUEs*. This is because the spatial correlation is directly mapped to the interference, e.g., with the Maximum Ratio Transmission (MRT) precoder, the power of the inter-user interference (between the $i$-th and $k$-th user) rises proportionally to $\Theta_{r,i,k}^2$. The next condition that the $k$-th user must meet is to increase the *sumRate* within RB $r$. This is performed in steps 14-18 of the algorithm. For scalability purposes, each RU has a limit of $N_{\mathrm{L}}$ spatial layers; if this limit is reached, the RU is no

longer considered for serving users by setting $\mathbf{D}_{i,l} = \mathbf{0}_{M_l}$ for this RU. Next, the Zero-Forcing (ZF) precoder is calculated for each RU in step 15. Note that the precoding weights are normalized to ensure $\|\mathbf{w}_{i,l,r}\|^2 = 1$. Although the ZF precoder has higher computational complexity than the MRT precoder, it has an important ability to suppress interference between users. This was shown in initial studies to be very beneficial for the considered UCCF M-MIMO network. It should be noted that we assume an architecture where precoding is performed independently for each RU. Moreover, we place a limitation on the number of spatial layers that the scheduler can create. As a result, the radio channel matrix, which is subject to ZF precoding, has a maximum size of $M_l \times N_{\mathrm{L}}$. The maximum number of spatial layers per RU is selected to ensure a reasonable processing time for ZF precoding. In step 16, power is allocated by splitting it equally among all spatial layers, independently within each RU. Power allocation in the UCCF M-MIMO network is a topic of significant importance. While some recent works address this problem, they are not designed for such a complicated system model utilizing an MCS, a scheduler, and a realistic radio channel. Moreover, it remains a challenging issue for the research community [6]. Existing power allocation algorithms are either optimized under a simplified system model, characterized by significant computational complexity, or unscalable. Instead, we utilize baseline power allocation, as presented in [3], which is characterized by low complexity and ensures the scalability of the UCCF M-MIMO network, i.e., equal power allocation among spatial layers within each RU. Having done this, the expected $S\tilde{I}NR_{i,r}$ can be computed for each UE that has the $r$-th RB scheduled using (4). The calculation of the SINR is performed in two places within the simulator: when scheduling users and when calculating the achieved rate. The first application is more challenging as it is based on channel estimates, calculated intra-serving cluster interference, and estimated inter-serving cluster interference. The channel between each UE and its serving RUs is estimated based on the uplink Sounding Reference Signal (SRS), and the knowledge of the utilized precoding can be used to calculate intra-cluster interference. Inter-cluster interference is assumed to be based on a user historical report similar to the Channel Quality Indicator (CQI), Reference Signal Received Quality (RSRQ), or SS-SINR, as outlined in the 5G specifications [23]. Using the expected $S\tilde{I}NR_{i,r}$, the *newSumRate* can be computed based on the Shannon formula. If the *newSumRate* is higher than the previously computed *sumRate*, the new spatial layer is created and the $k$-th UE has $\delta_{k,r}$ set to 1. Otherwise, it is removed from the *allocatedUEs*, and the loop breaks, as shown in steps 19-25 of the algorithm. After that, the procedure is repeated for the next RB.

### 4.4. MCS Selection

After the RBs, power, and precoder weights are allocated to the UEs, the proper MCS must be selected. We have implemented an algorithm where a single MCS is selected for all RBs allocated to a particular UE. Each MCS is associated with its spectral efficiency $SE_{mcs}$, $\beta_{mcs}$, and minimum $\mathrm{EESM}_{i,mcs}$, which are necessary to ensure a Block Error Rate (BLER) below 10%. Additionally, two parameters, $c_{mcs}$ and $b_{mcs}$, are required for the BLER calculation. Because parameters suitable for 5G are not easily accessible, we used the values proposed for MCS modeling in LTE. These values are summarized in Table 1 [24,25]. To select an MCS for a given UE, we compute $\mathrm{EESM}_{i,mcs}$ for each value of $\beta_{mcs}$ from Table 1 according to (5), using the expected $S\tilde{I}NR_{i,r}$ computed during the radio resource scheduling procedure. The selected MCS is the one associated with the highest $\mathrm{EESM}_{i,mcs}$ that exceeds the minimum requirement.

### 4.5. Simulation of Nonlinear Effects at PA

The fifth stage of the main simulation loop is the simulation of the nonlinear effects at the PA. While there exists an analytical framework for nonlinear distortion power calculation [26], it is limited, e.g., it requires the statistical properties of each wireless channel. Instead, link-level simulations are used. This is performed for all RUs and all scheduled UEs in the system. We simulate a batch of random QAM symbols, which are then subjected to precoding using the vectors already computed for all scheduled UEs, RBs,

and RUs. These samples are passed through the Rapp model of the PA according to (6). Based on the knowledge of both the input and output samples, one can estimate the power scaling coefficient matrix $\mathbf{A}_l$ and the power of nonlinear distortion $\sigma_{\text{dis},i,r}$ for each UE $i$ and RB $r$ using (8) and (9).

**Table 1.** MCS selection parameters based on [24,25].

| MCS | $SE_{mcs}$ (bit/Hz) | $\beta_{mcs}$ | Required EESM (dB) | $b_{mcs}$ | $c_{mcs}$ |
|---|---|---|---|---|---|
| 1 | 0.15 | 4.73 | −6.3 | 0.19 | 0.04 |
| 2 | 0.23 | 2.48 | −4.5 | 0.31 | 0.05 |
| 3 | 0.38 | 1.13 | −2.8 | 0.47 | 0.05 |
| 4 | 0.6 | 1.52 | −0.9 | 0.74 | 0.07 |
| 5 | 0.88 | 1.55 | 1.1 | 1.17 | 0.09 |
| 6 | 1.18 | 1.58 | 3.1 | 1.85 | 0.14 |
| 7 | 1.48 | 3.79 | 5.3 | 3.06 | 0.23 |
| 8 | 1.91 | 4.61 | 6.9 | 4.5 | 0.28 |
| 9 | 2.41 | 5.92 | 8.9 | 7.25 | 0.46 |
| 10 | 2.73 | 11.5 | 10.6 | 10.8 | 0.63 |
| 11 | 3.32 | 16.3 | 12.5 | 16.7 | 0.91 |
| 12 | 3.9 | 21.6 | 14.4 | 25.7 | 1.36 |
| 13 | 4.52 | 28.6 | 16.2 | 38.3 | 2.5 |
| 14 | 5.11 | 31.2 | 18.1 | 59.2 | 3.6 |
| 15 | 5.55 | 34.5 | 20.1 | 95.9 | 5.4 |

### *4.6. Calculation of Real SINR and BLER*

During the radio resource scheduling stage (Section 4.3), the expected $S\tilde{I}NR_{i,r}$ is used, which is based on the past inter-cluster interference reported by the UEs. However, the interference highly depends on the group of UEs scheduled within a particular time slot. Thus, the reported value usually differs from the real interference observed at a given UE, as well as the nonlinear distortion pattern. Thus, the next step of the main simulation loop is to calculate the real SINR using (4) with full knowledge of the radio channel coefficients, simulated nonlinear distortion, and scaling coefficients. With the calculated real $\text{SINR}_{i,r}$ for every UE and RB, along with the $\beta_{mcs}$ factor related to the selected MCS, one can calculate the real values of $\text{EESM}_{i,mcs}$. During the scheduling phase, it might happen that a particular UE wrongly estimated the inter-cluster interference, e.g., observing much higher real interference. This will influence the achieved rate. The real BLER can be calculated as follows:

$$\text{BLER}_{i,mcs} = 0.5 \cdot \text{erfc}\left(\frac{\text{EESM}_{i,mcs} - b_{mcs}}{\sqrt{2}c_{mcs}}\right), \tag{12}$$

where $b_{mcs}$ and $c_{mcs}$ are taken from Table 1 based on the MCS selected for the $i$-th UE.

### *4.7. Calculation of UE Rate*

The final stage of the main simulation loop is the calculation of the user throughput at the considered time slot. This is performed based on $SE_{mcs}$, which is associated with the selected MCS, and the calculated $\text{BLER}_{i,mcs}$. The throughput of the $i$-th UE is given by:

$$v_{i,mcs} = \frac{SE_{mcs} \cdot 12 \cdot 14 \cdot (1 - \text{BLER}_{i,mcs})}{T_{\text{slot}}}. \tag{13}$$

The numbers 12 and 14 are related to the fact that, according to the 3GPP specification [27], within a single RB, there are always 12 subcarriers in the frequency domain and 14 OFDM symbols within a single time slot. It should be noted that a UE is not always granted with RBs. Thus, to observe a reliable rate, the throughput should be averaged over multiple time slots.

### *4.8. Simulation Scenario*

To evaluate the considered UCCF M-MIMO network, we utilized an urban scenario developed for the purpose of the METIS project named the *Madrid Grid Model*, which included both a Line-of-Sight (LoS) park area and narrow street canyons with non-LoS (NLoS) radio conditions [28]. Within this area, we placed six RUs. The RU of index $l = 0$ corresponds to a macro-RU installed at a height of 45 m, with a maximal transmit power of $P_0 = 46$ dBm (128 PAs with $P_{\max,0} = 312.5$ mW) and an antenna array of $M_0 = 128$ elements (8 rows $\times$ 16 columns). The remaining RUs are micro-RUs installed at a height of 6 m, with a maximal transmit power of $P_l = 30$ dBm (32 PAs with $P_{\max,l} = 31.25$ mW) and equipped with $M_l = 32$ antennas (two panels with 8 rows $\times$ 2 columns). The remaining simulation parameters are listed in Table 2.

**Table 2.** Simulation parameters.

| Parameter | Value |
|---|---|
| Center frequency $f$ | 3.6 GHz |
| Number of RBs $N_{\text{rb}}$ | 69 |
| Time slot duration $T_{\text{slot}}$ | 0.5 ms |
| Subcarrier spacing | 30 kHz |
| Number of CU–DUs | 1 centralized and virtual |
| Number of RUs $N_{\text{ru}}$ | 6 (1 macro-RU, 5 micro-RUs) |
| RU installation height | macro-RU: 45 m; micro-RUs: 6 m |
| Rapp PA model smoothing factor $p$ | 12 |
| Transmit power $P_l$ | macro-RU: 46 dBm; micro-RUs: 30 dBm |
| Number of antennas $M_l$ | macro-RU: 128; micro-RUs: 32 |
| Threshold of correlation coefficient $\Delta$ | 0.7 |
| Maximum number of spatial layers $N_{\text{L}}$ | macro-RU: 32; micro-RUs: 8 |
| Wireless InSite configuration | 15 reflections, 1 diffraction |

## 5. Results

The UCCF M-MIMO network was evaluated using the advanced computer simulator described in Section 4. The simulation studies are divided into three parts: coverage analysis, throughput analysis without nonlinear effects, and throughput analysis considering nonlinear effects.

### *5.1. Coverage Analysis*

The first part of the simulation studies compares the coverage of the state-of-the-art network-centric architecture and that of the novel UCCF M-MIMO architecture. For this purpose, we generated radio channel coefficients for 3542 users uniformly distributed throughout the considered network area, with an inter-user space of 5 m. For each user and a varying number of serving RUs, we computed the Received Signal Strength (RSS) using the term *Desired signal* from (3), assuming that $p_{i,l,r} = \frac{P_l}{N_{\text{rb}}}$, and the MRT precoder. The results, presented as a map of the RSS averaged over the RBs, for both the network-centric architecture (each user can only be served by one RU providing the highest RSRP calculated using (10)) and the UCCF architecture with six serving RUs, are depicted in Figure 3. The benefits of utilizing the UCCF M-MIMO network architecture are especially visible in the alley on the right, where multiple micro-RUs were deployed. For the UCCF M-MIMO network architecture with six RUs serving the UEs, the radio signal within the alley maintains an average RSS oscillating around $-35$ dBm. On the other hand, for the network-centric architecture, clear boundaries between cells are visible, with the average RSS dropping below $-45$ dBm.

To gain better insights into the relationship between the observed RSS and the number of RUs serving a single UE, we examined the ratio between the RSS averaged over the RBs for the UCCF M-MIMO and network-centric architectures under varying numbers of RUs serving a single UE. The Cumulative Distribution Function (CDF) of this ratio is

depicted in Figure 4. We can see that the maximal gain related to the utilization of the UCCF M-MIMO network architecture over the network-centric approach is about 11 dB when using six RUs. This observation aligns with the findings from the coverage map. However, it can be seen that while a significant gain in the average RSS ratio can be observed between two and three RUs serving a single UE, for four, five, and six RUs, the gain is marginal. This somehow motivates the idea of forming serving clusters. It is worth mentioning that significant improvements in the average RSS can be observed for about 25% of UEs. This is because in many locations, the RSS from one RU is much higher than from others, e.g., the middle part of the considered area is mostly covered by the macro-RU, and the UEs placed therein benefit marginally from UCCF M-MIMO.

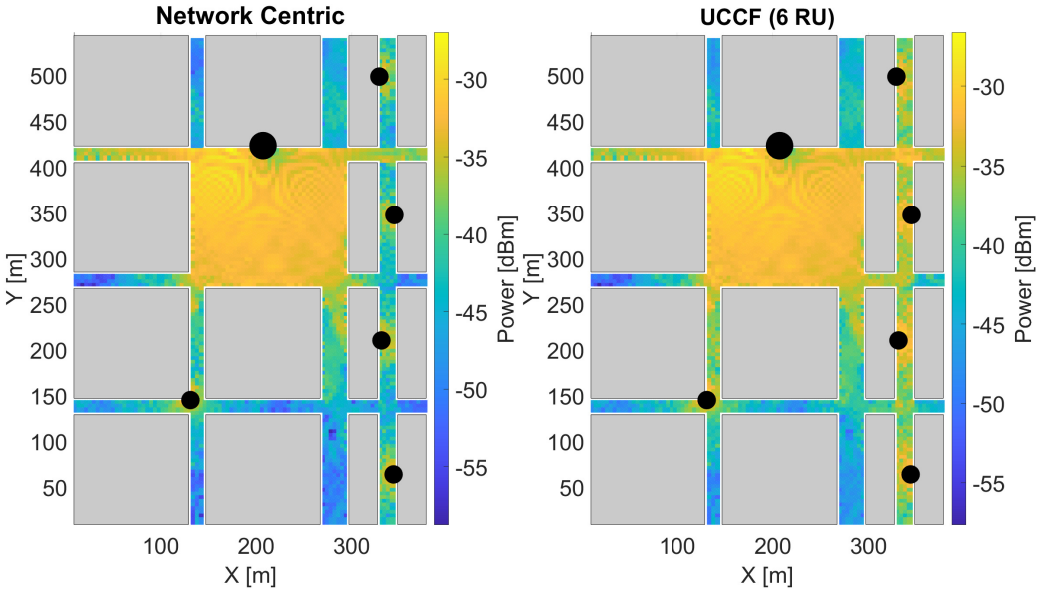


**Figure 3.** Comparison of RSS averaged over RBs between network-centric and UCCF approaches. The buildings are marked in gray, whereas RUs are marked with black dots (the larger dot corresponds to the macro-RU, whereas the smaller dots correspond to the micro-RUs).

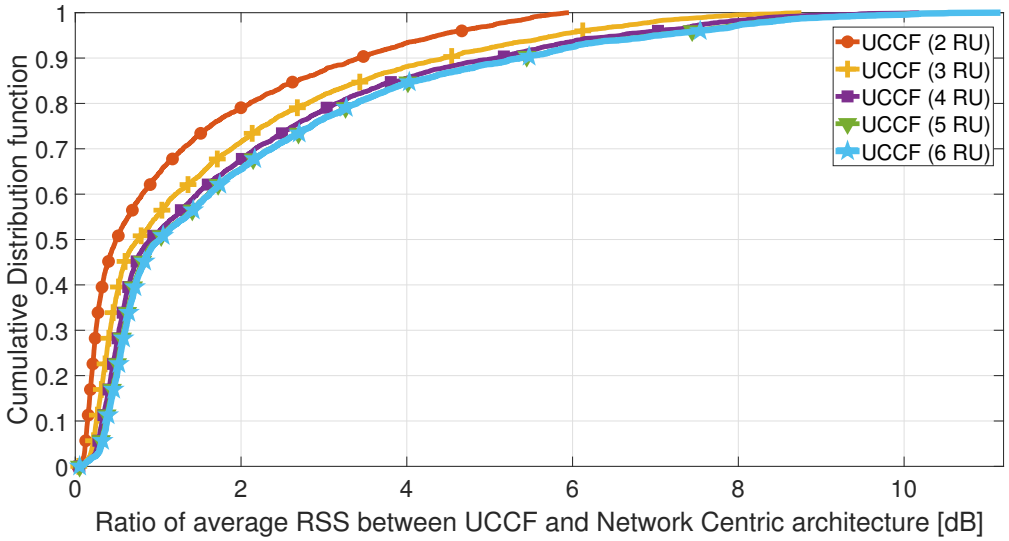


**Figure 4.** CDFs depicting the ratio between the RSS averaged over RBs achieved under a UCCF network architecture and that following a network-centric approach, with varying numbers of RUs.

### *5.2. Throughput Analysis without Nonlinear Effects*

After the coverage analysis, we conducted a system-level simulation of the UCCF M-MIMO network without taking into account the nonlinear effects at the PA. For this

purpose, we implemented the simulation environment described in Section 4 in MATLAB. We considered 20 users randomly placed in the alley (see Figure 4), where the effects of the selected network architecture were most visible during the coverage analysis. The initial positions of UEs followed a uniform distribution over the alley area. The users moved in random directions at a speed of 1.5 m/s, i.e., the azimuth of each user was uniformly distributed within the range of 0–360 degrees. Individual simulation runs involved continuous service and movement of these 20 users for 500 time slots (250 ms). During each time slot, the main loop depicted in Figure 2 was executed, but the fifth step was omitted. To achieve smooth plots, we conducted 30 independent simulation runs with different random generator seeds. Due to the high computational complexity of radio channel generation in the Wireless InSite 3D ray-tracer software, the realization of users' movements and the related channel coefficients for all simulation runs were pre-generated. This ensured a fair comparison, i.e., UEs followed the same paths and had identical radio channel coefficients in each simulation run, independent of the number of serving clusters.

#### 5.2.1. Rayleigh Channel

First, we evaluated the UCCF M-MIMO network and compared it against a state-of-the-art network-centric approach under the idealistic i.i.d. Rayleigh channel, which is widely used in the literature, e.g., [4,7]. The resulting CDFs of the average UE rates under the Rayleigh radio channel for both the network-centric approach and the UCCF M-MIMO network architecture, with varying numbers of RUs serving a single UE, are depicted in Figure 5. The CDF for the network-centric architecture exhibits an interesting stair-like shape. The stairs correspond to the maximum user throughput that can be achieved under a given MCS (vertical lines). This is because, under an uncorrelated Rayleigh radio channel, there are no spatial correlations between UEs. More specifically, when a high number of antennas is used, the radio channels between users become orthogonal, and as a result, there is no interference, i.e., the so-called *favorable propagation* occurs. While the number of UEs is relatively small and each UE can be served by only a single RU, the maximum number of spatial layers is not exceeded. As a result, all UEs experience almost static radio conditions, and in every time slot, the scheduling decision is exactly the same. This is not the case when considering the UCCF approach, where a single UE can create spatial layers within multiple RUs, causing situations where some UEs are not scheduled within a particular time slot (or are granted a limited set of RBs), which affects the decisions of the scheduler in the subsequent time slots. This is why the CDFs for the UCCF M-MIMO network architecture have smooth shapes. However, one can see that only the UCCF architecture with two RUs serving a single UE provides significant gains for users characterized by the worst radio conditions (10th percentile), without deteriorating the median or 90th percentile of the average UE rate distribution. Increasing the number of RUs to three, four, five, and six causes significant degradation. This is the result of equal power allocation, i.e., while there is no interference under an uncorrelated Rayleigh radio channel, the system becomes noise-limited. In such a case, the fact that the transmit power must be distributed among more UEs is not always compensated by the benefits of the joint UCCF network. For example, in the extreme case of six RUs, the median gain in the average RSS from the UCCF network is about 1 dB (see Figure 4), but power is always divided among all spatial layers (in the case of micro-RUs, it is about a 9 dB reduction in the average RSS). Moreover, in some situations, the RU allocates the same power to users who are both close and far away from it. As a result, power allocated to the far UE is "wasted".

#### 5.2.2. Ray-Tracer Channel

The second step was to repeat the studies within the ray-tracer radio channel, which outputs a channel characterized by spatial correlations causing interference in M-MIMO networks. The resulting CDFs of the average UE rates for the network-centric approach and the UCCF M-MIMO network architecture, with varying numbers of RUs serving a single UE, are depicted in Figure 6. In this case, a significant gain can be observed when

adopting the UCCF network architecture. This is because of interference coordination, where a UE served by multiple RUs benefits from ZF precoding suppressing interference between UEs served by the common RU. In the extreme case of six RUs (all RUs serve all UEs), all interference is suppressed by ZF precoding in each RU. However, power allocation can still negatively impact the rates achieved by some UEs, particularly for five and six RUs serving a single UE. On the other hand, the utilization of many RUs causes an effect expected in the literature for UCCF M-MIMO networks: the distribution of average UE rates becomes close to uniform. This means that the Mobile Network Operator (MNO) can guarantee uniform QoS for almost all users. It remains an open question regarding which approach is better from the perspective of the MNO: Is it better to offer network users almost equal throughput at the cost of significant throughput degradation for the best users, or to improve the throughput of median users and those with the worst radio conditions while maintaining the QoS of the best ones? The answer to this question depends on the specific conditions and goals of the MNO. However, the UCCF M-MIMO network can provide flexibility in its implementation through the proper formulation of serving clusters.

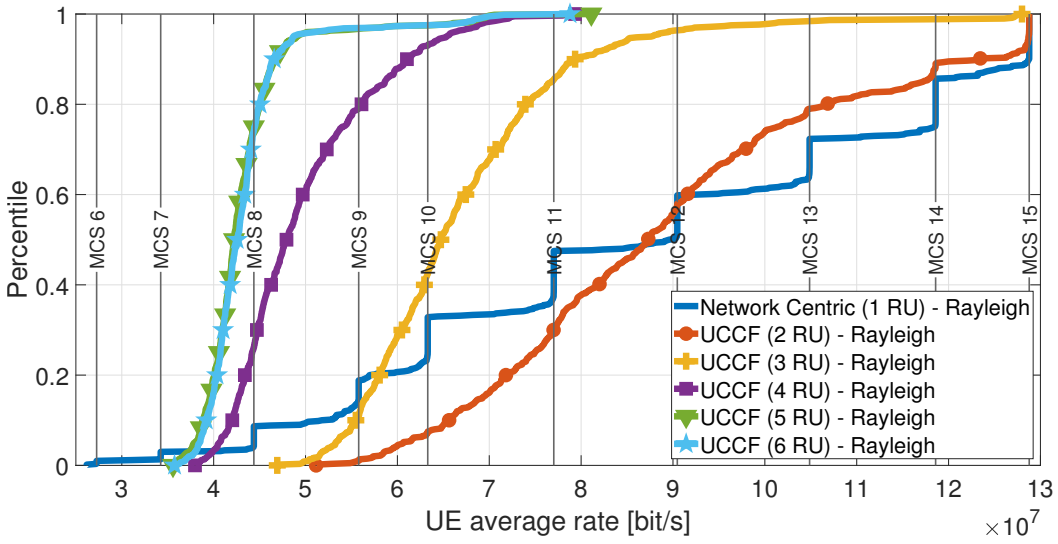


**Figure 5.** CDFs depicting the average UE rates for the network-centric and UCCF approaches, with varying numbers of RUs, under the Rayleigh radio channel.

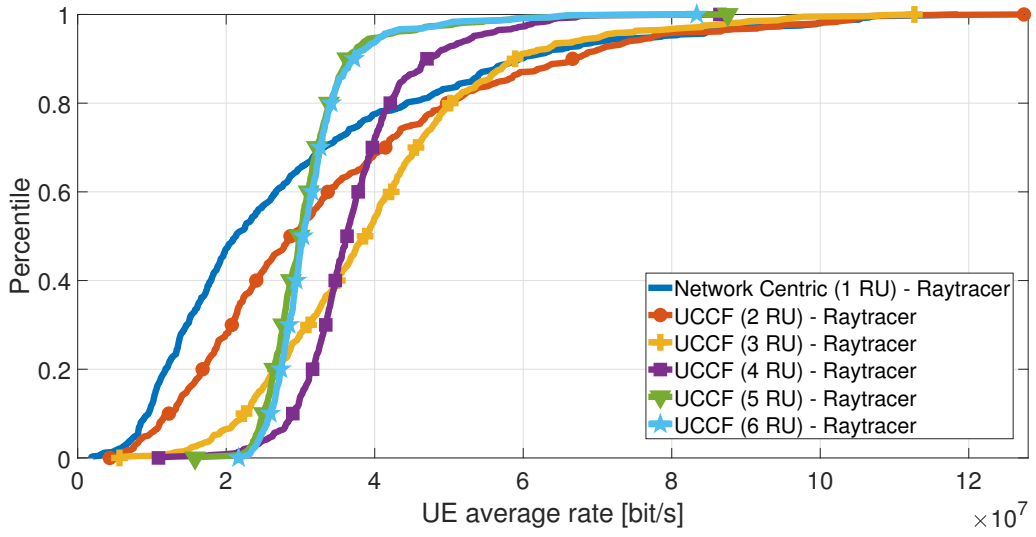


**Figure 6.** CDFs depicting the average UE rates for the network-centric and UCCF approaches, with varying numbers of RUs, under the realistic ray-tracer radio channel.

#### 5.2.3. Comparison

The results achieved for the Rayleigh and ray-tracer radio channels were compared in terms of the 10th, 50th (median), and 90th percentiles, as shown in Figure 7. The main observation is that the average UE rates achieved under the Rayleigh radio channel are much higher than those achieved under the ray-tracer channel. This is because the Rayleigh channel is not spatially correlated, which plays a crucial role in achieving the full performance of any M-MIMO system. From this perspective, the results obtained for this channel model may be overly optimistic, i.e., the UE rates are overestimated compared to real-world scenarios. However, even after rate normalization, the i.i.d. Rayleigh channel cannot accurately evaluate the relationship between the network-centric and UCCF M-MIMO network architectures. For example, while the highest median rate in the i.i.d. Rayleigh channel is achieved by the network-centric approach or UCCF M-MIMO architecture with two RUs, the ray-tracer-based simulations reveal that it is the best to use the UCCF M-MIMO network architecture with more than three RUs, depending on the MNO's goal. As a result, accurate radio channel models should be used for the evaluation of any M-MIMO system, especially when demonstrating the opportunities related to the UCCF M-MIMO network. By comparing the plots, it can also be seen that utilization of the UCCF M-MIMO network architecture in the considered network provides greater benefits for the realistic ray-tracer radio channel. This is because it allows for coordinated suppression of interference between RUs (achieved through ZF precoding applied within each RU) and increased array gain through the utilization of M-MIMO transmission from multiple RUs.

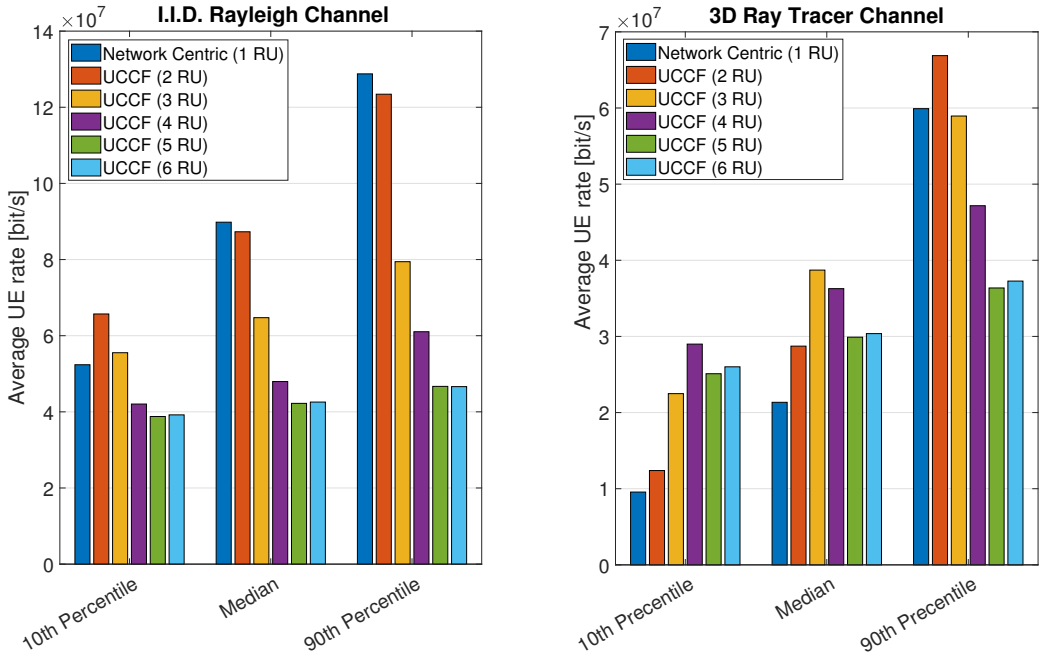


**Figure 7.** Comparison of 10th, 50th (median), and 90th percentiles from the distribution of the average UE rate for varying numbers of serving RUs and different radio channel models.

### *5.3. Throughput Analysis Considering Nonlinear Effects*

The last studies are related to system-level simulation considering nonlinearities. We followed the same setup and UE distribution used in Section 5.2, i.e., the number of UEs and their spatial distribution. However, here, all the steps of the main simulation loop were executed. We compared the results achieved without nonlinear effects, named *Perfect PA*, against the system with nonlinear distortion, with the IBO set to 0 dB and 6 dB, respectively. For the *Perfect PA* scenario, we assumed that the average system transmission power was $P_0 = 46$ dBm (macro-RU) and $P_l = 30$ dBm (micro-RUs, for $l > 0$). While this means that the IBO was equal to 0 dB for all RUs, causing severe nonlinear distortion effects, in reality, we omitted these in the *Perfect PA* scenario. As a result, $\mathbf{A}_l = \mathbf{I}_{M_l}$ for each RU, and no nonlinear distortion appeared, i.e., $\sigma^2_{\text{dis},i,r} = 0$. We are aware of the fact that in such a case, a comparison between *Perfect PA* and

real frontend cases is unfair, as the *Perfect PA* case uses higher useful power and is not penalized with nonlinear distortion that would result in higher throughput. However, this allows for a qualitative comparison of both schemes. For comparison under the i.i.d. Rayleigh channel, we selected the network-centric approach and the UCCF approach with two RUs serving a single UE, as it exhibited the highest rate improvements in Figure 7. The results are presented in Figure 8. It can be seen that under a high operation point of the PA (IBO 0 dB), the user throughput significantly degraded compared to the *Perfect PA* scenario and the results for the case of 6 dB IBO. This is due to the strong nonlinear distortion that was generated when the PA's operation point was low, i.e., close to 0 dB. On the other hand, lowering the operation point reduced the transmit power, but, as can be seen in this case, it only slightly affected the UE rates. This might be because in most cases, the lower transmit power did not degrade the SINR, resulting in the selection of a lower MCS for a given UE.

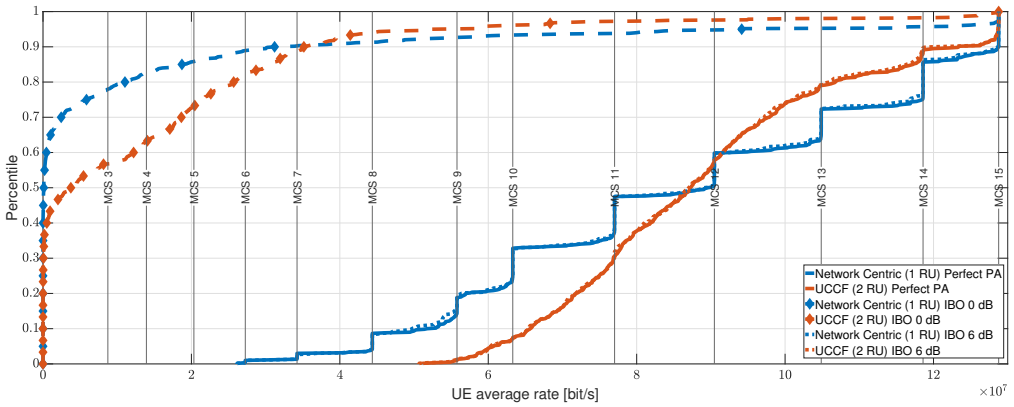


**Figure 8.** CDFs depicting the average UE rates for the network-centric and UCCF approaches, with varying numbers of RUs, under the Rayleigh radio channel, considering nonlinear effects.

The results obtained under the more realistic ray-tracer-based radio channel model are presented in Figure 9. For comparison, we selected the network-centric approach and the UCCF approach with three RUs serving a single UE. This configuration provided high average UE rate gains over the network-centric approach and did not deteriorate the rates achieved by any group of UEs (neither median nor 90th percentile), as visible in Figure 7. The observations are similar to those under the Rayleigh channel. The high operation point of the PA resulted in the generation of significant nonlinear distortion. However, under the realistic ray-tracer radio channel, a small drop in UE rates compared to the perfect PA case can be observed, related to the fact that the transmit power decreased by lowering the operation point of the PA by 6 dB. It might be that while each RU had a lower power to distribute among scheduled UEs, the allocation of a new spatial layer did not meet the condition of sum-rate improvement.

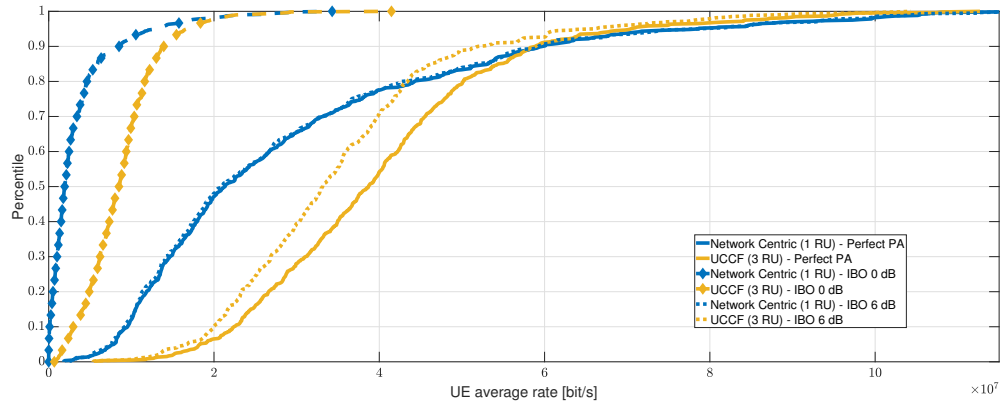


**Figure 9.** CDFs of average UE rates for network-centric and UCCF approaches, with varying numbers of RUs, under the Rayleigh radio channel, considering nonlinear effects.

## 6. Conclusions

In this paper, we evaluated a UCCF M-MIMO network using an advanced computer simulator under both state-of-the-art Rayleigh and realistic 3D ray-tracer-based radio channels, considering nonlinear effects at the PA. The results show that the behavior of the system is different under the idealistic radio channel and the realistic radio channel characterized by the spatial correlations between UEs. Moreover, we demonstrated the impact of the selection of the PA's operation point on the performance of the UCCF M-MIMO network. The main conclusion is that such a system should be evaluated using advanced computer simulators that consider multiple signal-processing stages and functional blocks within a 5G/6G communication system. Also, to avoid rate overestimation, close-to-real-world radio channels should be used, e.g., those based on 3D ray tracing. The operation point of the PA should be carefully chosen to achieve a balance between the transmit power and nonlinear distortion. Moreover, studies can be extended by evaluating the energy efficiency that depends on PA power consumption as a function of the IBO.

**Author Contributions:** Conceptualization, M.H. and P.K.; methodology, M.H.; software, M.H.; writing—original draft preparation, M.H.; writing—review and editing, P.K.; visualization, M.H.; supervision, P.K.; project administration, M.H. and P.K.; funding acquisition, M.H. and P.K. All authors have read and agreed to the published version of the manuscript.

**Funding:** Marcin Hoffmann was funded by the Polish National Science Centre, project no. 2022/45/N/ST7/01930. Pawel Kryszkiewicz was funded by the Polish National Science Centre, project no. 2021/41/B/ST7/00136.

**Institutional Review Board Statement:** Not applicable.

**Informed Consent Statement:** Not applicable.

**Data Availability Statement:** The radio channel coefficients obtained from the 3D ray tracer, and utilized in this publication are available in RepOD at https://doi.org/10.18150/NDGQ1P.

**Conflicts of Interest:** The authors declare no conflicts of interest.

## Abbreviations

The following abbreviations are used in this manuscript:

| | |
|---|---|
| BLER | Block Error Rate |
| BS | Base Station |
| CDF | Cumulative Distribution Function |
| CU | Central Unit |
| DU | Distributed Unit |
| EESM | Exponential Effective SINR Mapping |
| LoS | Line of Sight |
| MCS | Modulation and Coding Scheme |
| ML | Machine Learning |
| MNO | Mobile Network Operator |
| M-MIMO | Massive Multiple-Input-Multiple-Output |
| MU-MIMO | Multi-User MIMO |
| OFDMA | Orthogonal Frequency-Division Multiple Access |
| PA | Power Amplifier |
| PF | Proportional Fairness |
| RAN | Radio Access Network |
| RB | Resource Block |
| RF | Radio Frequency |
| RSRP | Reference Signal Received Power |
| RSS | Received Signal Strength |
| RU | Radio Unit |

| | |
|---|---|
| SINR | Signal-to-Interference-plus-Noise Ratio |
| UCCF | User-Centric Cell-Free |
| UE | User Equipment |
| ZF | Zero-Forcing |

## References


1. Akyildiz, I.F.; Kak, A.; Nie, S. 6G and Beyond: The Future of Wireless Communications Systems. *IEEE Access* **2020**, *8*, 133995–134030. [CrossRef]
2. Xu, Y.; Gui, G.; Gacanin, H.; Adachi, F. A Survey on Resource Allocation for 5G Heterogeneous Networks: Current Research, Future Trends, and Challenges. *IEEE Commun. Surv. Tutor.* **2021**, *23*, 668–695. [CrossRef]
3. Tugfe Demir, Ö.; Björnson, E.; Sanguinetti, L. Foundations of User-Centric Cell-Free Massive MIMO. *Found. Trends® Signal Process.* **2021**, *14*, 162–472. [CrossRef]
4. Buzzi, S.; D'Andrea, C. Cell-Free Massive MIMO: User-Centric Approach. *IEEE Wirel. Commun. Lett.* **2017**, *6*, 706–709. [CrossRef]
5. Ranjbar, V.; Girycki, A.; Rahman, M.A.; Pollin, S.; Moonen, M.; Vinogradov, E. Cell-Free mMIMO Support in the O-RAN Architecture: A PHY Layer Perspective for 5G and Beyond Networks. *IEEE Commun. Stand. Mag.* **2022**, *6*, 28–34. [CrossRef]
6. Ammar, H.A.; Adve, R.; Shahbazpanahi, S.; Boudreau, G.; Srinivas, K.V. User-Centric Cell-Free Massive MIMO Networks: A Survey of Opportunities, Challenges and Solutions. *IEEE Commun. Surv. Tutor.* **2022**, *24*, 611–652. [CrossRef]
7. Ngo, H.Q.; Ashikhmin, A.; Yang, H.; Larsson, E.G.; Marzetta, T.L. Cell-Free Massive MIMO: Uniformly great service for everyone. In Proceedings of the 2015 IEEE 16th International Workshop on Signal Processing Advances in Wireless Communications (SPAWC), Stockholm, Sweden, 28 June–1 July 2015; pp. 201–205. [CrossRef]
8. Björnson, E.; Sanguinetti, L. Scalable Cell-Free Massive MIMO Systems. *IEEE Trans. Commun.* **2020**, *68*, 4247–4261. [CrossRef]
9. Femenias, G.; Lassoued, N.; Riera-Palou, F. Access Point Switch ON/OFF Strategies for Green Cell-Free Massive MIMO Networking. *IEEE Access* **2020**, *8*, 21788–21803. [CrossRef]
10. Ammar, H.A.; Adve, R.; Shahbazpanahi, S.; Boudreau, G.; Srinivas, K.V. Downlink Resource Allocation in Multiuser Cell-Free MIMO Networks With User-Centric Clustering. *IEEE Trans. Wirel. Commun.* **2022**, *21*, 1482–1497. [CrossRef]
11. Zheng, J.; Zhang, J.; Björnson, E.; Li, Z.; Ai, B. Cell-Free Massive MIMO-OFDM for High-Speed Train Communications. *IEEE J. Sel. Areas Commun.* **2022**, *40*, 2823–2839. [CrossRef]
12. Larsson, E.G.; Van Der Perre, L. Out-of-Band Radiation From Antenna Arrays Clarified. *IEEE Wirel. Commun. Lett.* **2018**, *7*, 610–613. [CrossRef]
13. Kolomvakis, N.; Bavand, M.; Bahceci, I.; Gustavsson, U. A Distortion Nullforming Precoder in Massive MIMO Systems With Nonlinear Hardware. *IEEE Wirel. Commun. Lett.* **2022**, *11*, 1775–1779. [CrossRef]
14. Mokhtari, Z.; Dinis, R. Sum-Rate of Cell Free Massive MIMO Systems With Power Amplifier Non-Linearity. *IEEE Access* **2021**, *9*, 141927–141937. [CrossRef]
15. Hoffmann, M.; Kryszkiewicz, P. Reinforcement Learning for Energy-Efficient 5G Massive MIMO: Intelligent Antenna Switching. *IEEE Access* **2021**, *9*, 130329–130339. [CrossRef]
16. Sohrabi, F.; Yu, W. Hybrid Digital and Analog Beamforming Design for Large-Scale Antenna Arrays. *IEEE J. Sel. Top. Signal Process.* **2016**, *10*, 501–513. [CrossRef]
17. Hanzaz, Z.; Schotten, H.D. Analysis of effective SINR mapping models for MIMO OFDM in LTE system. In Proceedings of the 2013 9th International Wireless Communications and Mobile Computing Conference (IWCMC), Sardinia, Italy, 1–5 July 2013; pp. 1509–1515. [CrossRef]
18. Kryszkiewicz, P. Efficiency Maximization for Battery-Powered OFDM Transmitter via Amplifier Operating Point Adjustment. *Sensors* **2023**, *23*, 474. [CrossRef]
19. Azolini Tavares, C.H.; Marinello Filho, J.C.; Panazio, C.M.; Abrão, T. Input Back-Off Optimization in OFDM Systems Under Ideal Pre-Distorters. *IEEE Wirel. Commun. Lett.* **2016**, *5*, 464–467. [CrossRef]
20. Riera-Palou, F.; Femenias, G.; Lopez-Perez, D.; Piovesan, N.; De Domenico, A. Sleep Mode Strategies for Energy Efficient Cell-Free Massive MIMO in 5G Deployments. In Proceedings of the 2023 IEEE International Conference on Communications Workshops (ICC Workshops), Rome, Italy, 28 May–1 June 2023; pp. 618–624. [CrossRef]
21. Ito, M.; Kanno, I.; Amano, Y.; Kishi, Y.; Chen, W.Y.; Choi, T.; Molisch, A.F. Joint AP On/Off and User-Centric Clustering for Energy-Efficient Cell-Free Massive MIMO Systems. In Proceedings of the 2022 IEEE 96th Vehicular Technology Conference (VTC2022-Fall), London, UK, 26–29 September 2022; pp. 1–5. [CrossRef]
22. Yoo, T.; Goldsmith, A. On the optimality of multiantenna broadcast scheduling using zero-forcing beamforming. *IEEE J. Sel. Areas Commun.* **2006**, *24*, 528–541. [CrossRef]
23. Dahlman, E.; Parkvall, S.; Skold, J. *5G NR: The Next Generation Wireless Access Technology*, 1st ed.; Academic Press, Inc.: Cambridge, MA, USA, 2018.
24. Bossy, B.; Kryszkiewicz, P.; Bogucka, H. Optimization of energy efficiency in the downlink LTE transmission. In Proceedings of the 2017 IEEE International Conference on Communications (ICC), Paris, France, 21–25 May 2017; pp. 1–6.
25. Hanzaz, Z.; Schotten, H.D. Performance evaluation of Link to system interface for Long Term Evolution system. In Proceedings of the 2011 7th International Wireless Communications and Mobile Computing Conference, Istanbul, Turkey, 4–8 July 2011; pp. 2168–2173. [CrossRef]

26. Mollén, C.; Gustavsson, U.; Eriksson, T.; Larsson, E.G. Spatial characteristics of distortion radiated from antenna arrays with transceiver nonlinearities. *IEEE Trans. Wirel. Commun.* **2018**, *17*, 6663–6679. [CrossRef]
27. 3GPP. NR; Physical channels and modulation (Release 18). TS 38.211 v.18.0.0, 3GPP, 2023. Available online: https://portal.3gpp.org/desktopmodules/Specifications/SpecificationDetails.aspx?specificationId=3213 (accessed on 17 January 2024).
28. METIS. Mobile and wireless communications Enablers for the Twenty-twenty Information. In *Deliverable D6.1, Simulation Guidelines v1.0*; 2013. Available online: https://cordis.europa.eu/docs/projects/cnect/9/317669/080/deliverables/001-METISD61v1pdf.pdf (accessed on 17 January 2024).

## 7.14 Publication [P14]

M. Hoffmann, P. Kryszkiewicz, and G. P. Koudouridis, "Modeling of real time kinematics localization error for use in 5G networks," *EURASIP Journal on Wireless Communications and Networking*, vol. 2020, no. 1, p. 31, 2020.

MNiSW Points: 70

Number of citations:

- according to Web of Science: 8
- according to Google Scholar: 15

mgr inż. Marcin Hoffmann
Instytut Radiokomunikacji, Politechnika Poznańska
ul. Polanka 3, 60-965 Poznań

Poznań, 10 kwietnia 2021 r.

# OŚWIADCZENIE W SPRAWIE AUTORSTWA PRACY

Oświadczam, że w pracy:

*M. Hoffmann, P. Kryszkiewicz, G. P. Koudouridis, "Modeling of Real Time Kinematics localization error for use in 5G networks" EURASIP Journal on Wireless Communications and Networking, tom 31, styczeń 2020*

mój udział polegał na:

- Opracowaniu koncepcji modelowania błędu lokalizacji związanego z technologią Real Time Kinematics
- Implementacji generatora błędu lokalizacji
- Przeprowadzeniu symulacji
- Przygotowaniu wstępnej wersji treści artykułu

Mój procentowy udział w powstanie pracy szacuję na: 65%

.....

Podpis

dr hab. inż. Paweł Kryszkiewicz, prof. PP
Instytut Radiokomunikacji, Politechnika Poznańska
ul. Polanka 3, 60-965 Poznań

Poznań, 14 sierpnia 2025 r.

# OŚWIADCZENIE W SPRAWIE AUTORSTWA PRACY

Oświadczam, że w pracy:

*M. Hoffmann, P. Kryszkiewicz, G. P. Koudouridis, "Modeling of Real Time Kinematics localization error for use in 5G networks" EURASIP Journal on Wireless Communications and Networking, tom 31, styczeń 2020*

mój udział polegał na:

- Zainicjowaniu i koordynacji prac nad artykułem
- Dyskusji nad proponowanymi rozwiązaniami, uzyskanymi wynikami, propozycji modyfikacji i kolejnych kroków.
- Zaproponowaniu struktury artykułu, iteracyjna modyfikacja notacji matematycznej i tekstu.
- Przeprowadzeniu procesu wysłania pracy, odpowiedzi na recenzje i przygotowanie ostatecznej wersji pracy

Mój procentowy udział w powstanie pracy szacuję na: 25%

Podpis

Dr Georgios P. Koudouridis
Huawei Technologies,
Stockholm, Sweden

Stockholm, 13th of April 2021

# AUTHORSHIP AND ENGAGEMENT DECLARATION

Hereby, I declare that regarding the publication underneath:

> *M. Hoffmann, P. Kryszkiewicz, G. P. Koudouridis, "Modeling of Real Time Kinematics localization error for use in 5G networks" EURASIP Journal on Wireless Communications and Networking, vol. 31, January 2020*

my contribution was the following:

- Quality review of the overall article;
- Discussing the research work objectives and the material, shaping the manuscript, and writing/reviewing text.

I assess my contribution to this paper to be around 10%.

With kind regards,

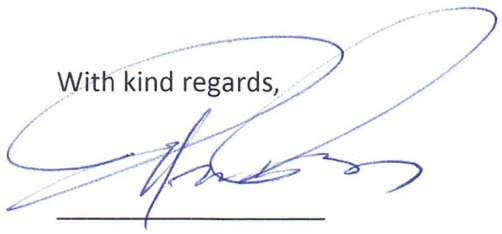

signature

Hoffmann *et al. EURASIP Journal on Wireless Communications and Networking* (2020) 2020:31
https://doi.org/10.1186/s13638-020-1641-8

EURASIP Journal on Wireless Communications and Networking

RESEARCH Open Access

# Modeling of Real Time Kinematics localization error for use in 5G networks

Marcin Hoffmann[1], Paweł Kryszkiewicz[1*] and Georgios P. Koudouridis[2]

**Abstract**

In 5G networks information about localization of a user equipment (UE) can be used not only for emergency calls or location-based services, but also for the network optimization applications, e.g., network management or dynamic spectrum access by using Radio Environment Maps (REM). However, some of these applications require much better localization accuracy than currently available in 4G systems. One promising localization method is Global Navigation Satellite System (GNSS)-based Real-Time Kinematics (RTK). While the signal received from satellites is the same as in traditional GNSS, a new reception method utilizing real-time data from a nearby reference station (e.g., 5G base station) results in cm-level positioning accuracy. The aim of this paper is to obtain a model of the RTK localization error for smartphone-grade GNSS antenna under open-sky conditions, that can be used in 5G network simulators. First, a tutorial-style overview of RTK positioning, and satellite orbits prediction is provided. Next, an RTK localization simulator is implemented utilizing GNSS satellites constellations. Results are investigated statistically to provide a simple, yet accurate RTK localization error framework, which is based on two Gauss-Markov process generators parametrized by visible satellites geometry, UE motion, and UE-satellite distance error variance.

**Keywords:** Radio environment maps, Localization, Real-Time Kinematics, Global positioning system, Error modeling

## 1 Introduction

The development of localization methods in cellular networks started with the formulation of the enhanced 911 (E911) location requirements by the Federal Communications Commission (FCC) of the USA in the 1990s [1]. The aim of the E911 requirements were to locate user equipment (UE) emergency calls with the root-mean square error (RMSE) of 125 m in 67% of all cases [1]. In cellular networks from 2G to 4G, firstly standardization effort was put into fulfil government requirements. With the networks development UE localization information began to be attractive for operators from a commercial point of view, resulting in introduction of location-based services (e.g. social networking, advertising) [1].

5G networks come with a set of new use cases where UE localization information is necessary, not only for emergency and user-plane applications, but also for Intelligent Transportation Systems Aerial Vehicles or Industrial Applications [2]. Moreover in 5G systems localization, data will be utilized for network optimization applications such as self-organizing networks (SON), network management, or dynamic spectrum access (DSA) [1].

Implementation of the mentioned network optimization applications may be based on the Radio Environment Maps (REMs) for both SON [3] and DSA [4]. REM can be understood as a real-time model of the real-world radio environment using multi-domain information (e.g., available radio links, wireless channel parameters) [5]. However, the implementation of REM requires accurate and robust localization information, firstly during data acquisition, and secondly when serving REM users. Localization can be achieved either by means of trilateration [6–8], triangulation [9], or fingerprinting [10]. However, the most suitable localization method for REM under outdoor and open-sky conditions is the Real Time Kinematics (RTK) [11] which is based on Global Navigation Satellite System (GNSS). It provides centimeter-level accuracy based on standard satellite-based GNSS signal while requiring constant connection to a reference station of known coordinates, e.g., 5G base station (BS). Although the localization error of the conventional GNSS is well investigated [12], there is no RTK error model that takes

*Correspondence: pawel.kryszkiewicz@put.poznan.pl
[1]Chair of Wireless Communications, Poznan University of Technology, Polanka 3, 60-965 Poznan, Poland
Full list of author information is available at the end of the article

into account the localization error as a function of daytime and geographical localization.

The aim of this paper is to study on the RTK localization error for smartphone-grade antenna under open-sky conditions, assuming line-of-sight (LoS) propagation between UE and each of the satellites. For better understanding of the RTK localization approach, detailed tutorial-style mathematical description is also provided. Based on simulations and statistical analysis important factors are extracted and a simplified yet accurate framework for the generation of RTK localization error is proposed. The framework takes into account UE motion, UE location and time of a day influencing geometry of visible satellites. One additional parameter is the cutoff angle allowing to consider only GNSS satellites exceeding given elevation above horizon. This allows for mimicking RTK operation in the urban environment where buildings block LoS propagation between some satellites and an UE. The resultant error both follows the proper distribution and is time continuous. The proposed model is of high importance when simulating 5G systems that utilize REM technology in outdoor environment with relatively low altitude buildings. Step-by-step description of the proposed algorithm is presented to simplify its implementation.

This paper is organized as follows: related work is discussed in Section 2. Section 3 provides brief description of REM concept and highlights some of the REMs applications where accurate localization may be required. Section 4 introduces the concept of RTK in relation to the conventional GNSS localization. Section 5 describes mathematical models of RTK, almanac-based satellites orbits prediction, and theory related with Gauss-Markov process including its generation with autoregressive model. Section 6 discusses the simulation results of the RTK localization error. The simplified framework for generation of RTK localization error under open-sky conditions is proposed in Section 7. Conclusions are formulated in Section 8.

## 2 Related work

As mentioned there are various ways to obtain user position. Some of them utilize trilateration, e.g., Observed Time Difference of Arrival (OTDoA) defined for cellular networks in LTE Positioning Protocol (LPP) [6], 802.15.4a ultra wide band (UWB) [7], or different implementations of GNSS, e.g., Global Positioning System (GPS) or Galileo [8]. Other ones, may use triangulation. This approach requires accurate Angle of Arrival (AoA) measurements, thus it is expected to be used in 5G systems utilizing massive MIMO (M-MIMO) technology [9]. Another interesting localization technique is utilization of radio frequency pattern matching (RFPM), called also fingerprinting. User position is estimated by comparing measured value (e.g., received signal strength (RSS)), with the fingerprint (previously measured RSS, tagged with geographical localization) from database. User position is the localization tag of the best matching fingerprint [10]. Fingerprinting is not explicitly defined in LPP; however, there are some works describing its implementation on the basis of the LTE positioning infrastructure [13, 14].

On the other hand RTK is defined in LPP [6] and foreseen for 5G networks [15]. The RTK method is mostly useful when REM is utilized in 5G network under outdoor conditions. With its centimeter-level accuracy it is currently widely used in geodesy or agriculture. Furthermore, it has been shown that RTK may be available for smart phones and provide cm-level accuracy in the open-sky conditions [16]. However, its performance can be degraded in urban environment, e.g., due to the cycle-slips phenomenon [17, 18].

While considering localization techniques as important features of the 5G systems, questions arise on the reliability of acquired localization data and the influence of the localization error on the network performance. The localization error of the conventional GNSS can be modeled as a bivariate normal distribution with $x$ (e.g., North-South) and $y$ (e.g., East-West) direction errors being uncorrelated [12]. In the case of RTK such a model, suitable, e.g., for 5G network simulations, is not available. In [19], authors analyzed localization error components of the RTK variant utilizing several cooperating base stations arranged in network, i.e. network RTK (NRTK). The final localization error obtained on the basis of the mathematical models and raw measurements is given only in terms of root-mean square (RMS). However, no information could be found about distribution, influence of satellites constellation or correlation of error in time. Studies in [20] are focused on the impact of the air humidity and sky obstruction on RTK localization error, but with no proposal of global RTK error model.

In [21], an error model is proposed, but its parameters are obtained only on the basis of the raw RTK measurements related to specific geographical localization. Also, the impact of the visible satellites geometry on RTK localization error was not taken into account.

## 3 5G radio environment maps

As it was mentioned in the Section 1, REMs are going to be a significant part of the future 5G networks. Their main aim is to improve the efficiency of the network and radio resources management. This section will firstly briefly describe REM concept and secondly discuss some of the 5G REMs applications, where accurate localization can be required.

### 3.1 REM concept

REM can be described as a live-changing model of a real-world radio environment using multi-domain information [5]. REM stores and processes information to support prediction and intelligent network management. Data stored in REM can be divided into long-term information (e.g., base station antenna parameters, local country law restrictions) and short-term information (e.g., available radio links, wireless channel parameters) [22].

Figure 1 depicts an example structure realization of REM as suggested in [23]. The context information tagged with localization and time is provided by so-called measurement capable devices (MCDs), e.g., UEs or BSs. Capturing the data from the MCDs is managed by the so-called REM acquisition module, and the information is further stored in REM storage structure. REM users sends service requests tagged with its current localization to the REM manager. REM manager is an intelligent part of the REM responsible for processing data from REM storage module and handling REM users requests.

### 3.2 Possible RTK applications in 5G REMs

As depicted in Fig. 1, REMs require localization information firstly to tag MCDs measurements with location, and secondly when REM user requests service from REM manager. There are many applications of 5G REMs which require accurate positioning, e.g.,

- *Interference coordination: [24]* where power density maps allow to perform interference coordination between users in a network.
- *M-MIMO [25]* where a database of the UEs AoAs related to the localization is proposed to manage Spatial Division Multiple Access (SDMA) in MIMO networks.
- *Location-based protocols in vehicular networks [26]* where REM provides location-specific transmission parameters for each vehicle.

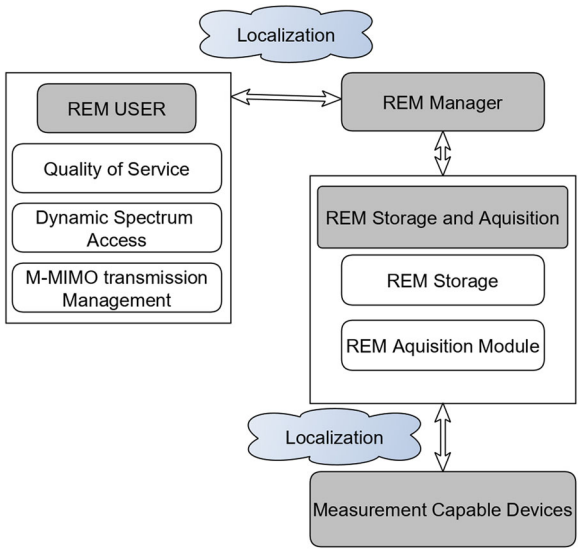


**Fig. 1** The example REM structure

In the *spectrum sensing* and *M-MIMO*, an accurate localization method like RTK can reduce errors related to the database measurement grid. This can allow for more accurate information especially in higher frequencies. In the case of *location-based protocols in vehicular networks* RTK can be utilized for much more precise definition of transmission areas.

## 4 GNSS localization

This section provides a brief description of the conventional positioning with GNSS, and later introduces the concept of RTK. In addition some features of RTK, e.g., UE-satellite range error, energy consumption, are discussed in relation to the conventional GNSS.

### 4.1 Conventional GNSS

A GNSS receiver uses the trilateration method to compute its position based on the distances measured to at least four satellites of known coordinates. A conventional GNSS receiver computes the distance between a UE and a satellite by obtaining the time offset between spread spectrum code transmitted by the satellite and a local code replica (code phase measurements). A chipping rate for basic civil L1 GPS signal is 1.023 Mcps. Even though the received signal is sampled at frequencies higher than the chip rate, due to, e.g., the multipath propagation and the receiver noise the UE-satellite range error equals for the state of art receivers about 1 m [8]. Additional source of error is the propagation through the troposphere and the ionosphere. The signal propagation speed and direction is changing while passing through these atmosphere layers. Moreover, non-perfect clocks synchronization, especially caused by relatively low quality UE's local oscillator, causes the satellite-UE clock offsets. These are another sources of propagation error causing the final UE-satellite range error for the stand-alone single-frequency receiver to equal around 6 m [8].

### 4.2 RTK

Real-Time Kinematics refers to the obtaining position estimation of moving UE in real time (i.e. without additional post-processing), with the help of a reference station, and on the basis of the carrier phase measurements [20]. Similarly, as in concventional GNSS receiver, RTK also provides UE position estimate based on the trilateration method. The difference lies in the method for obtaining the distance between the UE and the satellite. While conventional GNSS receiver utilizes code phase

measurements, in RTK, the UE-satellite range computation is based on the phase difference between the carrier signal received from the satellite and the local carrier replica (carrier phase measurements). Second difference in relation to the conventional GNSS is taking advantage of the so-called relative positioning, where a reference station of known coordinates is utilized, as shown in Fig. 2. The position of UE in relation to the reference station position is obtained with the help of assistance data provided by the reference station (e.g., its localization and raw carrier phase measurements data) [8].

The UE-satellite range influences the received signal phase which is normalized to a carrier wavelength. The distance between satellite and UE is presented as the sum of an integer and a fractional number of carrier wavelengths. By the solving proper equation, the receiver can find this integer number of wavelengths, and thus solve the so-called "integer ambiguity" shown in Fig. 3. At the same time, UE position approximating mostly the received carrier phase from all visible GNSS satellites is established. The fractional phase $\phi(t)$ estimate allows for tracking UE position with sub-wavelength accuracy. The RTK receiver initialization time which is referred to as time to ambiguity resolution (TAR) [16], corresponds to the time necessary for resolution of the integer ambiguities. The maximum error in carrier phase measurement is below 1 carrier wavelength which for the L1 GPS signal frequency, i.e., 1575.42 MHz, equals about 19 cm [8].

The carrier phase measurements are affected by the same types of phenomena like code phase measurements: multipath propagation, receiver noise, atmospheric propagation errors, and satellite and UE clock biases. However, thanks to the relative positioning, atmospheric propagation errors, and clock biases may be canceled out as discussed in Section 5.1. UE-satellite range error for carrier phase measurements is typically in the range from 0.5 to 1 cm and is mainly caused by the multipath propagation

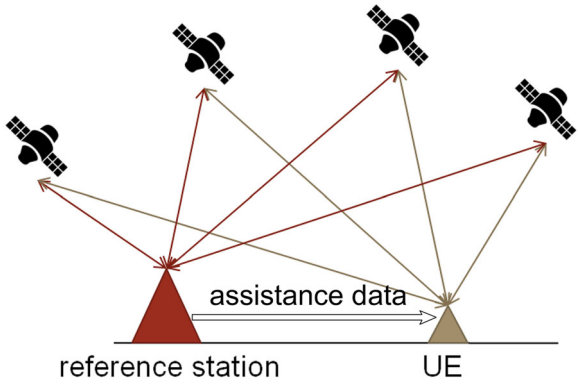


**Fig. 2** Concept of the reference station providing assistance data (mainly it's raw measurements) to the UE

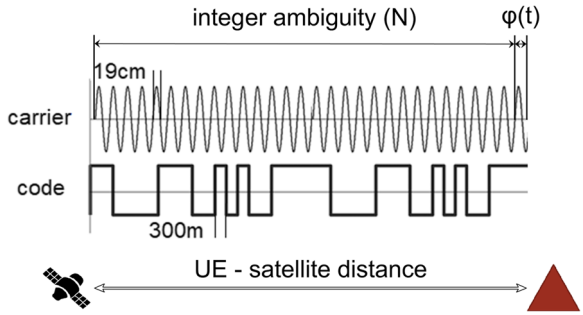


**Fig. 3** Comparison between code and carrier phase measurements

of GNSS signals, while best UE-satellite range accuracy achieved using code phase measurements is about 1 m [8]. Such high RTK performance is achieved at the cost of increased power consumption in the order of 100 mW as compared to about 10 mW for code phase measurements [16]. Additionally, continuous raw measurements data from the reference station (e.g., 5G BS) have to be provided to the UE. However, such a mechanism is already standardized in LPP [6].

## 5 RTK positioning and error

A general RTK description from the previous section can be extended to form a mathematical model. In this section, the state of the art about RTK positioning, and the satellite orbits prediction are presented in a tutorial-style to simplify implementation by interested readers. Both the utilization of the autoregressive model for UE-satellite distance error modeling, and the RTK error estimation simulation environment are proposed by the authors.

The phase of a GPS signal is measured as the number of wavelength cycles in $\frac{rad}{2\pi}$ [1] i.e., a standard phase changing from 0 to $2\pi$ over single carrier period can be divided by $2\pi$ to form values from 0 to 1. Denoting $f(\hat{t})$ as an instantaneous GNSS signal frequency at time instant $\tau$, the signal phase at the time $t$, $\varphi(t)$, depends on the phase at time instance $t_0$ as [8]:

$$\varphi(t) = \varphi(t_0) + \int_{t_0}^{t} f(\hat{t}) d\hat{t}. \tag{1}$$

Assuming perfect clocks measuring time epochs $t_0$ and $t$, and $f(\tau)$ being constant, $f(\tau) \approx f_0$, for short time interval, we can write

$$\varphi(t) = \varphi(t_0) + f_0 \cdot (t - t_0). \tag{2}$$

The signal phase changes linearly and proportionally to the time difference. If the GNSS signal travels from satellite to UE, a delay of $\Delta t$ is introduced by the propagation. At the time, instant $t$ the GNSS receiver will detect phase

$$\varphi(t - \Delta t) = \varphi(t) - f_0 \Delta t. \tag{3}$$

[1] this unit will be used to express phase in all subsequent equations

The satellite-receiver carrier phase distance measurement can be now expressed as a measured fraction of the wavelength cycle and an unknown integer number of full cycles (integer ambiguity) [8]:

$$\phi(t) = \varphi_r(t) - \varphi_s(t - \Delta t) + N, \tag{4}$$

where $N$ is an integer ambiguity, $\varphi_r(t)$ is the local carrier replica phase, and $\varphi_s(t - \Delta t)$ is the phase of the carrier received from satellite delayed by the propagation time $\Delta t$. When the receiver acquires a phase lock with the satellite signal, then $\varphi_r(t) = \varphi_s(t)$. Based on Eq. (3), Eq. (4) can be expressed as

$$\phi(t) = f\Delta t + N = \frac{r}{\lambda} + N, \tag{5}$$

where $r$ is the satellite-receiver distance in meters and $\lambda$ is the carrier wavelength in meters. However, the measured phase is distorted by the satellite and the receiver clock biases, $\delta t_s$, $\delta t_r$ , caused by the non-ideal synchronization between satellites and receivers clocks. Secondly, the measured phase suffers from the troposphere propagation error ($T$, in meters) and the ionosphere propagation error ($J$, in meters). Moreover, the receiver noise and the multipath propagation introduces an additional error $\epsilon$, so that the final measured carrier phase can be expressed as [8]

$$\phi = \frac{r + J + T}{\lambda} + \frac{c}{\lambda}(\delta t_r - \delta t_s) + \epsilon + N. \tag{6}$$

Errors from the above equation can be split into the slow and fast varying. Slow varying errors are atmospheric delays ($J$, $T$) and clock biases ($\delta t_s$, $\delta t_r$), which can persist for tens of minutes [8]. Fast varying errors are related to multipath propagation, and receiver noise ($\epsilon$). They are claimed to be zero mean i.e. $E[\,\epsilon\,] = 0$, and uncorrelated between measurements related to the different satellites i.e. $E[\,\epsilon^i \epsilon^j\,] = 0$, for $i \neq j$, and $E[\,\epsilon^i \epsilon^j\,] = \sigma_\phi^2$, for $i = j$. Indices $i$, $j$ denote satellite $i$, and $j$ respectively [8].

### 5.1 Relative positioning

To cancel out propagation errors ($T$, $J$) and clock biases ($\delta t_s, \delta t_r$), the RTK is taking advantage of the so-called relative positioning. The position of a user receiver is estimated on the basis of its own measurements and the raw measurements from a reference base station of known coordinates (possibly a 5G base station). The position is estimated as an offset to the reference station coordinates [8].

#### 5.1.1 Single difference

A general carrier phase measurement formula is given by (6). Let us denote the phase of the $i$th satellite signal measured at the UE as $\phi_u^i$, and the phase of the $i$th satellite signal measured at the reference station as $\phi_r^i$. After subtracting Eq. (6), related with UE and reference station we get

$$\phi_{ur}^i = \phi_u^i - \phi_r^i = \lambda^{-1}\left[\left(r_u^i - r_r^i\right) - \left(J_u^i - J_r^i\right) + \left(T_u^i - T_r^i\right)\right] + \frac{c}{\lambda}\cdot(\delta t_u - \delta t_r + \delta t_s^i - \delta t_s^i) + (N_u^i - N_r^i) + (\epsilon_u^i - \epsilon_r^i). \tag{7}$$

When the UE is close enough to the reference station i.e., less than 5 km of distance [16], the ionosphere and troposphere propagation errors are proven to be the same ($J_u^i - J_r^i = 0$ and $T_u^i - T_r^i = 0$) [16], which can simplify (7) to

$$\phi_{ur}^i = \lambda^{-1} r_{ur}^i + \frac{c}{\lambda}\cdot\delta t_{ur} + N_{ur}^i + \epsilon_{ur}^i, \tag{8}$$

where $(\bullet)_{ur}^i = (\bullet)_u^i - (\bullet)_r^i$.

#### 5.1.2 Double difference

While atmospheric errors and satellite clock bias are canceled out by the *single difference* operation, UE and reference station clock biases ($\delta t_{ur}$) may be canceled out by double difference. Having single difference related to the $i$th satellite ($\phi_{ur}^i$), and single difference related to the $j$th satellite ($\phi_{ur}^j$), we can subtract them to get double difference [8]:

$$\phi_{ur}^{ij} = \phi_{ur}^i - \phi_{ur}^j = \lambda^{-1}\left(r_{ur}^i - r_{ur}^j\right) + \frac{c}{\lambda}\cdot(\delta t_{ur} - \delta t_{ur}) + \left(N_{ur}^i - N_{ur}^j\right) + \left(\epsilon_{ur}^i - \epsilon_{ur}^j\right) = \lambda^{-1} r_{ur}^{ij} + N_{ur}^{ij} + \epsilon_{ur}^{ij}, \tag{9}$$

where $(\bullet)_{ur}^{ij} = (\bullet)_{ur}^i - (\bullet)_{ur}^j$.

It can be observed that the result of *double difference* operation is affected only by an error caused by receiver noise and multipath propagation $\epsilon_{ur}^{ij}$. Studies show that the dominant distortion is introduced by the multipath propagation. While receiver noise introduces about 1–2 mm rms error, in the UE-satellite range the UE-satellite rms range error caused by combined receiver noise and multipath propagation varies from 0.5 to 1 cm [8]. UE position estimation process utilizes a set of double difference Eq. (9) to estimate integer ambiguities ($N_{ur}^{ij}$) and obtain final UE position.

#### 5.1.3 Double difference correlations

As already mentioned fast varying errors of the carrier phase measurement between UE and satellite ($\epsilon_u^i$ in Eq. (7)) are uncorrelated and have the same variance and zero mean. The undifferenced measurements error covariance matrix may be expressed as

$$\mathbf{R} = E\left[\left[\,\boldsymbol{\phi_u} - E[\,\boldsymbol{\phi_u}]\,\right]\left[\,\boldsymbol{\phi_u} - E[\,\boldsymbol{\phi_u}]\,\right]^H\right] = E\left[\boldsymbol{\epsilon_u}\boldsymbol{\epsilon_u}^H\right], \tag{10}$$

where $\boldsymbol{\phi_u} = [\,\phi_u^1, \phi_u^2, \ldots, \phi_u^K]^T$, $\boldsymbol{\epsilon_u} = [\,\epsilon_u^1, \epsilon_u^2, \ldots, \epsilon_u^K]^T$ and $H$ denotes Hermitian transpose. After taking into account our assumptions, it can be shown that, Eq. (10) can be simplified to

$$\mathbf{R} = \sigma_u^2 \mathbf{I}_{K\times K}, \tag{11}$$

where $\sigma_u^2$ is the variance of the measured phase difference related to the UE, $\mathbf{I}$ is the $K \times K$ identity matrix, and K is the number of visible satellites. Note that the same reasoning can be applied in case of reference station-satellite undifferenced phase measurement error covariance.

The single difference operation from (7) can be presented for the $i$th and the $j$th satellites using matrix notation as

$$\boldsymbol{\phi}_{sd} = \begin{bmatrix} \phi_{ur}^i \\ \phi_{ur}^j \end{bmatrix} = \begin{bmatrix} 1 & -1 & 0 & 0 \\ 0 & 0 & 1 & -1 \end{bmatrix} \begin{bmatrix} \phi_u^i \\ \phi_r^i \\ \phi_u^j \\ \phi_r^j \end{bmatrix}. \tag{12}$$

Carrier phase measurements related to the UE and reference station have different error variances $\sigma_u^2$, $\sigma_r^2$, respectively [16]. It can be shown that for any $K$ visible satellites single difference covariance matrix is given by

$$\begin{aligned} \mathbf{R_{sd}} &= E[\,[\,\boldsymbol{\phi}_{sd} - E[\,\boldsymbol{\phi_{sd}}]\,]\,[\,\boldsymbol{\phi_{sd}} - E[\,\boldsymbol{\phi_{sd}}]\,]^H\,] = \\ &= (\sigma_u^2 + \sigma_r^2) \cdot \mathbf{I}_{K\times K}. \end{aligned} \tag{13}$$

In other words, single difference operation results are also uncorrelated, and their variances are two times greater.

By taking three single differences related with the $i$th satellite ($\phi_{ur}^i$), the $j$th satellite ($\phi_{ur}^j$), and the $k$th satellite ($\phi_{ur}^k$) we can write the corresponding pair of double differences in matrix notation [8]:

$$\boldsymbol{\phi}_{dd} = \begin{bmatrix} \phi_{ur}^{ji} \\ \phi_{ur}^{ki} \end{bmatrix} = \begin{bmatrix} 1 & -1 & 0 \\ 1 & 0 & -1 \end{bmatrix} \begin{bmatrix} \phi_{ur}^i \\ \phi_{ur}^j \\ \phi_{ur}^k \end{bmatrix}. \tag{14}$$

For a given pair of double differences the covariance matrix can be expressed as

$$\begin{aligned} \mathbf{R}_{dd} &= E[\,[\,\boldsymbol{\phi_{dd}} - E[\,\boldsymbol{\phi_{dd}}]\,]\,[\,\boldsymbol{\phi_{dd}} - E[\,\boldsymbol{\phi_{dd}}]\,]^H\,] = \\ &= (\sigma_u^2 + \sigma_r^2) \begin{bmatrix} 2 & 1 \\ 1 & 2 \end{bmatrix}. \end{aligned} \tag{15}$$

It can be shown that for any $K$ visible satellites the double difference covariance matrix is given by [16]

$$\mathbf{R}_{dd} = \frac{(\sigma_u^2 + \sigma_r^2)}{2} \begin{bmatrix} 4 & 2 & \cdots & 2 \\ 2 & 4 & & \vdots \\ \vdots & & \ddots & 2 \\ 2 & \cdots & 2 & 4 \end{bmatrix}_{K-1\times K-1} \tag{16}$$

As it can be seen, double differences are correlated even if raw phase measurements and phases differences are not. This observation, together with (16) will be used in Section 5.4.1 to obtain RTK covariance matrix.

#### 5.1.4 Linear model for position estimation

In the relative positioning, our target is to estimate the position of UE relative to the reference station [8]:

$$\mathbf{x}_{ur} = \mathbf{x}_u - \mathbf{x}_r, \tag{17}$$

where $\mathbf{x}_r = (\text{east}_r, \text{north}_r, up_r)^T$ is the vector of known reference station coordinates, herewith given using east-north-up (ENU) coordinates system ( see Appendix A), $\mathbf{x}_u = (\text{east}_u, \text{north}_u, up_u)^T$ is the vector of UE coordinates (fixed over the measurement period but not known at the UE), and $\mathbf{x}_{ur}$ is the UE relative position vector to be established by RTK. Let's choose $\mathbf{x}_0$ (could be $\mathbf{x}_0 = \mathbf{0}$ in practice [8]) as our initial estimate of the UE relative position vector $\mathbf{x}_{ur}$, then [8]:

$$\mathbf{x}_{ur} = \mathbf{x}_0 + \delta\mathbf{x}, \tag{18}$$

where $\delta\mathbf{x}$ is the unknown correction to the initial position estimate $\mathbf{x}_0$.

Our target now is to introduce $\mathbf{x}_{ur}$ into the double difference given by (9). Figure 4 depicts the single difference measurement UE ($\mathbf{x}_u$)-reference station ($\mathbf{x}_r$)-satellite geometry. When UE is ina smaller distance than 10 km from reference station we can assume that unit vector pointing from reference station to the satellite $i$ ($\mathbb{1}_r^i$) is equal to the unit vector pointing from UE to the satellite $i$ ($\mathbb{1}_u^i$) i.e., $\mathbb{1}_r^i = \mathbb{1}_u^i$ [8]. Now $r_{ur}^i$ from Eq. (8) can be approximated as follows [8]:

$$r_{ur}^i = r_u^i - r_r^i = -\mathbb{1}_r^i \cdot \mathbf{x}_{ur}. \tag{19}$$

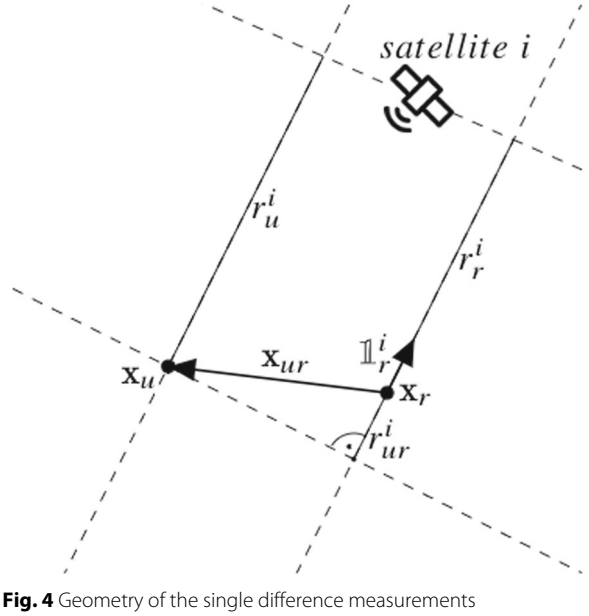


**Fig. 4** Geometry of the single difference measurements

In the east-north-up (ENU) coordinates ( see Appendix A) $\mathbb{1}_r^i$ is given by [8]:

$$\mathbb{1}_r^i = \left( \cos el^{(i)} \sin az^{(i)} \;\; \cos el^{(i)} \cos az^{(i)} \;\; \sin el^{(i)} \right), \tag{20}$$

where $el^{(i)}$ is the satellite $i$ elevation angle and $az^{(i)}$ is the satellite $i$ azimuth angle.

On the basis of the (19) $r_{ur}^{ij}$, from the double difference given by (9), can be expressed as

$$r_{ur}^{ij} = r_{ur}^{i} - r_{ur}^{j} = -\left(\mathbb{1}_r^i - \mathbb{1}_r^j\right) \cdot \mathbf{x}_{ur}. \tag{21}$$

Combining (18) and (21) we get [8]

$$\begin{aligned} r_{ur}^{ij} &= -\left(\mathbb{1}_r^i - \mathbb{1}_r^j\right) \cdot \mathbf{x}_{ur} \\ &= -\left(\mathbb{1}_r^i - \mathbb{1}_r^j\right) \cdot \mathbf{x}_0 - \left(\mathbb{1}_r^i - \mathbb{1}_r^j\right) \cdot \delta\mathbf{x} \\ &= r_0^{ij} - \left(\mathbb{1}_r^i - \mathbb{1}_r^j\right) \cdot \delta\mathbf{x}, \end{aligned} \tag{22}$$

where $r_0^{ij}$ is estimated on the basis of $\mathbf{x}_0$ UE-reference station distance.

Combining (22) with (9) we obtain [8]

$$\phi_{ur}^{ij} = \lambda^{-1} r_0^{ij} - \lambda^{-1}\left(\mathbb{1}_r^i - \mathbb{1}_r^j\right) \cdot \delta\mathbf{x} + N_{ur}^{ij} + \epsilon_{ur}^{ij}. \tag{23}$$

By setting $y_{ur}^{ij} = \phi_{ur}^{ij} - \lambda^{-1} r_0^{ij}$, and $\mathbf{g}^{ij} = -\lambda^{-1}\left(\mathbb{1}_r^i - \mathbb{1}_r^j\right)$, (23) can be rewritten as a linear equation [8]:

$$y_{ur}^{ij} = \mathbf{g}^{ij} \cdot \delta\mathbf{x} + N_{ur}^{ij} + \epsilon_{ur}^{ij}. \tag{24}$$

Having $K$ satellites visible, indexed $1, \ldots, K$, $K-1$ independent linear Eq. (24) can be formulated, e.g., by setting $j = 1$ and $i = 2, ..., K$. Under the assumption that all measurements are done in the same time period and that a single frequency receiver is utilized, these equations can be presented in vector-matrix notation as follows [8]:

$$\begin{bmatrix} y_{ur}^{21} \\ y_{ur}^{31} \\ \vdots \\ y_{ur}^{K1} \end{bmatrix} = \frac{-1}{\lambda} \begin{bmatrix} \mathbb{1}_r^2 - \mathbb{1}_r^1 \\ \mathbb{1}_r^3 - \mathbb{1}_r^1 \\ \vdots \\ \mathbb{1}_r^K - \mathbb{1}_r^1 \end{bmatrix} \cdot \delta\mathbf{x} + \begin{bmatrix} N_{ur}^{21} \\ N_{ur}^{31} \\ \vdots \\ N_{ur}^{K1} \end{bmatrix} + \begin{bmatrix} \epsilon_{ur}^{21} \\ \epsilon_{ur}^{31} \\ \vdots \\ \epsilon_{ur}^{K1} \end{bmatrix}, \tag{25}$$

or

$$\mathbf{y} = \mathbf{G} \cdot \delta\mathbf{x} + \mathbf{n} + \mathbf{e}, \tag{26}$$

where $\mathbf{y}$ is the $K-1$ element vector of the differences between double differences of measured phase data and estimated double differences for initial position $\mathbf{x}_0$ (that can be projected to a proper value of $r_0^{ij}$) , $\mathbf{G}$ is the $K-1 \times 3$ matrix describing UE-reference station-satellite geometry, $\mathbf{n}$ is the $K-1$ element vector of the double difference integer ambiguities to be estimated, $\mathbf{e}$ is the $K-1$ element vector of the double difference errors, and $\delta\mathbf{x}$ is the correction to the initial UE position estimate, to be estimated.

The target is to estimate the real-valued $\delta\mathbf{x}$, and the integers $\mathbf{n}$ denoted as $\delta\hat{\mathbf{x}}$ and $\hat{\mathbf{n}}$. This can be done by solving the following least-squares optimization problem [8]:

$$\min_{\hat{\mathbf{n}}, \delta\hat{\mathbf{x}}} \|\mathbf{y} - \mathbf{G}\delta\hat{\mathbf{x}} - \hat{\mathbf{n}}\|^2 \tag{27}$$

Methods for integer ambiguity resolutions are comprehensively described in [8]. [27] discusses reducing time to integer ambiguity resolution with receiver random motion for smartphone grade GNSS antennas. For further computer simulations, $\mathbf{n}$ is assumed to be already estimated.

### 5.2 Undifferenced carrier phase measurement error

No zero error in UE localization estimate, i.e., $\delta\hat{\mathbf{x}} \neq \delta\mathbf{x}$, is caused by non-zero $\epsilon_{ur}^{ij}$ values in (24). The main source of this error is multipath propagation. The double difference errors $\epsilon_{ur}^{ij}$ are caused by raw phase measurements errors, e.g., $\epsilon_r^i$ and $\epsilon_u^i$ as visible in (7). These can be modeled by a Gauss-Markov (GM) process are shown in [27]. The GM process is specified by its variance $\sigma^2$ and its correlation time - $\tau$ with the autocorrelation function for discrete time systems given by [28]

$$R_{\epsilon\epsilon}(m) = \sigma^2 e^{\frac{-|mT_s|}{\tau}}, \tag{28}$$

where $T_s$ stands for sample period, and $m$ is an integer number representing autocorrelation sample index. It has to be noted that the sample period is here related with the time intervals between consecutive position estimations and not the GNSS receiver sample rate.

#### 5.2.1 *Autoregressive model*

A discrete stationary random process can be generated from white noise with the use of linear filter of transmittance $H(z)$, as depicted in Fig. 5. If the stationary random process is a GM process then $H(z)$ consists only of the poles. This case is called autoregressive (AR) model.

AR model parameters, i.e., the filter coefficients ($a_k$), and the input white noise variance ($\sigma_s^2$) can be computed with the following formula [29]:

$$R_{xx}(m) = \begin{cases} -\sum_{k=1}^{p} a_k R_{xx}(m-k), & m > 0 \\ -\sum_{k=1}^{p} a_k R_{xx}(-k) + \sigma_s^2 & m = 0 \\ R_{xx}^*(-m) & m < 0 \end{cases}, \tag{29}$$

where $R_{xx}(m)$ is the $m-th$ autocorrelation sample of the desired random process, and $p$ denotes the order of AR model.

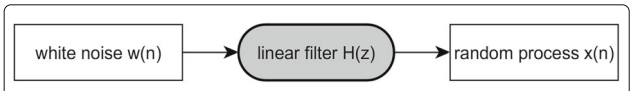


**Fig. 5** Generation of stationary random process by filtering input white noise

#### 5.2.2 Autoregressive model parameters for Gauss-Markov process

Adopting a first order model AR(1) for the GM process and writing (29) for $p = 1$, and combining with (28) results to the following set of equations:

$$\begin{cases} \sigma^2 e^{\frac{-|mT_s|}{\tau}} = -a_1\sigma^2 e^{\frac{-|(m-1)T_s|}{\tau}} & m > 0 \\ \sigma^2 = -a_1\sigma^2 e^{\frac{-T_s}{\tau}} + \sigma_s^2 & m = 0 \\ R_{xx}(m) = R_{xx}^*(-m) & m < 0 \end{cases}, \tag{30}$$

where $\sigma_s^2$ stands for the input white noise variance. Because in the first equation $m > 0$, we can write $|mT_s| = mT_s$, and $|(m-1)T_s| = mT_s - T_s$. Equation (30) can be simplified to

$$\begin{cases} e^{\frac{-mT_s}{\tau}} = -a_1 e^{\frac{-mT_s}{\tau}} e^{\frac{T_s}{\tau}} & m > 0 \\ \sigma^2\left(1 + a_1 e^{\frac{-T_s}{\tau}}\right) = \sigma_s^2 & m = 0 \\ R_{\epsilon\epsilon}(m) = R_{\epsilon\epsilon}^*(-m) & m < 0 \end{cases}. \tag{31}$$

After further transforms, we can obtain

$$\begin{aligned} a_1 &= -e^{-\frac{T_s}{\tau}} \\ \sigma_s^2 &= \sigma^2\left(1 - e^{\frac{-2T_s}{\tau}}\right) \end{aligned} \tag{32}$$

which can be used directly for the generation of the required GM process.

#### 5.2.3 Fitting Gauss-Markov process parameters

Now a reverse problem can be considered: having samples of the random process $x(n)$, the target is to model it with the GM process and obtain parameters: $\hat{\sigma}^2$ and $\hat{\tau}$. While variance $\hat{\sigma}^2$ can be computed directly from $x(n)$ samples, the estimation of the correlation time is more complicated.

By transformation of (32), $\hat{\tau}$ is given by

$$\hat{\tau} = \frac{-T_s}{ln(-a_1)}. \tag{33}$$

The filter coefficient $a_1$ can be estimated based on (29) as [29]:

$$a_1 = -\frac{\hat{R}_{xx}(1)}{\hat{R}_{xx}(0)}, \tag{34}$$

where $\hat{R}_{xx}(m)$ is the estimated autocorrelation function of $x(n)$. This approach is sufficient when $x(n)$ is an ideal GM process as it is impossible to create over-determined set of equations from (29) in that case. In practice simulation results presented in further sections (e.g., Fig. 12) would have autocorrelation not being ideal function described by (28).

#### 5.2.4 Proposed $\mathbf{a}_1$ estimation algorithm

In such a non-ideal case it is reasonable to use more than two autocorrelation function samples. Equations (29) can be rewritten in matrix notation as [29]:

$$\begin{bmatrix} \hat{R}_{xx}(0) & \hat{R}_{xx}(1) & \cdots & \hat{R}_{xx}(p) \\ \hat{R}_{xx}(1) & \hat{R}_{xx}(0) & \cdots & \hat{R}_{xx}(p-1) \\ \vdots & \vdots & \cdots & \vdots \\ \hat{R}_{xx}(p) & \hat{R}_{xx}(p-1) & \cdots & \hat{R}_{xx}(0) \end{bmatrix} \begin{bmatrix} 1 \\ a_1 \\ \vdots \\ a_p \end{bmatrix} = \begin{bmatrix} \sigma_s^2 \\ 0 \\ 0 \\ 0 \end{bmatrix}. \tag{35}$$

Consider now extending autocorrelation matrix to dimensions $N \times p$, where $N$ is number of the autocorrelation samples used for coefficients vector estimation. After discarding components related with $\sigma_s^2$ estimation, as this will be estimated using standard $x(n)$ variance estimator, and some minor transforms (35) can be rewritten as

$$\begin{bmatrix} \hat{R}_{xx}(0) & \hat{R}_{xx}(1) & \cdots & \hat{R}_{xx}(p-1) \\ \hat{R}_{xx}(1) & \hat{R}_{xx}(0) & \cdots & \hat{R}_{xx}(p-2) \\ \vdots & \vdots & \cdots & \vdots \\ \hat{R}_{xx}(N-1) & \hat{R}_{xx}(N-2) & \cdots & \hat{R}_{xx}(N-p) \end{bmatrix} \begin{bmatrix} a_1 \\ a_2 \\ \vdots \\ a_p \end{bmatrix} = -\begin{bmatrix} \hat{R}_{xx}(1) \\ \hat{R}_{xx}(2) \\ \vdots \\ \hat{R}_{xx}(N) \end{bmatrix} \tag{36}$$

For the considered first order AR model, (36) simplifies to

$$\begin{bmatrix} \hat{R}_{xx}(0) \\ \hat{R}_{xx}(1) \\ \vdots \\ \hat{R}_{xx}(N-1) \end{bmatrix} \cdot a_1 = -\begin{bmatrix} \hat{R}_{xx}(1) \\ \hat{R}_{xx}(2) \\ \vdots \\ \hat{R}_{xx}(N) \end{bmatrix}, \tag{37}$$

by introducing

$$\mathbf{d} = \begin{bmatrix} \hat{R}_{xx}(0) \\ \hat{R}_{xx}(1) \\ \vdots \\ \hat{R}_{xx}(N-1) \end{bmatrix}, \tag{38}$$

$$\mathbf{c} = \begin{bmatrix} \hat{R}_{xx}(1) \\ \hat{R}_{xx}(2) \\ \vdots \\ \hat{R}_{xx}(N) \end{bmatrix} \tag{39}$$

equation (37) can be written in vector notation as

$$\mathbf{d} \cdot a_1 = -\mathbf{c}. \tag{40}$$

The estimation of $a_1$, using least squares criterion is given by

$$\hat{a}_1 = \left(\mathbf{d}^T\mathbf{d}\right)^{-1}\mathbf{d}^T(-\mathbf{c}). \tag{41}$$

As $\mathbf{d}$ is a vector, (41) can be rewritten as

$$\hat{a}_1 = -\frac{\mathbf{d}^T}{\|\mathbf{d}\|_2^2}\mathbf{c}, \tag{42}$$

where $\| \bullet \|_2$ denotes the Euclidean norm. Now $\hat{\tau}$ can be estimated from (33).

### 5.3 GPS satellites orbits prediction

Apart from UE (reference station)-satellite range errors, also the geometry of the visible satellites influences the final position error in RTK. This is visible, e.g., in (27) by **G** varying with the satellites geometry. Because GPS is the most popular GNSS systems, in this paper, we will focus on estimating GPS satellites constellation. However, similar algorithms could be used for other systems, e.g., for Glonass [30].

#### *5.3.1 Ideal elliptical orbit parameters*

For simplicity, it is assumed that the GPS satellite motion can be modeled with ideal elliptical orbit. This approach results in 1–2 km standard deviation of the error in estimating satellites position [8], but remains good enough for evaluation of satellites constellation geometry influence on UE position error. The influence of satellites position accuracy on the performance of proposed UE localization error is evaluated by simulations in Section 6. Satellite position at specified time epoch on such orbit can be described with Keplerian elements defined below (see Fig. 6) [8]:

- GPS satellite ellipse orbit size and shape can be described by two parameters:
  - *Semi-major axis* ($a$)
  - *Eccentricity* ($e$)
- The next two parameters are describing relation between orbital plane, and the Earth's equatorial plane, and the direction of vernal equinox:
  - *Inclination* ($i$), angle measured between the satellite orbital plane and the Earth's equatorial plane.
  - *Longitude of the ascending node* ($\Omega$), angle in Earth's equatorial plane measured between the vernal equinox direction, and the ascending node which is the point on the satellite's orbit where it crosses the equatorial plane, moving in the northerly direction.
- The following single parameter characterizes orientation of the ellipse in orbital plane:
  - *Argument of perigee* ($\omega$), angle in the plane of the orbit, measured between the ascending node and the perigee, which is point in the satellite orbit, where the satellite is closest to the center of the Earth.
- The last Keplerian orbit parameter determines satellite position on its orbit in given time epoch:
  - *True anomaly* ($\nu$), angle measured in orbital plane between perigee, and the satellite position at given time.

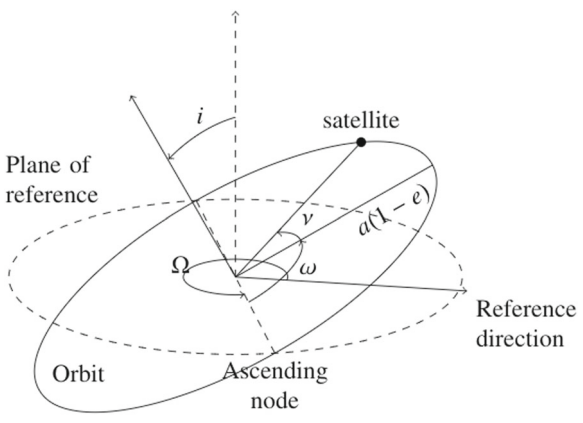


**Fig. 6** Characterization of an ideal orbit and satellite position by Keplerian elements, where the reference direction is the vernal equinox direction, and the plane of reference is the Equatorial plane

#### *5.3.2 System effectiveness model almanac*

Each GPS satellite distributes simple ephemerides (Keplerian orbit parameters) for whole constellation (so-called almanac). Receiving full almanac data takes 12.5 min [8]. A more practical and flexible approach is to use System Effectiveness Model (SEM) almanac available online instead of obtaining almanac transmitted by a GPS satellite. The definition of the SEM almanac content can be found in [31].

#### *5.3.3 Satellite position computation algorithm*

With the data from SEM almanac, it is possible to obtain a coarse position of all satellites in the GPS system constellation. The satellite position computation algorithm is presented below [32].

1. In the first step, two World Geodetic System 84 (WGS 84) constants must be introduced [32]:

$$\mu = 3.98605 \times 10^{14} \left[\frac{m^3}{s^2}\right], \tag{43}$$

which is WGS 84 value of the Earth's gravitational constant for GPS users [32]. The second constant is the WGS 84 value of the Earth's rotation rate given by

$$\dot{\Omega}_e = 7.2921151467 \times 10^{-5} \left[\frac{rad}{s}\right] \tag{44}$$

2. The satellite mean motion ($n_0$) is computed using square root of semi major axis from SEM almanac ($\sqrt{a}$):

$$n_0 = \sqrt{\frac{\mu}{a^3}} \tag{45}$$

3. Now, the difference between almanac time (defined by GPS Week Number - $t_{aw}$ and GPS time of applicability - $t_{as}$), and the desired time (defined by weeks number - $t_{dw}$ and seconds number - $t_{ds}$) is computed from the following formula:

$$\Delta t = t_{ds} - t_{as} + (t_{dw} - t_{aw}) \cdot s, \tag{46}$$

where $s$ is the number of seconds in a single week.

4. In this step, mean anomaly for desired time is obtained using mean anomaly for almanac time ($M_0$) from SEM almanac, and the values obtained from Eq. (45) and (46):

$$M = \tilde{M}_0 + n_0 \cdot \Delta t, \tag{47}$$

where $\tilde{M}_0 = \pi \cdot M_0$, is converted to radians (1 semicircle $= \pi$ radians), as SEM gives $M_0$ in the units of semicircles.

5. Eccentric anomaly ($E$ measured in radians) can be found by solving the so-called Kepler's equation given by

$$M = E - e \sin E, \tag{48}$$

where $e$ is the eccentricity from SEM almanac. Kepler's equation can be iteratively solved with one of the several available methods [33].

6. Having eccentric anomaly calculated, the GPS satellite position on the Keplerian orbit can be defined by true anomaly:

$$\nu = \arctan \frac{\sqrt{1-e^2}\sin E}{\cos E - e}, \tag{49}$$

and the radius by

$$r = a(1 - e\cos E) \tag{50}$$

7. After transformation of the satellites coordinates from radial to Cartesian, we get

$$\begin{cases} x = r\cos(\nu + \omega) \\ y = r\sin(\nu + \omega) \end{cases} \tag{51}$$

8. Next, the satellite coordinates in Keplerian orbit plane are transformed to ECEF ( see Appendix A) coordinates. Two parameters are obtained to perform this operation. First, the inclination is given by

$$i = \tilde{i}_0 + \delta\tilde{i}, \tag{52}$$

where both $i_0$ and $\delta i$ are given in the SEM almanac in semicircles units and must be converted to radians ($\tilde{i}_0 = \pi \cdot i_0$, and $\delta\tilde{i} = \pi \cdot \delta i$). Next, the longitude of the ascending node is

$$\Omega_p = \tilde{\Omega}_0 + (\dot{\tilde{\Omega}} - \dot{\Omega}_e)\Delta t - \dot{\Omega}_e t_{as}, \tag{53}$$

where $\tilde{\Omega}_0 = \pi \cdot \Omega_0$ and $\dot{\tilde{\Omega}} = \pi \cdot \dot{\Omega}$, because $\Omega_0$ and $\dot{\Omega}$ are given in SEM almanac in the units of semicircles, and semicircles/second, which are converted to the units of radians and radians/second, respectively.

9. The final step is to obtain the GPS satellite position in ECEF coordinates with the following formulas:

$$\begin{cases} x_{\text{ECEF}} = x\cos\Omega_p - y\cos i\sin\Omega_p \\ y_{\text{ECEF}} = x\sin\Omega_p + y\cos i\cos\Omega_p \\ z_{\text{ECEF}} = y\sin i \end{cases} \tag{54}$$

#### 5.3.4 Algorithm implementation and validation

The presented GPS satellite position estimation algorithm had been implemented in Python programming language. To validate the implemented algorithm, visible satellite list had been captured from USB-GPS antenna. USB antenna outputs the data via serial port using National Marine Electronics Association (NMEA) protocol. To this end, a C++ program has been developed to capture only data frames containing information about visible satellites and log them to text file (see Fig. 7). Satellite coordinates are the azimuth ($az$) and the elevation ($el$) angles seen from GPS antenna position (52.3921476900N, 16.7982299300E). Observations were performed in a 24 h period between 29 and 30 of December 2018.

Results of the comparison between the computed and the captured satellites coordinates are presented in Fig. 8. The former are derived by using the algorithm described in Section 5.3.3, with SEM almanac obtained 28 December 2018 19:56:48 UTC, while the latter are extracted from NMEA messages. There are two sources of errors: the first source of error is related to the 1° quantization of NMEA data (even though internally GPS receivers use much more accurate satellites positioning), while satellite coordinates computed with SEM almanac data domain is continuous. Up to 0.5° of error can be expected. The second source of errors is related to the computing satellites coordinates, i.e., the utilized satellites position forecasting, on the basis of ideal elliptic orbit, while in fact there are some temporary deviations in the satellites orbits.

As it can be observed in Fig. 8, satellites orbits prediction error doesn't grow over the analysed time period. This turns satellite constellation obtained on the basis of the algorithm described in Section 5.3.3 to be a reasonable tool for 24 hours long simulations. Also prediction errors around 1° seems to have no significant impact on the error modeling, as it is shown in Section 6.2.3.

```
================================================================
date: 29.12.18 time: 14:59:09
[PRN:   5   SNR:  24 dB    Azimuth: 207 deg   Elevation:  21 deg  ]
[PRN:   7   SNR:  12 dB    Azimuth:  81 deg   Elevation:   8 deg  ]
[PRN:   8   SNR:   9 dB    Azimuth:  24 deg   Elevation:   9 deg  ]
[PRN:  11   SNR:  24 dB    Azimuth:  65 deg   Elevation:   3 deg  ]
[PRN:  13   SNR:  18 dB    Azimuth: 245 deg   Elevation:  82 deg  ]
[PRN:  15   SNR:  34 dB    Azimuth: 294 deg   Elevation:  47 deg  ]
[PRN:  17   SNR:  16 dB    Azimuth: 134 deg   Elevation:  13 deg  ]
[PRN:  20   SNR:  26 dB    Azimuth: 327 deg   Elevation:  11 deg  ]
[PRN:  24   SNR:  26 dB    Azimuth: 266 deg   Elevation:  15 deg  ]
[PRN:  28   SNR:  12 dB    Azimuth:  91 deg   Elevation:  64 deg  ]
[PRN:  30   SNR:  24 dB    Azimuth:  79 deg   Elevation:  39 deg  ]
================================================================
```

**Fig. 7** Example set of the visible satellites coordinates (1° resolution) extracted from NMEA data captured by G-Mouse USB antenna and logged into text file

### 5.4 RTK error estimation simulation environment

A block scheme illustrating initial framework for UE localization error modeling in RTK system under open-sky conditions is presented in Fig. 9. The simulation environment consists of several functional blocks presented in previous subsections: Gauss-Markov noise generators (Section 5.2.2), SEM almanac-based satellites orbit prediction (Section 5.3.3), and linear model for position estimation (Eq. (26)).

For a given time instance, a list of visible satellites is computed on the basis of SEM almanac with the 7° elevation cutoff angle, i.e., satellites close to the horizon are treated as not visible for the UE receiver [8]. Next, on the basis of reference station position, and UE "true" position satellite-reference station, and the satellite-UE ranges are computed for each visible satellite. With the use of the independent GM process generators (with the given fix parameters: variance $\sigma^2$ and correlation time $\tau$) obtained ranges are noised. Noised ranges and visible satellites coordinates are then used in linear model

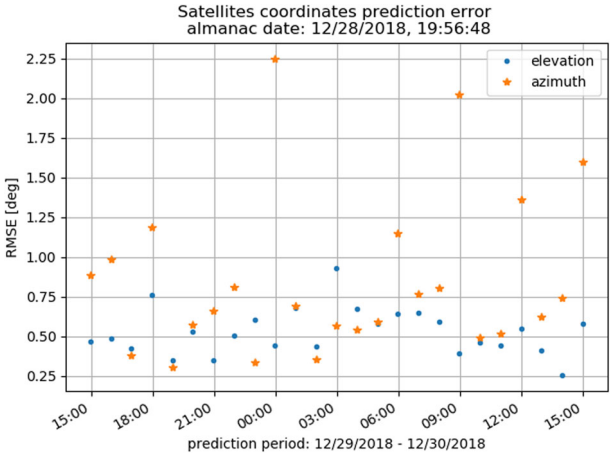


**Fig. 8** Comparison between visible satellites coordinates computed with algorithm from Section 5.3.3, and those obtained from NMEA data provided by USB antenna

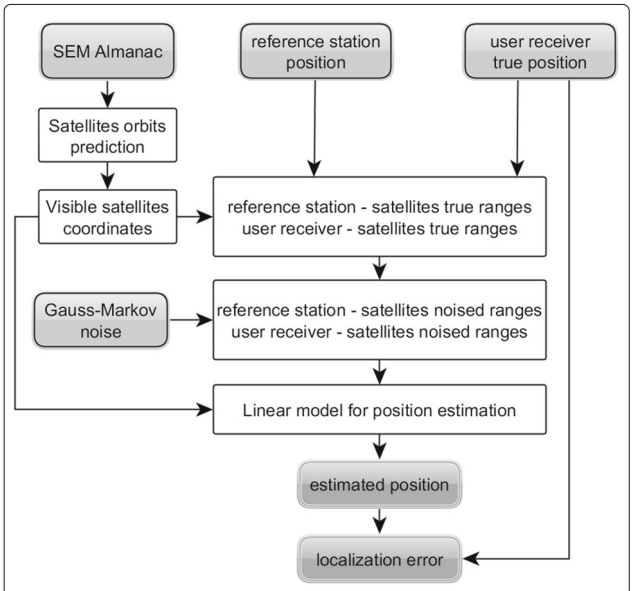


**Fig. 9** Block scheme illustrating simulation environment for the RTK positioning error estimation

for position estimation to formulate Eq. (27) under the assumption of having resolved integer ambiguities. Finally the position error is computed as the difference between true UE coordinates, and the ones computed from the noised reference station-satellite and the UE-satellite ranges.

#### 5.4.1 *RTK positioning error covariance matrix estimation*

In the other less computationally complex approach, the RTK positioning error covariance matrix may be estimated with the analytic formula, describing the least squares estimator covariance matrix and given by [8]

$$\mathrm{cov}(\delta\mathbf{x}) = \left(\mathbf{G}^T\mathbf{G}\right)^{-1}\mathbf{G}^T \cdot \boldsymbol{R}_{dd} \cdot \mathbf{G}\left(\mathbf{G}^T\mathbf{G}\right)^{-1}, \qquad (55)$$

where $\mathbf{G}$ is the satellite-reference station-UE geometry matrix (Eq. (26)) , and the $\mathbf{R}_{dd}$ is the double difference correlation matrix (Eq. (16)). Unfortunately, in this approach, random variables variances, can be only obtained, with no information on the positioning error distribution. Moreover, autocorrelation function cannot be estimated.

## 6 Simulation results and discussion

For evaluation purposes, the environment described in Section 5.4 is implemented in python programming language. Several computer simulation experiments have been performed for various sets of input parameters. Three places globally had been chosen for simulations. These are listed in Table 1. *Loc1* refers to the first author's home near Poznan in Poland, *Loc2* to the point where prime meridian intersects equator, and *Loc3* to the Huawei headquarters in the Chinese city of Shenzen.

**Table 1** Coordinates of the reference station and UE used in the simulations

| Scenario name | Reference station geodetic coordinates | UE geodetic coordinates |
|---|---|---|
| Loc1 | 52.3921476900N<br>16.7982299300E<br>117.19200 m | 52.3911476900N<br>16.7972299300E<br>117.19200 m |
| Loc2 | 0.00000000000N<br>0.00000000000E<br>0.00000 m | 0.00100000000N<br>0.00100000000E<br>0.00000 m |
| Loc3 | 22.6530360000N<br>114.060506000E<br>110.00000 m | 22.6540360000N<br>114.061506000E<br>110.00000 m |

The UE-reference station distance is chosen to be 130 m, 157 m, and 151 m for *Loc1*, *Loc2*, and *Loc3*, respectively. Choosing such distances ensures the UE and reference station are affected by the same atmospheric propagation delays, as explained in Section 5.1. This is reasonable for a dense 5G network and allows for the simplification of error modeling by assuming that errors related with ionosphere and troposphere delays are equal at UE and reference station.

The input parameters for GM process generators, which models the UE-satellite, and reference station-satellite distance error are specified based on the measurements with the use of smartphone-grade and survey-grade GNSS antenna, respectively, under open-sky conditions done in [16]. The values of the GM process parameters are shown in Table 2. Static correlation time refers to the scenario when the receiver antenna does not move, i.e., the reference station is always static. Dynamic correlation time refers to the scenario, when UE moves randomly within the GPS L1 carrier signal wavelength. The trajectory of the receiver is modeled as a GM process and has an average speed of 7.65 $\frac{km}{h}$ [16].

In all simulations, SEM almanac is utilized (almanac date: 28 December 2018 19:56:48 UTC). For all simulations, start date is 29 December 2018 14:58:09 UTC, and end date is 30 December 2018 14:58:09 UTC. Longer than a 24 h simulation period is not necessary due to the fact that visible satellites constellation repeats every 23 h and 56 min [8].

### 6.1 Continuous 24 h scenario

The first computer simulation is performed for *Loc1*, with *static* GM noise parameters. There are 15, 24-h-long simulation runs; UE position is computed in 1 *s* intervals. During the whole simulation experiment, the satellite constellation is continuously changing.

**Table 2** GM process parameters for modeling of undifferenced carrier phase measurement error for a static reference station

| | $\sigma$ | $\tau$ - static | $\tau$ - dynamic |
|---|---|---|---|
| Reference station | 2.5 mm | 100 s | — |
| UE | 6 mm | 300 s | 0.01 s |

#### 6.1.1 *Localization error distribution*

The first field of study for this simulation scenario is localization error empirical probability density function. Figure 10 present the localization error distribution in the east and north directions with fitted Gaussian functions. As can be seen, distributions have shape of the Gaussian distribution.

#### 6.1.2 *Autocorrelation analysis*

Apart from the localization error distribution, also the autocorrelation functions are analyzed. If the localization error can be described by GM process, autocorrelation function can be given by Eq. (28). Here, it appears the problem of fitting GM process parameters already discussed in Section 5.2.3. Correlation time is estimated with the use of (42). However, the number of the utilized autocorrelation function samples must be established. Figure 11 illustrates RMSE between the empirical autocorrelation function and fitted GM autocorrelation function while changing the number of the empirical autocorrelation function samples (N) used in the fitting process. As it can be seen, higher $N$ results in lower RMSE. However, the improvement is negligible for $N > 500$. As such $N = 500$ is used in all subsequent simulation experiments.

Autocorrelation functions for east and north directions are presented in Fig. 12. In each figure there is the autocorrelation obtained from the simulation results, and two fitted GM processes: using Eq. (42) with $N = 500$ and using (34). It can be seen that the fitted GM process autocorrelation function approximates the one obtained from simulation results very well. This, along with the localization error samples following the Gaussian distribution, leads

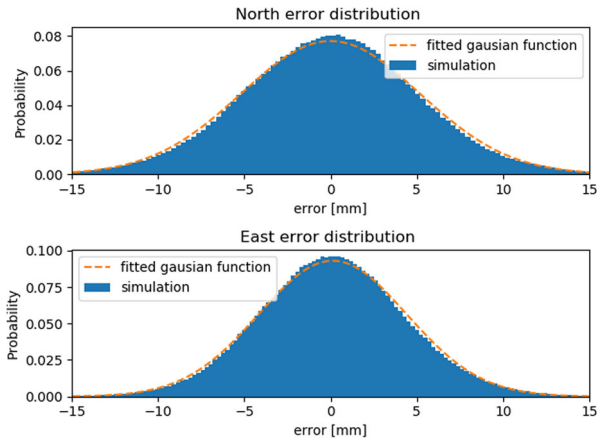


**Fig. 10** Localization error distribution

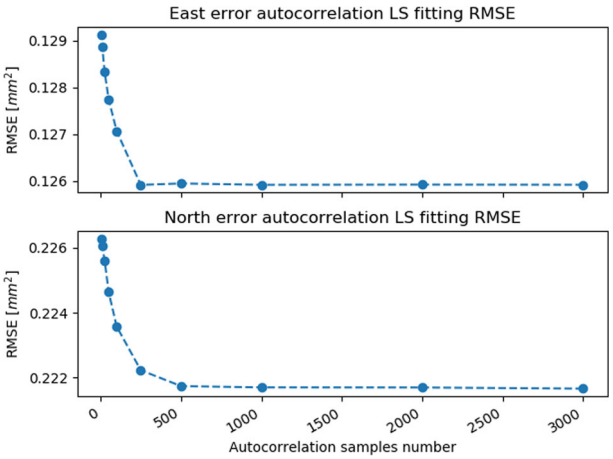


**Fig. 11** Dependence between number of utilized autocorrelation function samples used for GM process fitting and the resultant RMSE

to the conclusion that the UE localization error in RTK system may be modeled as a GM process.

To check if there is a correlation between RTK localization error in the east and north directions, the correlation coefficient (see [34]) has been computed with the result of $-$ 0.0669. A correlation coefficient close to 0 leads to the conclusion that east and north localization errors are uncorrelated and can be modeled independently. With other words independent GM process generators can be utilized to produce east and north localization error.

### 6.2 Step 24 h scenario

All previous simulations revealed that RTK localization errors in east and north directions are uncorrelated and may be modeled as a GM process. Next, we study the influence of the visible GPS satellites geometry on the RTK localization error at a given time and geographical position.

Simulation is performed in a "step mode." Every single step is related to a constant satellites constellation, and 15 independent simulation runs, each utilizing a different random generator seeds. During each simulation run, 3600 UE position error samples are collected at 1 Hz sampling frequency. From 29 December 2018 14:58:09 UTC to 30 December 2018 14:58:09 UTC, a new satellite constellation is computed every 10 min, and the corresponding simulations are performed, resulting in 144 steps. The simulations are performed for all locations in Table 1, static reference station and *static*/*dynamic* UE.

#### 6.2.1 *Variance analysis*

Firstly, RTK localization error variance obtained with the use of the simulation environment presented in Section 5.4 is compared with the one estimated using analytical formula (55), as it is depicted in Fig. 13 for *Loc1*. The variance obtained with (55) visibly overlap with simulation results for the *dynamic UE*. In the *static UE* scenario variance obtained on the basis of simulation and Eq. (55) differs more. This can be caused by longer correlation time (300 s) that results in smaller number of independent localization error samples over the simulated period. However, it can be stated that the estimated variance is independent of UE motion. Additionally, it is confirmed that the localization variance can be generated using (55) instead of performing full system simulations. In Fig. 14, localization error variances obtained on the basis of (55) for all considered geographical localizations are compared for the same time instances. It can be observed that the results differ significantly. This implies that RTK localization error variance depends on the visible satellites geometry.

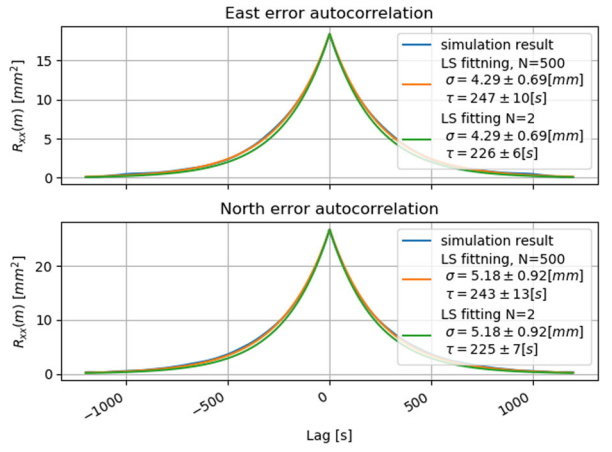


**Fig. 12** Autocorrelation of the localization error in *Loc1*, computed on the basis of: simulation, Eq. (42) with $N = 500$, and Eq. (34). $\sigma$ and $\tau$ parameters are estimated with 95% confidence intervals

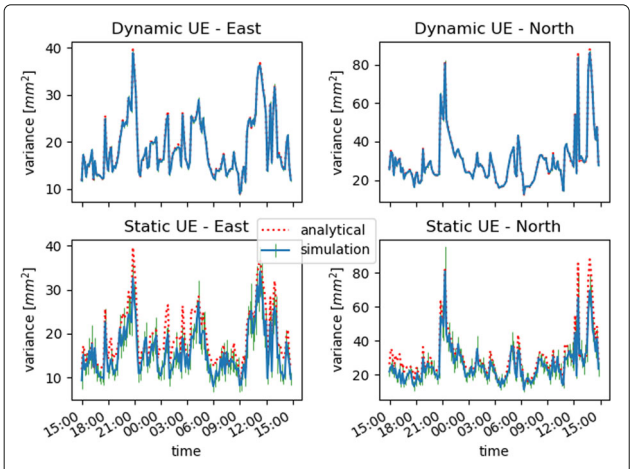


**Fig. 13** Comparison between RTK localization error variance in *Loc1* obtained from simulations, and computed with Eq. (55)

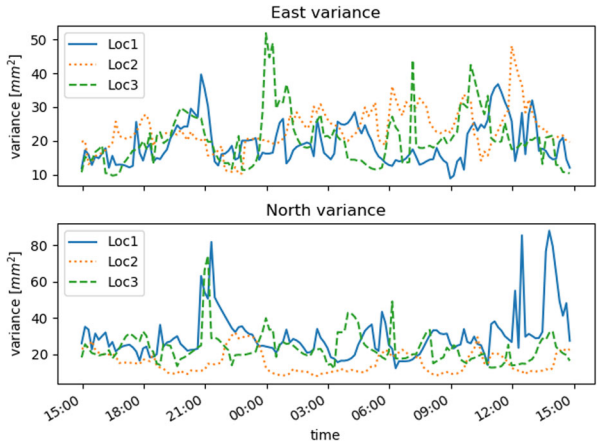


**Fig. 14** Comparison between RTK localization error variances obtained at different geographical localization

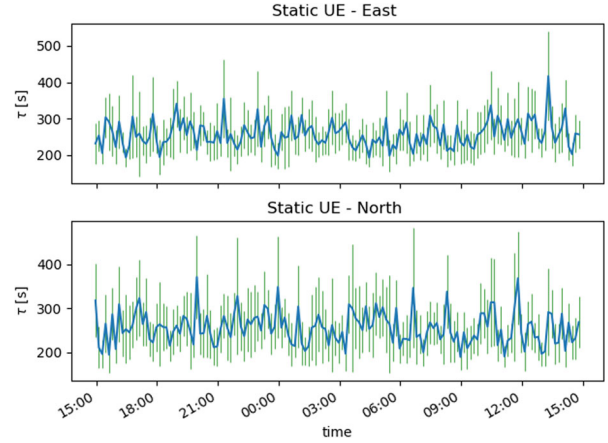


**Fig. 16** Correlation time obtained on the basis of simulation results in *Loc1*,and for the static UE

#### *6.2.2 Correlation time analysis*

Apart from the variance, the GM process is also described by correlation time. As an example, simulation results obtained for *Loc1* are presented in Fig. 15, in the case of dynamic UE, and Fig. 16, in the case of static UE. In both presented examples, the correlation time seems to be randomly fluctuating around a mean value, with no dependence of daytime or geographical localization. This hypothesis is validated by means of analysis of variance (ANOVA) statistical test on the correlation time data. ANOVA is a statistical test that allows to check if several data sets have statistically equal means, by analysis of their variance [35]. The ANOVA test has been independently performed for each simulation scenario and for all data sets related with static and dynamic UE respectively. The aim of the ANOVA test was to reject or not hypothesis $h_0$ that all data sets (correlation time over daytime and geographical localization) have the same mean value. To reject or not hypothesis, the ANOVA test output, i.e., $p$ value, is compared with the so-called significance level ($\alpha$), i.e., the probability of rejecting hypothesis which is actually true (typical $\alpha$ value is 0.05) [35]. The hypothesis may be rejected with significance level $\alpha$ when $p$value $< \alpha$. The corresponding ANOVA results are presented in Table 3. The hypothesis is rejected only in the case with dynmic UE in east direction and *Loc2*.

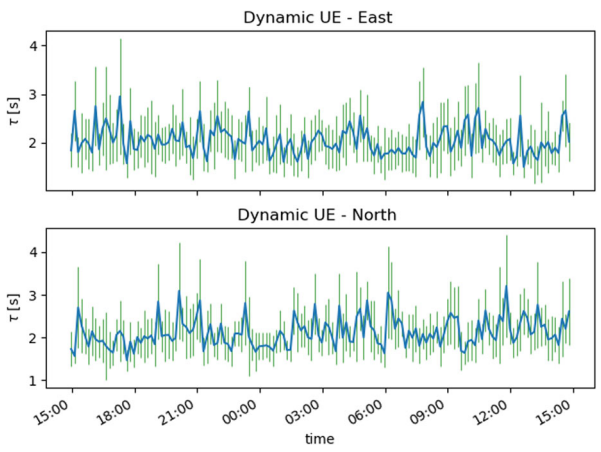


**Fig. 15** Correlation time obtained on the basis of simulation results in *Loc1* and for the dynamic UE

In conclusion, the RTK localization error correlation time depends only on undifferenced carrier phase measurement error and is independent of daytime and geographical localization, i.e., visible satellites constellation. The mean values of correlation time, averaged over all 144 steps, for all of studied geographical locations are presented in Table 4. For *dynamic UE* localization error

**Table 3** ANOVA statistical tests results for localization error correlation times

| Dataset | $p$ value | $h_0$ |
|---|---|---|
| Dynamic UE | | |
| Loc1 - east | 0.57 | Not rejected |
| Loc1 - north | 0.10 | Not rejected |
| Loc2 - east | 0.014 | Rejected |
| Loc2 - north | 0.93 | Not rejected |
| Loc3 - east | 0.19 | Not rejected |
| Loc3 - north | 0.17 | Not rejected |
| all (excluding Loc2 - east) | 0.17 | Not rejected |
| Static UE | | |
| Loc1 - east | 0.30 | Not rejected |
| Loc1 - north | 0.42 | Not rejected |
| Loc2 - east | 0.43 | Not rejected |
| Loc2 - north | 0.36 | Not rejected |
| Loc3 - east | 0.12 | Not rejected |
| Loc3 - north | 0.71 | Not rejected |
| all | 0.25 | Not rejected |

**Table 4** RTK east and north localization error correlation times, averaged over 24 h with 95% confidence intervals

| Localization | East error correlation time [s] | North error correlation time [s] |
|---|---|---|
| Dynamic UE | | |
| Loc1 | 2.0429 ± 0.0404 | 2.1172 ± 0.0441 |
| Loc2 | 2.0392 ± 0.0388 | 1.9983 ± 0.0403 |
| Loc3 | 2.0517 ± 0.0414 | 2.0738 ± 0.0421 |
| Static UE | | |
| Loc1 | 257.04 ± 4.78 | 255.94 ± 5.04 |
| Loc2 | 251.96 ± 4.50 | 258.45 ± 4.90 |
| Loc3 | 251.84 ± 4.62 | 255.97 ± 4.70 |

correlation time in both east and north directions can be assumed to be 2 s. The mean value of the correlation times in the case of *static UE* (in both east and north directions) is 255.2 s and fits in the confidence intervals in Table 4.

#### 6.2.3 Visible satellites coordinates resolution analysis

The proposed RTK localization error framework rely on visible satellites coordinates. The utilized satellites localization prediction uses SEM almanac introducing typically 1–2 km error (as mentioned in Section 5.3). The aim of this section is to verify whether degradation of satellites coordinates accuracy significantly impacts the final UE localization error. On the basis of Eq. (55), the localization error variance for *Loc1* geographical localization is computed with the visible satellites coordinates rounded to 1° and compared with the full-accuracy results in Fig. 17. As it can be seen, the presented results are almost identical.

#### 6.2.4 Adaptation of the proposed scheme for urban environment

In addition, the proposed RTK localization error framework may be applied to provide initial estimate of the localization error in urban environment, i.e., without taking into account NLoS UE-satellite signals propagation or cycle-slip occurrence. This can be done by increasing the elevation cutoff angle $\alpha_{el}$ from the default 7° to the value related to street geometry: width $W$ and neighboring buildings height $H$ as depicted in Fig. 18. This approach mimics signals from some GNSS satellites being blocked by buildings.

Dependence between street geometry of width $W$, and height $H$, and elevation angle cutoff $\alpha_{el}$ is given by

$$\alpha_{el} = \arctan\left(\frac{2H}{W}\right). \tag{56}$$

A simulation was performed to estimate RTK localization error variance in *Loc1* while changing $\alpha_{el}$. The elevation angle was increased to the value of 18° that corresponds to the $\frac{H}{W}$ street geometry ratio equal to 0.162. Results are depicted in Fig. 19. As expected, a higher elevation cutoff angle causes fewer satellites visibility. This finally results in a larger localization error in relation to the one obtained with default 7° elevation cutoff angle.

## 7 Final RTK localization error modeling algorithm

On the basis of the previous results a RTK localization error model for smartphone-grade GNSS antenna under open-sky conditions is proposed. Simulation experiments from Section 6.1 shown that RTK localization errors in both east and north directions are uncorrelated and may be modeled as a GM process. Further simulations from Section 6.2 proved that there is a dependence between localization error variance and geographical localization and daytime as a result of the different visible satellites geometry. The localization error correlation time seems to be related to the UE motion. The proposed model considers correlation time for two scenarios. First, it is appropriate for *static* UEs, e.g., people sitting on the bench in a park. Second, it can be applied for *dynamic* UEs, e.g., fast walking pedestrians. However, additional studies would be required to obtain a mathematical formula to

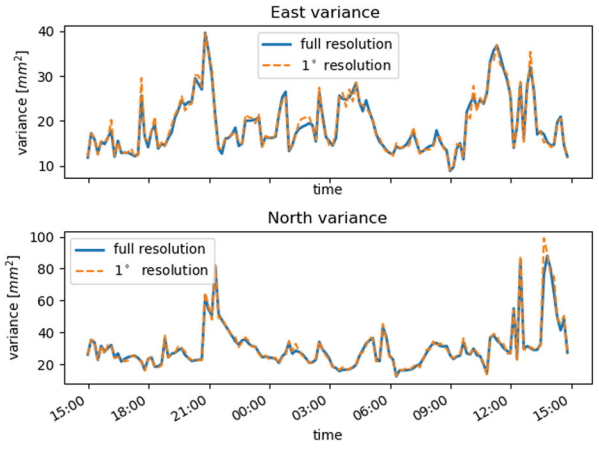


**Fig. 17** RTK localization error variance, computed with Eq. (55), for non-rounded and rounded to 1° satellites coordinates (*az*, *el*) in *Loc1*

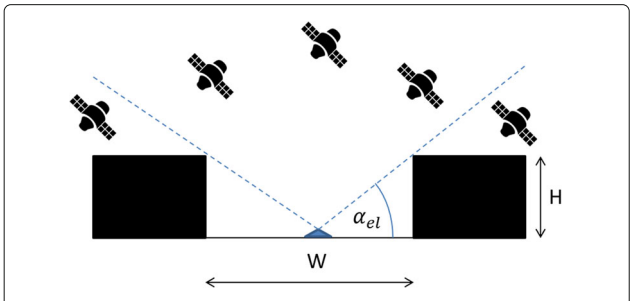


**Fig. 18** RTK LoS under urban conditions, modeled by adjusting elevation cutoff angle $\alpha_{el}$ to the street geometry: width $W$ and height $H$

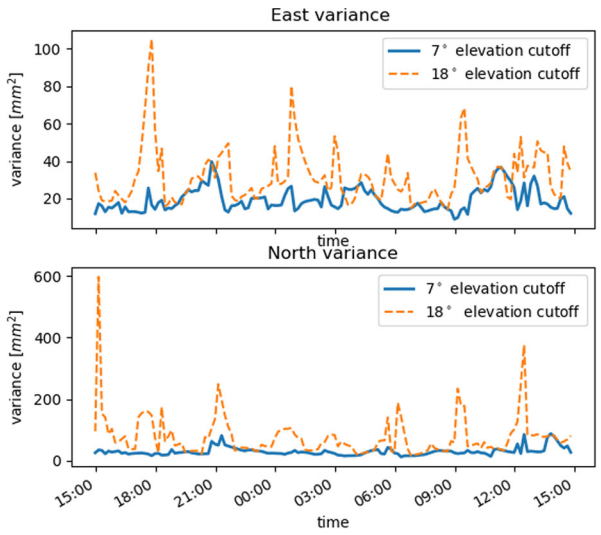


**Fig. 19** RTK localization error variance obtained at *Loc1* for open-sky and urban scenario modeled with elevation cutoff angles 7° and 18°, respectively

express the dependence of UE speed and RTK error correlation time, necessary for dealing with a big amount of other cases.

Figure 20 illustrates a block diagram representing the proposed RTK localization error generator. There are two independent GM process generators (see Section 5.2.2), one for error generation in the east direction and another one for the error generation in north direction, as the east and north localization errors are assumed to be uncorrelated. Furthermore, the GM process is described by two parameters: correlation time $\tau$ and variance $\sigma^2$, and can be generated as depicted in Fig. 21. Equation (32) explains how to convert given GM process parameters: correlation

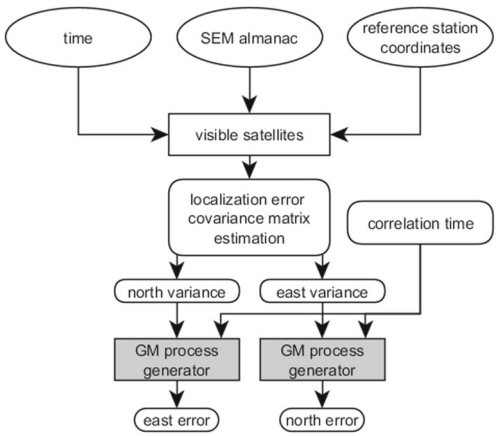


**Fig. 20** Block diagram of the RTK localization error generator

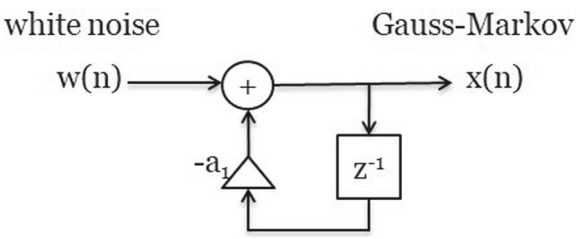


**Fig. 21** GM process generator structure

time and variance, into the generator parameters ($a_1$ and $\sigma_s^2$ from Fig. 21).

Simulation results show that localization error correlation time depends only on the UE motion. For static UEs, it is assumed to be the 255.2 s, while for dynamic UEs (moving with average speed of 7.65 $\frac{km}{h}$), it is assumed to be 2 s.

The variances of east and north localization errors change over geographical localization and daytime. Therefore, variance in both east and north directions will be computed with Eq. (55) using geometry matrix (see Eqs. (26, 25)). First, the GPS satellites coordinates (for every satellite in the constellation) are obtained on the basis of SEM almanac (see Section 5.3.2), with the use of the algorithm described in Section 5.3.3. Then visible satellites are those for which elevation angle (measured from the reference station) is greater than 7°.

Finally, undifferenced error standard deviation values obtained on the basis of experimental measurements in [16] and related to the UE ($\sigma_u = 2.5$ mm) and reference station ($\sigma_r = 6$ mm), required in the Eq. (55) are taken from Table 2.

Additionally, RTK localization error under urban conditions can be initially modeled by adjusting the elevation cutoff angle to the street geometry as proposed in Section 6.2.4.

## 8 Conclusions

The UE localization in 5G networks will be used not only for commercial and emergency purposes, but also for network optimization, intelligent transportation systems, and industrial applications. One of the most promising localization methods already described in LPP and foreseen for NR is GNSS-based RTK method providing centimeter-level accuracy.

The aim of this paper is to study daytime, geographical localization, and UE motion impact on the resulting RTK localization error and its distribution under open-sky conditions. For evaluation purposes a simulation environment is proposed and implemented including implementation and validation of the GM process generators, implementation of the satellite position computation algorithm (on the basis of the SEM almanac), and implementation of

the program capturing real visible satellite data (with the use of the NMEA protocol).

A series of simulations have been performed to study the impact of geographical position, daytime, and UE motion on the RTK localization error variance and correlation time. As a conclusion, the RTK localization error may be modeled with a Gauss-Markov process, described by time-varying variance, dependent on UE geographical position and daytime, and constant correlation time dependent on UE motion.

Finally, on the basis of the simulation results, the RTK localization error model has been proposed. It could be a useful tool for simulations studying performance of the future 5G networks utilizing REMs or intelligent transportation systems.

Future work include the study of imperfections in the UE-reference station side link quality and their impact on the RTK localization error.

## Appendix A: Coordinates Systems

In this paper, various global coordinates systems (e.g., Earth-Centered Earth-Fixed, east-north-up) are mentioned in several places. The purpose of this appendix is to describe them, and introduce transformations between them.

All coordinates systems described here refer to the World Geodetic System 1984 (WGS 84), which is currently the official geodetic system for navigation, mapping and charting purposes [8]. WGS 84 defines the Earth-Centered Earth-Fixed (ECEF) cartesian coordinate frame, geometric model of Earth's shape, the Earth's gravity field, and a set of constants (e.g., Earth's gravitational constant, Earth's rotation rate, used in Section 5 during GPS satellites orbits computation process) [8].

### Geodetic

Geodetic coordinate system (Fig. 22) characterizes point near Earth's surface with the following set of coordinates [36]:

- longitude $\lambda$ in the range of ($-$ 180° to 180°) measured between Prime Meridian and desired point
- latitude $\phi$ - in the range of ($-$ 90° to 90°) measured between the equatorial plane and the normal of the reference ellipsoid that passes through the measured point
- The height $h$ (or altitude) is the local vertical distance between the measured point and the reference ellipsoid surface

### Earth-centered Earth-fixed

ECEF coordinate system (Fig. 22) is an inertail coordinates system (rotates with Earth). In result, any chosen fixed point on the Earth surface has fixed set of coordinates. The origin of ECEF coordinate system is located in the center of Earth, and the axes are defined in following form: [36]

- $Z$-axis is along the spin axis of the Earth, pointing to the north pole
- $X$-axis intersects the sphere of the Earth at 0° latitude and 0° longitude
- $Y$-axis is orthogonal to the $Z$- and $X$-axes with the usual right-hand rule

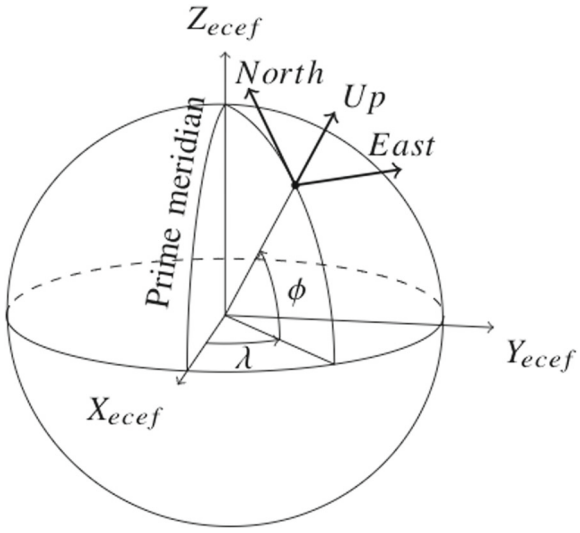


**Fig. 22** Comparison of Earth-Centered Earth-Fixed (ECEF), East-North-Up (ENU) and geodetic coordinate systems

### East-north-up

East-north-up (ENU) coordinate system (Fig. 22) is so-called local-level-system. Its origin is defined at the given position (e.g., reference station position), axis are defined in following form [8]:

- Axis-1 points east
- Axis-2 points north
- Axis-3 points upward

### Coordinates transformations

Coordinates systems transformations that are necessary for computer simulations of the RTK localization error will be described here. For details please refer to [36], [8].

#### *Geodetic-ECEF*

To perform transformation between geodetic coordinates $(\lambda, \phi, h)$ to ECEF $(x, y, z)$ two parameters from WGS 84 describing Earth's Meridian ellipse (defined as connection between all points on the ellipsoid with $\lambda = \text{const}$ [8]) must be introduced [36]:

$$\begin{cases} a_{wgs} = 6378137m \\ e_{wgs} = 0.08181919, \end{cases} \tag{57}$$

where $a_{wgs}$ is the semi major axis and $e_{wgs}$ is the eccentricity of the meridian ellipse.

Let's define now constant $N$ to simplify calculations [36]:

$$N = \frac{a_{wgs}}{\sqrt{1 - e_{wgs}^2 sin^2 \phi}}. \tag{58}$$

Geodetic to ECEF transformation is given with the following formula [36]:

$$\begin{bmatrix} x \\ y \\ z \end{bmatrix} = \begin{bmatrix} (N+h) \cdot \cos\phi \cos\lambda \\ (N+h) \cdot \cos\phi \sin\lambda \\ (N(1-e_{wgs}^2)+h) \cdot \sin\phi \end{bmatrix} \tag{59}$$

Inverse coordinates transformation is more complex and will not be discussed, because it is not necessary for the implementation of simulation environment.

### *ECEF-ENU*

As mentioned before, ENU is a local-level-system, performing transformation of the point in ECEF system (e.g., satellite coordinates $\mathbf{x}_s = (x_s, y_s, z_s)^T$), reference point (e.g. reference station) coordinates in ECEF ($\mathbf{x}_0 = (x_0, y_0, z_0)^T$), and Geodetic ($\lambda_0, \phi_0, h_0$)) systems are necessary.

The main part of the transformation is the rotation matrix $\mathbf{R}_{\text{enu}}$. This matrix rotates ECEF axes to make them coincident with the ENU axes. $\mathbf{R}_{\text{enu}}$ is given as [8]:

$$\mathbf{R}_{\text{enu}} = \begin{bmatrix} -\sin\lambda_0 & \cos\lambda_0 & 0 \\ -\sin\phi_0\cos\lambda_0 & -\sin\phi_0\sin\lambda_0 & \cos\phi_0 \\ -\cos\phi_0\cos\lambda_0 & -\cos\phi_0\sin\lambda_0 & \sin\phi_0 \end{bmatrix}. \tag{60}$$

Now $\mathbf{x}_s$ in ENU coordinates ($\mathbf{x}_{s_{\text{enu}}} = (e_s, n_s, u_s)^T$) is given with the following formula [8]:

$$\mathbf{x}_{s_{\text{enu}}} = \mathbf{R}_{\text{enu}}(\mathbf{x}_s - \mathbf{x}_0) \tag{61}$$

Sometimes it is more useful to express position in ENU system with the azimuth ($az$) and elevation ($el$) angles (e.g., satellite position with respect to the reference station). Azimuth angle ($0° - 360°$) is measured clockwise from the north, and elevation angle ($0° - 90°$) is measured from local horizon (positive up coordinate). ENU can be transformed to $az$ and $el$ with the following formulas [8]:

$$\tan az = \frac{e_s}{n_s} \tag{62}$$

$$\sin el = \frac{u_s}{\sqrt{e_s^2 + n_s^2 + u_s^2}} \tag{63}$$

#### Abbreviations

ANOVA: Analysis of variance; AoA: Angle of arrival; AR: Autoregressive; BS: Base station; DSA: Dynamic spectrum access; E911: Enhanced 911; ECEF: Earth-centered Earth-fixed; ENU: East-north-up; FCC: Federal Communications Commission; GM: Gauss-Markov; GNSS: Global Navigation Satellite system; GPS: Global Positioning System; LoS: Line of sight; LPP: LTE positioning protocol; M-MIMO: Massive multiple-input multiple-output; MCD: Measurement Capable Device; NMEA: National Marine Electronics Association; NRTK: Network Real-Time Kinematics; OTDoA: Observed time difference of arrival; REM: Radio Environment Map; RFPM: Radio frequency pattern matching; RMS: Root-mean square; RMSE: Root-mean-square-error; RSS: Received signal strength; RTK: Real Time Kinematics; SDMA: Spatial Division Multiple Access; SEM: System Effectiveness Model; SON: Self-organizing networks; TAR: Time to ambiguity resolution; UE: User equipment; UWB: Ultra wide band; WGS 84: World Geodetic System 84

#### Acknowledgements

Not applicable.

#### Authors' contributions

MH was responsible for literature study, proposal of the error generating algorithm, generation of results, and initial text preparation. PK and GK were responsible for discussing the material, shaping the manuscript, and writing/reviewing text. All authors read and approved the final manuscript.

#### Funding

This work was supported by Huawei Technologies within project 'RSM Based Radio Resource Provisioning for Spectral-, Energy- and Computational Efficiency in 5G Networks'. Project no. 08/81/PRJG/8139.

#### Availability of data and materials

The datasets used and/or analysed during the current study are available from the corresponding author on reasonable request.

#### Competing interests

The authors declare that they have no competing interests.

#### Author details

[1]Chair of Wireless Communications, Poznan University of Technology, Polanka 3, 60-965 Poznan, Poland. [2]Huawei Technologies, 164 40 Stockholm, Sweden.

Received: 14 October 2019 Accepted: 2 January 2020
Published online: 31 January 2020

#### References

1. J. A. del Peral-Rosado, R. Raulefs, J. A. López-Salcedo, G. Seco-Granados, Survey of cellular mobile radio localization methods: From 1g to 5g. IEEE Commun. Surveys Tutor. **20**(2), 1124–1148 (2018). https://doi.org/10.1109/COMST.2017.2785181
2. I.RACON. COST Action CA15104, T. Pedersen, B. Fleury, Whitepaper on New Localization Methods for 5G Wireless Systems and the Internet-of-Things. COST Action CA15104, IRACON (2018). https://vbn.aau.dk/en/publications/whitepaper-on-new-localization-methods-for-5gwireless-systems-an
3. A. Prasad, M. A. Uusitalo, Z. Li, P. Lunden, in *2016 IEEE Globecom Workshops (GC Wkshps)*. Reflection environment maps for enhanced reliability in 5g self-organizing networks, (2016), pp. 1–6. https://doi.org/10.1109/GLOCOMW.2016.7849019
4. A. Kliks, B. Musznicki, K. Kowalik, P. Kryszkiewicz, Perspectives for resource sharing in 5g networks. Telecommun. Syst. **68**(4), 605–619 (2018). https://doi.org/10.1007/s11235-017-0411-3
5. H. B. Yilmaz, T. Tugcu, F. Alagöz, S. Bayhan, Radio environment map as enabler for practical cognitive radio networks. IEEE Commun. Magazine. **51**, 162–169 (2013)
6. 3GPP, Evolved Universal Terrestrial Radio Access Network (E-UTRAN); Stage 2 functional specification of User Equipment (UE) positioning in E-UTRAN. Tech. Specification (TS) 36.305. https://portal.3gpp.org/desktopmodules/Specifications/SpecificationDetails.aspx?specificationId=2433
7. D. Dardari, A. Conti, U. Ferner, A. Giorgetti, M. Z. Win, Ranging with ultrawide bandwidth signals in multipath environments. Proc. IEEE. **97**(2), 404–426 (2009). https://doi.org/10.1109/JPROC.2008.2008846
8. P. Misra, P. Enge, *Global Positioning System: Signals, Measurements, and Performance*. (Ganga-Jamuna Press, 2006). https://books.google.pl/books?id=pv5MAQAAIAAJ. Accessed 24 Jul 2019
9. F. Wen, H. Wymeersch, B. Peng, W. P. Tay, H. C. So, D. Yang, A survey on 5g massive mimo localization. Digital Signal Process. (2019). https://doi.org/10.1016/j.dsp.2019.05.005
10. Q. D. Vo, P. De, A survey of fingerprint-based outdoor localization. IEEE Commun. Surveys Tutor. **18**(1), 491–506 (2016). https://doi.org/10.1109/COMST.2015.2448632

11. M. Hoffmann, H. Bogucka, in *Cognitive Radio-Oriented Wireless Networks*, ed. by A. Kliks, P. Kryszkiewicz, F. Bader, D. Triantafyllopoulou, C. E. Caicedo, A. Sezgin, N. Dimitriou, and M. Sybis. Localization techniques for 5g radio environment maps (Springer International Publishing, Cham, 2019), pp. 232–246
12. P. Ranacher, R. Brunauer, W. Trutschnig, S. Van der Spek, S. Reich, Why gps makes distances bigger than they are. Int. J. Geogr. Inf. Sci. **30**(2), 316–333 (2016). https://doi.org/10.1080/13658816.2015.1086924
13. 3GPP, Radio Frequency (RF) pattern matching location method in LTE. Tech. Rep. (TR) 36.809. https://portal.3gpp.org/desktopmodules/Specifications/SpecificationDetails.aspx?specificationId=2488
14. J. Turkka, T. Hiltunen, R. U. Mondal, T. Ristaniemi, in *2015 International Symposium on Wireless Communication Systems (ISWCS)*. Performance evaluation of lte radio fingerprinting using field measurements, (2015), pp. 466–470. https://doi.org/10.1109/ISWCS.2015.7454387
15. 3GPP, Technical Specification Group Radio Access Network; Study on NR positioning support. Technical Report (TR) 36.305, 3rd Generation Partnership Project (3GPP) (March 2019). Version 2.1.0
16. K. M. Pesyna, Advanced techniques for centimeter-accurate gnss positioning on low-cost mobile platforms. PhD thesis, (2015). https://repositories.lib.utexas.edu/handle/2152/33256?show=full
17. M. Fortunato, J. Critchley-Marrows, M. Siutkowska, M. L. Ivanovici, E. Benedetti, W. Roberts, in *2019 European Navigation Conference (ENC)*. Enabling high accuracy dynamic applications in urban environments using ppp and rtk on android multi-frequency and multi-gnss smartphones, (2019), pp. 1–9. https://doi.org/10.1109/EURONAV.2019.8714140
18. J. Miguez, J. Gisbert, J. A. Garcia-Molina, P. Zoccarato, P. Crosta, L. Ries, R. Perez, G. Seco-Granados, C. Massimo. Multi-gnss dynamic high precision positioning in urban environment, (2017), pp. 408–416. https://doi.org/10.33012/2017.15197
19. R. Emardson, P. Jarlemark, J. Johansson, S. Bergstrand, M. Lidberg, B. Jonsson, Measurement accuracy in network-rtk. Bollettino Geod. Sci. Affini (2009)
20. J. Chung, An accuracy study of rtk gnss positioning applied to comparing maps for bentgrass habitat modeling. PhD thesis (2017). Doctoral Dissertations. 1604. https://opencommons.uconn.edu/dissertations/1604
21. J. Hwang, H. Yun, Y. Suh, J. Cho, D.-H. Lee, Development of an rtk-gps positioning application with an improved position error model for smartphones. Sensors (Basel, Switzerland). **12**, 12988–3001 (2012). https://doi.org/10.3390/s121012988
22. M. Pesko, T. Javornik, A. Kosir, M. Štular, M. Mohorcic, Radio environment maps: The survey of construction methods. KSII Trans. Internet Inf. Syst. **8** (2014). https://doi.org/10.3837/tiis.2014.11.008
23. J. Perez-Romero, A. Zalonis, L. Boukhatem, A. Kliks, K. Koutlia, N. Dimitriou, R. Kurda, On the use of radio environment maps for interference management in heterogeneous networks. IEEE Commun. Magazine. **53**(8), 184–191 (2015). https://doi.org/10.1109/MCOM.2015.7180526
24. R. Di Taranto, S. Muppirisetty, R. Raulefs, D. Slock, T. Svensson, H. Wymeersch, Location-aware communications for 5g networks: How location information can improve scalability, latency, and robustness of 5g. IEEE Signal Process. Magazine. **31**(6), 102–112 (2014). https://doi.org/10.1109/MSP.2014.2332611
25. D. Slock, in *2012 5th International Symposium on Communications, Control and Signal Processing*. Location aided wireless communications, (2012), pp. 1–6. https://doi.org/10.1109/ISCCSP.2012.6217868
26. N. Wen, R. Berry, in *2006 40th Annual Conference on Information Sciences and Systems*. Information propagation for location-based mac protocols in vehicular networks, (2006), pp. 1242–1247. https://doi.org/10.1109/CISS.2006.286655
27. K. M. Pesyna, T. E. Humphreys, R. W. Heath, T. D. Novlan, J. C. Zhang, Exploiting antenna motion for faster initialization of centimeter-accurate gnss positioning with low-cost antennas. IEEE Trans. Aerospace Electron. Syst. **53**(4), 1597–1613 (2017). https://doi.org/10.1109/TAES.2017.2665221
28. P. Lamon, *The Gauss–Markov Process*. (Springer, Berlin, Heidelberg, 2008), pp. 93–95. https://doi.org/10.1007/978-3-540-78287-2_9. https://doi.org/10.1007/978-3-540-78287-2_9
29. J. G. Proakis, D. G. Manolakis, *Digital Signal Processing - Principles, Algorithms and Applications (2. Ed.)* (Macmillan, 1992)
30. M. J. M. Y. J.un. Wang, in *Proceedings of the 24th International Technical Meeting of the Satellite Division of The Institute of Navigation (ION GNSS 2011)*. Predicting glonass satellite orbit based on an almanac conversion algorithm for controlled ionosphere scintillation experiment planning, (2011), pp. 3118–3124
31. S. C. 300N. SepulvedaBlvd. SAICGPSSE&I, Navstar gps control segment to user support community interfaces. Technical Report (TR) ICD-GPS-870. https://www.gps.gov/technical/icwg/ICD-GPS-870A.pdf. Accessed 03 Aug 2019
32. S. Applications International Corporation, *Interface Specification IS-GPS-200 Revision E. Navstar GPS Space Segment/Navigation User Interfaces*. (Space and Missile Systems Center (SMC) Navstar GPS Joint Program Office (SMC/GP), 2010). https://www.gps.gov/technical/icwg/IS-GPS-200J.pdf
33. M. Murison, *A Practical Method for Solving the Kepler Equation*. (U.S. Naval Observatory, 2006). https://doi.org/10.13140/2.1.5019.6808
34. B. Madsen, *Statistics for Non-Statisticians*. (Springer, 2011). https://books.google.pl/books?id=JrC7DAEACAAJ. Accessed 19 Aug 2019
35. M. Reichenbächer, J. W. Einax, *Statistical Tests*. (Springer, Berlin, Heidelberg, 2011), pp. 37–77. https://doi.org/10.1007/978-3-642-16595-5_3. https://doi.org/10.1007/978-3-642-16595-5_3
36. G. Cai, B. Chen, T. Heng Lee, *Unmanned Rotorcraft Systems*. (Springer, 2011). https://doi.org/10.1007/978-0-85729-635-1


## Publisher's Note

## 7.15 Publication [P15]

M. Hoffmann, P. Kryszkiewicz, and A. Kliks, "Federated learning-based interference modeling for vehicular dynamic spectrum access," in *International Conference on Mobile and Ubiquitous Systems: Computing, Networking, and Services*, pp. 431–454, Springer, 2022.

MNiSW Points: 70

mgr inż. Marcin Hoffmann
Instytut Radiokomunikacji, Politechnika Poznańska
ul. Polanka 3, 60-965 Poznań

Poznań, 2 luty 2023 r.

# OŚWIADCZENIE W SPRAWIE AUTORSTWA PRACY

Oświadczam, że w pracy:

*M. Hoffmann, P. Kryszkiewicz, A. Kliks "Federated Learning-Based Interference Modeling for Vehicular Dynamic Spectrum Access," EAI MobiQuitous 2022 - 19th EAI International Conference on Mobile and Ubiquitous Systems: Computing, Networking and Services*

mój udział polegał na:

- Zaproponowaniu wspólnie z pozostałymi autorami metody modelowania interferencji wykorzystującej uczenie federacyjne na potrzeby dynamicznego dostępu do widma w scenariuszu komunikacji pomiędzy pojazdami
- Implementacji środowiska symulacyjnego
- Przeprowadzeniu eksperymentów symulacyjnych
- Przygotowaniu pierwszej wersji tekstu artykułu

Mój procentowy udział w powstanie pracy szacuję na: 60%

Marcin Hoffmann

Podpis

dr hab. inż. Paweł Kryszkiewicz, prof. PP
Instytut Radiokomunikacji, Politechnika Poznańska
ul. Polanka 3, 60-965 Poznań

Poznań, 14 sierpnia 2025 r.

# OŚWIADCZENIE W SPRAWIE AUTORSTWA PRACY

Oświadczam, że w pracy:

*M. Hoffmann, P. Kryszkiewicz, A. Kliks "Federated Learning-Based Interference Modeling for Vehicular Dynamic Spectrum Access," EAI MobiQuitous 2022 - 19th EAI International Conference on Mobile and Ubiquitous Systems: Computing, Networking and Services*

mój udział polegał na:

- Koordynacji prac badawczych
- Definicji problemu i miary zagregowanej interferencji wykorzystującej pojemność kanału radiowego
- Dyskusji ze współautorami metody zastosowana uczenia federacyjnego w zaproponowanym systemie
- Analiza uzyskanych wyników i propozycja metod ich prezentacji
- Iteracyjnym nanoszeniu poprawek na tekst

Mój procentowy udział w powstanie pracy szacuję na: 20%

Podpis

dr hab. inż. Adrian Kliks, prof. PP
Instytut Radiokomunikacji, Politechnika Poznańska
ul. Polanka 3, 60-965 Poznań

Poznań, 2 luty 2023 r.

# OŚWIADCZENIE W SPRAWIE AUTORSTWA PRACY

Oświadczam, że w pracy:

*M. Hoffmann, P. Kryszkiewicz, A. Kliks "Federated Learning-Based Interference Modeling for Vehicular Dynamic Spectrum Access," EAI MobiQuitous 2022 - 19th EAI International Conference on Mobile and Ubiquitous Systems: Computing, Networking and Services*

mój udział polegał na:

- zaproponowaniu pomysłu badawczego i współudziale w dyskusji merytorycznej
- udziału w edycji oraz sprawdzaniu tekstu pracy.

Mój procentowy udział w powstanie pracy szacuję na: 20%

Adrian Kliks

.....

Podpis

# Federated Learning-Based Interference Modeling for Vehicular Dynamic Spectrum Access*

Marcin Hoffmann[1], Pawel Kryszkiewicz[1], and Adrian Kliks[1]

Institute of Radiocommunications, Poznań University of Technology, Polanka 3, 61-131 Poznań, Poland
marcin.ro.hoffmann@doctorate.put.poznan.pl

**Abstract.** A platoon-based driving is a technology allowing vehicles to follow each other at close distances to, e.g., save fuel. However, it requires reliable wireless communications to adjust their speeds. Recent studies have shown that the frequency band dedicated for vehicle-to-vehicle communications can be too busy for intra-platoon communications. Thus it is reasonable to use additional spectrum resources, of low occupancy, i.e., secondary spectrum channels. The challenge is to model the interference in those channels to enable proper channel selection. In this paper, we propose a two-layered Radio Environment Map (REM) that aims at providing platoons with accurate location-dependent interference models by using the Federated Learning approach. Each platoon is equipped with a Local REM that is updated on the basis of raw interference samples and previous interference model stored in the Global REM. The model in global REM is obtained by merging models reported by platoons. The nodes exchange only parameters of interference models, reducing the required control channel capacity. Moreover, in the proposed architecture platoon can utilize Local REM to predict channel occupancy, even when the connection to the Global REM is temporarily unavailable. The proposed system is validated via computer simulations considering non-trivial interference patterns.

**Keywords:** Federated Learning · Radio Environment Map · Vehicle-to-Vehicle Communications · Vehicular Dynamic Spectrum Access · Interference Modeling

## 1 Introduction

A platoon-based driving [33, 29, 7] is a technology allowing vehicles to follow each other at short distances, i.e., of a few meters [40]. There are several significant benefits originating from this innovative approach. First, due to short inter-car distances, the road capacity can be improved by placing more vehicles on the road [41]. Second, vehicles following each other benefit from better aerodynamic conditions. This further implies fuel savings, and reduction of emitted pollution [10]. Most important, those gains from the platoon-based driving pattern

* The work has been realized within project no. 2018/29/B/ST7/01241 funded by the National Science Centre in Poland.

are achieved with no need for additional road infrastructure, e.g., expensive and time-consuming building of additional road lanes. One, typically first, vehicle in the platoon is a so-called platoon leader. Depending on the concept, it can be either an autonomous vehicle or a vehicle with a human driver [18, 36]. In most cases, the platoon leader is responsible for the platoon behavior, and other vehicles not only adjust their speed to the platoon leader but also follow its maneuvers, e.g., line change. However, it is a non-trivial task, especially, when the platoon leader is forced to sudden breaking. Research has shown that for the purpose of safe driving while maintaining short inter-vehicle distances, it is not enough to rely on the onboard sensors or cameras [45]. Additionally, reliable wireless communication must be established between the vehicles within the platoon to exchange control information, e.g., messages related to speed adjustment [39]. There are several protocols already defined that are aimed at wireless communications between vehicles (known as a vehicle-to-vehicle scheme, V2V), between vehicles and network infrastructure (called vehicle-to-infrastructure communications, V2I), and between vehicles and pedestrians (named vehicle-to-pedestrians V2P) [2]. These are collectively referred to as vehicles-to-everything (named widely V2X). In general, the idea of V2X communications can be realized either in a centralized way with the use of cellular technology (i.e., Cellular-V2X, C-V2X [1, 20]), or in a distributed fashion by means of, e.g., Dedicated-Short-Range-Communication (DSRC) [22]. The DSRC solution can utilize 802.11p and Wireless Access in Vehicular Environment (WAVE) standards, in physical, and medium access layers, respectively [3]. Although there are dedicated frequency bands for both DSRC and C-V2X, these might not be sufficient when road traffic is high. Some research has shown that with a growing number of vehicles utilizing DSRC interference in this part of the spectrum will drastically grow, decreasing the reliability of the wireless communications [34, 8]. Similar results were observed for C-V2X [43]. The low reliability is caused by the fact that under the high level of interference the DSRC and C-V2X-dedicated frequency bands will not be able to ensure the capacity of the wireless channel required by the platoon. This would further imply a need to increase the inter-vehicle spaces within the platoon to prevent potential intra-platoon crashes causing e.g., lower fuel savings. This contradicts the overall concept of a platoon-based driving pattern discussed above.

Therefore, it seems reasonable to look for alternative frequency bands where intra-platoon communication can be offloaded. Although almost all frequency bands are assigned to some wireless systems, the majority of these spectral resources are underutilized [24]. However, the frequency availability can vary with location or time. A platoon can potentially use a frequency band if it is not used at a given time in a given location. This requires detecting the radio activities of the so-called primary users (PUs), who are licensed to transmit in a particular frequency band. If PUs activity is not detected in this frequency band, this part of the spectrum can be opportunistically used by other systems. This approach is known in the literature as a Dynamic Spectrum Access (DSA) [49], and when

it relates to V2X communications, the Vehicle DSA (VDSA) scenario is then considered [12]. In our work, we concentrate on the latter scheme.

Detection of the PU's signal presence may be done by means of the so-called spectrum sensing (such as energy detection). However, stand-alone spectrum sensing has limited performance. In addition, knowledge about the radio environment is out-dates fast as a result of vehicle movement in VDSA. An entity that can be used to retain and aggregate knowledge about the radio environment is a database called a Radio Environment Map (REM) [47]. The REM stores, updates, and process location-dependent information about the present PU's signal, which from the perspective of the unlicensed, so-called secondary user (SU) may be treated as interference. Such processing of historical data about interference possibly from many devices provides more insight into the availability of secondary spectrum channels. Moreover, please note that REMs may save also information about other ongoing SU transmissions.

The main challenge while utilizing a REM for VDSA is accurate modeling of interference caused by PU's signals along the route of the vehicle. In this context, the state-of-the-art models of interference utilized by REM are very simple, i.e., they characterize observed PU's signal power in a given location by its first-order statistics - the mean received power of unwanted signal [25, 27, 42]. Such a simple approach was reliable enough when DSA was applied to the terrestrial television band, as the transmitted digital terrestrial television (DTT) signals are stable over frequency and time. However, in the general case, especially when unlicensed bands are considered, the PUs can utilize various algorithms for medium access controls and different transmission schemes. In such situations, more sophisticated models must be used to deal with complex interference distributions. This observation fits well with the considered VDSA scheme, where the observed unwanted signal distributions vary as a function of the road (location) and time. The creation of stable and precise models of unwanted signals may be time-consuming, and in practice, only a limited number of interference samples can be collected at one time. Thus, proper mechanisms for updating interference models in REM must be proposed. These mechanisms should be designed so as to enable the simultaneous contribution of several data sources, e.g., multiple platoons.

In this paper, to deal with potentially complex distributions of interference generated by PUs, a Gaussian Mixture Model (GMM) [35] will be used. GMM can model a Probability Density Function (PDF) of interference samples power, as a weighted sum of Gaussian distribution PDFs. Based on the model a wireless channel capacity can be calculated and the optimal frequency obtained using the algorithm proposed by us in [21]. However, that paper did not deal with a merger of knowledge from many sources. As the GMM model of interference varies in space, we proposed to store GMM-location pairs in the REM. Moreover, we propose a two-layer architecture of REM dedicated for VDSA, consisting of a Global, and a Local REM respectively. In our approach platoons can download the estimated GMM from Global REM to its Local REM, and update Local REM during ride based on local spectrum sensing. Later on, the locally updated

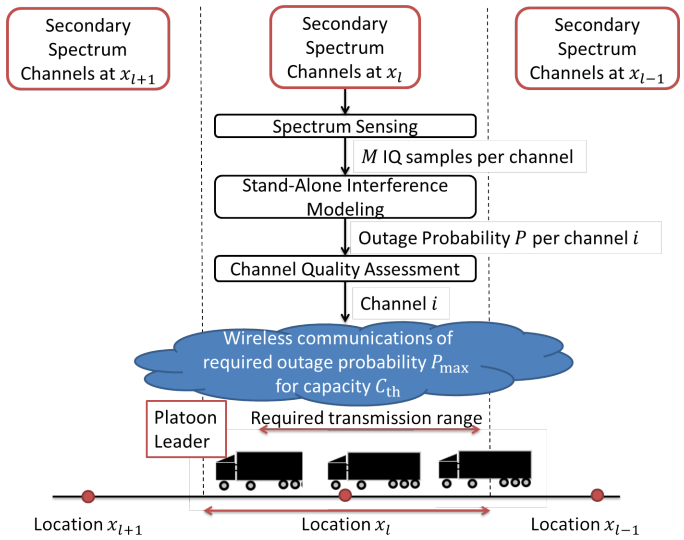


**Fig. 1.** Illustration of the stand-alone system model.

GMM models from potentially many platoons are sent back to the Global REM to be merged into a single model therein. Such an architecture is enabled via Federated Learning (FL) [26, 28]. We confirm the effectiveness of this scheme via computer simulations and compare it against local sensing. The local interference modeling, without REM utilization, provides much worse insight into the distribution of interference for the platoon. Moreover, we show that the more platoons contribute to the update of Global REM the higher accuracy interference models can be obtained.

The paper is organized as follows: In Sec. 2 a stand-alone system model is described, i.e., without REM. The proposed two-layered REM architecture together with formulas for an update of both local and global models is presented in Sec. 3. The simulation setup is described in Sec. 4. The results are discussed in Sec. 5. Finally, the conclusions are formulated in Sec. 6.

## 2 Stand-Alone System Model

Let us consider the generic case, where platoons offload a portion of their traffic from congested CV2X/DSRC bands to other frequency ranges, already occupied by the PU. All $U$ platoons apply the VDSA scheme trying to select the best frequency channels from all $\mathcal{I}$ candidate channels of bandwidth $B$. However, no additional edge intelligence, e.g., REM is used. A single platoon of index $u$ is formulated by $N_u$ vehicles, as depicted in Fig. 1. At a given time instance a platoon $u$ is located at position $\mathbf{x}_l$ being a vector of geographical coordinates related to platoon location expressed in arbitrary chosen coordinates system

e.g., earth-centered earth-fixed (ECEF). The behavior of the platoon, including maintaining proper inter-vehicle distances and management of intra-platoon communications, is realized by the first vehicle, which acts as a platoon leader. It sends proper management information to the remaining $N_u - 1$ vehicles using wireless communications. To benefit from the platoon-based driving pattern, vehicles must drive at a very short distance. This implies wireless communication to meet high requirements on QoS. In our scenario, VDSA is assumed, so each platoon is looking for the secondary spectrum channel that would meet the platoon communication requirements. The selection of $i$-th frequency channel out of setting $\mathcal{I}$, consists of several steps (see Fig. 1), mainly spectrum sensing, interference modeling, and channel quality assessment These steps are described below from the perspective of a single platoon, yet all $U$ platoons are performing them independently.

### 2.1 Capture of Samples

The first step is to capture power samples from secondary spectrum channels available at location $\mathbf{x}_l$. We assume that every vehicle in the platoon can be potentially involved in this process. Thus samples can be simultaneously collected from several secondary spectrum channels. In each channel, a batch of $M$ in-phase and quadrature (IQ) received signal samples is collected in total.

### 2.2 Channel Quality Assessment

Although in Fig. 1 *Interference Modeling* stands for the second step, it will be easier to understand the whole idea when the Channel Quality Assessment (CQA) would be described first. Moreover, some mechanisms used in interference modeling are related to the proposed CQA method.

First, when discussing the CQA, the challenge is to choose the proper evaluation metric. From the perspective of overall communications reliability, one of the most important aspects is to monitor the latency [14]. However, it is not straightforward to estimate it, as latency highly depends on the utilized radio access technology and medium access protocol. Both are in general not known when considering secondary spectrum channels, especially when many systems of different radio access technologies may operate. Moreover, according to the state-of-the-art models to assess latency, the knowledge of the arrival rate distribution of the incoming packets is necessary [48]. Its estimation is also case-dependent. On the other hand, a well-established metric is the Shannon capacity of a wireless channel being the upper bound estimate of the real system throughput. This metric is irrespective of the properties of the particular communication system, e.g., medium access control, and modulation schemes. Thus, in this paper, we follow this approach to assess channel quality.

We compute the capacity of channel $i$ of bandwidth $B$ as a sum over $N_\mathrm{f}$ narrow sub-channels, which is motivated by the following observations. First, in the secondary spectrum, there may be potentially many interference sources of various frequency-dependent transmission characteristics, e.g., some of them

may be narrow-band, and some wide-band. Second, in most of the contemporary communication protocols dedicated to V2V the multicarrier modulation scheme (Orthogonal-Frequency-Division-Multiplexing, OFDM) is applied, e.g., in IEEE 802.11p or CV2X using LTE or 5G networks. We consider the communication between the platoon leader and the last vehicle, as it is the most challenging because of the highest path loss. In consequence, at location $\mathbf{x}_l$ the Shannon capacity of the secondary spectrum channel $i$, between the two most distant vehicles within the platoon is given by:

$$c^{(i,\mathbf{x}_l)} = \frac{B}{N_\mathrm{f}} \sum_{f \in \mathcal{F}} \log_2 \left( 1 + \frac{P_\mathrm{tx}^{(i,\mathbf{x}_l)} \cdot H(i,\mathbf{x}_l)}{\sigma_\mathrm{n}^2 + I_f^{(i,\mathbf{x}_l)}} \right), \tag{1}$$

where $\mathcal{F}$ is a set of usable sub-channels (indexed by $f$), $H(i,\mathbf{x}_l)$ is a large scale channel gain (including transmit and receive antenna gains) at location $\mathbf{x}_l$ between the platoon leader and the last car. Next, $P_\mathrm{tx}^{(i,\mathbf{x}_l)}$ is the transmitter power per sub-channel, $\sigma_\mathrm{n}^2$ is the noise power over one sub-channel $f$, and $I_f^{(i,\mathbf{x}_l)}$ stands for the interference power on sub-carrier $f$. According to the field measurements, communication between vehicles following each other in the close distance, i.e., below 60 m, is expected to be mainly under Line-Of-Sight (LOS) conditions for roof-top antennas [32]. This observation can be applied to the communication between the platoon leader, and the last vehicle in a platoon consisting of a few vehicles, e.g. 3-4. As a result we expect channel to be relatively stable and flat. On the other hand interference in secondary spectrum potentially comes from the variety of sources having different transmission schemes. Therefore, our main focus is on the interference impact on the channel capacity.

While interference varies randomly, the capacity also becomes the random variable. From the perspective of the intra-platoon communication it is crucial to determine how likely is that channel capacity $c^{(i,\mathbf{x}_l)}$ falls below the acceptable level $C_{th}$, i.e., to derive the outage probability $\mathcal{P}(c^{(i,\mathbf{x}_l)} < C_\mathrm{th})$. Having (1) as a starting point, in our previous work, we proposed to utilize Shannon capacity simplification proper for low Signal to Noise Ratio (SNR), in order to obtain the formula for the computation of the outage probability on the basis of interference distribution, and remaining transmission parameters, e.g., bandwidth, transmission power [21]:

$$\mathcal{P}\left( \chi^{(i,\mathbf{x}_l)} < \ln \frac{\ln 2 \cdot C_\mathrm{th} \cdot N_\mathrm{f}}{\mathrm{B} \cdot P_\mathrm{tx}^{(i,\mathbf{x}_l)} \cdot H(i,\mathbf{x}_l)} \right), \tag{2}$$

where $\chi^{(i,\mathbf{x}_l)}$ is a random variable logarithm of aggregated interference and noise given by:

$$\chi^{(i,\mathbf{x}_l)} = \ln \left( \sum_{f \in \mathcal{F}} \frac{1}{I_f^{(i,\mathbf{x}_l)} + \sigma_n^2} \right). \tag{3}$$

With the use of the above equations quality of the available secondary spectrum, channels can be assessed, and the platoon leader can make the decision on the

transmission channel to be in use. The detailed mathematical reasoning aimed at transformation of (1) into the (2) can be found in [21].

### 2.3 Interference Modeling

After the introduction of the CQA metric given by (2), it can be observed that this metric requires an accurate model of interference term $\chi^{(i,\mathbf{x}_l)}$. The secondary spectrum channels can be occupied by many interference sources of different emission powers, diverse radio access technologies, various modulations, and not identical bandwidths. As a result the interference term $\chi^{(i,\mathbf{x}_l)}$ can follow a non-trivial, multi-modal distribution. It has been shown that such multi-modal distributions can be efficiently modeled with the use of the so-called Gaussian Mixture Model (GMM) [6]. The idea behind the GMM is to represent an arbitrary Probability Density Function (PDF), as a properly weighted sum of $J$ Gaussian distribution PDFs. In the considered case $\chi^{(i,\mathbf{x}_l)}$ is a one-dimensional random variable, thus GMM would be given by:

$$p(\chi^{(i,\mathbf{x}_l)}) = \sum_{j=1}^{J} \pi_j \mathcal{N}(\chi^{(i,\mathbf{x}_l)} | \mu_j, \sigma_j), \tag{4}$$

where $p(\chi^{(i,\mathbf{x}_l)})$ denotes the distribution of $\chi^{(i,\mathbf{x}_l)}$, $\pi_j$ is the $j$-th mixture component weight, i.e., the probability that $\chi^{(i,\mathbf{x}_l)}$ comes from the $j$-th mixture component. Next, $\mathcal{N}(\chi^{(i,\mathbf{x}_l)} | \mu_j, \sigma_j)$ is the conditional Gaussian distribution of $\chi^{(i,\mathbf{x}_l)}$, i.e., Gaussian distribution of $\chi^{(i,\mathbf{x}_l)}$, under assumption that it comes from the $j$-th mixture component with mean $\mu_j$ and standard deviation $\sigma_j$. To obtain parameters of a random distribution it is common to use a closed-form maximum likelihood estimator, i.e., closed form expressions are computed through maximization of the likelihood function. Unfortunately. in the case of GMM the log-likelihood function is a sum over the exponential functions, and no closed-form estimator exists [6]. Instead an iterative algorithm named Expectation Maximization (EM) is widely in use [15].

In this work the EM algorithm will be used to compute the parameters of GMM on the basis of $N_\mathrm{s} = \frac{M}{N_\mathrm{f}}$ samples of interference term $\chi^{(i,\mathbf{x}_l)}$. These samples are obtained from $M$ IQ samples captured each time any of the $U$ platoons visits location $\mathbf{x}_l$. The $M$ IQ samples are first divided into $N_\mathrm{s}$ non-overlapping segments, each of $N_\mathrm{f}$ samples. For each of these segments a Discrete Fourier Transform of size $N_\mathrm{f}$ is applied. Next, the power samples are computed within each sub-channel. Finally, by applying (3) a single value of $\chi^{(i,\mathbf{x}_l)}$ is obtained for each of these segments. These $N_\mathrm{s}$ samples of variable $\chi^{(i,\mathbf{x}_l)}$ constitutes an input to the EM algorithm. In the stand-alone approach discussed in this section, the platoon $u$ can rely only on the temporarily computed GMM to obtain the least occupied secondary spectrum channel $i$. In other words, the platoon senses the channel $i$ for the assumed period (obtaining $N_\mathrm{s}$ samples of interference term $\chi^{(i,\mathbf{x}_l)}$), and generates the GMM interference model following the traditional EM approach. Once it is done, it decides on the spectrum occupancy and prospective

capacity as described in Sec. 2.2. We will refer to this schema as *Stand-Alone Interference Modeling* (SAIM) throughout the rest of this paper, as it models the spectral usage characteristic without additional information provided by other entities, e.g., REM. We treat it as a reference solution.

The SAIM approach has a significant drawback. The GMM model is computed only on the basis of a limited number of locally collected samples. To make the generated GMM reliable, the simplest approach would be to set $N_\mathrm{s}$ to a large value. However, the primary goal of wireless communications within the platoon is to maintain safety on the road, especially when the inter-car distances are very short. Thus, it would be inefficient for the platoon to spend too much time on sensing, and thus $N_\mathrm{s}$ is expected to be low, creating a risk of inaccurate interference modeling through the GMM. In the following section (Sec. 3) we show how to overcome this issue by equipping the network infrastructure with REM modules utilizing a Federated Learning algorithm in order to enable continuous improvement of interference distribution models.

## 3 REM and Federated Learning for Interference modeling

In order to overcome the drawbacks of the SAIM approach we propose to utilize historical knowledge gathered about the interference observed in the location $\mathbf{x}_l$ for better spectrum utilization estimation. We also propose the application of the federated learning approach for improving the interference modeling by exchanging interference awareness between all interested platoons.

### 3.1 REM For Interference Modeling

From the perspective of spectrum management and the best channel selection, the REM may be treated as an intelligent database containing location-dependent information about various signal sources (both, wanted and of interference type) observed in the wireless communication system [47]. The users can communicate with REM via a side link to e.g. obtain information about the interference related to their positions or provide REM with their own measurement data. The entries in the database may have various forms, from raw measurements to some averaged figures of merit such as averaged received power in the band of interest. Although such REM databases may be applied to any frequency band and to any application, in the context of DSA the terrestrial television band was often in focus [38, 23, 37]. In this frequency band, the interference is usually homogeneous, i.e., it has a stable average level over time and at a given location. In such a case, the interference can be easily modeled by the average power of the observed signal. However, as already mentioned, this idea can be extended to build a REM database capable of modeling more complicated distributions, e.g., with interference power varying in time and frequency. Mainly, instead of average power, the parameters of GMMs related to the secondary spectrum channels $\mathcal{I}$ can be stored for each location $\mathbf{x}_l$. This structure of the data in REM is depicted in Fig. 2. One can observe that each location is

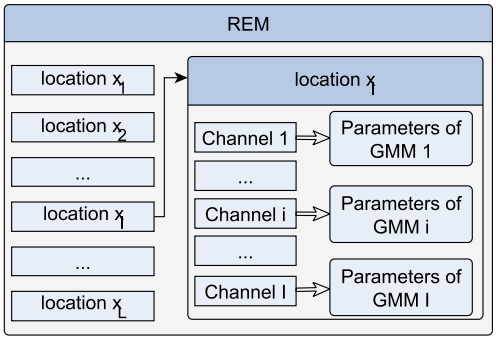


**Fig. 2.** The structure of data in REM.

associated with the dictionary of tuples: channel and related GMM model parameters. From the architectural perspective, we propose a two-layered scheme, as depicted in Fig. 3, where Global REM and Local REMs are shown. Global REM is a part of the network infrastructure (belonging to, e.g., mobile network operator). It stores the global interference models, distributes them to the Local REMs, i.e., platoons, and is capable to combine them together in order to update its own global interference model. In turn, the Local REM is deployed and managed (updated) at each platoon $u$. Thus, in our case, in the first step, the Local REM will be populated by the data downloaded from the Global REM. Next, these entries will be updated locally every time the platoon captures new $N_\mathrm{s}$ samples of interference term $\chi^{(i,\mathbf{x}_l)}$. Once processed locally, they will be used for updating the global REM, when the link to it is available. The idea behind the two-layered REM architecture aims at increasing the reliability of the system. While every platoon has its own Local REM, it can still use the interference models even when the side link to the Global REM is temporarily unavailable. Local REM is being updated on the basis of the raw samples, associated with the local environment, so it can reflect the current situation in the network and update the received model accordingly. As mentioned above, Local REM may also contribute to updating the Global REM models by sending back local observations or trained parameters. However, as the Local REM contains the whole GMM model it is enough to send only the model parameters to the Global REM instead of raw measurements. This results in significant traffic load reduction, i.e., order of tens parameters per GMM model vs hundreds of captured raw samples that have to be sent over the side link. Such an approach is inspired by the popular federated learning scheme [46, 30, 44], where the trained model details are exchanged between the central and surrounding nodes in order to better train the model and better reflect the local environment observed by each node. The procedure of secondary spectrum channel selection which utilizes interference modeling based on REM and FL is summarized in Fig. 4. It can be

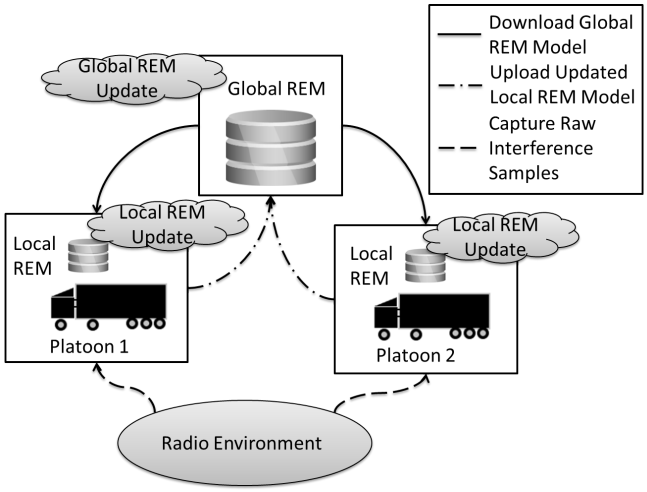


**Fig. 3.** Two-Layer REM architecture with FL cycle marked.

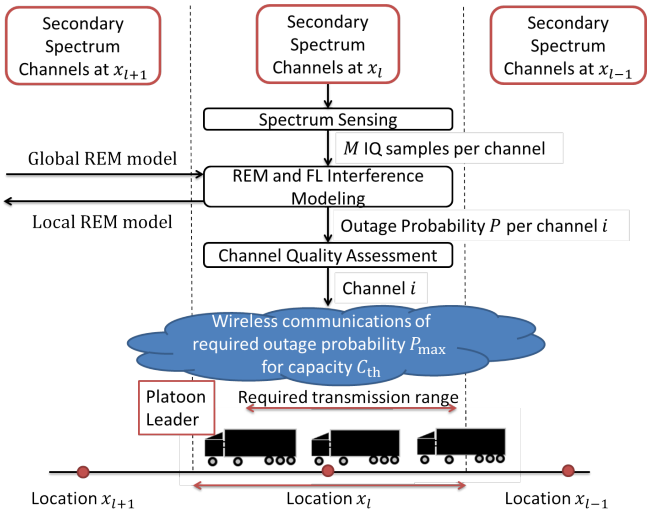


**Fig. 4.** Illustration of the REM and FL-based system model.

seen that it is an extension of the state-of-the-art SAIM approach presented in Sec. 2.

### 3.2 Local REM Update

Let us denote the set of GMM parameters in Local REM related to the channel $i$, location $\mathbf{x}_l$, and platoon $u$ as $g_u(\mathbf{x}_l, i)$. These GMM parameters are obtained

from the total number of samples equal to $N_{\mathrm{r},u}(\mathbf{x}_l, i)$. Every time when the location $\mathbf{x}_l$ is visited by the platoon $u$, only $N_\mathrm{s}$ new samples of interference term $\chi^{(i,\mathbf{x}_l)}$ per each secondary spectrum channel $i$ can be captured. These new samples are used to update the parameters of Local REM model $g_u(\mathbf{x}_l, i)$. The update procedure starts from computation of a temporal GMM model of $J$ components from those new $N_\mathrm{s}$ samples. The set of parameters of this temporal GMM model is denoted as $\tilde{g}_u(\mathbf{x}_l, i)$. The same number of GMM components $J$ for both $g_u(\mathbf{x}_l, i)$, and $\tilde{g}_u(\mathbf{x}_l, i)$. In general, $J$ can be established every time a new temporal GMM model of parameters set $\tilde{g}_u(\mathbf{x}_l, i)$ is built, by creating several models and comparing them against each other in terms of the chosen metric, e.g., Akaike Information Criterion (AIC), which is the function of model log-likelihood, and the number of parameters [5]. To reduce the number of GMM parameters to be sent between Local and Global REM we decided to use the shared-covariance variant of GMM, where a single variance is computed and shared among all $J$ components.

The parameters set of GMM model from Local REM $g_u(\mathbf{x}_l, i)$ consists of: shared variance $\sigma_u^2(\mathbf{x}_l, i)$, vector of means $\boldsymbol{\mu}_u(\mathbf{x}_l, i) = \{\mu_{u,j}(\mathbf{x}_l, i)\}_{j=1}^J$, vector of components proportions $\boldsymbol{\pi}_u(\mathbf{x}_l, i) = \{\pi_{u,j}(\mathbf{x}_l, i)\}_{j=1}^J$. The parameters set of temporal GMM model $\tilde{g}_u(\mathbf{x}_l, i)$ computed from the new $N_\mathrm{s}$ samples of interference term $\chi^{(i,\mathbf{x}_l)}$ is created by: $\tilde{\sigma}_u^2(\mathbf{x}_l, i)$, $\tilde{\boldsymbol{\mu}}_u(\mathbf{x}_l, i) = \{\tilde{\mu}_{u,j}(\mathbf{x}_l, i)\}_{j=1}^J$, $\tilde{\boldsymbol{\pi}}_u(\mathbf{x}_l, i) = \{\tilde{\pi}_{u,j}(\mathbf{x}_l, i)\}_{j=1}^J$. For implementation purpose of combining together corresponding pairs of Local REM model parameters $g_u(\mathbf{x}_l, i)$ and temporal GMM model parameters $\tilde{g}_u(\mathbf{x}_l, i)$ we recommend to sort the vectors $\boldsymbol{\mu}_u(\mathbf{x}_l, i)$, $\boldsymbol{\pi}_u(\mathbf{x}_l, i)$, according to the $\boldsymbol{\mu}_u(\mathbf{x}_l, i)$ values, and vectors $\tilde{\boldsymbol{\mu}}_u(\mathbf{x}_l, i)$, $\tilde{\boldsymbol{\pi}}_u(\mathbf{x}_l, i)$ according to the $\tilde{\boldsymbol{\mu}}_u(\mathbf{x}_l, i)$.

Now the parameters of the Local REM model $g_u(\mathbf{x}_l, i)$ are updated utilizing modified formula of incremental GMM learning [11]:

$$\begin{aligned}
\sigma_u(\mathbf{x}_l, i) &\leftarrow \frac{N_{\mathrm{th},u}(\mathbf{x}_l, i) \cdot \sigma_u(\mathbf{x}_l, i) + N_\mathrm{s} \cdot \tilde{\sigma}_u(\mathbf{x}_l, i)}{N_{\mathrm{th},u}(\mathbf{x}_l, i) + N_\mathrm{s}}, \\
\mu_{u,j}(\mathbf{x}_l, i) &\leftarrow \frac{N_{\mathrm{th},u}(\mathbf{x}_l, i) \cdot \mu_{u,j}(\mathbf{x}_l, i) + N_\mathrm{s} \cdot \tilde{\mu}_{u,j}(\mathbf{x}_l, i)}{N_{\mathrm{th},u}(\mathbf{x}_l, i) + N_\mathrm{s}}, \\
\pi_{u,j}(\mathbf{x}_l, i) &\leftarrow \frac{N_{\mathrm{th},u}(\mathbf{x}_l, i) \cdot \pi_{u,j}(\mathbf{x}_l, i) + N_\mathrm{s} \cdot \tilde{\pi}_{u,j}(\mathbf{x}_l, i)}{N_{\mathrm{th},u}(\mathbf{x}_l, i) + N_\mathrm{s}}, \\
N_{\mathrm{r},u}(\mathbf{x}_l, i) &\leftarrow N_{\mathrm{r},u}(\mathbf{x}_l, i) + N_\mathrm{s},
\end{aligned} \tag{5}$$

where $N_{\mathrm{th},u}(\mathbf{x}_l, i) = \min\{N_{\mathrm{r},u}(\mathbf{x}_l, i), k \cdot N_s\}$, and $k$ is a positive integer. The $N_\mathrm{th}$ parameter is defined so as to ensure that model can potentially follow the environment changes, it can be think of as a learning rate, i.e., how much impact on the model new data have. The larger the $k$ is the less impact the parameters of temporal GMM model $\tilde{g}_u(\mathbf{x}_l, i)$ have on the update of Local REM model parameters $g_u(\mathbf{x}_l, i)$. In the case when at a given platoon location $\mathbf{x}_l$ there is no information about interference model in REM, the values of GMM model parameters in Local REM are assumed to be initialized with set of temporal GMM model parameters $\tilde{g}_u(\mathbf{x}_l, i)$.

### 3.3 Global REM Update

In general, we can expect that multiple platoons can follow the same or partially overlapping route. A platoon $u$ will update its Local REM, following the procedure described in Sec. 3.2. Suppose there are $U$ platoons that updated their Local REMS and send updated models back to the Global REM. The question arises of how to combine the $U$ models from Local REMs into the Global REM model. One could notice that this concept fits well into the idea of FL, where multiple clients train their local models, which are sent to server and processed to update the global model [4]. Thus, in order to update the Global REM, We have decided to implement the state-of-the-art FL algorithm named FedAvg [31]. The FedAvg formula for updating the Global REM is defined as a weighted average of the parameters from the Local REMs. The detail update rule of GMM model parameters in Global REM related to channel $i$, and location $\mathbf{x}_l$ is presented below:

$$\begin{aligned}
\sigma_g(\mathbf{x}_l, i) &\leftarrow \frac{\sum_{u=1}^{U} N_{\mathrm{th},u}(\mathbf{x}_l, i) \cdot \sigma_u(\mathbf{x}_l, i)}{\sum_{u=1}^{U} N_{\mathrm{th},u}(\mathbf{x}_l, i)} \\
\mu_{g,j}(\mathbf{x}_l, i) &\leftarrow \frac{\sum_{u=1}^{U} N_{\mathrm{th},u}(\mathbf{x}_l, i) \cdot \mu_{u,j}(\mathbf{x}_l, i)}{\sum_{u=1}^{U} N_{\mathrm{th},u}(\mathbf{x}_l, i)} \\
\pi_{g,j}(\mathbf{x}_l, i) &\leftarrow \frac{\sum_{u=1}^{U} N_{\mathrm{th},u}(\mathbf{x}_l, i) \cdot \pi_{u,j}(\mathbf{x}_l, i)}{\sum_{u=1}^{U} N_{\mathrm{th},u}(\mathbf{x}_l, i)},
\end{aligned} \tag{6}$$

where $\sigma_g(\mathbf{x}_l, i)$ is the standard deviation shared among all GMM components, $\mu_{g,j}(\mathbf{x}_l, i)$ is the mean of $j$-th GMM component, and $\pi_{u,j}(\mathbf{x}_l, i)$ is the proportion of $j$-th GMM component.

### 3.4 Federated Learning Cycle

The procedure of Local REM update described in Sec. 3.2, together with the procedure of Global REM update described in Sec. 3.3 would follow each other in a cyclic manner in order to learn Global REM with interference distributions. This constitutes an FL cycle, that according to the principles defined in [4], can be specified as shown in Algorithm 1. This FL cycle can be visible also in the proposed two-layer REM architecture in Fig. 3.

## 4 Simulation Scenario

Training of the GMM models requires a lot of data to be processed, especially when multiple platoons are considered. To guarantee the reliability of the model, a dedicated and detailed simulation environment has been built in order to generate interference samples along with the consecutive platoon locations. We consider three non-overlapping Wireless Local Area Network (WLAN) channels having 2.412 GHz, 2.437 GHz, and 2.462 GHz center frequencies, respectively. At

**Algorithm 1** FL Cycle for Update of Global REM

```
Distribute parameters of Global REM model among U platoons in the location x_l
for each platoon u ∈ U do
    for each channel i ∈ I do
        Capture M new IQ interference samples
        Obtain N_s samples of interference term χ^(i,x_l)
        Compute set of temporal GMM model
         parameters g̃_u(x_l, i) from N_s aggregated
         interference samples using EM algorithm
        Update parameters of Local REM model
         g_u(x_l, i) with the use of eq. (5)
    end for
end for
Send sets of Local REM's models parameters g_u(x_l, i) from U platoons to Global
 REM
Update Global REM following the eq. (6)
```

the same time, they formulate a set of available secondary spectrum channels $\mathcal{I}$, for which we model the interference using the proposed algorithms. Choice of this frequency band (i.e. ISM band) is motivated by the fact that there are many devices of potentially various medium access control algorithms, and modulations transmitting therein. As a result, non-trivial interference distributions are expected to be observed, which makes the modeling process challenging. The set of platoon locations $\mathbf{x}_l$ together with the deployment of interfering access points is depicted in Fig. 5. We are considering a 1 km long fragment of the route, which is split into 30 equally spaced segments (platoon locations) $\mathbf{x}_l$. Moreover, there are in total 11 wireless access points deployed along the considered platoon route. They generate interference over 3 different radio channels that correspond to orange, purple, and yellow triangles, respectively.

Every time a platoon $u$ visit location $\mathbf{x}_l$, a batch of $N_\mathrm{s}$ new aggregated interference samples is calculated according to (3). We assume bandwidth $B = 10$ MHz, number of sub-channels $N_\mathrm{f} = 64$, and number of used sub-channels $|\mathcal{F}| = 48$ with spacing set to 156.3 kHz, as defined in the 802.11p specification [3]. To generate interference from the access point a four-state model of spectrum occupancy is used [19]. In this model idle state between acknowledgment message and transmission of new data, the block is modeled by an exponential distribution of traffic rate parameter $\lambda = 0.0054$ ms$^{-1}$. The remaining busy states including the transmission of data and acknowledgment message last jointly 0.81 ms under the assumption of 512-byte packet size. To compute the large-scale fading coefficient of the radio channel between an access point and a platoon, a two-slope model proper for vehicular communications is used [13]. The small-scale variations of the radio channel are generated using Rayleigh distribution, and power-delay profile proper for the scenario where the platoon route is crossing an urban area [17]. Finally, the Gaussian-distributed thermal noise of power proper for the temperature of 20° C is considered.

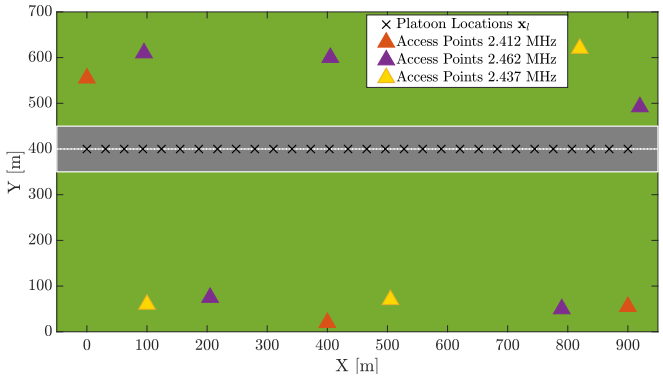


**Fig. 5.** Simulation scenario with platoon locations (black "x"), and access points locations (orange, purple, and yellow triangles respectively)

**Table 1.** Parameters of Simulation Scenario

| Parameter | Value |
|---|---|
| number of vehicles in a platoon $N_{\mathrm{u}}$ | 3 |
| platoon-leader to $N_{\mathrm{u}}$-th vehicle distance | 50 m |
| distance traveled by the platoon | 1 km |
| number of the platoon location | 30 |
| number of access points | 11 |
| secondary spectrum channels $\mathcal{I}$ | 2.412, 2.437, 2.462 GHz |
| secondary channel bandwidth $B$ | 10 MHz |
| transmitted power per sub-carrier $\mathrm{P_{tx}}$ | 3.19 dBm |
| desired capacity $C_{\mathrm{th}}$ | 3 Mbit/s |
| number of sub-channels $\mathrm{N_f}$ | 64 |
| number of usable sub-channels $\lvert\mathcal{F}\rvert$ | 48 |
| traffic rate parameter $\lambda$ | 0.0054 $\mathrm{ms}^{-1}$ |

The considered location can be simultaneously visited by the $U \geq 1$ platoons. In each platoon, the distance between the platoon-leader and the last $N_{\mathrm{u}}$-th vehicle is equal to 50 m. It corresponds to a 3-truck platoon. It is the minimum number of vehicles that are required to capture interference samples from all sets of three secondary spectrum channels $\mathcal{I}$. Transmitted power per subcarrier $\mathrm{P_{tx}}$ value is the maximum allowed in the 2.4 GHz band [16] and set to 3.19 dBm, including antenna gains. Finally, 3 Mbit/s is set to be the desired capacity $C_{\mathrm{th}}$. It is the lowest supported bitrate in 802.11p, claimed to be used for emergency messages [9].

The simulation parameters are summarized in Tab. 1.

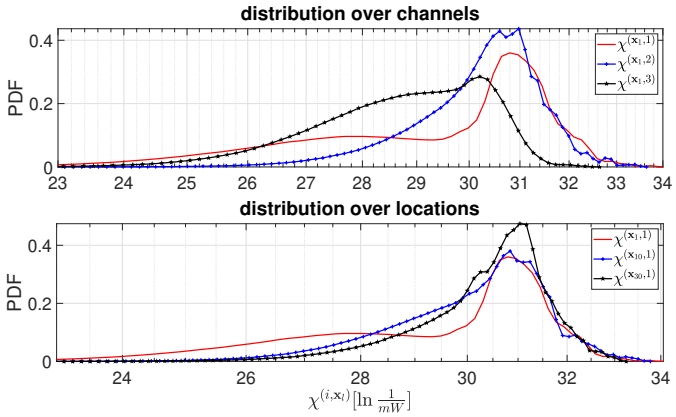


**Fig. 6.** Distribution of the aggregated interference $\chi^{(\mathbf{x}_l,i)}$ over different channels and platoon locations

## 5 Results

In this Section the evaluation of the algorithms proposed in Sec. 2, and Sec. 3 is performed using the simulation environment described in Sec. 4.

### 5.1 Baseline Model

At the first stage, we have analyzed an interference distribution $\chi^{(i,\mathbf{x}_l)}$ on the basis of large batch of captured samples, i.e., $M = 39321600$ IQ samples, that corresponds to the $N_\mathrm{s} = 614400$ samples of aggregated interference. This reflects a scenario where all data captured by the platoons were reported to REM, and once the statistically large number of samples has been collected, the proper GMM models can be computed. To prove our claim that interference can follow non-trivial, multi-modal distributions, there are representative examples of probability density functions related to $\chi^{(i,\mathbf{x}_l)}$ distributions depicted in Fig. 6. As it can bee observed, the distributions are complex, and they are varying over locations, and between channels. On the basis of these results, GMM models have been created for every secondary spectrum channel in each of the 30 platoon locations. They will serve as baseline models for evaluation of the proposed algorithms: SAIM, and based on REM and FL. Set of parameters of these GMM models are denoted as $g_\mathrm{B}(\mathbf{x}_l, i)$. In order to determine the number of components $J$ for the GMMs, we have built baseline models of $J \leq 15$ components on the basis of 90 data sets, i.e., 30 locations and 3 frequencies. The $g_\mathrm{B}(\mathbf{x}_l, i)$ models are evaluated in terms of their AIC. The average AIC is depicted in Fig. 7. It can be seen that after the number of GMM components is above $J = 7$ the AIC remains stable, and the observed AIC improvement is very small. Thus, we decided to fix this number, i.e., $J = 7$ in the following simulations. Clearly, in practice, the value of $J$ has to be adjusted to each situation, based on observed

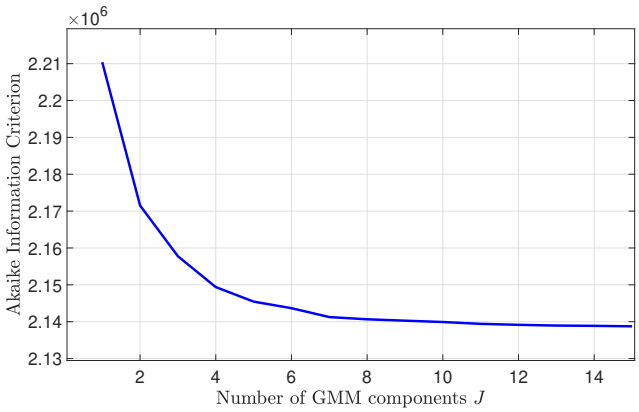


**Fig. 7.** Average AIC related to the GMM models of $J$ components. There are 90 training data sets considered.

and sensed interference sources, and based on the length of the considered road fragment.

### 5.2 Single Platoon Scenario

We first evaluate the accuracy of the proposed method of interference modeling in the scenario where the number of the platoons that simultaneously travel the considered route is set to one, i.e., $U = 1$. In this scenario, our main aim is to evaluate the algorithm of the Local REM update as described in Sec. 3.2. In one simulation run, the platoon travels the same route 25 times, i.e., Local REM is updated 25 times at each location $\mathbf{x}_l$. To smooth the results, up to 50 simulation runs are performed. There are two parameters to be evaluated: the number of captured aggregated interference samples $N_\mathrm{s}$, and the learning rate $N_{\mathrm{th},u}(\mathbf{x}_l, i)$ driven by the parameter $k$, as defined by (5). First, $k$ is arbitrary set to 5, and the impact of the number of captured aggregated interference samples $N_\mathrm{s}$ on the Local REM update is under consideration. The Root-Mean-Square-Error (RMSE) computed between the outage probability estimated with the use of updated Local REM and the baseline model is depicted in Fig. 8. It can be seen that after about 15 updates of Local REM, i.e., after the platoon traveled the considered route 15 times, all results tend to stabilize, and no further improvement of the RMSE could be observed. However, the level of stabilization depends on the number of captured aggregated interference samples $N_\mathrm{s}$. For the lowest $N_\mathrm{s} = 1024$ RMSE is approximately equal to 0.007, while for the $N_\mathrm{s} = 4096$ is about 0.0055, that is over 20% improvement with $N_\mathrm{s}$ increase. Obviously, it can be further improved by increasing $N_\mathrm{s}$, but the cost to be paid is less time for the intra-platoon communications. On the other hand, the initial analysis not presented here shows that decreasing the $N_\mathrm{s}$ leads to computational instability while estimating the set of GMM model parameters $\tilde{g}_u(\mathbf{x}_l, i)$.

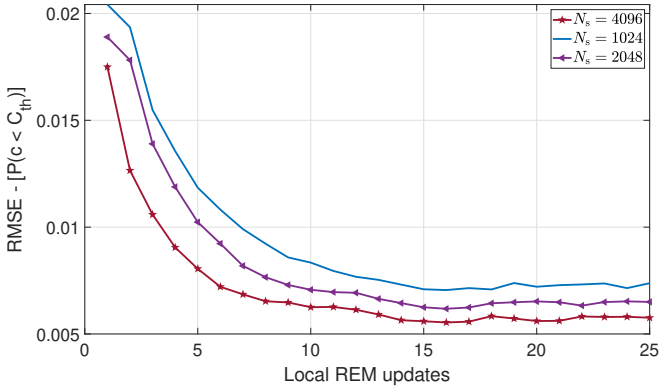


**Fig. 8.** RMSE computed between the outage probability estimated with the use of updated Local REM and the baseline model, for $k = 5$. Results are averaged over 50 simulations.

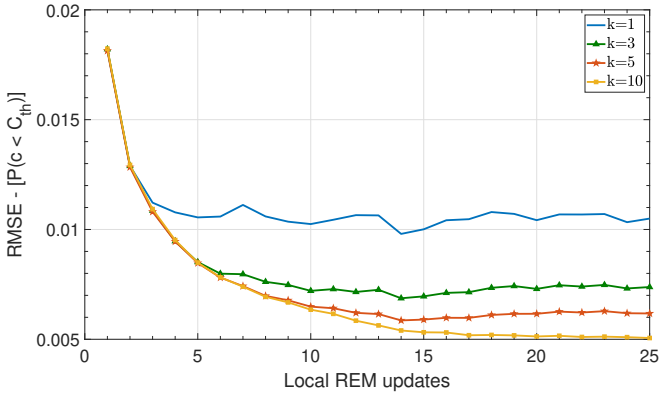


**Fig. 9.** RMSE computed between the outage probability estimated with the use of Local REM and the baseline model, for $k = 5$. Results are averaged over 50 simulations.

Later on, we have investigated the impact of the parameter $k$ defining the learning rate on the Local REM updates. This time the number of collected aggregated interference samples $N_s$ is set to the 4096. The related RMSE between the outage probability computed with the use of Local REM and baseline model, respectively, is depicted in Fig. 9.

It can be seen that the higher the parameter $k$, the better the RMSE. However, one should note that in the considered case interference being produced by each of the access points is a stationary random process. In the practical systems, it might not be true, thus it is reasonable not to choose very big $k$ allowing adaptation to the changing radio conditions, e.g., turn-off of an ac-

cess point. Moreover, it can be seen that when $k = 1$, results are unstable. It is because in this case newly computed GMM model possibly of low accuracy because of a limited number of samples $N_s$, has the same weight as the GMM model stored in Local REM. After the stabilization of the results, RMSE values obtained for $k = 10$ are approximately 5 times better than those for $k = 1$. The final conclusion is that $k$ should be large enough to provide stable results, but small enough to follow the radio environment changes.

### 5.3 Multiple Platoons Scenario

Having the algorithm of Local REM updates evaluated now is the time to move to the general case where $U \geq 1$ platoons can capture interference samples simultaneously at a given location $\mathbf{x}_l$, and participate in the process of improving the Global REM model, following the proposed FL-based approach. In this scenario, $U$ platoons travel through the set of locations 15 times. This procedure is repeated 50 times in order to average the results. Now, we set number of aggregated interference samples $N_s$ to 4096, and the $k$ parameter to 5. Our focus is put on the impact of the number of platoons $U$ on the Global REM improvement. Similar to the previous plots, the outage probability computed with the Global REM and baseline models are compared in terms of RMSE in Fig. 10. In addition, the plot contains a result that refers to the scenario where the interference model is computed independently at each platoon only on the basis of the currently captured $N_s$ samples, i.e., SAIM. The first observation is that benefits from the utilization of historical data in REM and FL are significantly compared to the SAIM scenario. In the case of a single platoon, $U = 1$ RMSE after many REM updates is about 3 times lower than RMSE obtained for SAIM which is not improving as a result of lack of memory in REM. Moreover, in the case of simultaneous Global REM updates by $U = 7$ platoons, a 4.5 fold reduction of the RMSE can be observed after 25 REM updates referring to the SAIM. Comparing the systems utilizing Global REM Updates, the biggest difference is between the single platoon scenario and the $U = 3$ platoon scenario, i.e., about 27% after 25 REM updates. While increasing further the number of simultaneously sensing platoons only a very little improvement can be observed, e.g., comparing between $U = 5$ and $U = 7$ the improvement is at the level of about 3%.

### 5.4 Channel Selection

It is important to take into account that the proposed algorithm of interference modeling realized with the use of a REM and FL is not the target itself. It is a tool to enable the selection of a proper secondary spectrum channel, as described in Sec. 2. On the basis of the interference models stored in REMs, platoons can decide which channels should be chosen along their route, e.g., on the basis of Dijkstra's algorithm, as discussed in [21]. In this paper, the simplest approach is evaluated, where a platoon chooses a wireless channel characterized by the lowest outage probability. In Fig. 11 there is an index of channel offering the

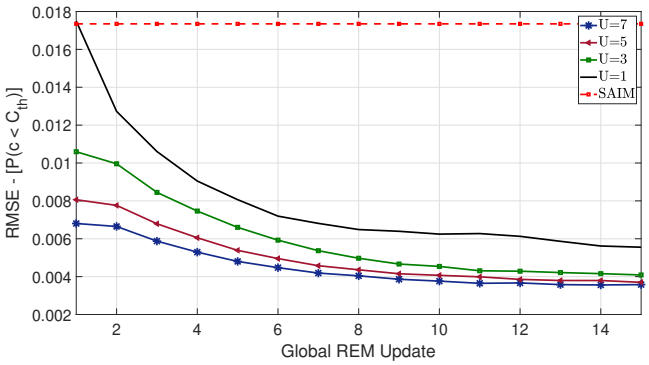


**Fig. 10.** RMSE computed between the outage probability estimated with the use of Global REM and the baseline model, for $N_s = 4096$, $k = 5$, and the varying number of platoons $U$. Additionally, the results of the SAIM scheme are included. Results are averaged over 50 simulations.

lowest outage probability in the consecutive platoon locations computed on the basis of the baseline model, the model utilizing REM (with Local and Global REM updates), and SAIM. We assume that the Global REM that is used is built from data captured by the $U = 7$ platoons during 15 route travels, and the considered parameters are: $N_s = 4096$, and $k = 5$. It can be seen that the channels marked as the best on the basis of the interference model from REM cover up with the ones computed using the baseline model in all cases, which is highly expected and proves the correctness of the proposed method. On the other hand, results based on SAIM correctly indicate the best radio channels only in 24 out of 30 platoon locations. It means that on the basis of only currently available interference samples the best secondary spectrum channel can be selected only in 80 % of cases. It is important to note that such a mistake can have a significant impact on the quality of wireless communications between vehicles formulating a platoon. This can further imply decreased fuel saves or platoon crash in extreme case.

## 6 Conclusion

In this paper, we proposed a two-layer architecture of REM, that together with FL and local spectrum sensing can be effectively used to provide platoons with an accurate model of interference. We have shown that the GMM accurately models the non-trivial distributions of interference in VDSA scenarios. Through the extensive computer simulations studies, we came to conclusion that historical data from REM can much improve the accuracy of interference models used by the platoon to predict radio channel occupancy in relation to the state-of-the-art SAIM approach. Moreover, it has been observed, that due to utilization of the

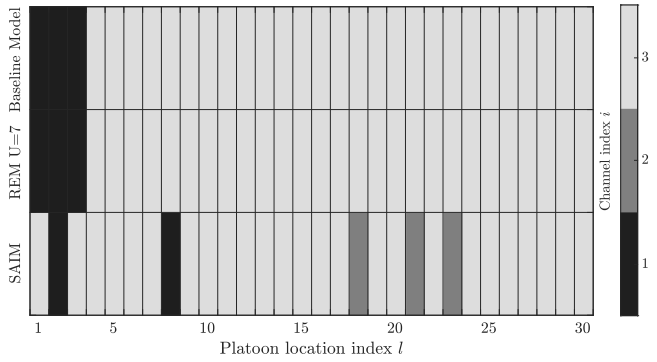


**Fig. 11.** Index $i$ of channel offering the lowest outage probability in the consecutive platoon locations $\mathbf{x}_l$ computed on the basis of baseline, Global REM, and *Spectrum Sensing* interference model.

FL multiple platoons can contribute to the improvement of Global REM interference models even more. Up to 4.5 fold reduction in channel capacity estimate RMSE was observed while comparing algorithm based on REM and FL against standard SAIM approach. It is important to notice that the proposed two-layer REM architecture have low requirements on the capacity of control channel. This is because only the GMM parameters are exchanged between the Local and the Global REM, instead of direct spectrum sensing results. Finally, equipping every platoon with Local REM ensures that channel capacity can be predicted even, when the side link to the Global REM is temporarily unavailable. What increases the system's reliability. In the future the measurement campaign can be conducted in order to verify the proposed algorithms in real-world scenario.

## References

1. 3GPP: LTE; 5G; Overall description of Radio Access Network (RAN) aspects for Vehicle-to-everything (V2X) based on LTE and NR. Technical Report (TR) 37.985, 3rd Generation Partnership Project (3GPP) (07 2020), version 16.0.0
2. Abboud, K., Omar, H.A., Zhuang, W.: Interworking of dsrc and cellular network technologies for v2x communications: A survey. IEEE Transactions on Vehicular Technology **65**(12), 9457–9470 (2016). https://doi.org/10.1109/TVT.2016.2591558
3. Abdelgader, A.M., Le-nan, W.: The Physical Layer of the IEEE 802.11p WAVE Communication Standard: The Specifications and Challenges (2014)
4. Abdulrahman, S., Tout, H., Ould-Slimane, H., Mourad, A., Talhi, C., Guizani, M.: A survey on federated learning: The journey from centralized to distributed on-site learning and beyond. IEEE Internet of Things Journal **8**(7), 5476–5497 (2021). https://doi.org/10.1109/JIOT.2020.3030072
5. Akaike, H.: A new look at the statistical model identification. IEEE Transactions on Automatic Control **19**(6), 716–723 (1974). https://doi.org/10.1109/TAC.1974.1100705

6. Bishop, C.M.: Pattern Recognition and Machine Learning (Information Science and Statistics). Springer-Verlag, Berlin, Heidelberg (2006)
7. Bonnet, C., Fritz, H.: Fuel consumption reduction in a platoon: Experimental results with two electronically coupled trucks at close spacing. In: Future Transportation Technology Conference & Exposition. SAE International (aug 2000). https://doi.org/https://doi.org/10.4271/2000-01-3056, https://doi.org/10.4271/2000-01-3056
8. Böhm, A., Jonsson, M., Uhlemann, E.: Performance comparison of a platooning application using the IEEE 802.11p MAC on the control channel and a centralized MAC on a service channel. In: 2013 IEEE 9th International Conference on Wireless and Mobile Computing, Networking and Communications (WiMob). pp. 545–552 (2013). https://doi.org/10.1109/WiMOB.2013.6673411
9. Campolo, C., Molinaro, A., Vinel, A., Zhang, Y.: Modeling Event-Driven Safety Messages Delivery in IEEE 802.11p/WAVE Vehicular Networks. IEEE Communications Letters **17**(12), 2392–2395 (2013). https://doi.org/10.1109/LCOMM.2013.102913.131863
10. Chan, E.: Overview of the SARTRE Platooning Project: Technology Leadership Brief. In: SAE Convergence 2012. SAE International (oct 2012). https://doi.org/https://doi.org/10.4271/2012-01-9019, https://doi.org/10.4271/2012-01-9019
11. Chen, C., Zhang, N., Shi, S., Mu, D.: An efficient method for incremental learning of gmm using cuda. In: 2012 International Conference on Computer Science and Service System. pp. 2141–2144 (2012). https://doi.org/10.1109/CSSS.2012.532
12. Chen, S.: Vehicular dynamic spectrum access: using cognitive radio for automobile networks. Ph.D. thesis, Worcester Polytechnic Institute (2012)
13. Cheng, L., Henty, B.E., Stancil, D.D., Bai, F., Mudalige, P.: Mobile vehicle-to-vehicle narrow-band channel measurement and characterization of the 5.9 ghz dedicated short range communication (dsrc) frequency band. IEEE Journal on Selected Areas in Communications **25**(8), 1501–1516 (2007). https://doi.org/10.1109/JSAC.2007.071002
14. de Oliveira Souza, F., Torres, L.A.B., Mozelli, L.A., Neto, A.A.: Stability and Formation Error of Homogeneous Vehicular Platoons With Communication Time Delays. IEEE Transactions on Intelligent Transportation Systems **21**(10), 4338–4349 (2020). https://doi.org/10.1109/TITS.2019.2939777
15. Dempster, A.P., Laird, N.M., Rubin, D.B.: Maximum Likelihood from Incomplete Data via the EM Algorithm. Journal of the Royal Statistical Society. Series B (Methodological) **39**(1), 1–38 (1977), http://www.jstor.org/stable/2984875
16. Edgard Vangeel: Wideband transmission systems; Data transmission equipment operating in the 2,4 GHz band; Harmonised Standard for access to radio spectrum HS Wideband transmission systems 2,4 GHz . Standard EN 300 328, ETSI, Sophia Antipolis Cedex, France (2019), https://www.etsi.org/deliver/etsi-en/300300-300399/300328/02.02.02-60/en-300328v020202p.pdf
17. ETSI: Intelligent Transport Systems (ITS); Access Layer; Part 1: Channel Models for the 5,9 GHz frequency band). TR 103 257-1 V1.1.1, European Telecommunications Standards Institute (May 2019)
18. Fernandes, P., Nunes, U.: Platooning with ivc-enabled autonomous vehicles: Strategies to mitigate communication delays, improve safety and traffic flow. IEEE Transactions on Intelligent Transportation Systems **13**(1), 91–106 (2012). https://doi.org/10.1109/TITS.2011.2179936

19. Geirhofer, S., Tong, L., Sadler, B.M.: A measurement-based model for dynamic spectrum access in wlan channels. In: MILCOM 2006 - 2006 IEEE Military Communications conference. pp. 1–7 (2006). https://doi.org/10.1109/MILCOM.2006.302405
20. Harounabadi, M., Soleymani, D.M., Bhadauria, S., Leyh, M., Roth-Mandutz, E.: V2x in 3gpp standardization: Nr sidelink in release-16 and beyond. IEEE Communications Standards Magazine **5**(1), 12–21 (2021). https://doi.org/10.1109/MCOMSTD.001.2000070
21. Hoffmann, M., Kryszkiewicz, P., Kliks, A.: Frequency selection for platoon communications in secondary spectrum using radio environment maps. IEEE Transactions on Intelligent Transportation Systems **23**(3), 2637–2650 (2022). https://doi.org/10.1109/TITS.2021.3136681
22. IEEE: Ieee standard for information technology– local and metropolitan area networks– specific requirements– part 11: Wireless lan medium access control (mac) and physical layer (phy) specifications amendment 6: Wireless access in vehicular environments. IEEE Std 802.11p-2010 (Amendment to IEEE Std 802.11-2007 as amended by IEEE Std 802.11k-2008, IEEE Std 802.11r-2008, IEEE Std 802.11y-2008, IEEE Std 802.11n-2009, and IEEE Std 802.11w-2009) pp. 1–51 (2010). https://doi.org/10.1109/IEEESTD.2010.5514475
23. Katagiri, K., Sato, K., Fujii, T.: Crowdsourcing-assisted radio environment database for v2v communication. Sensors **18**(4) (2018). https://doi.org/10.3390/s18041183, https://www.mdpi.com/1424-8220/18/4/1183
24. Kliks, A., Kryszkiewicz, P., Perez-Romero, J., Umbert, A., Casadevall, F.: Spectrum occupancy in big cities - comparative study - Measurement campaigns in Barcelona and Poznan. In: ISWCS 2013; The Tenth International Symposium on Wireless Communication Systems. pp. 1–5 (2013)
25. Kliks, A., Kryszkiewicz, P., Umbert, A., PéRez-Romero, J., Casadevall, F., Kulacz, L.: Application of radio environment maps for dynamic broadband access in tv bands in urban areas. IEEE Access **5**, 19842–19863 (2017). https://doi.org/10.1109/ACCESS.2017.2751138
26. Konečný, J., McMahan, H.B., Ramage, D., Richtárik, P.: Federated optimization: Distributed machine learning for on-device intelligence. CoRR **abs/1610.02527** (2016), http://arxiv.org/abs/1610.02527
27. Liang Yin, Jiayue Li, Sixing Yin, Shufang Li: Cognitive spectrum handoff game in the TV white space with radio environment map. In: 2012 IEEE 14th International Conference on Communication Technology. pp. 369–373 (2012). https://doi.org/10.1109/ICCT.2012.6511245
28. Liu, S., Yu, G., Chen, X., Bennis, M.: Joint user association and resource allocation for wireless hierarchical federated learning with iid and non-iid data. IEEE Transactions on Wireless Communications pp. 1–1 (2022). https://doi.org/10.1109/TWC.2022.3162595
29. Maiti, S., Winter, S., Kulik, L.: A conceptualization of vehicle platoons and platoon operations. Transportation Research Part C: Emerging Technologies **80**, 1–19 (2017). https://doi.org/https://doi.org/10.1016/j.trc.2017.04.005, https://www.sciencedirect.com/science/article/pii/S0968090X17301110
30. McMahan, H.B., Moore, E., Ramage, D., Hampson, S., Aguera y Arcas, B.: Communication-efficient learning of deep networks from decentralized data. In: Singh, A and Zhu, J (ed.) ARTIFICIAL INTELLIGENCE AND STATISTICS, VOL 54. Proceedings of Machine Learning Research, vol. 54, pp. 1273–1282. MICROTOME PUBLISHING, 31 GIBBS ST, BROOKLINE, MA 02446 USA (2017),

20th International Conference on Artificial Intelligence and Statistics (AISTATS), Fort Lauderdale, FL, APR 20-22, 2017
31. McMahan, H.B., Moore, E., Ramage, D., Hampson, S., y Arcas, B.A.: Communication-efficient learning of deep networks from decentralized data (2017)
32. Nilsson, M.G., Gustafson, C., Abbas, T., Tufvesson, F.: A Measurement-Based Multilink Shadowing Model for V2V Network Simulations of Highway Scenarios. IEEE Transactions on Vehicular Technology **66**(10), 8632–8643 (2017). https://doi.org/10.1109/TVT.2017.2709258
33. Qin, Y., Wang, H., Ran, B.: Stability analysis of connected and automated vehicles to reduce fuel consumption and emissions. Journal of Transportation Engineering, Part A: Systems **144**(11), 04018068 (2018). https://doi.org/10.1061/JTEPBS.0000196
34. Reddy G, R., R, R.: "An Empirical study on MAC layer in IEEE 802.11p/WAVE based Vehicular Ad hoc Networks". Procedia Computer Science **143**, 720 – 727 (2018). https://doi.org/https://doi.org/10.1016/j.procs.2018.10.443, `http://www.sciencedirect.com/science/article/pii/S1877050918321410`, 8th International Conference on Advances in Computing & Communications (ICACC-2018)
35. Reynolds, D.A.: Gaussian mixture models. Encyclopedia of biometrics **741**(659-663) (2009)
36. Robinson, T., Chan, E., Coelingh, E.: Operating platoons on public motorways: An introduction to the sartre platooning programme. In: 17th world congress on intelligent transport systems. vol. 1, p. 12 (2010)
37. Sroka, P., Kryszkiewicz, P., Kliks, A.: Radio Environment Maps for Dynamic Frequency Selection in V2X Communications. In: 2020 IEEE 91st Vehicular Technology Conference (VTC2020-Spring). pp. 1–6 (2020). https://doi.org/10.1109/VTC2020-Spring48590.2020.9128655
38. Sybis, M., Kryszkiewicz, P., Sroka, P.: On the context-aware, dynamic spectrum access for robust intraplatoon communications. Mobile Information Systems **2018** (2018). https://doi.org/10.1155/2018/3483298
39. Thunberg, J., Lyamin, N., Sjöberg, K., Vinel, A.: Vehicle-to-vehicle communications for platooning: Safety analysis. IEEE Networking Letters **1**(4), 168–172 (2019). https://doi.org/10.1109/LNET.2019.2929026
40. Tsugawa, S., Kato, S.: Energy its: another application of vehicular communications. IEEE Communications Magazine **48**(11), 120–126 (2010). https://doi.org/10.1109/MCOM.2010.5621978
41. van Arem, B., van Driel, C.J.G., Visser, R.: The Impact of Cooperative Adaptive Cruise Control on Traffic-Flow Characteristics. IEEE Transactions on Intelligent Transportation Systems **7**(4), 429–436 (2006)
42. van de Beek1, J., Lidström, E., Tao Cai, Yong Xie, Rakovic, V., Atanasovski, V., Gavrilovska, L., Riihijärvi, J., Mähönen, P., Dejonghe, A., Van Wesemael, P., Desmet, M.: REM-enabled opportunistic LTE in the TV band. In: 2012 IEEE International Symposium on Dynamic Spectrum Access Networks. pp. 272–273 (2012). https://doi.org/10.1109/DYSPAN.2012.6478140
43. Wang, P., Di, B., Zhang, H., Bian, K., Song, L.: Cellular V2X Communications in Unlicensed Spectrum: Harmonious Coexistence With VANET in 5G Systems. IEEE Transactions on Wireless Communications **17**(8), 5212–5224 (2018). https://doi.org/10.1109/TWC.2018.2839183
44. Wang, S., Tuor, T., Salonidis, T., Leung, K.K., Makaya, C., He, T., Chan, K.: Adaptive federated learning in resource constrained edge computing systems. IEEE Journal on Selected Areas in Communications **37**(6), 1205–1221 (2019). https://doi.org/10.1109/JSAC.2019.2904348

45. Xu, L., Wang, L.Y., Yin, G., Zhang, H.: Communication Information Structures and Contents for Enhanced Safety of Highway Vehicle Platoons. IEEE Transactions on Vehicular Technology **63**(9), 4206–4220 (2014)
46. Yang, Q., Liu, Y., Chen, T., Tong, Y.: Federated machine learning: Concept and applications. ACM TRANSACTIONS ON INTELLIGENT SYSTEMS AND TECHNOLOGY **10**(2) (FEB 2019). https://doi.org/10.1145/3298981
47. Yilmaz, H.B., Tugcu, T., Alagöz, F., Bayhan, S.: Radio environment map as enabler for practical cognitive radio networks. IEEE Communications Magazine **51**(12), 162–169 (2013). https://doi.org/10.1109/MCOM.2013.6685772
48. Zeng, T., Semiari, O., Saad, W., Bennis, M.: Joint communication and control for wireless autonomous vehicular platoon systems. IEEE Transactions on Communications **67**(11), 7907–7922 (2019). https://doi.org/10.1109/TCOMM.2019.2931583
49. Zhao, Q., Sadler, B.M.: A Survey of Dynamic Spectrum Access. IEEE Signal Processing Magazine **24**(3), 79–89 (2007). https://doi.org/10.1109/MSP.2007.361604

## 7.16 Publication [P16]

M. Hoffmann and P. Kryszkiewicz, "Radio Environment Map and Deep Q-Learning for 5G Dynamic Point Blanking," in *2022 International Conference on Software, Telecommunications and Computer Networks (SoftCOM)*, pp. 1–3, 2022.

MNiSW Points: 70

Number of citations:

- according to Web of Science: –
- according to Google Scholar: 4

mgr inż. Marcin Hoffmann
Instytut Radiokomunikacji, Politechnika Poznańska
ul. Polanka 3, 60-965 Poznań

Poznań, 2 luty 2023 r.

# OŚWIADCZENIE W SPRAWIE AUTORSTWA PRACY

Oświadczam, że w pracy:

*M. Hoffmann and P. Kryszkiewicz, "Radio Environment Map and Deep Q-Learning for 5G Dynamic Point Blanking," 2022 International Conference on Software, Telecommunications and Computer Networks (SoftCOM), Split, Croatia, 2022, pp. 1-3*

mój udział polegał na:

- Zaproponowaniu algorytmu bazującego na głębokim uczeniu ze wzmocnieniem, który na podstawie położeń użytkowników wygasza niektóre stacje bazowe, w celu zmniejszenia interferencji.
- Implementacji algorytmu i przeprowadzeniu eksperymentów symulacyjnych.
- Przygotowaniu pierwszej wersji tekstu artykułu

Mój procentowy udział w powstanie pracy szacuję na: 90%

Marcin Hoffmann

Podpis

dr hab. inż. Paweł Kryszkiewicz, prof. PP
Instytut Radiokomunikacji, Politechnika Poznańska
ul. Polanka 3, 60-965 Poznań

Poznań, 14 sierpnia 2025 r.

# OŚWIADCZENIE W SPRAWIE AUTORSTWA PRACY

Oświadczam, że w pracy:

*M. Hoffmann and P. Kryszkiewicz, "Radio Environment Map and Deep Q-Learning for 5G Dynamic Point Blanking," 2022 International Conference on Software, Telecommunications and Computer Networks (SoftCOM), Split, Croatia, 2022, pp. 1-3*

mój udział polegał na:

- Koordynacja prac badawczych
- Dyskusja z pierwszym autorem koncepcji badań.
- Analiza uzyskanych wyników i propozycja metod ich modyfikacji/poprawy
- Korekty artykułu: merytoryczne i językowe

Mój procentowy udział w powstanie pracy szacuję na: 10%

Podpis

# Radio Environment Map and Deep Q-Learning for 5G Dynamic Point Blanking

Marcin Hoffmann
*Institute of Radiocommunications*
*Poznań University of Technology*
Poznań, Poland
marcin.ro.hoffmann@doctorate.put.poznan.pl

Paweł Kryszkiewicz
*Institute of Radiocommunications*
*Poznań University of Technology*
Poznań, Poland
pawel.kryszkiewicz@put.poznan.pl

***Abstract*—Dynamic Point Blanking (DPB) is one of the Coordinated MultiPoint (CoMP) techniques, where some Base Stations (BSs) can be temporarily muted, e.g., to improve the cell-edge users throughput. In this paper, it is proposed to obtain the muting pattern that improves cell-edge users throughput with the use of a Deep Q-Learning. The Deep Q-Learning agent is trained on location-dependent data. Simulation studies have shown that the proposed solution improves cell-edge user throughput by about 20.6%.**

***Index Terms*—5G, Massive MIMO, Radio Environment Map, Dynamic Point Blanking, Deep Q-Learning**

## I. Introduction

The CoMP techniques are introduced for mobile networks in Release 11 of Long Term Evolution Advanced (LTE-A) [1]. The main idea behind the CoMP is that BSs cooperate, e.g., to improve the throughput of the cell edge users. Several CoMP techniques are investigated in the literature, e.g., Joint Transmission (JT) stands for simultaneous transmission to the User Equipments (UEs) from several BSs, or Dynamic Point Selection (DPS), where a UE is connected to a single BS but can be switched almost instantly to another BS [2]. On the other hand, the much less investigated CoMP scheme is a so-called Dynamic Point Blanking (DPB). The idea of DPB is to mute particular BSs in frequency and time, e.g., to reduce interference, and improve the cell-edge users throughput [3]. The challenge is to properly choose the muting pattern that is appropriate for given network conditions, e.g., the spatial distribution of users in a cell. This problem especially arises while considering the 5G Massive Multiple-Input Multiple-Output (M-MIMO) BSs in the Heterogeneous Network (HetNet). In such a network architecture inter-cell interference is much affected by the spatial channel correlations [4].

The state-of-the-art solutions proposed for muting pattern selection in DPB mostly rely on the instantaneous Channel State Information (CSI) proper for single antenna BSs [3]. This approach can be insufficient to model a realistic 5G M-MIMO HetNet consisting of several interacting functional blocks: precoder, user to BSs assignment, scheduler, and most importantly under a realistic, spatially-correlated radio channel.

The simulations were based on the QCM simulator from Huawei Technologies Sweden Research Center. The presented work has been funded by the Polish Ministry of Education and Science within the status activity task "Optimization of wireless network operation and compression of test data" in 2021, no. 0312/SBAD/8159.

The aim of this paper is to propose an intelligent DPB algorithm, that targets the improvement of the cell-edge users' throughput. The proposed solution is based on the location-dependent data being stored and processed in the so-called Radio Environment Map (REM) [5]. Instead of using instantaneous CSI, the historical information about the observed cell-edge users' throughput related to the given spatial distribution of users, and the muting pattern is stored in REM. In our previous works, we have utilized the REM to implement a so-called table-based Reinforcement Learning scheme [6]. In that approach, each spatial distribution of users, the muting pattern, and the resultant network performance metrics create a separate REM entry. However, while in a real network the number of possible user locations is large, the size of REM would rapidly grow. Thus in this work, we propose to train a so-called Deep Q-Network (DQN) [7]. The DQN still needs data from REM for the training purpose, but after the training phase, the DQN can potentially infer how to act under the unknown spatial distribution of users. The proposed solution based on DQN is validated within the realistic system-level simulator using an accurate 3D-Ray-Tracing radio channel model.

## II. Radio Environment Map and Deep Q-Learning

The diagram of the considered system is depicted in Fig. 1. It is assumed that the CoMP cluster covers a single HetNet cell consisting of one Macro BS (MBS) and several pico BSs (PBS). DPB process is centralized and managed by the MBS, which is not considered for muting to provide general coverage in a cell. Due to the assumption of ideal backhaul PBSs can be muted immediately. Just before muting a particular PBS, users connected to this PBS, are assigned to on of the active BSs, that provides the highest Received Signal Strength (RSS). The proposed algorithm aims to increase the cell-edge users' throughput (10th percentile from the distribution of user bitrates). To achieve this the MBS is extended with a dedicated REM module responsible for providing muting patterns proper for the currently observed spatial distribution of UEs. The REM consists of storage and the DQN model. During the learning phase, for each encountered spatial distribution of

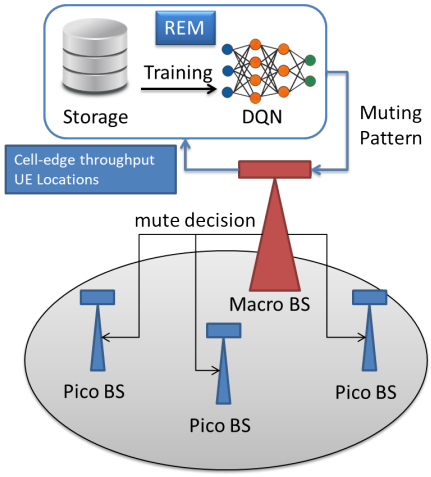


Fig. 1. Dynamic Point Blanking based on REM and DQN.

UEs, the REM tests all possible muting patterns and stores related cell-edge users' throughputs, i.e., an exhaustive search is performed. Later on, information from REM can be used to train a DQN. Training of DQN follows the standard RL scheme, where the agent observes the environment state, takes action, obtains a reward and the cycle repeats [8]. The only modifications in relation to the standard tabular RL methods are that DQN takes the state as an input and outputs approximated rewards for all possible actions. The difference between the real reward and DQN-approximated rewards is used to update the weights of DQN. In this paper the RL scheme components are defined as follows:

- **Environment** is the CoMP cluster in a single HetNet cell.
- **Agent** is a REM unit that chooses the muting pattern on the basis of users' location information. For this purpose Agent utilizes DQN. We assume that after the training phase agent acts greedy, i.e., takes action that will provide the best-approximated reward.
- **State** can be defined directly as a raw set of UE locations. However, under such an approach state recognition is challenging for the DQN, due to the varying number of UEs in the cell, and the shuffle of UE coordinates. To overcome these issues we propose to pre-process the localization data with the use of a K-Means clustering algorithm [9]. We split users into the number of clusters equal to the number of BSs in the considered HetNet cell. The algorithm starts with centers of clusters being set to the BSs' coordinates and outputs centers of clusters and the number of UE associated with each cluster. Flatten output of K-Means algorithm formulates state and is provided as an input to the DQN.
- **Action** is defined as the combination of active PBSs. There are $2^N$ possible actions, where $N$ is the number of PBSs in the CoMP cluster.
- **Reward** is the throughput of the cell-edge users, defined as a 10-th percentile from the distribution of user bitrates. The reward is equal to 0 for actions that result in disconnecting of any UE from the network. This prevents such actions to be selected.

## III. Simulation Results

The proposed DPB algorithm based on REM and DQN is validated through computer simulations. The deployment of BSs and a representative example of UE spatial distribution are depicted in Fig. 2. It is assumed that a HetNet is operating in a common frequency band of 300 MHz at a carrier frequency of 3.5 GHz. There is one MBS equipped with a 128-antenna array, and 5 PBSs equipped with 16-antenna arrays. The MBS and PBSs have a transmission power of 46 dBm, and 30 dBm, respectively. We have assumed a *full-buffer* traffic model, user to BSs association based on RSS, Regularized Zero-Forcing (RZF) precoder, and user scheduler aimed at providing proportional fairness. Radio channel coefficients are generated with the use of an accurate 3D-Ray-tracing model. More details on the simulation environment can be found in [10].

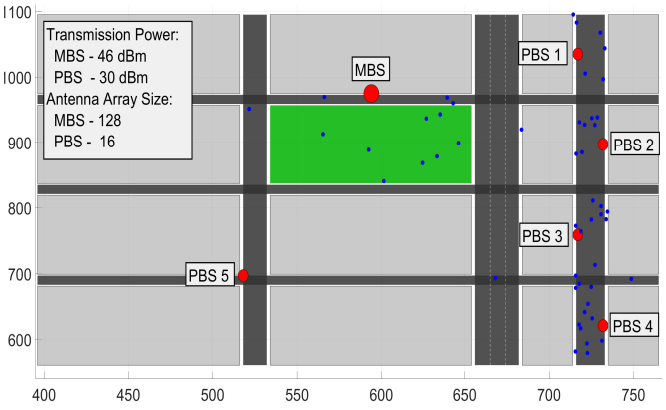


Fig. 2. Deployment of BSs (red dots), and representative example of UE spatial distribution (blue dots).

A total of 150 spatial distributions of UEs have been considered. Each exploits 50 UEs randomly distributed over the HetNet area (see Fig. 2). To provide REM with information about the cell-edge throughput related to all possible muting patterns, the simulation has been repeated 32 times under the same 150 UE spatial distributions. After that, the gathered data was used to train the DQN over 50000 epochs with a batch size of 8 samples. The DQN is designed arbitrarily to have four hidden layers of size 16, 64, 128, and 64, respectively.

Four algorithms have been evaluated. *No DPB* refers to the case where DPB is not applied. *Ref* stands for the DPB based on instantaneous CSI defined in [3]. *ES* refers to the utilization of an optimal muting pattern obtained on the basis of an exhaustive search. Finally, *DQN* refers to the DPB scheme based on the pre-trained DQN that is stored in REM, and used for inference of the muting pattern. In Fig. 3, there is a Cumulative Distribution function of cell-edge users throughput observed over 150 sets of randomly placed UEs for every algorithm. The observed states (UE locations) are the same, that were used during the training of DQN. It can be seen that

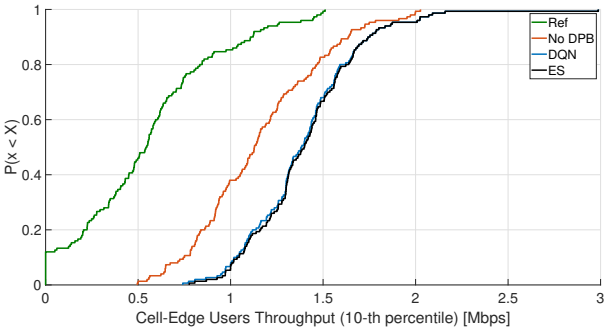


Fig. 3. The Cumulative Distribution function of cell-edge users throughput observed over 150 sets of randomly placed UEs.

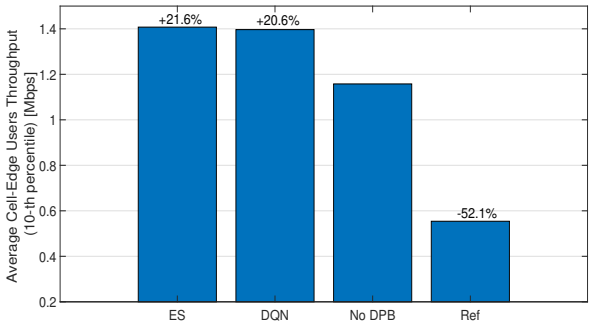


Fig. 4. Cell-edge users throughput averaged over 150 sets of randomly placed UEs.

*Ref* algorithm has the worst performance because the used CSI is not accurate enough in approximating user throughput in the M-MIMO network. On the other hand, it is clearly visible that the proposed *DQN* approach improved the cell-edge users throughput in every case. Moreover, the *DQN* performs almost as well as the optimal *ES* approach. Cell-edge throughput averaged over 150 sets of randomly placed UEs is presented in Fig. 4. The *Ref* algorithm due to its inability of accurate estimation of users throughput chooses the wrong muting patterns. This is why it causes about 52.1% degradation in cell-edge users throughput while comparing it against the *No DPB* algorithm. On the other hand, the utilization of *DQN* approach provides about 20.6% gain over the *No DPB* algorithm. It is because the *DQN* is trained on the historical data from the REM storage unit, that allows us to accurately infer the behavior of the system under various muting patterns. The *DQN* achieves on average about 99% of cell-edge users throughput gains obtained under a selection of the optimal muting patterns provided by the *ES* algorithm. Finally, in Fig. 5 there is presented a mean user throughput averaged over 150 sets of randomly placed UEs. It can be seen that in the case of a *DQN* algorithm the cell-edge user throughput gains, comes with a cost of only 5% degradation in mean user throughput while comparing to the scenario without DPB. On the other hand, the *Ref* algorithm decreases the mean user throughput by about 28%.

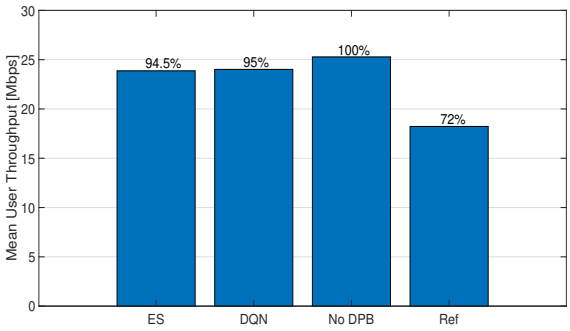


Fig. 5. Mean user throughput averaged over 150 sets of randomly placed UEs.

## IV. Conclusions

This paper shows that with the use of location-dependent information about cell-edge user throughput related to given muting patterns and UE spatial distributions stored in REM it is possible to effectively train and use DQN for the purpose of DPB. Simulations have shown that the proposed algorithm can improve the cell-edge users throughput by about 20.6% in relation to the algorithm without DPB. Moreover, the muting patterns selected by the DQN achieved 99% of the exhaustive search performance. In the future, more extensive training of DQN will be conducted considering, e.g., various UE mobility patterns, and different configurations of BSs' antenna arrays.

## References

[1] E. Dahlman, S. Parkvall, and J. Sköld, "Chapter 4 - LTE—An Overview," in *5G NR: the Next Generation Wireless Access Technology*, E. Dahlman, S. Parkvall, and J. Sköld, Eds. Academic Press, 2018, pp. 39–55. [Online]. Available: https://www.sciencedirect.com/science/article/pii/B9780128143230000041

[2] S. Bassoy, H. Farooq, M. A. Imran, and A. Imran, "Coordinated multi-point clustering schemes: A survey," *IEEE Communications Surveys Tutorials*, vol. 19, no. 2, pp. 743–764, 2017.

[3] H. Wang, X. Tao, and P. Zhang, "Adaptive Modulation for Dynamic Point Selection/Dynamic Point Blanking," *IEEE Communications Letters*, vol. 19, no. 3, pp. 343–346, 2015.

[4] L. Sanguinetti, E. Björnson, and J. Hoydis, "Toward Massive MIMO 2.0: Understanding Spatial Correlation, Interference Suppression, and Pilot Contamination," *IEEE Transactions on Communications*, vol. 68, no. 1, pp. 232–257, 2020.

[5] P. Tengkvist, G. P. Koudouridis, C. Qvarfordt, M. Dryjanski, and M. Cellier, "Multi-dimensional radio service maps for position-based self-organized networks," in *2017 IEEE 22nd International Workshop on Computer Aided Modeling and Design of Communication Links and Networks (CAMAD)*, 2017, pp. 1–6.

[6] M. Hoffmann and P. Kryszkiewicz, "Reinforcement learning for energy-efficient 5g massive mimo: Intelligent antenna switching," *IEEE Access*, vol. 9, pp. 130 329–130 339, 2021.

[7] V. Mnih, K. Kavukcuoglu, D. Silver, A. Graves, I. Antonoglou, D. Wierstra, and M. Riedmiller, "Playing Atari with Deep Reinforcement Learning," 2013.

[8] R. S. Sutton and A. G. Barto, *Reinforcement learning: An introduction*. MIT press, 2018.

[9] T. Kanungo, D. Mount, N. Netanyahu, C. Piatko, R. Silverman, and A. Wu, "An efficient k-means clustering algorithm: analysis and implementation," *IEEE Transactions on Pattern Analysis and Machine Intelligence*, vol. 24, no. 7, pp. 881–892, 2002.

[10] M. Hoffmann, P. Kryszkiewicz, and A. Kliks, "Increasing energy efficiency of massive-MIMO network via base stations switching using reinforcement learning and radio environment maps," *Computer Communications*, 2021. [Online]. Available: http://www.sciencedirect.com/science/article/pii/S0140366421000335